Report Title: Final Report for the ZERT Project: Basic Science of Retention Issues, Risk Assessment & Measurement, Monitoring and Verification for Geologic Sequestration

Type of Report: Final Scientific/Technical Report

Reporting Period Start Date: October 1, 2004

Reporting Period End Date: March 31, 2011

Principal Authors:
Lee Spangler, Principal Investigator (MSU)
Alfred Cunningham (MSU)
David Lageson (MSU)
Jesse Melick (MSU)
Mike Gardner (MSU)
Laura Dobeck (MSU)
Kevin Repasky (MSU)
Joseph Shaw (MSU)
Richard Bajura (WVU)
B. Peter. McGrail (PNNL)
Curtis M. Oldenburg (LBNL)
Jeff Wagoner (LLNL)
Rajesh Pawar (LANL)

Date Report was Issued: September 23, 2011

DOE Award Number: DE-FC26-04NT42262

Name and Address of Submitting Organizations:

Montana State University (MSU)
Energy Research Institute
P.O. Box 172465
Bozeman, MT 59717-2465

West Virginia University (WVU)
(subcontractor)
385 Evansdale Drive
Morgantown, WV 26506-6064

Lawrence Berkeley National Laboratory
(LBNL)
Earth Sciences Division 90-1116
1 Cyclotron Rd
Berkeley, CA 94720

Pacific Northwest National Laboratory
(PNNL)
3110 Port of Benton Blvd
MS K6-81
Richland, WA 99352

Lawrence Livermore National Laboratory
(LLNL)
P.O. Box 808
Livermore, CA 94551

Los Alamos National Laboratory (LANL)
Earth & Environmental Sciences Division
(EES-16)
Los Alamos National Laboratory, MS T003
Los Alamos, NM 87545

DISCLAIMER

ABSTRACT

ZERT has made major contributions to five main areas of sequestration science. Those areas, and major accomplishments within them, are listed below.

1. Improvement of computational tools
Major Accomplishments:

- Documented the design of the ECO_2N fluid property module to describe brine-CO_2 mixtures in TOUGH2, and demonstrated its application to problems of CO_2 storage
- Developed new correlations for phase partitioning in mixtures of brine and CO_2, and expanded the thermodynamic range of the TOUGH2/ECO_2N simulator
- Developed features for handling full range of CO_2 saturations (saturations from zero to one)
- Demonstrated a parallelized version of TOUGH2/ECO_2N to large-scale modeling of convectively enhanced CO_2 dissolution
- Parallel version of TOUGH2/ECO_2N was developed.
- Beta-version of TOUGH2 Hysteresis model completed.
- Improved TOUGHREACT reactive surface area algorithm for mineral-water reactions, and fugacity coefficient corrections for gas-water reactions
- Improved coupling of changes in rock and fluid properties
- EOS7C testing and documentation completed.
- Developed equation of state (GasEOS) for TOUGH2 gas mixture properties as a readily accessible stand-alone web application
- Parallelization of NETL's flow through fractured media code NFFLOW Run times reduced by a factor of 10 - Plan to simulate leaky cap rocks in FY2010
- A computational model was developed for coal-bed deformation with CO_2 injection within multiphase, multi-component flows coupled with adsorption/desorption and structural deformation.
- Computational models were developed for designing the layout of injection and collection wells for storage of carbon dioxide in coal seams while simultaneously gathering and producing methane from the seam.
- Added coupled flow-stress modeling capability to FEHM for CO_2 sequestration: FEHM had the capability to perform coupled fluid flow and stress simulations as well as coupled fluid flow and reaction simulations. We have extended the coupled flow and stress modeling capability in FEHM for CO_2 problems. While this capability is limited to linear elastic mechanical model for porous media, we will be extending it to non-linear elastic and plastic deformation regimes as part of this year's effort. We expect this capability to be used as part of the Southwest Regional Partnership project and potentially Big Sky Regional Partnership project.
- We have developed a novel approach in FEHM to incorporate wellbores and details of well completions (such as casing, cement, etc.) in large reservoir models. Our approach provides a user the flexibility to incorporate multiple wells in complex numerical meshes on the fly, without a need for regridding. The approach also results in computationally efficient numerical models that takes significantly less computational time compared to the traditional approach of local grid refinement. Finally, the approach captures the dynamics

of near wellbore conditions (pressure, saturation) much better compared to the traditional approaches. The final condition is critical for understanding and effectively characterizing release of CO_2 through wellbores.

2. Measurement and monitoring techniques to verify storage and track migration of CO_2

Major Accomplishments:

- Developed a first in the world facility to determine efficacy and detection limits for near surface detection that is now being copied in other countries.
- Accumulation chamber measurements were used to map the spatio-temporal evolution of surface CO_2 flux leakage signals associated with controlled subsurface CO_2 releases and quantify total leakage rate. Results were published.
- Net CO_2 surface fluxes were measured by an eddy covariance station during controlled CO_2 releases, background ecosystem fluxes were modeled and removed from total fluxes to enhance leakage signal detection, and least squares inversions of CO_2 fluxes and modeled footprint functions were conducted to map the surface CO_2 flux leakage signal and quantify leakage rate. Results were published.
- Miniature infrared gas analyzers continuously measured soil CO_2 concentrations and characterized the temporal evolution of shallow subsurface leakage signals during controlled CO_2 releases.
- Seepage characterization optimization approach for eddy covariance and other surface monitoring methods was developed and published.
- Used TOUGH2 simulations and Bayesian Belief Networks to design sequestration monitoring systems.
- Installed 32 tilt meters around a coal bed sequestration site and obtained baseline data before injection
- Last year we investigated modeling of time-lapse elastic wave scattering and attenuation. This technique has great potential to improve the resolution of seismic data interpretation as well as characterization of reservoir heterogeneities at different scales including those relevant to precipitation, dissolution processes and fluid saturation and transport properties.
- We explored the use of hyperspectral reflectance data to measure plant stress responses of indigenous vegetation to elevated soil CO_2 concentrations. In FY2010, we will analyze these data in the context of investigating the ability of the Japanese IBUKI (aka GOSAT) satellite to detect CO_2 releases.
- We also tested the capabilities of a new instrument for continuous CO_2 concentration and 13C/12C (δ13C) analysis offered by Los Gatos Research's (LGR's) Carbon Dioxide Isotope Analyzer (cavity ringdown laser spectrometer; CRDLS).
- Developed and deployed an underground, fiber optic and diode laser based method to measure soil gas. The instrument used a single section of hollow core fiber for measuring the CO_2 concentration. We are beginning to extend the capabilities by using multiple hollow core sections in multiple fibers to allow a single laser and receiver to be used to measure a large area.
- Provided a test site for R&D 100 winning tracer technology

3. Development of a comprehensive performance and risk assessment framework.
Major Accomplishments:

- We have performed a study at an analogue site focussed on understanding and characterizing risks associated with CO_2 leakage in groundwater, especially, shallow aquifers used for potable water supply. We are utilizing a natural analog at Chimayo, NM, where CO_2 from deep subsurface is migrating to shallow aquifer and is affecting the local groundwater chemistry. We are utilizing an integrated approach combining field observations, laboratory experiments and numerical modeling to characterize CO_2 leakage processes, its migration into shallow aquifers and resulting geochemical processes. We are using the analog site to characterize the risks to shallow groundwater chemistry including potential for heavy metal release and migration.
- We have made initial developments of a first-ever system modeling framework to predict long-term performance of geologic CO_2 storage sites. This framework (CO_2-PENS) and its associated system level model will be applied as part of the risk assessment for the Phase III demonstration projects within Southwest and Big-Sky regional partnerships.
- We began work on modeling and analysis of applications to CCS of risk assessment techniques from other analogous industries. We are continuing to examine risk profiling and assessment techniques for other types of long-term geologic storage projects that have some similarities with CCS. This includes analysis of tools used in other industries or applications, including the oil and gas production, nuclear waste repositories and natural gas storage.
- We have begun a test case study of predictive modeling capabilities for CO_2 leakage by history matching documented gas leaks through abandoned wells and faults in oil and gas fields in the Los Angeles Basin.

4. Fundamental geophysical, geochemical and hydrological investigations of CO_2 storage
Major Accomplishments:

- Imaged CO_2 in brine during CO_2 core flood at reservoir P, T conditions
- Laboratory facility developed for CT scanning of high-P,T flow-through experiments.
- High-resolution numerical simulations with TOUGH2 were carried out to interpret and extend the experimental results.
- We are applying the coupled flow-stress modeling capability in FEHM to understand and characterize the geomechanical response of large-scale CO_2 injection. We are investigating both near-wellbore and as well as far field geomechanical changes. We are developing models for changes in fault permeability due to large-scale stress changes.
- We have developed a core flood / flow testing system with *in situ* pH and conductivity probes.
- We have developed a basin scale model based on data from 30,000 wells that identifies five reservoir classes with varying depositional systems and rock mineralogy. Lithofacies classification at the tertiary level within formations results in a capture of heterogeneities with tens of meters of vertical resolution. Petrophysical properties from 3000 well logs are being added to allow multiphase flow modeling studies. To our knowledge, this is the highest resolution basin scale geostatic model constructed to date.

5. Investigate innovative, bio-based mitigation strategies

Major Accomplishments:

- Using this system our research team demonstrated that *Bacillus mojavensis* biofilms can reduce the permeability of rock cores by over two orders of magnitude (47 milidarcies down to 4 milidarcies). When challenged by $ScCO_2$ the permeability of the biofilm cores was raised by approximately 4% (Mitchell et al. 2009).
- We also showed in a separate study (Mitchell et al. 2008a) that microbial cells growing as biofilms were substantially more resistant to killing by $ScCO_2$ than the same cells in suspension (suspended cell cultures revealed a $3\log_{10}$ reduction while biofilm cultures showed a $1\log_{10}$ reduction in viable cell numbers).
- The investigation has evolved toward developing engineered biofilms which are capable of precipitating mineral deposits (i.e. calcium carbonate) within the biofilm matrix (Cunningham et. al., 2008 and Mitchell et al. 2008b). Biofilm communities in the subsurface are able to actively precipitate calcium carbonate minerals from the ambient Ca^{2+} and HCO_3^- in the subsurface water. However, by stimulating native subsurface microbial communities, or by adding specific microorganisms and growth media, we can engineer the biomineralization process in beneficial ways. Using ureolytic biomineralization, together with process engineering concepts, our study team has demonstrated "complete plugging" of porous media flow reactors ranging in size from 0.5mm glass beads to 1mm etched flow channels.
- Our research program has also discovered that ureolytic biomineralization is capable of sequestering anthropogenic CO_2 from the gas phase into the mineral phase as $CaCO_3$-- thereby facilitating a method for enhanced mineral-trapping of injected CO_2 in the subsurface as well as from waste streams above ground.
- We have found that ureolytic biomineralization enhances the capacity of the brine for $CO_2(g)$ and dissolved carbonate ions, thus increasing the solubility-trapping capabilities. These findings are reported in Mitchell et. al, submitted to *Environmental Science and Technology*, and Mitchell et. al, 2008b.
- Our research team has an ongoing collaboration with Dr. Rainer Helmig and Dr. Anozie Ebigbo of the Department of Hydromechanics and Modeling of Hydrosystems, University of Stuttgart, Germany. As a result of this collaboration a multiphase simulation model has been developed (Ebigbo et. al, Submitted to *Advances in Water Resources*) which is capable of simulating the growth of biofilm barriers in the deep subsurface, and the effects of these barriers on the migration of injected CO_2 plumes.

TABLE OF CONTENTS

EXECUTIVE SUMMARY

Overview

The Zero Emissions Research and Technology (ZERT) collaborative was formed to address basic science and engineering knowledge gaps relevant to geologic carbon sequestration. Many of the research activities fall between areas normally funded by different directorates at DOE and might be considered too applied for the basic science directorate and too basic in nature for other directorates. An executive committee comprised of institutional leads (and leaders in the field of carbon sequestration) met annually and talked via a monthly scheduled conference call to identify research gaps and research strengths among the ZERT institutions. The executive committee established the following major objectives:

- Improve computational tools for simulation of CO_2 behavior in the subsurface. This includes adding reactive transport, development of coupled models to include geomechanics, inclusion of hysteretic effects, parallelization, etc.
- Test efficacy of near-surface detection techniques, help establish detection limits for those techniques, and provide data to assist in development of transport models in the near-surface region. Development of a field site to help accomplish this objective.
- Develop a comprehensive risk assessment framework that will allow flexible coupling of multiple computational models for different components/processes of the system.
- Perform gap analysis to determine critical missing data for CO_2 properties in the subsurface including thermodynamic properties of CO_2 – brine mixtures, reaction rates, relative permeabilities, etc. In addition, perform laboratory based experiments to generate that key data.
- Investigate innovative leakage mitigation strategies

Many of these efforts were multi-institutional. Computational code improvement was undertaken by LBNL, LLANL, PNNL, and NETL, all ZERT institutions participated in the near-surface detection experiments, the systems level risk modeling was lead by LANL, but built to incorporate process level models developed by other ZERT institutions and utilizes information from ZERT investigations of natural analogs for escape mechanisms, and all institutions measured properties of CO_2 – brine and/or rock interactions.

Mitigation Methods

This research project, which is aimed at developing a microbially-assisted biomineralization process into an innovative technology for carbon dioxide (CO_2) leakage mitigation in geologic sequestration systems, has been accomplished in two phases. During Phase I, a high pressure biofilm and supercritical CO_2 testing apparatus was constructed to test the efficacy of growing microbial biofilms in rock cores under high pressure (8.9 MPa), moderate temperature (32 °C). These experiments showed that biofilm growth resulted in a two-order of magnitude reduction in initial rock permeability (47 milidarcies to 0.4 milidarcies) over a 200 hour period. Subsequent challenges using supercritical CO_2 resulted in a slight (1.5%) increase in permeability. Starvation of the biofilm for over 300 hours had no effect on the permeability of the biofilm-rock matrix

Phase II involved the use of microbial biofilms which are capable of ureolytic biomineralization to reduce permeability in porous media. This process first produces biofilm throughout the porous media matrix then, when calcium and urea are added, precipitation of calcium carbonate results thereby plugging free pore space with mineral precipitation. It was also observed that ureolytic biomineralization also modifies the geochemistry of brines to enhance CO_2 solubility and mineral precipitation. Experimental results obtained from this ZERT (Zero Emissions Research and Technology) task demonstrate that engineered biomineralization has the potential to become a viable technology for sealing unwanted CO_2 migration pathways through porous media. Because the fluids used to initiate biofilm formation and biomineralization are low viscosity aqueous solutions, this technology has the potential to seal small aperture leaks or the porous rock itself potentially providing a leakage mitigation technique that can address issues problematic for cement use.

Near Surface Detection Efficacy

ERT developed a facility on the Montana State University (MSU) campus in Bozeman, Montana capable of delivering a controlled release of CO_2 into the shallow subsurface. Known flux rates and the ability to start and stop flow to measure onset and recovery response times provide a test site which can be used to determine efficacy and detection limits of various near surface monitoring techniques as well as study the transport of CO_2. The field site was characterized before injection began. Modeling using site specific soil properties as input was extremely useful for designing monitoring strategies. Nine injections were performed over the summers of 2007-2010 with CO_2 flow rates ranging from 0.1 to 0.3 metric ton CO_2 /day. Researchers from six national labs, six universities, five companies, the United States Geological Survey, and the Electrical Power Research Institute have used more than 20 techniques to investigate CO_2 movement through soil, water, plants, and the atmosphere at the site. Even at relatively low flow rates, most techniques were able to detect levels of CO_2 in the soil, atmosphere, or water elevated above the natural background. Results from the ZERT experiments will help inform decisions about monitoring large scale carbon sequestration projects.

The ZERT project funded research at Lawrence Berkeley National Laboratory (LBNL) in three principal areas related to geologic carbon sequestration: (1) Performance prediction (model development and applications); (2) Measurement and monitoring; and (3) Fundamental laboratory investigations. LBNL significantly advanced the state of modeling and simulation through its development of ECO_2N, hysteretic capillary pressure and relative permeability functions, TOUGHREACT, and WebGasEOS. In the field of monitoring, LBNL demonstrated the utility of accumulation chamber and eddy covariance monitoring for CO_2 leakage studies including innovative data analysis and footprint modeling approaches, provided essential field support and model predictions and analysis of results for the ZERT shallow-release experiment, and developed theoretical modeling and analysis approaches for enhancing leakage detection. As for the laboratory studies, LBNL developed, built, and tested a core flood and imaging apparatus that was then used to study CO_2 and brine invasion processes in a natural rock core. These studies were augmented by pore-scale studies combining imaging and modeling of pore-scale two-phase invasion. These two approaches combined revealed the importance of heterogeneity in controlling invasion, and by inference CO_2 residual-phase trapping.

This research effort utilized existing Lawrence Livermore National Laboratory (LLNL) capabilities and relationships with the University of California, specifically UC Santa Cruz (UCSC). The specific tasks in this project created products that support and underscore the research of other organizations working with ZERT and NETL on carbon sequestration science. There were three overarching objectives to LLNL's role within ZERT: (1) reduce the uncertainty involved in subsurface storage; (2) improve characterization of risk elements, specifically assessment and monitoring of leakage; and (3) identify strategies to reduce risk elements.

Work under the ZERT I program at Pacific Northwest National laboratory (PNNL) has focused on basic and applied research related to long term geologic storage of carbon dioxide (CO_2). By combining advancements in modeling to include kinetic dissolution processes, coupled heat transport for nonisothermal environments, geochemical reactive transport, transition from sub-critical to supercritical as related to near surface processes, and boundary-fitted orthogonal grid systems, an entirely new generation of scalable computing capabilities was developed. As a result, subsurface science related to regional partnership pilot studies, industrial CCS projects, and the FutureGen project is being modeled by the coupled HTC-process simulator STOMP-CO_2 developed under this program. Equally important is the availability of thermodynamic data used to calculate critical parameters (mineral and gas solubility reactions, aqueous speciation, oxidation/reduction) necessary for modeling calculations in these computer codes. For the first time, a report was generated (Krupa et al., 2010) describing availability of thermodynamic data for aqueous and solid carbonates. Advancements in reaction mechanisms between rocks and $scCO_2$ with co-existing compounds (e.g. SO_2) were accomplished through laboratory based studies and molecular dynamic simulations. Communicated through a series of publications and presentations, chemical reactivity of water dissolved into $scCO_2$ was found to be significant when in contact with metals and minerals. Using molecular dynamics simulations, these reactions proceed through spontaneous activation and decomposition of CO_2 on the metal surface rather than formation of carbonic acid. Efforts associated with field studies resulted in the development of an enhanced soil gas flux CO_2 detection system deployed in Bozeman during 2008. Data collected over several years yielded highly heterogeneous flux patterns depending on the wind and groundwater movement. Finally, numerical modeling of caprock leakage was enhanced by correlating barometric pressure fluctuation to subsurface conditions. Through a combination of these research efforts, PNNL contributions significantly enhanced fundamental concepts related to monitoring technologies, reservoir modeling, leakage mitigation as well as advancing basic models linked to chemistry and hydrodynamic properties in $scCO_2$-brine mixtures.

The successful completion of NETL's efforts at the ZERT I facility in Bozeman Montana demonstrated the feasibility of using remote sensing for the ultra low level detection of atmospheric plumes of perfluorocarbon (PFC) tracers as means to monitor the near-surface leakage of sequestered CO_2. It is desirable to develop techniques that can monitor a large area and detect CO_2 leaks that may be very limited in magnitude and spatial extent. This problem is particularly challenging because CO_2 baseline levels are large and variable. Characterization of the tracer plume in the atmosphere is considered a "proof of concept" step to verify that tracer detection by remotely sampling with unmanned aerial systems (UAS) or at permanent tower installations is feasible under the leakage scenario simulated by the ZERT experiments.

Resistivity and electromagnetic induction surveys conducted as part of the study provided valuable near-surface geology/hydrology information pertinent to understanding potential near-surface migration pathways and in detecting soil changes indicative of CO_2 transport.

Pre-tracer injection surveys at the ZERT I Marshall County WV coal-bed methane injection facility identified light hydrocarbon anomalies (from both soil-gas and mobile atmospheric surveys) and other potential migration pathways for near-surface release (such as fault zones from lineament analysis). Based upon this information, a soil-gas monitoring grid was established and background surveys were taken. Additional objectives included monitoring for tracer in water wells and water well headspace, and monitoring of tracers in the produced gas from monitoring wells for application to reservoir modeling where breakthrough of CO_2 may be impossible to distinguish from CO_2 already present in the produced gas.

Near Surface Detection Efficacy: Technology Development

The research efforts have led to the development of instrumentation and techniques for near surface monitoring of carbon sequestration sites. The initial research effort was focused on the development of a free space above ground integrated path measurement of carbon dioxide (CO_2) concentration based on a tunable distributed feedback laser (DFB) with a center wavelength of 2.004 μm. This instrument was successfully deployed for two summer field experiments with daily average CO_2 concentrations measured the first year and continuous time CO_2 concentration measurements made the second year. Based on the experience gained with this initial instrument, a first generation sub-surface detector was developed utilizing the DFB laser with the light delivered to the absorption cell via an optical fiber. This instrument was successfully deployed for two summer release experiments. Work with the underground fiber sensor has lead to further funding through the Department of Energy and commercialization of the fiber sensor is underway through a Phase I Small Business Innovative Research (SBIR) project funded through the Environmental Protection Agency. Recognizing the need to monitor the large areas associated with geologic carbon sequestration sites, a differential absorption lidar (DIAL) was modeled as part of a feasibility study. The model of the DIAL performance was completed and a design for a DIAL instrument for spatially mapping CO_2 concentrations was completed. This work led to a separate funded project sponsored by the Department of Energy and work to commercialize the DIAL instrument is underway through the preparation of a Phase I SBIR proposal. Finally, a passive optical sensing technique based on random forest classification analysis was developed using a ground based hyperspectral imaging system. The success of this project led to follow on funding by the Montana Board of Research and Commercialization Technology (MBRCT). Commercialization of flight based hyperspectral imaging for large area monitoring of carbon sequestration sites is underway with a successful Phase I Small Business Technology Transfer Program (STTR) project and a funded Phase II STTR project by the Department of Energy.

Experiments have been conducted to demonstrate the feasibility of detecting CO_2 leaking from underground through observation of resulting changes in the reflectance spectrum of overlying vegetation. These observations were made with a multi-spectral imager that observes simultaneous images in a green, red and near-infrared spectral band. This imager was mounted

on a 3-m-tall scaffold to view a vegetation test region during controlled CO_2 release experiments at the ZERT site in Bozeman, Montana in the summers of 2007, 2008, and 2009. Absolutely calibrated images were processed to produce time series of reflectance for three different regions within the vegetation test area. Region 1 covered and extended 1.5 m (1.64 yards) beyond the buried CO_2 release pipe, region 2 was an intermediate region from approximately 1.5 to 3 m (1.64 to 3.28 yards) beyond the release pipe, and region 3 extended from approximately 3 to 5 m (3.28 to 5.47 yards) beyond the buried release pipe. Statistical analysis of the reflectance time-series plots showed that there were statistically significant differences in the "near," "middle," and "far" regions. The correlation was most reproducible and reliable for a data product called the "Normalized Difference Vegetation Index," calculated as the difference of near-infrared and red reflectance divided by the sum of these two bands. Data from the later experiments showed that the net effect of leaking CO_2 depends on the relationship between gas sink-source balance and vegetation density. Also, a consistently calibrated imager was able to see the effects of water and hail on the vegetation. Using best-practices calibration methods, it has been shown that this simple multi-spectral imager can be operated continuously through the day without experiencing difficulty from variable clouds or solar illumination angles and conditions. This system's easy setup, automation, all-day imaging capability, and low cost make it a very practical tool for plant stress measurements for the purpose of detecting leaking CO_2.

Risk Assessment: Natural analogs for Escape Mechanisms

Subsurface sequestration of anthropogenic carbon dioxide derived from coal-fired power plants is one of several environmental strategies needed to offset the rate of global warming. In this regard, understanding the geologic variables that contribute to long-term confinement of CO_2 in deep subsurface traps is a critically important research topic. One strategy used to understand these variables is to conduct research on subsurface accumulations of naturally occurring CO_2 in areas where confinement has occurred for millions of years. Southeast Idaho and Western Wyoming are ideally suited for a study of these confinement variables, given the following: well-documented accumulations of CO_2 in faulted anticlines within the Absaroka thrust sheet (Butler 1982) and up-dip exposures of reservoir and seal/cap rocks (and analogous structural traps) in the Salt River Range, Snake River Range, and Big Hole Mountains. Therefore, the major goals of this project were aimed at addressing the following questions: (1) what are the mesoscopic and microscopic attributes of these CO_2-bearing reservoir units, (2) which faults and fracture systems were the dominant "carriers" of CO_2, and (3) what are the characteristics of seal/caprock units that prevented CO_2 migration to the surface? Field work conducted in the Absaroka thrust sheet has shown that key reservoir formations (e.g., Triassic/Jurassic Nugget Sandstone, Jurassic Twin Creek Limestone, and Paleozoic carbonate formations) are pervasively fractured; these fracture sets include (1) hingeline-parallel (with respect to regional folding) and bedding-perpendicular fractures, (2) hingeline- and bedding-perpendicular fractures, and (3) conjugate shear fractures. The first two fracture sets are syntectonic open joints that played an important role in flushing the reservoir formations with large volumes of CO_2 + brine ± hydrocarbons; conjugate shear fractures formed early and were significantly "tighter" with respect to fluid transport. Major faults, including the Absaroka thrust and some imbricate faults in its hanging wall, also served as major conduits for fluid migration in an up-dip direction (regionally from west-to-east). The damage zone of the Absaroka thrust extends for tens of

meters into the hanging wall and is completely cemented with coarse, milky calcite, and dolomite from CO_2-saturated formation fluids; smaller imbricate thrust faults are similarly cemented and many thrust panels are so pervasively fractured/shattered and cemented, that one must conclude there was a huge volume of over-pressured, CO_2-rich brine moving through the system. At the reservoir scale, it appears that the Absaroka thrust sheet was a mega-cataclastite, being thoroughly fractured and flushed with fluids from down-dip sources, including CO_2-rich brines. A surprising discovery of this research is the realization that much of the subsurface fluid flow occurred via hydrothermal dynamic processes, including significant in situ brecciation; indeed, modern occurrences of CO_2 in SW Idaho may be classified by hydrothermal reservoirs. Seal/cap rocks that prevent CO_2 from leaking to the surface today in SE Idaho include the Jurassic Preuss Formation (red shale and sandy siltstone), and thick lower Cretaceous shale of the Bear River and Aspen Formations. Deeper shale units may have compartmentalized fluid flow laterally through the allochthon, such as the Triassic Dinwoody-Woodside, and also served to retard overall up-section fluid leakage to higher stratigraphic levels.

Los Alamos National Laboratory's (LANL) activities for the ZERT have fallen into three broad research areas:

- How do you reduce uncertainty in assuring prior to operation that an engineered geologic site will meet a specific performance goal (*e.g.*, <0.01% leak per year)?
- What are key monitoring needs for verifying that an engineered geologic site is meeting a performance goal?
- What are potential vulnerabilities for breeches in containment of CO_2, and how could they be mitigated either prior to operation or in the event that a threshold is exceeded?

We have utilized LANL's multi-disciplinary expertise and an integrated approach combining laboratory experiments, field observations and numerical simulations to address various research issues related to above-mentioned areas. While there have been a number of major milestones achieved as described in past quarterly reports, two of the major accomplishments resulting from LANL's efforts include:

- Development of the CO_2-PENS systems framework for long-term performance analysis of geologic CO_2 sequestration sites. CO_2-PENS is first-ever systems analysis tool designed for assessment of CO_2 sequestration sites.
- One of the few field studies to-date focused on understanding impact of CO_2 leakage on shallow groundwater chemistry. Two major conclusions of the study are as follows: the impact of co-contaminants transported with deeper brine on shallow groundwater quality is likely to be much larger than that of the CO_2 and CO_2-induced geochemical reactions and in certain geochemical environment the reactivity of pure CO_2 will not be sufficient to mobilize metals beyond background levels.

Basic Geoscience: Pore Scale

An experimental rock core flow-through reactor apparatus was developed to reproduce subsurface conditions relevant to geologic sequestration. Experiments were conducted at the core scale to simulate CO_2 injection, assess CO_2-brine-rock interactions, and geochemical and physical changes to the rock and brine composition. Monitoring capabilities included *in situ* pH,

EC, pressure, and temperature measurement and continuous logging of these variables. Two sets of experiments were conducted. The first set was conducted by flowing brine and/or supercritical CO_2 through the apparatus, with and without rock cores in line. Rock samples were limestones/dolostones from the Madison Formation, western Black Hills, South Dakota, which was selected based on its applicability as a potential large-scale geological CO_2 storage target. Brines were prepared in the laboratory of a similar composition to reported literature values for *in situ* Madison Formation fluids. The experiments indicate that samples of the Madison Formation with simulated *in situ* brines can be partially dissolved via exposure to supercritical CO_2. Similar processes would likely occur in the subsurface Madison Formation in response to addition of supercritical CO_2. A significant upgrade of the flow-through reactor apparatus was implemented prior to a second set of experiments. This second set of experiments used similar pressure, temperature, and brine conditions to those in the first set but also included sandstone core samples; quartz arenite from the Berea Formation were selected to represent ideal 'clean' sandstone. NMR images of fresh cores were compared with images of CO_2-brine challenged cores using a protocol for pixel-by-pixel comparison to determine the effects on bulk pore volume and geometry. Little change was evidenced in the samples from the sandstone (Berea Formation) but significant changes in the pore volume and geometry of limestone/dolostone (Madison Formation) were observed, which is in agreement with the geochemical analyses in the first set of experiments.

Basic GeoScience: Intermediate (Reservoir) Scale

The intermediate scale portion of the ZERT project was the thesis work for graduate student Keriann Pederson. Ms. Pedersen's thesis is included as Appendix A and is the final report for the intermediate scale portion of the ZERT I project. Below is the abstract in its entirety taken directly from the thesis.

Five formal members have been recognized through correlation of depositional stacking patterns as identified in well logs and cores in the Fiddler Creek and Clareton incised valley-fills, Powder River basin, Wyoming. These five units are consistent with identified members in other Muddy Sandstone incised valley-fills in the Powder River basin. Long-term sequestration of CO_2 necessitates an understanding of the internal porosity and permeability pathways. Net sandstone maps and interpreted stacking patterns were used to identify these pathways within the two incised valley-fills. Stacking pattern and environment of deposition were compiled from facies recognition in core (11 cores) and correlated to corresponding wireline logs (600 well logs). It is concluded that the Fiddler Creek system is not an incised valley-fill system, as defined in this work, due to its avulsion out of the valley walls after deposition of the earliest members in the system. It is also concluded that these valleys maintain the necessary porosity and permeability pathways for successful injection of CO_2. However because of difficulty monitoring and maintaining the 6000+ wells in these fields they are useful only as analogues for future sequestration sites.

Basic Geoscience: Basin Scale

This contribution summarizes an accurate method for characterization of geologic heterogeneity associated with geologic carbon storage (GCS) in subsurface reservoirs at the basin scale. The Powder River Basin is studied because it is representative of GCS onshore sites; it has a long history of diverse fluid production, and contains a unique, comprehensive, and robust subsurface dataset. The Ph.D. resulting from this research developed a workflow to retain, reproduce, and manage multiple scales of heterogeneity to accurately model basin-scale fluid behavior; created two geomodels utilizing the workflow; and evaluated the impact of this approach on conventional GCS screening methods for calculating net pore volumes.

High produced and resident fluids define five reservoir classes (RCs) listed below. Characterized by hierarchical stratigraphic sequences, the RCs represent approximately 40% of the 4-km (2.49 miles) thick basin-fill, and record over 300 m.y. of geologic time defined by 20 Paleozoic and Mesozoic geologic formations.

RC1. Shallow-marine and karsted carbonate platform (Madison Limestone)
RC2. Mixed carbonate, evaporite, and clastic coastal eolian (Minnelusa/Tensleep Formation)
RC3. Coastal to peidmont clastic valley-fills (Muddy Sandstone)
RC4. Remnant clastic deltaic and shallow-marine turbidites (Frontier Formation)
RC5. Wave-influenced, clastic delta/shelf (Mesaverde Group)

Detailed characterization of RC4 illustrates the modeling workflow: (1) define hierarchy of sedimentary attributes correlated to geologic heterogeneity spanning four orders of magnitude in scale, (2) erect a threefold sequence stratigraphic framework to vertically modulate heterogeneity, and (3) distribute heterogeneity within and between sequences using sedimentation regions.

Because the RCs are not characterized at the same level of detail, the basin geomodel is not ready for simulation, but these models do provide a starting point for future research and can be accessed via the iProject at iReservoir.com.

HISTORY AND EVOLUTION

Mitigation Methods

This ZERT task has conducted research on microbial biofilm processes and concepts which may ultimately be applied for beneficial CO_2 use. We have focused on sequestration of anthropogenic CO_2 in the deep subsurface in secure geological formations (referred to herein as Carbon Capture and Storage or CCS). CCS involves injection into underground formations including oil beds, deep un-minable coal seams, and deep saline aquifers with temperature and pressure conditions such that CO_2 will likely be in the supercritical state ($ScCO_2$). The pure phase $ScCO_2$, which is less dense and less viscous than the resident brine, will accumulate in the upper regions of the aquifer resulting in the potential for upward migration of CO_2 unless the storage aquifer is overlain by a suitable low-permeability cap rock formation. If preferential flow paths (i.e. fractures) are present in these cap rock formations, particularly near the injection well bore

region, it is important to have technologies in place to block these migration pathways and prevent CO_2 leakage from occurring. Our ZERT task was originally conceived to explore the use of microbial biofilms for this purpose. The foundation for the original ZERT Proposal was based on previous research (Cunningham et al. 2003) which developed biofilm barrier methods to contain and remediate organic contaminant plumes in the shallow subsurface.

At the start of Phase I this task was entitled "Investigation of subsurface biofilm barriers for enhanced geologic sequestration of CO_2". This title describes the long term goal for this task which is to develop engineered biofilm-related process which can be used to block unwanted upward migration pathways for CO_2 injected into deep geologic formations. During Phase I our research team focused on investigating the formation of microbial biofilms under high pressure and temperature. This led ultimately to the construction of a novel high pressure rock core testing system as described below. The construction of this high pressure rock core testing system began toward the end of Phase I and was completed early in Phase II. The subsequent experiments carried out using different microbial inocula and different rock cores, continued on throughout Phase II and into Phase III. There were no major changes in the Statement of Project Objectives (SOPO) for Phases I, II, and III. Publication of these biofilm-based results can be found in Mitchell, et al. 2009.

During Phase III our research team began experimenting with biofilms which are capable of hydrolyzing urea. Urea hydrolization causes an increase in pH which, if conditions are right, will cause the precipitation of calcium carbonate (as explained below). This process is termed "biomineralization" and results in the formation of mineral deposits which can conceivably form a permanent barrier to flow of CO_2. Once the biomineralization concept was identified, our research focused on developing methods to optimize this process for use as a CO_2 leakage mitigation strategy. As a result the task title for Phases IV and V was changed to "Investigation of subsurface biomineralization barriers for enhanced geologic sequestration of CO_2". Experimental investigation of biomineralization in porous media was conducted through Phase V and is presently continuing under ZERT. Results to date are presented in Cunningham et al., 2010 (Cunningham et al. 2010).

Near Surface Detection Efficacy

The ZERT shallow subsurface controlled release facility was built and experiments designed to be relevant to large scale geological carbon sequestration. The spatial scale of the horizontal pipe as well as the CO_2 release rates were chosen to provide results useful in evaluating how best to monitor large scale CO_2 storage projects.

The site chosen for the facility is a relatively flat plot of land on the MSU campus formerly used for agriculture. The soil, plants, groundwater, and meteorology of the field site were characterized before injection of carbon dioxide began. Before carrying out releases from the horizontal well, modeling studies were performed by LBNL to predict pressures and migration patterns of CO_2 in the ground. Site specific information from test pit logs and a small scale vertical injection was used as input for soil properties in the model. The horizontal pipe was installed in December of 2006. The first release from the horizontal well into the shallow

subsurface was performed in July of 2007. Carbon dioxide release rates and placement of detection instrumentation were decided in light of the modeling results. The goal was to produce a situation in which the level of CO_2 was detectable by most types of instrument but still challenging. Transport of CO_2 through the soil, water, plants, and air was investigated by MSU and visiting researchers. Release rates in subsequent injections were adjusted in response to experimental results obtained from the various detection techniques. Since the six zones within the well are independently controllable it is possible to flow different flow rates of CO_2 in different zones or inject into some zones and not others. The release configuration was modified as participants were added and as returning researchers' experimental questions evolved. Studying the same field site for over 4 years has helped to characterize natural variability on a seasonal and interannual scale.

The ZERT project at LBNL focused on three broad technical tasks from the outset of the project through to the conclusion in September 2010. These tasks were (1) Performance prediction for underground fate and transport of CO_2, (2) Measurement and monitoring to verify storage and track migration of CO_2, and (3) Fundamental geochemical and hydrological investigations of CO_2 storage. There were many significant accomplishments and progress made within the ZERT tasks as documented in 39 peer-reviewed journals, book-chapters, and edited-volume publications by LBNL authors (see appendix). The work in technical Task 1 evolved as new code capabilities for LBNL's TOUGH2 family of codes were developed and made available to the broader geologic carbon sequestration (GCS) community. Task 2 also saw significant evolution as theoretical and literature studies were carried out early in the project, followed by predictive modeling and design simulations for the shallow release experiment, and culminating in extensive field measurements using accumulation chamber and eddy covariance methods associated with the ZERT shallow release test. Interspersed between field seasons was interpretative analysis and modeling to improve the ability to detect CO_2 leakage. Finally in Task 3, work evolved as the laboratory equipment and capabilities were developed. The laboratory facility that was developed is capable of flow-through measurements at reservoir pressure and temperature along with x-ray CT (Computed Tomography) visualization. LBNL has made pioneering images of CO_2 and brine during drainage and imbibition cycles. In addition, original work involving imaging of pore space and related modeling of imbibition and drainage has been accomplished as capabilities have grown over the course of the project. Simulation capabilities from Task 1 were utilized in Tasks 2 and 3 to predict behavior (e.g., ZERT shallow release) and analyze results (brine displacement in core).

In the ZERT experiment conducted at Montana State University, a horizontal, segmented, underground well at a few meters depth and 100 meters long was injected with CO_2, giving ZERT partners opportunities to test a variety of techniques to detect the spread of the CO_2 in the soil as a function of distance from the well and duration of injection during the experiment. (LLNL) participated in assessment of hyperspectral imaging and other remote sensing techniques and in providing real-time CO_2 soil sensors, which were deployed in the field by UCSC and LBNL.

In 2009, the experiments at the MSU field site demonstrated that hyperspectral measurement of plant stress is a viable technique for monitoring buildup of CO_2 in soils as might occur from

leakage of a commercial-scale CO_2 sequestration site. A key question was whether viable remote sensing techniques exist for monitoring leakage and verification of CO_2 storage sites. Results indicated that the minimum CO_2 concentration needed in soil to stress vegetation appeared to be between 4% and 8% CO_2 by volume and plant stress becomes evident in their spectral signatures within days of exposure to excess CO_2. In light of these results, and the correspondence between the ground measurements and spectral measurement made by Resonon, Inc., the team sought two sources of remote data to compare with field measurements: additional airborne data and satellite data. The results from 2009 represent an important milestone in the proof-of-concept of hyperspectral data as a convenient and powerful monitoring and verification technology. Satellite data sources were identified and plans made to compare appropriate ground-based and airplane ZERT datasets with the Japanese satellite, IBUKI (GOSAT), datasets for future field sessions. The technical paper in Appendix D summarizes the results of this study.

Throughout the duration of the project, PNNL focused on subsurface science issues associated with geologic sequestration. The project consisted of five main tasks, which are briefly described below. The principal objective of Task 1, Scalable Computing of CO_2 Migration and Storage in Geologic Formations, is the development and demonstrated application of a scalable numerical simulator for geologic sequestration of greenhouse gases with capabilities for coupled process modeling. The geologic sequestration simulator being developed at the PNNL is actually a suite of operational modes of the Subsurface Transport Over Multiple Phases (STOMP) simulator (i.e., STOMP-CO_2, STOMP-CO_2e, STOMP-CO_2ae). STOMP-CO_2 is the isothermal version, STOMP-CO_2e is the nonisothermal version, and STOMP-CO_2ae is the nonisothermal version for modeling subsurface-surface interactions. All of these simulators include the possibility of coupling in the Equilibrium, Conservation, Kinetic Equation Chemistry (ECKChem) reactive transport module for modeling geochemistry.

Task 2, Fundamental Studies of Supercritical CO_2-Brine Mixtures, focused on several aspects of H_2O-CO_2 mixtures including 1) forced convective flow around the injection well, 2) dissolution rate of CO_2 into the brine, and 3) solvation of water and water reactivity with subsurface components in the CO_2 phase. For the case where supercritical CO_2 is injected into a deep saline formation, the important processes to be considered also include heat of solution as CO_2 dissolves into the formation brine. Based on independent measurements of supercritical CO_2 fluids (Swinney and Cummins 1968), it has been proposed that thermal diffusion, quantified in a parameter called the Soret coefficient (Chipman 1926), will play an important role in the evolution of composition of CO_2/H_2O fluids in CO_2 injection site. Therefore, the objective of this work was to use laser Raman spectroscopy to study the Soret effect in CO_2/H_2O mixtures across a temperature gradient. To better understand the reactivity of water solvated in the CO_2 phase, molecular dynamics simulations were conducted along with laboratory experiments to examine the impact of bound electrolyte ions, and changes in the interfacial mineral structure.

The focus of Task 3, Characterization of Sealing Performance of Caprock Horizons, was developed on previous work by Spane (2002) which demonstrated the successful use of barometric pressure fluctuation analysis for a variety of subsurface characterization applications. This previous work will be extended to develop statistical barometric response models that can be used to assess/quantify sealing performance of caprock horizons at the reservoir scale. The to-

be-developed barometric statistical models can be used to evaluate the existing, in-situ leakage characteristics of the caprock prior to, as well as the caprock integrity performance during and following CO_2 injection. The objectives of this task are: 1) to develop statistically-based, barometric leakage response models for assessing overlying caprock leakage, 2) apply the developed leakage models to actual formation/barometric response data sets for the purpose of assessing caprock sealing/leakage characteristics, and 3) quantify area-of-investigation/caprock distances for the barometric response analysis technique, using numerical model simulation (e.g., STOMP, MODFLOW).

Task 4, Thermodynamic Data Assessment for Geochemical Modeling of CO_2-Sequestration, was designed to enhance overall modeling capabilities. Computer simulators and geochemical models require thermodynamic data to calculate the aqueous speciation, oxidation/reduction, mineral and gas solubility reactions associated with laboratory studies and field-scale applications of CO_2 injection and sequestration in geologic formations. The adequacy of these modeling calculations depends on numerous factors, including the completeness of the thermodynamic data used for these computer codes. Under this task, a report was generated that described the availability of carbonate-containing gaseous, aqueous, and solid species and their associated thermodynamic values in databases used by geochemical reaction models (Krupka et al. 2010).

Task 5, Monitoring Capability Development and Field Testing, was focused on developed enhanced soil gas flux CO_2 detection instrumentation and conducting field trials at the ZERT test site in Bozeman, Montana to evaluate the equipment performance develop better understanding of processes that affect CO_2 emissions through soils. At the ZERT field site, our CO_2 surface-flux monitoring approach evolved significantly during the project. Initially (FY06), our approach was to use a mobile analyzer coupled to fixed soil-gas samplers to simply monitor CO_2 concentrations and thus delineate the boundaries of the release plume. During the first phase, when a vertical-well injection was performed, we quickly realized that an approach that could handle much larger concentrations than conventional infrared gas analyzers were capable of measuring, together with a rigorous method for determining flux densities, was needed. In the second phase of the project (FY07), therefore, we developed a steady-state surface-flux chamber coupled with a sample-dilution system that extended our measurement range 50-fold.

Field testing of this system during the first horizontal-well injection identified the need for an array of chambers to better sample the heterogeneous flux pattern, and for unattended operation to allow monitoring for longer periods of time. Our focus during the third phase of the project (FY08) was on developing a 25-chamber array linked to a stationary analyzer powered by an independent off-grid energy source to allow unattended operation for a month at a time, and a cellular modem link to allow remote control and data retrieval. Field testing of this system identified the need for a wider measurement range and highlighted the impact of major wind events on surface-flux data. During the fourth phase of the project (FY09), we modified our chamber design to mitigate possible artifacts caused by high winds, enhanced the measurement range another five-fold, and developed the first version of a web-based user interface for remote real-time data viewing and analyzer control. Field testing revealed a need to remove moisture from the chamber air prior to passing into the analyzer and suggested that soil moisture content

might also influence flux data. In the fifth phase (FY10), we used a different analyzer that eliminated the need for dilution, further enhanced the web-based user interface, and collected data on wind and soil moisture content in addition to CO_2 surface flux.

The experiment conducted in the Fall of 2006 consisted of an injection of CO_2 into a vertical pipe in the soil at a depth of 2.5 meters beneath the surface. The purpose of this phase was to simulate a point source leakage which could possibly occur due to failure of a deep well completion. For experiments conducted between 2007 and 2010, a horizontal well was drilled to a depth of 6 feet. The purpose of this experimental design was to simulate leakage through a line source such as a fault or fracture. In each year except 2010, 3 mls per 24 hours of co-injected perfluorocarbon tracers (PFTs) were added to the center packer section of the horizontal well over multiple days. (For 2010, the same injection ratio was maintained with 2.4 mls of tracer per day.) Tracer injection was begun soon after the start of CO_2 injection and continued until the tracer experiments were completed.

Work conducted in the summers of 2006 and 2007 focused on measuring spatial distribution of surface CO_2 fluxes, soil-gas composition and isotope ratios, on the detection of co-injected PFTs in soil-gas, and on the use of soil conductivity and resistivity techniques to characterize soil properties at the test site, and to detect the development of the CO_2 plume.

In 2008-2010, the development of atmospheric plumes of the tracer was studied under various meteorological conditions using horizontal and vertical grids of atmospheric tracer monitors. In 2008, a rectangular, horizontal grid of 90 atmospheric monitors was placed that was a superposition of 40, 20 and 10 meter grids, with the finest grid adjacent to the horizontal release zone. The grid was designed, through data reduction, to evaluate the ability of 10M, 20M and even courser grids to provide information about the location, size and shape of the atmospheric tracer plume. The goal was to simulate the application of increasingly finer grids to first detect a tracer plume, then to provide increasingly greater detail on the release point location and shape of the tracer plume.

In 2009, atmospheric tracer plumes were monitored using samplers attached to tethered balloons and arrays of ground-based monitors. These experiments serve as a basis for planning future experiments using unmanned aerial systems (UAS's) rather than the balloons. Ultimately, NETL aims to demonstrate the usefulness of PFC tracer monitoring using UAS's and a ground-based array of monitors to monitor leakage events via simulations, field and laboratory studies. The experiments conducted by NETL in 2009 established a framework for detection of the PFTs and a protocol for sampling with incorporation of atmospheric dispersion models into the sampling plan.

In 2010, atmospheric plume monitoring was extended to 8 meter fixed tower structures, including a remote sampling complex at about 825 meters from the release point. Other experiments conducted in 2010 included simulated UAS flights using the balloon tethered monitors and a collaborative study with WVU and the USGS of the relative rates of development of the tracer and CO_2 plumes in the vadose zone, with access to the vadose zone of the sixth packer section through an array of ground water wells.

Work to date at the Marshall County, West Virginia coal-bed sequestration test facility includes measurement of the background levels of PFC tracers and CO_2 soil flux during various seasons of the year. Tracer background levels were characteristic of worldwide background levels, and flux measurements were typical for the climate and vegetation found in Marshall County. This information will also help to provide statistical comparisons to assess potential leakage signals as set in the framework of a Bayesian belief network. Future plans call for the simultaneous co-injection of 500 ml of one PFT into injection well MH-18 and 500 ml of a second PFT into injection well MH-20. Completing the tracer injection should require about 3 ½ days at a ratio of 12.5 ml tracer per ton of CO_2. The development of any atmospheric tracer plume released from the syringe pumps or well head fittings will be monitored during tracer injection. Post-injection schedules call for 3 sets of soil-gas and atmospheric monitors to be exchanged during the first month, then at intervals of about every other month for 1-2 years post-injection.

Near Surface Detection Efficacy: Technology Development

Introduction. The evolution of the ZERT effort is describe below covering the five different phases of the research effort. Each of the next five sections discusses the goals from the statement of work, the goals achieved, and the actions taken as the research progressed.

Phase I. The goals of the first of the ZERT effort was focused on the development of a tunable laser source that could access the carbon dioxide (CO_2) absorption features near the two micron wavelength region. Researchers at Montana State University developed a tunable continuous wave (cw) Raman laser based on a tunable external cavity diode laser that was used to pump a Raman gain medium contained in a high finesse cell. This laser was built and demonstrated. During this time, tunable distributed feedback (DFB) diode lasers became commercially available with a nominal wavelength of 2.004 μm. One of these lasers was obtained and a comparison of the cw Raman laser and the DFB laser was made. It was determined that the DFB laser would provide a more robust laser source for the development of a field instrument. Initial spectroscopic measurements of CO_2 absorption features were made during this Phase I effort. The results from this first phase of the ZERT research effort lead to the development of the phase II research plans that included the development and modeling of the differential absorption instrument for monitoring CO_2.

Phase II. The goals of the second phase of the ZERT effort was aimed at developing a differential absorption measurement instrument for monitoring CO_2 along with a differential absorption instrument for measuring diatomic oxygen (O_2). A differential absorption instrument for above ground monitoring of CO_2 was modeled and built. This instrument utilized the DFB laser characterized in the phase I research effort. A tunable laser was developed, built and tested near the 760 nm wavelength where O_2 has absorption features. Both CO_2 and O_2 concentration measurements were made with these two instruments. The CO_2 instrument was also demonstrated at the ZERT field site with the second deployment allowing continuous measurements made for more than 30 days. The results from these experiments demonstrated the capability of the CO_2 differential absorption instrument to successfully monitor CO_2 concentrations with the accuracy needed for carbon sequestration site monitoring.

Phase III. The ability to use a tunable DFB laser for surface measurements lead to the idea of developing a fiber based sensor for subsurface monitoring of CO_2 for carbon sequestration site monitoring. Subsurface monitoring has several advantages including avoiding environmental conditions such as rain and snow cover. A fiber based subsurface detector was developed and deployed at the ZERT field site during the phase III research efforts. The successful demonstration of the initial fiber sensor work led to the idea of developing a fiber sensor array that will be discussed in the phase V section.

Phase IV. The goals of the fourth phase of the ZERT research effort involved the deployment of the surface and subsurface instrumentation to be deployed at a controlled underground release facility for controlled underground release experiments lasting up to thirty days per experiment.

Phase V. The goals for the fifth phase of the ZERT research effort involved deploying instruments at the ZERT field site developed during the phase IV efforts. The above ground differential absorption instrument, the subsurface fiber instrument, and hyperspectral imaging experiments were conducted during these summer release experiments. The above ground differential absorption instrument was deployed over two summers with the second summer data collected continuously for over thirty days successfully demonstrating the effectiveness of the cw differential absorption instrument for monitoring carbon sequestration sites. The fiber based subsurface detectors have been deployed over three summers with a fiber sensor array consisting of four sensors deployed during the last summer. Ground and flight based hyperspectral imaging data was collected during two summer field experiments demonstrating that classification tree analysis can be used to detect elevated CO_2 levels indirectly by monitoring vegetation stress.

Summary. The ZERT research effort allowed a differential absorption instrument to be constructed, modeling of a pulsed differential lidar instrument to be completed, a fiber sensor array to be developed and tested, and provided the opportunity to demonstrate hyperspectral imaging as a potential for large area monitoring of carbon sequestration sites. The success of the ZERT research effort has allowed additional research funding to be obtained through competitive grant processes and technology developed during the ZERT research effort is being transferred to commercial entities. Work with the underground fiber sensor has lead to further funding through the Department of Energy and commercialization of the fiber sensor is underway through a Phase I SBIR project funded through the Environmental Protection Agency. Recognizing the need to monitor the large areas associated with geologic carbon sequestration sites, a differential absorption lidar (DIAL) was modeled as part of a feasibility study. The model of the DIAL performance was completed and a design for a DIAL instrument for spatially mapping CO_2 concentrations was completed. This work led to a separate funded project sponsored by the Department of Energy and work to commercialize the DIAL instrument is underway through the preparation of a Phase I SBIR proposal. Finally, a passive optical sensing technique based on random forest classification analysis was developed using a ground based hyperspectral imaging system. The success of this project led to follow on funding by the Montana Board of Research and Commercialization Technology (MBRCT). Commercialization of flight based hyperspectral imaging for large area monitoring of carbon sequestration sites is

underway with a successful Phase I STTR project and a funded Phase II STTR project by the Department of Energy.

Phase II. This work began as preliminary imaging system design during ZERT Phase II, Task 1.0, subtask 1.4.3:

Phase II Task 1.0 – Development of Optical Methods for Carbon Dioxide MMV
Task 1.0 – Development of Optical Methods for Carbon Dioxide MMV
Subtask 1.4 (Month 1-Month 24) Determination of other optical methods of measuring surface CO_2 concentrations, fluxes, or effects.
Sub-Task 1.4.3 (Month 12 - 24) Inexpensive Normalized Differential Vegetation Detector

Phase III. We also installed a solar-powered weather station at the ZERT field site in September 2006 during the first CO_2 release experiment to characterize wind speed and direction and other meteorological parameters as part of the background data collection effort:

Task 4.0 – Development of a surface detection test site. MSU land will be used to develop a surface detection test site aimed at understanding detection limits and expected CO_2 fluxes.
Subtask 4.1. (Months 0-6) Collect baseline data at a surface detection test site.

Phase IV. During this phase we completed development of a multi-spectral imaging system and deployed it during the 2007 and 2008 CO_2 release experiments as part of Task 2.0.

Task 2.0 – Validation of near-surface CO_2 detection techniques and transport models

Phase V. In this phase we deployed a modified version of the multispectral imaging system designed and built in Phases III and IV in the 2009 CO_2 release experiment. We also began testing a preliminary prototype of a new custom-designed multispectral imager.

Task 1.0 – Investigation of low cost optical detection of CO_2 leakage
Subtask 1.2 Spectral Imaging
Sub -Task 1.2.1: Development of the multispectral imaging system.
Sub -Task 1.2.2 Construction and testing of a multispectral imaging system.

Risk Assessment

LANL is one of the founding partners of ZERT and has been an active project participant since its inception. Within the framework of ZERT's focus on addressing science needs for evaluating efficacy of geologic sequestration as a U.S. strategy for minimizing the impacts of atmospheric carbon dioxide on climate change, LANL's overall approach has been to utilize a science-based prediction approach to develop capabilities to predict long-term performance of CO_2 sequestration sites and fill the science gaps that limits comprehensiveness of the prediction approach. LANL's initial SOPO was focused on establishing the scientific basis for predicting the performance of engineered geologic CO_2 storage sites, identifying key monitoring needs for such sites and identifying remediation strategies should a site exceed performance thresholds. The initial SOPO resulted in development of an initial system framework that linked system-level performance of an engineered geologic sequestration sites to key coupled

processes/parameters at sites. The framework as well as monitoring and remediation needs were used to identify LANL activities in subsequent years. The second SOPO was focused on development of the first version of CO_2-PENS system-level model based on the framework developed during first year including linking the system level model to process-level models for various parts of the sequestration system (such as reservoir, wellbores, faults, etc.). In addition, we initiated activities focused on understanding impact of CO_2 leakage on shallow aquifers through study of a natural analog at Chimayo, New Mexico as well as participated in the ZERT controlled release experiment. The third SOPO continued to build on the activities during the previous year including enhancing the capabilities in CO_2-PENS system model (incorporating Princeton's semi-analytical wellbore leakage model), Chimayo analog study and participation in ZERT release experiment. In addition, the SOPO also included other activities, including, development of numerical modeling capabilities for simulating CO_2-cement interactions and determination of feasibility of non-linear acoustic methods to detect cement integrity. In the following year, the focus of LANL SOPO shifted from developing system-level modeling capabilities to filling science gaps in fundamental science of CO_2-reservoir-rock interactions at geologic CO_2 storage sites. We continued our efforts at Chimayo analog site as well as participated in the ZERT release experiment. In addition, we also initiated activities focused on developing efficient numerical simulation capability for modeling wellbore leakage in LANL's FEHM simulator. In the following SOPO, we continued our efforts related to Chimayo study and ZERT release experiment. We also initiated activities related to enhancing the coupled flow-stress processes simulation capabilities in FEHM. LANL efforts through the years have led to a number of accomplishments ranging from enhancing our understanding of CO_2 interactions with geologic media to development of novel modeling capabilities to simulate processes resulting from large-scale CO_2 injection and predicting long-term performance of geologic CO_2 sequestration sites for risk assessment. We provide details for two major accomplishments below.

Risk Assessment: Natural analogs for escape mechanisms

Phase IV. Tasks related to natural analogs for escape mechanisms began in phase IV of the ZERT project. Project objectives for this phase of research involved subsurface structural analysis of large, CO_2-bearing anticlines in the hanging wall of the Absaroka thrust fault (3.1). This involved the construction of local cross-sections based on surface and subsurface data. In addition, the larger objective focused on characterization of the main CO_2 reservoir rocks in the northern Salt River Range (3.2), including the Jurassic Twin Creek, Triassic/Jurassic Nugget Sandstone, and Mississippian Madison Group carbonates. These objectives did not change through the course of the work, although much more effort was placed on field- and laboratory-based characterization of CO_2 reservoir rocks, fracture/joint characterization of these same reservoir units, and "leaky" fault zone characterization.

Phase V. These subtasks focused on the collection of fault-zone materials that may have been conduits for CO_2 migration and microscopy/characterization of samples from the field. Other subtasks in this phase were essentially the same as subtasks in phase IV, differing only in the scope of the work. In addition to looking at new outcrops of the Nugget and Twin Creek, we also conducted an extensive study of deeper Paleozoic units that also have reservoir potential for

hydrocarbons and CO_2, building on the database collected during phase IV. It was during this phase of research that we discovered the widespread signature of hydrothermal brecciation and alteration of reservoir units, created by the buoyant ascent of warm brine+CO_2+hydrocarbon solutions through hydro-fractured breccia conduits, both parallel and perpendicular to bedding. The overall scope of the research remained a coherent project, focusing on CO_2 reservoir rock characterization and fault/fracture characterization.

Basic Geoscience: Pore Scale

Phases I & II. An initial flow-through core reactor apparatus was built in Phases I and II following discussions with colleagues (J. Kaszuba at Los Alamos National Labs and H. Rush at Albany Research Center). Design of our flow-through core reactor system was also guided by the experience of the system used by colleagues (R. Gerlach and A. Cunningham) in the Center for Biofilm Engineering (CBE) at MSU for the biofilm barrier research using rock cores on the ZERT grant. The initial flow-through system was very similar to the system in the CBE (Figure 1) and a proof-of-concept set of experiments using a limestone/dolostone core and brine-supercritical CO_2 mixture demonstrated increases in brine total dissolved solids (TDS) and thus partial core dissolution. The flow-through system was then upgraded to incorporate additional capabilities compared to that in the CBE, including the ability to run the reactor at higher temperatures (90-100 ^{o}C) and including probes for continuous measurement of pH, electrical conductivity (EC) – a measure of TDS, temperature, and pressure (Figure 2).

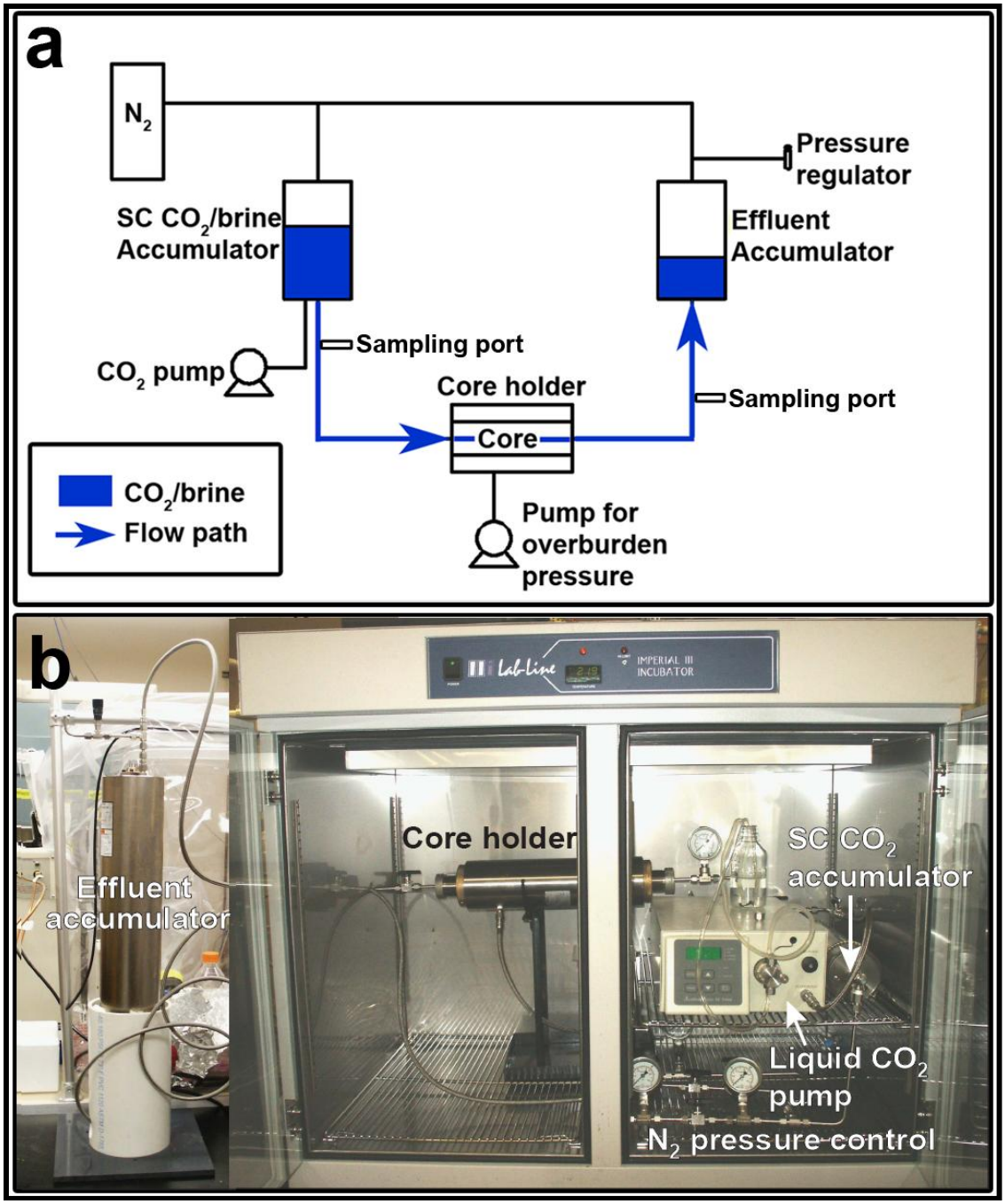

Figure 1. Version one of the flow-through reactor system. a) Schematic diagram. N_2 gas controls a pressure imbalance between the piston accumulators, driving **CO_2** through the system. b) Photograph. All components with the exception of the effluent accumulator were housed inside an incubator to maintain elevated system temperature.

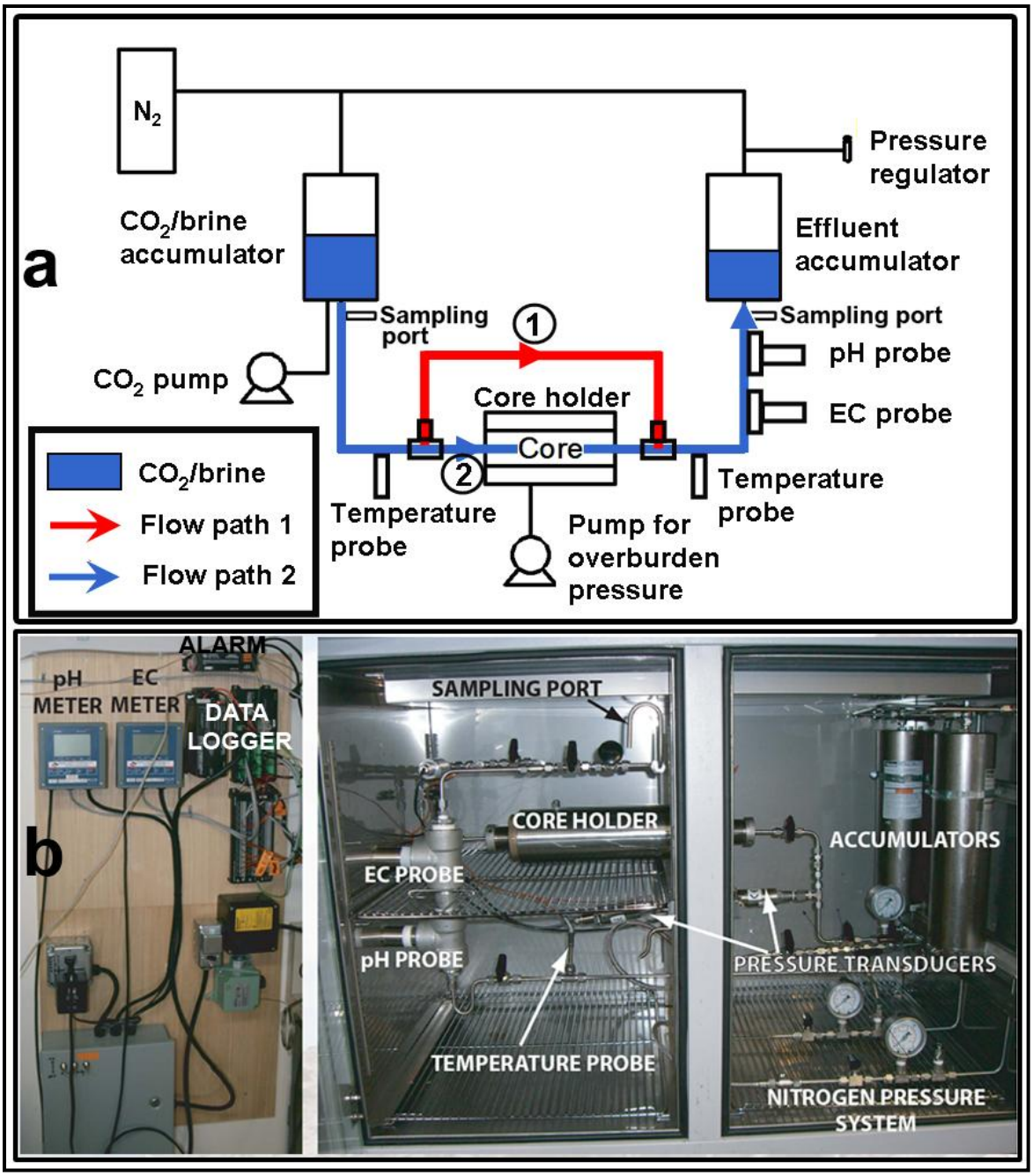

Figure 2. Version 2 of the flow-through reactor system. a) Schematic diagram of high pressure system. Flow path 1 bypassing the core holder was used in the experiments with no inline rock core and flow path 2 was used in the experiments with an inline rock core. b) Photograph of system including novel monitoring probes (right), and data collection and logging system, and alarm system (left).

Phase III & IV. This involved testing the flow-through core reactor apparatus using supercritical CO_2-brine mixtures with and without rock cores. Rock samples used were limestones/dolostones from the Madison Formation, western Black Hills, South Dakota, which was selected based on

its applicability as a potential large-scale geological CO_2 storage target (Fischer et al. 2005). Brine-CO_2 experiments were conducted over a range of temperatures (45-90 ^oC) and brine salinities (0.5-5 g L^{-1}) TDS based on formation water composition (Busby et al. 1995). Following these experiments a major refit and upgrade of the core reactor system was undertaken including a syringe pump for improved flow rate control compared to piston accumulators, custom built single block housing for pH and EC probes to reduce leakage and improve thermal stability, and modifications to the system plumbing to reduce dead volume/potential bubble points in the system (Figure 3).

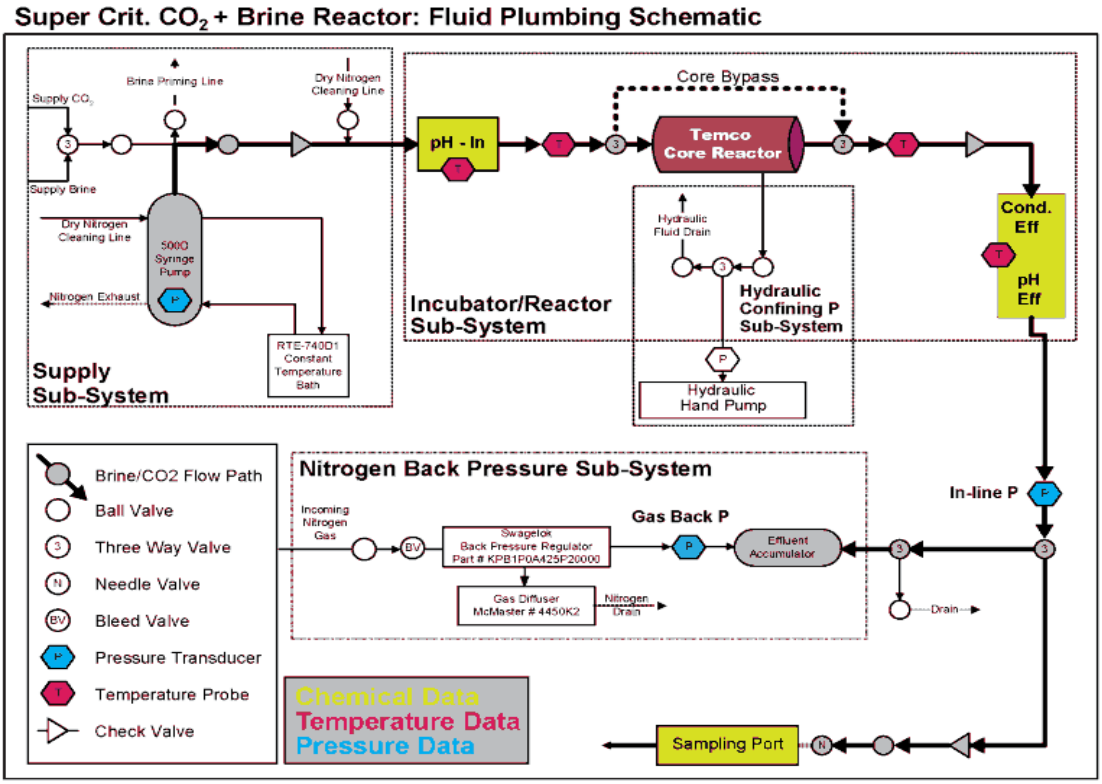

Figure 3. Version 3 of the flow-through reactor system. (A) Photograph and (B) Schematic diagram showing flow-through reactor used in experiments.

Confining pressures of 16-17 MPa were maintained within the TEMCO reactor cylinder (Figure 3). Internal fluid pressures of approximately 10-12 MPa were controlled by a syringe pump and nitrogen back pressure system. A constant-temperature bath preheated fluids in the syringe pump before introduction to the system. A modified incubator maintained primary system components at a constant temperature. Temperatures were maintained with 2-3° C of target for 50° C experiments and ~10° C for 100° C experiments.

Phase V. In this phase cores of quartz arenite from the well characterized and uniform Berea Formation (Ohio) were selected to represent ideal 'clean' sandstone, as an analog for a depleted clastic hydrocarbon reservoir as a geologic carbon sequestration target. Experimental parameters, pressure, temperature, and brine concentration were similar to those in the carbonate experiments in phase III. Additionally, brine saturated cores were imaged before and after CO_2 exposure in the flow reactor using nuclear magnetic resonance (NMR) imaging to determine the effects on bulk pore volume and geometry. A Madison Formation carbonate core was also tested under these experimental conditions for comparison. During the five phases of the project there has been development and systematic improvements in the core reactor system and also the incorporation of new and non-destructive imaging techniques to evaluate physical changes in core properties.

Basic Geoscience: Basin Scale

This contribution is based on dissertation research conducted in the Department of Earth Sciences by Jesse J. Melick, with funds supporting this effort made available in 2006. This initial work assisted with ongoing evaluation of intermediate-scale reservoir heterogeneity in major oil and gas fields and saline aquifers in the Rocky Mountain region being considered for geologic carbon storage (GCS). This revealed the limitation of isolated, small-scale reservoir studies in the assessment of industrial-scale geologic sequestration. The Powder River Basin was selected to study this problem at the basin scale.

The second phase of research (2007 and 2008) involved building the infrastructure and database. The effort centered on the key acquisition, from John Horne at RPI of Colorado and Dave Wheeler at El Paso Oil and Gas, of a comprehensive database consisting of 28,000 wells, 60 standardized stratigraphic tops and over 50 stratigraphic surfaces correlated across the Powder River Basin. The purchase of licenses for, and training on, Petra, Petrel, and GIS software provided the tools for geologic characterization and modeling. Multiple industry contacts were solicited, with Jason Taylor at TGS and Buzz Miller at IHS providing digital well data, including access from IHS to the Enerdeq database. MJ Systems discounted acquisition of over 60,000 raster log images. The bulk of the digital rock property data comes from a subset of 3500 well-log and petrophysical measurements from 1400 cores and outcrops. Concurrent literature review and reconnaissance outcrop investigations contributed to the selection of five reservoir classes for detailed study. Collaboration was initiated on the model design for basin-scale fluid simulation.

Preparation, conversion and normalization of digital, well-log and petrophysical data for modeling occupied phase III research (2009), involving MSU students Chris Franklin, John Porter, Allen Roy, Beth Helmke, and Travis Jester. Core sedimentological descriptions define the hierarchy of sedimentary attributes calibrated to subsurface data in the iterative analysis of cross sections and maps. Don Stone and Chris Zahm (structural geology); Mark Sonnenfeld (Madison Limestone); and Mark Kirschbaum, Laura Mark and Jeff May (Frontier Formation) reviewed the geology. Mike Uland provided mentoring, while Omar Angola, Ann Givan and Michael Beecher assisted with modeling during six months of on-site work at iReservoir.com in Denver, Colorado in 2009. The effort focused on petrophysical definition of effective reservoir properties and their geostatistical distribution in various scale geomodels. The first dissertation manuscript describing the modeling workflow was submitted to the Society of Petroleum Engineers (SPE) journal for publication.

The partially funded last phase (2010 and first half of 2011) involves completion of a dissertation that integrates and summarizes results in 16 published abstracts derived from presentations made at national and international scientific conferences during the course of this research. The second dissertation manuscript focuses on detailed geologic characterization of the Frontier Formation (RC4), demonstrating the value of this approach to GCS. Net pore volume calculations incorporating hierarchical stratigraphic sequences embedded with sedimentation regions reinforce these conclusions. Unfortunately, generation of the model dataset consumed the budgeted time and funding, with simulation not feasible with the resources provided.

EXPERIMENTAL METHODS

Mitigation Methods

Biofilm experiments. During phase I the high pressure biofilm and supercritical CO_2 testing apparatus was constructed as shown in Figure 4. This system was initially operated using a 40 millidarcy, 2.54 cm (one-inch) diameter Berea sandstone rock core under high pressure (8.9 MPa), moderate temperature (32 °C). Data showing the reduction in permeability along with the response to $ScCO_2$ challenge are shown in the following section entitled Results and Discussion.

Figure 4. High Pressure Biofilm and supercritical CO_2 testing apparatus: TOP- Series of valves and gauges that allow differential pressure setup BOTTOM LEFT - Accumulator for nutrient storage, supercritical CO_2 storage accumulator (far left), Hassler-type core holder with Berea sandstone core, (all housed inside an incubator for temp. control) BOTTOM RIGHT - Accumulator and sample port used to collect effluent samples.

Shewanella frigidamarina was selected as the inoculum for biofilm formation in the sandstone core. This organism was isolated from oil field brine and therefore had survived high salt environments and high pressures. The nutrient media contained 18g L^{-1} brain heart infusion (BHI), 0.75 g L^{-1} NH_4Cl, 40 g L^{-1} NaCl, and 3 g L^{-1} $NaNO_3$. The liquid that passed through the core into the effluent accumulator was pressurized into a flask. The resulting volume of the effluent was divided by the pulse time to determine a flow rate and subsequently the permeability of the core.

Biomineralization experiments. The column experiment apparatus used to conduct biomineralization experiments during phases IV and V is shown in Figure 5. The column was made of clear, 2.54 cm (one inch) PVC tubing, 60.96 cm (24 inches) in length filled with 0.5 mm quartz sand. Piezometers were put in place at the influent and effluent and the initial flow rate was set at approximately 3.5 mL/minute, but before the column was inoculated the flow rate was increased to 10 mL/min.

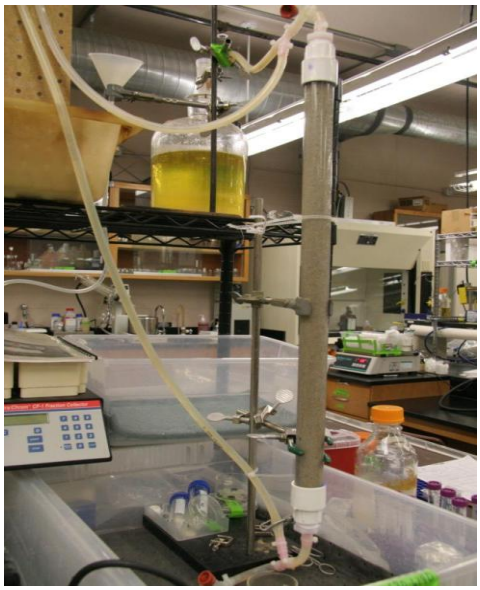

Figure 5. Experimental set up for conducting biomineralization experiments intended to develop a uniform distribution of calcium carbonate over the entire length of the quartz sand column

Sporosarcina Pasteruii was chosen as the ureolytic bacterial strain for these experiments. Three different filter-sterilized growth media were used:

- CMM- (minus); Difco Nutrient Broth 3g/L, Urea 20g/L, and Ammonium Chloride 10g/L
- CMM++ (plus plus); Difco Nutrient Broth 3g/L, Urea 20g/L, Ammonium Chloride 10g/L, Calcium Chloride Dihydrate 185g/L
- CMM--(minus minus); Difco Nutrient Broth 3g/L, Ammonium Chloride 10g/L

Following inoculation and biofilm formation, pulse flow of two media types was established to facilitate the precipitation of calcium carbonate uniformly throughout the column. First, CMM - - (minus minus) was pumped in at 10mL/min for approximately 30 minutes (~ two pore volumes) to neutralize the pH; this was followed by an equal volume of CMM++. After about 35 days the fluid in the influent piezometer reached the top and these readings were no longer taken. After 58 days and 36 CMM++ pulses, the column would no longer allow media to be pumped through and it was assumed to be plugged. At that point the influent and effluent tubing was disassembled and the column was inverted and allowed to drain. The column was then destructively sampled by sawing it into eight 3 inch sections. The contents of each section was removed and mixed, each mixture was further divided into three parts. These twenty-four samples were then analyzed for calcium and protein concentrations.

Near Surface Detection Efficacy

A detailed description of the field site and infrastructure can be found in Spangler et al. (2009). Briefly, a 100 m (109.36133 yards) long stainless steel pipe with the central 70 m (76.552931) slotted was installed by horizontal directional drilling at the field site. The average depth below ground surface of the pipe was 1.8 m (1.968504). This placed most of the well below the water

table during the injections. The well was partitioned into sox zones by rubber packers. A mass flow controller system delivered CO_2 to each zone independently. Water monitoring wells were installed in the farthest southwestern zone to sample shallow ground water and head space gas. Nine injections with CO_2 flow rates ranging from 0.1 to 0.3 metric ton CO_2 /day were performed over the summers of 2007-2010. Over the past four experimental seasons, researchers from six national labs, six universities, five companies, the United States Geological Survey, and the Electrical Power Research Institute have carried out studies at the site.

Figure 6. Field test facility at MSU

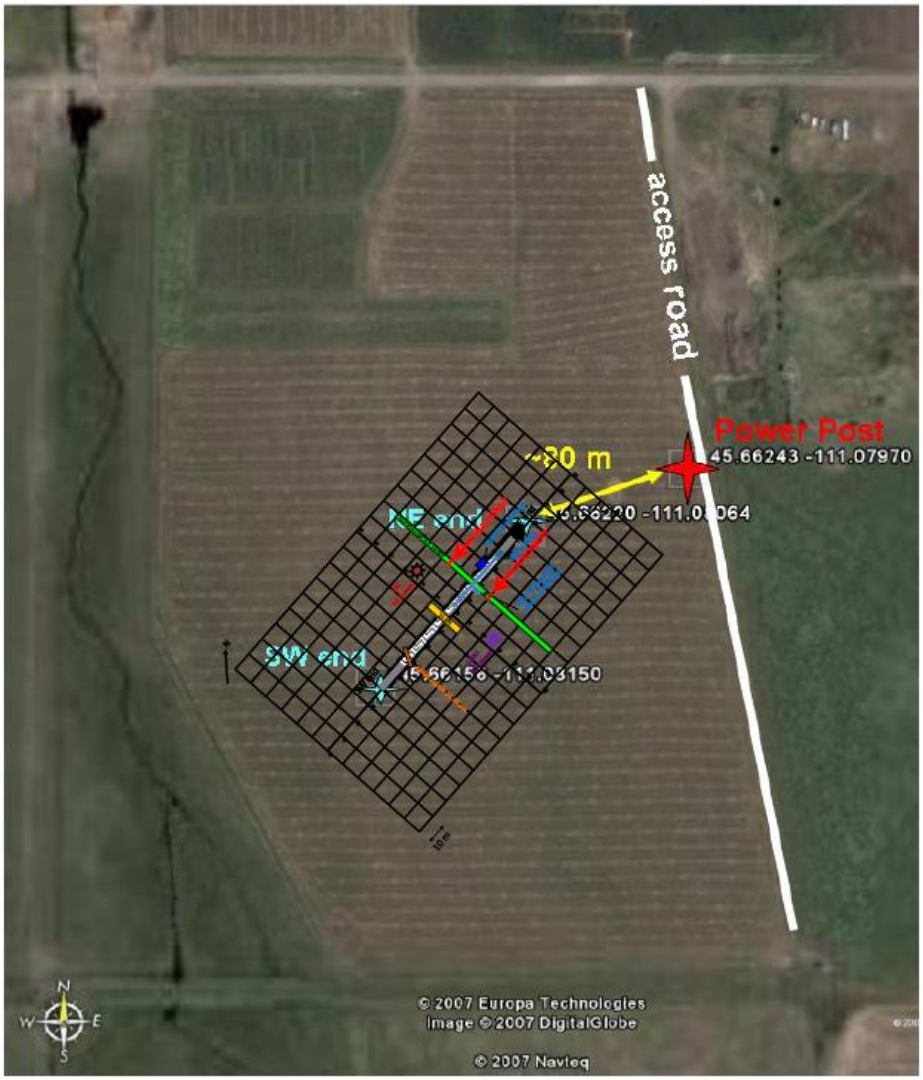

Figure 7. Horizontal well layout

Transport of CO_2 through soil, water, plants, and atmosphere was investigated. Steady-state and non-steady-state soil CO_2 flux were measured with accumulation chambers. Soil gas concentration was determined using perfluorocarbon tracers, laser-based differential absorption measurements, and non-dispersive infrared sensors. Inelastic neutron scattering was used to measure total carbon in soil. Changes in ground water chemistry and head space gas were used to follow transport of CO_2 in the water. Plant health was monitored using both hyperspectral and multispectral imaging as well as infrared radiometry and plant root imaging. Transport of CO_2 through the air was investigated with several techniques. Vertical profiles of perfluorcarbon tracer concentration were collected from towers as well as a tethered blimp. Radon as well as ratios of O_2 to CO_2 were monitored in the air. Laser-based differential absorption measurements were made of CO_2 in the air while frequency-modulated spectroscopy and two different commercial systems measured $\delta^{13}C$ using cavity ring down spectroscopy. A portable CO_2 sniffer was tested by Licor, a private company. Eddy covariance techniques were used to determine net CO_2 flux. Stable isotopes of CO_2 were measured in atmospheric, vegetation, soil, and

groundwater reservoirs. Soil properties such as soil moisture, temperature and conductivity were measured. Studies investigating the effect of CO_2 on microbes in the soil were carried out. Additionally, supporting data such as general meteorological conditions and vertical profiles of wind were measured by MSU and results provided to interested participants.

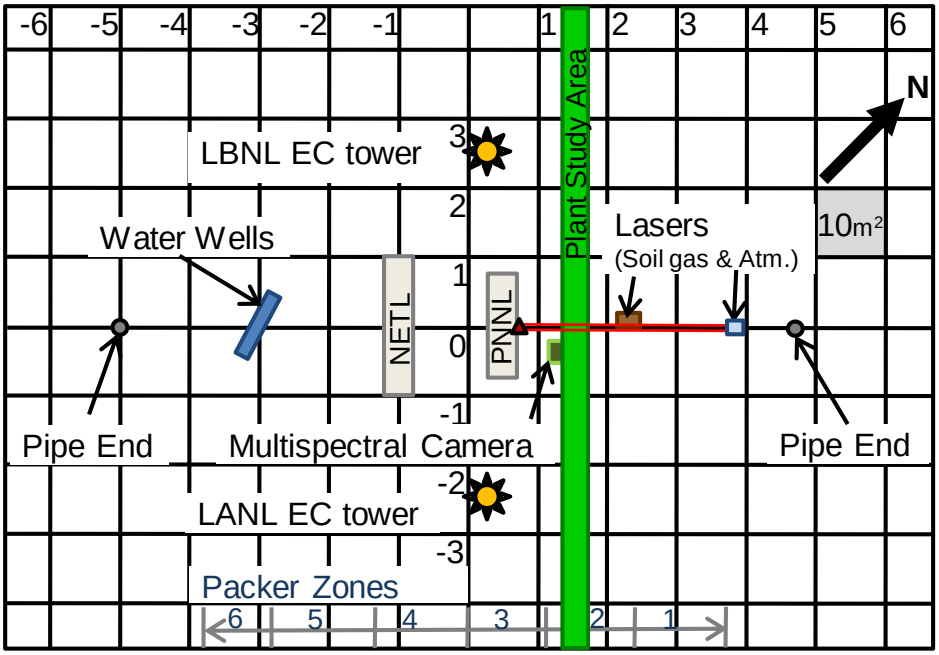

Figure 8. Schematic of 2007 field layout

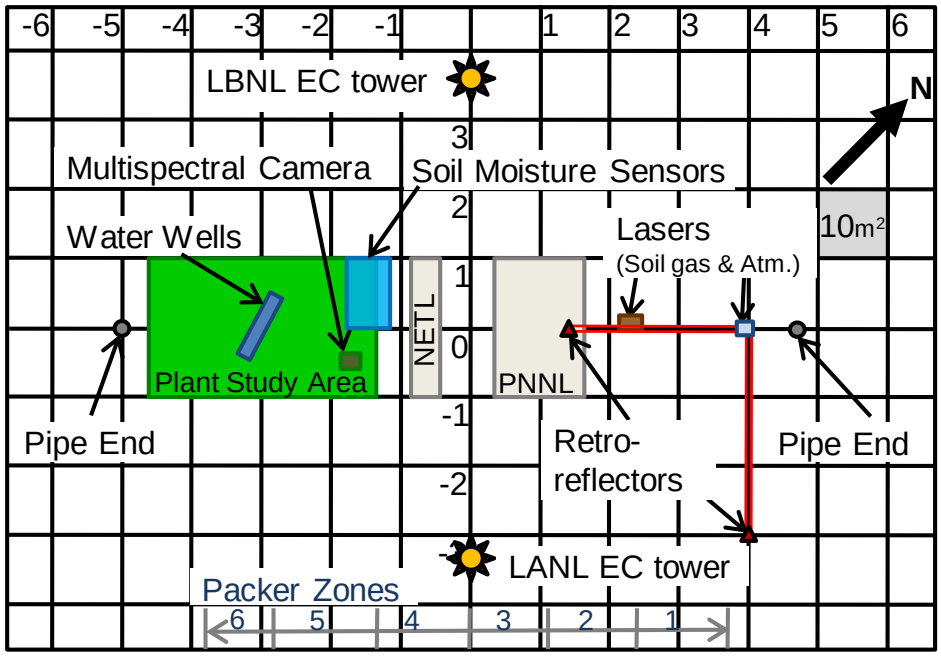

Figure 9. Schematic of 2008 field layout

Figure 10. Looking north across the field site in 2010

Experiments conducted under task 3 included high pressure tests with uniquely developed reactors. Measurements with Raman Spectroscopy and residual gas analyzers allowed for *in situ* characterization of supercritical fluids containing water and trace contaminant (H_2S, SO_2) gas components. For testing at the ZERT field site (Task 5), the experimental methods through the third phase of the project are summarized in Amonette and Barr (2009), Amonette et al. (2010), and Spangler et al. (2010). Subsequent modifications include a larger chamber vent tube diameter to minimize induced vacuum inside the chambers, insertion of drying columns in the sample train ahead of the analyzer, a new more robust solenoid valving system, and the use of four inexpensive pyroelectric CO_2 detectors (IRC-A1, Alphasense Ltd., Essex, UK) that cover the full range of CO_2 concentrations and eliminate the need for sample dilution. Volumetric soil moisture content in the top 15 cm of soil inside and adjacent to the chambers was measured by time-domain reflectometry (CS630, Campbell Scientific, Inc., Logan, UT).

The presence of PFTs in soil-gas or in the atmosphere is monitored using small, glass capillary absorption tubes containing the sorbent ambersorb. These tubes are then analyzed to the pico- and femto- levels (parts per quadrillion, v/v) at NETL's tracer laboratory in Pittsburgh using thermal desorption, and gas chromatography with chemical ionization, mass spectrometric detection. The tubes can be exposed in a passive mode by removing the cap from one end. In this

mode, the exposure rate is 200 ml of soil-gas or air exposed over a 24 hour period. The tubes can also be exposed in an active mode using a small air pump to draw soil-gas or air through the tubes at a specific flow rate for a specific amount of time. For soil-gas monitoring, the tubes are exposed near the bottom of a steel pipe driven one meter into the ground, then opened at the bottom to admit soil-gas, and sealed at the top to exclude exposure to air. Soil-gas depth profiling arrays consisted of multiple pipes driven to various depths. Passive atmospheric monitors were contained in weather protective chambers mounted on poles or towers. Atmospheric monitors used in the 2009 and 2010 efforts included remotely controlled multiple tube samplers developed for NETL by Apogee Scientific.

For the vertical injection of 2006, an experimental grid was established for passive tracer in soil-gas measurements covering the four compass directions from the injection well at distances up to 50 meters. The soil-gas monitoring grid for 2007 was laid out perpendicular to the horizontal well and offset 25 meters on both sides of the well. The grid for 2008 consisted of 90 passive atmospheric monitors placed in a rectangular, horizontal grid which was a superposition of a 20 meter grid and a 10 meter grid, with the finer grid adjacent to the horizontal release zone (Figure 12). In 2009, remotely controlled, multiple tube samplers on balloon tether lines were coordinated with 1 to 4 meter ground based towers. This work was extended to 8 meter towers in 2010 with the addition of a remote sampling complex downwind of the tracer release point in addition to simulated UAS 'flights' using the balloon samplers.

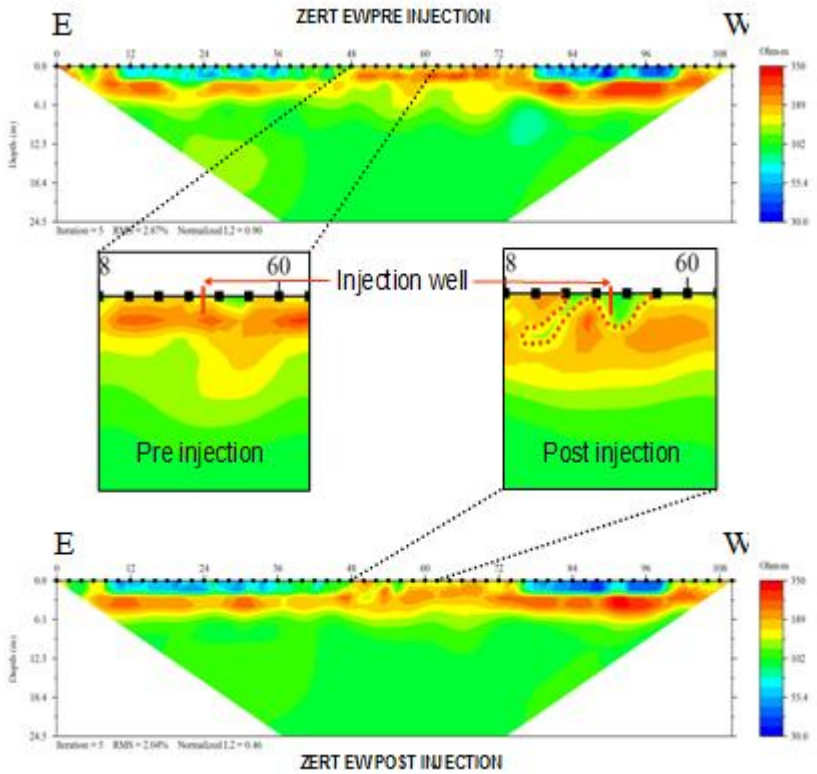

Figure 11. Resistivity/depth profiles acquired along an east/west line through the vertical injection well before (upper) and after (lower) CO_2 injection. Area made more conductive (less

resistive) by the injection of **CO_2** is depicted by dashed red line.

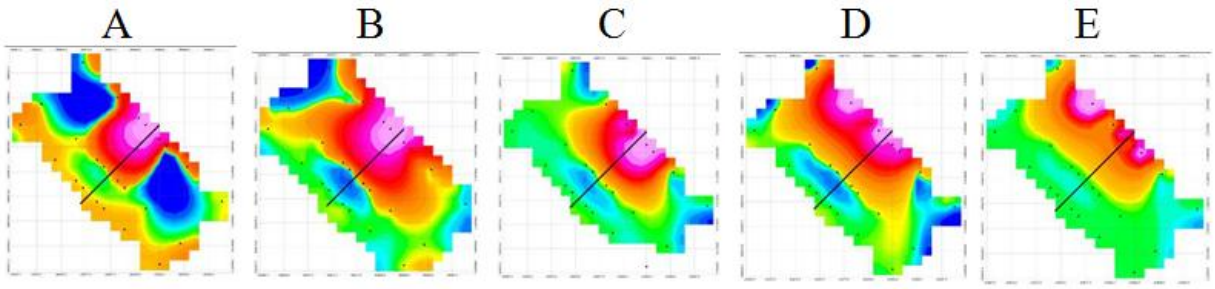

Figure 12. Contour plots representing soil-gas tracer concentrations at 1 meter depth measured at the points marked by black dots. Timing of samples is (A) during the 2 day tracer injection, (B) a six hour exposure taken on the day following completion of tracer injection, (C) a six hour exposure taken 2 days after the completion of tracer injection, (D) a six hour exposure taken 3 days after the completion of tracer injection, and (E) a 2 ½ day exposure initiated 4 days after the completion of tracer injection.

Soil-gas fluxes were measured using a LiCor 6400 photosynthesis chamber with the soil CO_2 flux chamber. Soil-gas CO_2 depth profile samples were taken by driving a probe (AMS Gas Vapor Probe 427.01) into the soil with an annular hammer. 2-D resistivity imaging profiles were collected over selected traverses at the ZERT study area using an 8-channel resistivity instrument (Advanced Geosciences SuperSting R8/IP) and a Swift dual-mode, 56-electrode cable. Each traverse consisted of a single deployment of 56 stainless steel electrodes spaced 2-m apart to obtain a 110-m long profile.

Near Surface Detection Efficacy: Technology Development

Integrated Path Differential Absorption Instrument. The above ground sensor (Humphries et al. 2008a. 2008b; Repasky et al. 2006; Barr et al. 2010; Humphries et al. 2006) is based on a tunable DFB laser with a center wavelength of 2.003 μm. The DFB laser is capable of tuning across two water vapor absorption features and four CO_2 absorption features in the 2.0015 – 2.0042 μm range. The output of the DFB laser is collimated with 4% of the outgoing light sent to a reference detector used to monitor the reference power of the DFB laser via a reflection from a wedged pickoff. An extended InGaAs photodiode with a responsivity cutoff of 2.2 μm is used to monitor the reference laser power. The light passing through the wedged pickoff is next incident on a mirror that can be moved into or out of the optical beam path by a computer controlled translation stage. With the mirror moved out of the optical beam path (parallel beam path), the light exits the instrument and is incident on a corner cube that directs the light back to the instrument. The light is then sent to another extended InGaAs photodiode which is used to monitor the transmitted optical power. With the mirror moved into the optical beam path (perpendicular optical path), the light exits the instrument perpendicular to the optical path when the mirror is moved out of the optical beam. This light is incident on a second corner cube that directs the light back to the instrument. The light directed back to the instrument is again incident on the moveable mirror that sends the light to the same detector that monitors the optical

transmission of the parallel path. A picture of the instrument deployed at the ZERT field site is shown in Figure 13.

Figure 13. Above ground instrument deployed at the ZERT field site

A computer is used to control the wavelength scanning of the above ground sensor in the following manner. The computer sets the temperature of the DFB laser and records both the reference and transmission detector voltages using a data acquisition board. The computer then steps the operating temperature of the DFB laser, which changes the DFB laser's operating wavelength and again reads the reference and transmission detectors. This process is repeated allowing a wavelength scan to be completed across several absorption features. A normalized transmission scan is then calculated by dividing the transmission signal by the reference signal. One scan is recorded with the laser in the parallel optical beam path. The computer moves the mirror into the optical path and again records a tuning scan with the laser in the perpendicular optical beam path. The process is repeated continuously. A plot of the normalized transmission as a function of wavelength is shown in Figure 14 for several scans taken during the CO_2 release experiment. The normalized transmission is then used along with ambient temperature and pressure measurements taken from a nearby weather station to calculate the CO_2 concentration (Repasky et al. 2006; Rothman et al. 2003).

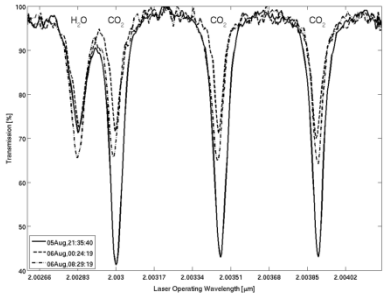

Figure 14. Wavelength scans showing the absorption features used to calculate the **CO_2** concentration

Sub-Surface Fiber Sensor. The below ground instrument (Barr 2010) uses a temperature tunable DFB diode laser with a center wavelength of 2.003 μm. A schematic of the below ground instrument is shown in Figure 15. Light from a temperature tunable DFB laser is coupled into a single mode fiber optic cable. The light is then transferred along the fiber to an in-line optical fiber splitter where approximately half the light is transferred to box 1 and the rest of the light is transferred to box 2. Each box is machined so that gas permeable membranes allow the CO_2 to

enter the boxes but do not allow water or dirt to enter. The light delivered to box 1 via the optical fiber encounters an in-line fiber optic splitter that transfers approximately half of the light to a reference detector, D1, and half of the light to a 1 m (1.093613 yards) long absorption cell. The light that is transferred down the absorption cell is incident onto the detector, D2. The light delivered to box 2 also encounters an in-line fiber optic splitter. In this box half of the light is transferred to a 0.3 m (0.328084 yards) absorption cell that is monitored by detector D3 while the rest of the light is delivered to 1 m (1.093613 yards) long hollow core photonic bandgap (PBG) fiber. The light passing through this hollow core photonic bandgap (PBG) fiber is incident on detector D4. The detectors D1-D4 are extended InGaAs detectors with a cutoff wavelength of 2.2 μm.

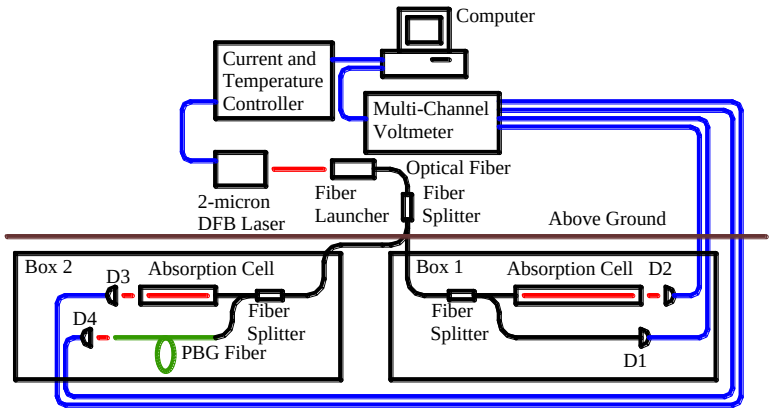

Figure 15. Schematic of the differential absorption instrument for measuring underground **CO_2** concentrations

PBG fibers use periodically arrayed set of air holes to guide light down a hollow core. The light confined to the hollow core of the PBG fiber can then interact with CO_2 allowing differential absorption measurements to be made using PBG fibers. Light is delivered to the underground PBG fiber using a standard single mode fiber (SMF-28) used for telecommunications. The single mode fiber is spliced to the PBG fiber using an Ericson FSU-995 fusion splicer. Special care was taken to insure that the core of the PBG fiber was not collapsed by the arc fusion but also to insure that the joining of the two fibers was as strong as possible.

The underground sensor collects and processes data in the following manner. The operating temperature and hence wavelength of the DFB diode laser is set by a computer operated temperature controller. The four detector voltages are then recorded by the computer using a multichannel voltmeter. The computer then steps the operating temperature and hence wavelength of the DFB diode laser and records the detector voltages again. This process is repeated generating a scan over the CO_2 absorption features as a function of wavelength. The normalized transmission spectra is then calculated by dividing the voltages read by detectors D2, D3, and D4 by the reference detector D1. The normalized transmission spectra are then used to calculate the concentration level of CO_2 (Repasky et al. 2006; Rothman et al. 2003). A plot of the three normalized transmission spectra can be seen in Figure 16.

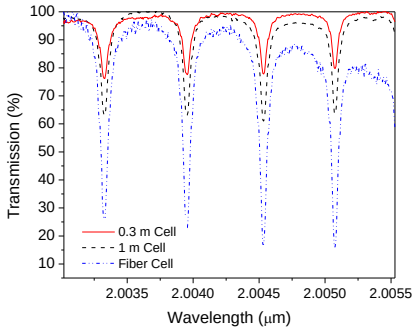

Figure 16. Plot of the normalized transmission as a function of wavelength for the three underground sensors.

Differential Absorption Lidar (DIAL) for Spatially Mapping Carbon Dioxide Concentrations. DIAL instruments (Kovalev and Eichinger 2004) use a pulsed tunable laser transmitter that can be tuned to an on-line wavelength associated with an absorption feature for the molecule of interest and then tuned to an off-line wavelength with no molecular absorption. The wavelengths of the DIAL transmitter are chosen so that the ratio of the return signal from the on-line and off-line wavelengths is directly related to the absorption from the molecules of interest. The difference in the strength of the return signals for the on-line and off-line wavelengths can then be related to a number density for the molecule of interest. Ranging information is obtained by measuring the time difference between when the laser pulse leaves the laser transmitter and when the scattered light is collected by the DIAL receiver. The range resolution of the DIAL instrument is related to the laser pulse duration.

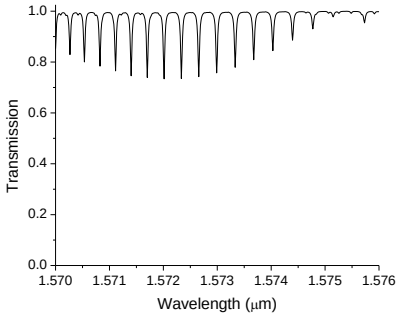

Figure 17. Transmission as a function of wavelength resulting from carbon dioxide.

Modeling the CO_2 DIAL instrument provides an estimate of the DIAL performance in terms of monitoring carbon sequestration sites. The modeling of the DIAL instrument starts by considering the absorption features of CO_2 using the Hitran database (Rotham 2003). A plot of the transmission as a function of wavelength near 1.573 μm associated with carbon dioxide is shown in Figure 17. A total path length of 4 km, an atmospheric pressure of 0.85 atm, and a concentration of carbon dioxide of 384 ppm was used to generate this plot. The absorption line chosen for modeling the DIAL instrument has a center wavelength of 1.5729919 μm, a linestrength of $S=1.729 \times 10^{-23}$ cm/molecule, and a linewidth (FWHM) of $\gamma_L=0.1524$ cm^{-1}. Since

this DIAL instrument will be used for horizontal measurements near the ground, pressure broadening will dominate allowing us to assume a Lorentzian lineshape. At line center, the cross section associated with this absorption feature is (Rotham 2003)

$$\sigma_0 = \frac{S}{\pi\gamma_L} \quad (1)$$

The DIAL equation can then be used to find the number density N(r) as a function of range r using the absorption cross section as (Kovalev and Eichinger 2004)

$$N(r) = \frac{1}{2\Delta r(\sigma_{on}(r)-\sigma_{off}(r))} ln \frac{P_{on}(r)P_{off}(r+\Delta r)}{P_{on}(r+\Delta r)P_{off}(r)} \quad (2)$$

Δr is the range bin size and is related to the pulse duration of the DIAL laser transmitter, P(r) is the optical power collected by the DIAL receiver from the range bin at range r, and the subscript on (off) refers to the DIAL laser transmitter being tuned on (off) the absorption feature. To find the power collected by the DIAL instrument, the lidar equation is used. The lidar equation is (Kovalev and Eichinger 2004)

$$P(\lambda, r) = P_t(\lambda)\frac{A}{r^2}\Delta r\beta(\lambda, r)T_A^2(\lambda, r)\varepsilon_0(\lambda, r)\varepsilon_R(\lambda)\varepsilon_D(\lambda) \quad (3)$$

where $P_t(\lambda)$ is the transmitted power, A is the area of the receiver telescope, $\Delta r = c\tau/2$ is the range bin size, c is the speed of light, and τ is the laser pulse duration, $\beta(\lambda,r)$ is the backscatter coefficient, T_A^2 is the round trip atmospheric transmission, $\varepsilon_0(\lambda,r)$ is the overlap function, $\varepsilon_R(\lambda)$ is the transmission of the receiver optics, and $\varepsilon_D(\lambda)$ is the detector efficiency. The round trip atmospheric transmission can be written in terms of the extinction, $\kappa(\lambda,r)$, and number density as

$$T_A^2 = \exp(-2\int_0^r \kappa(\lambda, r')dr')\exp(-2\int_0^r \sigma(\lambda, r')N(r')dr') \quad (4)$$

Using a lidar ratio (the ratio of the extinction to backscatter) at 1.57μm for dust estimated from the Constrained Ratio Aerosol Model (CRAM) (Reagan et al. 2006; 2007) of 30 and a backscatter coefficient of $0.5\text{x}10^{-5}$ $m^{-1}sr^{-1}$, the lidar returns can be estimated for both the on-line and off-line returns. These returns along with a signal to noise estimate can then be used to estimate the DIAL performance.

Hyperspectral Imaging to Monitor Carbon Dioxide Via Plant Stress. Hyperspectral imagery (Keith et al. 2009) was collected using a commercial imager (Resonon 2008) mounted on a tripod, placing the hyperspectral imager at a distance of about 1 m (1.093613 yards) from the plants being imaged. The hyperpsectral imager collected 640x640 pixel images covering a ground area of approximately 20 cm x 20 cm (7.874016 inches x 7.874016 inches). The hyperspectral imager has 160 spectral channels in the 400 to 900 nm spectral range with a spectral band resolution of 3.21 nm.

Much of the plant matter at the site had senesced at the time of the experiment. An exception was the alfalfa plants. A number of alfalfa plants were thus chosen for observation at various positions about the release line. Care was taken in choosing the plants such that they were of approximately the same health and flowering stage.

Data was collected by repeated measurements of the selected plants over the course of the CO_2 release. It was acquired at nearly the same time each day, about solar noon. The hyperspectral imager was positioned opposite to the sun such that the angle between the hyperspectral imager's field of view and vertical was about the same as between the sun and vertical.

Data collection began two days after the start of the release and finished one day after the end of the release. All of the plants selected were imaged each day except when inclement weather conditions prevented the completion of the data collection.

The Random Forest classifiers (Breiman 2001) use an ensemble (or forest) of tree-structured classifiers (Breiman et al. 1984), each of which uses a random subset of the training set. The training set contains data samples which have been labeled as belonging to definite classes before the analysis has begun. The tree-structured classifiers are constructed by separating the training set by recursive binary splitting, where the splits are chosen based on the explanatory variables of the training set samples. For each split, a random subset of the bands is considered for selecting the best split. Each tree is grown by continuing to split until each of the lowest nodes contains only a single class. When presented with new data, each tree in the forest returns its own classification of the data. The Random Forest then decides on the classification by taking the plurality vote of the classes returned by each of the trees. It has been shown (Breiman 2001) that the Random Forest does not overfit the learning set. The Random Forest misclassification rate approaches the Bayes misclassification rate as the number of trees grows large for training sets that well represent the population.

The primary method used in this research is to record multi-spectral images of vegetation surrounding the buried CO_2 release pipe at the ZERT field site, and perform correlation analysis on time-series plots of the reflectance at different wavelengths. The two wavelength bands of major interest are in the red and near infrared regions of the optical spectrum, separated by a "red edge" (i.e. a steep rise in vegetation reflectance) at 700 nm wavelength. As vegetation is stressed, the red edge shifts to shorter wavelengths and becomes less steep (Figure 18). In Figure 18, the gold line is a reflectance spectrum of a healthy plant, the blue line is the reflectance spectrum of an unhealthy plant, and the gray line is the spectrum of a dead plant (shifted upward for viewing). Healthy plants are highly reflective in the near infrared and more reflective in the green than in the red or blue, while unhealthy plants have higher reflectance with flatter spectral dependence.

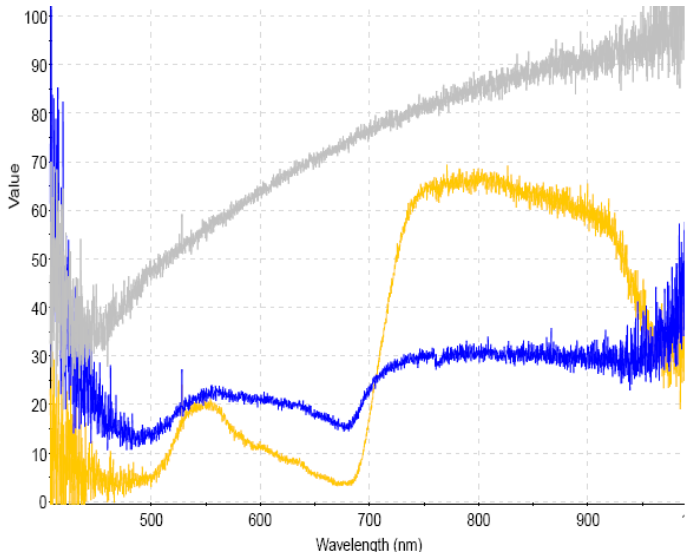

Figure 18. Spectrum of a healthy (gold), unhealthy (blue), and dead (grey) plants

The multispectral imager developed and used in this study records images in near infrared (NIR, 735-865 nm), red (630-700 nm), and green (500-580 nm) bands. Statistical analysis was performed on reflectance data at each of these bands, and on a product called Normalized Difference Vegetation Index (Rouse et al. 1974), or NDVI, defined as

$$NDVI = \frac{\rho_{NIR} - \rho_{RED}}{\rho_{NIR} + \rho_{RED}}. \quad (1)$$

In this equation, ρ_{NIR} is the NIR reflectance and ρ_{RED} is the red reflectance.

The vegetation reflectance can be caused to change by a variety of environmental factors such as the soil and atmospheric CO_2 levels, soil moisture, and temperature. It is actually possible for excess CO_2 to be helpful or harmful, depending on the CO_2 sink-source balance and the density of the vegetation (Arp 1991; Kimball 1993). No matter what the stress agent, with a change in chlorophyll and water content there will be a notable change in the reflectance spectrum of vegetation, but the use of separate test and control vegetation regions with similar moisture and heat conditions is important.

Multispectral imaging data were collected during CO_2 release experiments held in the summers of 2007, 2008, and 2009, each year with progressively more refined measurement and instrument calibration techniques. The CO_2 was released from a buried pipe, located along a nominally SSW-NNE axis to be orthogonal to the prevailing NNW and SSE winds, measured by the ZERT weather station we deployed beginning in September 2006 (Figure 19). A vegetation test area was reserved and protected from interference. In this vegetation area we imaged a 4×11 m (4.37x12.03 yards) section, with mown and un-mown subsections to determine if mowing was helpful or detrimental to the detection process (Figure 20).

Figure 19. Solar-powered weather station being installed at the ZERT field site in Bozeman, Montana in September 2006 (the solar panels are not yet installed here)

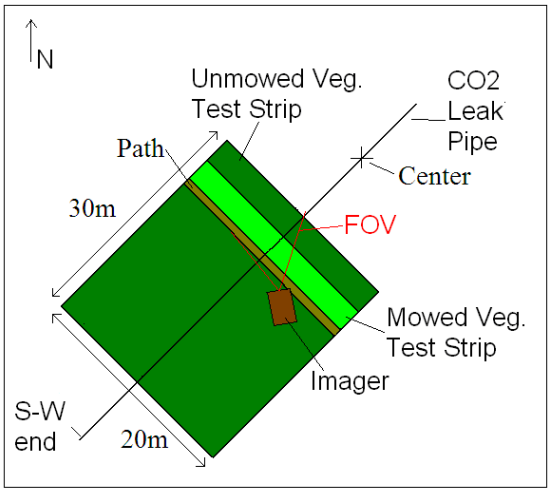

Figure 20. Vegetation test strip as configured in the 2008 release experiment

The imaging system was mounted on a 3-m-tall scaffold, with a -45^{o} viewing angle so that it viewed the ground directly above the buried release pipe out to about 10 m (10.94 yards) away from the pipe. Because of the small detector array size, it was necessary to use custom wide-angle optics on the front of the commercial camera lens (Figure 21) to achieve a field of view that could see the desired 10 m (10.94 yards) length of the vegetation test area. Figure 22 is a photograph showing the imager on the scaffold and the three data analysis regions. The

northwest edge of this rest area ("region 3") was used as a control, as it was the furthest from the release pipe. The edge nearest the imager and immediately adjacent to the release pipe ("region 1") was used as the primary test area (the intervening area was dubbed "region 2").

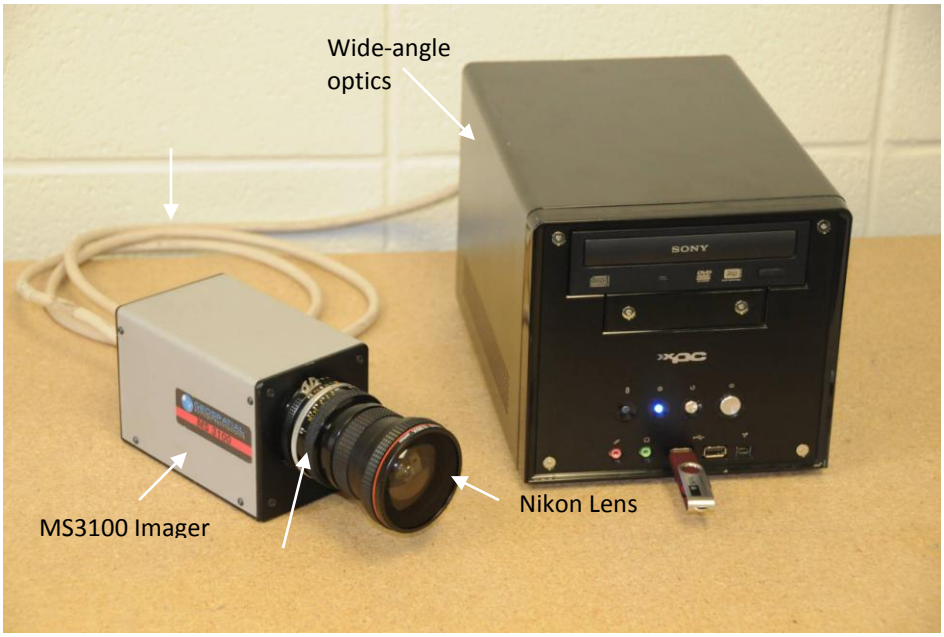

Figure 21. Imaging system including the MS-3100 three-CCD Imager with wide-angle front optics, alongside a small computer to run the system

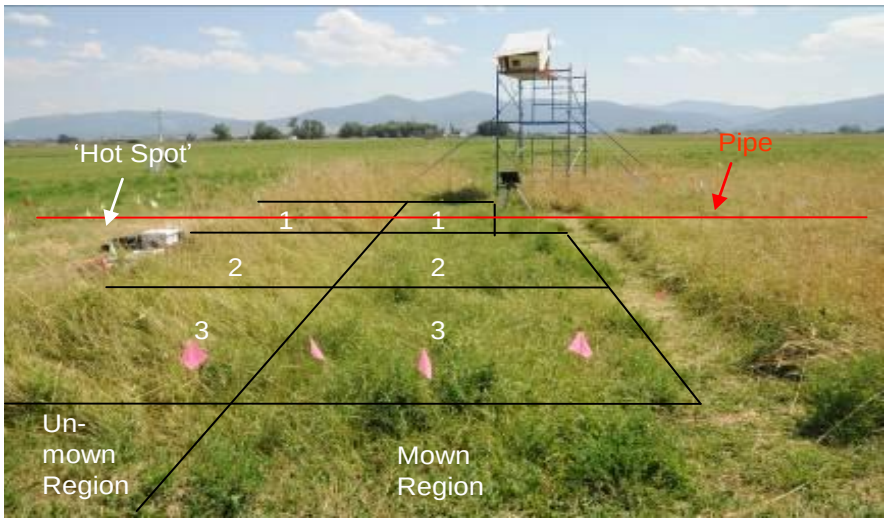

Figure 22. Multispectral imager on the scaffold, viewing the un-mown (left) and mown (right) segments of the vegetation test area. The 3 data analysis regions are also shown

The reflectance and NDVI data were analyzed with linear regression analysis based on the following general formulation:

$$y = \beta_0 + \beta_G x_G + \beta_R x_R + \beta_{NIR} x_{NIR} + \beta_{NDVI} x_{NDVI} + \tau + (x_G * \tau) + (x_R * \tau) + (x_{NIR} * \tau) + (x_{NDVI} * \tau) \quad (1)$$

Here y is the date/time (response variable), β_0 is the y-intercept (linear regression coefficient), β_G is the slope for the green band, x_G is the green reflectance (predictor variable), β_R is the slope for the red band, x_R is the red reflectance, β_{NIR} is the slope for the NIR band, x_{NIR} is the NIR reflectance, β_{NDVI} is the slope for the NDVI, and τ is the region number (categorical variable). After progressively removing terms that produced insignificantly to the result, a reduced model was obtained as follows:

$$Date = \beta_o + (\beta_{NDVI} * NDVI) + \tau_{I,1-2} + (\tau_{S,1-2} * NDVI) + \tau_{I,1-3} + (\tau_{S,1-3} * NDVI) + \tau_{I,2-3} + (\tau_{S,2-3} * NDVI) \quad (2)$$

Here Date is the response variable, β_o is the intercept, β_{NDVI} is the slope, NDVI is the predictor variable, $\tau_{I,1-2}$ is the vegetation region categorical variable that is affected by the relationship between the intercepts for regions 1 and 2, $\tau_{S,1-2}$ is the vegetation region categorical variable that is affected by the relationship between the slopes for regions 1 and 2, and $\tau_{I,1-3}$, $\tau_{S,1-3}$ and $\tau_{I,2-3}$, $\tau_{S,3-3}$ are the same as above except these are applied to regions 1 and 3 and regions 2 and 3.

Risk Assessment

Development of *CO_2*-PENS framework and system-level model

Large-scale implementation of geologic storage of CO_2 will require a large number of suitable storage sites (reservoirs). There is a need for a robust and reliable decision-making framework for evaluating the suitability of specific sites to ensure that they will perform up to required goals as well as to determine the risks associated with long-term storage of CO_2. The method needs to take into account the fundamental physical and chemical interactions resulting due to presence of CO_2 at multiple length and time scales and link fundamental scientific inputs to decisions based on a required performance goal. This means that a valid systematic approach will be required to limit site-specific evaluations to only the *critical factors* for the site (as opposed to all potential factors). We developed a framework and a coupled process-systems model based on the framework that can be used to study long-term performance of a wide range of geologic CO_2 storage sites utilizing the concept of *science-based prediction*. Science-based prediction links high level systems models, on which decisions can be based, to detailed models of physical and chemical processes by integrating theory, observation, experiment, and simulation. The foundation of predictions is built upon fundamental experimental (laboratory and field), theoretical and computational research into the behavior of individual subsystems and, as appropriate, the coupling between them. For some subsystems, the necessary information can be obtained from experimental data, but most of the complex subsystems involve an iterative approach among experiment, observation, theory and computation. Once an adequate understanding of the important subsystems is gained, the information is synthesized and simplified, accounting for uncertainties, and built into a systems model. The systems model accounts for all the couplings between subsystems and their uncertainties, and produces a

probabilistic prediction of the system behavior that can be used for decision-making. The key to the approach is how the transition is made between sub-systems level models and systems level models. For engineered geologic sites, this is done through probability functions that are developed explicitly or implicitly on detailed physics and chemistry. Site specificity is addressed by ensuring that the coupling of all possible performance controlling factors is included while recognizing that site particulars permit only a subset of all possible processes to be investigated in detail. This winnowing of processes is done systematically, providing confidence that the prediction for a site's performance has been comprehensive.

Risk Assessment: Natural Analogs for escape mechanisms

Experimentation was not conducted, as this was a field-based geological study. As such, this project was broken into two components, one involving the collection of samples and data in the field, and the other involving follow-up laboratory work and data analysis. Field sites were selected based on stratigraphic relevance (e.g., key reservoir or caprock units), structural position or significance, and accessibility. A sampling strategy was based on several transects across the fault contact of the Absaroka thrust and through several imbricate panels in the hanging wall of the Absaroka. At each sample site, data on fracture orientation, length, spacing, aperture, geometry, cross-cutting relations (i.e., relative age), geometry of vein-fill material (antitaxial versus syntaxial), and other variables were collected. Many samples were stained using "Dickson's method" with a solution of Alizarin Red-S and potassium ferricyanide dissolved in weak HCl; with this method, calcite turns pale pink to red, ferroan calcite turns purple to royal blue with >Fe, dolomite displays no color, and ferroan dolomite turns pale to deep turquoise with >Fe. Hand-samples were then examined with a Leica S8APO binocular microscope. Several standard and large-format thin-sections were prepared by outside vendors; some were selected for staining with alizarin red-S for visual discrimination of dolomite versus calcite under non-polarized light. Using a Leica DM2500P polarizing binocular microscope, thin-sections were analyzed for: 1) framework constituents, 2) porosity and permeability, 3) diagenetic history, 4) low-temperature hydrothermal alteration, 5) secondary tectonic fabrics (pressure-solution cleavage), and 6) cementation history related to past CO_2 storage. Since most rock samples are carbonates, the "white card" or "diffusive lighting" technique was used for textural and diagenetic analysis. Rock chips from CO_2 reservoir units (e.g., Madison, Nugget, Twin Creek) were taken to Imaging and Chemical Analysis Laboratory (ICAL) on the MSU campus (http://www.physics.montana.edu/ical) for further analysis with the XRD and SEM; gold coating worked best on carbonate chips to reduce "charging" while using the SEM. Lastly, some thin-sections (without cover slips) were analyzed with the new cathodoluminescence microscope in the Department of Earth Sciences "research petrography lab." Cathodoluminescence is an extremely powerful tool for identifying multiple generations of diagenetic cement in thin-sections of carbonate rocks (textures that are otherwise invisible with conventional transmitted light microscopy), particularly those cements containing variable amounts of trace elements (e.g. Mn^{2+}, Fe).

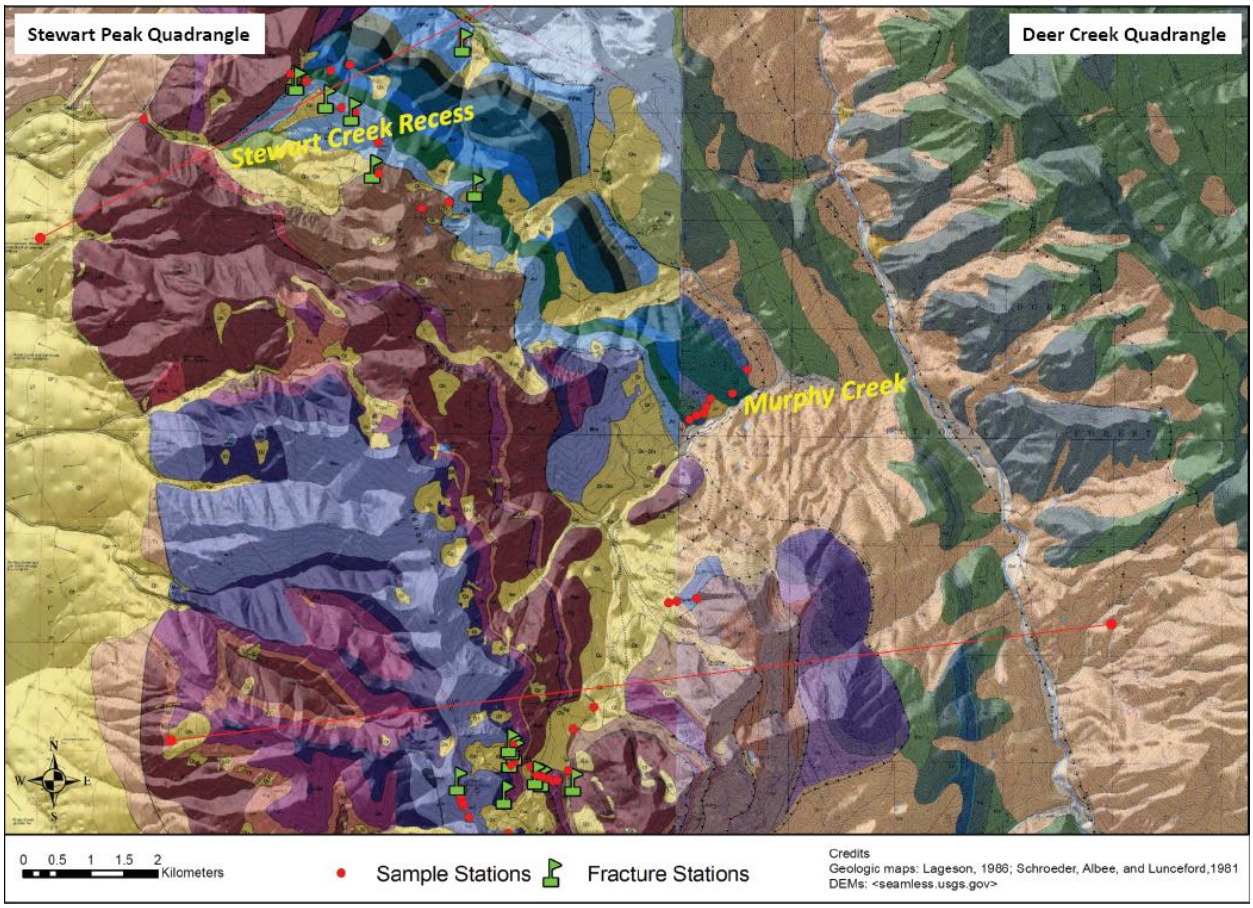

Figure 23. Geologic map of the Stewart Peak quadrangle in the northern Salt River Range, western Wyoming

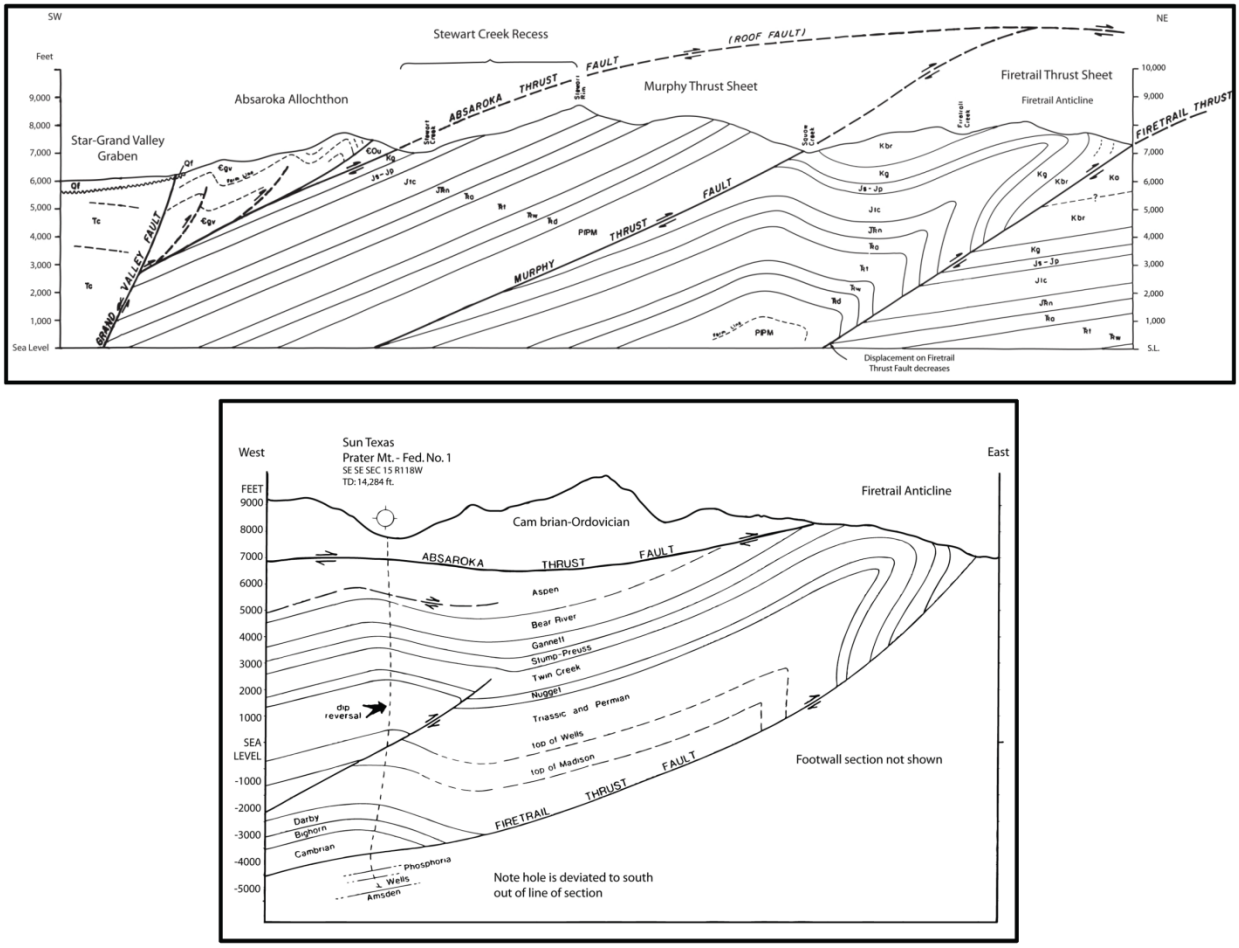

Figure 24. Structural cross-selection. Top: Structural cross-section across the northern part of the Stewart Peak duplex fault zone, northern Salt River Range, western Wyoming. This duplex was a large reservoir for hydrocarbons and CO_2 prior to Neogene uplift and exhumation. Bottom: Structural cross-section across the southern part of the Stewart Peak duplex fault zone, northern Salt River Range, western Wyoming. This cross-section shows the out-of-sequence geometry of the Absaroka thrust fault.

Understanding impact of *CO_2* leakage on shallow groundwater

One possible risk concern for geologic sequestration of CO_2 is impacts resulting from upward leakage through drinking water aquifers. Although CO_2 itself is not toxic, elevated CO_2 concentration could change the geochemical environment in the aquifer and cause aqueous and/or mineral precipitation/ dissolution reactions that might negatively impact drinking water quality. Modeling studies by Wang and Jaffe (2004) suggest that CO_2 leakage into potable aquifers has the potential to enhance trace metal dissolution. Although enhanced trace metal dissolution due to CO_2 has been observed at natural analogue sites such as Mammoth Mountain, CA, it is unknown how common this effect might be either in natural analogue sites or in engineered CO_2 storage systems. Studies of such impacts need to be performed in a broad range of aquifer types which will provide critical information for citing CO_2 storage facilities and

adequately monitoring associated aquifers. We have used an integrated approach combining field data, laboratory experiments, and geochemical modeling, to determine if CO_2 fluxes have caused trace metal mobilization at a natural analogue site in Chimayo, New Mexico (Figure 25). Elevated CO_2 has been documented in several wells in the aquifer in the Chimayo area and is most notably evident in a cold geyser which has erupted through a shallow well twice daily for over 30 years. We have collected and analyzed a number of water samples from the region (Figure 25) to establish groundwater chemistry both in the regional aquifer (at the basin scale) and in the local Chimayo community.

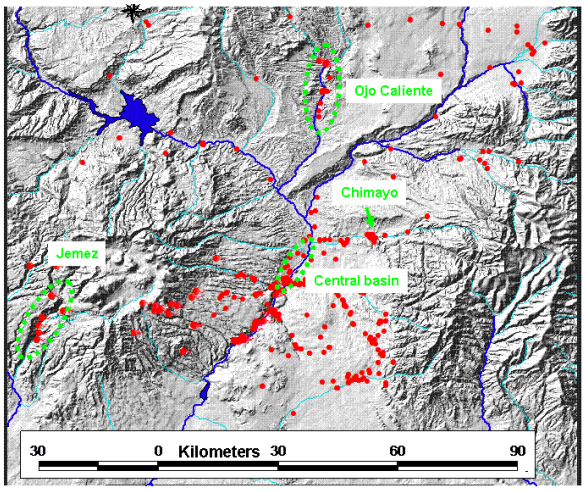

Figure 25. Location of wells and springs with groundwater chemistry data

One trace metal commonly elevated in the regional groundwater is uranium, which is either derived from weathering of granitic clasts in the sediments, roll-front deposits, and/or volcanic ash beds. Sampling of regional ground waters (typically with very low pCO_2 values) has shown very high spatial variability in uranium concentrations, with some evidence that high uranium is associated with high alkalinity (but sometimes with low alkalinity) and with oxidizing environments. The geyser water itself is elevated in uranium, but is well within the background values for waters which are typically in the normal range of pCO_2 (< -2.0). Measured uranium concentrations in the geyser are far below saturation for common uranium minerals, suggesting uranium concentrations are limited either by slow dissolution kinetics or mineral availability or both. In a well near the geyser (also very elevated in pCO_2) uranium is below detection. There are several possible reasons for this, but clearly there are factors controlling uranium concentrations here and elsewhere in the area that are more much important than pCO_2. Based on this evidence, if sequestered CO_2 were to leak through a uranium-containing aquifer the impact on U concentrations would be very difficult to detect.

Although we have not found compelling evidence for CO_2 effects in this aquifer, there are clear impacts of co-solutes originating at depth with the CO_2. For example, the CO_2-enriched geyser water is also elevated in F, Na, Cl, and SO_4. The origin of these co-solutes is unknown; possibly connate brines at depth or enhanced mineral weathering at depth due to the CO_2 plume. Processes occurring at depths well below the shallow drinking aquifers may cause contaminants to rise with the CO_2 and impact water quality through simple mixing. We used geochemical

modeling and major ion data based on field sampling to establish simple reaction paths (some unknown combination of mixing, aqueous complexation, and mineral precipitation /dissolution reactions) that are consistent with measured trends in observed Cl concentration, pCO_2, and pH. The emphasis on these variables was due to the importance of Cl and pCO_2 in defining the degree to which CO_2 and brine has mixed with the aquifer; and pH is both an indicator of mineral reactions (especially with carbonates) and a master variable that will impact trace metal mobility. Second, use the established reaction paths to predict expected trends in trace metal concentrations and compare with measurements.

Basic Geoscience: Pore Scale

Core testing: Version 1, flow-through reactor system (see Hansen 2009 for further details). Reacting fluids, reproduced formation water, and supercritical CO_2 were flowed through Madison Formation rock cores at 55° C, 10.34 MPa (1500 psi) flowing pressure for five days. The core was held at an overburden pressure of 13.79 MPa (2000 psi) for the duration of the experiments. Discrete fluid samples (~15 mL) were taken directly every 24 hours prior to accumulator recharge. Major cation and anion concentrations of the discrete samples were measured via ion chromatography following Montross (2007).

Core testing: Version 2, flow-through reactor system (see Hansen, 2009 for further details). A suite of experiments were conducted to measure various aqueous phase properties (*in situ* pH, EC, pressure, and temperature, and *ex situ* pH and EC) of the brine-CO_2 system under a range of system pressures and temperatures, testing hypotheses 1-3:

1. Mixing brine and supercritical CO_2 at supercritical conditions will reduce brine pH and increase brine electrical conductivity
2. Increased brine TDS will decrease CO_2 solubility
3. Increased temperature will decrease CO_2 solubility

All experiments were conducted in triplicate for 8-10 hour test duration. Experiments to assess the effects of CO_2 on brine pH and composition were conducted with brine only and repeated with a mixture of 0.8 L brine and 1 L CO_2 (measured at 25º C and 0.1 MPa) with each of two brine concentrations, 0.5 and 5 g L^{-1} TDS. Equilibrium pH was modeled using PHREEQC (Parkhurst 1995) for CO_2-brine reactions over the temperature range 45-95 ^oC at 10 ^oC intervals. The brine compositions are detailed in Table 1. Modeled pH values were calculated by equilibrating brines with CO_2 at atmospheric pressure (0.1MPa) as PHREEQC does not have the capacity to include supercritical CO_2 as a variable.

Table 1. Initial conditions for experimental and modeled brines

Brine Solution	T (ºC)	pH	Na^+ (mmol)	Cl^- (mmol)	SO_4^{2-} (mmol)	Mg^{2+} (mmol)	Ca^{2+} (mmol)	HCO_3^- (mmol)
0.5 g L^{-1}	25	6.5	3.2	9.1	0	0.06	2.9	0.06
5 g L^{-1}	25	6.5	32.0	90.7	0	0.6	29.4	0.6

Core-flood experiments were conducted to assess the effects of injecting supercritical CO_2 into brine-bearing Madison Formation rock cores. Each experiment was conducted utilizing Madison Formation rock cores and reproduced Madison formation water for 120 hour test duration. Experiments were conducted with a mixture of 0.8 L brine and 1 L CO_2 (measured at 25º C and 0.1 MPa) with each of two brine concentrations, 0.5 g L^{-1} and 5 g L^{-1} (Table 1), and each of two temperatures, 50° C and 90° C. These experiments were used to address the following hypothesis: reduced brine pH resulting from addition of CO_2 will promote solid-phase dissolution of rock cores. Further, increasing brine TDS and temperature will reduce this effect via hypotheses 2 and 3 (increased brine TDS will decrease CO_2 solubility and increased temperature will decrease CO_2 solubility). *In situ* pH, EC, pressure, and temperature were measured and logged each 30 seconds. Discrete fluid samples, collected at hours 0, 3, 6, 9, 12, 18, 24, 48, 72, 96, and 120 after the start of the experiment, were analyzed for major cation concentration via inductively-coupled plasma mass spectrometry (ICP-MS) in the Center for Biofilm Engineering at MSU. One inch plugs from each end of the tested rock cores were analyzed for porosity and permeability. Four additional core plugs not subjected to CO_2 flood were analyzed for porosity and permeability to assess the degree of natural heterogeneity of these parameters in the rock.

Core testing: Version 3, flow-through reactor system. Samples representing unreactive and reactive lithologies were tested to establish end-member models for the response of reservoir rocks to supercritical CO_2 flooding. Berea formation quartz arenite (>95% quartz) from Cleveland Quarries, Ohio was chosen to represent relatively inert quartz-rich clastic lithologies and Madison formation dolomitic limestone collected in the Black Hills, South Dakota was used to represent more reactive carbonate rock. Most target reservoir rocks are likely to have chemical reactivities somewhere between these bracketing end-members (e.g. carbonate cemented sandstone, impure limestone, marl etc.). In addition to lithology, experimental variables included temperature (~50° C and ~95° C) and brine concentration (~ 1 g L^{-1} and 10 g L^{-1}).

The experiments employed a flow-through core reactor equipped with in-situ pre-core influent pH and post-core effluent pH and conductivity probes for real-time monitoring of changes in fluid chemistry. Periodic discrete sampling of effluent fluids were used to measure changes in major ions in solution, as previously described. Core samples were brine saturated prior to supercritical CO_2 injection and imaged using non-destructive NMR. NMR imaging was used to distinguish between the liquid and solid phase in the core. The same cores were reimaged using NMR after the supercritical CO_2 challenge experiments. A protocol for pixel-by-pixel comparison was used on the pre- and post- CO_2 challenge images to determine the effects on bulk pore volume and geometry of sandstone and carbonate cores.

Basic Geoscience: Basin Scale

The Powder River Basin meets the site screening requirements for GCS shown in Figure 26 (USDOE/NETL, 2010, Table 3.1, p. 12). High produced and resident fluid volumes define five reservoir classes, which include potable water, brine, corrosive gas, oil, condensate, CO_2, and both biogenic and thermogenic gas as shown in Figure 27 and Figure 28, and Table 2 (Dolton 1995; Anna 2010). Published geologic maps and fault, lineament and fracture patterns define the

structural basin (Blackstone 1983; Slack 1981; Love and Christiansen 1985; Lisenbee 1988, 1993; Ellis and Colton 1994; Stone 1993; 2002; 2003). Three sources of data created using various tools in different phases of the research guide experimental methods centered on:

1. Geologic characterization using Petra database,
2. Construction of Petrel geomodels,
3. Assessment of conventional methods for calculating net pore volume.

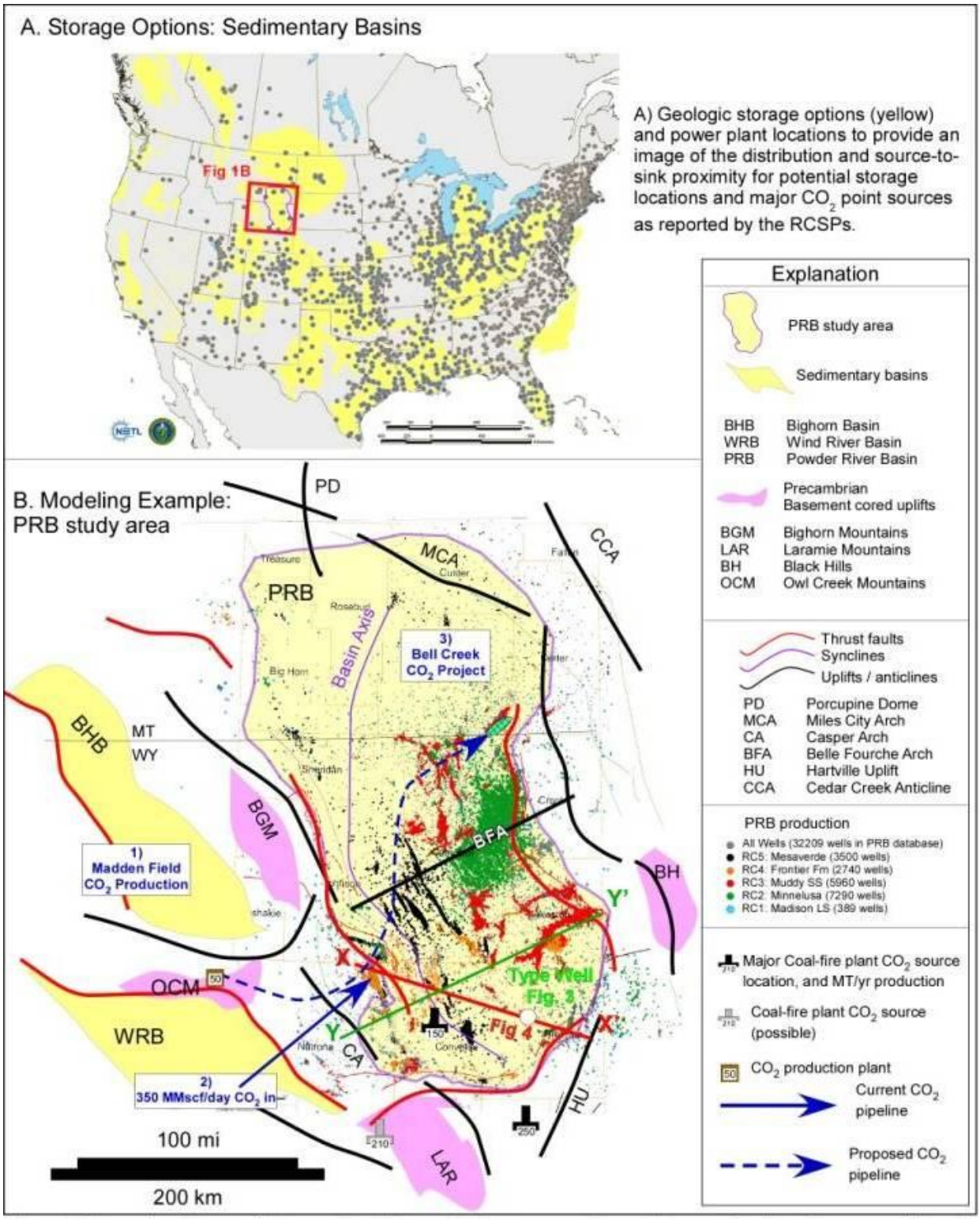

Figure 26. Maps of study area

Figure 26A is an overlay of the geologic storage options and power plant locations to provide an

image of the distribution and source-to-sink proximity for potential storage locations and major CO_2 point sources as reported by the Regional Carbon Sequestration Partnerships. Figure 26B is a summary map of PRB study area showing structural setting, data coverage and GCS infrastructure. Over 30,000 wells were used, from the more than 100,000, in geologic analysis and five main reservoir classes are penetrated (RC1-5), which are highlighted based on production type and formation at total depth. Coal-fired power plants, with present and proposed CO_2 pipelines are indicated. Note the type of the well in Figure 27 and structural cross section X-X' in Figure 28 shown.

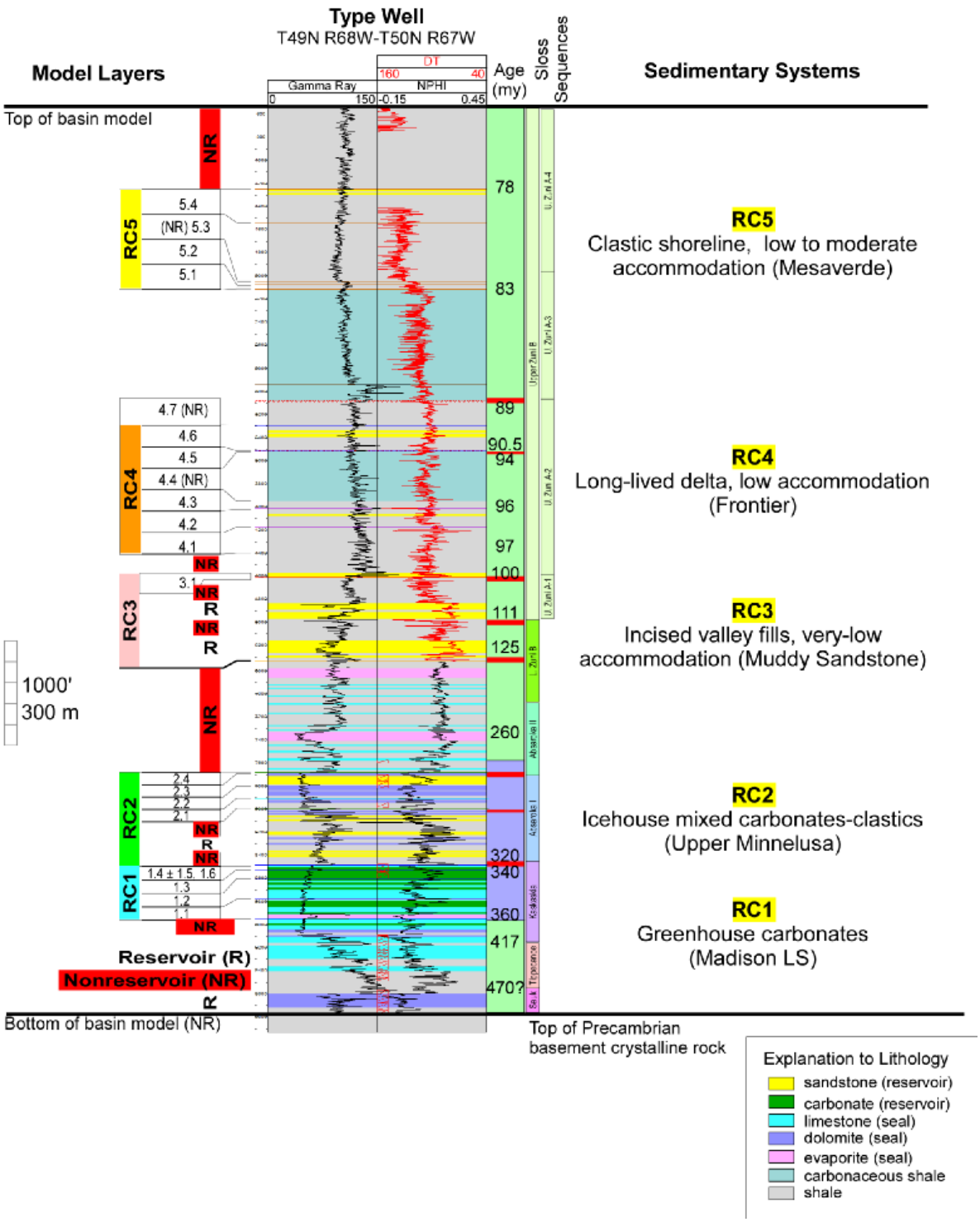

Figure 27. Composite type well showing how modeling structure relates to stratigraphy and the vertical distribution of RCs (RC1-5)

It is important to note in Figure 27 that RC4 is example interval for high-resolution methods. RCs have different sedimentary systems in each; the example used in this model for each is

indicated in parenthesis. These RCs represent approximately 40% of Paleozoic and Mesozoic fill. Also notice the schematic heterogeneity produced by the architecture of each RC in Figure 28.

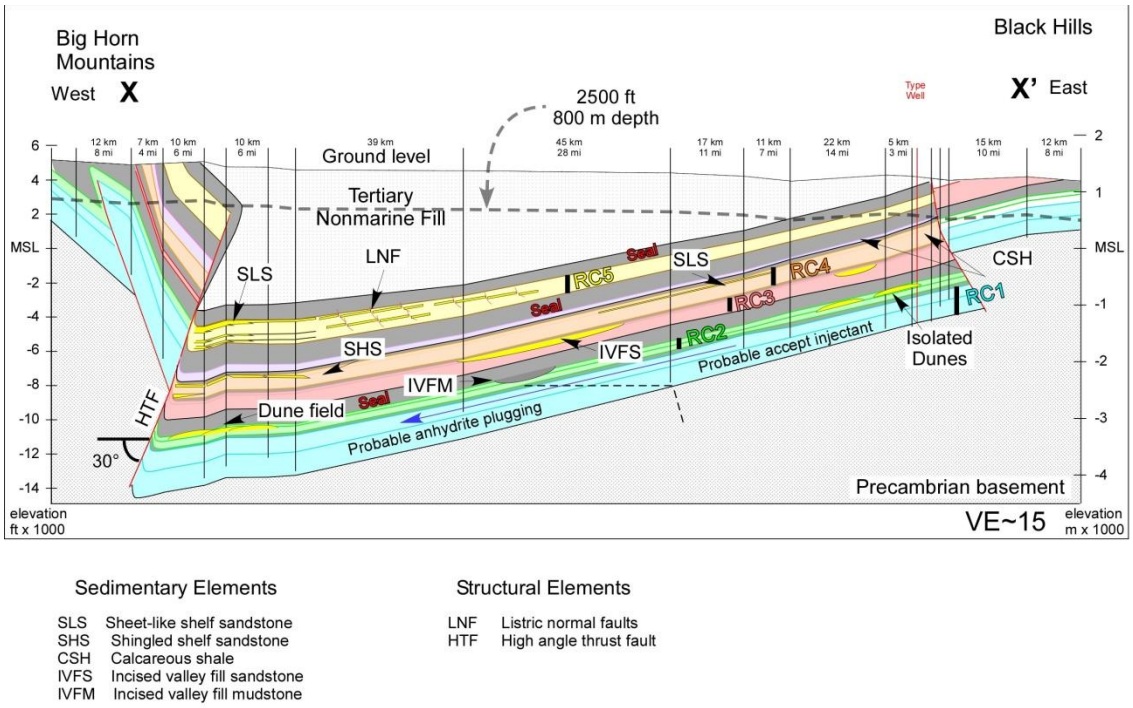

Figure 28. Structural cross section showing modeling structure and stratigraphic distribution of RCs (RC1-5) and basin bounding faults.

Table 2. Reservoir classes are defined by multivariate attributes at multiple scales

RC # and Sedimentary Attriubutes	1: Carbonate Platforms (Permian Madison LS)	2: Mixed Carbonate - Clastic Coastal Systems (Pennsylvanian -Permian Tensleep/Minnelusa)	3: Incised Valley Fill Systems (L. Cretaceous Lakota, Fall River, Muddy SS)	4: Low Accommodation Delta-shelf systems (M. to U. Cretaceous Frontier Fm)	5: Clastic Shorelines (U. Cretaceous U. Steele and L. Mesaverde)
Basin Type	cratonic	foreland	cratonic	Early foreland	Late foreland
Lithologies	Limestone: Φ: 0-5%; K: lo Dolomite: Φ: 15-35%; K: hi Evaporite: Φ: <3%; K: lo Karst breccia: Φ: 0-50%; K: lo-hi	Limestone Φ: <5%; K: V. lo Dolomite Φ: 10-15%; K: V. lo Evaporite: Φ: <3%; K: v. lo Sandstone: Φ: 15-20%; K: v. hi Mudstone	Fluvial SS: Φ 11%; K: v. hi Estuarine SS: Φ 4%; K: mod Shoreface (valley fill): Φ 12%; K v hi Mudstone	Shoreface SS: Φ 10-12%, K mod Reworked Shoreface SS: Φ 2-8% Hyperpycnite SS: Φ 1-11% Mudstone Carbonaceous Mudstone	Strandline shoreface: Φ 10-14%; K hi Offshore bar SS: Φ 8-10%; K hi Muddy slope: Φ <4% Mudstone
Total and net thickness Sed. accum. Rate	0-1400 ft 200-400 ft < 120 ft/my	0-600 ft 200-300 ft 150 ft/my	50-150 ft 40-75 ft 75 ft/my	Compensatory lobate deltaic clastic wedge	800-1000 ft <100' 250 ft/my
Well log data quantity and quality	100 wells 18% DN combo	800 wells 80% DN combo	1300 wells 90 % DN combo	1100 wells 60% DN combo	1300 wells 50% DN combo
Age Cycle forcing Duration Hierarchy	Mississippian (large continental seas) Greenhouse 11 my 3 orders (2-4th)	Lower Permian Icehouse - more hi frequency, hi mag SL changes 4-6 my 3 orders (2-4th)	Lower Cretaceous (Boreal/Tethian cratonic seas) Greenhouse 2 my 3 orders (2-4th)	Mid Cretaceous (Iniation of Western Cretaceous Seaway) Greenhouse 8 my 6 orders (2-6th)	Upper Cretaceous (Culmination of Western Cretaceous Seaway) Greenhouse 5 my 4 orders (2-5th)
Surface Types Seal Type	Karst Dissolution vugs Subaerial erosion Seal irregular and discontinuous	IVF unconf. Flooding surface Evarporite caps Shale drape	IVF unconf. Flooding surface Shale drape	IVF unc. Forced regression unc. Transgressive surface of erosion	Transgressive surface of erosion Shale drape
Sedimentation regions Shape Strataregions	laterally continuous cratonic carbonate platform with large shelf and many isolated buildups	coastal eolian shoreface, sabkha, wadi, shallow water carbonates	Flood-based back-filling valley fill encased in mudrocks long linear high perm bodies	Compensatory lobate deltaic (laterally discontinuous)-hyperpycnite (laterally continuous) clastic wedge	Linear, fault-controlled clastic Strandplain wedge partitioned by mudrocks
Connectivity Vertical Horizontal Lateral	Widespread high CPV layers bound by no flow limestones	clastic wedge segregated by widespread dolomites, hi Kh, low Kv	Long linear channel belts with high Kh/Kv	Isolated flow units, moderate Kh, variable Kv	Thin high Kh zones, very vertically partitioned
Connected Pore Volume	Largest pore volume resource	Variable high volume	Mod low	Mod hi	Mod high
CO2 migration Rate	low to very low	Locally high	High leakage pathway	Moderate	High leakage pathway Connected to faults

Explanation to colors

Favorable (e.g., lo risk + hi volume)	Mod. Favorable
Mod. unfavorable	Unfavorable (e.g., hi risk ± low vol)

Geologic Characterization using Petra Database. The Petra database contains well log and core data used to define the hierarchy of sedimentary attributes and correlate stratigraphic surfaces in maps and cross sections (Figure 29 and Figure 30). About 4000 of the 5260 digital wells contain quantitative *Log Ascii Standard* (LAS) measurements used to estimate porosity. This includes 1540 wells with high-quality, normalized density (RHOB) and neutron-porosity (NPHI) logs, and 1290 wells with good-quality density logs, and 1170 moderate-quality sonic logs. Core sedimentology relates process-facies and sedimentation events to formative processes affecting porosity and permeability and defines the small-scale heterogeneity (Willis and White 2000; Borer 2005). This is demonstrated in

Table 3. Sedimentary body analysis characterizes larger three-dimensional architectural elements whose arrangement determines connectivity and continuity affecting intermediate-scale heterogeneity. Correlation of architectural elements establishes the continuity and origin of stratigraphic surfaces that define stratigraphic sequences and component sedimentation regions; the latter representing spatial domains with similar attributes, like thickness, lithology, sedimentary bodies, sedimentation events, process facies, and rock properties (Figure 30). Time-significant surfaces (e.g., unconformities, condensed intervals recording sediment starvation, or volcanic ash event beds) bracket stratigraphic sequences of genetically related rock volumes of varying duration and resolution. These methods relate the hierarchy of formative geologic processes to multiple scales of heterogeneity.

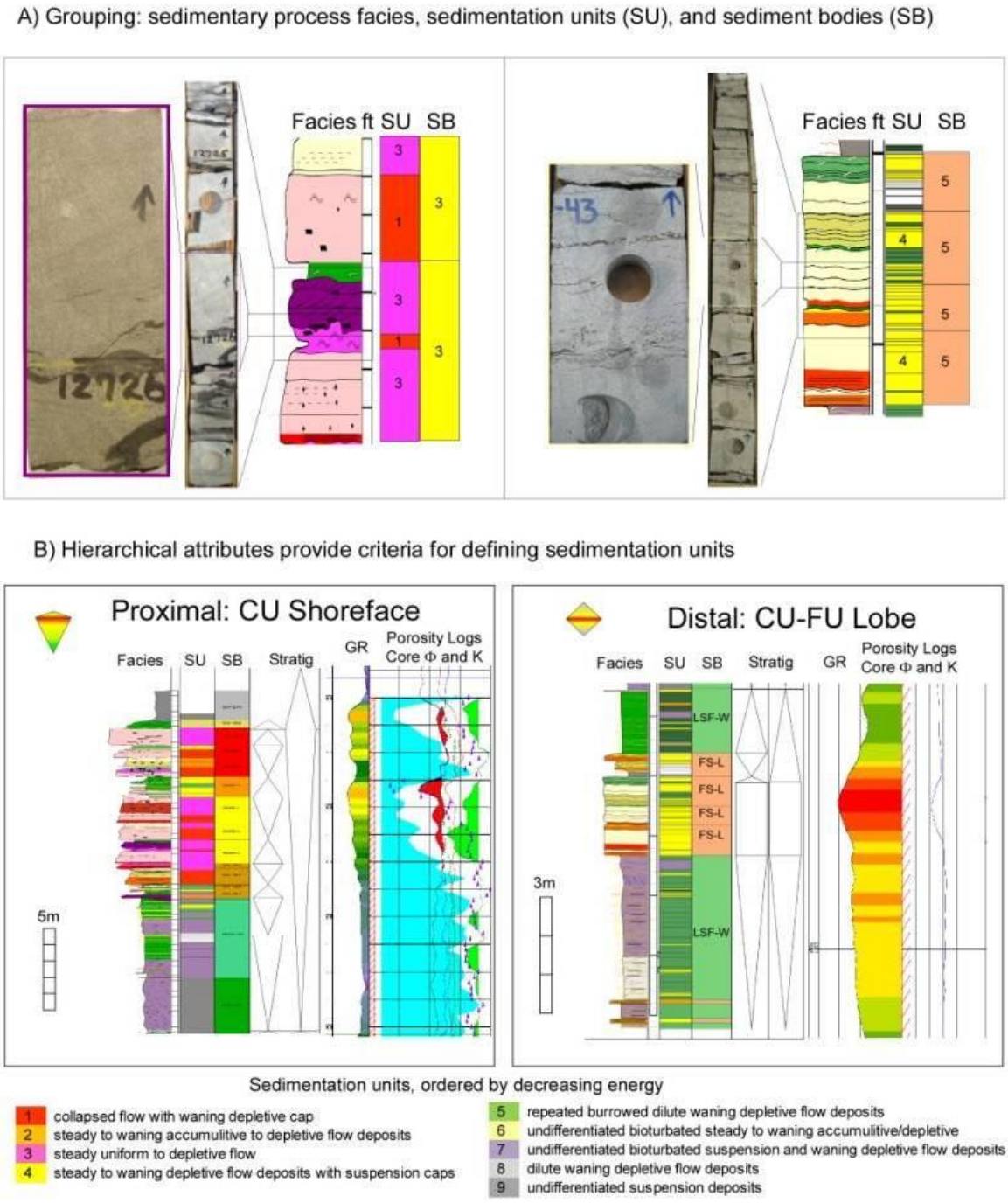

Figure 29. Steps taken for upscaling core facies (A) into sedimentation units and then sedimentary bodies (B) 3D Sedimentary bodies defined by facies and sedimentation units form characteristic log shapes represent sedimentation regions. See Table 2 and

Table **3** for Facies, Sedimentation Units and Bodies explanations.

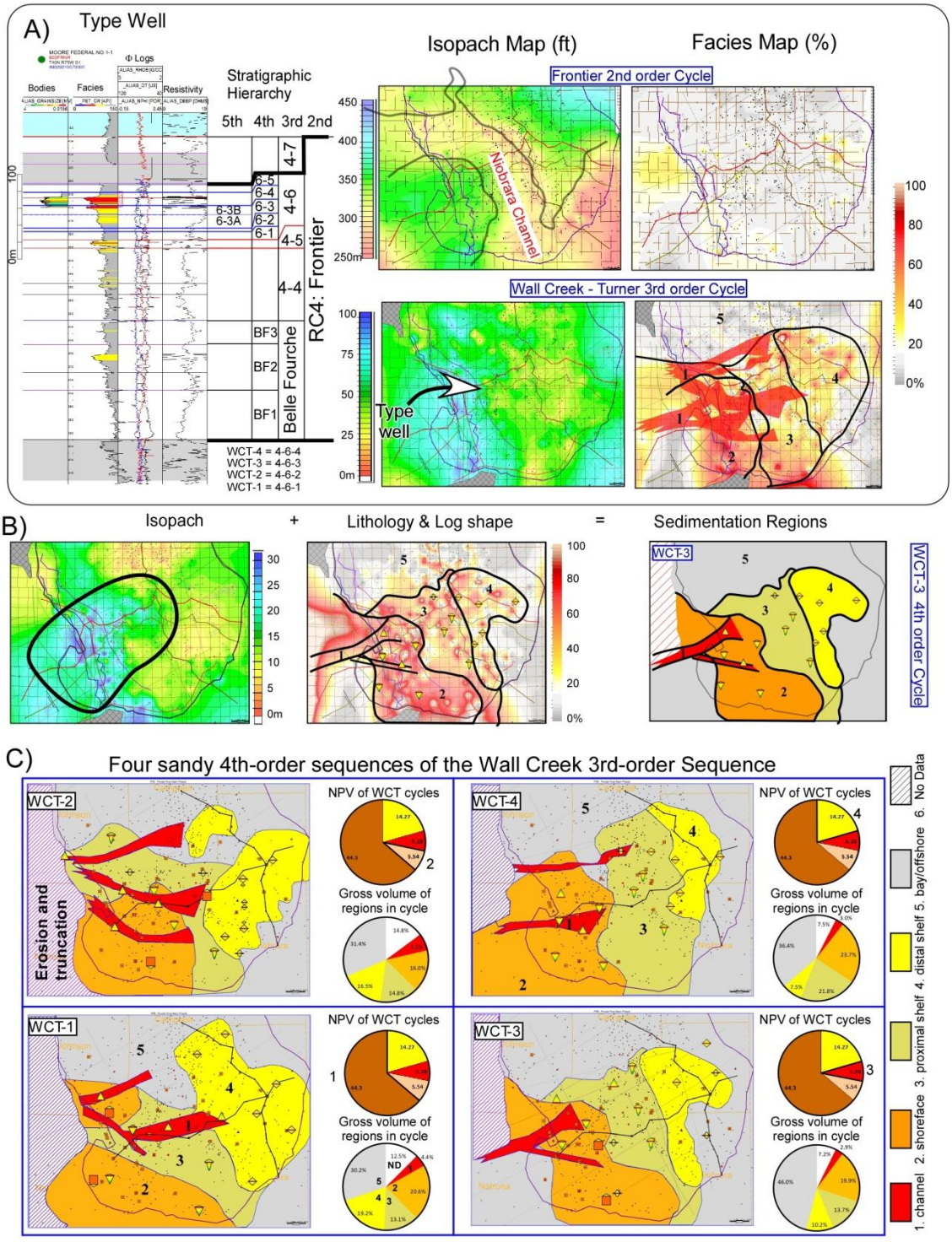

Figure 30. Defined hierarchy of sedimentary attributes and correlated stratigraphic surfaces in maps and cross sections derived from the Petra database

Sedimentation regions are best defined at the highest resolution possible, typically at the 4th or when possible 5th-order as shown in Figure 30A and B Thickness maps and facies and lithology maps are evaluated in conjunction with log shape to determine predominant architectural style in a mapping domain. Figure 30C provides boundaries for rock property distribution strategies. 1000 wells with high-quality logs, core reports and sedimentary profiles were used in all these maps in this figure.

Table 3. Facies descriptions and interpretations help define grouping strategies

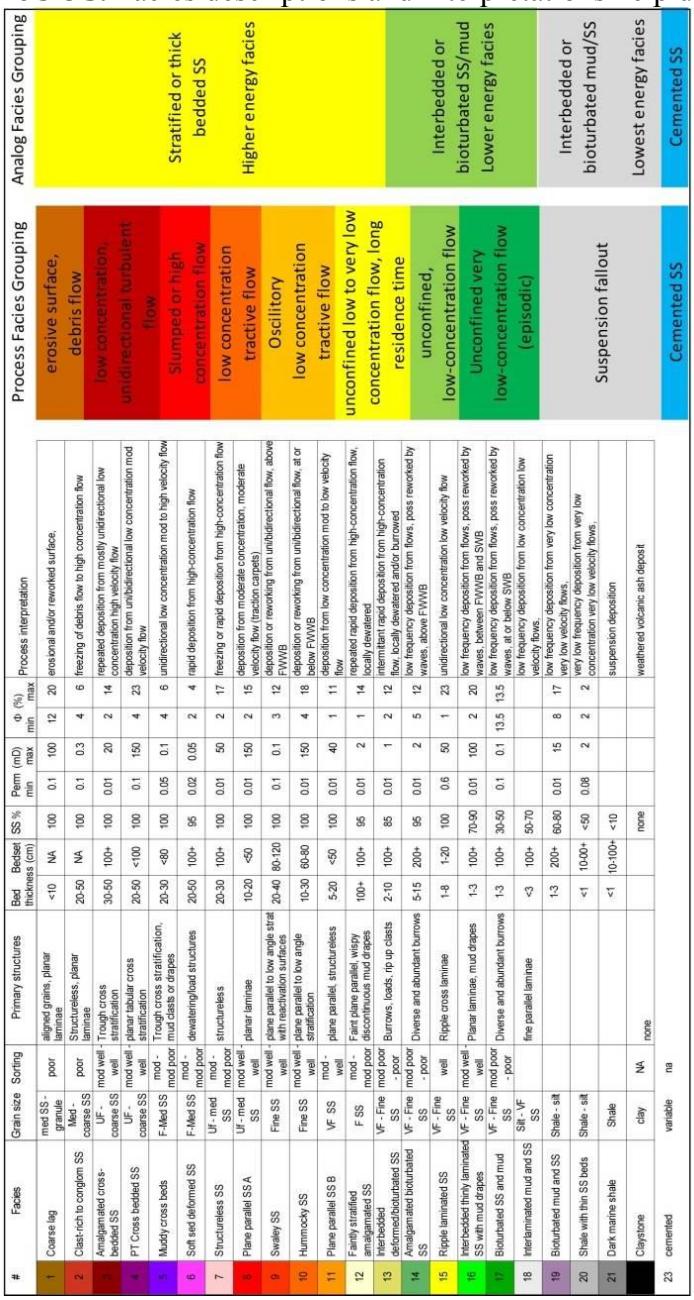

#	Facies	Grain size	Sorting	Primary structures	Bed thickness (cm)	Bedset (cm)	SS %	Perm (mD) min	Perm (mD) max	Φ (%) min	Φ (%) max	Process interpretation	Process Facies Grouping	Analog Facies Grouping
1	Coarse lag	med SS - granule	poor	aligned grains, planar laminae	<10	NA	100	0.1	100	12	20	erosional and/or reworked surface,	erosive surface, debris flow	Stratified or thick bedded SS
2	Clast-rich to conglom SS	Med - coarse SS	poor	Structureless, planar laminae	20-50	NA	100	0.1	0.3	4	6	freezing of debris flow to high concentration flow		
3	Amalgamated cross-bedded SS	UF - coarse SS	mod well - well	Trough cross stratification	30-50	100+	100	0.01	20	2	14	repeated deposition from mostly unidirectional low concentration high velocity flow	low concentration, unidirectional turbulent flow	
4	PT Cross bedded SS	UF - coarse SS	mod well - well	planar tabular cross stratification	20-50	<100	100	0.1	150	4	23	deposition from unidirectional low concentration mod velocity flow		
5	Muddy cross beds	F-Med SS	mod - mod poor	Trough cross stratification, mud clasts or drapes	20-30	<80	100	0.05	0.1	4	6	unidirectional low concentration mod to high velocity flow		
6	Soft sed deformed SS	F-Med SS	mod - mod poor	dewatering/load structures	20-50	100+	95	0.02	0.05	2	4	rapid deposition from high-concentration flow	Slumped or high concentration flow	
7	Structureless SS	Uf - med SS	mod - mod poor	structureless	20-30	100+	100	0.01	50	2	17	freezing or rapid deposition from high-concentration flow		
8	Plane parallel SS A	Uf - med SS	mod well - well	planar laminae	10-20	<50	100	0.01	150	2	15	deposition from moderate concentration, moderate velocity flow (traction carpets)	low concentration tractive flow	Higher energy facies
9	Swaley SS	Fine SS	mod well - well	plane parallel to low angle strat with reactivation surfaces	20-40	80-120	100	0.1	0.1	3	12	deposition or reworking from unibidirectional flow, above FWWB		
10	Hummocky SS	Fine SS	mod well - well	plane parallel to low angle stratification	10-30	60-80	100	0.01	150	4	18	deposition or reworking from unibidirectional flow, at or below FWWB	Oscillitory low concentration tractive flow	
11	Plane parallel SS B	VF SS	mod - well	plane parallel, structureless	5-20	<50	100	0.01	40	1	11	deposition from low concentration mod to low velocity flow		
12	Faintly stratified amalgamated SS	F SS	mod - mod poor	Faint plane parallel, wispy discontinuous mud drapes	100+	100+	95	0.01	2	1	14	repeated rapid deposition from high-concentration flow, locally dewatered	unconfined low to very low concentration flow, long residence time	
13	Interbedded deformed/bioturbated SS	VF - Fine SS	mod poor - poor	Burrows, loads, rip up clasts	2-10	100+	85	0.01	1	2	12	intermittant rapid deposition from high-concentration flow, locally dewatered and/or burrowed		Interbedded or bioturbated SS/mud Lower energy facies
14	Amalgamated bioturbated SS	VF - Fine SS	mod poor - poor	Diverse and abundant burrows	5-15	200+	95	0.01	2	5	12	low frequency deposition from flows, poss reworked by waves, above FWWB	unconfined, low-concentration flow	
15	Ripple laminated SS	VF - Fine SS	well	Ripple cross laminae	1-8	1-20	100	0.6	50	1	23	unidirectional low concentration low velocity flow		
16	Interbedded thinly laminated SS with mud drapes	VF - Fine SS	mod well - well	Planar laminae, mud drapes	1-3	100+	70-90	0.01	100	2	20	low frequency deposition from flows, poss reworked by waves, between FWWB and SWB	Unconfined very low-concentration flow (episodic)	
17	Bioturbated SS and mud	VF - Fine SS	mod poor - poor	Diverse and abundant burrows	1-3	100+	30-50	0.1	0.1	13.5	13.5	low frequency deposition from flows, poss reworked by waves, at or below SWB		
18	Interlaminated mud and SS	Slt - VF SS		fine parallel laminae	<3	100+	50-70					low frequency deposition from low concentration low velocity flows.		
19	Bioturbated mud and SS	Shale - slt			1-3	200+	60-80	0.01	15	8	17	low frequency deposition from very low concentration very low velocity flows,	Suspension fallout	Interbedded or bioturbated mud/SS Lowest energy facies
20	Shale with thin SS beds	Shale - slt			<1	10-00+	<50	0.08	2	2	2	very low frequency deposition from very low concentration very low velocity flows.		
21	Dark marine shale	Shale			<1	10-100+	<10					suspension deposition		
	Claystone	clay	NA	none			none					weathered volcanic ash deposit	Cemented SS	Cemented SS
23	cemented	variable	na											

When defining analog facies from log suites as shown in

Table 3, it is necessary to group based on the scale that the logs permit recognition. For example, all the facies 1-13 were indistinguishable from the IF-THEN statements, so were lumped into "higher energy facies". See Appendix B for statistical analysis of well-log generated analog facies.

Three-fold stratigraphic hierarchy is the minimum requirement for modeling large subsurface volumes. Error! Reference source not found. is an image of the the three-fold stratigraphic ierarchy. Time scale from Gradstone, 2004 and biozone data from Merewether et al., 2007.

Construction of Petrel Geomodels. Geomodel construction in Petrel requires the conversion of qualitative geologic data into quantitative analog data distributed within a 3D model grid of uniform cells. The cells are 800 m (874.89 yards) on each side and 1 to 3 m (1.09 to 3.28 yards) thick. Two calculated logs in Petra (total porosity and shale volume) establish the effective porosity (Asquith and Krygowski 2004) imported into the Petrel model. Petrophysical measurements of core permeability are used to estimate log permeability (Figure 31 and Figure 32). Numeric cutoffs applied to multiple, core-calibrated, well-log measurements (e.g., if-then statements, fuzzy logic, etc.) define analog facies (e.g., vertical changes in values from multiple log measurements). Vertical proportion curves control vertical probability distributions of analog facies, which together with log shape are used to estimate sedimentary bodies (Borer 2005). Isopach, lithology and areal proportion maps (including azimuth and lateral changes) are used to group well data into discrete modeling domains, here termed "sedimentation regions". These attributes are integrated with published outcrop studies (e.g., Kerr et al. 1986; Tillman et al. 1987; Gustason et al. 1988; Elrick 1990; Bhattacharya and Willis 2001; Montgomery et al. 2001) to guide property distributions, between-well correlations and region limits within model layers. Sparse data in the deepest reservoir class (Madison Limestone) is supplemented with comparable subsurface data from adjacent basins (Elrick and Read 1991; Smith et al. 2004; Sonnenfeld 1996; Sonnenfeld pers. comm. 2010) and hydrologic studies from the basin margin (e.g., Huntoon 1976; 1985; Downey 1984; Downey and Dinwiddie 1988).

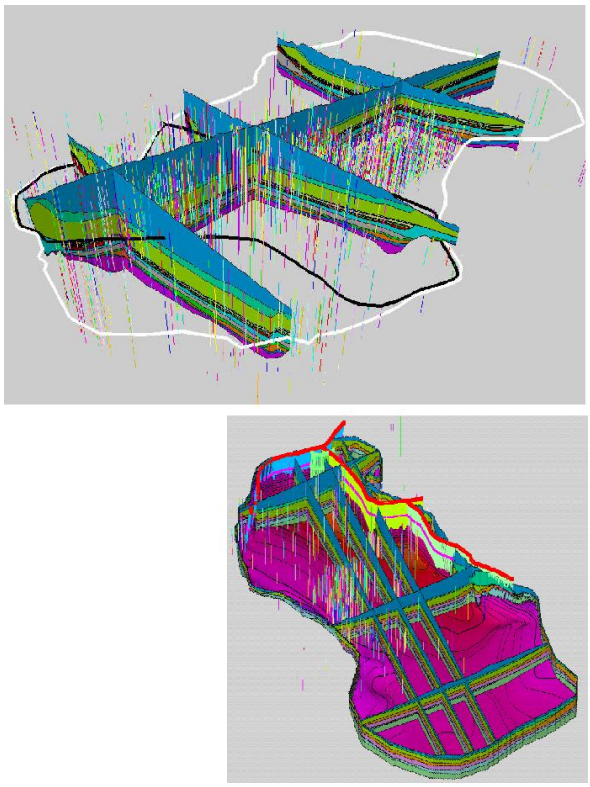

Figure 31. 3-D basin model showing wells and RC4 study area

Three thousand wells are shown in Figure 31 as sticks and fence which shows how RCs are distributed. PRB model shows basement surface with faults intersecting western side in the below figure. Modeling layers are highlighted on the basin rim. White outline of PRB study area is approximately 400 km (248.55 miles) north-south and 200 km (124.27 miles) west-east.

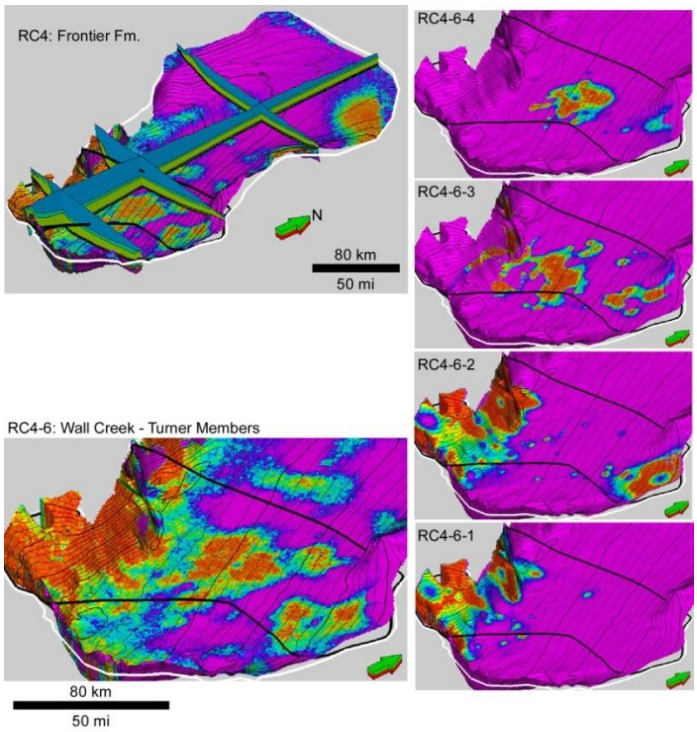

Figure 32. 3-D basin model demonstrating importance of hierarchy

Upper left image in Figure 32 shows porosity distribution in RC4 with fence diagram at 200-300 m (218.72-328.08 yards) thick. The lower left image shows sector model boundaries and general porosity distribution based on averaging the entire RC4-6 at 50-60 m (54.68-65.62 yards) thick interval. The right images from bottom to top display the four small-scale sequences at 10-20 m (10.94-21.87 yards) thick and better document the migration of porosity distribution upward through the medium-scale sequence of RC4-6. The black polygon is the approximate area of detailed study area.

Assessment of Conventional Methods for Calculating Net Pore Volume. Pore volume calculations multiply average porosity values (using published data from producing oil fields WGA, 2000; WOGCC 2008-2009) by sequence-based volumes using two methods: *factor* (one average value assigned to the entire volume) versus *region* (multiple averaged values constrained by different discrete spatial regions within the volume). Sequence-defined (second- through fourth-order, e.g., Mithchum and Van Wagoner, 1991) volumes are constrained by net porosity to gross (NTG) interval thickness maps generated by (1) creating NTG maps using porosity estimated using gamma-ray logs in Petra, (2) calculating logs porosity, (3) importing porosity logs into Petrel, (4) distributing porosity in Petrel model, and (5) using more data-rich Petra NTG maps to edit Petrel volumes. The field porosity values are not necessarily representative of the range of values in the model and do not account for heterogeneity.

The factor and region methods are applied to four different scenarios, each using thickness values based on the 3D surfaces rather than averaging sequence thickness at each data point. The first scenario estimates reservoir pore volumes using methods (i.e., area x thickness x average

porosity) similar to Fischer et al. (2005, pg. 10). The difference being porosity values from field data are constrained by their position within varying scale sequences in each reservoir class. The second scenario calculates RC pore volumes for up to five, third-order sequences. The third scenario uses third-order sequences, but adds up to five sedimentation regions to each sequence. The fourth scenario, only done for RC4, incorporates higher resolution, fourth-order sequences with regions (Figure 33).

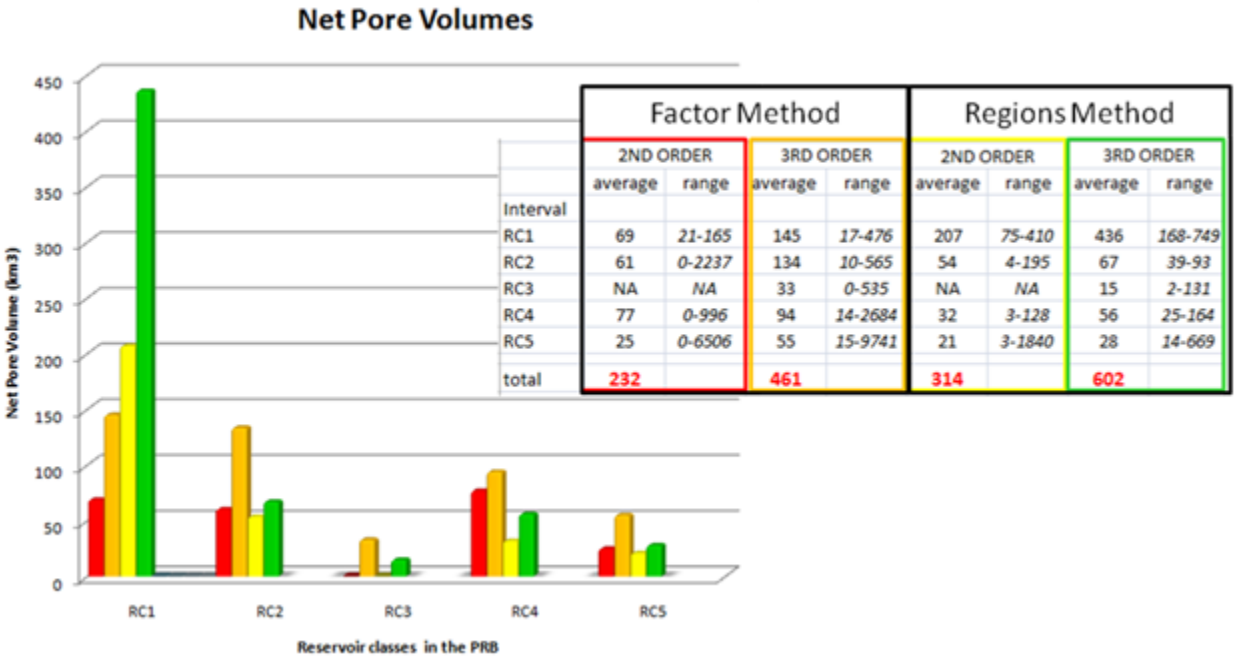

	Factor Method				Regions Method			
	2ND ORDER		3RD ORDER		2ND ORDER		3RD ORDER	
	average	range	average	range	average	range	average	range
Interval								
RC1	69	*21-165*	145	*17-476*	207	*75-410*	436	*168-749*
RC2	61	*0-2237*	134	*10-565*	54	*4-195*	67	*39-93*
RC3	NA	*NA*	33	*0-535*	NA	*NA*	15	*2-131*
RC4	77	*0-996*	94	*14-2684*	32	*3-128*	56	*25-164*
RC5	25	*0-6506*	55	*15-9741*	21	*3-1840*	28	*14-669*
total	232		461		314		602	

Figure 33. Graph summarizing impact of scale on net pore volumes

Figure 33 is a summary of the impact of hierarchical stratigraphic framework and sedimentation regions on net pore volume (km3). Calculations compared between factor (using one average value across entire interval) and regions methods (constraining average values to discrete modeling domains characterized by similar properties.

RESULTS AND DISCUSSIONS

Improvement of Computational Methods

In task 1, LBNL carried out development and applications of the TOUGH2 codes for GCS studies. For example, the equation of state module for water, brine, and CO_2 under gaseous and supercritical conditions was developed. This code, TOUGH2/ECO$_2$N, made possible accurate reservoir simulations for numerous GCS demonstration sites, in addition to many design and theoretical studies. Similarly, hysteretic capillary pressure and relative permeability methods were developed and implemented into TOUGH2 under task 1. TOUGHREACT (the second-most requested piece of software after TOUGH2 from the Energy Science and Technology Software Center) was also updated and extensively tested and applied under task 1. ZERT also

supported the use of TOUGH2/EOS7CA for the shallow subsurface modeling carried out for the Frio CO_2 release test. Finally, LBNL's ZERT task 1 supported the extension of LBNL's work on gas equations of state work to a web-based tool called WebGasEOS (http://esdtools.lbl.gov/gaseos/) that receives growing use from researchers all over the world.

In addition to the code development work and related releases to share this software with the broader community, the investigators also applied their codes to a variety of problems and they published numerous papers on their studies. Some highlights of results of LBNL simulation studies include (i) the finding that runaway CO_2 discharges up a fault appear unlikely due to phase interference effects, (ii) dry-out and pore clogging due to halite precipitation around CO_2 injection wells can be inhibited by fresh water injection, (iii) cycling flows of alternating water and CO_2 are likely up wells undergoing CO_2 leakage, (iv) special logic for hysteretic relative permeability modeling is needed for CO_2 injection into depleted gas reservoirs, (v) Pitzer and Debye-Hückel models predict roughly the same mineral trapping of CO_2, and (vi) supercritical CO_2 is the primary phase present (dominant over dissolved CO_2 in brine, e.g.) even after 1,000 years.

Accomplishments under task 1 over the course of the ZERT program funding include a number of advancements: 1) kinetic dissolution model, 2) coupled heat transport for nonisothermal environments, 3) geochemical reactive transport through the development of the ECKEChem module, 4) supercritical to sub-critical transition and near-surface processes including air, 5) pressure-limited injection well model, and 6) boundary-fitted orthogonal grid systems. These advancements have transformed the STOMP-CO_2 simulator from a single process simulator to a coupled HTC-process simulator that is being used in several regional partnership pilot studies, industrial CCS projects, and the FutureGen project.

Accomplishments under task 3 were obtained by developing a numerical model/well test simulations for a variety of leakage and hydrologic boundary scenarios within a multi-aquifer/caprock system. The numerical simulations provided synthetic aquifer pressure responses for various caprock leakage conditions subjected to barometric pressure fluctuations. The leakage/boundary conditions investigated included conditions commonly examined for hydrologic test conditions: constant-head and no-flow boundaries (Aquifer 1 and 3; Figure 34) and with and without caprock storage (Caprock 2 and 3; Figure 34). From these synthetic aquifer pressure response data sets, diagnostic barometric response plots will be developed that can be used to identify and characterize various caprock leakage conditions. These newly developed barometric response models will extend previous models developed for non-leaky confined aquifer systems.

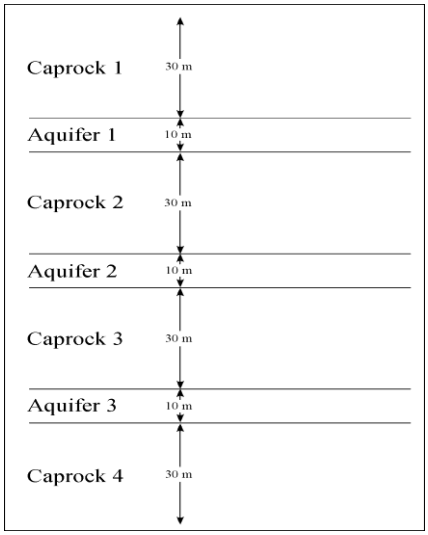

Figure 34. Conceptual multi-aquifer caprock. system

Mitigation Methods

Biofilm growth and permeability change under high pressure (Phase I, II, and III). Two high pressure experiments were performed in order to assess how biofilm would grow under high pressure, and how this would affect permeability of the sandstone core. During experiment 1 the core was challenged with supercritical CO_2 at 500 hours. During experiment 2, the core biofilm was (i) starved with a 4% brine solution at 300 hours, (ii) challenged with supercritical CO_2 at 694 hours, (iii) starved with a 4% brine solution beginning at 766 hours, and (iv) again challenged with supercritical CO_2 at 783 hours. A permeability decrease was observed in both experiments (Figure 35). Initial permeability was 39 and 47 md respectively in experiments 1 and 2, immediately prior to core inoculation. Permeability decreased rapidly by between 82% and 85% during the first 50 to 80 hours to ~ 7 md. This equated to a permeability decrease of 0.49 md hr^{-1} and 3.2 md hr^{-1} during experiments 1 and 2 respectively. Permeability in both the experiments then exhibited a slight increase up to 120 hours, and then decreased to < 2.5 md by 200 hours. The maximum reduction in permeability relative to the initial permeability of the core was 95 and 99 % in experiments 1 and 2 respectively.

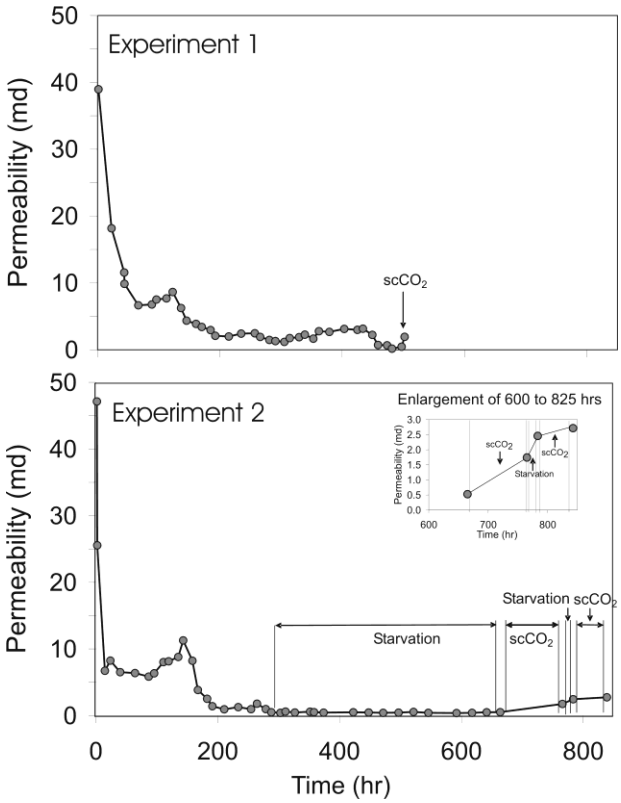

Figure 35. Changes in permeability over time during experiments 1 and 2.

Starvation challenge effect on permeability. During experiment 2, the nutrient media was switched to a 4% brine solution between 300 and 663 hours in order to starve the biofilm, and determine the effect to the resilience of the biofilm through subsequent changes in permeability. This 363 hour starvation period resulted in negligible changes in the permeability of the sandstone core, which remained at ~ 0.5 md throughout. A second starvation period was applied between 766 and 783 hours, which resulted in a slight increase in permeability between 1.74 and 2.45 md, which was only a 1.5% increase relative to the initial permeability of the core (Figure 35). These data demonstrate that starving the biofilm did not result in a significant increase in permeability, and the resilience of the biofilm remained intact under high pressure conditions.

Supercritical CO_2 *challenge effect to permeability.* Supercritical CO_2 challenges were performed at the end of experiment 1 between 497 and 502 hours (Figure 35). Permeability before the challenge was 0.46 md, which after a 5 hour $scCO_2$ challenge increased to 1.93 md. This was only a 3.8 % increase relative to the initial permeability of the core. During experiment 2, two $scCO_2$ challenges were performed. During the first, the permeability increased from 0.51 md before the challenge to 1.74 md after a 71 hour challenge between 694 and 765 hours (Figure 35). This was only a 2.6 % permeability increase relative to the initial permeability of the core. During the second challenge, the permeability increased from 2.45 md before the challenge, to 2.75 md after a 48 hour challenge. This was only a 0.64 % increase relative to the initial permeability of the core. These data clearly demonstrate that $ScCO_2$ challenges do not significantly increase the permeability of the core, even when the challenge lasts for prolonged periods up to 71 hours.

$CaCO_3$ Profile and Occupied Pore Space along Length of the Column (Phase IV and V). After 58 days, biofilm-mineral deposits resulted in complete plugging of the column (i.e. growth media could no longer be pumped through the column). The average calcium carbonate content, measured as mg $CaCO_3$ per gram of sand was 479 ± 29 mg $CaCO_3$/g sand in the first section near the inlet of the column. The mass was lower for the remaining five sections in the column, averaging 239 ± 26 mg/g (Figure 36). Similar results are anticipated for radial flow experiments. This somewhat constant mass distribution of calcium carbonate is encouraging for achieving uniform calcium carbonate distribution along the flow path, particularly when compared with similar results from other studies. However, the 490 mg $CaCO_3$/g sand value near the column entrance is still considered unacceptably high.

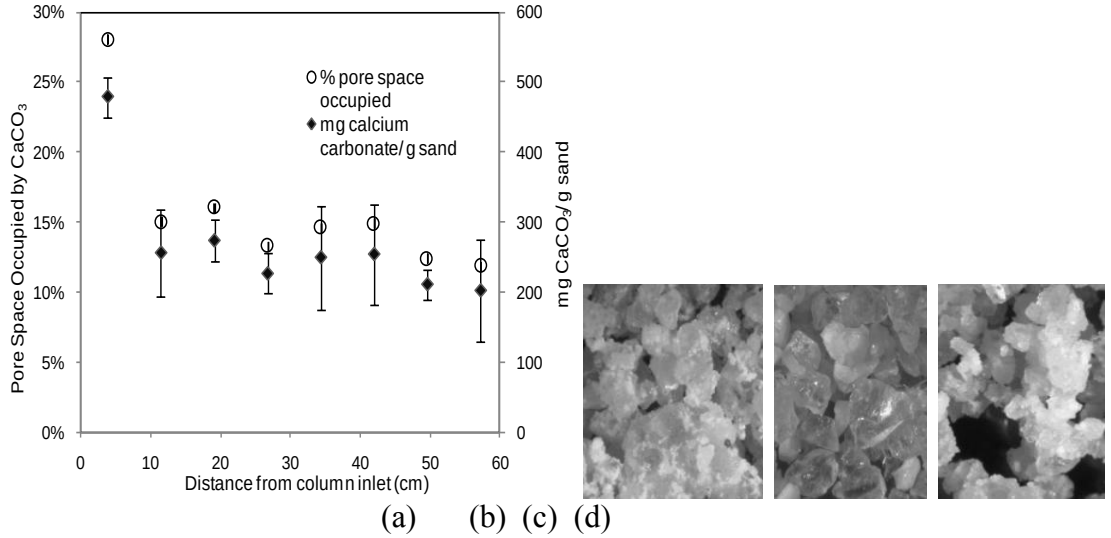

Figure 36. Results of biomineralization experiments in a packed sand column. (a) Volume fraction of calcium carbonate-occupied pore space and $CaCO_3$ concentrations over the distance of a 60 cm column. Stereoscopic analysis of (b) clean sand (control) and biofilm-calcium carbonate deposits (c - first 7.6 cm of column) and (d - last 7.6 cm of column) reveal significant calcium carbonate deposits. Similar results are anticipated for radial flow experiments.

Near Surface Detection Efficacy

Carbon dioxide has been successfully injected into the shallow subsurface at the ZERT site since 2006. Preinjection modeling (Oldenburg et al. 2010) was done to predict migration of CO_2 in the saturated and vadose zones and into the atmosphere. Experimental results for breakthrough times, evolution of the surface flux signals, and extent of spreading away from the well agreed very well with modeling predictions (Lewicki et al. 2007). Visiting researchers characterized background signals and measured transport of CO_2 in soil, water, plants and the atmosphere at the site. Performing experiments at the same site for four consecutive years has allowed us to characterize background on timescales from diurnal to interannual. Almost all techniques were able to detect CO_2 at flow rates of practical interest.

Carbon dioxide was easily detected in the soil gas by non-dispersive infrared (IR) sensors (Lewicki et al. 2010) and differential absorption measurements using a laser-based instrument buried in the shallow subsurface (Humphries et al. 2008; Barr et al. 2011). Spread of perfluorocarbon tracers injected with the CO_2 were mapped in the soil gas (Strazisar et al. 2009; Wells et al. 2010). Carbon dioxide flux out of the soil surface was detected with both steady-state (Amonette et al. 2010) and non steady-state accumulation chambers (Lewicki et al. 2007; Strazisar et al. 2009).

Rapid and systematic changes in the shallow groundwater (Kharaka et al. 2009) and head space gas (Strazisar et al. 2008) of the water monitoring wells were seen with injection of CO_2. Stress to plant health from injected CO_2 was measurable optically by hyperspectral (Male et al. 2010; Keith et al. 2009; Lakkaraju et al. 2010) and multispectral (Rouse et al. 2010) imaging.

Carbon dioxide injected into the well was seen in the atmosphere easily by several laser-based techniques. Laser-based differential absorption measurements detected CO_2 along a total path length of 86m (94.05 yards) over the well trace (Humphries et al. 2008). Injected CO_2 was distinguishable above CO_2 from natural biotic processes with an O_2/CO_2 ratio measurement system (Fessenden et al. 2010). Two different commercial cavity ring-down systems (for example, Krevor et al. 2010) as well as frequency modulated spectroscopy (Fessenden et al. 2010) were used to measure $\delta^{13}C$ signatures indicating the presence of injected CO_2. Elevated CO_2 levels in the air were also characterized by a portable sniffer from Licor as well as stationary non-dispersive IR sensors (Lewicki et al. 2010). In 2007 and 2008 eddy covariance measurements successfully recovered elevated CO_2 signal at the 0.3 t/d rate but not the 0.1 t/d rate (Lewicki and Hilley 2009a; 2009b). The atmospheric plume of CO_2 over the field site was inferred by mapping the distribution of the co-injected perfluorocarbon tracer (Wells et al. 2010). Stable isotopes of CO_2 were also collected to study transport in the atmospheric, vegetation, soil, and groundwater reservoirs.

The CO_2 injection rates for the ZERT experiments were selected to be scalable to leakage rates consistent with desirable retention rates in large scale geological carbon sequestration. Modeling with site specific input prior to injection proved to be extremely useful in predicting the behavior of the CO_2 and thus in designing sampling strategies. When the injection was performed, agreement between modeling and experiment was found to be excellent. Over 20 techniques have been brought to the site to investigate transport of CO_2 through the soil, groundwater, plants, and atmosphere. Almost all of the techniques tested at the site were able to detect CO_2 above background levels and variability of natural CO_2. Monitoring for a leak on a reservoir scale, which is likely the case for large scale geological sequestration projects, will surely prove much more challenging. Techniques tested at ZERT needed to identify a very localized anomaly within a relatively small area. The anomaly itself produced enough signal to fall well within the detection limit of most instrumentation, but because it is very localized the signal at distances not very far off the feature [on the order of 5 m (5.486 yards)] were often outside the range of detectability for many instruments. If one were searching for a feature like this over a large area, techniques able to survey larger areas (e.g. eddy covariance, imaging large vegetated areas for plant stress, laser based CO_2 detection, or atmospheric tracer detection arrays) would be more useful as opposed to point type measurements such as accumulation chamber measurements or

commercially available non-dispersive IR probes. Once the location of the leak is narrowed down point type measurements are entirely appropriate for quantifying and mapping the geometry of the leak. It may also be appropriate to invest resources into instrumenting locations more prone to leakage with high sensitivity point type sensors. Abandoned wells above the injected CO_2 reservoir would be an example of this.

Characterizing the natural variability of CO_2 will be extremely important for any near surface monitoring plan. The background signal for the site must be understood and accounted for as the natural fluctuations in background could easily be larger than a small leakage signal. Several timescales are relevant. Plant photosynthesis and respiration as well as microbial activity, for example, follow a diurnal cycle. Plant lifecycles follow the seasons. Weather patterns vary year to year (hot and dry vs. cold and rainy years). In addition to variability in time spatial heterogeneity should also be considered. Small scale local variations in the following have been seen at the ZERT site: soil temperature and moisture, soil mineralogy, and soil permeability. These directly influence, respectively, biological production of CO_2, water chemistry, and CO_2 transport through the soil. Having as complete an understanding as possible of the background signals at a site before injection of CO_2 will greatly increase the chances of correctly identifying a leak if one should occur.

In task 2, LBNL undertook theoretical studies of monitoring early in the ZERT project and field measurements later in the project. In the early studies, LBNL showed that optimization of seepage characterization can be carried out by near-surface monitoring using eddy covariance and accumulation chamber approaches along with Artificial Neural Networks (ANNs) and Particle Swarm Optimization (PSO) for detecting, pinpointing, and quantifying seepage. As part of the ZERT shallow-release study, LBNL provided the packer and tube system and associated CO_2 injection control infrastructure for the experiment. Prior to the experiments, LBNL design simulations predicted that an initial injection rate of 100 kg/d would provide a detectable seepage signal for flux- and concentration-based measurements. Also prior to the shallow-release tests, LBNL deployed eddy covariance system for background measurements of net CO_2 fluxes in preparation for the planned CO_2 release experiment. During all of the shallow-release experiments, LBNL participated by providing measurements and related flux maps. LBNL published under task 2 various footprint modeling and data filtering analyses to evaluate leakage detectability, and post-experiment simulations to investigate the causes of the focused emission pattern at the ZERT shallow-release experiment. Because of the importance of surface leakage to CO_2 exposure by humans and other animals, LBNL also carried out simulations of CO_2 surface seepage dispersion in a turbulent wind field and found the presence of a universal scaling relation involving wind speed and seepage flux.

The major scientific results under PNNL's task 5 (field testing) can be summarized in Figure 37. Flux rose and decayed rapidly during the injection and reached steady-state values between 3 and 5 d after the start of the injection (Figure 37, left). Major excursions to lower flux values in the PNNL chamber were highly correlated with major wind events. Both types of flux data yielded a decrease in flux during a 24-h long wind event at 240 h suggesting that significant depletion of surface-soil CO_2 occurs due to pumping action during prolonged wind events. Spatially-resolved data collected over several years (Figure 37, right) yielded highly heterogeneous (<1 m) flux

patterns and showed evidence for significant secondary flux emanating from CO_2 carried away from the horizontal well by groundwater and released to the soil several meters down-gradient.

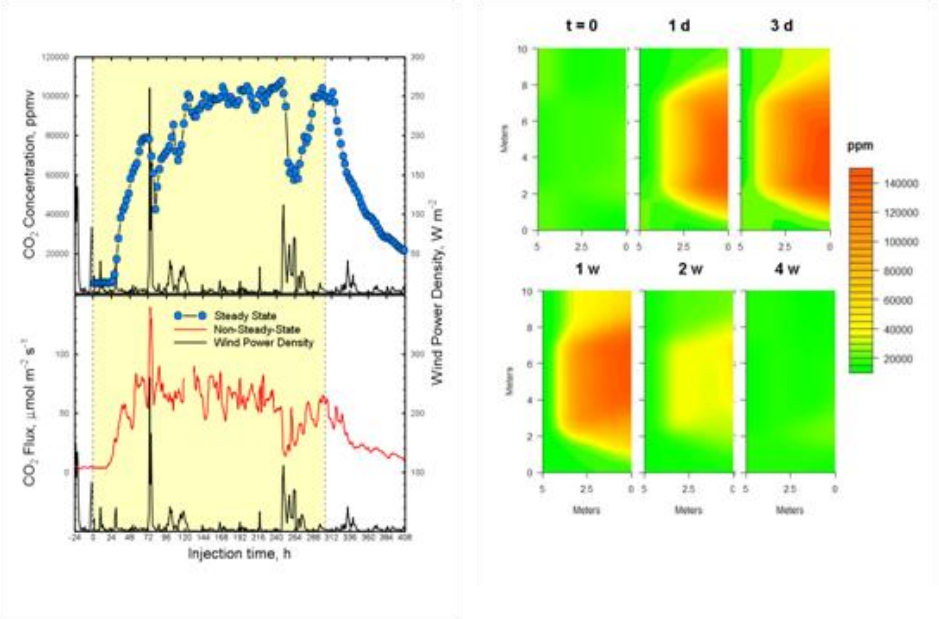

Figure 37. Typical time-resolved surface-flux monitoring and wind-power density data from summer of 2008 for PNNL's steady-state flux chambers (left, top) and non-steady-state chambers placed by MSU (left, bottom). Adapted from Amonette et al. (2010).

Tracer in soil-gas depth profiles (not shown) appear to show release of tracer from a 'reservoir' of tracer, presumably from the top of the water table or from the soil-cobble interface. In both experiments, the release of CO_2 was successfully detected and characterized by both direct soil gas methods and tracer detection. In the case of the vertical well, the integrated flux rate was within 10% of the known injection rate. A simple interpolations and integration of the fluxes over the area (by forcing radial symmetry) produced a total flux rate of 723 mL/minute. This compares very well with the actual injection rate of 800 mL/minute. Carbon isotope ratios monitored in 2006-2007 matched those of the injected CO_2. Within 1 meter of the hot spot, the measurements averaged -62.7 ± 1.7 for $\delta^{13}C$, consistent with the source tank.

Preliminary flux measurements made it clear that the NETL packer section contained two hot spots where the bulk of the CO_2 was being released. One hot spot was near the northeast end of the NETL packer section, and the other hot spot was near the southwest end. These locations correspond to the highest elevation of the pipe in two of the isolated sections of pipe, where CO_2 could accumulate before flowing to the surface.

In the 2007 experiments, tracer in soil-gas concentrations near the northeast anomaly corresponded to a maximum (or tracer hot spot), while those near the southwest anomaly corresponded to a minimum (or tracer hole) below the 'background' levels found following tracer injection (Figure 12). It was concluded that the hot spot in flux measurements to the southwest was due to gas flow from the neighboring section, which lacked tracer. The annulus

around the roots of living and dead plants might serve as channels for barometric pumping to occur as could the burrows of insects and other animals. The appearance of multiple release channels from a single hot spot release location evidenced in Figure 12 D & E suggests a mechanism for the spread of the underground plume at the water table interface. The development of these features is roughly perpendicular to the horizontal well, and in the direction of the measured flow of subsurface water. Resistivity depth profiling surveys conducted for the vertical well injection (Figure 11) revealed information on subsurface geology/hydrology as well as imaging the CO_2 plume development.

In the 2008 experiments, the effects of successively courser atmospheric monitoring grids and of various wind conditions were evaluated (Figure 38). Particularly significant was the conclusion that all of the grid spacings provided detection of tracer, and at least some information pertinent to the identification of a source. The selection of 'best possible wind conditions' was, however, critical to avoid misidentification of sources, and to ensure the detection of leakage, especially for permanent tower installations.

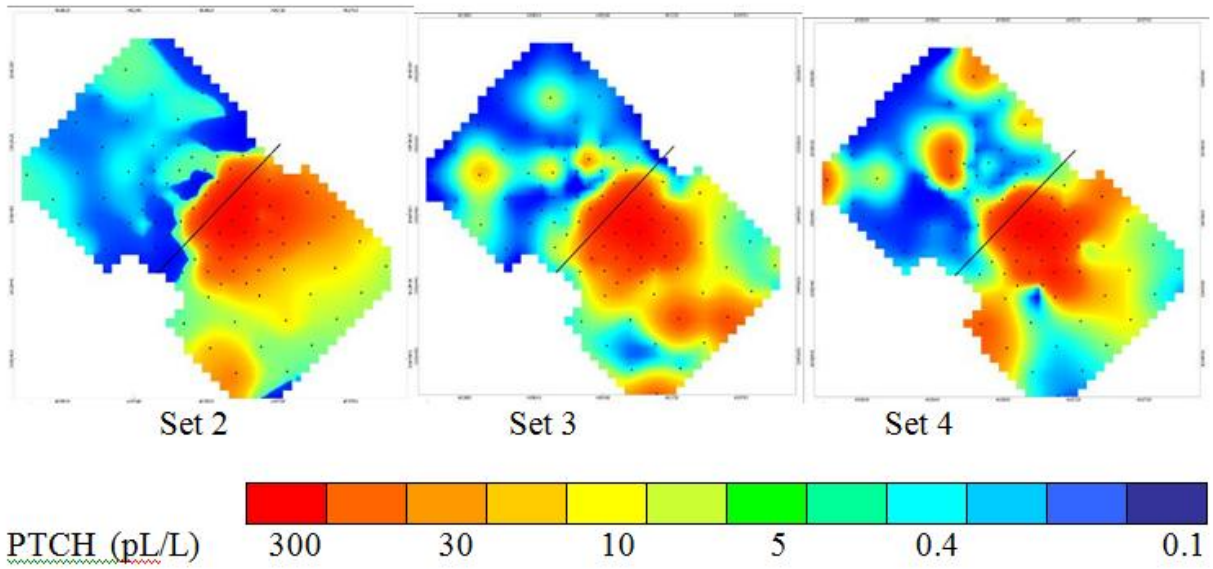

Figure 38. PTCH Atmospheric plumes for winds that were strong and steady (Set 2), light and steady (Set 3) and light and variable (Set 4)

In the 2009 experiments, the low lateral dispersion of the PFC tracers is instructive in determining density of the grid for a UAS flight plan or tower-based monitoring network. (The tethered balloon samplers revealed near background levels above 20 meters.)

In 2010, preliminary evaluation of the vadose zone studies demonstrated that following the start of tracer injection in packer section 6 (water well test zone), the tracer plume expanded much faster than did the initial CO_2 plume following the start of CO_2 injection. PFC tracers plumes may, therefore, be considered as 'conservative surrogates' for CO_2. Given the positive results demonstrated here, the AERMOD model could be incorporated into sampling scheme development at other CCS sites. With site-specific geological information and assumptions made

with respect to possible point, line, or area leak locations, dispersion modeling becomes a valuable tool in optimizing the monitoring grid and UAS flight plan. Frequent UAS surveys at a CO_2 sequestration site are not cost effective, and therefore, future experiments will establish a reasonable protocol for long-term sequestration site leak detection.

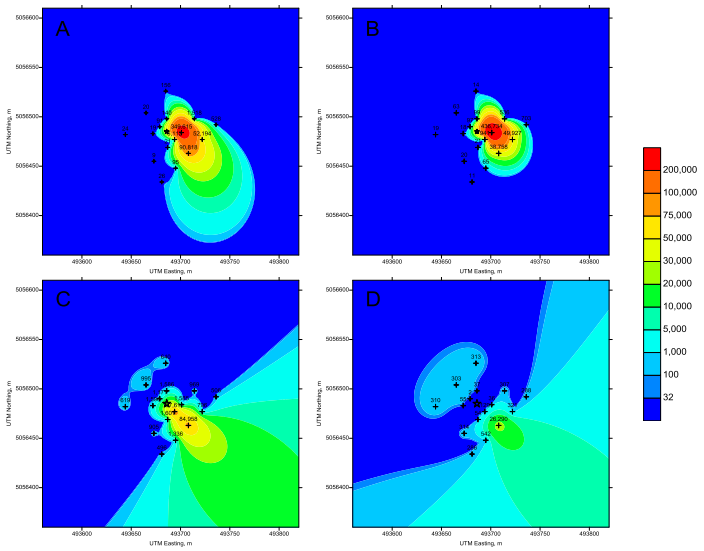

Figure 39. July 18, 2009: Tower-based monitoring results at 1m and 2m elevations (top 2 figures) and AERMOD modeled results at 1m and 2m elevations (bottom 2 figures). Concentrations in fL/L.

Near Surface Detection Efficacy: Technology development

Introduction. The results and discussion section is again broken into five sections including this brief introduction. The remaining four sections will include the major results from each of the instruments and techniques described in the Experimental Methods section. Most of the results shown here have been published in peer reviewed journals (Humphries et al. 2008a. 2008b; Repasky et al. 2006; Barr et al. 2010; Humphries et al. 2006; Keith et al. 2009).

Integrated Path Differential Absorption Instrument. The above ground sensor was operated continuously from July 1 through August 13, 2008. The above ground sensor was set up with the parallel optical path located directly over and along the direction of the release pipe and the second optical path perpendicular to the release pipe. The corner cube for the optical path located over the pipe was positioned 29.5 m (32.26 yards) away from the optical sensor provides a total integrated path length of about 59 m (64.52 yards). The corner cube for the optical path perpendicular to the release pipe was 31 m (33.9 yards) away from the optical sensor providing a total integrated path length of about 62 m (67.8 yards). Both optical beam paths were at a nominal height of 13 cm (5 inches) above the ground.

A plot of the CO_2 concentration as a function of time measured by the above ground sensor is shown in Figure 40. The solid line represents measurements made along the direction of the release pipe while the dashed line represents measurements made perpendicular to the release

pipe. The beginning and ending of the CO_2 injection are marked as vertical lines on July 9, 2008 and August 7, 2008. Before the injection begins, measurements made parallel to the release pipe and perpendicular to the release pipe have the same values. Once the CO_2 injection starts, measurements made perpendicular to the release pipe are similar to the measurements made before the CO_2 injection, but measurements made parallel to the release pipe increase indicating an elevated CO_2 concentration measured over the release pipe. Approximately one day after the CO_2 injection stops, measurements made parallel to the pipe and perpendicular to the pipe have similar values.

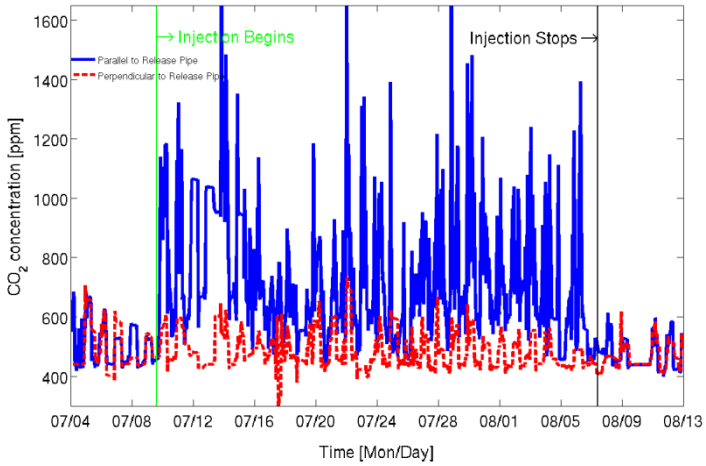

Figure 40. Plot of CO_2 concentrations measured during the 2008 controlled release by the above ground instrument in the parallel (solid line) and the perpendicular (dashed line) directions relative to the release pipe. The start and end of the injection are designated by vertical lines. The elevated CO_2 levels measured over the release pipe as indicated by the solid line are clearly evident in this figure compared to the background measurements made perpendicular to the release pipe as indicated by the dashed line.

One interesting feature seen in both the parallel and perpendicular measurements is the daily cycle of the CO_2 concentration. A plot of the CO_2 concentration as a function of time is shown in Figure 41 for July 31 – August 4, 2008. The CO_2 concentration measurements made perpendicular to the release pipe show a daily cycle with lower levels of CO_2 measured from mid-morning to mid-evening and higher levels of CO_2 measured from mid-evening to mid morning. A similar trend is seen for the CO_2 levels measured parallel to the release pipe. Since the elevated CO_2 levels measured over the release pipe result from the CO_2 injection, this diurnal cycle must result from weather conditions including the cooler nighttime temperatures and lower average wind speeds along with CO_2 concentration changes due to photosynthesis.

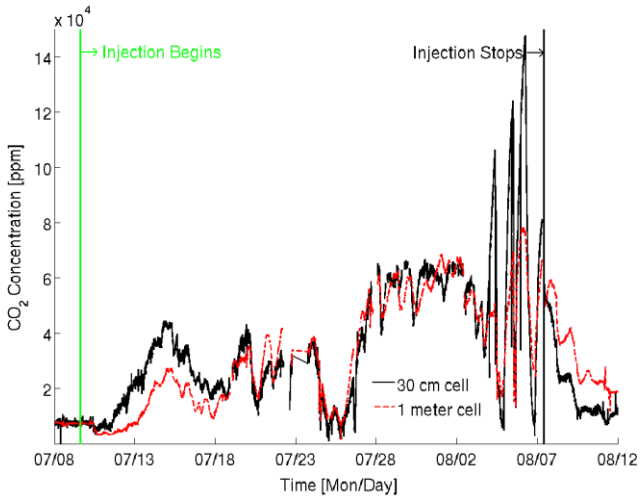

Figure 41. Underground **CO_2** concentration as a function of time. The solid black (dashed red) line indicates measurements made over the (1 m lateral from) the injection pipe. Rain events that occured during this release affected the diffusivity of teh soil causing the large fluctuations in the underground **CO_2** concentrations seen in the plot.

Sub-Surface Fiber Sensor. A plot of the CO_2 concentration as a function of time measured by the underground instrument is shown in Figure 41. The solid line represents measurements made using the 0.3 m (11 inch) absorption cell that was placed over the release pipe while the dashed line represents the 1 m absorption cell that was placed 1 m (1.09 yards) away from the pipe. Approximately 24 hours after the start of the underground injection, the 0.3 m (11 inch) cell begins to see an increase in underground CO_2 concentration. Approximately 64 hours after the start of the underground injection the 1 m (1.09 yard) cell begins to see an increase in the underground CO_2 concentrations. From this measurement, it takes about 40 hours for the CO_2 that is released to move 1 m (1.09 yard) laterally from the pipe.

A validation of the PBG fiber sensor was conducted during this release experiment. The PBG fiber sensor was inserted in the same underground box as the 0.3 m (11 inch) open path absorption cell allowing a comparison of the CO_2 concentration measured using the open path sensor and the PBG fiber sensor. This comparison is shown in Figure 42. The black line represents CO_2 concentration measurements made with the 0.3 m (11 inch) open path cell while the red line represents CO_2 concentration measurements made with the PBG fiber sensors. Figure 42 shows a strong correlation between the two cells with about a four hour lag time for measurements made with the PBG fiber sensor. This lag time results from the slow diffusion rate of the CO_2 into the hollow core of the PBG fiber.

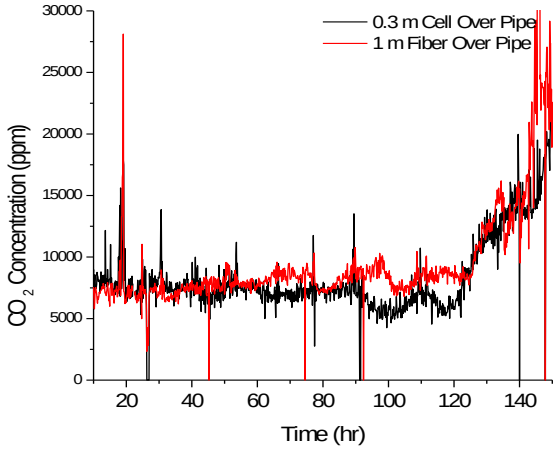

Figure 42. A comparison of the **CO_2** concentration measured using the open path absorption cell and the PBG fiber. Good agreement between these two measurements indicates that the PBG fiber is a viable sensor technology.

Differential Absorption Lidar (DIAL) for spatially mapping Carbon Dioxide Concentrations. A plot of the number density as a function of range is shown in Figure 43. The solid squares represent the number density profile used in the model. A carbon dioxide concentration of 400 ppm was assumed at all range bins except at the range bin located near 1500 m (1,640.42 yards). The range bin at 1500 m (1,640.42 yards) was assumed to have an average concentration of 1200 ppm, indicative of the CO_2 level above the release pipe described in the above paragraph and indicative of the lower level of CO_2 concentrations that needs to be detected for successful carbon sequestration site monitoring. The error bars indicate the estimated performance of the DIAL instrument associated with an averaging time of one minute for the on-line returns and one minute for the off-line returns and shows the potential of this instrument to measure range resolved CO_2 number densities. The instrument parameters used for this model include a 1.5μJ pulse energy with a 500 ns pulse duration providing a range bin size of 75 m (82.02 yards). The telescope was assumed to be 11 inches in diameter and the receiver optics was assumed to have a transmission of 0.2 while the detector was assumed to have a quantum efficiency of 0.2. The laser and the field of view of the telescope were assumed to be in full overlap by 500 m (546.80 yards). The results of this modeling indicate that the proposed DIAL instrument is capable of detecting elevated CO_2 levels and has the potential for monitoring areas of approximately 6 square kilometers (3.73 square miles) if the DIAL is scanned through one hundred eighty degrees with a range resolution of 75 m (82.02 yards). Based on the results from this modeling, further funding from the Department of Energy was received to develop a scanning DIAL for mapping CO_2 concentrations.

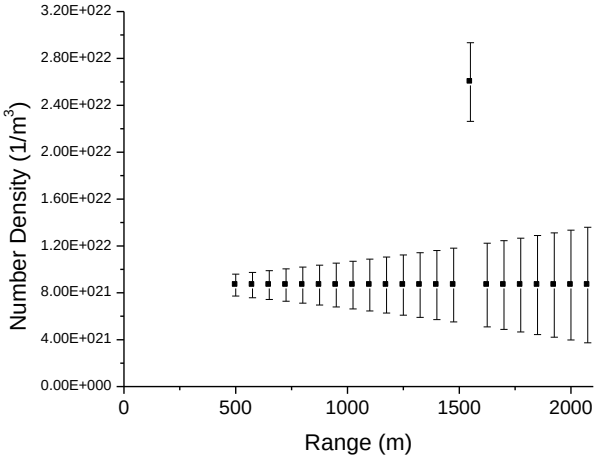

Figure 43. Modeled performance of a DIAL instrument for measuring range resolved carbon dioxide concentrations.

Hyperspectral Imaging to Monitor Carbon Dioxide via Plant Stress. The results of the analysis indicate a threshold response of plant health to the injected CO_2. The logarithm transform of the distance values gave more significant regressions for all of the data. The regressions from the health measure to distance have lower significance values for the days of August 5-8. The significance of the regressions is far greater than for the earlier days on August 10 and 11. In each group of days before and after the apparent threshold has been reached, there is no clear trend to the significance of the regressions, indicating a threshold response of the plant health to the elevated sub-surface CO_2 resulting from the injection.

This method of analysis assesses the health of plant spectra. The important bands used in the classifier, shown in Figure 44, are near the red edge of the spectra associated with the chlorophyll in the plant. These spectral bands near the red edge change as a plant's health changes. Applying the classifier to hyperspectral images in the manner described gives a measure of health for plants in the images that vary with distance from the CO_2 release in an expected manner. For the 0.3 tons CO_2/day injection rate, the plant health deteriorated the most within a perpendicular distance of 0.5 m (0.547 yards) on either side of the release pipe. A plot of the number of pixels classified as healthy as a function of perpendicular distance from the injection pipe is shown in Figure 45. The plot on the left resulted from classification early in the release while the plot on the right resulted from classification late in the release. The vegetation becomes more stressed later in the release as indicated by the drop in the percentage of pixels classified as healthy. The stressed vegetation is within 1 – 2 m (1.093 – 2.187 yards) of the injection pipe consistent with other monitoring results and modeling.

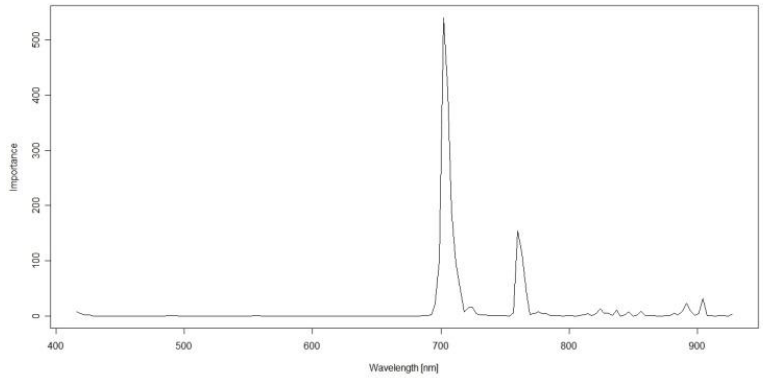

Figure 44. Plot of the percentage of the pixels classified as healthy as a function of the perpendicular distance from the release pipe. The left hand plot represents data taken early in the release while the right hand plot represents data taken late in the release.

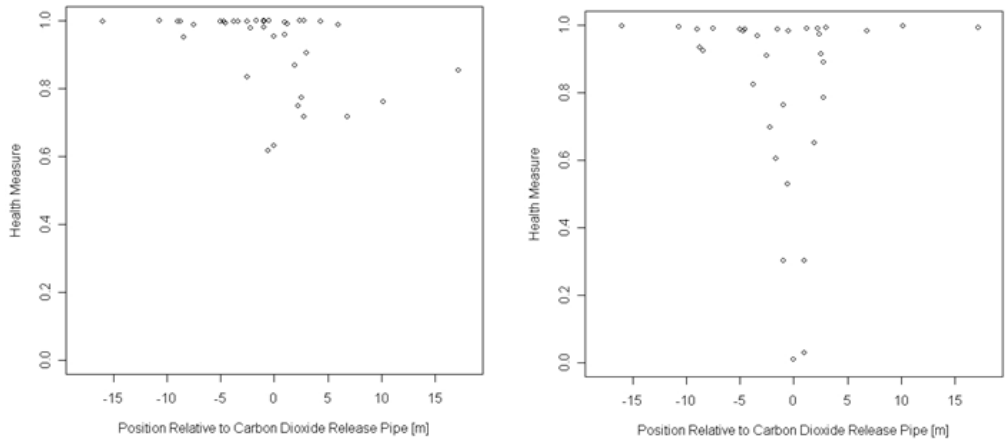

Figure 45. Plot of the percentage of the pixels classified as healthy as a function of the perpendicular distance from the release pipe. The left hand plot represents data taken early in the release while the right hand plot represents data taken late in the release.

The ZERT research efforts demonstrate that optical detection of CO_2 provides one method for near surface monitoring of carbon sequestration sites. Two active optical detection instruments based on 2.004 μm wavelength DFB lasers, including integrated path measurements of CO_2 and sub-surface fiber sensors provide moderate area coverage for CO_2 monitoring. Flight based hyperspectral imaging has been demonstrated and provides a means of monitoring larger areas. Finally, the DIAL technique offers an eye-safe method of spatially mapping CO_2 concentrations over larger areas.

Research efforts supported by the ZERT effort have led to other research projects that received follow-on funding through peer review proposals with an effort to commercialize instrumentation and techniques for carbon sequestration site monitoring. The early work with the fiber sensors probes is continuing with funding from the Department of Energy and the Environmental Protection Agency to develop a field deployable 1 X N fiber sensor array. The

fiber sensor probes have been designed, built, and tested as shown in Figure 46 with a 1 X 100 electro-optic switch currently under development by a Montana based photonics company. The preliminary work on hyperspectral imaging as a means of monitoring CO_2 via plant stress has received follow on funding from the Montana Board of Research and Commercialization Technology (MBRCT), and Phase I and Phase II STTR funding from the Department of Energy. This work has allowed a demonstration of flight based hyperspectral imaging at the ZERT field site demonstrating the capability of flight based hyperspectral imaging to detect elevated CO_2 as shown in Figure 47. This work is in collaboration with a Bozeman based company that has developed compact flight ready hyperspectral imaging systems. Finally, follow on funding from the Department of Energy has been obtained to develop and deploy a DIAL for spatial mapping of CO_2. A picture of this instrument is shown in Figure 48 and initial data collected over a two hour period is shown in Figure 49. Work on transferring this technology for commercialization is also under way with a phase I SBIR proposal in preparation with a Bozeman based photonics company to develop a field deployable scanning CO_2 DIAL.

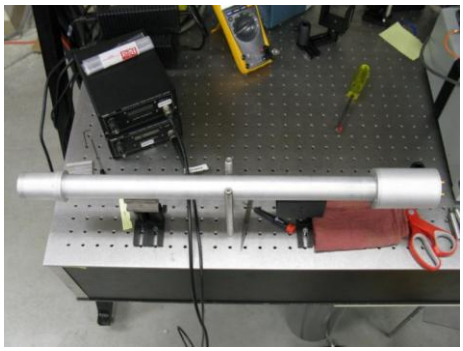

Figure 46. Fiber optic probe currently under development as part of a 1 X N fiber sensor array

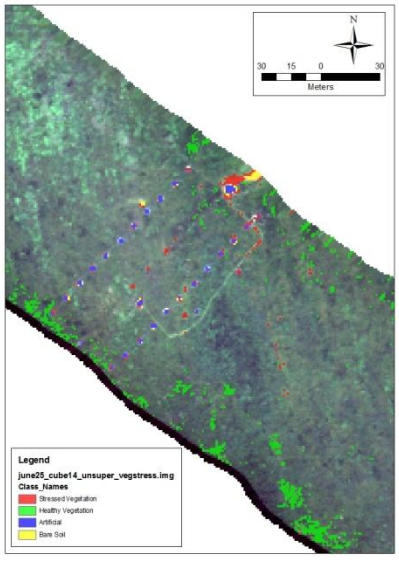

Figure 47. Flight based hyperspectral imaging showing plant stress resulting from a controlled CO_2 injection.

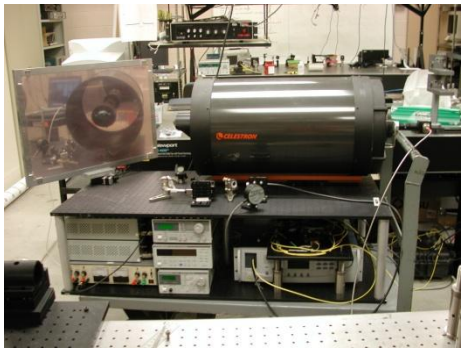

Figure 48. Scanning DIAL instrument for spatially mapping CO_2 concentrations.

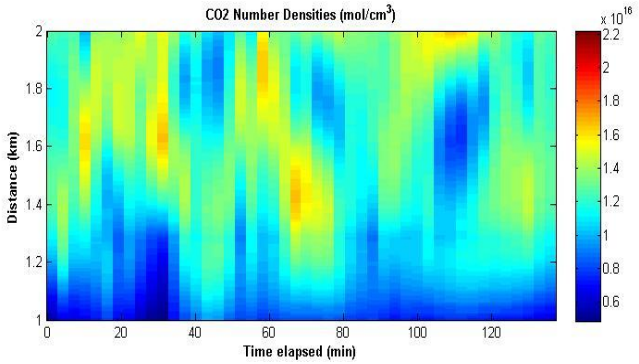

Figure 49. False color plot of the **CO_2** number density as a function of range and time

The statistical analysis of this entire data set (Rouse et al. 2010) showed that the NDVI was the data product that most consistently allowed detection of a vegetation response to the changing CO_2. The results from different years were repeatable, within the naturally occurring variation of meteorological conditions at the ZERT field site. In general, the time evolution of the spectral imager data produced a statistically significant correlation with the spatial and temporal patterns of CO_2 flux. The statistical analysis of multispectral reflectance imagery was successfully correlated with the CO_2 flux in both the mown and un-mown regions, although the latter became more complicated as tall dead grass obscured the underlying surface vegetation in late summer. The data also showed shorter-term responses to weather events, with the NDVI increasing within a day following significant rain events (indicating increased plant health) and with the NDVI briefly decreasing following a heavy hail storm (indicating decreased plant health).

The results of the 2008 release experiment are shown as representative results. One fairly unique characteristic of this particular season was an unusually high number of heavy rain events and one particularly plant-damaging hail storm. Because of the large amount of rain in mid-to-late summer, the vegetation health in the mown segment actually increased during the experiment, whereas the more common pattern is for it to decrease because of a combination of hotter, dryer conditions plus the increased CO_2 concentrations created by the release.

Figure 50 shows that the reflectance values exhibited the expected stress-induced pattern of decreasing in the NIR and increasing in the red (Figure 50). The NDVI values, however, exhibit

a somewhat less obvious response. Figure 51 shows that the NDVI values in the un-mown segment all decreased over time, with the lowest plant-health decay slope in region 3 (the control region far from the CO_2 release) and the highest decay slope in region 1 (the test region closest to the release). This shows that, while all the vegetation became increasingly stressed through natural processes as summer progressed, the higher CO_2 concentration near the release pipe enhanced the plant stress.

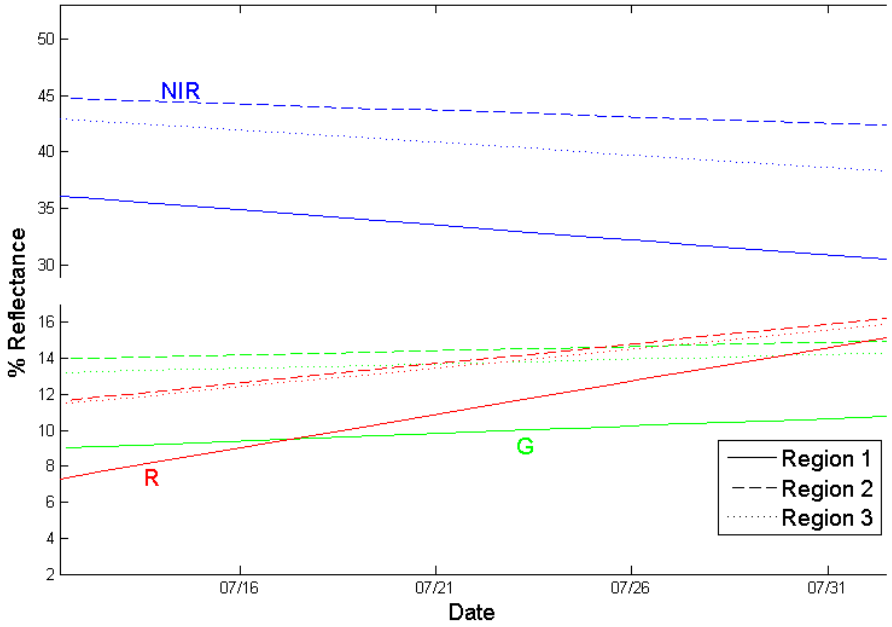

Figure 50. Reflectance plotted vs. time for the 2008 un-mown segment (green, red, and NIR reflectances for regions 1=solid, 2=dash, and 3=dot)

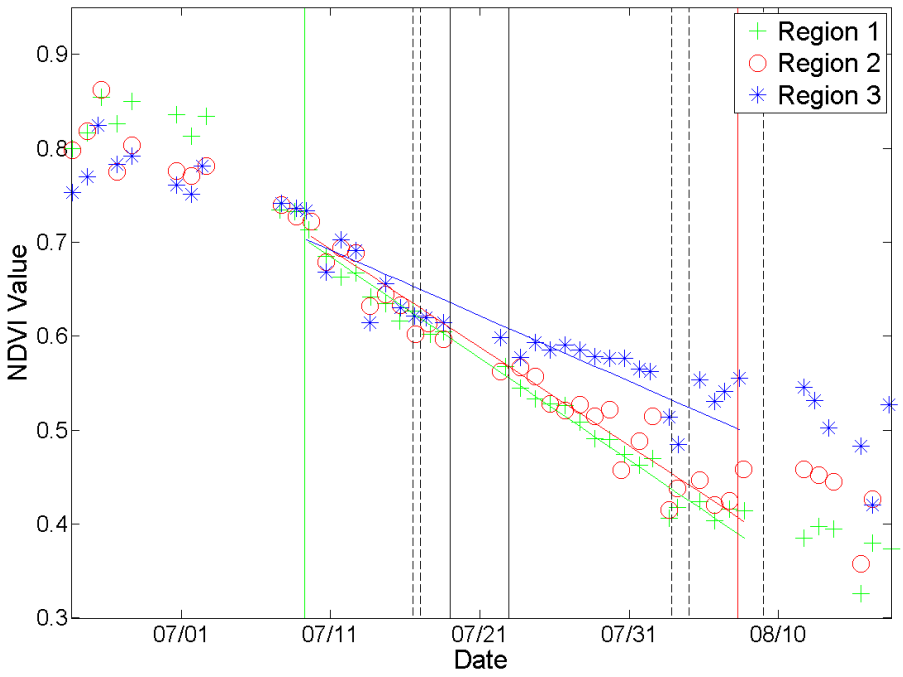

Figure 51. Plot of NDVI vs. time for the un-mown segment in the 2008 release

Because of a total lack of tall dead grasses obscuring the surface vegetation, the NDVI time-series plot for the un-mown region, shown in Figure 52, is somewhat different. Here the NDVI values for all three regions actually increased as summer progressed (a result of the unusually frequent and heavy rains). However, the region 1 data had the smallest slope, while regions 2 and 3 had higher slopes that indicated less negative influence of the distant CO_2.

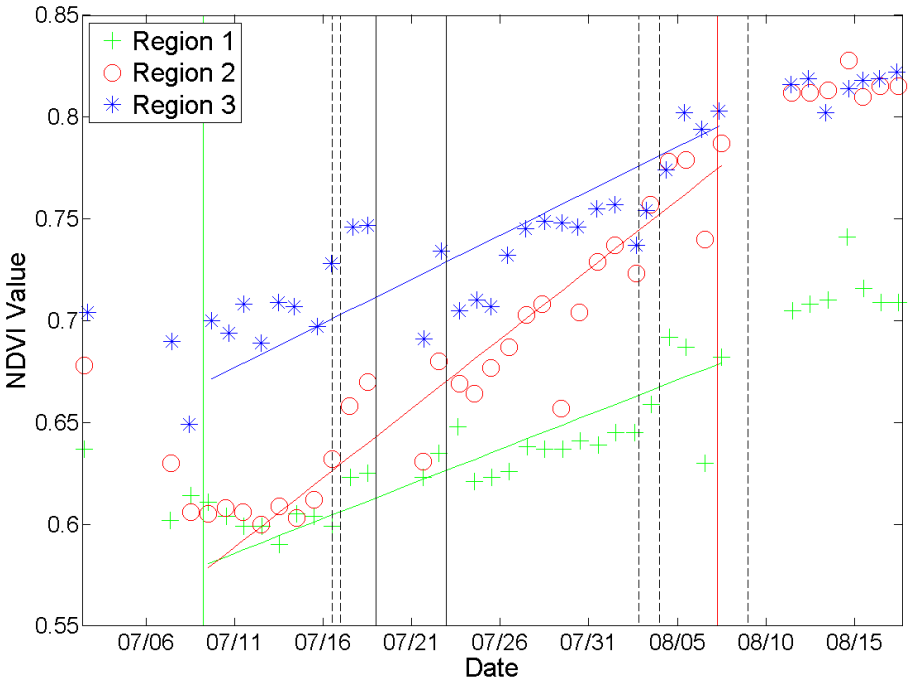

Figure 52. NDVI plotted vs. time for the mown region in the 2008 release experiment

The significance of the statistical results can be best characterized by the R^2 and p values from the regression analysis, as summarized for the mown segment in Table 4 and Table 5. The corresponding values for the mown regression analysis of data obtained in the un-mown segment are shown in Table 6 and Table 7.

Table 4. 2008 mown segment date-versus-NDVI regression R^2 and p-values

	Regression R^2	Regression p-value
NDVI	0.73	<0.01

Table 5. 2008 mown segment date-versus-NDVI regression p-values that distinguish between vegetation regions

	p-Value		
	Regions 1, 2	Regions 2, 3	Regions 1, 3
Intercept Term	0.000881	0.00436	0.604922
Slope Term	0.000305	0.01291	0.172055

Table 6. 2008 un-mown segment date versus NDVI regression R^2 and p-values

Regression R^2	Regression p-value

NDVI	0.9	<0.01

Table 7. 2008 un-mown segment dateversus NDVI regression p-values that distinguish between vegetation regions

	p-Value		
	Regions 1, 2	Regions 2, 3	Regions 1, 3
Intercept Term	0.538	6.32E-06	8.33E-07
Slope Term	0.721	8.36E-05	2.59E-05

In this study it has been found that the NDVI may have advantages over any other combination of spectral bands available on the imager used with or without NDVI for statistically detecting differing levels of plant stress and explaining the variability in plant health. The NDVI is able to distinguish between both mown and un-mown vegetation regions that have been stressed, compared to non-stressed regions, but the NDVI is much stronger when the vegetation region has not been mown. Also, the NDVI explains variability in plant health better in un-mown regions, but not by much. Spectral bands may not be the best solution to detect differences in the health of vegetation in different regions since they are best used to explain the variability in the spectral response of vegetation over time.

Risk Assessment

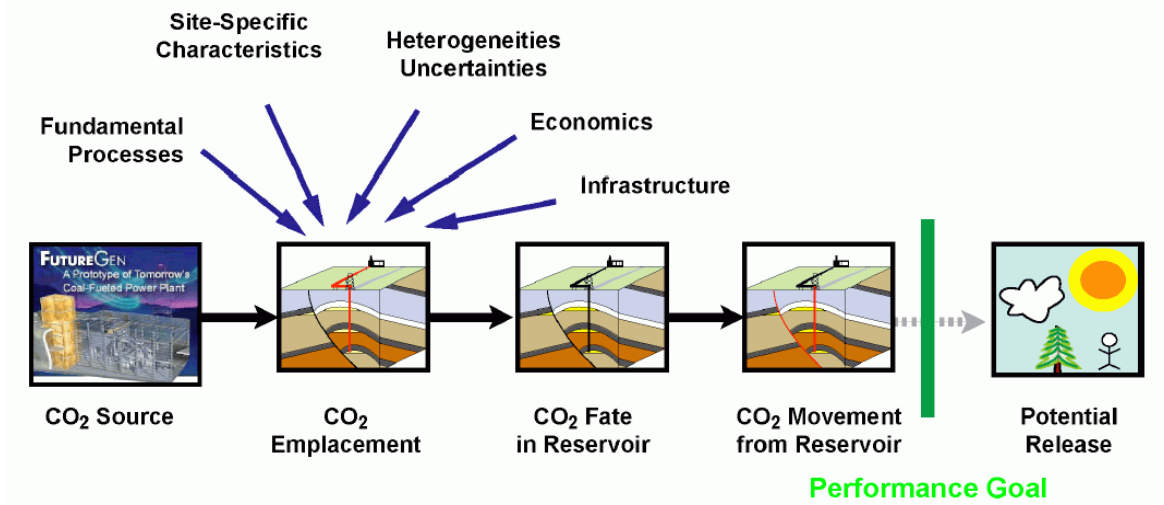

Figure 53. Schematic diagram showing a high level systems model for any **CO_2** sequestration project

A comprehensive model for any CO_2 sequestration project would include all the sub-systems, from the source for CO_2 such as a power plant, to the sub-systems affected by potential release of CO_2 such as the terrestrial environment near a geologic repository. Such a model can be used to analyze performance of any site based on any desired metric ranging from economics to health and safety. The sub-systems that make up the model shown in Figure 53 are themselves

comprised of sub-systems. These lower level sub-systems can be further sub-divided until the process levels are reached. The sub-systems which follow the "CO_2 Source" sub-system in Figure 53 represent the geologic repository and the environment in its vicinity. This is the main area of interest for long-term performance and risk assessment. The framework that can be used to study and analyze this area of interest is shown in further details in Figure 54. The main components of this framework include storage reservoirs, seals, potential release mechanisms, CO_2 transport beyond primary storage reservoir and CO_2 release at surface. This approach is effectively a graphical approach to the features/events/process (FEPs) method that has been demonstrated to be effective in addressing other engineered geologic systems. The framework described here can be used to predict fate of CO_2 in the reservoir. It can also be used to determine fate of CO_2 outside the primary reservoir in case of potential release from the reservoir. This provides the flexibility to perform both performance assessment and risk assessment calculations. The framework can be used to answer questions such as what is the ultimate sequestration capacity of the reservoir and what is the total injectivity of the reservoir. It can also be used to answer questions such as what is the probability of a wellbore failure at the sequestration site and in case of failure what are the consequences. Using the framework described above, we have developed a computational model using GoldSim® (Figure 55). GoldSim is a commercially available systems modeling package which has been tailored with the unique needs of engineered geologic systems in mind, particularly, uncertainty and heterogeneity. It can be linked directly to process level models such as reactive-transport codes.

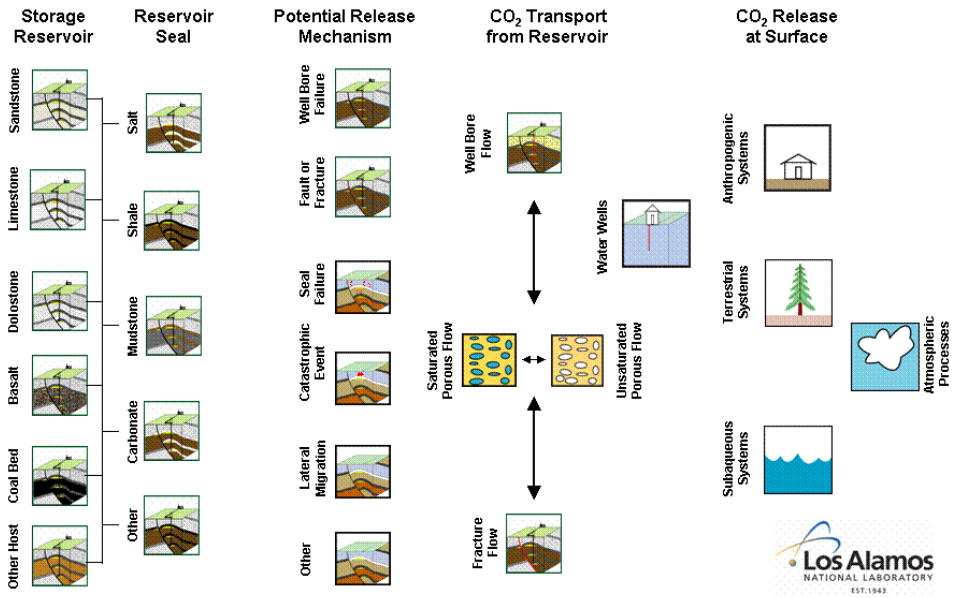

Figure 54. Framework for assessment of performance of an engineered geologic **CO_2** storage site

Figure 55. First version of the GoldSim systems model, **CO_2**-PENS, developed at LANL

Risk Assessment: Natural Analogs for escape mechanisms

Although samples from potential CO_2 reservoir formations throughout the stratigraphic section were studied in detail, the focus of this summary will be on those units that are known to contain CO_2 in the subsurface today, namely the Mississippian Madison Limestone (e.g., Shute Creek field, Moxa arch, western Wyoming) and the Triassic/Jurassic Nugget Sandstone and Jurassic Twin Creek Limestone (Caribou Range, SE Idaho). These are the main reservoir units that would most likely be targeted for subsurface sequestration projects in the future.

Madison Group Carbonates. The Mississippian Madison Group crops out along the crest of the Northern Salt River Range and Snake River Range. The upper unit (Mission Canyon Limestone) is approximately 305 m (333.55 yards) thick and consists of medium- to massively-bedded, light gray, and bioclastic and oolitic-sparry limestone. In thin-sections, the cement between fossil fragments consists of multiple-generation calcite with blocky and fibrous crystal habit; neomorphic recrystallization and late silicification has occurred in localized zones, suggestive of late-stage (low-temperature hydrothermal) diagenesis. The lower unit of the Madison Group (Lodgepole Limestone) consists of 274 m (299.65 yards) of resistant, dark blue-gray, thinly bedded, fossiliferous, argillaceous micritic limestone. The basic, first-order differences between the Mission Canyon and Lodgepole Limestones are the result of differing depositional environments. However, there is also a significant late diagenetic overprint on these carbonates that is important relative to reservoir quality for CO_2 sequestration and understanding migration pathways of CO_2 solutions through the carbonate-rich Paleozoic section. The following features are collectively indicative of late-stage diagenesis involving warm formation fluids (i.e., low-temp hydrothermal alteration): pervasive neomorphic recrystallization, multiple-generation cements, localized silicification, bitumen residue, and anastomosing calcite/dolomite-filled veins ("stylo-breccia"). The southern-most field area near Prater Mountain in the northern Salt River Range yielded a major hydrothermal breccia pipe in the Mississippian Madison Limestone in the

hanging wall of the Absaroka thrust, as well as a host of other hydrothermal and fracture/vein measurement sites at different stratigraphic levels. The Madison breccia pipe is upwardly-branching with pervasive breccia at all scales, saddle dolomite, bitumen, sulfides, boiling textures (boxwork), and silicification (herkimer quartz prisms). Nearly identical breccia pipes have been described in the Canadian Rockies where they represent the Mississippi Valley-Type (MVT) hydrothermal Pb-Zn-dolomite systems, as discussed in ZERT quarterly reports. These structurally-controlled systems form major conduits for CO_2-brine-hydrocarbon migration through higher levels of the stratigraphic section and, based on bottom-hole reservoir conditions, are representative of modern, subsurface CO_2 accumulations in SE Idaho.

Triassic/Jurassic Nugget Sandstone. Surface outcrops of the Nugget Sandstone throughout the northern part of the Idaho-Wyoming fold-and-thrust belt are generally well-cemented and dense, with very low intergranular porosity. The Nugget is a texturally mature, moderate- to well-sorted, dominantly fine-grained subarkose to arkose. Figure 56 shows a sample of the Nugget Sandstone from the northern Salt River Range (Murphy Creek drainage) in the proximal footwall of the Absaroka thrust fault. In contrast to other surface outcrops in the region, this outcrop is very similar to Nugget cores from the hydrocarbon-producing region of the fold-and-thrust belt in SW Wyoming (and CO_2-producing Nugget in SE Idaho) in that it is bleached, friable, highly porous, and contains hydrocarbon residue. Bleaching of sandstones is widely believed to be the result of Fe-reduction due to the migration of hydrocarbons and brine solutions through the sedimentary sequence (Parry et al. 2009). In addition, carbonate-filled fractures, networks of calcite-filled hairline fractures, secondary porosity (micro-vugs), and bitumen in the Nugget are consistent with hydrothermal alteration processes which may have been synchronous with CO_2-brine migration through the sedimentary succession. Several hydrothermal breccia pipes were discovered in the Nugget Sandstone directly beneath the Absaroka thrust fault in the vicinity of the Stewart Creek recess. These pipes are perpendicular to bedding and contain large angular blocks of altered, bleached Nugget Sandstone; their presence underscores the importance of forceful fluid migration upwards through the stratigraphic section driven by the thermal buoyancy of deep formation water/brine + hydrocarbons + CO_2.

Figure 56. Slab photograph of Triassic/Jurassic Nugget Sandstone

Jurassic Twin Creek Limestone. The upper and middle members of the Twin Creek Limestone consist of pale yellow-gray, medium-bedded, oosparite limestone with some micritic limestone (Giraffe Creek), and medium- to dark-brown, thinly-bedded, nonfossiliferous micritic limestone which breaks along smooth, concoidal fractures (Leeds Creek), respectfully. Calcite cement is pervasive in samples from surface outcrops. Porosity-reducing features, such as pressure-solution stylolites, are also very common. The Leeds Creek consists of blocky, calcite-filled extensional fractures indicating enhanced fracture-permeability during and immediately after deformation followed by post-kinematic cementation from warm CO_2-rich fluids; closely-spaced fractures, in addition to matrix porosity, accounts for excellent hydrocarbon production from the Twin Creek in southwest Wyoming as well as porosity for natural CO_2 in anticlines to the west of this field locality. Figure 57 shows white, blocky calcite that has filled open fractures in dark-gray, oolitic limestone of the Twin Creek Formation. Some blocks of limestone can be easily relocated to their sites of origin on the margin of the fracture, indicating minimal transport with fluids in the open fracture. Other fracture clasts appear to be shattered with calcite cement filling spaces between small, very slightly displaced pieces. Small-scale pseudo-brecciation is typical of fluid hydrofracture textures and suggest that CO_2 brines were forceful as they migrated upwards through the rock and that fracturing and cementation was a one-time, rapid event.

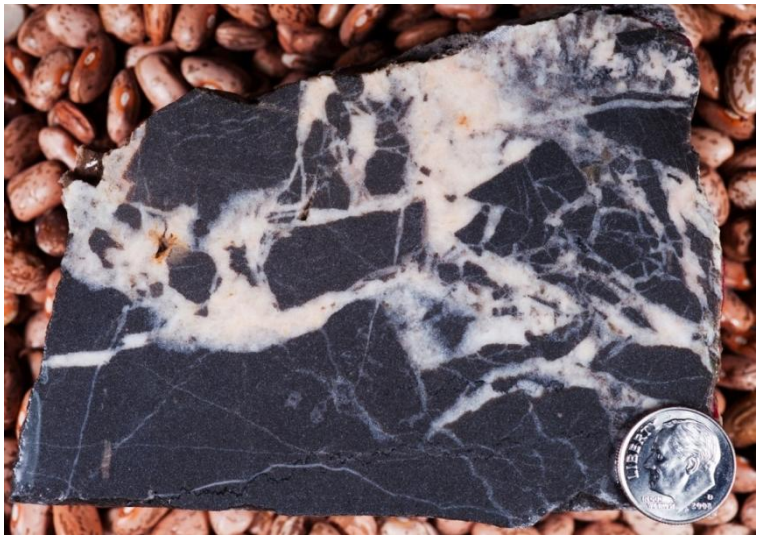

Figure 57. Slab photograph of Jurassic Twin Creek Limestone

Fracture systems. Figure 58 shows statistical fracture data from the Northern Salt River Range. Also shown are tabulations of fracture length (cm), spacing (cm), and aperture (mm). Three groupings or sets of fractures stand out. Set #1 (red in top diagram) is oriented almost north-south. These fractures tend to be somewhat longer and more widely spaced than the other sets and they have the widest apertures; therefore, these may be the youngest fractures, probably related to east-west regional extension at the eastern margin of the Intermountain Seismic Belt. Set #2 (blue) is parallel to the overall trend of the Stewart Peak structural culmination and is an extensional, mode-I, "a-b" fracture set. Set #2 fractures may have originated in two ways: (a) simply as extensional fractures parallel to the culmination's hingeline at the top of the Grand Valley ramp, or (b) as early, closely-spaced tectonic stylolites ($\perp$ bedding) that were

subsequently dilated by flexural-folding at the top of the Grand Valley ramp. In either case, they appear to be older than set #1 and somewhat "tighter." Set #3 (green) is parallel to the shortening direction during the Sevier orogeny and may be classified as syntectonic, extensional "a-c" fractures. The inset photograph shows large, anastomosing, open, and calcite-filled fractures belonging to set #3. The vein-fill material is syntaxial (i.e., progressive opening in the center) and clearly demonstrates multiple fluid-flow/precipitation events involving large fluxes of water. Conjugate shear fractures are not broken out, but are represented by fracture trends bisected by set #3. These fractures formed during the early stages of thrusting during layer-parallel compression and were not significant conduits for fluid + CO_2 migration.

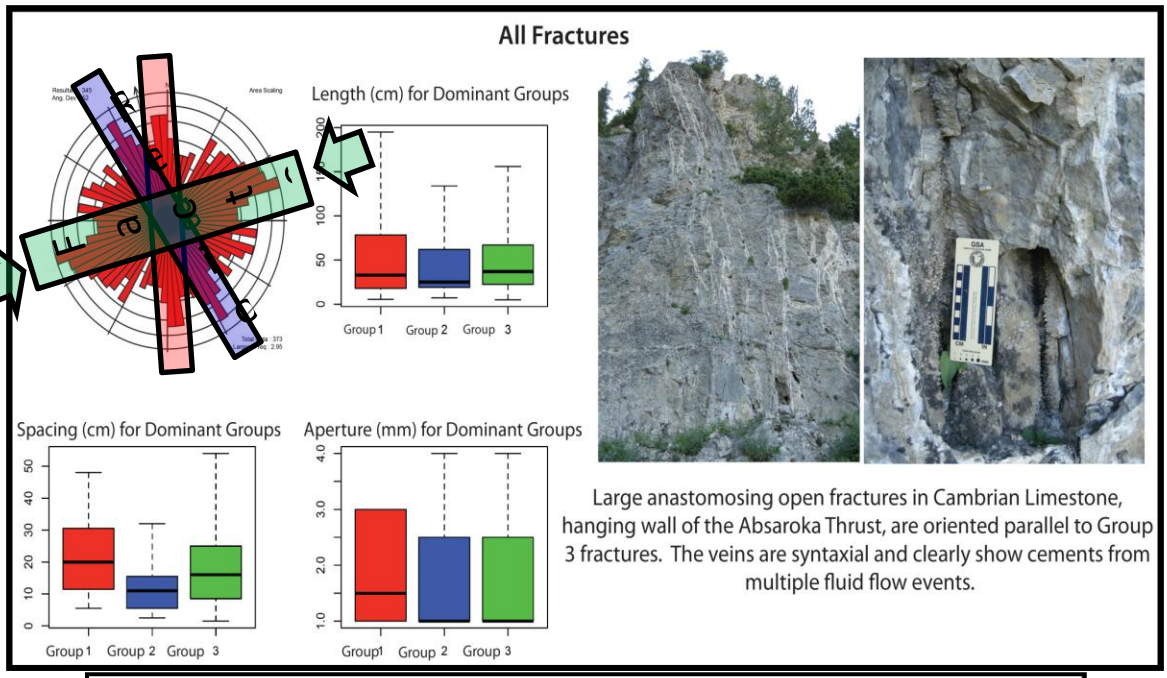

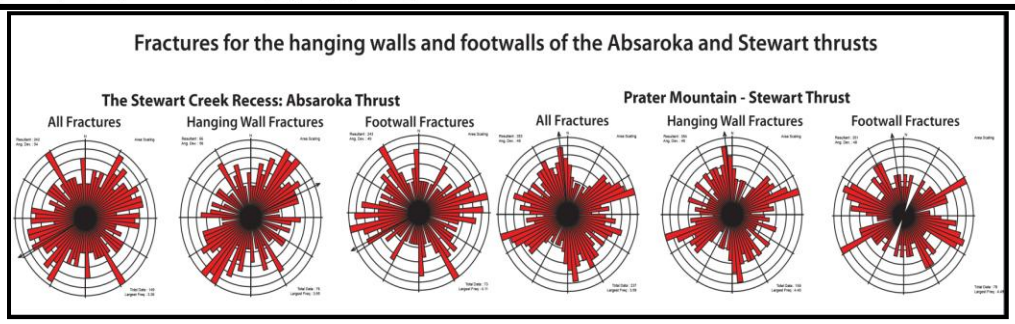

Figure 58. Fracture data from the Northern Salt River Range. Group 1 fractures (red in top diagram) are oriented north-south and may be the youngest, related to Basin and Range extension; group 2 fractures (blue) are parallel to the trend of folding and are interpreted as extensional "a-b" fractures; group 3 fractures (green) are parallel to the shortening direction during the Sevier orogeny and are interpreted as extensional "a-c" fractures.

It must be stressed again that, in addition to the above fracture patterns, the stratigraphic section at the Jurassic level and deeper shows pervasive evidence for a significant hydrothermal overprint. We believe these hydrothermal textures and mineral associations are the fingerprint of

CO_2 boiling (effervescence) created as ascending, hot brine solutions followed paths of least resistance (both upwards and laterally) through the Absaroka thrust sheet. Sometimes there is a correlation between the orientation of hydrothermal conduits and the fracture sets described above. For example, hydrothermal breccia "walls" in the Jurassic Twin Creek Formation are oriented perpendicular to the regional trend of folds, suggesting they were controlled by set #3 fractures ("a-c"). Therefore, relative timing suggests that dilational jointing occurred in response to folding and thrust faulting, followed by the influx of CO_2 infused hydrothermal brine solutions that exploited these joints.

Fault zones characterization. Regarding the practical aspects of long-term, subsurface carbon sequestration, it is critical to understand how, why, and when faults act as barriers versus conduits, and to understand the potential for discontinuous leaks of CO_2 along faults. This is one of the most important facets of this research. Significant cataclastic deformation has occurred along all thrust faults in the field area, most notably the Absaroka, with a well-developed damage zone extending tens of meters into the hanging wall and several meters into the footwall. The actual brecciated fault zone of the Absaroka thrust is remarkably consistent in thickness, averaging ~4m (4.38 yards) in the hanging wall. Within this zone, the average fragment size was found to be ~1.2mm (0.047 inches) (Zone A), but jumped to 5.2 mm (0.205 inches) for several meters beyond (Zone B). Cataclastic rocks from Zone A are typically loose and crumbly, lacking in a significant percentage of secondary cement (typically calcite/dolomite). The small amount of cement present is yellowish-tan, "silty" dolomite that has been (a) reconstituted from the original dolomitic limestone (Cambrian) during cataclasis, and/or (b) introduced via hydrothermal brine + CO_2 migrating along the fault. The individual breccia fragments are medium-to-dark gray carbonate clasts; there is no visible foliation or internal fabric to the breccia zones, except for locally developed zones of finely comminuted rock that approaches gouge in size. Overall, Zone A is poorly cemented, reflecting either original porosity and permeability left over from the time of thrust sheet emplacement (unlikely, since that was over 60 million years ago), or secondary porosity and permeability created post-kinematic fluid flow through the fault zone (hydrothermal brine + CO_2). Zone B is significantly less brecciated and more coherent than Zone A, even though the rocks are of identical lithology and age. Zone B represents a transition between the intense cataclasis of Zone A and non-fractured rocks above; as such, Zone B is a true "damage zone" in the hanging wall of the Absaroka thrust fault. From detailed analysis it is clear to us that the Absaroka thrust and its hanging wall imbricate thrusts were highly permeable conduits for fluid flow during and after their motion history. Regarding the degree of fault zone permeability from fault to fault, the main controlling factors are (1) hanging wall lithology (e.g. dolomite is more brittle than limestone, accounting for its lower ductility before failure at a given confining pressure), and (2) dip-separation on the fault (resolved as heave and throw). The Absaroka thrust has by far the greatest dip-separation in the region and was a major pipeline for fluid/CO_2 flow. Vertical confinement for this highly faulted and fractured "sponge" of Paleozoic through Jurassic strata was provided by the seal/cap intervals discussed in the "Executive Summary."

One of the most important goals of this project was to determine which faults and fracture systems carried CO_2 and which did not. In knowing this, prediction of the structural integrity of future CO_2 sequestration sites may be possible. By virtue of the tectonic setting (fold-and-thrust belt), virtually all of the faults we studied in the field are characterized by intense cataclasis

extending farther into the hanging wall than the footwall, a well-defined fault plane with slickenlines (i.e., polish and slip striae), calcite/dolomite cement and, in the case of large faults like the Absaroka, a zone (up to a few meters thick) of loose, open breccia interlaced with narrow zones of finely comminuted gouge. Clearly, the major faults were the main conduits for fluid migration through the stratigraphic section and these faults remain open permeability pathways today (in the absence of eroded seal/cap rocks). Therefore, the amount of dip-separation appears to be one of the criteria in determining if a particular fault will be sealed or be a conduit. Based on the magnitude of fault displacements in this area, a reasonable cut-off would be 2 km (1.243 miles). Imbricate thrust faults with <2 km dip separation have not developed sufficient damage and breccia zones for subsequent fluid migration; conversely, large-displacement faults like the Absaroka are long-lived pipelines for subsurface fluids. Fracture networks in the field area also served as fluid migration pathways, particularly those dilatants/extensional sets that are either parallel or perpendicular to the trend of regional folding; these sets were also exploited by rising hydrothermal brines + CO_2 in the past.

Given the present-day high-temperature subsurface environment of CO_2 brines in SE Idaho and elsewhere in the region, we believe a strong case can be made for linking hydrothermal diagenesis to fluid migration processes associated with naturally occurring CO_2 systems. Thermal advection via migration of hydrothermal brines through a stratigraphic section may significantly alter the chemistry of reservoir rocks and control CO_2 movement (both vertically and horizontally) in unpredictable ways. Therefore, it is vitally important to understand these anomalous reservoir conditions prior to the onset of pilot injection/sequestration projects. For example, the faults and fractures described in the discussion section are often the main permeability pathways in conventional hydrocarbon reservoirs, in conjunction with matrix permeability zones in reservoir rocks. However, the advection of hydrothermal brine + CO_2 through a stratigraphic section may or may not follow these rather predictable fracture and fault patterns; hydrothermal "breakouts" may occur almost anywhere, channeling fluids both laterally and vertically in a maze of anastomosing breccia pipes. Having said this, many of the breccia pipes and breccia walls in the Absaroka thrust sheet do display some degree of structural control, either following thrust faults or one or more fracture sets, albeit highly modifying the route.

In summary, the basic structural requirements for deep subsurface sequestration of CO_2 (applicable to the Northern Rockies) include the following:

1. Porous and permeable reservoir rocks in the deep subsurface, capped by impermeable seal rocks (e.g., thick Cretaceous shale succession), that are not compromised by through-going, open faults and deeply-penetrating fracture sets that could leak CO_2 to the surface;
2. Four-way closure on large anticlines or domes with sufficient vertical amplitude to create large storage volumes at key reservoir levels;
3. Secondary structures (such as small-displacement, fault-propagation folds) that compartmentalize larger structures and thus provide the potential for stacked traps for CO_2 sequestration;
4. Abundant subsurface formation fluids (often these are warm hydrothermal brines) capable of carrying large volumes of dissolved CO_2;

5. A proven, in situ, natural, undersaturated CO_2 reservoir of that has maintained reservoir integrity for millions of years thus mitigating risk factors (examples include SE Idaho, the LaBarge Platform of western Wyoming, and the Kevin Dome in northern Montana).

Understanding impact of *CO_2* leakage on shallow groundwater

Shallow groundwater in the vicinity of Chimayo is distinctive from other basin waters in that it is very high in dissolved CO_2, higher in TDS and not as enriched with respect to sodium as the other relatively high TDS waters in the. High pCO_2 wells are clustered along a north-south trending fault (Figure 59). By calculating pCO_2 for all waters in the dataset, we compare the variability in pCO_2 within the Chimayo locality and the larger region. The Chimayo waters have anomalously high pCO_2 values. Regional waters have pCO_2 values somewhat higher than waters in equilibrium with the atmospheric (pCO_2 = -3), probably reflecting the consequence of mineral weathering (carbonates and/or silicates). Values as high as those measured in Chimayo waters can only be explained by invoking an internal source at depth. In Figure 60, we present the relationship between calculated pCO_2 (using PHREEQC) and measured Cl in Chimayo waters. Based on these data and assuming that the only source of Cl is deep connate brine and that Cl is a conservative species, we conclude that upwelling CO_2 is not always associated with deep connate brine (as it is in the Roberts Geyser). There are two distinct groups of high pCO_2 waters, one with background levels of Cl (shown in red, Group 2), one with high levels of Cl (shown in blue, Group 4), and intermediate waters (shown in green, Group 3). Samples colored black (Group 1) represent background waters, minimally affected by either CO_2 or connate brine. We used geochemical modeling to determine the potential reaction paths that can help describe the observed data. We explored two reaction paths: diffusion of pure CO_2 into the shallow aquifer and migration of deeper brine/CO_2 mix into shallow aquifer. Geochemical models using PHREEQC showed that the second reaction path matched the observed data better (Figure 61).

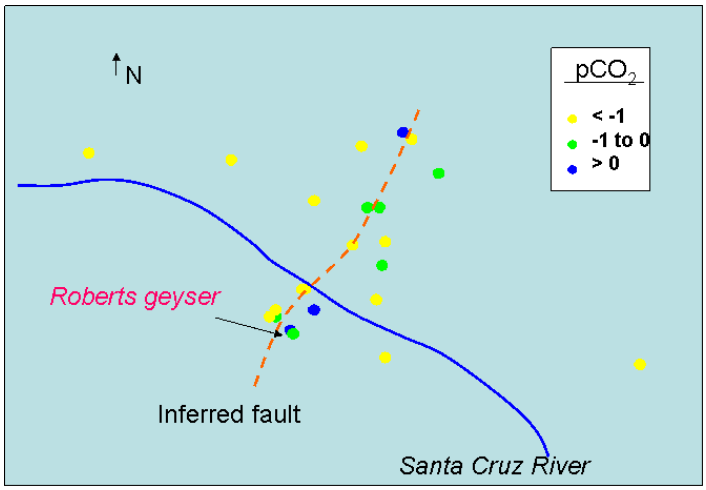

Figure 59. Map of wells in Chimayo. Color of dots indicate p**CO_2**.

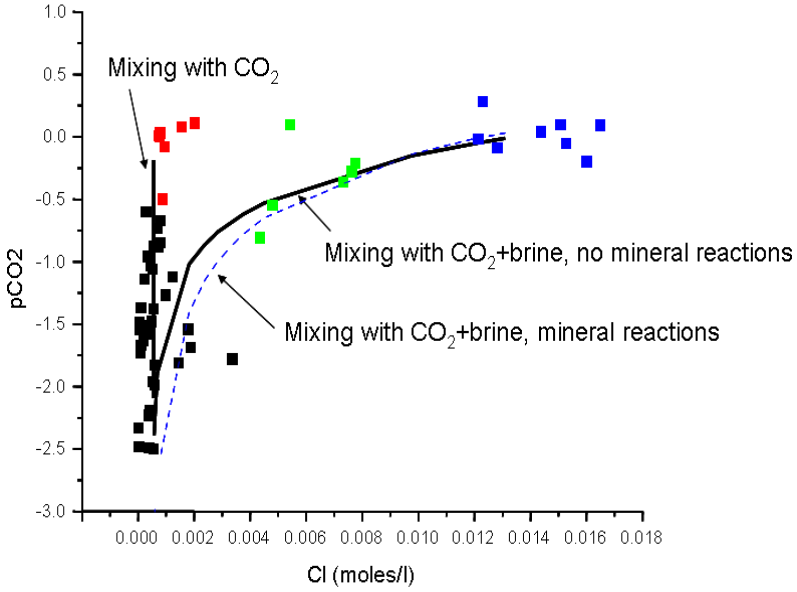

Figure 60. Measured variations in p$\mathbf{CO_2}$ and Cl in Chimayo waters. Lines indicate reaction paths described in text.

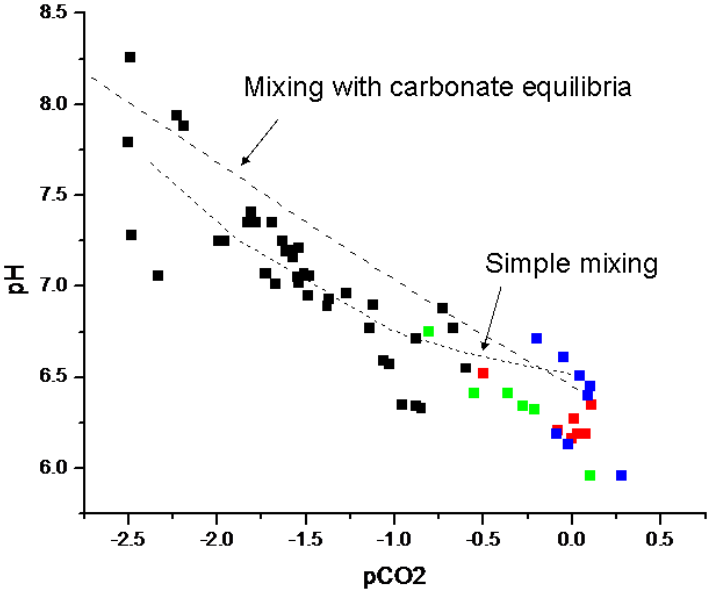

Figure 61. Measured variations in p$\mathbf{CO_2}$ and pH in Chimayo waters. Lines indicate simulations of mixing with $\mathbf{CO_2}$-brine (geyser water) and background groundwater.

This model was used to examine the potential for uranium to be mobilized by the CO_2 plume. Roberts Geyser has measured concentrations of 160 ppb. This water is undersaturated with respect to common uranium minerals (see Table 8), suggesting the potential for uranium dissolution.

Table 8. Saturation indices with respect to common uranium minerals

B-UO2(OH)2	-7.4	$UO_2(OH)_2$
Coffinite	-8.7	$USiO_4$
Gummite	-12.5	UO_3
Rutherfordine	-5.4	UO_2CO_3
Schoepite	-7.2	$UO_2(OH)_2{:}H_2O$
U(OH)2SO4	-26.4	$U(OH)_2SO_4$
U3O8(c)	-19.5	U_3O_8
U4O9(c)	-29.4	U_4O_9
UO2(a)	-13.0	UO_2
UO3(gamma)	-9.7	UO_3
Uraninite(c)	-8.6	UO_2
Uranophane	-15.8	$Ca(UO2)_2(SiO_3OH)_2$

Furthermore, high alkalinity produced by CO_2 is known to complex U and further enhance U mineral solubility. Although available data for dissolved uranium at this site is very limited, examination of the data in the context of regional data and in the context of calculated saturation indices for common uranium minerals leads us to conclude that in the regional context there is no relationship between pCO_2 and [U] (see Figure 62), and furthermore, our highest pCO_2 sample (Roberts Geyser) has [U] concentrations which are elevated, but well within background levels.

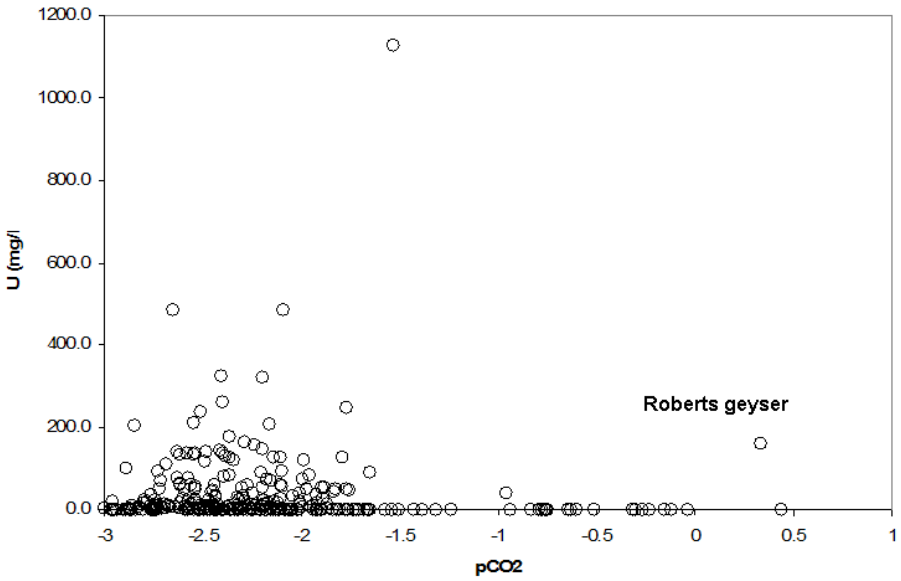

Figure 62. Measured variations in dissolved uranium and pCO_2

Secondly, as the CO_2/brine water mixes with background waters, [U] is reduced from 160 ppb to below detection. This strongly suggests that any [U] either transported upward with the CO_2/brine or brought into solution locally by high pCO_2 concentrations can rapidly re-precipitate due to mixing with background waters or due to other non-CO_2 related processes.

In summary, we conclude based on geochemical modeling and available data that enhanced mobility of trace metals due to CO_2 is unlikely at this site. This study focused on groundwater in Chimayo, New Mexico, where high levels of dissolved carbon dioxide have been measured in shallow (< 200 ft deep) wells. We examined existing data for this site and regional groundwaters, supplemented the data with limited additional sampling in the vicinity of the high CO_2 waters, and conducted geochemical modeling to examine the potential impacts of mixing, aqueous reactions, and buffering due to carbonate mineral equilibrium on iron and uranium mobility. Results suggest enhanced trace metal mobility due to elevated CO_2 is either nil or too small to be detected within the context of natural background variability. Although the dataset presented and geochemical modeling do support our conclusion regarding trace metal mobility, it begs the basic question "are we not seeing effects because our sample size is so small" or, to phrase this another way, "if we collected more data or did a more exhaustive geochemical modeling study, would we begin to see clear trace-metal mobility effects?" Of course the honest answer is "yes, this is possible", but is also true that neither the existing data nor geochemical theory suggest that this would be likely. The Chimayo site, in fact, shares many of the features that will cloud any natural analogue study of a CO_2 emerging through a shallow aquifer. At many sites, rather than emerging as pure CO_2, the CO_2 is likely to rise with co-contaminants such as heavy metals (common in thermal waters), trace elements associated with residue from depleted oil reservoirs, and//or high levels of common ions (Na, Cl, SO_4, etc.) associated with saline brines. The impact of these co-contaminants on shallow groundwater quality is likely to be much larger than that of the CO_2 and CO_2-induced geochemical reactions, thus, detection of a "CO_2" effect, per se, will

be extremely difficult if not impossible. The Chimayo site offers one advantage in this respect; the data do show evidence of both "pure" CO_2 mixing with shallow waters and a CO_2-brine mixing with shallow waters. Geochemical modeling suggests pure CO_2 will be much more reactive, yet, in this geochemical environment the reactivity will not be sufficient to mobilize metals beyond background levels. If this result can be generalized to other sedimentary basin-fill aquifers (which are common in the arid southwest) it is encouraging for the prospect of carbon sequestration in this region.

Basic Geoscience: Pore Scale

Core testing: Version 1, flow-through reactor system. A significant increase in $Mg^{2+}_{(aq)}$ was observed in the first 96 hours with minimal subsequent change. Changes in other analytes were recorded during the experiments; however, their concentrations after 120 hours were similar to initial concentrations at t = 0. $HCO_3^-{}_{(aq)}$ was not measured via IC but is the complementary anion to $Mg^{2+}_{(aq)}$ as determined via charge balance, given no significant changes in $Cl^-_{(aq)}$ and $SO_4^{2-}{}_{(aq)}$. These data indicate dissolution of the limestone/dolostone rock core.

Core testing: Version 2, flow-through reactor system. Addition of CO_2 to brine at all tested conditions significantly reduced brine pH. Dilute brine (0.5 g L^{-1}) pH was reduced to a greater degree, a reduction of ~3.5 pH units, than the concentrated brine (5 g L^{-1}), a reduction of ~2.5 pH units (Figure 63). A minor increase in pH of ~ 0.1 units was observed with increasing temperature from 45-95 ^oC for the 0.5 g L^{-1} brine. However, this falls within the error envelope of the measurements and thus is not considered statistically significant. A minor decrease in pH of ~ 0.1-0.2 units was observed with increasing pressure from 1200-1600 psi; however, the further increases in pressure to 2000 psi did not result in any further change in pH. No statistically significant change in EC was observed for any experiment.

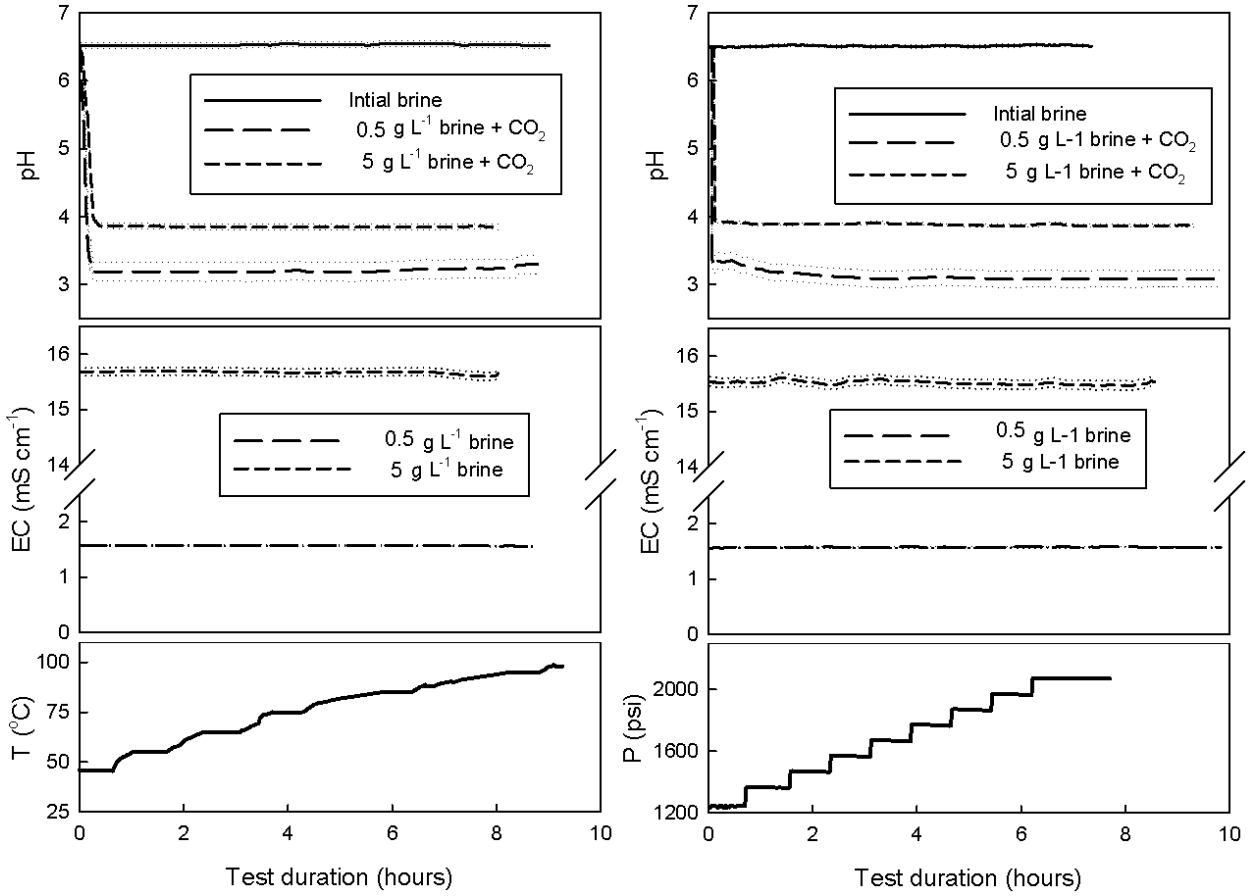

Figure 63. pH and EC versus experiment duration as a function of variable temperature (left panel) and variable pressure (right panel). Each line represents data from triplicate experiments (major lines) plotted with an error envelope (minor, dashed lines) of ± one standard deviation. Error envelopes fall within the thickness of plotted lines where no error envelope is visible.

Discrete bench pH measurements agree well with *in situ* pH probe data for experiments conducted with brine only, i.e. no added CO_2. A reproducible difference of ~ 0.5-1.25 pH units is observed between discrete bench measurements and the *in situ* pH probe data in experiments conducted with CO_2 for 5 g L^{-1} brine and 0.5 g L^{-1} brine respectively. In all cases the discrete pH measurements are higher than the measured *in situ* pH values. Results of geochemical modeling at ambient pressure of 1 atm (0.1MPa) were compared to *in situ* (continuous) at elevated pressure and *ex situ* (discrete) pH measurements also at ambient pressure (Figure 64). The modeled rise in pH in response to elevated temperatures was not observed in either the *in situ* or bench pH data and the modeled data agreed most closely with the empirical bench pH data at higher temperatures (>75 ^{o}C). PHREEQC predicted higher pH values, up to 1.2 pH unit difference in all modeled scenarios than the *in situ* pH data The discrepancy was ~ 0.3 to 0.5 pH units for the 5 g L^{-1} brine and 0.7-1.2 pH units for the 0.5 g L^{-1} brine with the difference increasing at higher temperatures. This highlights the limitation of current geochemical models e.g. PHREEQC in representing scenarios that include supercritical CO_2.

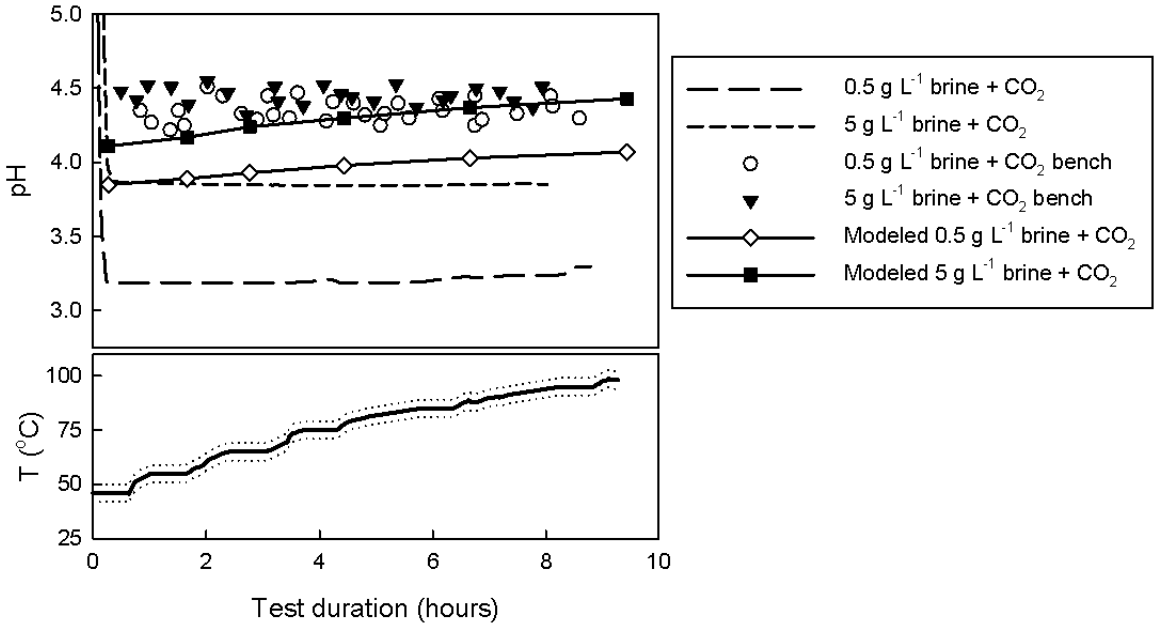

Figure 64. Comparison of continuous *in situ* pH and EC (solid and dashed lines), discrete bench measurements, and modeled results using PHREEQC versus time as a function of varying system temperature. Error envelopes have been excluded for simplicity.

Injection of the CO_2/brine mixture into Madison Formation rock cores decreased brine pH in all four experiments (Figure 65). There was a sharp initial reduction of 1 pH unit in the 90 ^oC experiments with both the 0.5 and 5 g L^{-1} brine. At 50 ^oC the initial pH reduction was 1.5-1.8 pH units with the lowest value recorded with the 0.5 g L^{-1} brines. A gradual increase in pH occurred in all experiments over the following hours with a plateau in pH being measured at 40 hours for the 50 ^oC 0.5 g L^{-1}, 80 hours for the 90 ^oC 0.5 g L^{-1} and 100 hours for the 90 ^oC 5 g L^{-1}. Only in the 50 ^oC 5 g L^{-1} experiment did the pH continue to rise gradually over the 120 hour experiment. After ~ 30 hours the pH profile for the 50 ^oC experiments was largely similar, to within ~ 0.1 pH units with both brine concentrations. The pH profiles in the 90 ^oC experiments were also somewhat similar with the 5 g L^{-1} solution consistently higher than the 0.5 g L^{-1} solution by ~ 0.1 pH units from 4-78 hours.

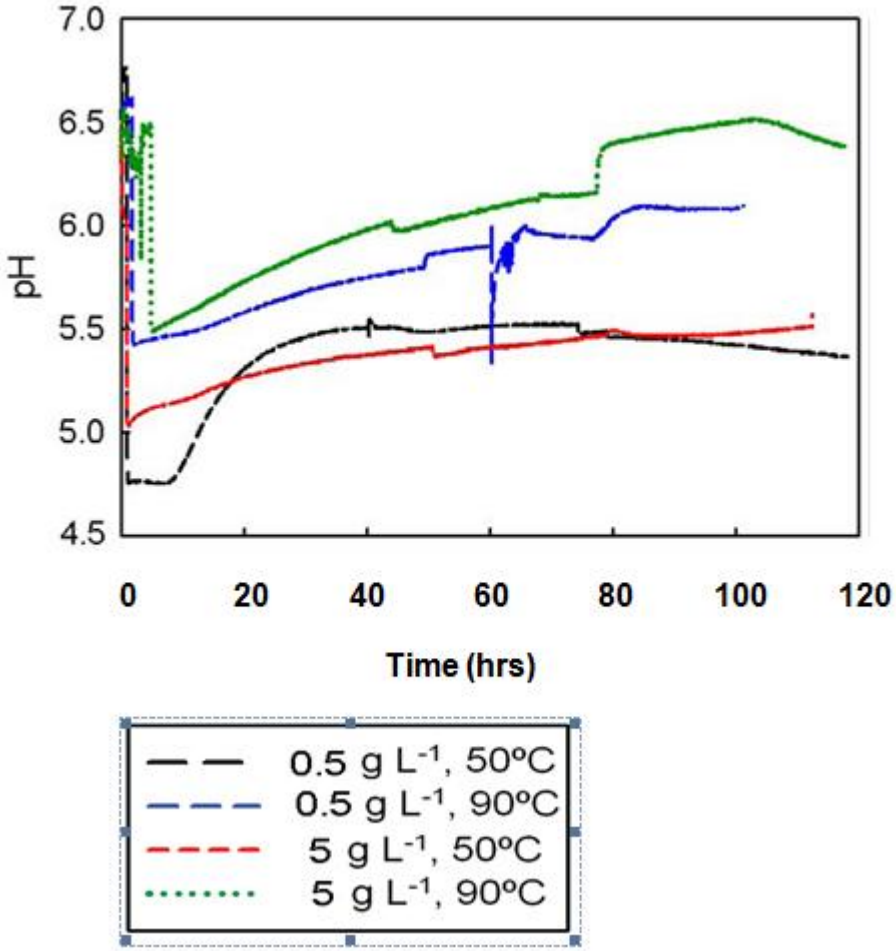

Figure 65. Continuous pH record from in situ pH probe for four core flood experiments.

Core analysis did not show significant trends relating exposure to CO_2 to changes in rock properties (Figure 66). Overall, samples with higher porosity generally had higher permeability, and in general, post-flood samples had higher porosity and permeability than unchallenged samples. However, this was not the case for all samples. The three highest porosity values were in flooded samples (22.0%, 19.5%, and 18.6%) but the highest measured permeability was for an unflooded core plug (57.5 mD). This variability may reflect the inherent heterogeneity within a particular block or rock from which cores were sub-sampled (e.g. Henriette et al. 1989)

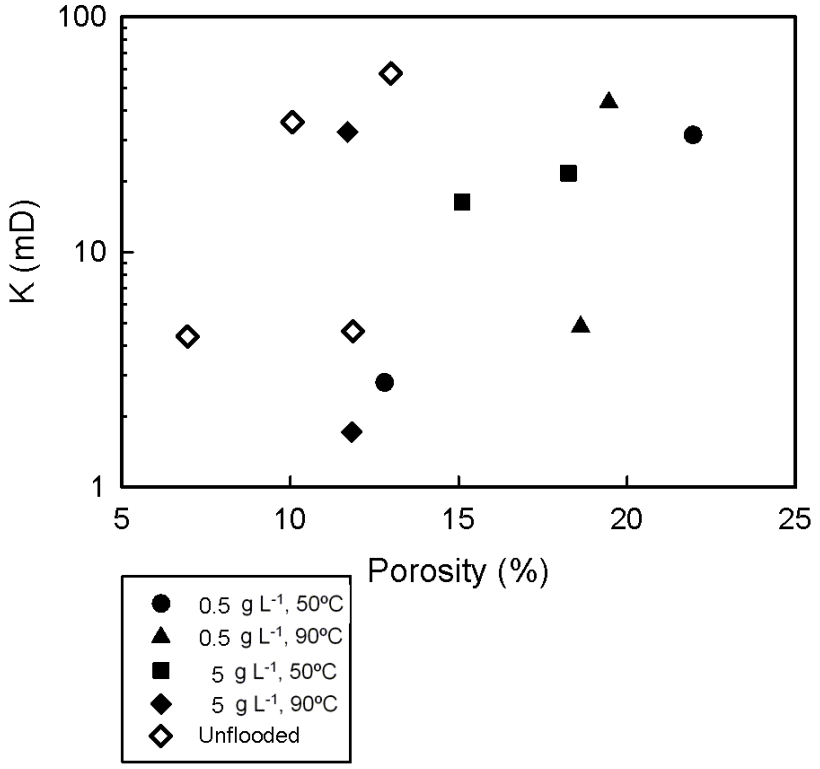

Figure 66. Porosity versus permeability for four unflooded core samples and eight core samples subjected to brine-$\mathbf{CO_2}$ injection (open and closed icons, respectively).

Magnesium concentrations (Mg^{2+}) in the brine effluent increased in all the experiments; however, a clear relationship between net dissolution and temperature or net dissolution and fluid TDS was not evident. While some of the differences observed may result from core composition heterogeneity, these results highlight the need for further studies to better understand the effects of primary variables such as temperature and TDS on supercritical CO_2-brine-rock interactions.

Core testing: Version 2, flow-through reactor system. NMR images of fresh cores were compared with images of cores following CO_2-brine mixture challenges using a protocol for pixel-by-pixel comparison to determine the effects on bulk pore volume and geometry of sandstone and carbonate cores (Figure 67). The carbonate core showed evidence for an increase in pore volume along existing high-porosity features suggesting pore increase by enlargement of existing pores and/or fractures. 3-D images of the carbonate cores before and after the brine-CO_2 challenge were constructed from individual cores slices, and showed an increase in the volume and 3-D connectivity of the pore network (Figure 68). Flow rate and differential pressure were monitored in the core experiments to provide a measure of changes in permeability (Figure 69). The permeability of the sandstone cores remained constant over the range of temperature and brine concentrations tested, but an increase in permeability of the carbonate core was demonstrated. These results are consistent with Hansen, (2009), where dissolution and was recorded in supercritical CO_2-brine challenge experiments on carbonate cores of the Madison formation.

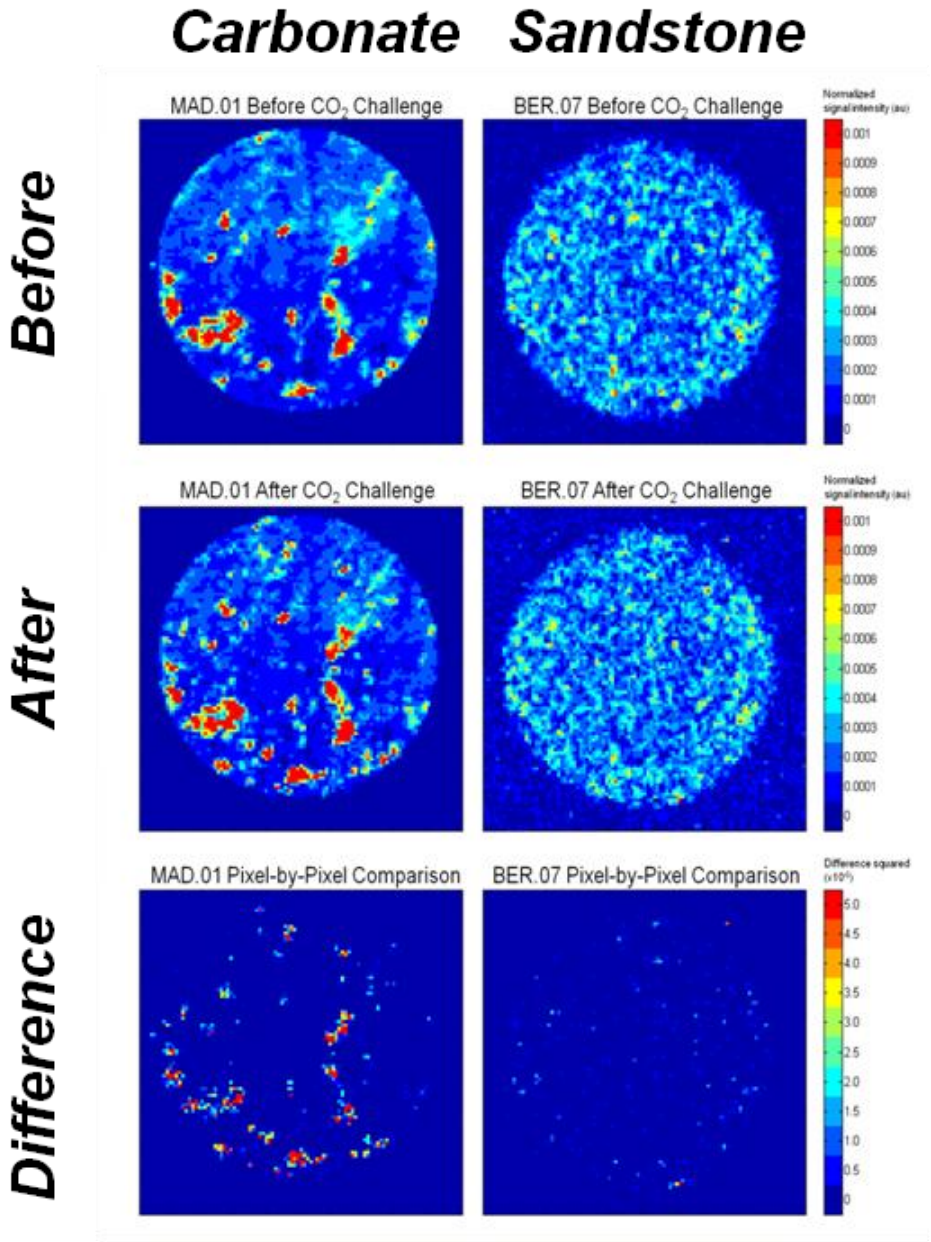

Figure 67. NMR image slice comparison.

Representative spin echo slice images of carbonate (limestone/dolostone) (MAD.01 – left column) and quartz arenite sandstone (BER.07 – right column) are shown in Figure 67. Each experiment consisted of 12 axial slices with thickness 1.5mm and in-plane resolution of 0.27mm x 0.27mm. Slices were separated by 2.5mm. Two experiments were performed with interleaving slices on both the bottom and top of each core. The rocks were then challenged with CO_2 and the experiments were repeated with the cores in the same position. Images are normalized with total signal intensity from the middle part of the core. We interpret high signal intensity as an indication of a high density of fluid-filled pore space. The bottom set of images show pixel-by-

pixel comparison between before and after images. Images were produced by taking the square of the difference in normalized signal intensity between 'before' and 'after' images. Areas where fluid-filled pore density increased after the challenge show as warm colors.

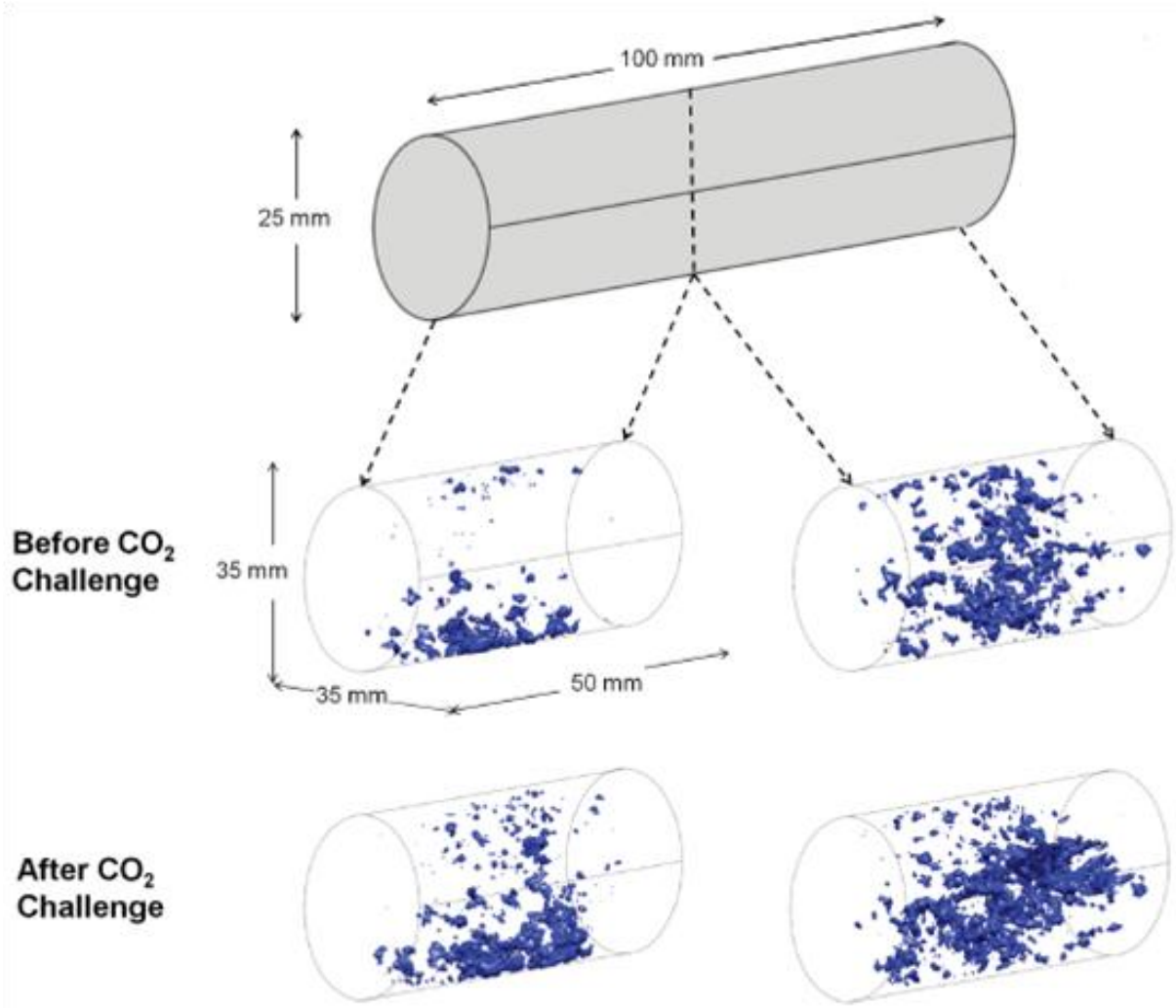

Figure 68. 3-D spin echo images of pore structure of carbonate core (MAD.01) before and after **CO_2** challenge

Resolution of images shown in Figure 45 is 0.47mm x 0.55mm x 0.55mm. The Images show the increase of pore volume in both the top and bottom of the sample, as also evidenced by porosity and permeability measurements. The signal intensity was normalized to the total signal intensity for each experiment, and the same threshold of 0.025% of the total intensity was then used for all four images.

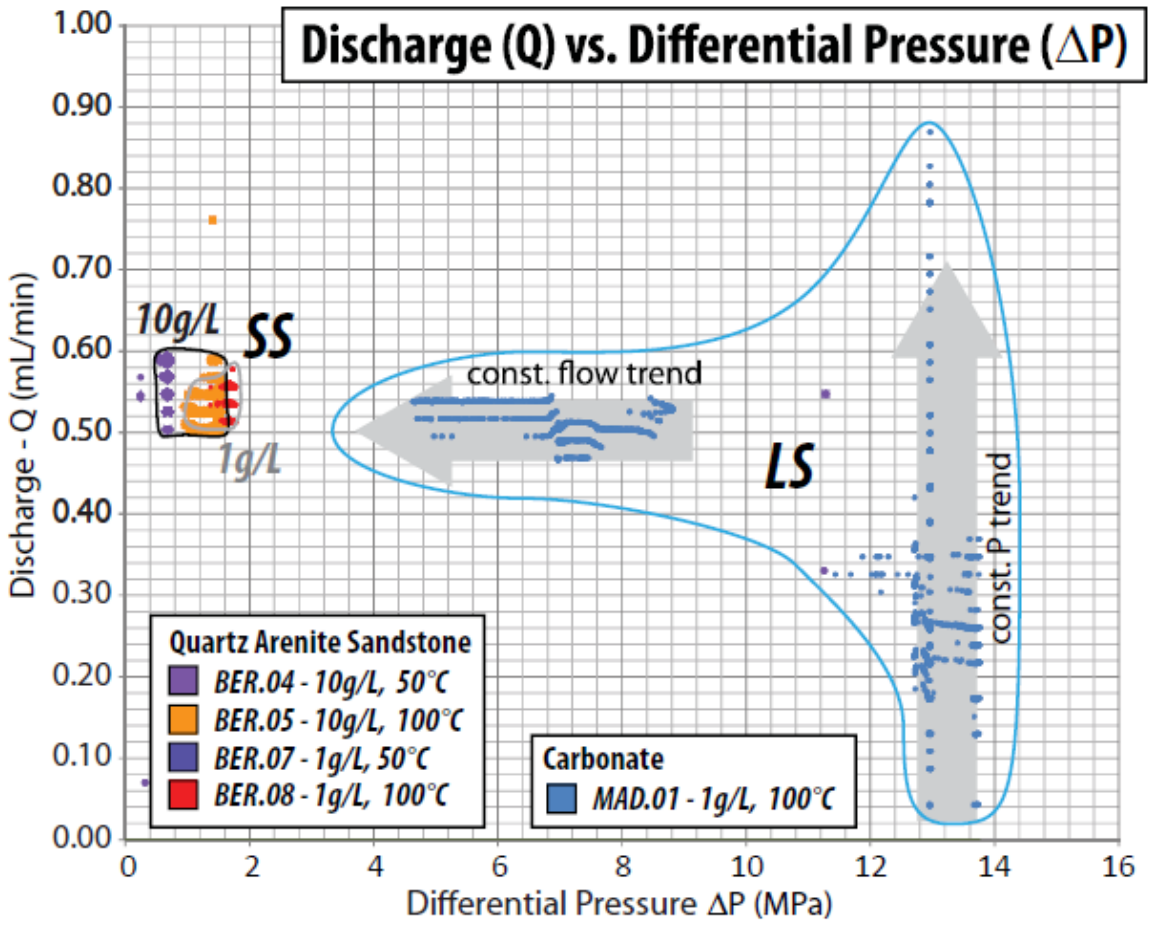

Figure 69. Plot of discharge (flow rate) vs. differential pressure from real-time measurements for all experiments

Figure 46 demonstrates that data from four separate sandstone (SS) experiments form a tight cluster. Data from the carbonate (LS) experiment is dispersed along a time-evolution path. Because of system limitations the first part of the LS experiment was conducted at constant P. Discharge accelerated after introduction of CO_2. After switching to constant flow, differential pressure decreased over time.

The key outcomes of this research are the successful development and testing of laboratory core-flooding technology for experimentally assessing effects of supercritical CO_2-brine mixtures including novel inline, *in situ* measurements of variables such as temperature, pressure, pH, and EC. Further the research has demonstrated the utility of non-destructive NMR imaging to track changes in the physical properties of rock cores in response to CO_2-brine floods. Experimental results demonstrated mixing supercritical CO_2 and brine significantly reduced brine pH under all tested conditions; however, this effect was partially buffered by in-line carbonate rock cores, but no significant buffering was evident with the sandstone cores. No measurable change in porosity was evident in sandstone cores following supercritical CO_2-brine exposure as measured by NMR but an increase in porosity concentrated near pre-existing pore-space and an increase in the 3-D

connectivity of the pore network was evident in carbonate cores. Permeability of the sandstone cores remained constant; though, a 6-fold increase in permeability of the carbonate core was measured. Collectively these results suggest that chemical dissolution concentrated in pre-existing pore networks effectively enhances permeability. Nevertheless, the experimental results did not show a clear relationship between net dissolution and temperature or net dissolution and fluid TDS with the carbonate cores. Future work would be necessary to further investigate this.

Basic Geoscience: Basin Scale

Discussion of results is presented in the order of the data analysis and research phases summarized in the previous sections of this report. Though separated in the discussion, these sections describe steps in an iterative progression that facilitates data integration.

Geologic Characterization. The hierarchical approach to geologic characterization accounts for heterogeneity and its spatial distribution at different scales (Figure 70). The Petra database provides core-to-log calibration, enabling high-resolution mapping within a consistently constructed stratigraphic framework. Core-calibrated, well log, and petrophysical measurements define 17 sedimentary attributes in five categories (tectonics, sedimentology, sedimentary bodies, paleogeography and stratigraphy). Correlation of 30 stratigraphic surfaces bracket 13 second-order and 25 third-order sequences populated with sedimentary attributes distributed within 25 sedimentation regions. Sedimentation regions vary in size, shape, and arrangement within stratigraphic sequences. At the scale of fourth- and higher-order sequences, only defined in RC4, the nine sedimentation regions approximate preserved environments of deposition and define the components of the depositional sequence (e.g., systems tracts, Vail et al. 1977). Sedimentation regions migrate in accordance to Walther's Law (e.g., Middleton 1973) in conformable successions of strata recording high accommodation (Gardner, 1995; Gardner et al. 2004). Sedimentary patterns are more complex when incompletely preserved under low accommodation conditions, and represented by depositional remnants and more time-significant surfaces (Merewether and Cobban 1983; Ryer and Lovekin 1986; Gardner et al. 1995; Martinsen 2003a. 2003b; Merewether et al. 2007; Plint and Kreitner 2007).

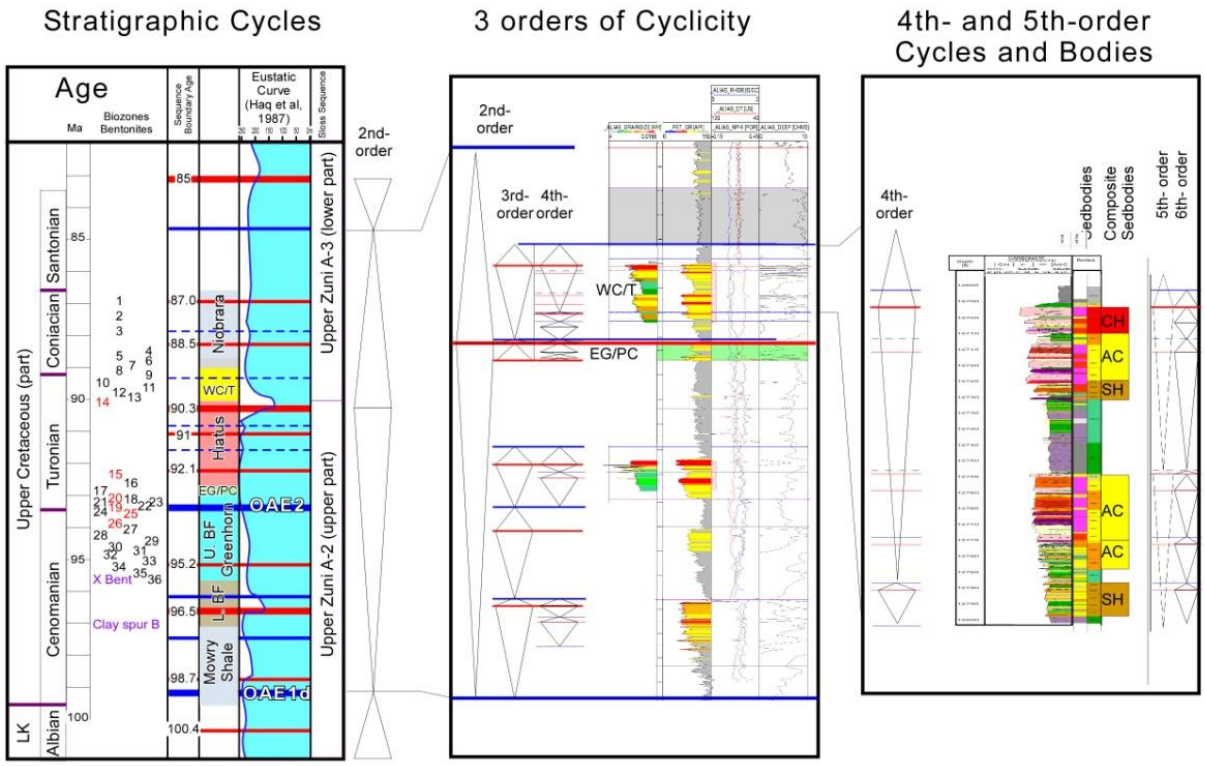

Figure 70. Three-fold stratigraphic hierarchy

It is important to note that in lower resolution sequences, sedimentation regions are composite spatial domains combining multiple environments of deposition. The increased resolution in higher-order sequences (i.e., shorter duration fourth-order or higher) contains more sedimentary attributes to account for variations produced by sequence stacking patterns. This enables comparison of sedimentation regions to modern environments of deposition. Correlation of thickness and lithology distributions in the Frontier Formation (RC4) to modern environments of deposition contributes to the prevailing paleogeographic interpretation of a delta in the Powder River Basin (Haun 1953; Weimer 1960; Barlow and Haun 1966; McGookey et al. 1972; Merewether et al. 1979; Winn et al. 1983; Roberts and Kirschbaum 1995; Bhattacharya and Willis 2001, Kirschbaum et al. 2009, among many others). The hierarchy of sedimentary attributes, within this high-resolution and basin-wide stratigraphic framework, documents the incomplete preservation of depositional components with remnants of a deltaic system distributed in stratigraphic sequences spread out across a broad area that extends beyond the limits of the Powder River Basin. Gravity and magnetic anomaly maps, integrated with crustal provenance maps, define basin topology and variable subsidence of anisotropic continental crust (Slack 1981; Marrs and Raines 1984; Kluth 1986; Anna 1986; Tonnsen 1986; Peterson and Smith 1986; Ye et al. 1996; Woodward 1988; Dickinson et al. 1988; Baars et al. 1998; Bally 1989; Snoke 1993). This comparison supports a tectonic control on remnant sedimentation patterns that don't exist in modern deltas (Barrell 1912; Fisk 1955; Wright and Coleman 1973; Harms et al. 1975; Elliot 1986; Bhattacharya and Walker 1992). These results highlight the information required to effectively incorporate geologic analogs in site characterization and reservoir modeling.

Geomodeling Workflow. The model building workflow emphasizes the retention of multiple scales of heterogeneity explicitly correlated to formative geologic process. The (1) correlation of reservoir properties to a hierarchy of sedimentary elements (2) modulated within a hierarchical stratigraphic framework, and embedded with (3) sedimentation regions constraining spatial heterogeneity distributions within reservoir layers. Heterogeneity retention utilizes established methods derived from outcrop studies that reproduce sedimentary architecture using existing reservoir modeling software and techniques (Borer 2005). Populating properties within a model grid is required to simulate fluid flow (e.g., Blunt et al. 2002); what differs in this workflow is the geologic context assigned to the data and its rigorous correlation to formative process (Gardner et al. 1992; Willis 1998; Willis and White 2000; Atan et al. 2001; Borer 2005). This approach correlates heterogeneity to its geologic source to enable reproducibility and interrogation of multiple reservoir scenarios and realizations. The two geomodels resulting from this research enable interrogation of different simulation scales and grid designs (Atan et al. 2005; Wells et al. 2006; Carneiro 2009).

Pore Volume Determination. Pore-volume calculations by reservoir class are presented based on factor and region methods applied to four different scale scenarios. Results highlight the impact of resolution and scale on detection of net pore volumes affecting storage capacity. The different sequence and region measurements are considered relevant to different scales of geologic heterogeneity, model designs, and sample density.

RC1: Fewer wells penetrate the deepest RC and produce high values that reflect non-geologic differences in sample density rather than geologic trends associated with karsted, shallow-marine platform carbonates (Sando 1988; Erlick and Read 1991; Sonnenfeld 1996b; Westphal et al. 2004; Smith et al. 2004). Color-coding of wells by reservoir class in Figure 27 illustrates the decrease in well penetration with depth. Consequently, approximately 2/3 of the NPV is calculated from shallower wells in the northern part of the basin. Many proposed storage sites target deep saline aquifers (Fischer et al. 2005; Birkholzer et al. 2009; Kopp et al. 2009a. 2009b; DOE/NETL-401/090808, 2010; N.E.T.L. 2010), where sparse data favors statistical averaging techniques and calculations are biased to shallower data recording a different burial and diagenetic history (Dutton and Willis 1998).

RC2: Both factor and region methods produce similar results, but the range in values is 2.5 orders of magnitude lower using the region method. While these results highlight the value of using regions within reservoir layers, they also illustrate the need to geologically constrain region size. Regions are particularly important to RCs with diverse rock types, but when poorly defined they over-emphasize lateral continuity (high horizontal permeability). In this case, the high number of small fields producing from eolian dune sandstone reservoirs, isolated by depositional topography and incision by mudstone valley-fills, indicates more reservoir complexity than NPV calculations reveal (Tenney 1963; Trotter 1963; 1984; Van West 1971; Moore 1975; Tromp et al. 1981; Curry 1984; Fryberger 1984; Kerr et al. 1986; Frederick et al. 1995).

RC3: Pronounced spatial partitioning of reservoir and non-reservoir strata makes this the RC most sensitive to region-based pore volume calculations. Regions halve values because they

discriminate between narrow and elongate coastal paleo-valleys, filled with reservoir sandstone, and encased by non-reservoir marine mudrocks (Weimer et al. 1984; Gustason et al. 1988; Dolson et al. 1991; Dolson and Miller 1994; Gardner 2001). Higher resolution intervals are required to capture the >20 percent variation in reservoir porosity (e.g., Berg 1976; Wheeler et al. 1988). This increases the potential error with using average field values to characterize the wide range in porosity.

RC4: The most detailed geologic characterization documents the remnant delta RC and illustrates the impact of scale on NPV. Calculations of fourth-order sequences with regions double the NPV compared to values from third-order sequences. Increased resolution also reduces the range in NPV values (one order of magnitude lower). These results also reflect widespread sandstone distributions related to truncation and redistribution associated with seaward-stepping shallow-marine sequences and sedimentation from hyperpycnal flows (Weimer and Flexer 1985; Larue 1995; Fitzsimmons and Johnson 2000; Plint and Nummedal 2000; Bhattacharya and Willis 2001; Sadeque and Bhattacharya 2004).

RC5: Sedimentation regions are required to capture the spatial repetition and isolation of reservoir and non-reservoir intervals. In this case, regions account for the shoreline-parallel, shelf sandstone ridges isolated by mudstone belts (Brenner 1978; Hobson et al. 1982; Rice and Shurr 1983; Swift and Rice 1984; Tillman and Martinsen 1987; Tillman and Merewether 1994; Tilman 1997). Regions reduce the range in values by an order of magnitude, but the estimates reflect the lower resolution in the third-order sequences.

Geologic characterization of the Powder River Basin for industrial-scale GCS emphasizes the need to consider scale in the definition of the assessment problem. The presence of multiple scales of heterogeneity in sedimentary rocks is well known, as is its correlation to both temporal and spatial sedimentary hierarchies in stratigraphy (Barrell 1917; Sloss 1962; Weimer 1984; Haq et al. 1987, Tyler 1988; Galloway 1989; Van Wagoner 1990; Gardner et al. 1992; Larue and Yue 2003; Miller et al. 2005; Vakarelov et al. 2006). The treatment of this geological information determines the accuracy of estimates of storage, injectivity, and migration of fluids in a basin (Wells et al. 2006; Litynski et al. 2008; Oldenburg et al. 2009). Consequently, GCS models must be built to address the scale of the problem and this is at the basin scale (Nicot 2008; Birkholzer and Zhou 2009; Yamamoto et al. 2009; Zhou et al. 2010). This study provides three relevant contributions:

1) Documentation of a hierarchical approach to reservoir characterization
2) Development of modeling workflow to retain multiple scales of heterogeneity
3) Demonstration of relevance through pore volume calculations from five reservoir classes

One of the many challenges facing GCS modeling is the retention of multiple scales of heterogeneity for realistic simulation of long-term fluid movement in a sedimentary basin. Hierarchical reservoir characterization enables correlation of geological processes operating at different temporal scales to multiple spatial scales of heterogeneity. Stratigraphic modulation of heterogeneity distributions must address the additive and dampening affect created by superimposing different temporal scales of stratigraphic cyclicity (e.g., Gardner 1995). These

conclusions are relevant because they enable higher resolution sedimentary responses to be accounted for in lower resolution geomorphic landscapes in which they are embedded. When these hierarchical sedimentary elements cannot be reconciled, it does not mean they are unrelated or don't exist, but rather their incomplete preservation and expression has reduced correlation and detection (Bhattacharya and MacMeacharn 2006; Gani and Bhattacharya 2007). Multiple scales of heterogeneity exist within all sedimentary systems and are necessary and sufficient for the simulation of supercritical fluids in GCS models, irrespective of scale.

This study highlights the problem with predicting Earth systems from limited data (i.e., limited well data) or by simplification of complex phenomena (i.e., homogeneous modeling of heterogeneous media). This does not mean Earth systems cannot be predicted, but existing methods oversimplify the complexity. They fail to account for the hierarchy of Earth processes and responses that operate over geologic time. This is why geologic models with multiple scales of heterogeneity must be used to understand the long-term fate of unprecedented volumes of supercritical CO_2 that will be stored in them (Pacala and Socolow 2004; Sneider and Young 2009; Charles 2009).

The workflow developed in this study deploys field-scale methods at the basin scale to retain multi-scale heterogeneity in geomodels for a variety of reservoir classes. Region stacking patterns within sequences help manage non-uniform property distributions within the model (Figure 32). Analyzing different scales of geologic heterogeneity change predictions of storage capacity and complexity. For example, homogeneous models of supercritical CO_2 displacing denser brine in a saline aquifer over-emphasize buoyancy and vertical well-bore leakage. Geologic heterogeneity creates non-uniform and unsteady variations in flow rate (well-documented behavior in fluid production from subsurface reservoirs), which cannot be assessed using single-well, pilot studies that fail to consider dynamic basin aquifer systems (Doughty et al. 2008; Chiaramonte et al. 2008). Consequently, all GCS in future power plant design and deployment must be studied at the basin scale (Damen et al. 2009).

The net pore volume calculations demonstrate the limitation of simplistic conclusions resulting from GCS models based on homogeneous media (Celia 2008). Skewed and inaccurate results reflect the over-simplistic correlation of porosity to interval thickness, which assumes no variation in properties and/or heterogeneity in stratigraphic intervals spanning up to ten million years (Fischer et al. 2005). Vertical flow barriers in the upper half of RC1 points to the error in using uniform property distributions (Smith et al. 2004). The increased uncertainty created by a low sample density requires more deterministic, high-resolution sequence frameworks, embedded with spatial regions, to manage sparsely sampled storage sites. This analysis also illustrates how each RC has unique resolution requirements. Third-order sequences sufficient to capture heterogeneity in one system can be inadequate for description of another.

Basic Sequestration Science

A core-flood and imaging apparatus was built, tested, and used to study CO_2-brine displacement in a Berea sandstone core. The main conclusion from these laboratory studies is that heterogeneity affects CO_2 invasion at all scales. Using micro CT and the method of multiple

inscribed spheres (MIS), effects of heterogeneity were observed at the pore scale. At the core scale, even relatively homogeneous core has porosity variations that prevent complete replacement of brine by CO_2 by flow processes. The importance of surface tension in controlling capillary pressure effects motivated initiation of work to measure surface tension of $scCO_2$ which will continue in the ZERT project.

Progress under PNNL's task 2 was significant throughout the duration of this program and resulted in a number of presentations and publications. Laboratory experiments exploring reactivity of trace amounts of water in $scCO_2$ were reported by McGrail et al. (2009) and showed (Figure 71) that the most important chemical reactivity and impacts on steel components occurred in the liquid CO_2 phase instead of water where most attention has been focused. Another area of focus under Task 2 was the in-depth investigation of the fundamental interactions of $scCO_2$ in the presence of co-existing compounds (e.g. H_2O, $SO_{2)}$, and/or at the interface of these condensed media with metal or mineral surfaces. Unlike the well-established reactivity in aqueous environments, reactivity is $scCO_2$ is not well understood. These discoveries have led to a new BES effort to advance the fundamental science of wet $scCO_2$ interactions with silicates and a PNNL laboratory-level LDRD investment to develop a new set of high-pressure capable instruments to enable in situ investigation of wet $scCO_2$ reactions with various natural minerals and engineered materials such as steels and cements.

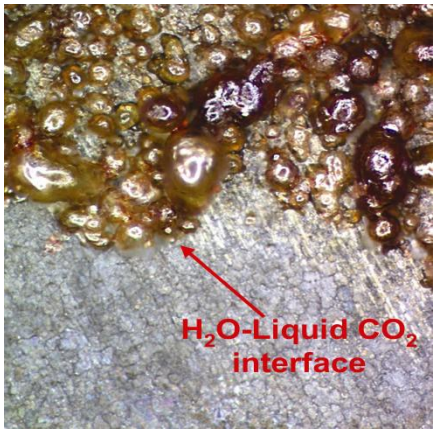

Figure 71. Optical photograph of corroded steel surface resulting from exposure to a liquid **CO_2** and H_2O for six days (1000 psig **CO_2** in excess water.).

Examination of fundamental interactions of CO_2 and H_2O on the Fe(100) surface with molecular dynamics simulations indicated corrosion and CO_3 formation proceeds through the spontaneous activation and decomposition of CO_2 on the surface rather than formation of carbonic acid (Glezakou and Dang 2009; Glezakou et al. 2010). Additional studies within the periodic cell approximation as well as experimental studies showed that traces of water assist in the process by hydroxylating the adsorbed O-sites, thus lowering the energy barrier to CO_2 addition to form CO_3, while water is re-generated after the CO_3 formation (McGrail et al., 2009). Hydrogen bonding was identified as a key component in this mechanism. DFT-based dynamics of sc-$CO_2/(H_2O)_n$, n=1-4, reveal that traces of water do not affect the internal structure of CO_2, which also explains why the formation of carbonic acid is not possible in this case (Glezakou et al., 2010).

PNNL's task 4.0 was completed by the issuance of a literature review (Krupa et al., 2010) identifying published studies related to computer modeling simulation, field injection site, natural analogue site, and laboratory fluid-rock and mineral studies of the carbonate reactions associated with the subsurface injection and sequestration of CO_2 and acid gases. All references included in our review were first examined to identify the names of geochemical reaction codes used to predict geochemical changes in fluid and mineral compositions resulting from CO_2 sequestration or to interpret geochemical reactions that occurred in laboratory experiments or at field sites from CO_2 sequestration. This information was used to identify what thermodynamic data are available for the carbonate gaseous, aqueous, and mineral species in sources most commonly utilized for the thermodynamic databases that are in these computer models.

CONCLUSION

Modeling

ZERT efforts have significantly advanced the state of modeling and simulation through its development of ECO_2N, hysteretic capillary pressure and relative permeability functions, TOUGHREACT, and WebGasEOS. Additionally, by combining advancements in modeling to include kinetic dissolution processes, coupled heat transport for nonisothermal environments, geochemical reactive transport, transition from sub-critical to supercritical as related to near surface processes, and boundary-fitted orthogonal grid systems, an entirely new generation of scalable computing capabilities was developed. As a result, subsurface science related to regional partnership pilot studies, industrial CCS projects, and the FutureGen project is being modeled by the coupled HTC-process simulator STOMP-CO_2 developed under this program.

Basic Geosciences

Equally important is the availability of fundamental data used to calculate critical parameters (mineral and gas solubility reactions, aqueous speciation, oxidation/reduction) necessary for modeling calculations in these computer codes. For the first time, a report was generated (Krupa et al., 2010) describing availability of thermodynamic data for aqueous and solid carbonates. Advancements in reaction mechanisms between rocks and scCO_2 with co-existing compounds (e.g. SO_2) were accomplished through laboratory based studies and molecular dynamic simulations. Communicated through a series of publications and presentations, chemical reactivity of water dissolved into scCO_2 was found to be significant when in contact with metals and minerals. Using molecular dynamics simulations, these reactions proceed through spontaneous activation and decomposition of CO_2 on the metal surface rather than formation of carbonic acid. A new core flood and imaging apparatus was developed, built, and tested that was then used to study CO_2 and brine invasion processes in a natural rock core. These studies were augmented by pore-scale studies combining imaging and modeling of pore-scale two-phase invasion. These two approaches combined revealed the importance of heterogeneity in controlling invasion, and by inference CO_2 residual-phase trapping. Additional laboratory core-flooding apparati were developed for experimentally assessing effects of supercritical CO_2-brine

mixtures including novel inline, *in situ* measurements of variables such as temperature, pressure, pH, and EC. Further the research has demonstrated the utility of non-destructive NMR imaging to track changes in the physical properties of rock cores in response to CO_2-brine floods. Experimental results demonstrated mixing supercritical CO_2 and brine significantly reduced brine pH under all tested conditions; however, this effect was partially buffered by in-line carbonate rock cores, but no significant buffering was evident with the sandstone cores. No measurable change in porosity was evident in sandstone cores following supercritical CO_2-brine exposure as measured by NMR but an increase in porosity concentrated near pre-existing pore-space and an increase in the 3-D connectivity of the pore network was evident in carbonate cores. Permeability of the sandstone cores remained constant; though, a 6-fold increase in permeability of the carbonate core was measured. Collectively these results suggest that chemical dissolution concentrated in pre-existing pore networks effectively enhances permeability. Nevertheless, the experimental results did not show a clear relationship between net dissolution and temperature or net dissolution and fluid TDS with the carbonate cores.

Near Surface Detection Efficacy

Mutiple near-surface detection technologies were tested and compared at a field site developed for that purpose in the ZERT program. The CO_2 injection rates for the ZERT experiments were selected to be scalable to leakage rates consistent with desirable retention rates in large scale geological carbon sequestration. Modeling with site specific input prior to injection proved to be extremely useful in predicting the behavior of the CO_2 and thus in designing sampling strategies. When the injection was performed, agreement between modeling and experiment was found to be excellent. Over 20 techniques have been brought to the site to investigate transport of CO_2 through the soil, groundwater, plants, and atmosphere. Almost all of the techniques tested at the site were able to detect CO_2 above background levels and variability of natural CO_2. Monitoring for a leak on a reservoir scale, which is likely the case for large scale geological sequestration projects, will surely prove much more challenging. Techniques tested at ZERT needed to identify a very localized anomaly within a relatively small area. The anomaly itself produced enough signal to fall well within the detection limit of most instrumentation, but because it is very localized the signal at distances not very far off the feature [on the order of 5 m (5.486 yards)] were often outside the range of detectability for many instruments. A technology gap was identified through this work which has resulted in the ZERT team developing relatively low cost, moderate to large area detection methods such as DIAL and low cost hyperspectral imaging.

Risk Assessment

Process level models discussed above, as well as information being gleaned from studies of natural analogs for escape mechanisms are being integrated in a systems level model for risk assessment and management, CO_2-PENS.

Mitigation Methods

Experimental results obtained from this ZERT task demonstrate that engineered biomineralization has the potential to become a viable technology for sealing unwanted CO_2

migration pathways through porous media. Because the fluids used to initiate biofilm formation and biomineralization are low viscosity aqueous solutions, this technology has the potential to seal small aperture leaks or the porous rock itself potentially providing a leakage mitigation technique that can address issues problematic for cement use.

GRAPHICAL MATERIALS LIST

List of Figures

List of Tables

REFERENCES

Amonette, J. E. and J. L. Barr. 2009. *Multi-Channel Auto-Dilution System for Remote Continuous Monitoring of High Soil-CO_2 Fluxes.* PNNL-18229, Pacific Northwest National Laboratory, Richland, Washington.

Amonette, J. E., J. L. Barr, L. M. Dobeck, K. Gullickson, and S. J. Walsh. 2010. "Spatiotemporal Changes in CO_2 Emissions During the Second ZERT Injection, August-September 2008." *Environ. Earth Sci.* **60**(2):263-272.

Arp, J.W. 1991. "Effects of source-sink relations on photosynthetic acclimation to elevated CO_2, Plant," *Cell, Environ.*, **14**, 869-875.

Atan, S., Almatrook, M., Kazemi, H., and Gardner, M.H. 2005. Dual-Mesh Simulation of Reservoir Heterogeneity in Single- and Dual-Phase Porosity Problems, Society of Petroleum Engineers, Reservoir Simulation Symposium, Special Publication, Paper No. 93294

Barr, J.L., Humphries, S.D., Nehrir, A.R., Repasky, K.S., Dobeck, L.M., Carlsten, J.L., and Spangler, L.H. 2010. "Laser Based Carbon Dioxide Monitoring Instrument Testing During a Thirty Day Controlled Underground Carbon Release Field Experiment", Accepted for publication in the International Journal of Greenhouse Gas Control, 5: 138-145

Bhattacharya, J.P. and Willis, B.J. 2001. Lowstand deltas in the Frontier Formation, Powder River Basin, Wyoming: Implications for sequence stratigraphic models, AAPG Bull., 85/2: 261–294.

Blackstone, D. L., Jr. 1983. Laramide compressional tectonics, southeastern Wyoming: Contributions to Geology, University of Wyoming, Rocky Mountain Geology, v. 22, p. 1–38.

Borer, J. M. 2005. Outcrop Analysis and Geologic Modeling of Submarine Channel and Related Strata, Permian Middle Brushy Canyon Formation, West Texas, USA: unpublished Ph.D. thesis, Colorado School of Mines, Golden, Co, 269p.

Breiman, L. 2001. Random forests. Machine Learning, 45, 5– 32.

Breiman, L., Friedman, J.A., Olshen, R.A., and Stone, C.J. 1984. *Classification and regression trees*. Belmont, CA: Wadsworth International Group.

Busby, J.F., B.A. Kimball, J.S. Downey, and K.D. Peter. 1995. "Geochemistry of Waters in Aquifers and Confining Units of the Northern Great Plains in Parts of Montana, North Dakota, South Dakota, and Wyoming." U.S. Geological Survey Professional Paper 1402-F. United States Government Printing Office, Washington.

Butler, A.W., III, 1982, Case history of the north Caribou prospect, Bonneville County, Idaho, in, Powers, R.B., ed., Geologic studies of the Cordilleran thrust belt, volume II: Rocky Mountain Association of Geologists, Denver, p. 649-655.

Chipman, J. 1926. "The Soret Effect." *J. Am. Chem. Soc.* **48**:2577-2589.

Cunningham, A.B, R. R. Sharp, R. Hiebert and G. James. 2003. Subsurface Biofilm Barriers for the Containment and Remediation of Contaminated Groundwater. *Bioremediation Journal.*7(3/4) 151-164.

Cunningham, A.B., R. Gerlach, L. Spangler, L. Schultz and A.C. Mitchell. 2008. Microbially Enhanced Geologic Containment of Sequestered Supercritical CO_2. Proceedings, 9th International Conference on Greenhouse Gas Technologies, November, 2008. Available through *Energy Procedia* at http://www.sciencedirect.com/science/journal/18766102.

Cunningham ,A.B., R. Gerlach, L. Spangler, A.C. Mitchell, S. Parks, and A. Phillips (In Review). 2010. Reducing the risk of well bore leakage of CO_2 using engineered biomineralization barriers. Submitted September 2010 to Energy Procedia.

Davies, G.R., and Smith, L.B., Jr., 2006, Structurally controlled hydrothermal dolomite reservoir facies: An overview: American Association of Petroleum Geologists Bulletin, vol. 90, no. 11, p. 1641-1690.

Ebigbo A., R. Helmig, A. B. Cunningham, H. Class, R. Gerlach**,** (In Review). Modeling biofilm growth in the presence of carbon dioxide and water flow in the subsurface. Submitted to *Advances in Water Resources*, October 2009.

Fessenden, J. E., S. M. Clegg, et al. 2010. "Novel MVA tools to track CO_2 seepage, tested at the ZERT controlled release site in Bozeman, MT." Environmental Earth Sciences 60(2): 325-334.

Fischer, D.W., S.A. Smith, W.D. Peck, J.A LeFever, R.D. LeFever, L.D. Helms, J.A. Sorensen, E.N. Steadman, and J.A. Harju. 2005. "Sequestration Potential of the Madison of the Northern Great Plains Aquifer System (Madison Geological Sequestration Unit)." Plains CO_2 Reduction (PCOR) Partnership Professional Paper.

Glezakou, V. A. and L. X. Dang. 2009. "Spontaneous Activation of CO_2 and Possible Corrosion Pathways on the Low-Index Iron Surface Fe(100)." *J. Phys. Chem. C* **113**(9):3691-3696.

Glezakou, V. A., R. Rousseau, L. X. Dang, and B. P. McGrail. 2010. "Structure, Dynamics and Vibrational Spectrum of Supercritical CO_2/H_2O Mixtures from *Ab Initio* Molecular Dynamics as a Function of Water Cluster Formation." *Phys. Chem. Chem. Phys.* **12**:8759–8771.

Hansen, L. 2009. Design and Experimental Testing of a High Pressure, High Temperature Flow-Through Rock Core Reactor Using Supercritical Carbon Dioxide. MSc. thesis, Department of Earth Sciences, Montana State University. 70pp.

Have, Ton ten, and Heijnen, Wim, 1985, Cathodoluminescence activation and zonation in carbonate rocks: an experimental approach: Geologie en Mijnbouw 64, p. 297-310.

Henriette, A., Jacquin, C. G., and Adler, P. M. 1989. "The effective permeability of heterogeneous porous media." PhysicoChemical Hydrodynamics, **11 (**1), 63–80.

Humphries, S.D., Nehrir, A.R., Keith, C.J., Repasky, K.S., Dobeck, L.M., Carlsten, J.L., Spangler, L.H. 2008a. Testing carbon sequestration site monitor instruments using a controlled carbon dioxide release facility. Applied Optics, 47(4):548–555, February.

Humphries, S.D., Nehrir, A.R., Keith, C.J., Repasky, K.S., Dobeck, L.M., Carlsten, J.L., and Spangler, L.H. 2008b. “Testing Carbon Sequestration Site Monitoring Instruments Using a Controlled Carbon Dioxide Release Facility”, Applied Optics, 47, 548-555.

Humphries, S.D., Nehrir, A.R., Repasky, K.S., Carlsten, J.L., Shaw, J.A., and Spangler, L.H. 2006. “Differential absorption measurements of carbon dioxide and diatomic oxygen”, Seth Proceedings of the Carbon Sequestration Conference.

Keith, C.J., Repasky, K.S., Lawrence, R.L., Jay, S.C., and Carlsten, J.L. 2009. “Monitoring Effects of a Controlled Subsurface Carbon Dioxide Release on Vegetation Using a Hyperspectral Imager”, International Journal of Greenhous Gas Control, doi:10.1016/j.ijggc2009.03.003, 3(5): 626-632.

Kharaka, Y., J. J. Thordsen, et al. 2009. "Changes in the chemistry of shallow groundwater related to the 2008 injection of CO_2 at the ZERT field site, Bozeman, Montana." Environmental Earth Sciences 60(2): 273-284.

Kimball B. A., J. R. Mauney, F. S. Nakayama, S. B. Idso. 1993. “Effects of increasing atmospheric CO_2 on vegetation,” *Plant Ecology* **104**, 105:65-75 1993.

Kovalev, Vladimir A. and Eichinger, William E. 2004. **Elastic Lidar, Theory, Practice, and Analysis Methods**, (John Wiley and Sons, New Jersey)

Krevor, S., J.-C. Perrin, et al. 2010. "Rapid detection and characterization of surface CO_2 leakage through the real-time measurement of delta(13) C signatures in CO_2 flux from the ground " International Journal of Greenhouse Gas Control 4(5): 811-815.

Krupka, K. M., K. J. Cantrell, and B. P. McGrail. 2010. *Thermodynamic Data for Geochemical Modeling of Carbonate Reactions Associated with* CO_2 *Sequestration – Literature Review.* PNNL-19766, Pacific Northwest National Laboratory, Richland, Washington.

Lakkaraju, V. R., X. Zhou, et al. 2010. "Studying the vegetation response to simulated leakage of sequestered CO_2 using spectral vegetation indices." Ecological Informatics 5(5): 379-389.

Leach, D.L., Plumlee, G.S., Hofstra, A.H., Landis, G.P., Rowan, E.L., and Viets, J.G., 1991, Origin of late dolomite cement by CO_2-saturated deep basin brines: evidence from the Ozark region, central United States: Geology, vol. 19, p. 348-351.

Lewicki, J. L. and G. E. Hilley 2009. "Eddy covariance mapping and quanitfication of surface CO_2 leakage fluxes." Geophysical Research Letters 36: L21802.

Lewicki, J. L., C. M. Oldenburg, et al. 2007. "Surface CO_2 leakage during two shallow subsurface CO_2 releases." Geophysical Research Letters 34(24): L24402.

Lewicki, J. L., G. E. Hilley, et al. 2009. "Eddy covariance observations of surface leakage during shallow subsurface CO_2 releases." Journal of Geophysical Research - Atmospheres 114: D12302.

Lewicki, J. L., G. E. Hilley, et al. 2010. "Dynamics of CO_2 fluxes and concentrations during a shallow subsurface CO_2 release." Environmental Earth Sciences 60(2): 285-297.

Male, E. J., Pickles, W. L., Silver, E. A., Hoffman, G. D., Lewicki, J., Apple, M., Repasky, K. and Burton, E. A. 2010. "Using hyperspectral plant signatures for CO_2 leak detection

during the 2008 ZERT CO_2 sequestration field experiment in Bozeman, Montana." Environmental Earth Sciences 60(2): 251-261.

McGrail, B. P., H. T. Schaef, V. A. Glezakou, L. X. Dang, and A. T. Owen. 2009. "Water Reactivity in the Liquid and Supercritical CO_2 Phase: Has Half the Story Been Neglected?" *Energy Procedia* **1**(1):3415-3419.

Middleton, G. W. 1973. Johannes Walther's Law of the Correlation of Facies: Geological Society of America Bulletin, v. 84, p. 979-988.

Mitchell , A.C, A. Phillips, M. Hamilton, R. Gerlach, J.Kuszuba, and A.B. Cunningham. 2008a. Resilience of planktonic and biofilm communities to supercritical CO_2. *Journal of Supercritical Fluids*. Vol 47, Issue 2, 318-325.

Mitchell, AC, A. Phillips, J. Kaszuba, H.K. Hollis, R. Gerlach, A.B. Cunningham, 2008b. Microbially enhanced carbonate mineralization and containment of CO_2.*Geochimica et Cosmochimica Acta.* 72 (12), A636.

Mitchell A.C., K. Dideriksen, L.H. Spangler, A. B. Cunningham, R. Gerlach. 2009. (submitted). Microbially enhanced carbon capture and storage by mineral-trapping and solubility-trapping. Submitted to *Evironmental Science and Technology,* October 2009.

Mitchell, A.C., A. Phillips, R. Hiebert, R. Gerlach, and A.B. Cunningham. 2009. Biofilm enhanced subsurface sequestration of supercritical CO_2, *International Journal Greenhouse Gas Control,* Vol (3), No1, 90-99. doi:10.1016/j.ijggc.2008.05.002

Montross, S.N. 2007. "Geochemical Evidence for Microbially Mediated Subglacial Mineral Weathering." Montana State University, Department of Earth Sciences, M.Sc. thesis.

Oldenburg, C. M., J. L. Lewicki, et al. 2010. "Modeling Gas Transport in the Shallow Subsurface During the ZERT CO_2 Release Test." Transport in Porous Media 82(1): 77-82.

Parkhurst, D.L. 1995. "User's guide to PHREEQC – A computer program for speciation, reaction-path, advective-transport, and inverse geochemical calculations." U.S. Geological Survey Water-Resources Investigations Report 95-4227, 143 p.

Pawar, R. J., An example performance assessment of SACROC with the CO_2-PENS framework. 2008. Proceedings of the 7th Annual Conference on Carbon Capture & Storage, Pittsburgh, PA, May.

Reagan, J.A., McPherson, C., Hostetler, C., Hair, J., and Ferrare, R., 2007. "Initial CRAM Aerosol Retrievals from CALIPSO and Supporting Airborne HSRL Measurements", *IEEE IGARSS*, Barcelona, Spain, July.

Reagan, J.A., Wang, X., Cattrall, C., and Thome, K. 2006. "Lidar Aerosol Retrievals from ICESat Using a Model-based Constrained Ratio Approach," AMS 12th Conference on Atmospheric Radiation, Madison, WI, July 10-14.

Repkasy, K.S., Humphries, S.D., and Carlsten, J.L. 2006. Differential absorption measurements of carbon dioxide using a temperature tunable distributed feedback diode laser. Review of Scientific Instruments, 77(11):113107.

Rothman, L.S., Barbe, A., Benner, D.C., Brown, L.R., Camy-Peyret, C., Carleer, M.R., Chance, K., Clerbaux, C., Dana, V., Devi, V.M., Fayt, A., Flaud, J.-M., Gamache, R.R., Goldman,

A., Jacquemart, D., Jucks, K.W., Lafferty, W.J., Mandin, J.-Y., Massie, S.T., Nemtchinov, V., Newnham, D.A., Perrin, A., Rinsland, C.P., Schroeder, J., Smith, K.M., Smith, M.A.H., Tang, K., Toth, R.A., Vander Auwera, J., Varanasi, P. and Yoshino, K. 2003. The HITRAN molecular spectroscopic database: edition of 2000 including updates through 2001. Journal of Quantitative Spectroscopy & Radiative Transfer, 82:5–44, March 2003.

Rouse, J. H., J. A. Shaw, R. L. Lawrence, J. L. Lewicki, L. M. Dobeck, K. S. Repasky, L. H. Spangler. 2010. "Multi-spectral imaging of vegetation for detecting CO_2 leaking from underground." Environmental Earth Sciences. DOI: 10.1007/s12665-010-0483-9. 60(2): 313-323.

Sonnenfeld, M.D. 1996. An integrated sequence stratigraphic approach to reservoir characterization of the Lower Mississippian Madison Limestone, emphasizing Elk Basin field, Bighorn Basin, Wyoming: Unpublished Ph.D. dissertation, Colorado School of Mines, Golden Colorado 437 p.

Spane, F. A. 2002. "Considering Barometric Pressure in Groundwater Flow Investigations." *Water Resour. Res.* **38**(6):14/1-18.

Spangler, L. H., L. M. Dobeck, K. S. Repasky, A. R. Nehrir, S. D. Humphries, J. L. Barr, C. J. Keith, J. A. Shaw, J. H. Rouse, A. B. Cunningham, S. M. Benson, C. M. Oldenburg, J. L. Lewicki, A. W. Wells, J. R. Diehl, B. R. Strazisar, J. E. Fessenden, T. A. Rahn, J. E. Amonette, W. L. Pickles, J. D. Jacobson, E. A. Silver, E. J. Male, H. W. Rauch, K. S. Gullickson, R. Trautz, Y. Kharaka, J. Birkholzer, and L. Wielopolski. 2010. "A Shallow Subsurface Controlled Release Facility in Bozeman, Montana, USA, for Testing near Surface CO_2 Detection Techniques and Transport Models." *Environ. Earth Sci.* **60**(2):227-239.

Stone, D.S. 1993. Basement-involved thrust-generated folds as seismically imaged in the subsurface of the central Rocky Mountain foreland, Special Paper - Geological Society of America, vol. 280: 271-318,

Stone, D.S. 2002. Morphology of the Casper Mountain uplift and related, subsidiary structures, central Wyoming; implications for Laramide kinematics, dynamics, and crustal inheritance, AAPG Bulletin, 86/8: 1417-1440.

Stone, D.S. 2003. New Interpretations of the Piney Creek thrust and associated Granite Ridge tear fault, northeastern Bighorn Mountains, Wyoming, Rocky Mo8ntain Geology, 38/2: 205-235.

Strazisar, B. R., A. W. Wells, et al. 2008. "Soil Gas Monitoring for 1he ZERT Shallow CO_2 Injection Project." Prepr. Pap.-Am. Chem. Soc., Div. Fuel Chem. 53(2): in press.

Strazisar, B. R., A. W. Wells, et al. 2009. "Near-surface monitoring for the ZERT shallow CO_2 injection project." International Journal of Greenhouse Gas Control 3(6): 736-744.

Swinney, H. L. and H. Z. Cummins. 1968. "Thermal Diffusivity of CO_2 in Critical Region." *Phys. Rev.* **171**(1):152-160.

U.S.D.O.E./N.E.T.L. 2010. Best practices for: Site screening, site selection, and initial characterization for storage of CO_2 in deep geologic formations, http://www.netl.doe.gov/technologies/carbon_seq/refshelf/BPM_PublicOutreach.pdf .

Viswanathan, H.S., Pawar, R.J. , Stauffer, P. H. , Kaszuba, J.P. , Carey, J.W. , Olsen, S.C. , Keating, G.N., Kavestski, D. and Guthrie, G.D. 2008. Development of a hybrid process and system model for the assessment of wellbore leakage at a geologic CO_2 sequestration site, Environ. Sci. Technol., 42, 7280-7286.

Wang, S. and Jaffe, P.R., 2004. Dissolution of a mineral phase in potable aquifers due to CO_2 releases from deep formations; effect of dissolution kinetics. Energy conversion and management, 45: 2833-2848.

Wells, A. W., B. R. Strazisar, et al. 2010. "Atmospheric tracer monitoring and surface plume development at that ZERT pilot test in Bozeman, Montana, USA." Environmental Earth Sciences 60(2): 299-305.

LIST OF ACRONYMS AND ABBREVIATIONS

μm	micron
a-c fractures	Fractures that form perpendicular to the hingeline of a fold (and perpendicular to bedding) and tend to form down-dip lineations on dipping bedding surfaces; such fractures are also extensional in origin, otherwise known as “mode-I fractures.
ANN	Artificial Neural Network
b-c fractures	Fractures that form parallel to the hingeline of a fold (and perpendicular to bedding) and tend to radiate around the crest of a folded rock unit; such fractures are extensional in origin, otherwise known as “mode-I fractures.
CCS	Carbon Capture and Sequestration
CO_2	Carbon Dioxide
CT	Computed Tomography
DFB Laser	Distributed Feedback Laser
DIAL	Differential Absorption Lidar
ECKEChem	Equilibrium, Conservation, Kinetic Equation Chemistry
FWHM	full width half maximum
GCS	Geologic Carbon Sequestration
GCS	Geologic Carbon Storage
GT	Gigaton
IR	infrared
Km	kilometer
LBNL	Lawrence Berkeley National Laboratory
MBRCT	Montana Board of Research and Commercialization Technology
MIS	Multiple Inscribed Spheres
MODFLOW	Modular Finite-Difference Flow Model
MSU	Montana State University
MVT	Mississippi Valley-Type hydrothermal Pb-Zn-dolomite ore systems
NDVI	Normalized Difference Vegetation Index
NIR	Near Infrared
NMR	Nuclear Magnetic Resonance
PBG	Photonic Bandgap
PNNL	Pacific Northwest National Laboratory
ppm	parts per million
PSO	Particle Swarm Optimization
RC	Reservoir Class
SBIR	Small Business Innovative Research
$ScCO_2$	Supercritical carbon dioxide
$scCO_2$	supercritical carbon dioxide
SMF	Single Mode Fiber
STOMP	Subsurface Transport Over Multiple Phases
STOMP-CO_2	isothermal version
STOMP-CO_2ae	nonisothermal version for ground-surface interaction
STOMP-CO_2e	nonisothermal version

STTR	Small Business Technology Transfer Program
TDS	Total Dissolved Solids
UCSC	University of California Santa Cruz
ZERT	Zero Emission Research and Technology

Appendices

Appendix A

Basic GeoScience: Intermediate (Reservoir)-Scale Report

STRATIGRAPHIC FRAMEWORK AND RESERVOIR CHARACTERIZATION OF CLARETON AND FIDDLER CREEK FIELDS, EARLY CRETACEOUS MUDDY SANDSTONE FORMATION, POWDER RIVER BASIN, WYOMING: EFFECTS OF SEDIMENT SUPPLY ON INCISED VALLEY-FILL SYSTEM ARCHITECTURE

Thesis by Keriann Hope Pederson

STRATIGRAPHIC FRAMEWORK AND RESERVOIR CHARACTERIZATION OF CLARETON AND FIDDLER CREEK FIELDS, EARLY CRETACEOUS MUDDY SANDSTONE FORMATION, POWDER RIVER BASIN, WYOMING: EFFECTS OF SEDIMENT SUPPLY ON INCISED VALLEY-FILL SYSTEM ARCHITECTURE

by

Keriann Hope Pederson

A thesis submitted in partial fulfillment
of the requirements for the degree

of

Master of Science

in

Earth Sciences

MONTANA STATE UNIVERSITY
Bozeman, Montana

May 2010

APPROVAL

of a thesis submitted by

Keriann Hope Pederson

This thesis has been read by each member of the thesis committee and has been found to be satisfactory regarding content, English usage, format, citation, bibliographic style, and consistency, and is ready for submission to the Division of Graduate Education.

Dr. David W. Bowen _____
Signature

Approved by the Department of Earth Sciences

Dr. Steven J. Custer _____
Signature

Approved for the Division of Graduate Education

Dr. Carl A. Fox _____
Signature

STATEMENT OF PERMISSION TO USE

In presenting this thesis in partial fulfillment of the requirements for a master's degree at Montana State University, I agree that the Library shall make it available to borrowers under rules of the Library.

If I have indicated my intention to copyright this thesis by including a copyright notice pate, copying is allowable only for scholarly purposes, consistent with "fair use" as prescribed in the U.S. Copyright Law. Requests for permission for extended quotation from or reproduction of this thesis in whole or in part may be granted only by the copyright holder.

Keriann Hope Pederson

May 2010

ACKNOWLEDGEMENTS

This work would not have been possible without the help and assistance of David Bowen and his work with the Zero Emissions Research and Technology grant. Special thanks to my thesis committee Mike Gardner and Jim Schmitt, and to my Z.E.R.T. research colleagues Jesse Melick and Logan Hansen.

MJ Systems generously donated well logs for this study. The USGS Core Laboratories in Denver, CO provided cores for description. Some cores were uncut at the beginning of this work and were expertly cut by the Butcher, and beautifully photographed by his wife Terry. Thanks to Dave Eby and his wife ---- for letting me stay at their condo while I described core in Denver, and for the gift of truly beautiful music and great wine.

Special thanks to Travis Jester for his relentless support of me through every step in this process. His influence made this work the success it is today.

Thanks to my family and friends who helped me prepare and acted as sounding boards through this entire process. Finally thanks to the faculty and students of the Earth Science Department at Montana State University.

Any opprobrium within these pages is due to the obdurate author, and does not reflect those who assisted in this work.

TABLE OF CONTENTS

LIST OF TABLES

LIST OF FIGURES

LIST OF FIGURES CONTINUED

LIST OF FIGURES CONTINUED

ABSTRACT

Five formal members have been recognized through correlation of depositional stacking patterns as identified in well logs and cores in the Fiddler Creek and Clareton incised valley-fills, Powder River basin, Wyoming. These five units are consistent with identified members in other Muddy Sandstone incised valley-fills in the Powder River basin. Long-term sequestration of CO_2 necessitates an understanding of the internal porosity and permeability pathways. Net sandstone maps and interpreted stacking patterns were used to identify these pathways within the two incised valley-fills. Stacking pattern and environment of deposition were compiled from facies recognition in core (11 cores) and correlated to corresponding wireline logs (600 well logs). It is concluded that the Fiddler Creek system is not an incised valley-fill system, as defined in this work, due to its avulsion out of the valley walls after deposition of the earliest members in the system. It is also concluded that these valleys maintain the necessary porosity and permeability pathways for successful injection of $C0_2$. However because of difficulty monitoring and maintaining the 6000+ wells in these fields they are useful only as analogues for future sequestration sites.

1. INTRODUCTION TO RESEARCH

Introduction

The primary objective of this study is to develop the stratigraphic framework of two coeval incised valley-fill systems that produce oil and natural gas at the Clareton and Fiddler Creek Fields (eastern Powder River basin, Wyoming) and to characterize their reservoir architecture. This research will address two principal research issues. First, through comparison of the stratigraphic architecture of each valley-fill it will be possible to more completely understand how sediment supply, as an independent variable, affects the preserved sedimentary record of these incised valley-fill systems. Second, these reservoirs are ideally suited to be a sector model for lower Cretaceous incised valley-fill systems in the Powder River Basin. This work is part of a three-fold study at Montana State University to better understand issues related to geologic sequestration of carbon dioxide (CO_2) at the basin scale (Melick 2007), reservoir scale (Pederson 2007; and this study), and pore scale (Hansen 2008).

The Fiddler Creek and Clareton fields are early Cretaceous (Albian) in age (Obradovich and Cobban 1978) and are situated on the eastern edge of the Powder River basin (figure 1). Both fields are economically important oil fields and have been producing since the early 1900's (Cupps et al. 1964; Hintze 1914). After nearly 100 years of production there have been extensive studies that interpret the depositional environment of the features. The current accepted depositional model is that these fields

Figure 1:

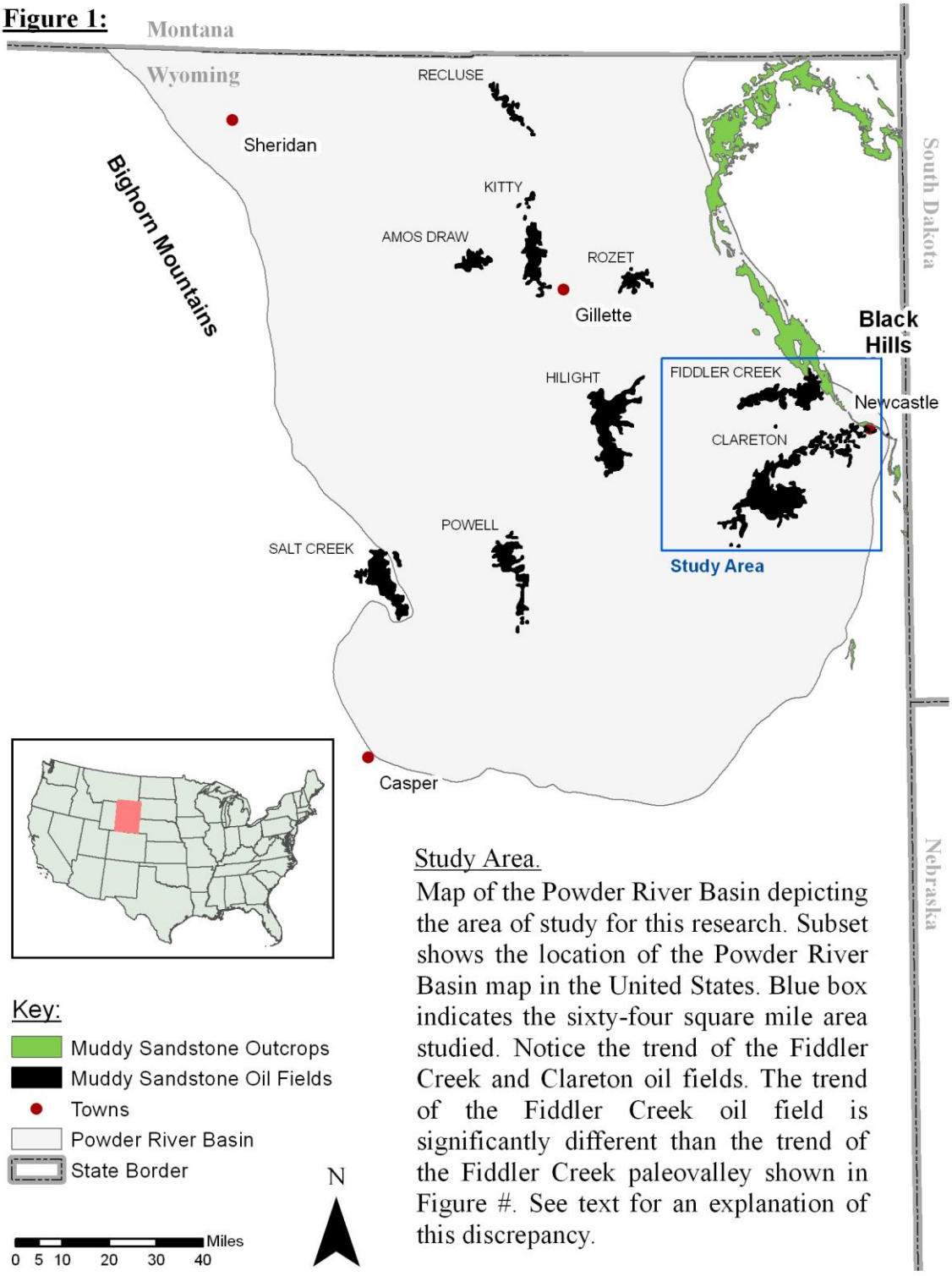

Study Area.

Map of the Powder River Basin depicting the area of study for this research. Subset shows the location of the Powder River Basin map in the United States. Blue box indicates the sixty-four square mile area studied. Notice the trend of the Fiddler Creek and Clareton oil fields. The trend of the Fiddler Creek oil field is significantly different than the trend of the Fiddler Creek paleovalley shown in Figure #. See text for an explanation of this discrepancy.

are early Cretaceous incised valley-fills (IVFs).[1] This model is rigorously evaluated in this study.

Importance of Research

Incised Valley-Fills and Stratigraphic Architecture: As stated by Van Wagoner et al. (1990) incised valley-fills, though relatively infrequent in the rock record, constitute a significant portion of petroleum reservoirs. In addition to economic importance, scientifically each incised valley-fill is a record of a detailed experiment involving the interplay between sea-level[2], sediment supply, climatic, and tectonic variables. In a sense, incised valley-fills are a simplified proxy of the stratigraphic record as a whole (Dalrymple, 2006). Through careful interpretation of valley-fills within a sequence stratigraphic framework, the complex, interdependent relationship of these variables to the stratigraphic architecture of resultant deposits can be better understood. Additionally, porosity and permeability pathways inherent to these systems can be better predicted.

As a result of their economic and scientific importance, these distinctive features have been well-studied (Aldinucci et al. 2007; Baines et al. 2002; Bowen and Weimer 2005; Cotter and Driese 1998; Dalrymple and Zaitlin 1994; Eberth 1996; Foyle and Oertl 1997; Greene et al. 2007; MacDonald et al. 1998; Mattheus et al. 2007; Nordfjord et al. 2006; Plint and Wadsworth 2003; Stephen and Dalrymple 2002; Willis 1997; etc.). As a

[1] For more detailed description of current and past geologic models for these fields please see the Previous Work section in Chapter 3.
[2] In this work, sea-level will be used as a general term describing the variable controlling stratigraphic architecture. This includes the eustatic (global) control and relative (global plus local) control on changes.

result incised valley-fills are one of the most completely understood clastic depositional systems. However, despite a plethora of information about the depositional system, criteria for recognizing spatial and temporal variability in valley-fill systems are still poorly understood.

The Clareton and Fiddler Creek incised valley-fills of the Muddy Sandstone[3] in eastern Wyoming are not unusual in economic value, scientific worth, nor amount of scientific study and understanding (Cotter and Driese 1998; Dalrymple and Zaitlin 1994; Emme 1981; Graham 2000; Hajash 1980; Higley et al. 2003; Siguaw et al. 2001; Van Wagoner et al. 1990; Wulf 1962; etc). However these two valley-fills provide a rare study opportunity for understanding valley-fill stratigraphic architecture.

According to conventional wisdom, the variables controlling stratigraphic architecture in any depositional system (i.e. tectonics, sea-level, climate, baselevel[4], and sediment supply) are inherently dependent (figure 2). In investigating any depositional system, it is rare that any control on stratigraphic architecture can be isolated and evaluated independently of other dependent variables. Figure 2 displays this dependent relationship by showing three of the major controls on stratigraphic architecture, eustasy, tectonics, and sediment supply, in a spectrum. For example according to figure 2, as the influence of sediment supply decreases, the stratigraphic record becomes more strongly influenced by either tectonics or eustasy. However, the proximity and coeval genesis of

---

[3] Also known as the Newcastle Formation. The term Muddy Sandstone will be used exclusively for the purpose of this study. See figure 6 and Chapter 3 for explanation.

[4] Baselevel in this work refers only to stratigraphic baselevel *sensu* J. Barrell (1917) and H. E. Wheeler (1959). Specifically baselevel will refer to the surface at which neither sedimentation nor erosion can take place, regardless of cause.

these two particular incised valley-fills provide a unique opportunity to evaluate a single control on incised valley-fill stratigraphic architecture.

The two incised valley-fills evaluated in this work experienced the same climate, the same tectonic influences, and were subject to the same relative changes in sea-level, as well as baselevel. However the valleys differ in one crucial aspect. The Clareton system was a piedmont valley whose sediment source was from the hinterlands of the Black Hills uplift (Emme, 1981). As such, the Clareton valley had a large amount of sandy sediment flowing through the system. Conversely, the Fiddler Creek system was a coastal plain valley, which had a limited supply of mostly muddy sediment. Because of the unique history of these two systems, it is possible to separate sediment supply out as an independent variable in the process of filling these two systems (figure 3). It is simple to think of this relationship as a simple algebraic equation. As figure 3 demonstrates, if A+B+C=D and A, B, and D are known variables, it is simple to solve for the unknown variable, C.

Carbon Dioxide Sequestration: It is widely accepted that anthropogenic greenhouse gasses (GHG's) are having an affect on the earth's natural climate cycles. An increase in GHG's, such as carbon dioxide (CO2) and methane (CH4), has been documented since the industrial revolution. According to Byrant (1997), CO2 is responsible for approximately two-thirds of the increase in global temperatures. Because of CO2's dominant role in affecting Earth's climate, it is the primary target for emission reduction. Scientists around the world are in the process of developing methods, and technology, for reducing the anthropogenic output of CO2 into earth's atmosphere.

Geologic storage (sequestration) of CO_2 is one of the proposed methods for stabilizing atmospheric levels of CO_2. For decades enhanced oil recovery (EOR) utilizing CO_2, a potential methodology for geologic sequestration of CO_2, has been used to increase production from partially depleted oil reservoirs. In both its liquid and dense gaseous state, CO_2 is a powerful solvent for hydrocarbons. Therefore, when injected into an oil reservoir, it has the capability to extract small molecules of hydrocarbons trapped within the pore space of a geologic reservoir (White et al. 2003). Because EOR is already a widely used practice, the infrastructure, technology, and understanding for geologic storage of CO_2 makes it an attractive method for the sequestration of CO_2.

In selecting a site for geologic sequestration of CO_2, extensive research must be carried out in order to ensure that carbon dioxide, once injected, will remain trapped in the geologic reservoir into which it was injected. While generally thought of as innocuous[5], in high concentrations CO_2 can be an asphyxiant to plants and animals. Concerns also exist regarding leakage of injected CO2 in safe water drinking aquifers. For this reason, storage sites for geologic sequestration of CO_2 must be thoroughly characterized in order to avoid unintended consequences.

Through determining the stratigraphic architecture and associated porosity and permeability pathways of the Fiddler Creek and Clareton incised valley-fills this study will, as a result, also determine the suitability of these two incised valley-fills for long-term storage of CO_2; an important first step toward the implementation of CO_2

---

[5] CO_2 is consumed daily in large amounts through respiration, and the consumption of soda pop and other fizzy beverages, etc.

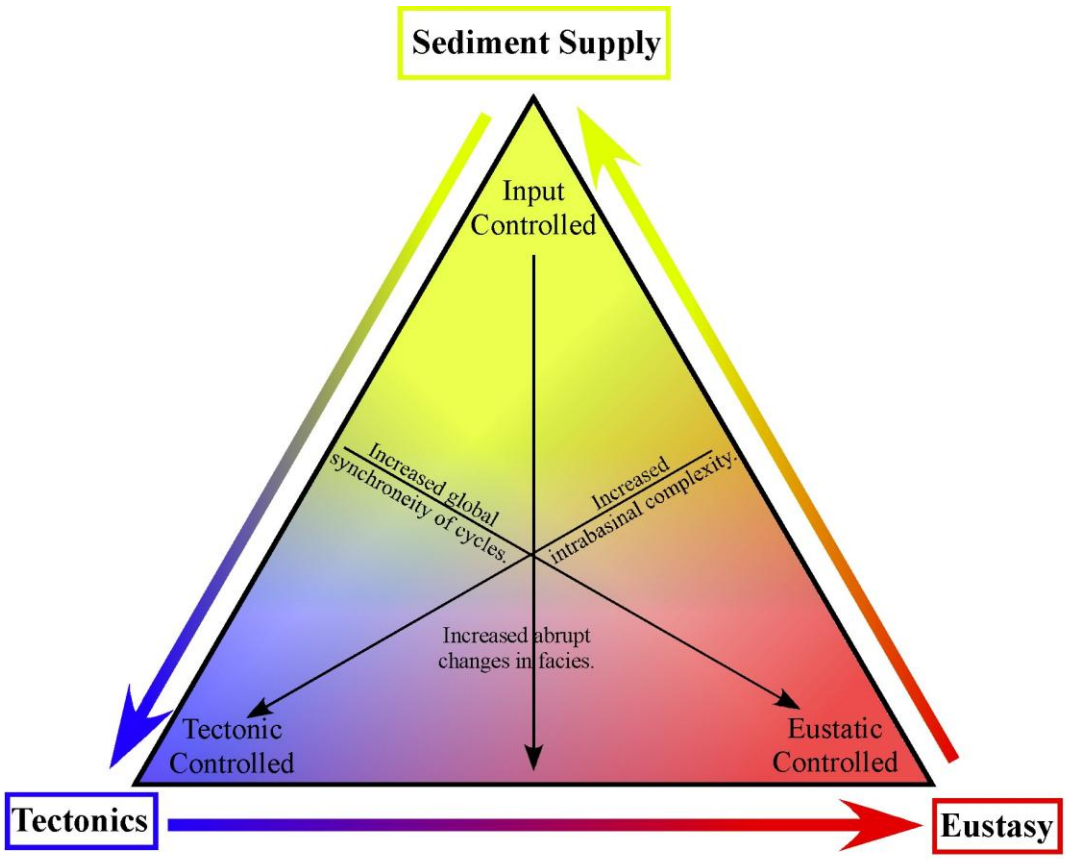

Figure 2:

Controls on Stratigraphic Architecture.

Diagram showing the relation of three primary controls on stratigraphic architecture. Notice with increase in eustatic control there is an increase in synchroneity of cycles, with an increase in tectonic control there is an increase in intrabasinal complexity, and a *decrease* in input control increases abrupt changes in facies. In this study, both eustasy and tectonic inputs are known constant variables for the two paleovalleys. Modified from Coe, 2003.

If:

A+B+C= SA and **A+B+C= SA**

where:
A is tectonic influence,
B is eustatic influence,
C is sediment supply influence,
SA is the resulting stratigraphic architecture,
and with **Fiddler Creek fill factors in blue** and **Clareton fill factors in red**.

Then since:

A = **A** and **B** = **B**

C = **SA** and **C** = **SA**.

Figure 3:

Mathematical Analogy.

The way that this work will determine the affect of sediment supply on stratigraphic architecture can be explained with a simple <if : then> mathematical statement.

In this statement, not only the tectonic and eustatic influences both known values, but they are also had exactly equal influence because of the paleovalleys coeval genesis (see text for further explanation). The resulting stratigraphic architecture is also a known value, as the result of this study. This allows us to 'solve' for the one remaining unknown constant, sediment supply. Comparing and contrasting the two stratigraphic architectures in relation to each other will result in a better understanding of how sediment supply, as a control, affects stratigraphic architecture.

sequestration. This work also serves as a sector model for other incised valley-fills in the Powder River Basin, which may be candidates for CO_2 sequestration, or could be potential leakage pathways in the basin.

2. BACKGROUND AND SETTING

Geologic Setting

Situated on the eastern flank of the Powder River basin, the early Cretaceous Fiddler Creek and Clareton incised valley-fills both result in notable oil fields within the Powder River basin. Structurally, the Powder River basin is one of the Tertiary aged Laramide foreland basins. During early Cretaceous time, the region was along the eastern margin of the epeirogenic seaway that periodically occupied the western North American continent from the Arctic to the Gulf of Mexico. This region was submerged and exposed multiple times by relative sea level changes of the Western Interior Cretaceous Seaway.

The valleys themselves coevally carved into the Aptian aged Skull Creek Shale[6], and then concurrently were backfilled during the ensuing irregular rise in relative sea-level during Albian time.

Due to their economic importance, scientists have been studying the depositional environments of the Fiddler Creek and Clareton fields since the early 1920's (Hancock 1920). The current tectonic model for this study area was first proposed by Donald Baker in 1962, and has since been well documented by Robert Weimer (1988), Jim Emme (1981), Cathy Farmer (1981), Paul Slack (1981), and by Robert Kidney and Thomas Davis (1981). This model indicates that basement fault blocks controlled the geographic location of the systems and baselevel changes through time in the Newcastle area,

---

[6] Also Thermopolis Shale.

including the incision of the Fiddler Creek and Clareton valleys into the Skull Creek Shale and filling of the Muddy Sandstone into the features in a later transgression. (Kidney and Davis 1981; Slack 1981).

The current accepted facies model of the Fiddler Creek and Clareton systems is that they are two incised valley-fill systems. The history of how this facies model came to be is discussed in more detail in the following section (see Chapter 2, Previous Work, Sedimentologic Timeline). However, prior to the general acceptance of the current facies model, the Muddy Sandstone had been interpreted to result from many different types of depositional systems including a migrating, locally swampy, shoreline with shifting longshore currents controlling the deposition of sand (Skolnick 1958); a large subaqueous deltaic plain interspersed with small forested islands (Peppers 1959); and an alluvial plain deposit completely separate from any marine, or marginal-marine, influences (Baker 1962).

According to the tectonic model the trend of the features, the Clareton feature in particular, directly follows two northeast-southwest trending lineaments interpreted as basement fault block half-grabens. Slack (1981) asserts “virtually all stratigraphic production from the diverse assemblage [of the Powder River baisn] [. . .] can be directly related to subtle repeated movements along newly identified structural trends.” (p. 730). Slack goes on to state that the Belle Fourche Arch resulted from the culmination of these movements in Cretaceous time. According to this depositional model, movement of the fault blocks in the late Aptian, early Albian period were great enough to control fluvial trends in this area, and thereby incision and subsequent filling of both the Clareton and Fiddler Creek features.

Previous Work

The history of study of the Muddy Sandstone near Newcastle Wyoming can be categorized into three groups. (1) The sedimentologic timeline, which follows the various interpretations of depositional environment through time, (2) the stratigraphic nomenclature timeline which lays out how the rocks have been correlated lithologically and time-stratigraphically, and (3) the production timeline which details the history of oil production from the Fiddler Creek and Clareton Fields. A generalized timeline of previous work on the Muddy Sandstone is depicted in figure 4. This figure depicts not only what work was published on these rocks and when, but also whether the unit was referred to as Muddy or Newcastle, as a formation or member of another formation, and when the term Newcastle sandstone became obsolete according to the North American Stratigraphic Code on nomenclature.

Sedimentologic Timeline

The first known interpretation of the Muddy Sandstone near Newcastle, Wyoming was by C.H. Collier in 1922. He reported that the unit was deposited in a shallow-water environment proximal to a forested land surface (Skolnick 1958). Sommerford et al. (1990) interpreted the lenticular sandstone bodies within these rock units to be due to a laterally shifting strandline, with the strandline sands then re-worked by waves and currents into their present day lenticular form (Skolnick 1958). Gries (1954) and Roadifer

(1962) both speculated that the sandstone near Newcastle was a tongue of the Dakota Sandstone extending westward from a delta plain east of the Black Hills (Baker 1962).

In 1962 Donald Baker took an entirely different approach and interpreted the lenticular sandstone bodies as alluvial deposits. He argued that previous publications had assumed a marine, or marginal marine, influence in the rocks simply because the sandstone bodies were underlain and overlain by marine shales. Instead Baker interpreted the deposits as an alluvial non-marine deposit, which filled a "valley-like erosional depression" (1962, p. 161). Baker's work is the first to interpret the sandstone as deposited within an erosionally confined 'valley-like' system. His work became the basis for the current depositional model as described in the previous section.

Nomenclature Timeline

The term "muddy sand" was first coined by drillers in Wyoming in the early 20th century (Hintze, 1914). The first person to publish on the rocks was F.F. Hintze in his 1914 publication "The Basin and Greybull oil and gas field." Hintze describes a white sandstone, which contrasts the black shale layers above and below. However he goes on to say that "The 'Muddy Sand' has no special importance [. . .] but it is nearly always recognized in drilling" (Hintze, 1914, pg 21). The Newcastle sandstone was not recognized in publication until 1920 when E.T. Hancock described the Newcastle as a member of the Graneros shale.

In 1951 the Newcastle was redefined by Crowley as a member of the Skull Creek Shale rather than the Graneros Shale. This establishes the Newcastle as late Cretaceous in age rather than early Cretaceous. One year later, in 1952, two separate papers were

published raising the Newcastle to formation status (Cobban and Reeside 1952; Grace 1952). However, both publications restricted the use of 'Newcastle' to the Powder River and Williston basins, specifically the area around the Black Hills. Despite these two publications the Newcastle was not widely recognized as a formation until the mid-1960's.

In 1955 Karl Waage published an overview of the Dakota Group, which was the first detailed correlation of the Newcastle sandstone. In this work the Newcastle sandstone, shown as an informal member of the Skull Creek Shale, and the Muddy sandstone, shown as an informal member of the Thermopolis Shale, were depicted as depth and lithologic equivalents, but not time-stratigraphic equivalents. It was not until 1965 that the Muddy Sandstone was raised to formational status in his work that correlated the Muddy Sandstone throughout Colorado and Wyoming.

Until 1972 the term Newcastle was only applied to rocks in and around the Black Hills area while the term 'Muddy' was applied to the stratigraphic equivalent rocks throughout the rest of the Great Plains (Montana, Wyoming, Colorado, and North Dakota). In 1972 William Stone was the first person to apply the 'Muddy' terminology to the early Cretaceous (Albian) rocks around the Black Hills. According to the North American Stratigraphic Code, Stone's peer reviewed publication established the Newcastle as a synonymic term to Muddy. Because the term Muddy was first published six years before the term Newcastle, it is the view of this author that the term Newcastle should have been discontinued as a result of the Stone publication. Therefore this publication will refer only to the Muddy Sandstone, a unit having formation status.

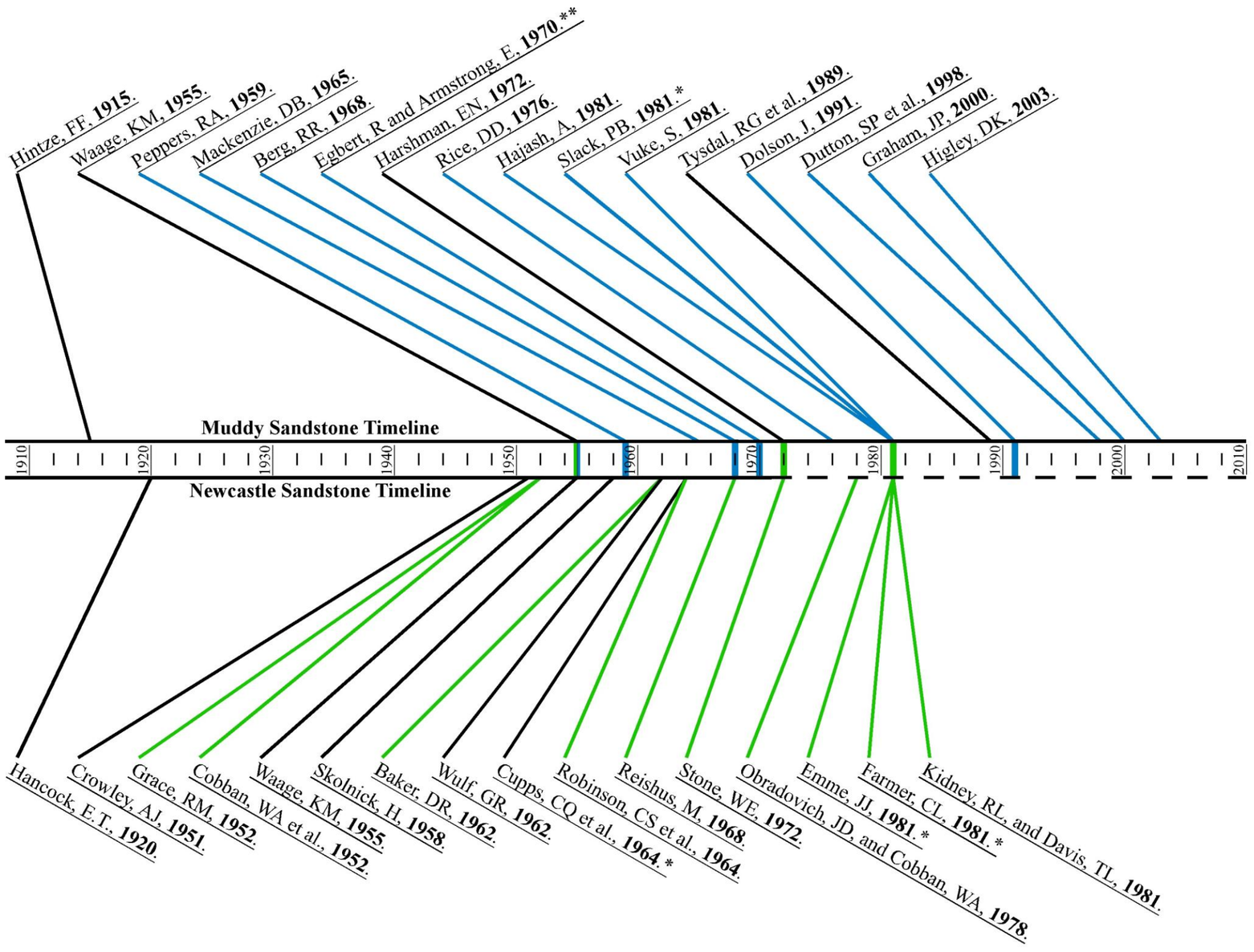

Figure 4:

Previous Work.

Time line detailing previous work on the Muddy and Newcastle Sandstones. The top line indicates work which uses the term Muddy Sandstone. The black lines indicate where the rocks are referenced as a member of another formation, the blue lines where the Muddy is referred to as its own formation. Likewise, the bottom timeline indicates work which uses the term Newcastle. Again, black lines indicate where Newcastle is used to refer to a member of another formation, green lines where Newcastle is referred to as a formation. The colored bars across the timeline indicate work which correlates the Newcastle and Muddy Sands as syndepositional rocks. Starred references (*) indicate work which specifically looks at the two paleovalleys from this study.

The dashed line on the Newcastle timeline after 1972 indicates the time after the Muddy and Newcastle Formations had been established as synonymic formations (Stone, WE, 1972). According to the North American Stratigraphic Code, after this publication it is appropriate to use the term Muddy Sandstone and not Newcastle Sandstone for the rocks in this study.

** This paper uniquely identifies the Newcastle as a member within the Muddy Formation.

Production Timeline

Production at Fiddler Creek Field was established in 1919 by the Henry Oil Company (WGA Symposium 1981). The nearby Clareton Field's discovery well, the #1 Millhouse, was drilled in May 1944 (WGA Symposium 1981) by the Western Oil and Gas Trust. As of 2008 the Clareton Field had produced a minimum of 6,541,530 billion barrels of oil (BBO) and 7,074,871 million cubic feet of gas (MCFG) (Wyoming Oil and Gas Conservation Commission website, 2009). Detailed information on the history of the two oil and gas fields is published in the Wyoming Geological Association's 1981 Symposium on the Oil and Gas fields of the Powder River basin.

3. METHODS OF RESEARCH

Methods

The database for this study is predominantly subsurface in origin from the extensive oil and gas drilling in the study area. It includes wireline well logs (figure 6), slabbed whole core, and production information. The subsurface data correlate directly to outcrops at the eastern margin of the study area where the Muddy Sandstone is well-exposed. Those outcrops were described in detail by Gustason et al 1988, and others and those results are integrated with the data collected for this study to yield an integrated interpretation. From this data set a grid of cross-sections were constructed to determine a stratigraphic framework of the study area. Facies data from the description of slabbed whole cores were integrated with the stratigraphic framework constructed from well logs. When analyzed, these data allowed for interpretation of key surfaces including flooding surfaces, disconformities, and unconformities that were critical to the sequence stratigraphic interpretation. Isochore maps of significant components of the incised valley-fills were created to define the distribution of those geobodies that comprise the detailed internal stratigraphic architecture of the two incised valley-fills.

Facies shifts and within-feature flooding surfaces were picked in more than 6,000 wireline resistivity and sonic logs. This resulted in the definition of five surfaces that could be correlated throughout both incised valley-fills (figure 5, 6). Figure 5 shows the stratigraphic interpretation used in this study correlated to the lithostratigraphic correlation typically used in this area *sensu* Martinsen, 1994. Note that the lowest lithostratigraphic members, Rozet Member and Lazy B Member are not present in this

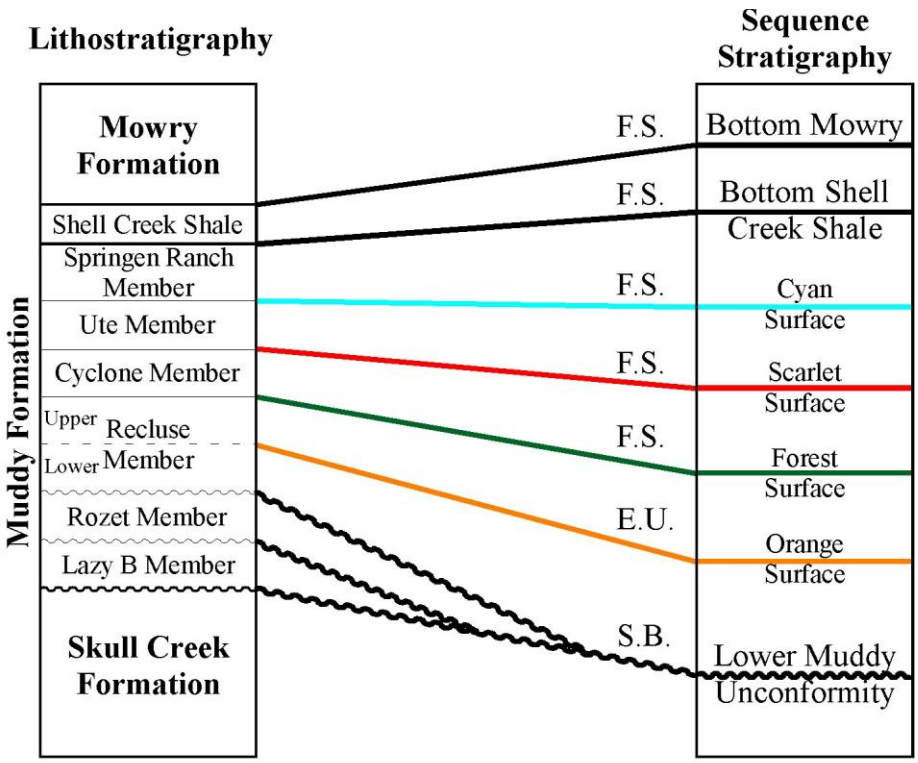

Figure 5:

Stratigraphic Correlation:

Figure showing correlation of Sequence Stratigraphic terms to Lithostratigraphic terms used in this work. Sequence Stratigraphic terms were created by the author and recognized using wire-line logs in the study area. They were later correlated to established lithostratigraphic members of the Muddy Sandstone in the Powder River basin from Martinsen (1994). Notice that the Rozet and Lazy B lithomembers are not present in this area. Upper Recluse and Lower Recluse members are separated by a dashed line indicating that they are not always distinguishable as two separate units. These terms will be used throughout this work.

F.S.= Flooding Surface; E.U.= Erosional Unconformity; S.B.= Sequence Boundary.

part of the section. It is interpreted here that the erosive boundary below the Rozet and Lazy B Members merges with the basal sequence boundary at the base of these valleys forming a composite boundary.

When available, resistivity logs were checked against gamma-ray logs for verification of sandstone and shale content. Twenty-seven cross sections, which characterize the internal down-dip and strike stratigraphic variations of the surfaces within the valley-fill trends, were constructed from well logs (appendix A). Figure 6 shows the location of the primary wells used in this study. The green and red arrows indicate the trend of the Fiddler Creek and Clareton paleosystems respectively. These trends are based on the trend of the producing oil wells in each system.

Ten isochore maps were then constructed illustrating relative thicknesses between each picked surface (see chapter 6). An isochore of the Muddy Sandstone formation in this area can be seen in figure 7. Notice how, in the isochore in figure 7 the apparent trend of the Fiddler Creek system is a tributary to the Clareton system, forming a Y. This is contrary to the apparent trend of the Fiddler Creek system as shown in figure 6 by the trend of the producing wells in the Fiddler Creek. This disparity is discussed at length in chapters 6 and 7.

Meticulous graphic description of approximately 600 feet (200 meters) of Muddy Sandstone core (11 cores total) were described through the Fiddler Creek and Clareton trends. Graphic core descriptions detail the grain size, sedimentary structures, lithology, bounding surfaces, ichnology, approximate porosity, and other characteristics of the cores (appendix B). The 11 cores were correlated with their respective wireline logs, and used

to define facies, and verify unconformities and flooding surface picks within the incised valley-fills.

Facies were defined and described from the core descriptions according to color, sediment size, grain sorting and roundness, sedimentary structures, and intensity and type of bioturbation. Facies were then described according to hydrodynamic interpretation (see Chapter 4). Individual facies were grouped according to depositional environment into six facies associations.

Net sandstone thicknesses were picked on gamma-ray wireline logs for each of the five members, which are defined by the within feature surfaces determined earlier. Net sandstone was determined by a gamma signature, which stood well below background shale values. Unfortunately, due to differing vintages of gamma logs, specific gamma radiation levels could not be used to delineate sandstone versus shale. Wells for net sandstone interpretation were picked on a one well per square mile (i.e. section) basis. An isochore map for each individual member was drawn by hand, to allow for geologic interpretation, then digitally drafted and loaded into the Petra database.

Finally, stacking patterns for each member within each system were compiled based on available well data, wireline logs, core description, facies and associations, member isochores, and net sandstone isochores. These stacking patterns, when combined, establish the stratigraphic architecture of each system.

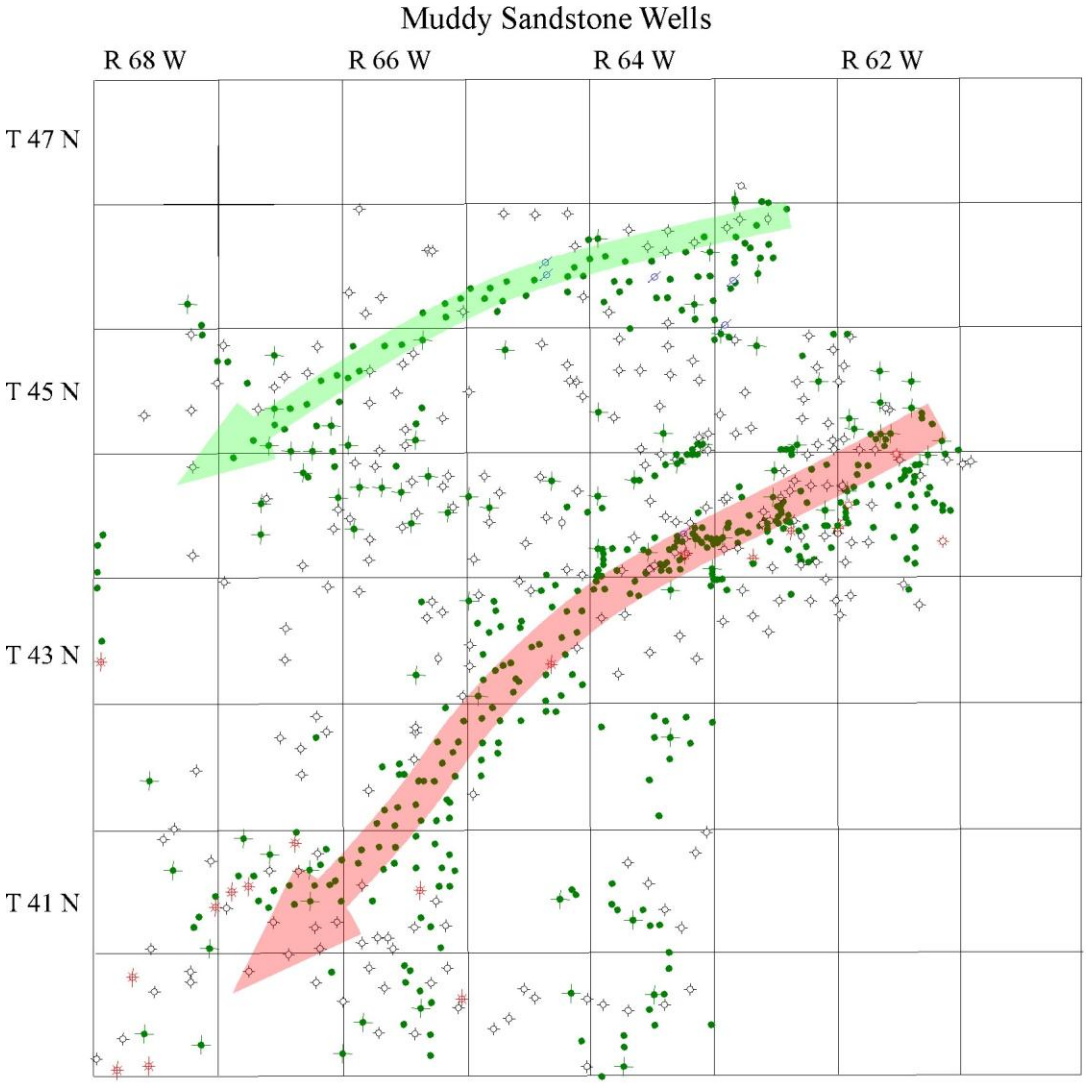

Figure 6:

Muddy Sandstone Well Map:

Map displaying the approximately 600 most useful wells from the study. Green wells indicate producing oil wells, red producing gas wells, and black, open, crossed circles dry holes. Transparent green arrow indicates apparent dip direction of Fiddler Creek from well trends. Transparent red arrow indicates apparent depositional direction of Clareton system from well trends. These depositional trends very closely follow the basement fault blocks mapped by Slack (1981).

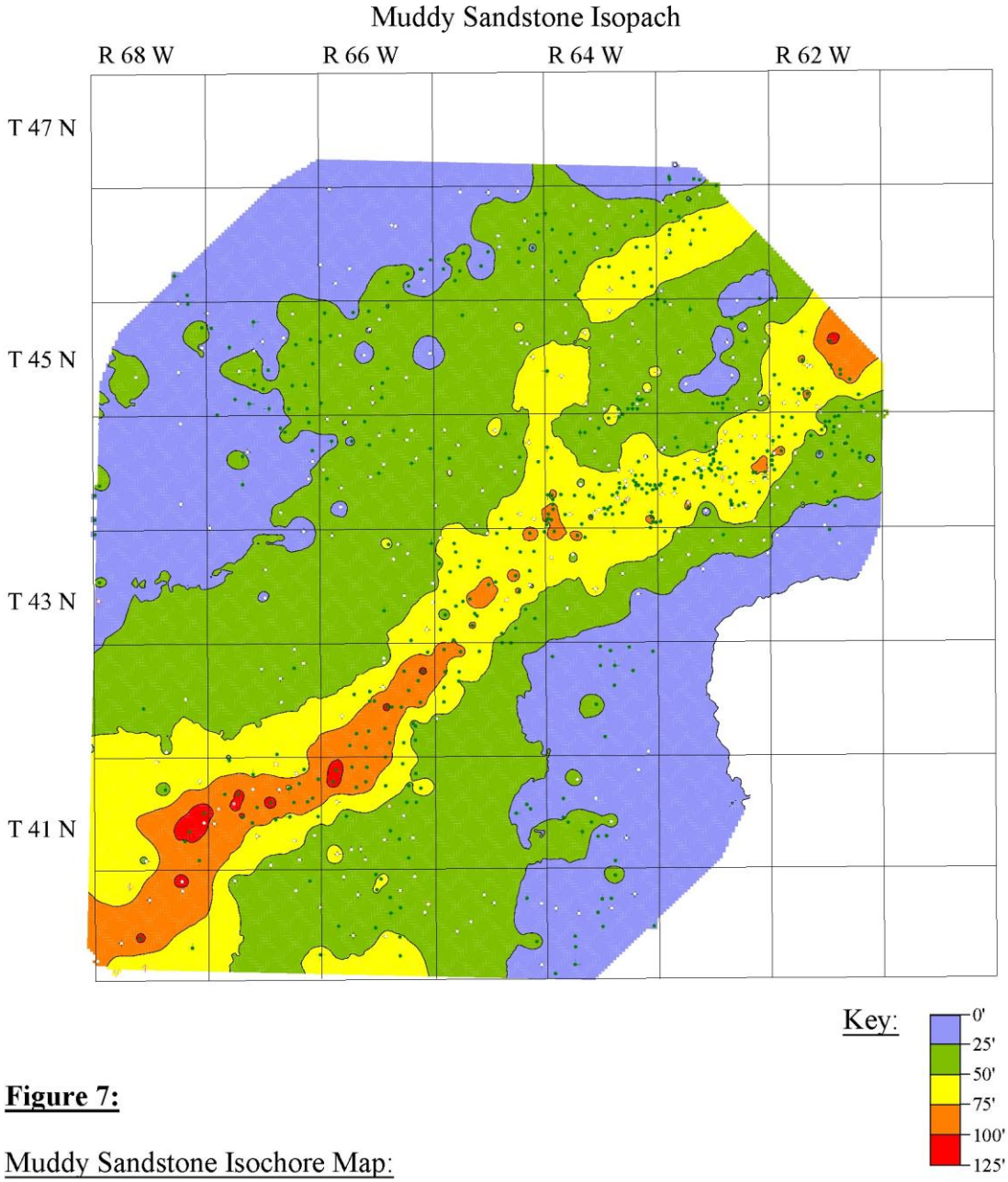

Figure 7:

Muddy Sandstone Isochore Map:

Isochore map of the Muddy Sandstone from the base of the Shell Creek Shale, to the base of the Muddy Sandstone. Map drawn with 25' contour interval. Notice how the depositional 'deep' of the Fiddler Creek, the 'Y' feature in the northeastern quadrant of the map, differs from the trend line of the wells from figure 6.

FACIES DESCRIPTIONS

Introduction to Facies Descriptions

Sixteen facies were derived from eleven Muddy Sandstone cores described as a part of this study. The sixteen facies are grouped lithologically into three mudstone facies (figure 8), seven silty sandstone or sandy siltstone facies (figures 9.A, B, and C), and six sandstone facies (figure 10.A and B).

Abbreviations for facies names were created using nomenclature proposed by Miall (1985), which is only slightly modified where necessary. The first upper case letter describes rock type, i.e. sandstone, siltstone, etc. Where more than one upper case letter is combined the first upper case letter indicates the dominate rock type and the second a subsidiary rock type. Thus a sandy siltstone is delineated by 'FS,' and silty sandstone by 'SF.' Lower case letters indicates the type of bedding structure present. Tables 1.1 and 1.2 describe this nomenclature in more detail.

Table 1.1 - Rock Type

S	Sandstone	Lower very fine to very coarse consolidated sand
F	Siltstone, Mudstone	Silt and mud, often intermixed with varying amounts of sand
C	Carbonaceous	Organic material

Table 1.2 - Bedding Structures

m	Massive	No apparent bedding structures
b	Bentonite	White bentonite clay
l	Laminated	Parallel to sub parallel or wavy lamination
r	Ripples	Isolated or stacked ripples
rc	Climbing Ripples	Series of stacked ripples
hl	Horizontal Lower Plane Bed	Lower flow regime plane beds
hu	Horizontal Upper Plane Bed	Upper flow regime plane beds

d	Deformed	Beds and bedding structures deformed beyond recognition
p	Planar Crossbeds	Cross stratified beds

Each facies is described very briefly in the text. Detailed description and interpretation are given in the tables of figures 8, 9.A-C, and 10 A and B. The descriptions and interpretations in these figures are associated with an image of the facies from core, and are meant to be the primary source of descriptive information for each facies.

Mudstone Facies

The mudstone facies (figure 8, facies FCl, FCm, and Fb) are most prominent in the Skull Creek section of the cores. The massive carbonaceous mudstone facies (FCm) is very rarely found within the Muddy Sandstone itself. Conversely, the laminated siltstone (figure 8, facies FCl), and white claystone (figure 8, facies Fb) are found exclusively within the Muddy Sandstone section of these cores.

Laminated Carbonaceous Mudstone (FCl)

This facies (figure 8) is only found in the Muddy Sandstone section of the cores, and only in very thin intervals. It ranges from 2 cm to 10 cm thick. This facies is not very common, and occurs in only 1% of the described core.

Facies FCl consists of very organic black sandy siltstone with grain sizes ranging from very fine lower sand to silt. Laminae are subparallel to wavy and range in thickness from < 1 mm to 3 mm. Facies FCl is infrequently interbedded with very fine lower well

Mud and Silt Facies:

FCl - Laminated Carbonaceous Siltstone:

Description:
Black organic sandy siltstone. Very fine lower sand to silt, poorly sorted and well rounded grains. Sub-parallel to wavy laminations ranging from <1 to 3 mm, occasionally interbedded with very fine lower, well sorted standstone. Bioturbation ranges from infrequent to very frequent mud filled burrows.

Hydrodynamic Interpretation:
Suspension fall-out, deposited in a little to no current, very low energy environment. High organic content suggests deposit accumulated proximal to vegetation, or with periodic influx from a vegetated area.

FCm - Massive Carbonaceous Mudstone

Description:
Dark grey to black, very organic rich mudstone. Very organic, may contain 1 to 3 mm organic particulates. Occasionally heavily bioturbated with lined horizontal burrows, otherwise no sediment structures apparent.

Hydrodynamic Interpretation:
Suspension fall-out of silt, mud, and organic material deposited in very low energy, quiet waters.

Fb - White Claystone (Bentonite):

Description:
White bentonite clay. Occasional organic particulates ranging from <1 to 3 mm. Heavily bioturbated in places, horizontal, unlined, bentonite filled burrows.

Hydrodynamic Interpretation:
Deposition through suspension fallout from airborne volcanic ash. Underwent bioturbation in some areas prior to alteration to claystone.

Figure 8: The three mud and silt facies of the Fiddler Creek and Clareton Cores recognized from the USGS Core Library. Facies defined by grain size and sorting, sedimentary structures, and composition.

sorted sandstone. Very little burrowing is present in this facies, but when present are horizontal and vertical mud filled burrows.

Facies FCl is interpreted as suspension fall-out deposited in an environment with little to no current, very low energy (Nichols et al. 1991; Dalrymple et al. 1992; Anthony et al 1996; Koch and Brenner 2009). High organic content suggests deposit accumulated proximal to vegetation, or with periodic influx from a vegetated area.

Massive Carbonaceous Mudstone (FCm)

Unlike FCl, the FCm facies (figure 8) is most the most common facies in the Skull Creek section of the cores. It makes up approximately 90% of the Skull Creek in the cores investigated. FCm is the most common facies core, it accounts for the 19% of the total described core.

FCm is dark grey to black organic rich mudstone. FCm may contain organic particles < 1 mm to 3 mm in size, and may have very heavy bioturbation in places. Bioturbation are lined horizontal burrows. No other sedimentary structures are apparent in FCm.

Facies FCm is interpreted as the suspension fall-out of silt, mud, and organic material deposited in low energy, quiet waters with little or no current influence (Nichols et al. 1991; Dalrymple et al. 1992; Anthony et al 1996; Koch and Brenner 2009).

White Claystone (Fb)

Facies Fb is starkly white compared to the rest of the core. It contains no sandstone, and is nearly always unconsolidated. In sections it contains 1 to 3 mm organic

particles. Facies Fb is generally 10 to 30 cm thick, however in one core this facies is several meters thick. Like FCl, facies Fb only accounts for 1% of the total core described.

Fb is a bright white shrink swell claystone that is heavily bioturbated in places with unlined burrows that are filled with the same white shrink swell claystone.

Facies Fb is interpreted as the suspension fall-out from airborne volcanic ash. In places the ash underwent bioturbation prior to alteration to clayston, but more often presents as massive claystone.

Silty Sandstone and Sandy Siltstone Facies

The silty sandstone facies, figure 9.A, 9.B, and 9.C are the most prominent facies within the Muddy Sandstone, however they also occur intermittently in the Skull Creek as relatively thin, 10 – 20 cm thick, beds. Facies with a muddy matrix and mud filled burrows are often easily recognized because of the high clay content in the mud. When the core is sprayed with water, the clay swells noticeably. It is interpreted here that the primary source of clay in the mud is from the multiple bentonite layers, facies Fb (figure 8), present in the valley-fills.

Massive Silty Sandstone (SFm)

Facies SFm is extremely rare in the core described for this study. This facies is present in only one of the facies associations, and comprises less than 2% of the association. In total facies SFm makes up 2% of the entire core described. Its hydrodynamic interpretation is non-unique in that this facies alone is not indicative of any specific environment of deposition.

SFm is light to dark grey muddy sandstone. Grain size ranges from very fine upper sand to silt, is poorly sorted, well rounded grains. SFm is massive, unlaminated with no to very frequent, mud or sand filled horizontal unlined burrows.

Facies SFm is interpreted as suspension fall-out deposit accumulated in low energy unidirectional or bidirectional current (Nichols et al. 1991; Dalrymple et al. 1992; Anthony et al 1996). However, it is possible that SFm has been homogenized by bioturbation.

Laminated Silty Sandstone (SFl)

This facies ranges in thickness in core from 5 cm to 50 cm, however is most commonly between 10 cm and 20 cm thick. It is present in 16% of the described core, and occurs in both the Muddy Sandstone and Skull Creek Shale portions of the cores. Facies SFl is one of the more common facies found in core.

SFl is white to light grey muddy sandstone. Grain size ranges from fine upper sand to very fine upper sand in a silty matrix with poorly sorted, well rounded grains interspersed with organic particles ranging from 1mm to 3mm. Discontinuous sub-parallel wavy laminations with some evidence of soft sediment deformation present. Burrows are silt filled, unlined, vertical and horizontal burrows.

SFl is interpreted as low energy, suspension fall-out of sand and silt in a weak, unidirectional current (Nichols et al. 1991; Dalrymple et al. 1992; Anthony et al 1996; Koch and Brenner 2009).

Ripple Laminated Carbonaceous Sandy Siltstone (FSCr)

This facies has one of the widest ranges in thickness of all the facies. It ranges from 5 cm thick, to 200 cm thick, however it is most commonly between 10 cm and 20 cm thick. FSCr is also one of the more common facies; it comprises approximately 12% of the described core.

FSCr ranges from dark to light grey and is finely laminated lenticular sandstone bodies interbedded with organic rich laminae of sand, silt, and mud. Sand grain sizes ranges from fine lower to very fine upper, and are well rounded. Lamina are between 1mm and 6mm thick. Deposit is heavily bioturbated with unlined horizontal and vertical burrows that are predominately sand filled.

Facies FSCr is interpreted as the accumulation of sediment in alternating current and slack water conditions. If ripple cross stratification was ever present is has since been destroyed by bioturbation (Nichols et al. 1991; Dalrymple et al. 1992; Anthony et al 1996; Koch and Brenner 2009).

Ripple Laminated Sandy Siltstone (FSr)

This facies is relatively rare in core, occurring in only 6% of all described core. However, when present, it can range from 10 cm to 200 cm thick. It most commonly occurred in thicknesses greater than 20 cm.

Facies FSr is light to dark grey sandstone with mud. Gran sizes range from fine lower to very fine lower, moderately sorted well rounded grains with mud present. Wavy laminae range from 1mm to 5mm thick sand layers interspersed with < 1mm muddy organic layers. No, to very little bioturbation is present, but when identified were sand filled unlined horizontal burrows.

Silty and Muddy Sandstone Facies:

SFm - Massive Silty Sandstone:

Description:
Light to dark grey muddy sandstone. Very fine upper sand to silt, poorly sorted, well rounded grains. Massive unlaminated, with no to very frequent, mud or sand filled, horizontal, unlined burrows.

Hydrodynamic Interpretation:
Suspension fall-out deposit, accumulated in very low energy unidirectional or bidirectional current. It is also possible that this facies was not originally massive, but has become homogenized by bioturbation.

SFl - Laminated Silty Sandstone:

Description:
White to light grey muddy sandstone. Fine upper sand to very fine upper sand in silty matrix, poorly sorted, well rounded grains interspersed with organic particles ranging from 1 to 3 mm. Discontinuous sub-parallel wavy laminations with some evidence of soft sediment deformation. Silt filled, unlined, vertical and horizontal burrows.

Hydrodynamic Interpretation:
Low energy, suspension fallout of sand and silt in weak unidirectional current.

FSCr - Laminated Carbonaceous Sandy Siltstone:

Description:
Light to dark grey or black laminated sand mud and organic material. Fine lower to very fine upper, moderately sorted, well rounded sand grains. Sand laminae appear lenticular and range from 1 to 3 mm thick. Lenticular sand is heavily interbedded with organic rich sand and mud laminae ranging from 1 to 6mm thick. Deposit is heavily bioturbaded with unlined, horizontal and vertical burrows that are predominately sand filled.

Hydrodynamic Interpretation:
Accumulation of sediment under alternating current and slack-water conditions. If cross-stratification was ever present, it was destroyed by bioturbative activity.

Figure 9.A: The six silty and muddy sand facies of the Fiddler Creek and Clareton Cores recognized from the USGS Core Library. Facies defined by grain size and sorting, sedimentary structures, and composition.

Silty and Muddy Sandstone Facies (Continued):

FSr - Ripple Laminated Sandy Siltstone:

Description:
Light to dark grey sandstone with mud. Fine lower to very fine lower, moderately sorted, well rounded grains in a muddy matrix. Wavy laminated one to five mm sand layers interspersed with <1mm muddy organic layers. No, to very infrequent, sand filled, unlined horizontal burrows.

Hydrodynamic Interpretation:
Lenticular sand bodies bounded with mud and organic particles indicates cyclic conditions of quiescence, and unidirectional current. Bioturbative activity appears to be most active during periods of quiescence, after which burrows were filled with the next deposition of sand.

SFCl - Laminated Carbonates and Silty Sandstone:

Description:
Black organic coal with sand and mud laminations. Sand is very fine upper to fine upper, well sorted, well rounded grains. Mud is light grey in color. Coal laminae contain organic fragments ranging from 1 to 3 mm. Laminations are wavy, no bioturbation or soft sediment deformation present.

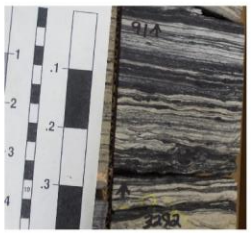

Hydrodynamic Interpretation:
Suspension deposition of mud and organic material frequently punctuated by very low energy deposition of sand.

SFd - Deformed Silty Sandstone:

Description:
Dark grey to black marled silty sandstone. Grain size ranges from very fine upper, to very fine lower, well rounded, mature sand. Wavy laminations are occasionally present, however unit is extensively bioturbated and deformed. Laminae are often unrecognizable. Bioturbation, when recognizable, consists of unlined vertical and horizontal burrows.

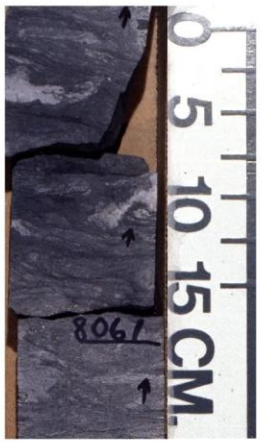

Hydrodynamic Interpretation:
Predominate silt and organic particulates, interspersed with mixed sandy units indicate deposition in relatively deep water with periods of increased flow resulting in sand deposition. Relative lack of sandy deposits in comparison with other facies indicates a more distal deposition than other facies.

Figure 9.B: The six silty and muddy sand facies of the Fiddler Creek and Clareton Cores recognized from the USGS Core Library. Facies defined by grain size and sorting, sedimentary structures, and composition.

In facies FSr lenticular sand bodies are bounded with mud and organic material indicating cyclic conditions of alternating quiescence and unidirectional current. Bioturbative activity appears to be mostly active during periods of quiescence after which burrow are filled with sand from the next laminae (Nichols et al. 1991; Dalrymple et al. 1992; Anthony et al 1996; Koch and Brenner 2009).

Laminated Carbonaceous Silty Sandstone (SFCl)

SFCl is one of the least common facies in the described core. It is present in 2% of the described core. In addition it is never present in sections greater than 10 cm thick.

This facies is black organic rich coal with laminations of sand and mud. Sand grains are fine upper to very fine upper well sorted and well rounded. Mud laminae are light grey in color. Coal laminae contain organic fragments 1mm to 3mm thick. Laminations are wavy, with no or very little bioturbation present.

Facies SFCl is interpreted as the suspension deposition of mud and organic material punctuated by low energy deposition of sand (Nichols et al. 1991; Dalrymple et al. 1992; Anthony et al 1996; Koch and Brenner 2009).

Deformed Silty Sandstone (SFd)

Along with facies FSr and FSCr this facies can range up to 200 cm thick. It occurs in approximately 6% of the described core and is found exclusively in the Muddy Sandstone portion of the cores.

SFd is a dark grey to black marled sandy siltstone. Sand grains are very fine upper to very fine lower in size, well rounded, and well sorted. Wavy laminations may be present, however most of this facies is extensively bioturbated and deformed obscuring

original sedimentary structures. Bioturbation, when recognizeable are unlined vertical and horizontal burrows.

Facies SFd's silt and organic particles interspersed with mixed sandy units indicate deposition in relatively deep water with periods of increased flow resulting in sand deposition (Nichols et al. 1991; Dalrymple et al. 1992; Anthony et al 1996; Koch and Brenner 2009). Lack of sandy deposition relative to other facies indicates a more distal environment of deposition than other facies described here.

Sandstone Facies

The sandstone facies, figure 10.A and 10.B, occur rather infrequently in the described cores. However, when they are present they are often oil stained. The sandstone facies are the only facies to contain oil staining.

Massive Sandstone (Sm)

Facies Sm ranges from 10 cm to 50 cm thick and only appears in a relatively small portion, approximately 5% of the described core.

Sm is light brownish-red to light grey, mature, massive sandstone. Grains are very fine upper in size, well sorted, and well rounded no laminations are visible. Moderate to light bioturbation presents as sand filled, lined and unlined, vertical and horizontal burrows.

Facies Sm is interpreted as high energy upper plane bed sandstone deposits. Parallel to sub-parallel laminations are likely present but indistinguishable due to the homogenous nature of the deposit. This facies is likely not an event deposit due to the

Sandstone Facies:

Sm - Massive Sandstone:

Description:
Light brownish-red to light grey mature massive sandstone. Very fine upper, well sorted, well rounded sand grains. No visible laminations. Infrequent to frequent sand filled unlined and lined, vertical and horizontal burrows.

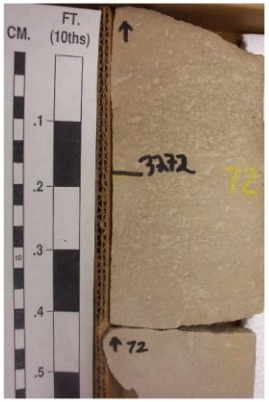

Hydrodynamic Interpretation:
Relatively high energy upper plane bed sand deposit. Parallel to sub-parallel laminations are likely present, but indistinguishable due to the homogenous nature of the deposited sediment. This facies is likely not an event deposit due to the nature of the bioturbation,

Shl - Lower Plane Bed Sandstone:

Description:
White/light tan to dark brown sandstone. Fine upper to very fine upper, well sorted, well rounded grains. Infrequent organic rich laminae.

Bedding ranges from parallel to sub parallel 2 to 5mm's in width. Moderate amounts of bioturbation consisting of sand filled, lined and unlined, vertical burrows.

Hydrodynamic Interpretation:
Smaller grain size, increased bioturbation, and higher frequency of organic laminations indicate lower-flow regime plane beds deposited by unidirectional current.

Sr - Ripple Laminated Sandstone:

Description:
Light grey sandstone. Fine lower to very fine upper, well sorted, well rounded grains. Parallel to cross stratified laminations marked by organic particulates. No bioturbation.

Hydrodynamic Interpretation:
Relatively high energy ripples and upper plane beds from unidirectional flow conditions. Tabular cross bedding formed by the down-current migration of small ripples.

Figure 10.A: The six sand facies of the Fiddler Creek and Clareton Cores recognized from the USGS Core Library. Facies defined by grain size and sorting, sedimentary structures, and composition.

Sandstone Facies (Continued):

Src - Climbing Ripple Sandstone:

Description:
Light tan to dark brown trough cross-laminated sandstone. Grains are fine lower to fine upper, mature, well sorted, and well rounded. 1 to 3mm thick laminae truncate underlying beds. Laminae are often obscured by bioturbation with unlined, sand filled, horizontal burrows.

Hydrodynamic Interpretation:
Ripple cross-laminations. Ripple crests may occur in-phase or out-of-phase (in-phase pictured above). Deposited rapidly under relatively high energy, unidirectional current.

Sp - Cross-Stratified Sandstone:

Description:
White sandstone. Fine upper to very fine upper, well sorted, well rounded grains. High angle tabular cross-beds with infrequent organic rich laminae. Moderate bioturbation consisting of sand filled, lined, vertical burrows.

Hydrodynamic Interpretation:
Angled cross stratification interspersed with bioturbated plane beds indicates low energy to medium energy plane bed and ripples deposited in unidirectional current.

Shu - Parallel Laminated Sandstone:

Description:
Reddish brown to light brown fine upper to very fine upper sandstone. Well sorted, well rounded grains. Parallel to sub-parallel laminations. Very little to no bioturbation. Occasionally oil stained in core.

Hydrodynamic Interpretation:
Transport and deposition of sand in upper flow regime currents. Because of uniform grain size laminae are often only visible due to diagenitic color operations, either iron oxide staining, or oil staining.

Figure 10.B: The six sand facies recognized from the Fiddler Creek and Clareton Cores from the USGS Core Library. Facies defined by grain size and sorting, sedimentary structures, and composition.

nature of bioturbation in the facies (Nichols et al. 1991; Dalrymple et al. 1992; Anthony et al 1996; Koch and Brenner 2009).

Lower Plane Bed Sandstone (Shl)

Facies Shl is rarely present in core, and is always erosively truncated at the top. It ranges in thickness from 10 cm to 50 cm and is present exclusively in the Muddy Sandstone portion of the cores. The Shl facies occurs in 3% of the total described core.

Facies Shl is white or light tan to dark brown sandstone. Grains are fine upper to very fine upper in size, well sorted and well rounded. Very thin (< 1mm) organic rich laminae are present, but sparse. Laminations range from parallel to sub-parallel, and are 2mm to 5mm thick. Moderate amounts of bioturbation present as sand filled lined and unlined vertical burrows.

Facies Sm is interpreted as deposited in the lower flow regime plane beds by unidirectional current. This interpretation is based on the small grain size, larger amounts of bioturbation, and larger number of organic laminations in this facies as compared to others (Nichols et al. 1991; Dalrymple et al. 1992; Anthony et al 1996; Koch and Brenner 2009).

Ripple Laminated Sandstone (Sr)

Sr has an anomalously wide range of thickness in core. Facies Sr can be anywhere from 5 cm up to 100 cm thick. However facies Sr is most commonly between 5 cm to 10 cm thick. Sr is present in 8% of the core.

Facies Sr is light grey sandstone with fine lower to very fine upper sand grains that are well sorted, and well rounded. Parallel to cross stratified laminations are marked by very thin organic laminations (< 1mm thick). No bioturbation is present in facies Sr.

Facies Sr is interpreted to have been deposited as relatively high energy ripples and upper plane beds from unidirectional flow conditions. Tabular cross bedding is formed by the down current migration of small ripples (Nichols et al. 1991; Dalrymple et al. 1992; Anthony et al 1996; Koch and Brenner 2009).

Climbing Ripple Laminated Sandstone (Src)

Climbing ripples are quite infrequent in core, only occurring in sections from 10 cm to 20 cm thick and in 2% of the total described core.

Facies Src is light tan to dark brown trough cross laminated sandstone with fine upper to fine lower, mature sand grains. Laminations are 1mm to 3mm thick and tend to truncate the underlying laminations. Laminations in facies Src can be obscured with unlined sand filled horizontal burrows.

Facies Src is interpreted as ripple cross laminations deposited in unidirectional current. Ripple crests may occur either in-phase or out-of-phase. Facies Src is interpreted to have been deposited relatively quickly under high energy unidirectional current (Nichols et al. 1991; Dalrymple et al. 1992; Anthony et al 1996; Koch and Brenner 2009).

Cross Stratified Sandstone (Sp)

Facies Sp is one of the more common facies in core. Sp occurs in intervals ranging from 10 cm to 120 cm thick. However it is most commonly between 30 cm to 50

cm thick. Facies Sp is relatively common in core; it comprises 12% of the total described core.

Sp is white sandstone with fine upper to very fine upper, well sorted, well rounded sand grains. High angle tabular cross-beds with infrequent organic rich laminae are present. Bioturbation is moderate and consists of sand filled, lined and unlined vertical burrows.

Facies Sp is interpreted as angled cross stratification interspersed with bioturbated plane beds indicating low energy to medium energy plane bed and ripples deposited in unidirectional current (Nichols et al. 1991; Dalrymple et al. 1992; Anthony et al 1996; Koch and Brenner 2009).

Upper Plane Bed Sandstone (Shu)

Facies Shu in core ranges from 5 cm to 50 cm thick. The Shu facies is present exclusively in the Muddy Sandstone portion of core, and makes up 6% of the total core.

Shu is reddish-brown to light brown sandstone with fine upper to very fine upper sand grains that are well sorted and well rounded. Laminations are parallel to sub-parallel. There is very little or no bioturbation present in this facies. However, facies Shu can present as oil stained in core.

Facies Shu is interpreted as deposited by the transport and deposition of sand in upper flow regime currents. Because of the uniform grain size, laminae are often only visible due to diagenitic color operations, either by iron oxide staining, or by oil staining (Nichols et al. 1991; Dalrymple et al. 1992; Anthony et al 1996; Koch and Brenner 2009).

5. FACIES ASSOCIATIONS

Introduction to Facies Associations

Five facies associations were described from the rock data in the study area. The facies associations then allow interpretation of the rock units to unique depositional environments responsible for their deposition. The five facies associations recorded in the rocks of this study are the central basin association (CB), bay head delta association (BHD), tidal influenced fluvial channel association (TFC), flood basin association (FB), and marine association (MA). A bentonite association is also discussed in this chapter. While the bentonite facies (BT) are not in themselves an association, they are of particular stratigraphic importance for correlation, and so are discussed as a part of this chapter.

Central Basin Association (CB)

Description: This association consists of facies FSCr, FSr, SFCl, and SFd as shown in figure 11. While each individual facies ranges in thickness from well to well, facies FSCr, FSr, and SFd are the dominate facies, and can range in thickness from 10 centimeters to 200 centimeters (cm). Each of these facies makes up approximately 30% of the association. Facies SFCl is the least common making up 10% of the association as described in core.

The facies which compose this facies association always grade into each other within the association. The ratio of sandstone to mudstone in each facies varies throughout each CB association unit. Where some CB association units display uniform

sandstone to mudstone ratios, others grade from more mud at the bottom to more mud at the top and visa versa. This association is usually bounded gradationally or abruptly at the top by the Bay Head Delta (BHD) association, or Marine (MA) association. At its base this association is usually abruptly bounded, and can precede any of the other facies associations.

Interpretation: This association is interpreted as the predominately fair-weather deposition of sand and mud in a lagoon or bay environment of a central basin complex. In this environment, the small scale bedding, fine grain size, and occasional sandstone stringers (most easily seen in facies SFCl) are indicative of the small scale fluctuations in energy of the central basin (Dalrymple 1992; MacEachern and Pemberton 1994; Anthony 1996). While unequivocal tidal structures are lacking, the finely laminated organic and muddy sandstone, or pinstripe nature of the deposits (see facies FSr and SFCl) and occasional current ripples do indicate some tidal influence on the deposits. The tidal influence in current ripples is displayed by the very fine sediment drape across the top of each set of current ripples. This indicates a slight decrease in fluvial current flow leading up to and at high tide.

The fluctuating ratio of sandstone to mudstone throughout the association is interpreted as an indicator of the proximity of the deposit to the sandstone rich bay head delta, or estuarine mouth and therefore shoaling water depths (Dalrymple 1992; MacEachern and Pemberton 1994; Anthony 1996).

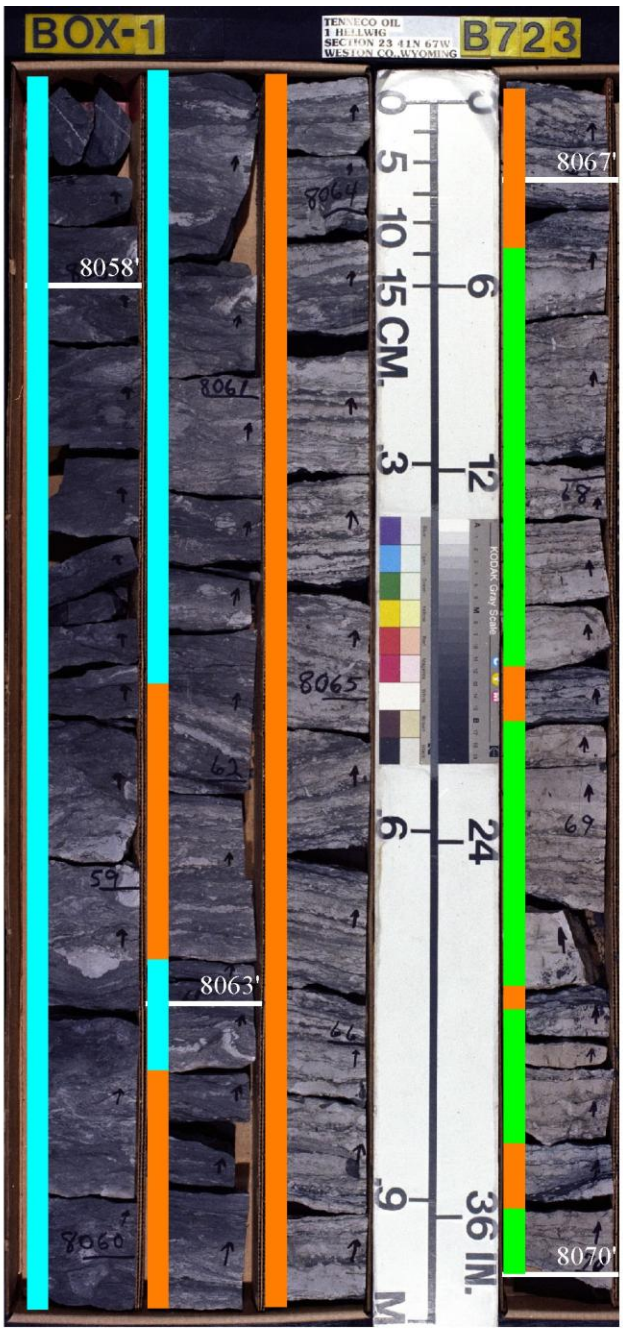

Figure 11:

Central Basin Association:

Example of the Central Basin Facies Association from Tenneco Oil's USA #1 Hellwig core, UWI number 4904505097 in the Petra database, and USGS library no. B723. Notice the increase in mud in the system from the base of the section, depth 8070', up through the top of the core at 8057' (footages marked in white).

Facies pictured include predominately Fsr (light green) at the base of the core with some of facies FSCr (orange) present, grading into entirely facies FSCr around 8067', and finally completely grading into facies SFd (cyan) around 8063'.

Bay Head Delta Association (BHD)

Description: The BHD is composed of seven facies. An example of the BHD is shown in figure 12. The seven facies are FCl, SFl, FSCr, Sm, Shl, Sr, and Sp. The least common facies in the BHD is facies FCl, it is present in core less than 1% of the time ranges in thickness from 2 cm to 5 cm. Likewise, facies SFl is also very rare in the BHD. Facies SFl makes up 4%, or less, of the association. It ranges in thickness from 5 cm to 20 cm, and usually grades into the preceding and subsequent facies. Facies Sm is present in 5% of the association, Sm is usually bounded above and below gradationally, and can be anywhere from 10 cm to 50 cm thick.

Facies FSCr and facies Shl make up approximately 15% of the core each. Facies FSCr is generally thin in this association, ranging from 5 cm to 10 cm thick and is usually abruptly bounded by the next facies in the association. Facies Shl is generally more thick than facies FSCr, ranging from 10 cm to 50 cm, however it is less abundant than FSCr. Facies Shl tends to be present at or near the top of the association, and therefore is usually abruptly bounded by the succeeding facies, or association, and is generally gradationally bounded below by the preceding facies within the association.

Facies Sr and Sp are the most abundant facies observed, making up a total of nearly 60% of the association. Facies Sr makes up 35% of the association and ranges from 5 cm to 100 cm thick. Facies Sr is usually bounded either above, below, or both, by facies Shl. The two facies nearly always grade into each other, often phasing from one to another and back several times within one association. Facies Sp takes up the last 25% of the association, and can be anywhere from 20 cm to 70 cm thick.

Mud laminae are infrequent in this association, however when they do occur, they occur at the top of an association unit. Bioturbation in this association is infrequent, and nearly always occurs as lined, horizontal burrows. This association is often bounded by erosive, sometimes rooted surfaces but can also grade into association CB.

Interpretation: This association is interpreted as the fair-weather and storm deposits of a bay head delta system. High angle cross beds of facies Sp are most likely trough cross-stratified, however are usually unrecognizable as such in core (this is not true in the example BHD of figure 12). High angle trough cross-stratified beds were most likely deposited as a sub-aqueous dune. Horizontal planar and ripple laminated beds were deposited as either overbank sheetflow, or delta-front style sediment gravity flows (MacEachern and Pemberton 1994). Massive sandstones, like those in facies Sm are likely the result of rapid sediment deposition during flood stage fluvial environments with associated dewatering and liquefaction (Dalrymple 1992; MacEachern and Pemberton 1994; Anthony 1996).

The infrequent occurrence of facies FCl, SFl and FSCr display a clear tidal influence demonstrated by the frequent mud drapes and thin layers of organic material. These facies were most likely deposited on the delta topset with limited fluvial influence except during flood stage and storm weather conditions.

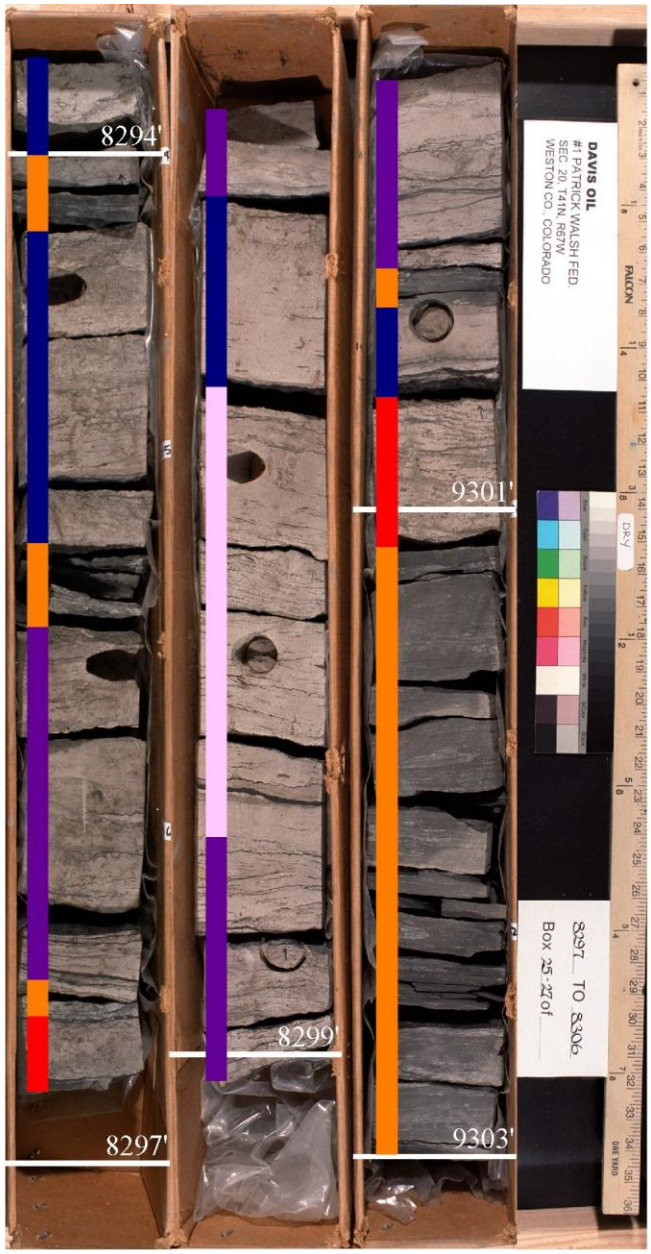

Figure 12:

Bay Head Delta Association:

Example of the Bay Head Delta Association from Davis Oil's #1 Patrick Walsh Federal core. UWI number 4904521730 in the Petra Database, and USGS library no. S601. BHD facies begin slightly below 9301' and ends at 8294'.

This BHD unit has significantly more ripple cross laminations (facies Sr in dark purple) than other BHD associations from this study area. Also note, facies Sp (in light pink) is clearly trough cross bedded. The clear representation of trough cross stratification is rare in core. Mud content in this BHD unit increases toward the top abrupt contact with the next association (next association not pictured).

Other facies from the BHD association displayed in this example include facies SFl (red), facies Shl (dark blue), and facies FSCr (orange).

Tidal Influenced Fluvial Channel Association (TFC)

Description: This facies association consists of facies Sm, Sr, Src, Sp and Shu as shown in figure 13. Approximately one half (45%) of the association is composed of facies Sp which can be anywhere from 10 cm to 120 cm thick. Facies Src is included in the 45% occurrence of facies Sp because facies Src never occurs in core except when gradationally bounded above and below by facies Sp. Facies Src is never more than 20 cm, and never less than 10cm thick.

The next most common facies is facies Shu, making up approximately 30% of the association. Facies Shu ranges in thickness from 5 cm to 50 cm thick in any given interval. Facies Sm is also rather common in this association, comprising 20% of the association and ranging in thickness from 20 cm to 50 cm. The least common facies in the TFC is facies Sr, which comprises only 5% of the association as a whole. Facies Sr can be anywhere from 5 cm to 20 cm thick, however is most commonly between 5 cm and 10 cm thick.

The entire association has very similar grain sizes, ranging from lower very fine sand, to upper fine sand. In this homogenous sediment, laminations are made visible by the very slight increase in mud, and organic material at the laminae boundaries. All facies in this association contain zero bioturbation, excepting the occasional burrowed boundary at the top of an association.

All of the contacts between facies associated with this association are gradational. The top of the association is usually sharply bounded and usually bioturbated by the next association. However the top of the association may also grade into the BHD. The base of

the association is nearly always a sharp, erosional contact with the underlying association. Often mud rip-up clasts are present in the base of the association.

Interpretation: This association was deposited in a fluvial channel, which was influenced, albeit slightly, by tidal processes. The erosional boundary at the base is interpreted as the initial erosional channel scour. The associated mud rip-up clasts in the basal facies of the association are from the continued erosion of the system, and further iterate the interpretation of a fluvial channel deposit. It appears the majority of facies in this association were deposited during fair-weather 'normal' fluvial conditions. However some of facies Sm (massive sandstones) appear to have been rapidly deposited during either flood stage, or storm conditions within the fluvial system.

The slightly mud rich laminae within the fluvial deposits is interpreted to be from a decrease in stream flow velocities during high tide. The laminae packages do not exactly work out to neap and spring tides, as you would expect to find in a true tidal rythmite. However the increase of mud in the fluvial sandstone, while maintaining a very consistent grain size throughout the entire association is most simply explained by a decrease in flow velocities at high tide (Dalrymple 1992; MacEachern and Pemberton 1994; Anthony 1996).

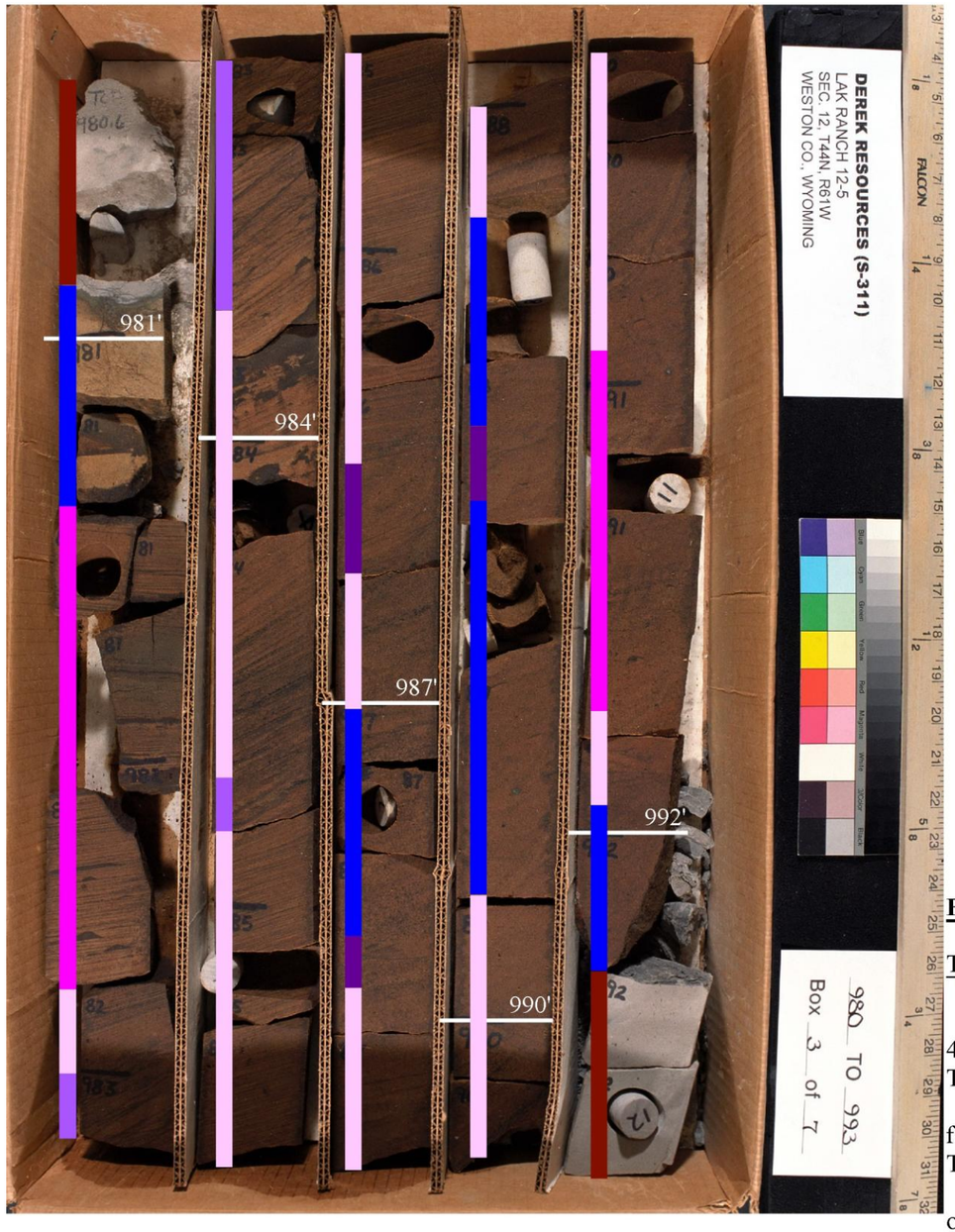

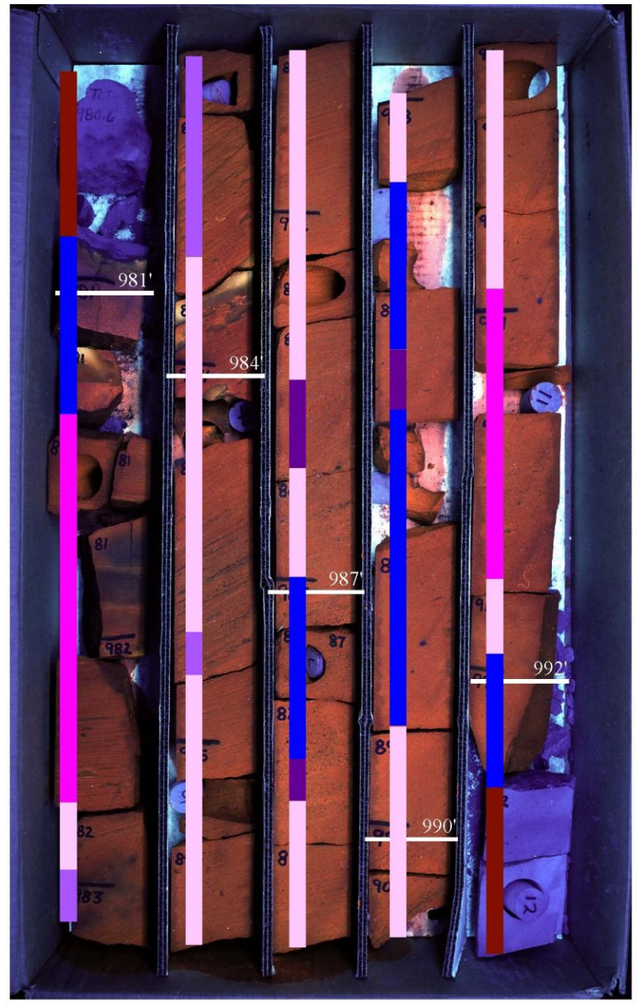

Figure 13:

Tidal Influenced Fluvial Channel Association:

Example of the TFC facies association. Taken from Derek Resources' Lak Ranch 21-5 well. UWI number 4904522495 from the Petra Database, USGS library no. S311. The well is located in Wyoming Sec. 12 T44N R61W. The TFC association begins at depth 992' and ends just above 981'.

The facies presented in this TFC example are facies Sm (Blue), facies Shl (Light Pink), facies Shu (Dark Pink), facies Sr (Dark Purple), facies Src (Light Purple). Above and below the TFC association is facies SFm (Dark Red). The TFC association is erosionally bounded at the base, with some mud rip-up clasts present in the base of the section.

This particular TFC association is oil stained, which is the cause of the dark brown color of the facies. The photo on the left is of the core in natural light, the photo on the right shows the same core under ultra-violet light. Notice how the oil stained core floresces under the UV light.

Flood Basin Association (FB)

Description: Facies association FB is composed dominately of facies SFl, but also contains facies SFm, FSCr and very rarely facies FCl, or facies Fb. Facies SFl comprises 80% of this association and ranges in thickness from 10 cm to 50 cm. Similarly, facies FSCr occurs in 15% of the association, and can be 10 to 30 cm thick. The other two facies comprise the final 5% of the association, and are never more than 5 or 10 cm thick. When present, the three additional facies usually occur at, or near, the top of the association and are gradationally bounded with facies SFl. Each individual FB unit is rarely more than 50 cm thick.

All the intra-facies boundaries within the FB are sharp contacts. However many of them are difficult to ascertain due to the extremely fissile nature of the predominate facies SFl.

Facies SFl within the association is always heavily bioturbated and commonly displays carbonaceous horizontal root fragments. Wavy organic laminations are pervasive in this facies, and are always disjointed, never continuous. However, facies FSCr, where present, commonly displays vertical to sub-vertical, and horizontal unlined burrows. The sandstone in facies FSCr generally appears lenticular, and completely surrounded by silt and mud. These facies are predominately composed of mud and silt, with some interspersed lower to upper very fine sand.

The top of a FB unit is usually abruptly truncated. Mud laminae, and mud filled burrows may be present at the top of a truncated association. The base of the association

may be either gradational with the preceding association, or a sharp contact. This association occurs most commonly in combination with the TFC.

Interpretation: This association is interpreted as having been deposited in a flood plain (or flood basin) environment. Sand, silt, and mud were deposited during intermittent fluvial flood stage conditions. During periods of non-deposition of silt, sand, and mud depositional events the sediments were significantly re-worked by roots, and burrows. In facies SFl bioturbative activity has thoroughly mixed the sand, silt, and mud, eliminating any sedimentary structures, which may have been present at one time. Sedimentary structures were generally preserved in facies FSCr, however in places where horizontal burrows are dominant some of the original structures are unclear. The fact that this association always occurs in conjunction with the TCF facies further iterates the depositional interpretation of a flood basin adjacent to an active fluvial system (Dalrymple 1992; MacEachern and Pemberton 1994; Anthony 1996).

Figure 14:

Flood Basin Association:

Left: Example of the FB facies taken from Davis Oil's #1 Bitterroot State core. UWI number 4904521559, USGS Library no. R-309. This well is in Weston County, Wyoming, Sec. 28, T41N, R67W. The FB association is the only association pictured here. This segment of the core starts at a depth of 8112' and ends at 8104', and represents a series of multiple FB association units.

The section of core to the left displays facies SFl (Red), facies FSCr (Orange), facies FCl (Black, just above 8111'), and facies Fb (White, just above 8107').

Right: Example of the FB facies taken from Derek Resources 12-5 LAK Ranch core. UWI number 4904522495 in the Petra database, USGS library no. S-311. This well is located in Weston County, WY, Sec. 12, T44N, R61W. Core begins at 1037' below the surface, and ends at 1034.5'.

This section of core more clearly displays facies SFl (Red). Notice the rooted, muddy, sharp contact between facies SFl and facies FSCr (Orange).

Marine Association (MA)

Description: This association consists predominately, approximately 95%, of facies FCm (figure 15). In the MA facies FCm is generally greater than 1 meter (m) thick, and may be as much as 6 m thick. Facies FCl, facies Fb, facies FSCr, and facies SFl occur in varying amounts making up the final 5% of the association and never occur in intervals more than 20 cm thick. When facies FSCr and facies SFl are present they are usually at, or near, the top of the association unit and are usually erosionally truncated by the next association unit. Facies FCl and Fb occur in less than 1% of the total association and always with gradational boundaries at the base and top of the facies.

In core, this association was commonly very fissile, and as a result, unslabbed which made detailed sedimentologic analysis difficult. In places the association is heavily bioturbated (figure 15) with what appear to be lined burrows which consolidated the unit. The association is always abruptly truncated at the bottom, and usually at the top as well, however the top may appear to grade into CB facies. This association contains the lowest sandstone content of the system. Marine association may occur in small beds, less than 50 cm, in the Muddy Sandstone interval, it is the only association found in the Skull Creek unit in core.

Interpretation: This association is interpreted as a record of suspension fall out from calm, relatively open marine system. Ripple laminations and lenticular nature of the infrequent sandstone beds in the system indicate deposition from storm or flood condition deposits from the adjacent fluvial system (Dalrymple 1992; MacEachern and Pemberton 1994; Anthony 1996).

Figure 15:

Marine Association:

Example of the MA facies taken from Davis Oil's #1 Bitterroot State core. UWI number 4904521559, USGS Library no. R-309. This well is in Weston County, Wyoming, Sec. 28, T41N, R67W. The MA association is the only association pictured here. This segment of the core starts at a depth of 8169' and ends at 8160', and does not represent the entirety of this MA association unit.

At the very base of the core is a very small package of facies FCl (Black, shown with a white border). Facies FSCr (Orange) appears at the base, and near the top of this image. Facies FCm makes up the bulk of this image (Grey, shown with a white border). Facies FCl and FCr are shown with white borders to help differentiate the facies line from the grey surrounding rock.

Bentonite Association (BT)

Description: This association consists of only facies Fb. However this facies may appear in any of the other associations as mud laminae, or reworked into mud filled burrows. When it occurs on it's own it ranges in thickness from 5 cm (most common), to 5 meters (occurs only once in core). Bioturbation is generally very infrequent; however in places it can be extremely frequent, very much like the bioturbated segments of the MM.

Interpretation: While bentonite isn't strictly a facies association in and of itself, it is of particular significance stratigraphically. Unlike the other surfaces and rock units present in these valley-fills, un-altered bentonite facies are time significant events and can be used as time lines for inter-valley correlation. When unaltered, bentonite is interpreted as the suspension fall out of volcanic ash. Even 'un-reworked' deposits have most likely been transported by fluvial processes until final deposition in calm waters.

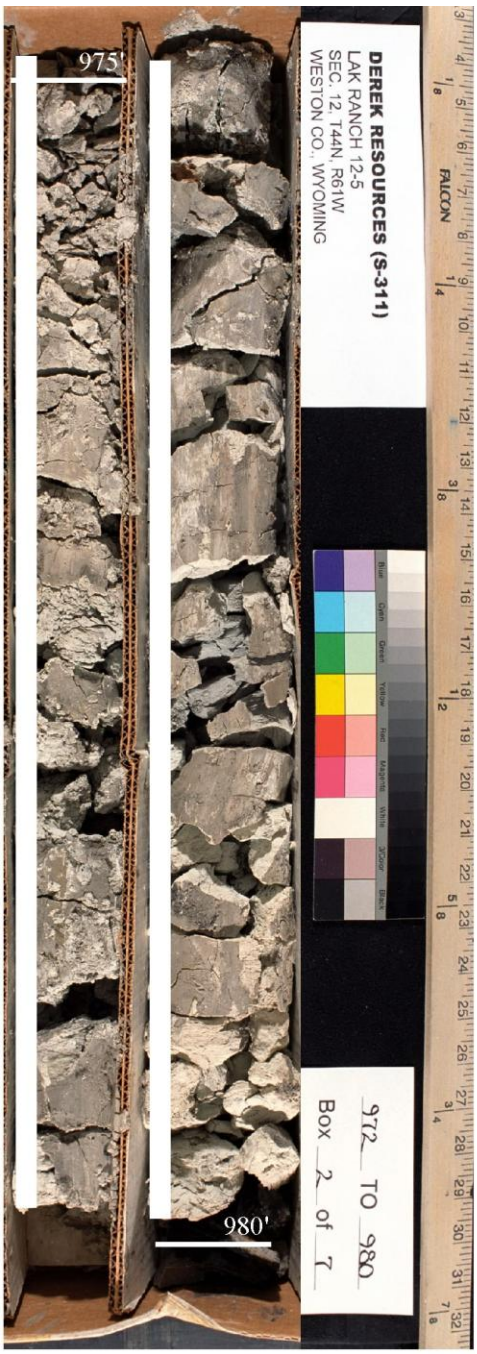

Figure 16:

Bentonite Association:

This example of the BT association comes from Derek Resources 12-5 LAK Ranch core. UWI number 4904522495 in the Petra Database, USGS library no. S-311. The well is located in Weston County Wyoming, Sec. 12, T44N R61W. The displayed core begins at a depth of 980' and ends at 975'.

The only facies pictured int his BT association photo is facies Fb (White). This is an anomalously thick appearance of the bentonite facies. There are no intra-facies, or intra-association boundries present in this photo.

6. STRATIGRAPHIC INTERPRETATIONS

Introduction to Stratigraphic Interpretations

Member isochore maps, net sandstone isochore maps, and structure contour maps were used in conjunction with facies associations and core descriptions in order to determine the internal stratigraphic architecture of each valley-fill.

Throughout both valley-fills stratigraphic preservation appears to increase through time. In other words, there is more time recorded as rock in the younger members of the valleys than in the older members of the valleys. This relationship of increasing preservation of rock versus time is interpreted based on the decreasing amount of erosive surfaces in the youngest members as opposed to the oldest members, and a decrease in significance of erosive surfaces in younger members than in older members of these valley-fills.

These observations are consistent with general conceptions of incised valley-fills. Valleys are initially carved during in-phase, eustatic falls, during these massive erosive events time is preferentially preserved as a surface in the rock record, and little, to no, time is recorded as rock within the valley itself. Any sediment that is deposited in a low order, out-of-phase eustatic rise would be quickly eroded during the next in-phase fall (low order fall on an overall eusatic fall). As sea level begins to rise the low order rises are in-phase with the high order rises and time begins to be preferentially recorded as rock, rather than a surface.

Clareton Valley-Fill

The Clareton valley-fill, as discussed earlier, was a piedmont valley-fill *sensu* Zaitlin et al. (1994). This means the Clareton valley-fill was a thoroughgoing valley, who's sediment source was in the hinterlands. The Clareton valley-fill had a relatively high amount of sandy sediment supply whose source was in the emerging black hills uplift to the east (Emme 1981). In the study area the Clareton valley-fill contains five individual members, representing five distinct periods of deposition. The environment of deposition (EOD) of each member is discussed separately in the following sections beginning with the earliest (oldest) deposited member and continuing through the final (youngest) fill in the valley-fill. Each member and its stratal relations to the others can be seen in figure 5.

Lower Recluse Member

The lower Recluse member of the Clareton valley-fill, pictured in figure 17, is the first record of deposition after the prolonged erosive event, which carved the valley. It is bounded at the base by an unconformity, the basal surface of the Muddy Sandstone, and above by the informally designated Orange surface of this study (figures 17, 18, 19). This member is present in most of the Clareton valley-fill; however it is anomalously missing from several wells.

This member is predominately composed of facies association CB at the down-dip end of the valley-fill, grades into the facies association BHD mid way up the valley-fill, and displays a small amount of the TFC facies association in the up-dip most portion of the valley-fill. Overall this member records a landward step in facies, CB facies

association above facies association BHD, and facies association BHD above facies association TFC. However, there are deposits from two distinct minor regressive episodes within the overall framework of transgressive deposits. The regressive periods are recorded by a significant down valley step in facies placing BHD facies associations above CB facies associations. CB facies associations are then emplaced over the BHD facies assciations again with the next transgression, as seen in figure 18.

This member is always erosionally bound at the base by the surface which marks the base of the Muddy Sandstone, however in core the surface is not always prevalent due to amalgamation of the same, or similar facies over the contact. The contact may contain root traces, but in core is usually recognized by an abrupt change from MA facies to either CB or BHD facies. The top of the Lower Recluse member, designated by the Orange surface in this work, is most commonly an erosional surface. This surface is often marked by root traces, and a very sharp facies contact.

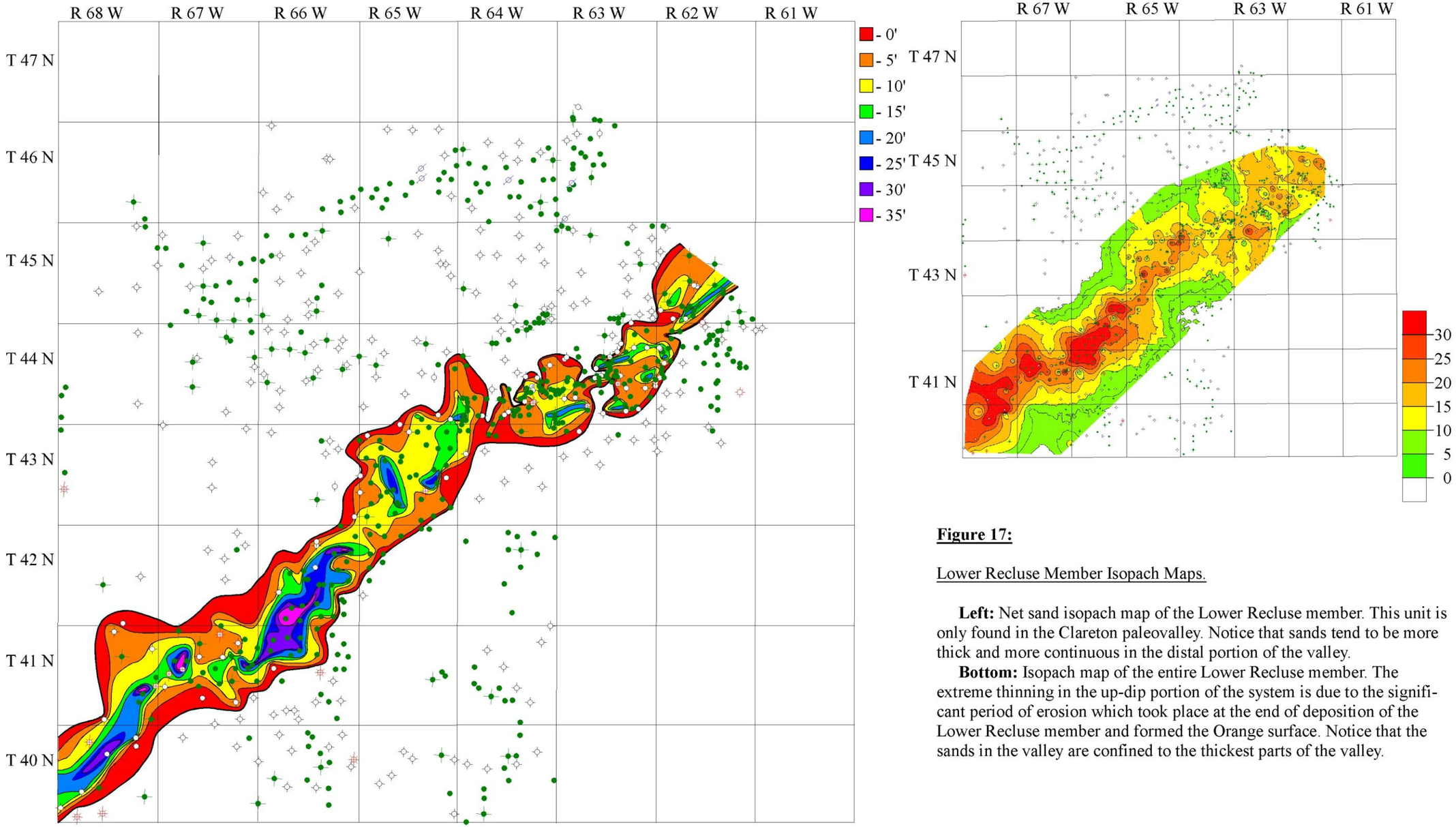

Figure 17:

Lower Recluse Member Isopach Maps.

Left: Net sand isopach map of the Lower Recluse member. This unit is only found in the Clareton paleovalley. Notice that sands tend to be more thick and more continuous in the distal portion of the valley.

Bottom: Isopach map of the entire Lower Recluse member. The extreme thinning in the up-dip portion of the system is due to the significant period of erosion which took place at the end of deposition of the Lower Recluse member and formed the Orange surface. Notice that the sands in the valley are confined to the thickest parts of the valley.

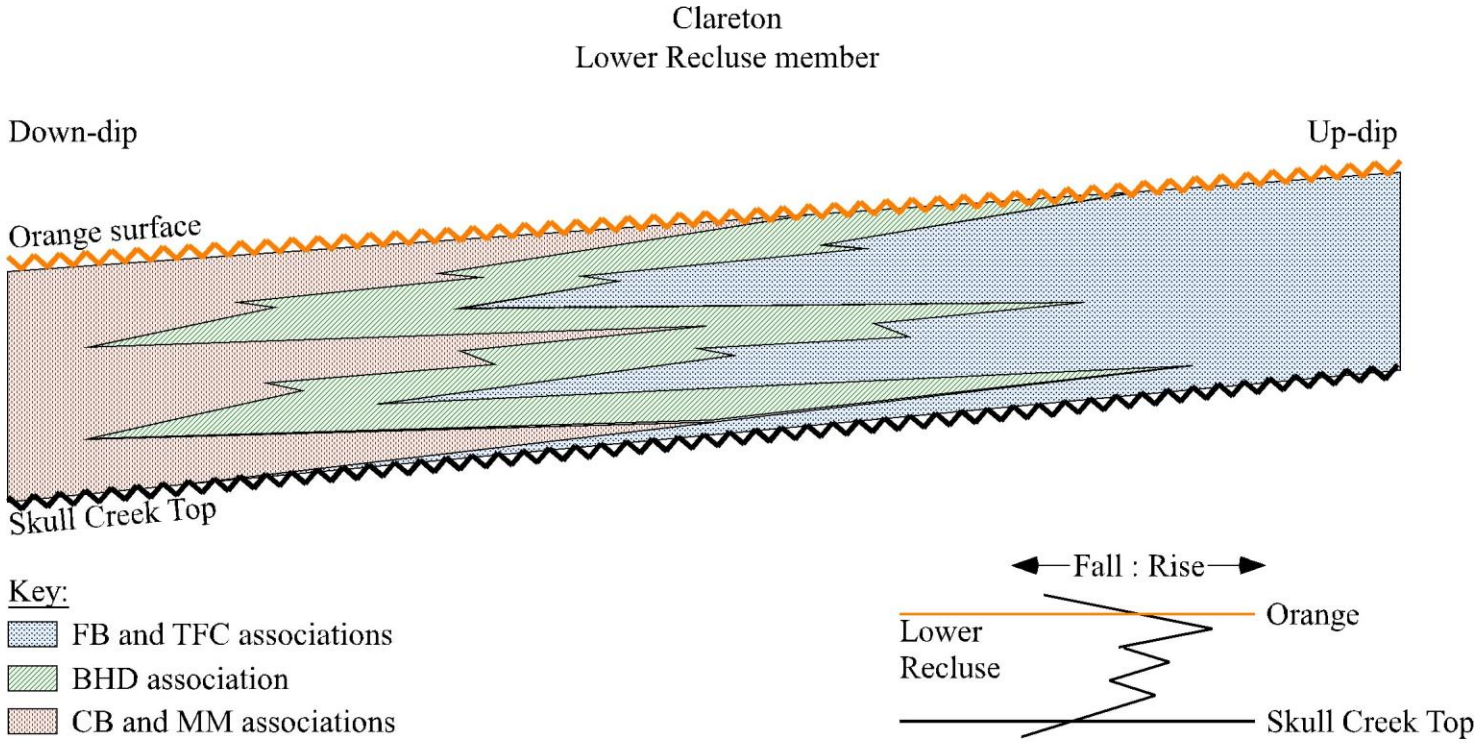

Figure 18:

Lower Recluse Stratigraphic Architecture:

Dip cross section of the Clareton system showing the generalized stacking pattern of the Lower Recluse member of the Clareton system. This member is the only to display two very low order transgressive-regressive cycles within the overall low order transgression. Total thickness of this unit is approximately 30'. The generalized sea-level curve derived from this member's stacking pattern is shown in the lower right. Note the two orders of rise and fall episodes in the curve, two rises and falls in the lowest order, and one higher order rise and fall. The Orange surface is marked at the maximum rate of fall indicating that the surface records an erosion event.

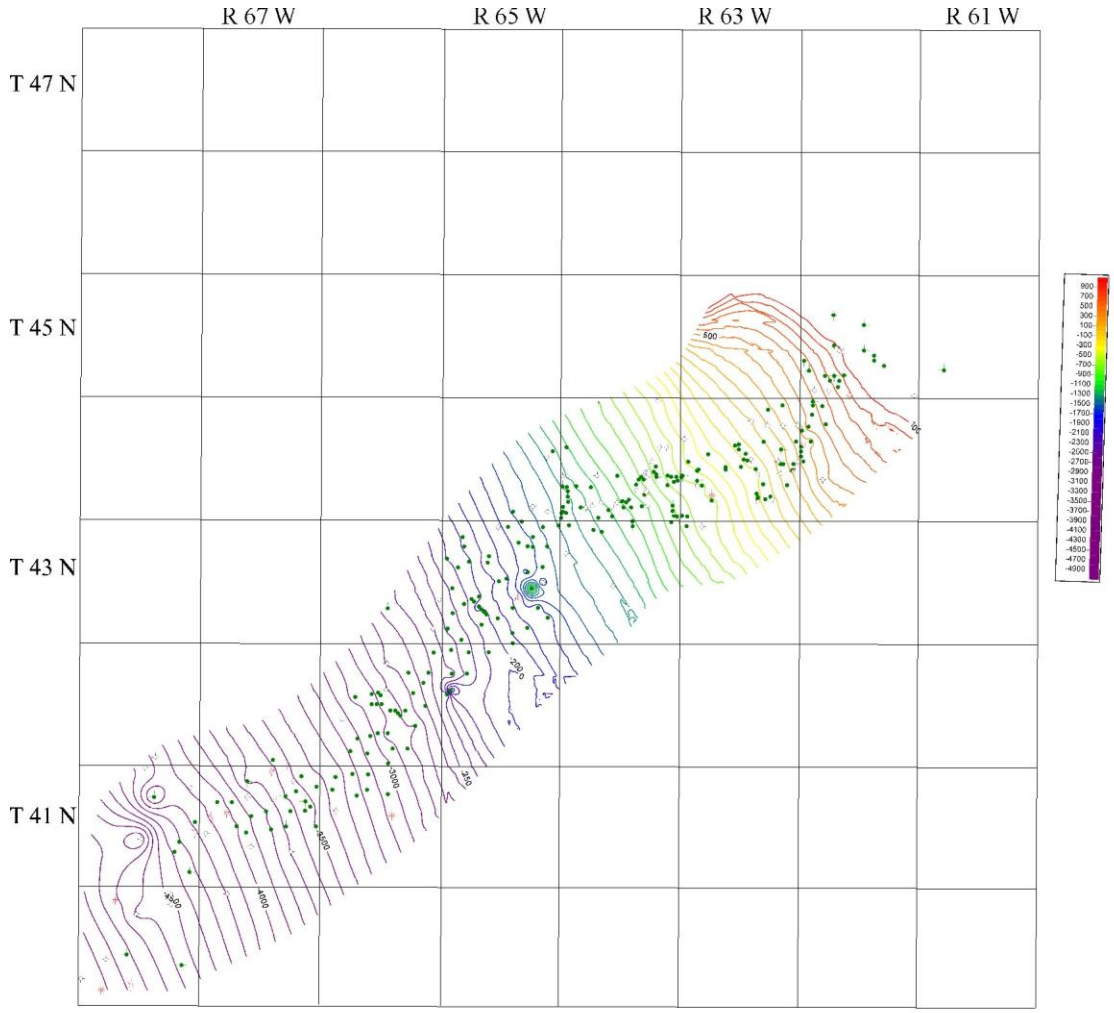

Figure 19:

Lower Recluse Structure Map:

Structure contour map of the Orange Surface, the orange surface marks the top of the Lower Recluse member. Wells displayed are only those where the Orange Surface is present. Because the Orange Surface is only present in the mid- and lower portion of the Clareton valley system, the structure map only covers the Clareton Valley.

Upper Recluse Member

The Upper Recluse member is defined in this work as bound above by the Forest surface, and below by the Orange surface, or by the erosional boundary with the Skull Creek Shale. This member represents the second period of filling within the Clareton valley-fill (figures 20, 21, and 22).

At the up-dip most part of the valley this member is dominated by a series of facies associations TFC and FB. Minor amounts of association CB may be present but only appear at the top of the member. The mid portion of the Clareton valley-fill is dominated with the CB association, with some MA present. Farther down-dip in the valley the MA becomes more prevalent in the older deposits of the member, and the CB associations become less prevalent. In the down-dip segment the MA facies generally grade upward into BHD at the top of the member.

The Upper Recluse member is interpreted to have been initially deposited during a relatively rapid rise in sea-level, directly after a period of baselevel fall and resultant erosion (figure 21). Omission of the Lower Recluse member, when the Upper Recluse member sits directly on the basal unconformity of the Muddy Sandstone, indicates a significant period of erosion after the initial deposition of the Lower Recluse member. Furthermore the core directly below the Orange surface often contains prominent root traces, and an abrupt change in facies to facies association MA directly above the surface. This combination of roots directly overlain by the Marine facies association represents a significant landward shift in facies, and is interpreted as a flooding surface. Also, the isochore of this member (figure 20) shows a significant thickening of the unit in the

center of the valley (up to 30'), which indicates erosion prior to deposition of this member.

In the lower portion of the valley the basinward step in facies, association BHD over facies association CB and facies association MA, indicates a minor regression at the end of deposition of the Upper Recluse member demonstrated by progradation of facies association BHD to prograde over the previously deposited marine facies.

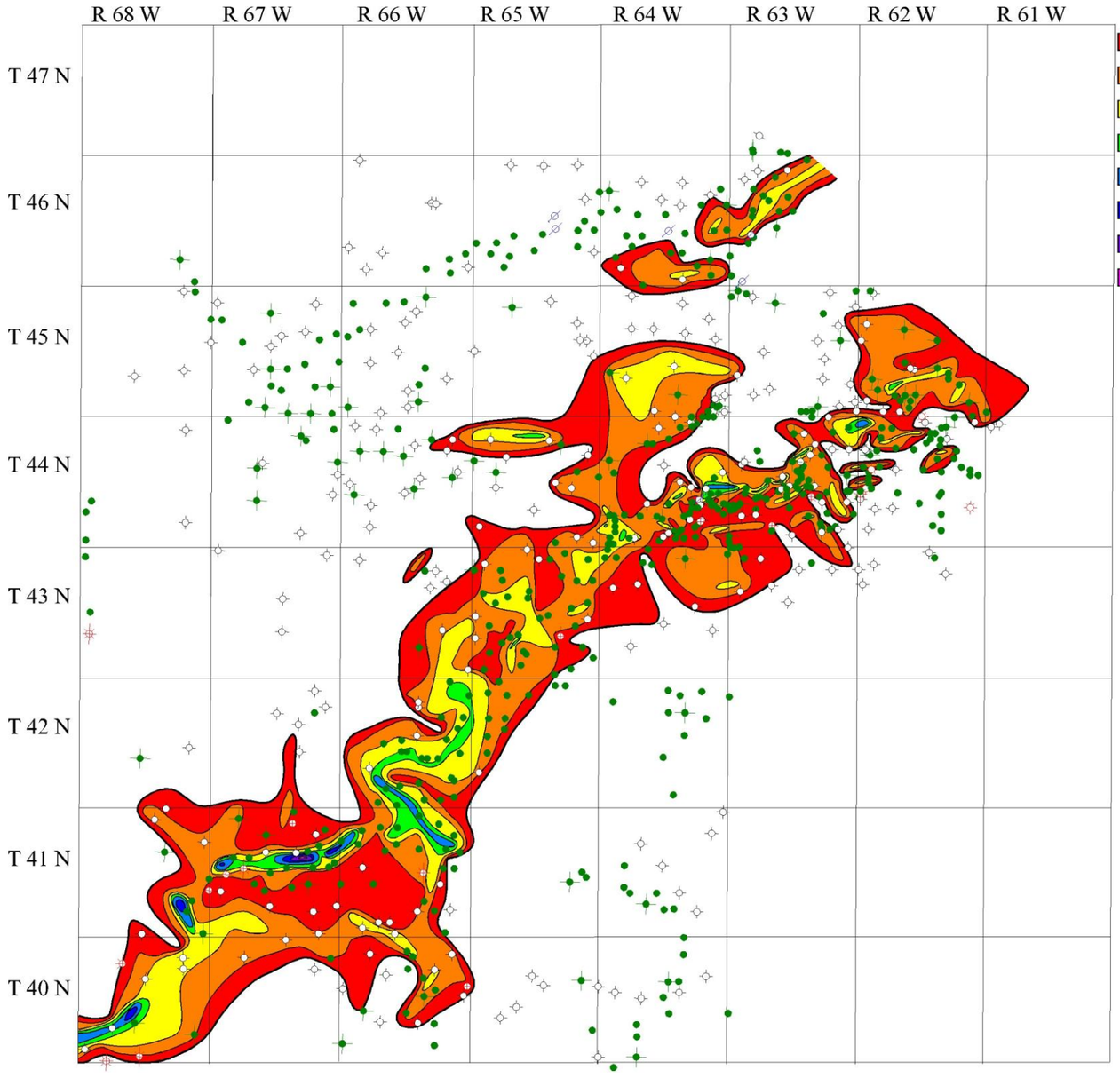

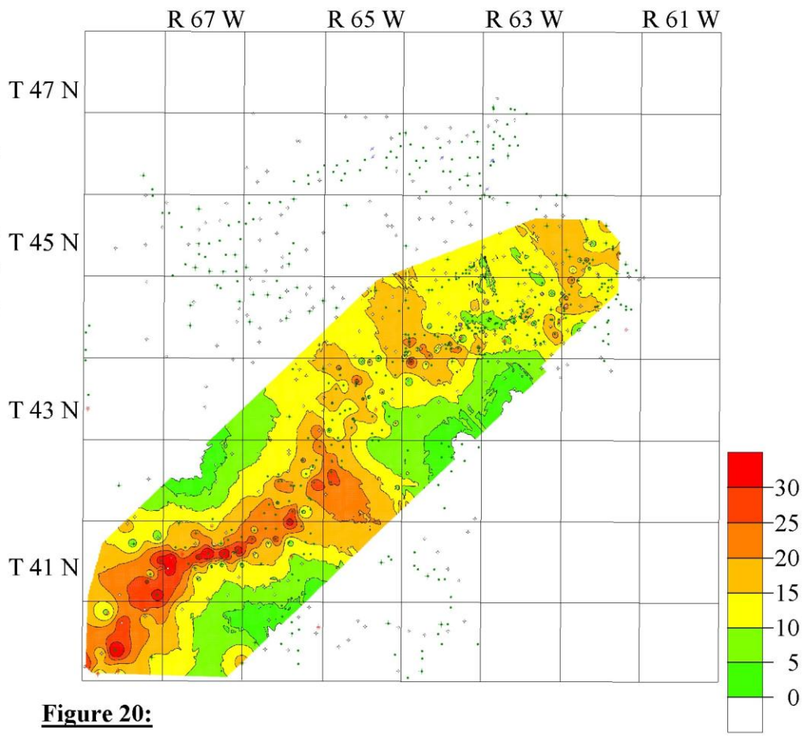

Figure 20:

Upper Recluse Member Isopach Maps.

Left: Net sand isopach of the Upper Recluse member. This is the first member recorded in the deposition of the Fiddler Creek valley. On the 'tuning fork' feature, the upper prong is the Fiddler Creek system, and the loer prong is the Clareton system. Notice the difference in the width of the area where sand was deposited in this member as opposed to the Lower Recluse member. the thickest packages of sand are relatively discontinuous, sometimes only connected by extremely thin sand packages.

Bottom: This is a member isopach for the Clareton system only. As mentioned in the text, the Upper Recluse member has a different lower bounding surface in the Fiddler Creek system than in the Clareton system. A figure displaying an isopach map for the Upper Recluse in the Clareton system can be found in the Fiddle Creek - Upper Recluse section of this chapter.

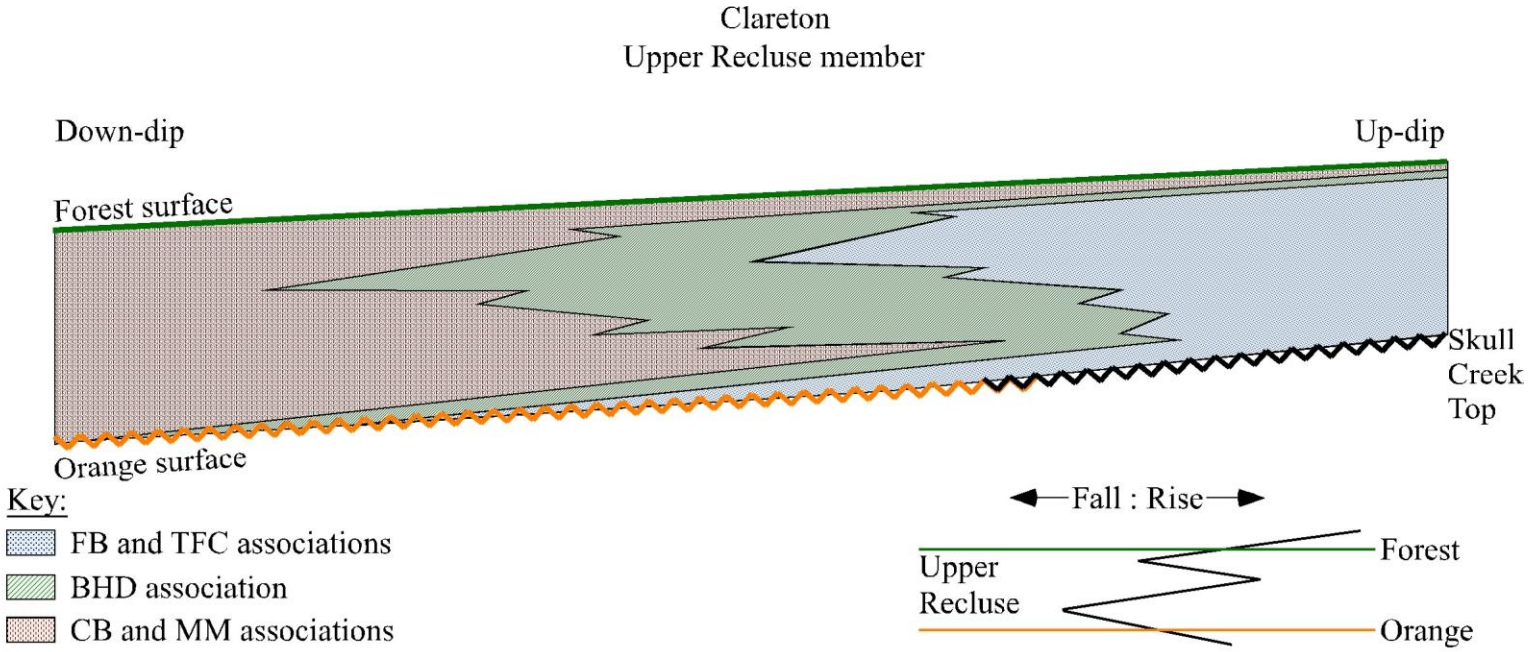

Figure 21:

Upper Recluse Stratigraphic Architecture:

Dip cross section of the Clareton system showing the generalized stacking pattern of the Upper Recluse member. This member recorded a single rise - fall cycle, followed by a rapid rise which marked the end of deposition of this member. Entire member reaches a maximum of 25' thick in the down-dip portion of the system. Note that in the up-dip portion of the section the facies sit directly on the Skull Creek top, this is to indicate that in places throughout the valley the Upper Recluse member sits directly on the Skull Creek Shale. The generalized sea-level curve derived from this member's stacking pattern is shown in the lower right. Note the Forest surface is marked at the maximum rate of transgression indicating this surface is the record of a flooding event.

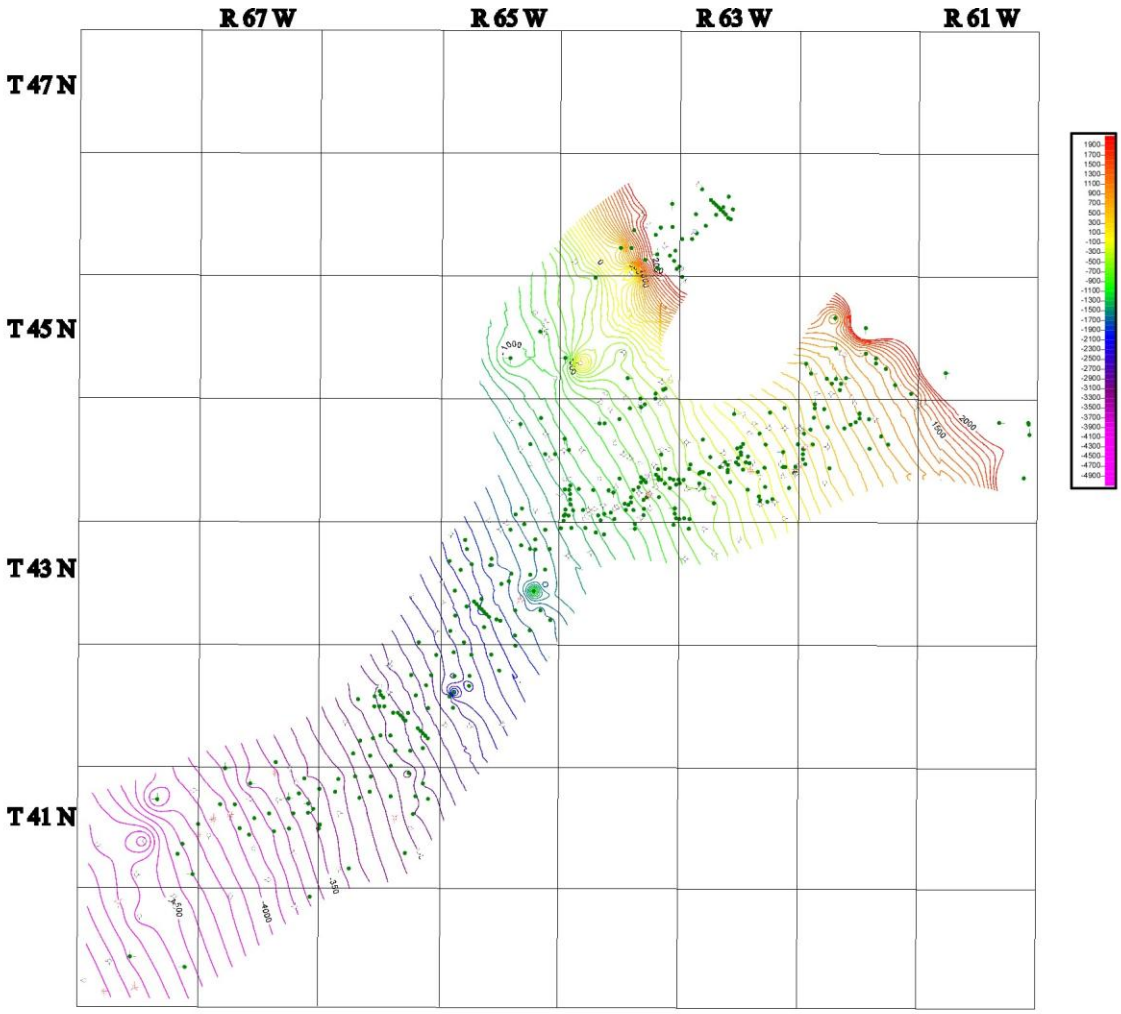

Figure 22:

Upper Recluse Structure Map:

Structure contour map on the Forest Surface, the Forest Surface marks the top of the Upper Recluse member. Wells displayed are only those where the Forest Surface is present. The Forest Surface is the first surface above the Top of Skull Creek erosive surface in the Fiddler Creek valley, and the second surface above the top of Skull Creek erosive surface in the Clareton valley. Notice how the trend of wells in this map indicate that at this point in time the Fiddler Creek is still a tributary system to the Clareton System.

Cyclone Member

The Cyclone member is bounded below by the Forest surface, and above by the Scarlet surface, which are interpreted as flooding surfaces. Neither the Forest, nor the Scarlet surfaces appear to have any significant erosion associated with them in the Clareton system. The Cyclone member is the third recorded depositional filling of the Clareton valley-fill (figures 23, 24, 25).

FB and TFC facies associations dominate the up-dip segment of the valley, and CB facies association units dominate the down-dip segment of the valley. There is no direct core data from the mid section of the valley-fill, however from the well-log data and net-sandstone isochore maps it is interpreted that facies association BHD should be present in the mid section of the valley-fill. Specifically the BHD facies association is interpreted to occur around township 43N 65W (see figure 23).

The rate of sea-level rise is interpreted to be low during the deposition of this member. This interpretation is based on the fact that the high sediment supply from the Clareton system was able to keep up with sea-level rise. As a result, the up-dip portion of the valley records deposition of the facies association TFC throughout deposition until the final flood that marked the end of Cyclone member deposition.

The CB units in the down-dip portion of the valley uniformly show a muddying upwards trend. This trend indicates a slow rise in sea-level, and therefore landward stepping trend in facies throughout Cyclone member deposition.

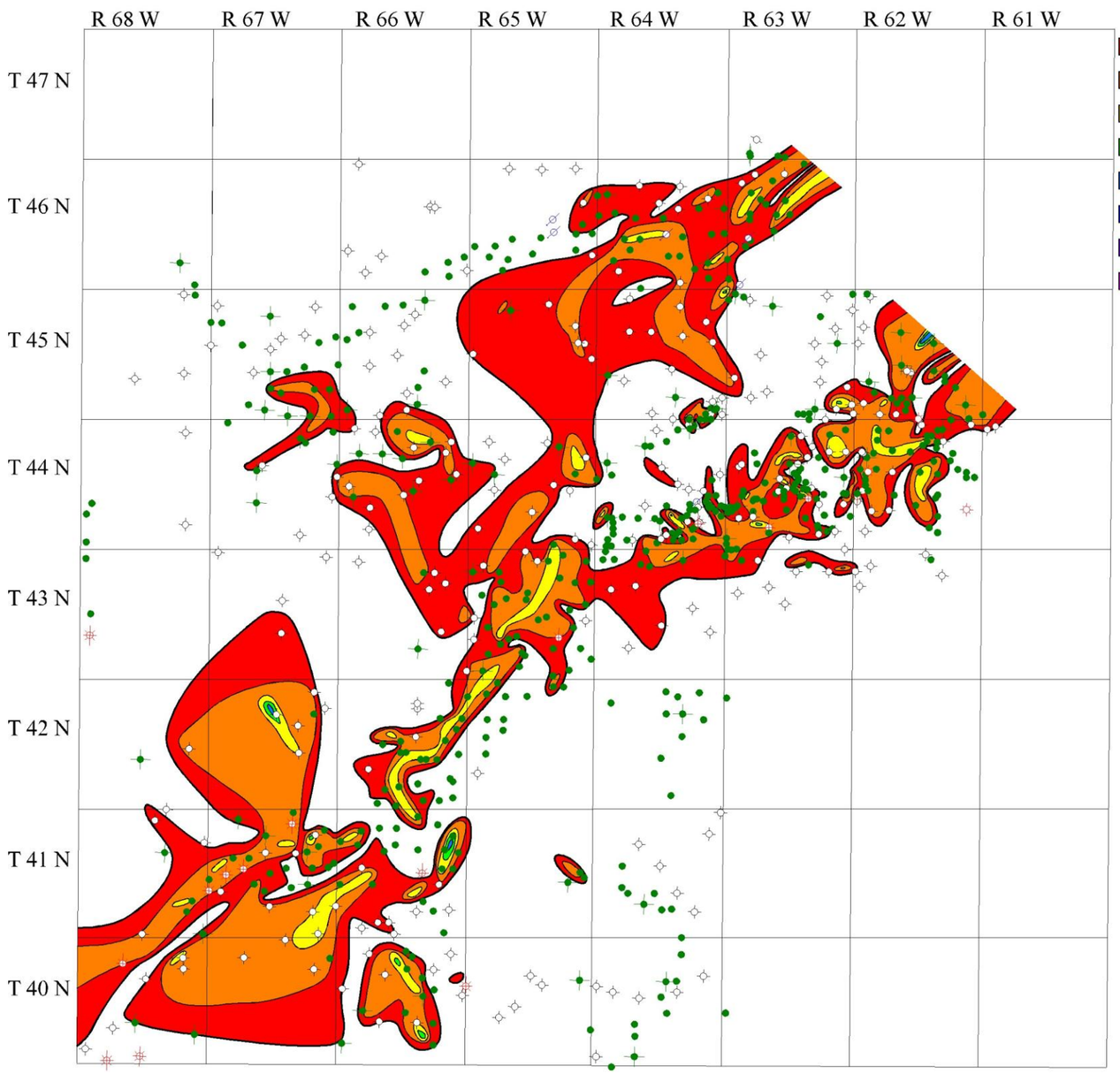

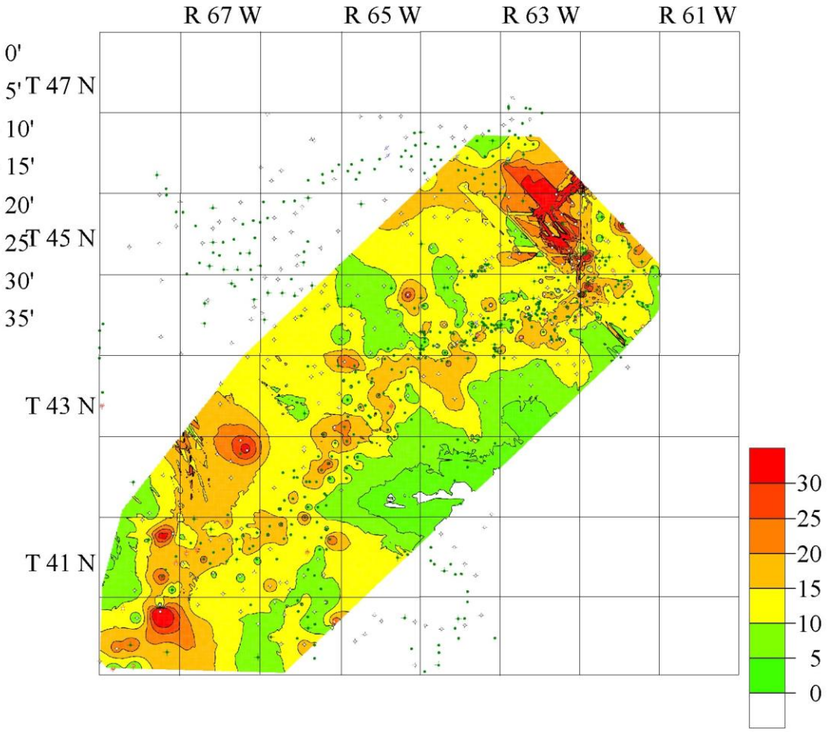

Figure 23:

Cyclone Member Isopach Maps.

Left: Net sand isopach map for the Cyclone member. Notice in the Clareton system a significant thinning of sand packages in the upper and mid sections of the valley, and widening of the sand deposits in the lower section of the valley. In the Fiddler Creek system there is a significant widening of sand deposits. Also sand packages are significantly more thin overall than in the Upper and Lower Recluse members.

Bottom: Isopach map of the entire Cyclone member. Notice that when the thickness of the entire member is compared with the thickness of the sand, it becomes apparent that the majority of deposits in this member are sand, with very little mud, except on the edges of the valleys.

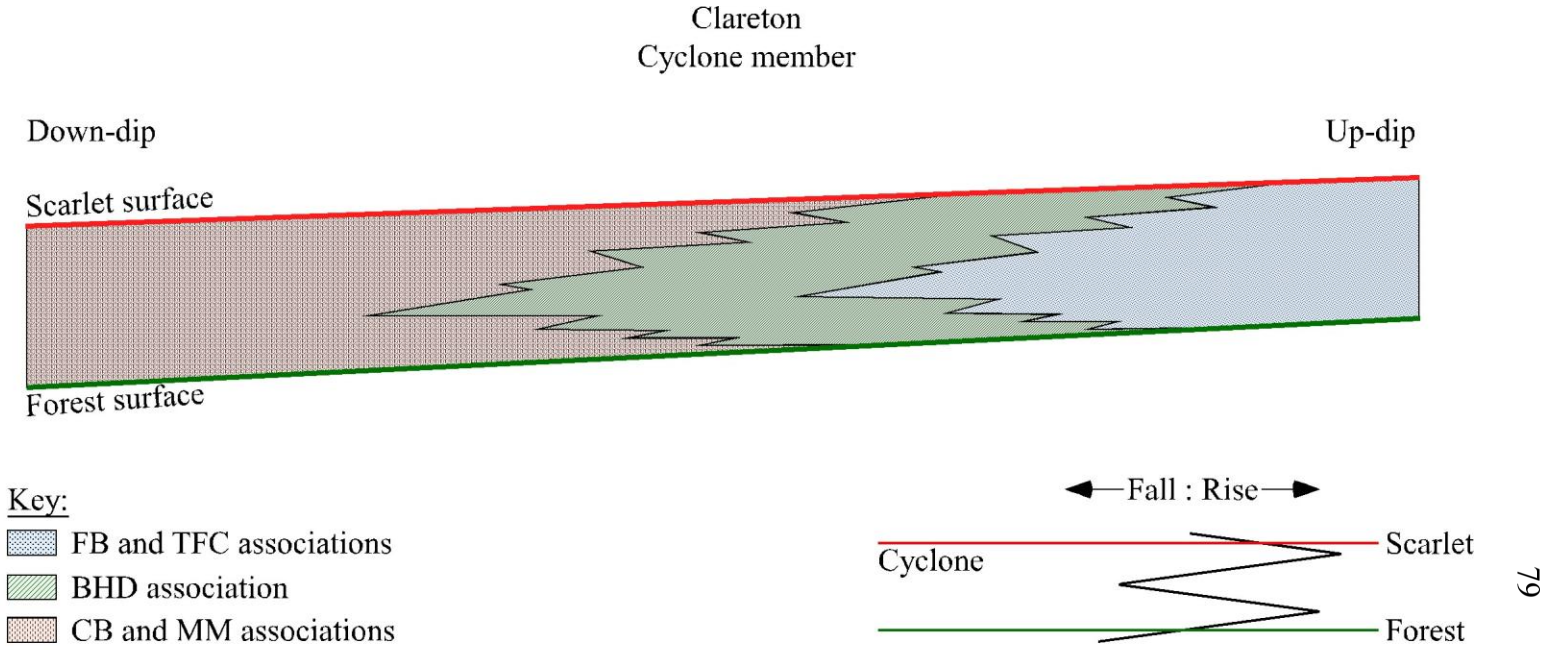

Figure 24:

Cyclone Stratigraphic Architecture:

Dip cross section of the Clareton system showing the generalized stacking pattern of the Cyclone member. This member recorded a single fall - rise cycle. The entire member is approximately 20' thick. This member is bound relatively conformably below and above by the Forest and Scarlet surfaces respectively. As mentioned in the text the Scarlet surface occasionally appears erosive, while this is not displayed in this generalization, it is shown by the placement of the Scarlet surface on the sea-level curve. The generalized sea-level curve derived from this member's stacking pattern is shown in the lower right. Note the Scarlet surface is marked at the maximum rate of regression indicating this surface is the record of a erosive event.

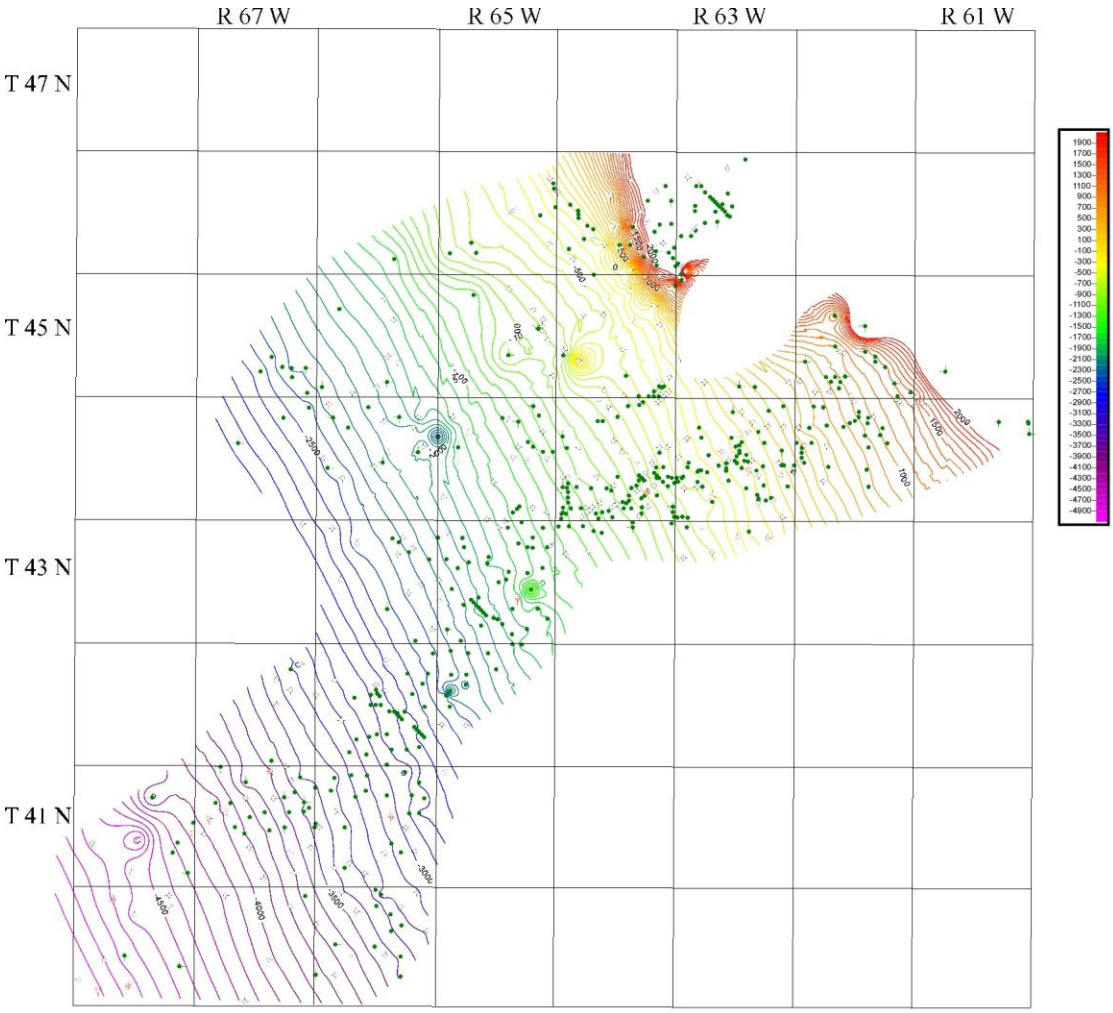

Figure 25:

Top Cyclone Member Structure Map:

Structure map on the Scarlet surface, the Scarlet surface marks the top of the Cyclone member. Wells displayed are only those where the Scarlet Surface is present. The Scarlet Surface is the first to display the Fiddler Creek trend as an independent distributary system from the Clareton trend.

Ute Member

The Ute member is defined below by the Scarlet surface and above by the Cyan surface. Within the Clareton system the Scarlet surface appears in places as an erosive surface. However the amount of erosion appears minor, and in most wells the Scarlet is recorded as a flooding surface or transgressive surface of erosion (figures 26, 27, 28).

As with the other members, fluvial facies associations FB and TFC dominate deposition in the up-dip portion of the valley, and marine influenced facies association CB units dominate deposition in the down-dip portion of the valley. In the Ute member, CB facies associations dominate over more of the Clareton system than in previously deposited members. Also there is a significant lateral narrowing of the BHD facies association in this member, as compared to other members.

Deposition of this member is interpreted to have begun with a sea-level rise as indicated by the landward shift in facies associations. After the initial rise, there was a period of progradation where BHD facies were deposited over CB facies, and FB and TFC facies over BHD facies. This progradation event was likely caused by either a decrease in the rate of sea-level rise from tectonic events, or by an increase in sediment supply to the system. After the progradation event the rate of sea-level rise began to increase and the associations began to step in a landward direction again.

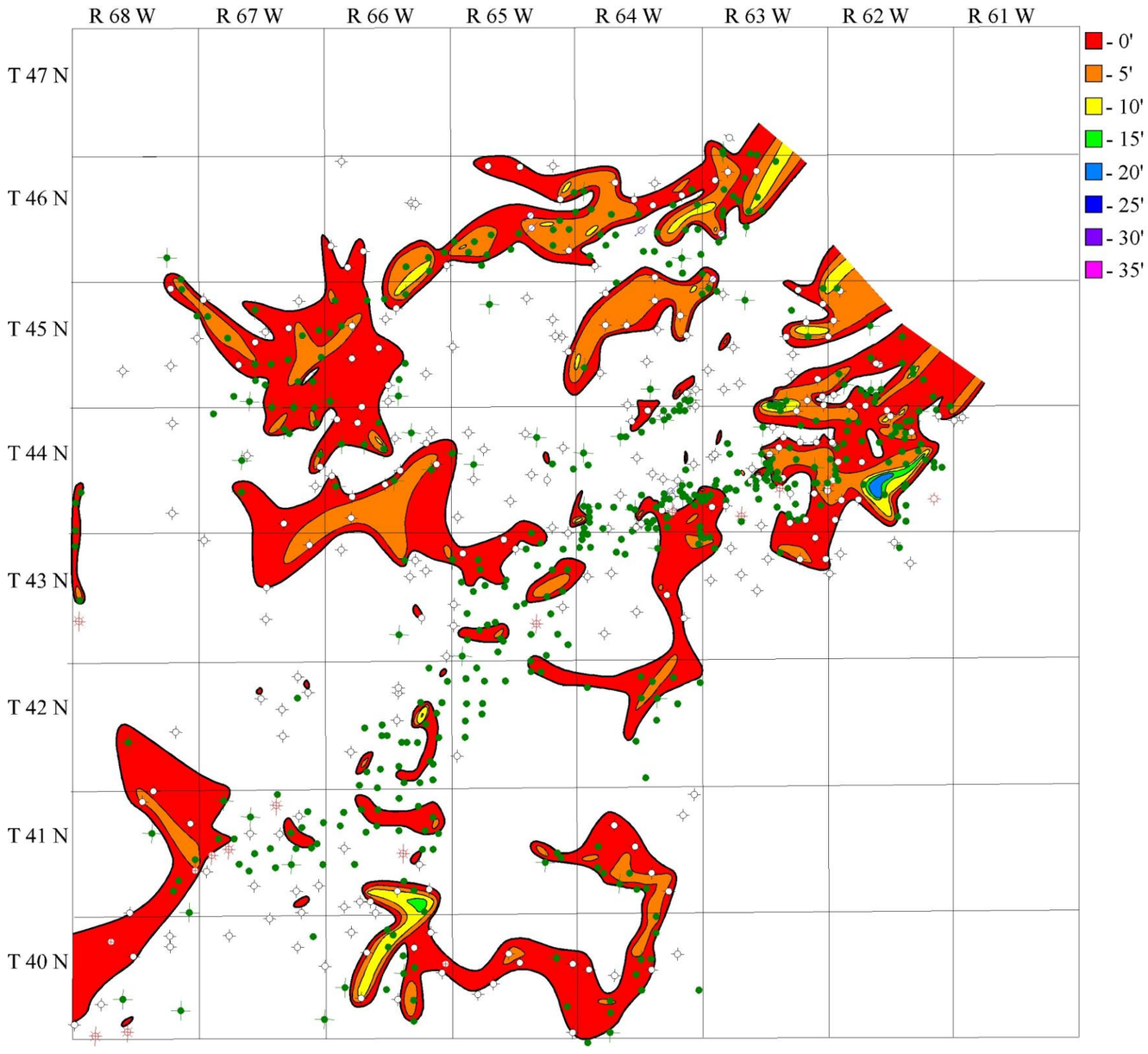

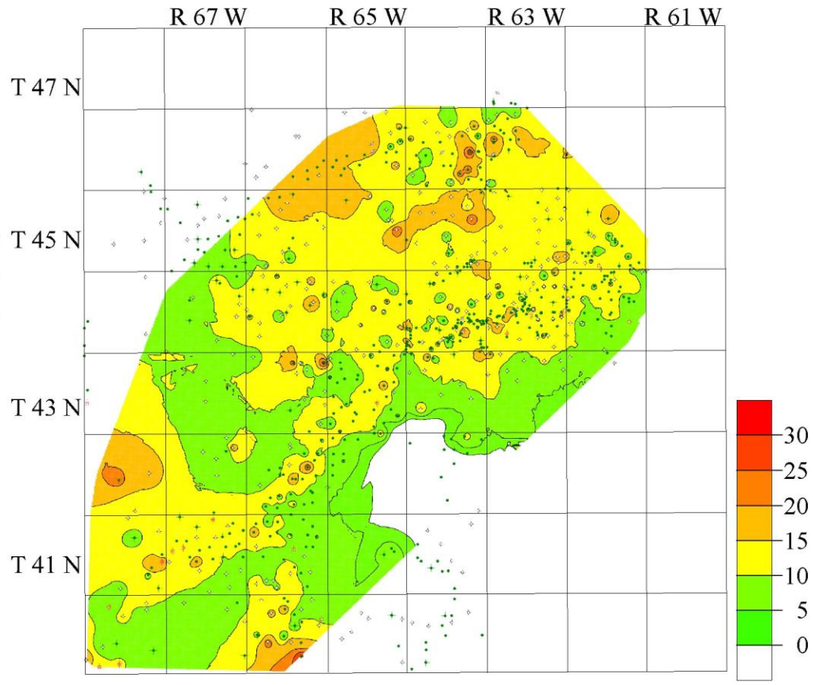

Figure 26:

Ute Member Isopach Maps.

Left: Net sand isopach map of the Ute member. Notice that the sand in the Clareton valley of this system is significantly more disjointed than in the previous Cyclone, Lower and Upper Recluse members. In contrast, the Fiddler Creek still displays relatively continuous sands. Note that at this point the Fiddler creek distributary system has changed direction and no longer connects with the Clareton system.

Bottom: Isopach map of the Ute member. Notice how the member has a relatively uniform thickness and covers a much larger area than previous members. Note that while the upper portion of the map (T45 to 46N and R63 to 65W) record the deposition of the Fiddler Creek, in the rest of the Fiddler Creek system the Ute member's lower bounding surface is the top of the Skull Creek shale. A member isopach map of the lower portion of the Fiddler Creek system can be seen in the Fiddler Creek - Ute section of this chapter.

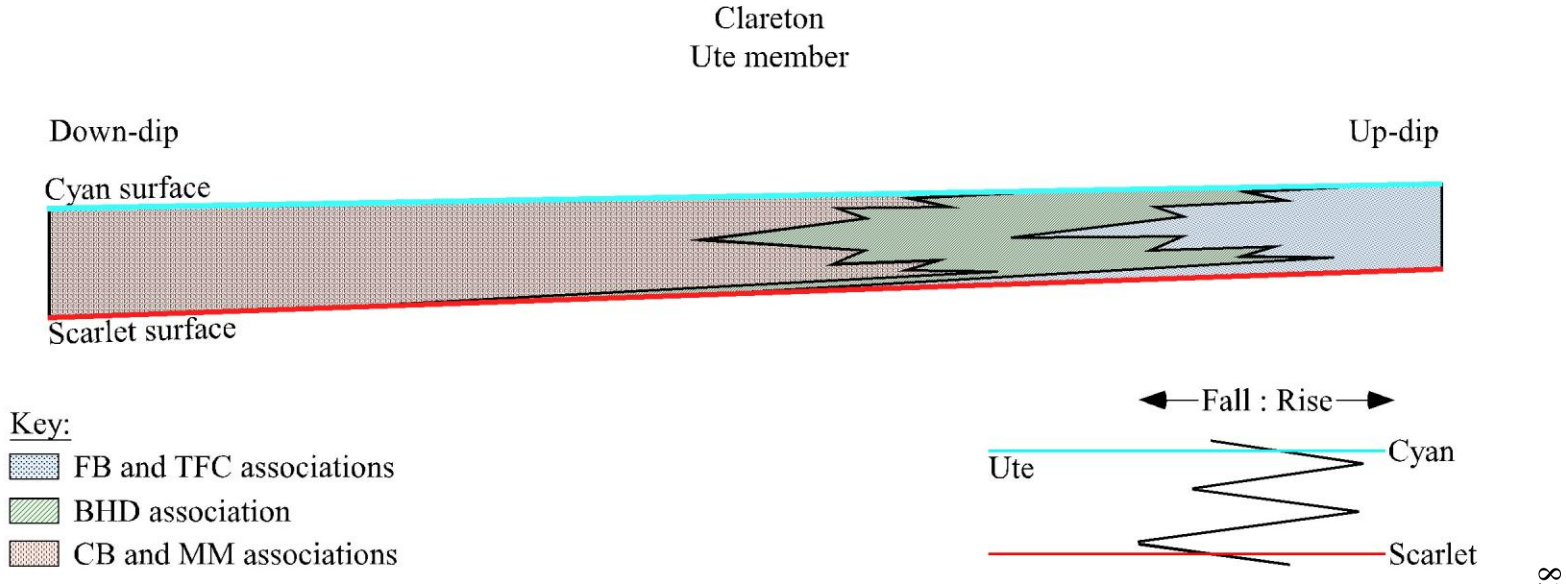

Figure 27:

Ute Stratigraphic Architecture:

Dip cross section of the Clareton system showing the generalized stacking pattern of the Ute member. This member recorded a rise - fall - rise cycle. The member is approximately 15' thick at the thickest. This member is bound relatively conformably below Scarlet surface, and above conformably by the Cyan surface. The generalized sea-level curve derived from this member's stacking pattern is shown in the lower right. Note the Cyan surface is marked at the maximum rate of fall indicating this surface is the record of a erosion event. However the Cyan surface may be present as a condensed surface which is the surface that marks both the fall and the rise of the next incursion.

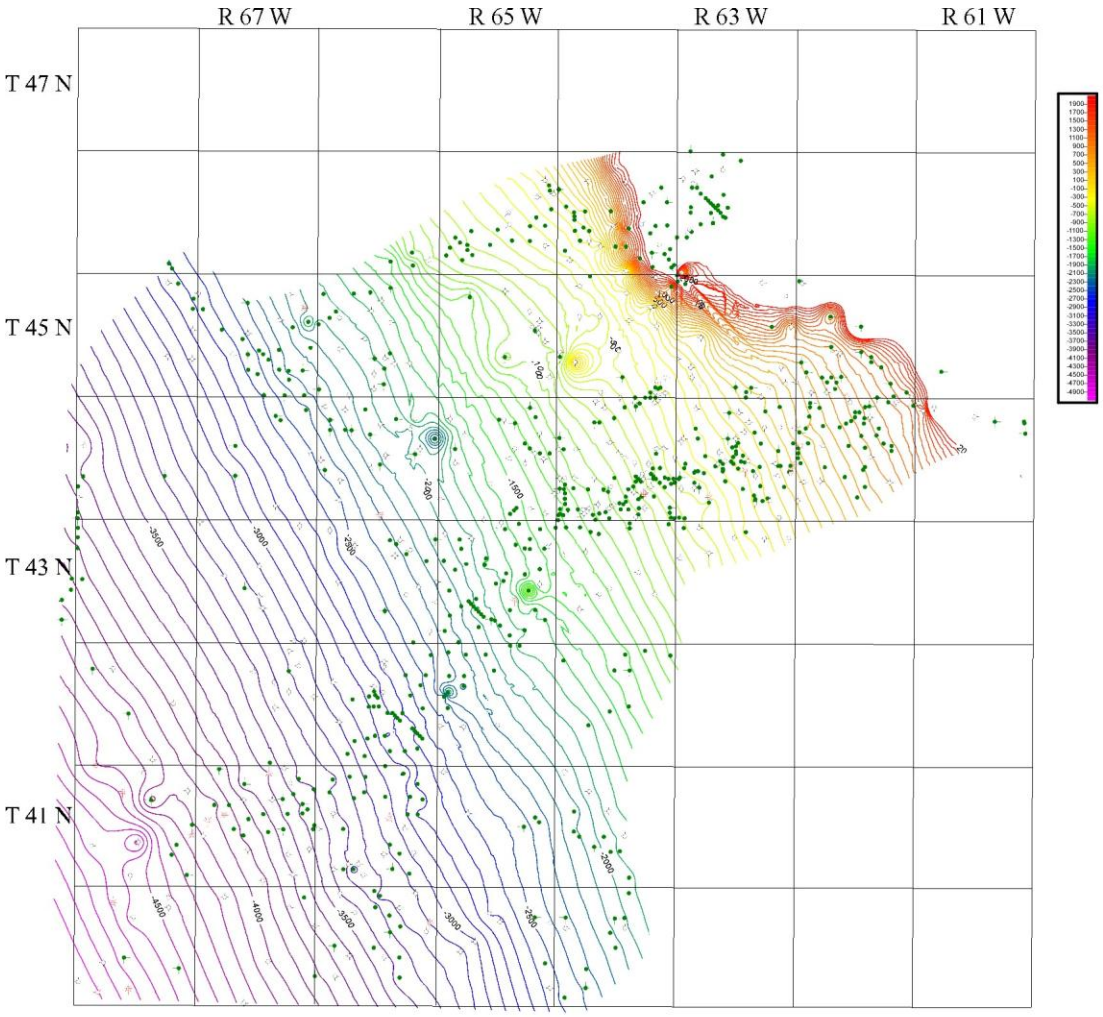

Figure 28:

Top Ute Member Structure Map:

Structure contour map of the Cyan surface, the Cyan surface marks the top of the Ute member. Wells displayed are only those where the Cyan Surface is present. The Cyan is the final valley influenced surface in the Clareton valley-fill. The Cyan surface marks the beginning of deposition of the Springen Ranch member. This surface is the final flooding surface that is constrained by the valley walls.

Springen Ranch Member

The Springen Ranch member is the youngest unit within the Clareton valley-fill. This member is interpreted as having been deposited without topographic restriction by valley-fill walls. The Springen Ranch member is bound below by the erosive Cyan transgressive surface of erosion, and above by the erosive transgressive surface, which is the base of the Shell Creek Shale (figures 29, 30, 31).

The down-dip portion of the Springen Ranch member is predominately muddy MA and CB facies at the base. There are occasional thin elongate sandstone packages present in this portion of the member, which are interpreted to represent storm deposits. In the down-dip portion of this member the sandstone is very thin, never more than 5 feet thick, and entirely isolated.

Unlike all other members, there is no fluvial facies present at the up-dip portion of this member. Less than 10 feet of BHD facies association are present, and are the facies most often seen in Clareton valley-fill outcrops. These BHD facies were at one time likely connected with up-dip FB and TFC facies that have been eroded away by modern processes.

In the Springen Ranch member, all facies associations demonstrate slow, yet steady transgression throughout deposition. The top of the Muddy Sandstone is marked by a significant erosive event. Large root traces are common, indicating subaerial exposure. Facies association MA in the Shell Creek Shale unit immediately overlies rooted portions of the core.

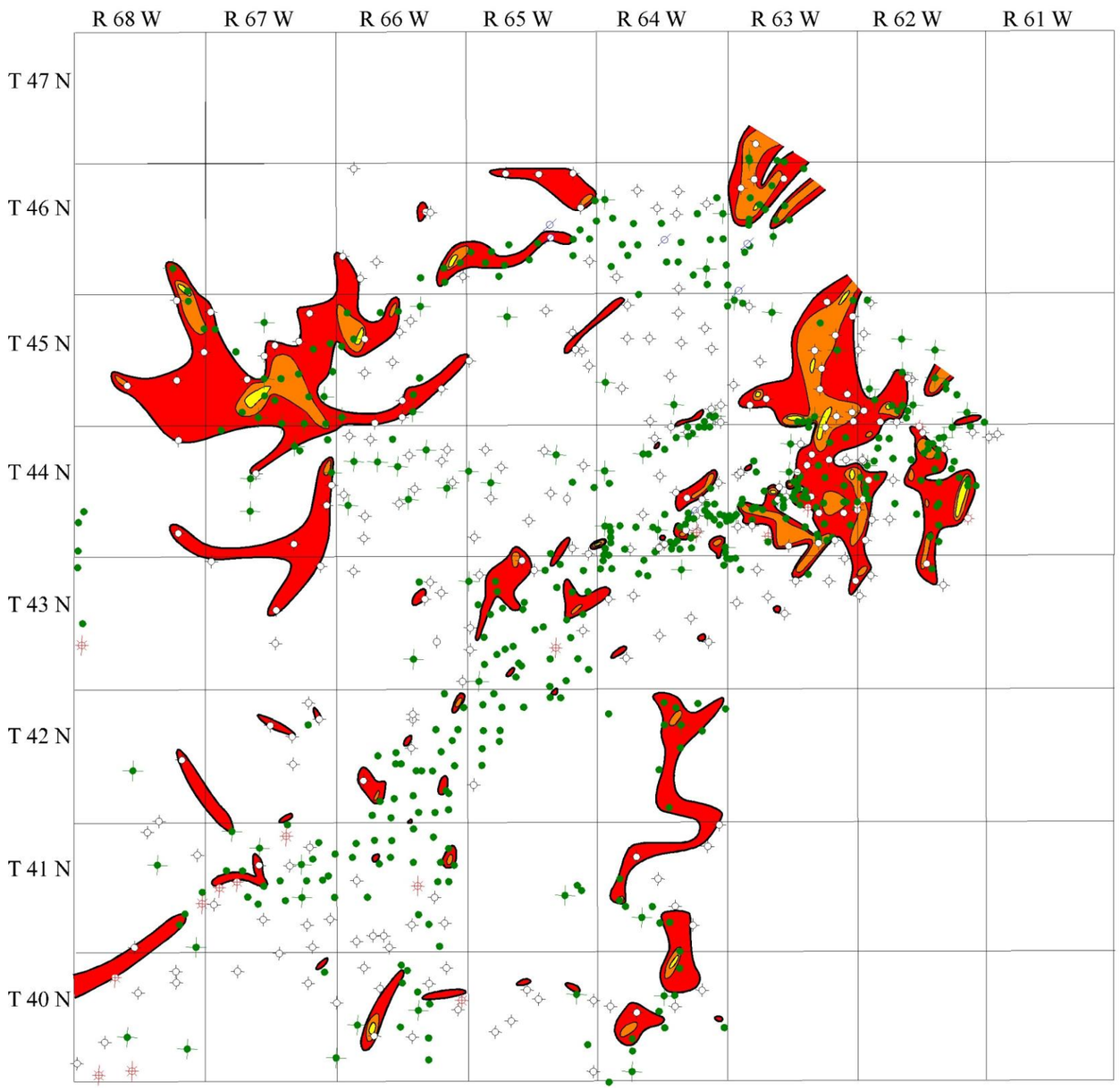

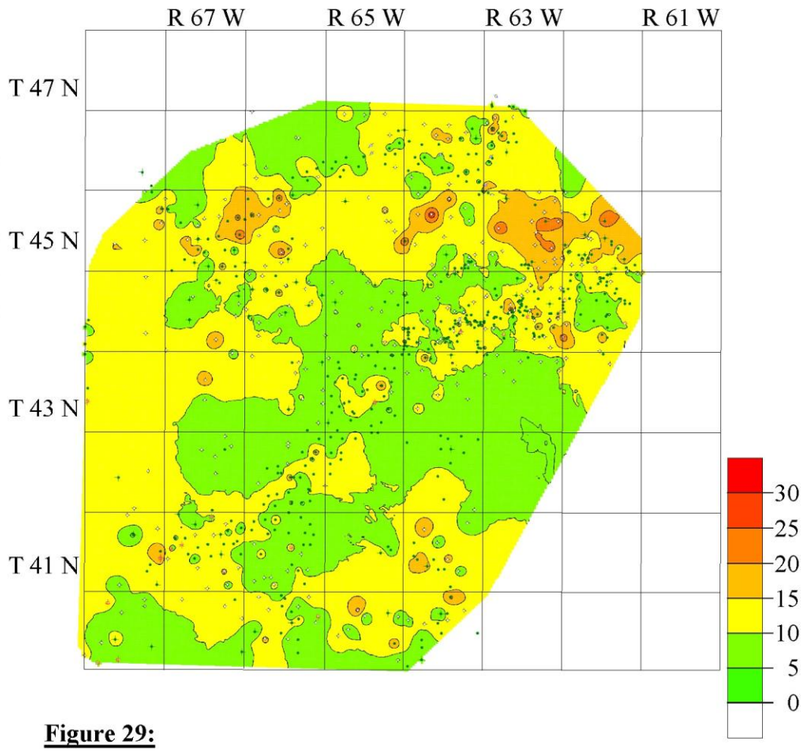

Figure 29:

Springen Ranch Member Isopach Maps.

Left: Net sand isopach map of the Springen Ranch member. Sand packages in both the Clareton and Fiddler Creek systems in this member are extremely thin and very discontinuous. Also, the sand in this member appears to be essentially unbound by valley walls.

Bottom: Springen Ranch member isopach map. Notice the apparent uniform thickness of this member across both the Clareton and Fiddler Creek systems. There is a slight thickening of the member at the up-dip most portion of the Clareton system (T45 to 46N, R63 to 64W) that corresponds to the thickest, and most continuous deposition of sand from the figure on the left. Uniform deposition of sediment over the entire breadth of this member also indicates that deposition in this member was unconfined by valley bounds.

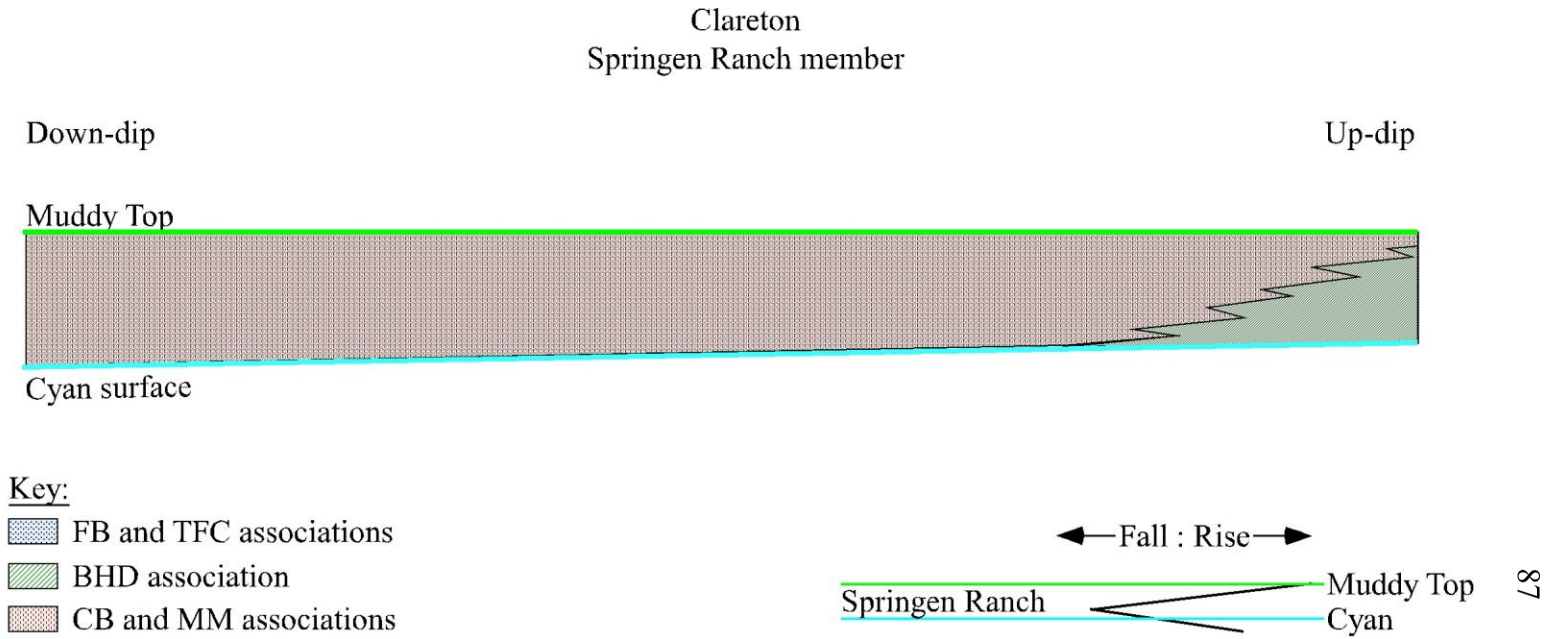

Figure 30:

Springen Ranch Stratigraphic Architecture:

Dip cross section of the Clareton system showing the generalized stacking pattern of the Ute member. This member recorded a single fall - rise cycle. The member is approximately 10' thick at the thickest. This member is bound relatively conformably below Cyan surface, and above unconformably by the top of the Muddy Sandstone formation. The generalized sea-level curve derived from this member's stacking pattern is shown in the lower right.

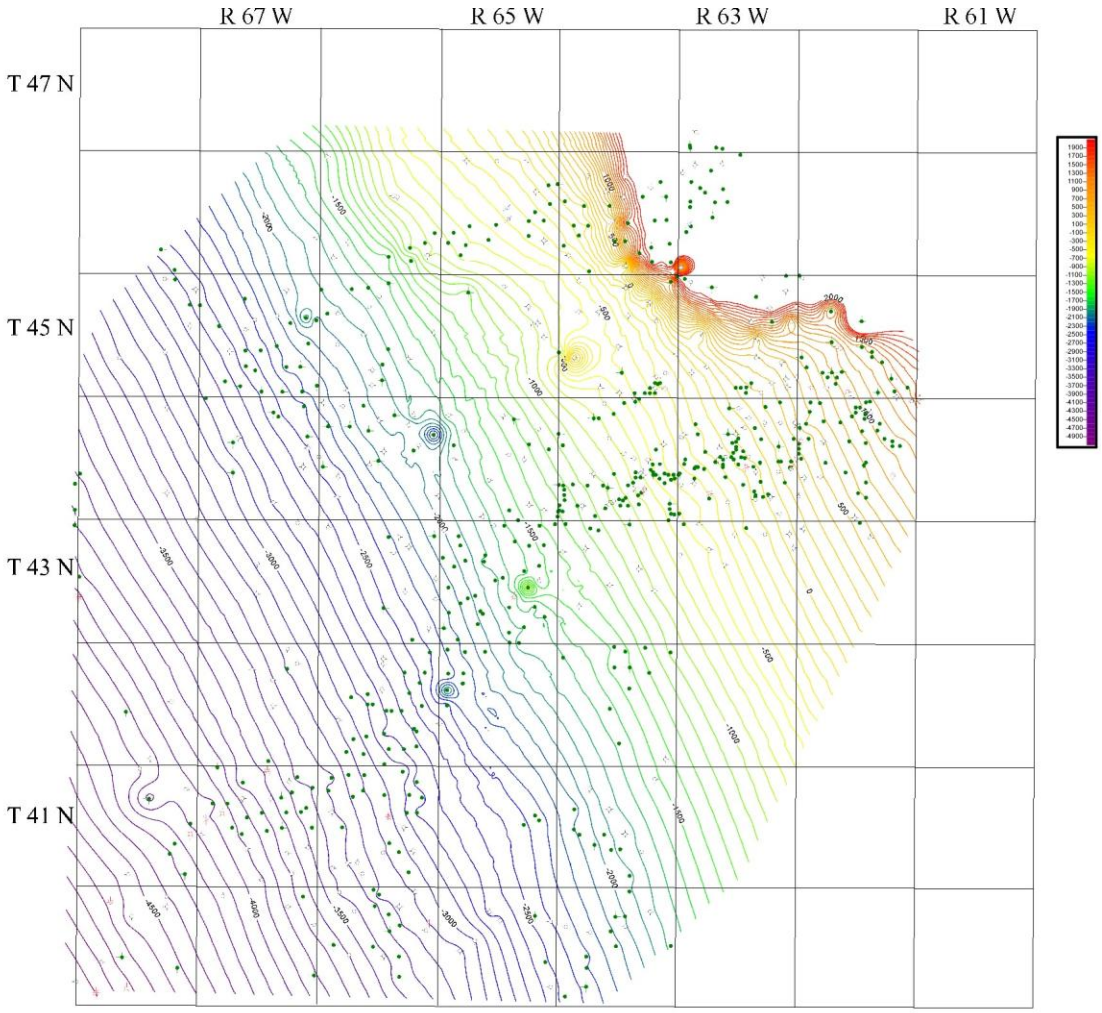

Figure 31:

Top Springen Ranch Member Structure Map:

Structure map on the top of the Springen Ranch Member, this surface also marks the top of the Muddy Sandstone Formation. Wells displayed represent all the wells with logs used in this study. The Springen Ranch member is the uppermost member in the muddy sequence and is the only member not influenced by the bounds of the incised valley. This surface marks the end of deposition of the Muddy Sandstone.

Overall Clareton Fill

Deposits comprising the Clareton valley-fill represent deposition during a relative sea-level rise interpreted by several distinct higher frequency relative falls of sea-level. Fluvial FB and TFC facies associations are absent in the down-dip portion of the valley-fill, and are only found in the mid section of the valley-fill in the oldest members, the Lower Recluse and Upper Recluse (figure 32).

The Lower Recluse member is the thickest (up to 35 feet), and best-connected sandstone body (figures 17, 18, and 32). Connectivity is determined based on mapped continuity of facies associations and thickness of each association as well as the apparent continuity of sand as mapped by the net sandstone maps. Sand prone facies associations that are mapped as very thick, and have very laterally extensive net sandstone patterns are assumed to have the best connectivity. The Lower Recluse member is the primary producing member in the Clareton valley-fill. In the Lower Recluse member sandstone is mapped as a continuous body from the head to the mouth of the valley-fill through the facies associations BHD and TFC (figures 17, 18, and 32).

The Upper Recluse member is unit stratigraphically above the Lower Recluse, and is second in terms of sandstone connectivity, and thickness to the Lower Recluse (figures 20, 21, and). The Upper Recluse also produces oil from the distal portion of the valley-fill.

TFC facies associations are oil productive in the Clareton field from the Ute and Cyclone members. According to the net sandstone, and facies association maps (figures 23, 24, 26, 27, and 32) these channel sandstones appear as relatively thin, less than 20

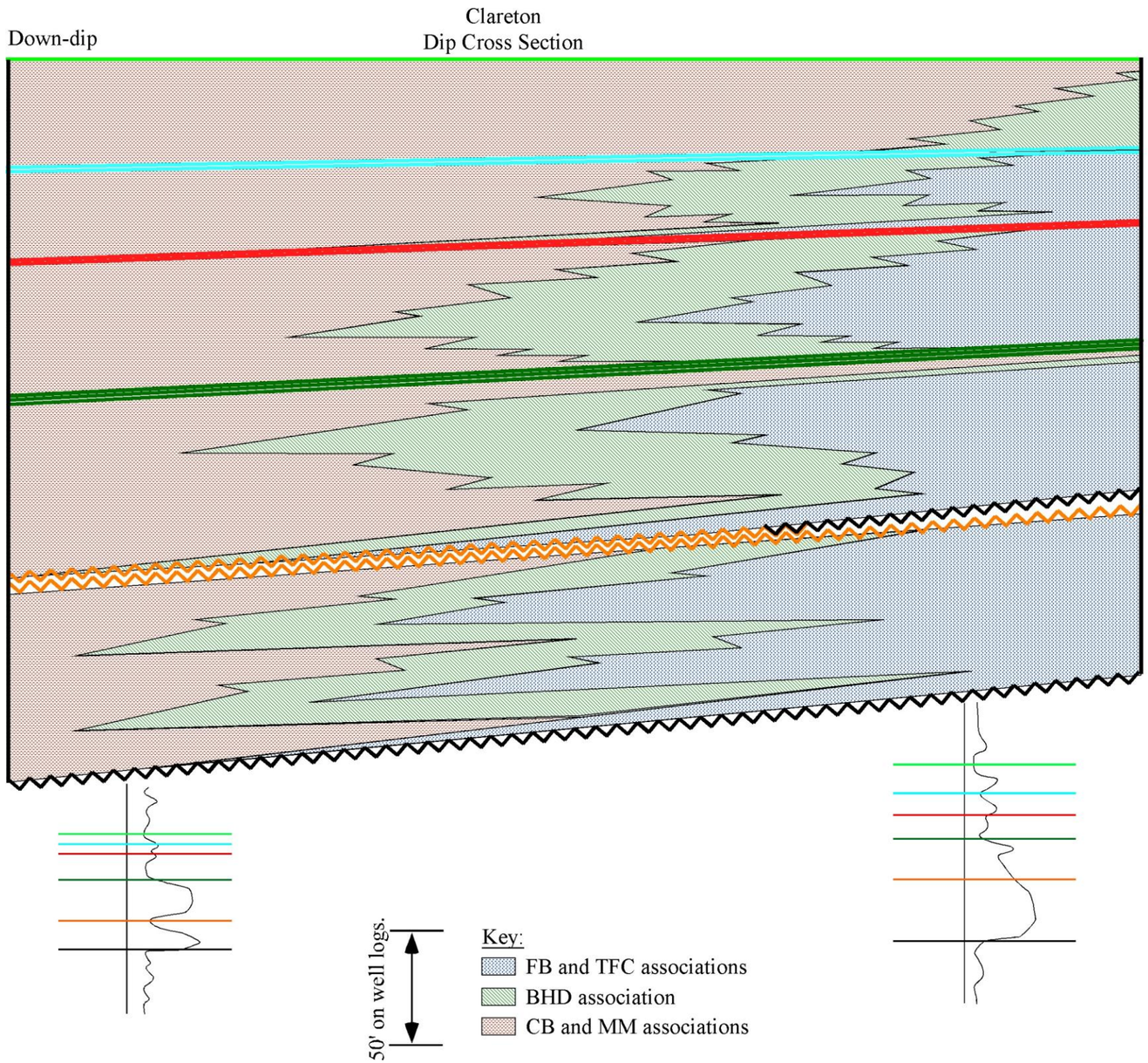

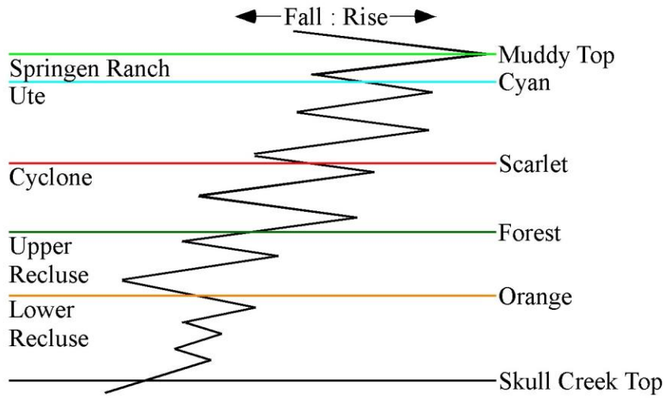

Figure 32:

Clareton Dip Cross Section.

Schematic dip cross section of the Clareton paleovalley showing the overall stacking pattern of the entire system. As discussed in the text the paleovalley displays an overall backstepping pattern as the valley filled. Also the amount of backstep between each member changes vertically through the section. There is a moderate backstep after the Lower Recluse member, which is preceded by the Orange surface, which is a significant surface of erosion. The facies appear to stack vertically between the Upper Recluse and Cyclone members, then backstep drastically between next members. This indicates that the rate of fall, or rise, in the Upper Recluse and Cyclone members was relatively slow, and followed by a more rapid rate of rise during deposition of the Ute and Springen Ranch members.

The correlated sea-level curve is shown to the right. Note that the pattern displays an overall rise, punctuated by the lower frequency rises and falls which determined the deposition within each member.

A well log is shown from both up-dip and down-dip in the valley below the schematic cross section. Logs are Induction Resistivity logs from T44N R64W S36 (up-dip log) and T41N R67W S2 (down-dip log).

feet thick, laterally connected units. Vertically the two members are baffled in places by the silty FB facies association (figures 24, 27, and 32). However channel erosion of the upper member into the lower member is interpreted to have connected enough of the TFC facies association between the two members such that all TFC facies association is connected in the Ute and Cyclone members of the Clareton valley-fill system (figures 23, 24, 26, 27, and 32). The Ute and Cyclone members are stratigraphically capped by the predominately muddy, marine influenced Springen Ranch member (figures 29, 30, and 32). In no place in the Clareton valley-fill does the Springen Ranch member produce.

Fiddler Creek Valley-Fill

The Fiddler Creek valley-fill, as discussed earlier in this paper, was a coastal plain valley-fill that had a muddy sediment supply. In previous work this system has been described as a tributary to the Clareton system (Emme 1981, Farmer 1981). This work re-interprets the genetic relationship of the Fiddler Creek system to the Clareton valley-fill system.

The interpretation of the stratigraphic architecture of the Fiddler Creek valley-fill is significantly more limited than that of the Clareton valley-fill. The complications are twofold. First, the depositional history of the Fiddler Creek valley-fill is significantly more complex than that of the Clareton system. Second, there were only two cored intervals available from the Fiddler Creek valley-fill. Because of these two obstacles, the stratigraphic interpretation of the Fiddler Creek valley-fill relies heavily on well-log cross sections, member isochore maps, and net sandstone isochore maps.

Lower Recluse Member

The Lower Recluse member is absent from the Fiddler Creek valley-fill. Because a significant period of erosion is interpreted at the end of Lower Recluse deposition in the Clareton system, it is interpreted that all of the Lower Recluse deposits were eroded during the relative sea-level fall that formed the Orange surface.

Upper Recluse Member

Because the Lower Recluse is not present in the Fiddler Creek system, the bounding surfaces of the Upper Recluse member differ from those of the Clareton system. In the Fiddler Creek valley-fill, the Upper Recluse member is bound above by the Forest surface and below by the erosional base of the Muddy Sandstone a composite surface of the basal unconformity and the orange surface.

Despite the difference in bounding surfaces, the depositional pattern of the Upper Recluse member in the Fiddler Creek valley-fill is very similar to that of the same unit in the Clareton valley-fill. After the period of erosion, which followed deposition in the Lower Recluse member, a rapid transgression resulted in deposition of the CB and MA facies associations in the lowermost portion of the member. After this rapid transgression a very slow regression deposited prograding facies associations BHD, and TFC and FB over the top of the initial CB facies association. Finally the rate of transgression overtook the rate of sediment input and a very rapid backstepping of facies tracts occurred creating a flooding surface at the top of this member. This flooding surface is recognized as the Forest surface in well logs.

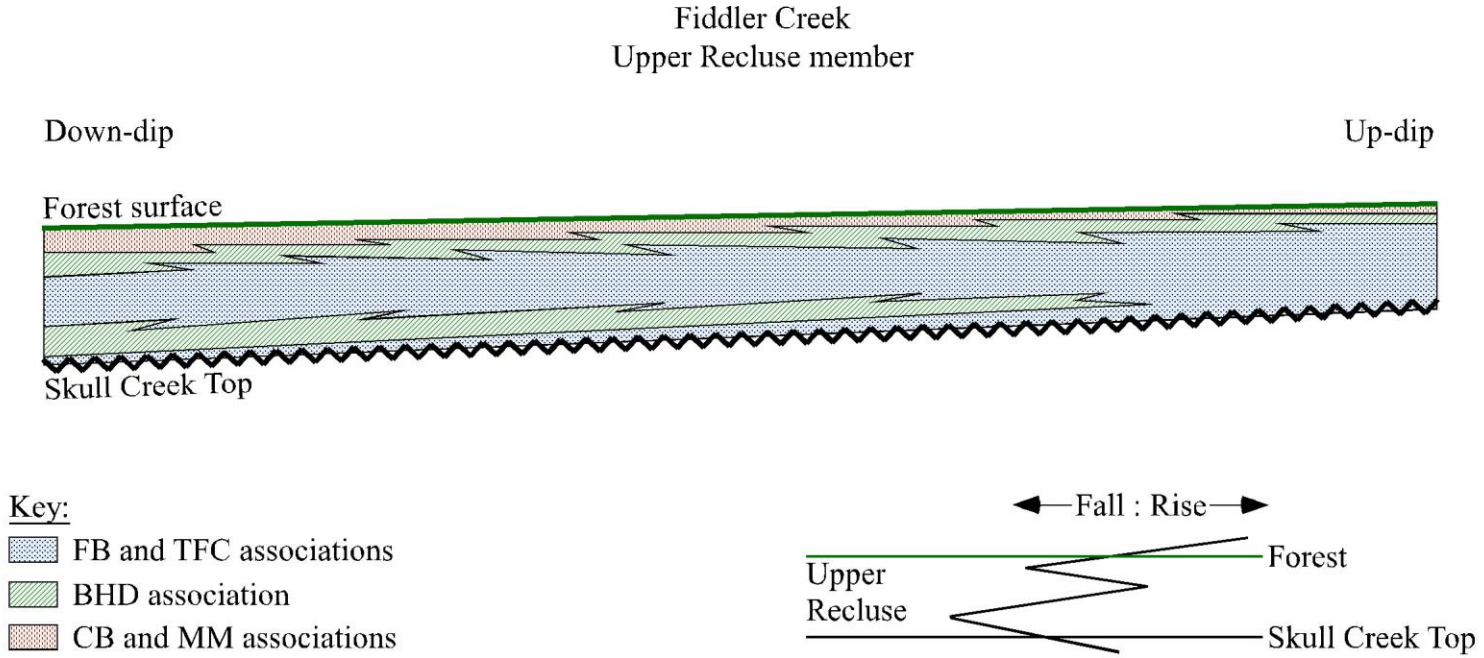

Figure 33:

Upper Recluse Stratigraphic Architecture:

Dip cross section of the Fiddler Creek system showing the generalized stacking pattern of the Upper Recluse member. This member recorded a single rise - fall cycle, followed by a rapid rise which marked the end of deposition of this member. Entire member reaches a maximum of 20' thick. Note that the unconformable base of this member is the Skull Creek top, not the Orange surface as in the Clareton system. The generalized sea-level curve derived from this member's stacking pattern is shown in the lower right. Note the Forest surface is marked at the maximum rate of transgression indicating this surface is the record of a flooding event.

The Upper Recluse member the Fiddler Creek valley-fill is interpreted to be a tributary system to the Clareton valley-fill and enters that system in the SW ¼ of township 44N, range 64W. The intersection of the two systems is demonstrated by the net sandstone isochore map for this member, figure 20. It is interpreted that the general transport for this system was in a relatively narrow belt traveling in a south, and south-south-westerly direction beginning at township 46N range 63W and ending in the connection to the Clareton valley-fill described above.

Cyclone Member

The sequence stratigraphic relationship of the Cyclone member in the Fiddler Creek system is the most similar to that of the Clareton system. In both systems this member is bound below by a flooding surface (Forest surface), and above by another flooding surface (Scarlet surface). As in the Clareton system the Cyclone member here displays a dominantly landward stepping deposition of facies indicating overall transgression. In the Fiddler Creek system the BHD is the most prevalent, and makes up the majority of the Cyclone fill.

An important distinction between this member and the previous member (Upper Recluse) in the Fiddler Creek valley-fill is the location of the intersection of the Fiddler Creek tributary system with the Clareton system. The actual intersection of these two systems in this member is at the NW ¼ of township 43N range 65W (figure 23). This is a six mile shift of the entry point from the previous member. In addition, the width of deposition during this period is significantly wider than in the previous period of deposition.

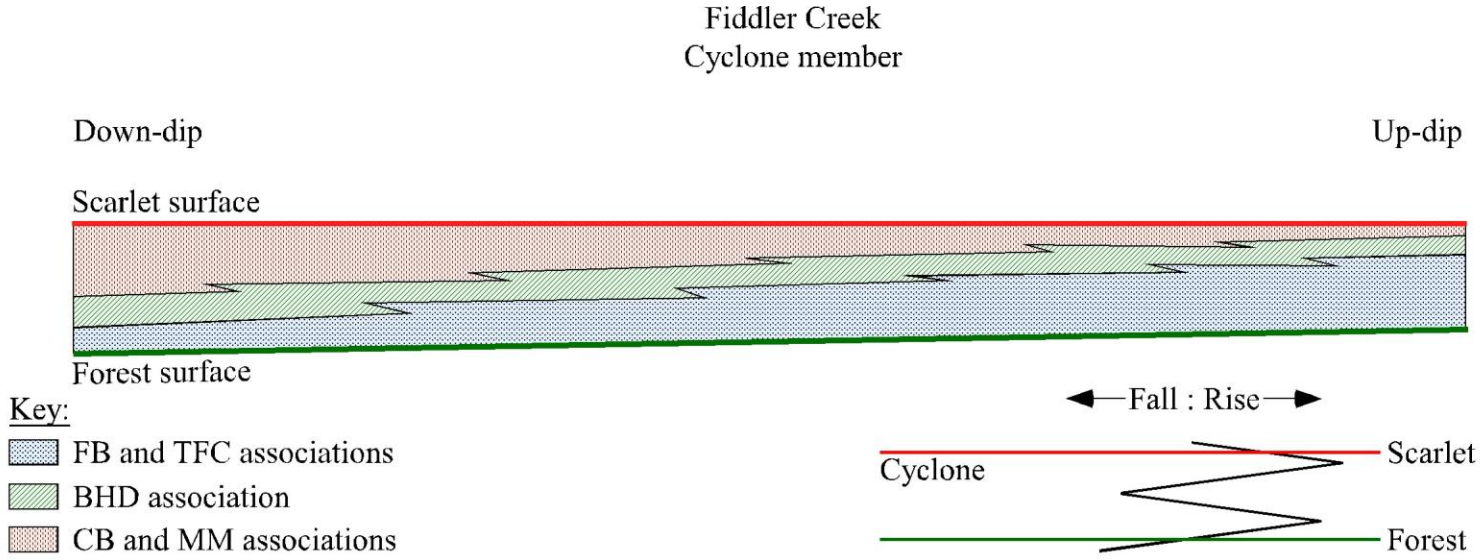

Figure 34:

Cyclone Stratigraphic Architecture:

Dip cross section of the Fiddler Creek system showing the generalized stacking pattern of the Cyclone member. This member recorded a single fall - rise cycle. The entire member is approximately 10' thick. This member is bound relatively conformably below and above by the Forest and Scarlet surfaces respectively. As mentioned in the text the Scarlet surface occasionally appears erosive, while this is not displayed in this generalization, it is shown by the placement of the Scarlet surface on the sea-level curve. The generalized sea-level curve derived from this member's stacking pattern is shown in the lower right. Note the Scarlet surface is marked at the maximum rate of regression indicating this surface is the record of a erosive event.

Ute Member

The Ute member in the Fiddler Creek system has different bounding surfaces than those in the Clareton system. Both are bound above by the Cyan surface, however in places in the Fiddler Creek this member is below by the Scarlet surface as in the Clareton, but in other places, it is bound below by the erosional base of the Muddy Sandstone[7]. There is also a significant difference between this member of the Fiddler Creek valley-fill, and all other Fiddler Creek members, which have been discussed thus far. In this member, the primary depositional fairway connects directly to the transgressing shoreline. Beginning with this member, the Fiddler Creek system is no longer a tributary to the Clareton system.

This change is most easily seen in the net sandstone isochore map (figure 26). In this figure it is clear that the primary deposition of this member is no longer on a SSW trend connecting with the Clareton trend at the SW quadrant of township 44N range 65W. Rather, deposition in the Fiddler Creek follows a more WSW trend through the NW quadrant of township 46N range 63W, to the SE quadrant of township 45N range 67W.

As in the Ute member of the Clareton system the facies display a general coarsening upward succession, which indicates overall progradation of associations during a slow rate of sea-level rise. The lowermost deposition of MA and CB associations in the unit indicate initial flooding of the entire system. These facies then

[7] See next chapter for more detailed description of the surface relationship.

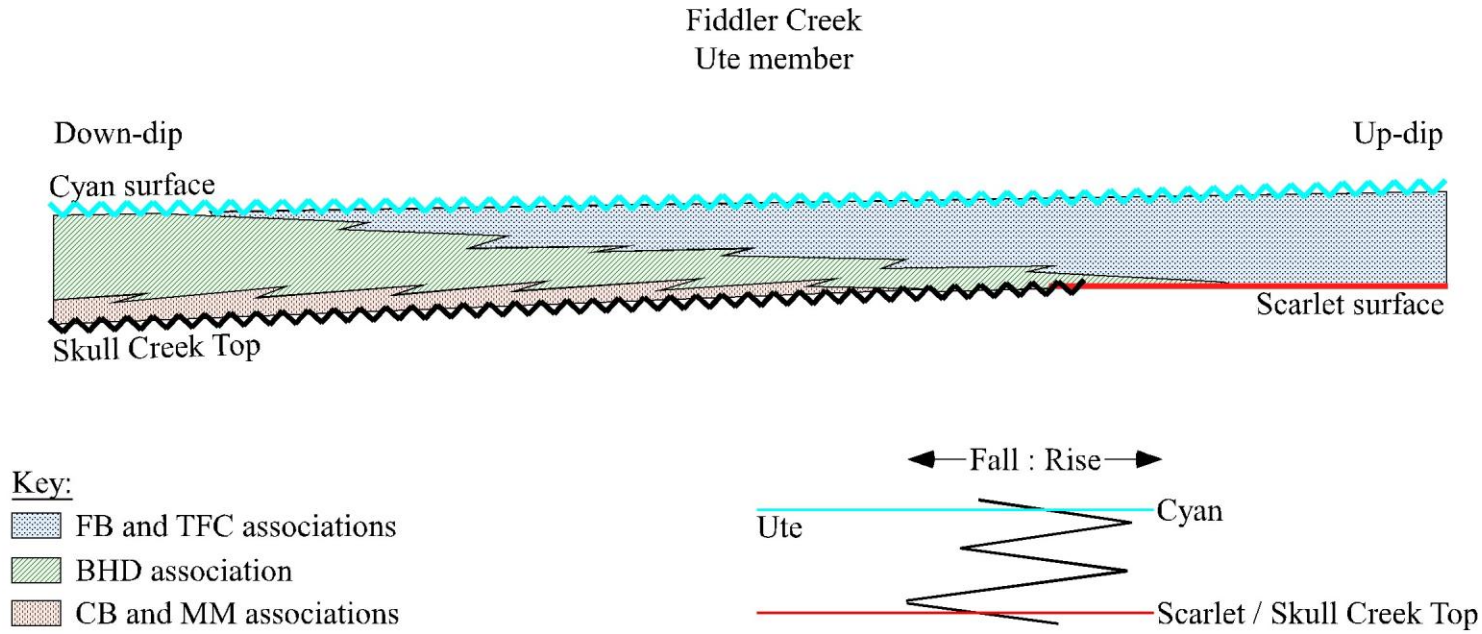

Figure 35:

Ute Stratigraphic Architecture:

Dip cross section of the Fiddler Creek system showing the generalized stacking pattern of the Ute member. This member recorded a single rise - fall cycle. The member is approximately 15' thick at the thickest. This member is bound relatively conformably below Scarlet surface in the up-dip portion, and unconformably below by the Skull Creek top in the mid and down-dip portions. It is bound above unconformably by the Cyan surface. The generalized sea-level curve derived from this member's stacking pattern is shown in the lower right. Note the Cyan surface is marked at the maximum rate of fall indicating this surface is the record of a erosion event.

grade upward into BHD and finally TFC and FB. At the end of deposition in the Ute member of the Fiddler Creek, the fluvial system reached a maximum down-dip position of the SW ¼, of the SE ¼ of township 46N, range 66W.

The end of deposition of the Ute member in the Fiddler Creek system is marked by a period of erosion and non-deposition, which form the Cyan surface. Extensive burrowing and some root traces are present in core below this surface.

Springen Ranch Member

Just as in the Clareton system the Springen Ranch member in the Fiddler Creek system is bound below by the Cyan surface, and above by the base of the Shell Creek Shale. The down-dip portion of the Springen Ranch member in the Fiddler Creek is dominated by very mud rich sandstones. The sandstones are generally lenticularly bedded, or ripple laminated with interstratified mud and organic layers. Overall the facies present are those of the BHD showing a general deepening upward relationship into facies association CB and eventually facies association MA.

In the up-dip, and mid portion of the system, very little sandstone was deposited. Facies associations FB and TFC are dominant; however the system is so mud rich at this point that sandstone connectivity is extremely poor. As in the down-dip portion of the system, the up-dip and mid portions demonstrate deepening upward facies trends eventually ending in a final flooding surface with MA facies deposited over the entire unit.

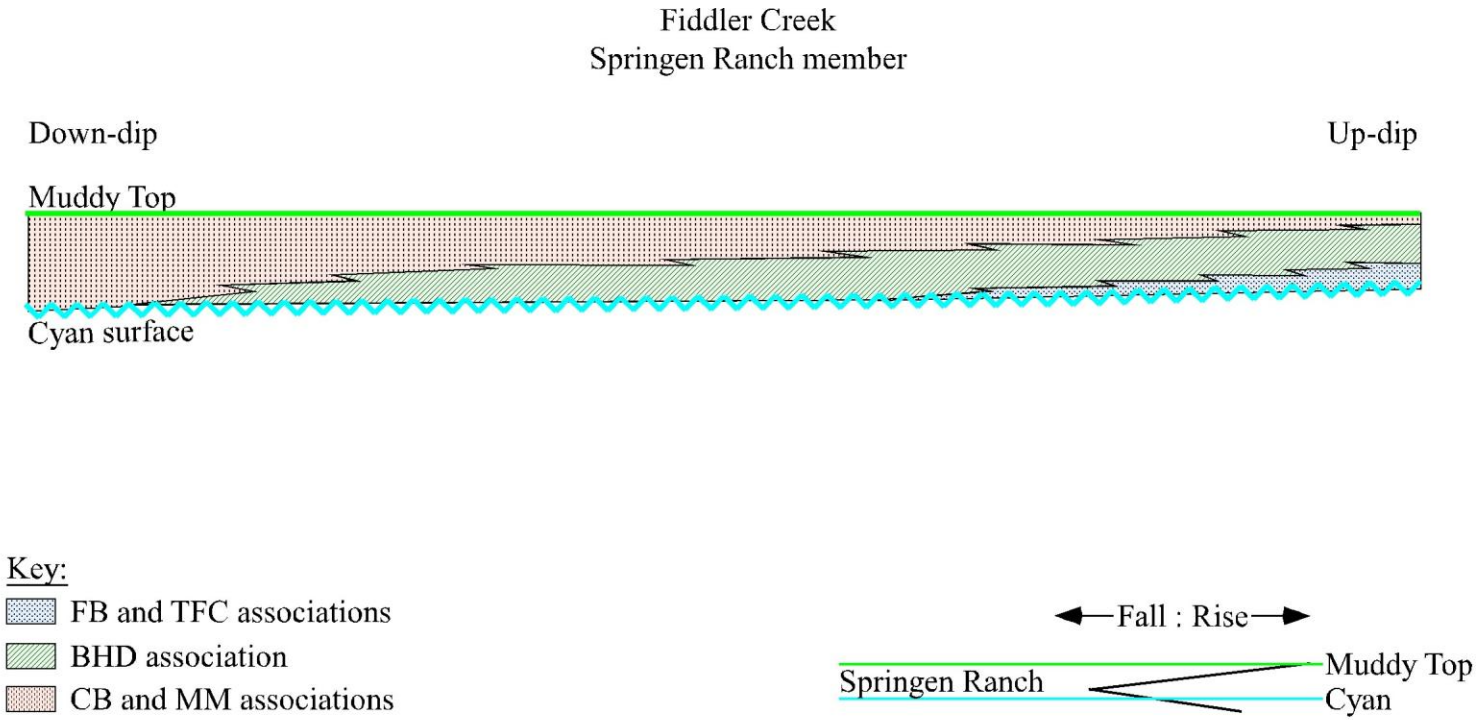

Figure 36:

Springen Ranch Stratigraphic Architecture:

Dip cross section of the Fiddler Creek system showing the generalized stacking pattern of the Springen Ranch member. This member recorded a single fall - rise cycle. The member is approximately 10' thick at the thickest. This member is bound unconformably below Cyan surface, and above unconformably by the top of the Muddy Sandstone formation. The generalized sea-level curve derived from this member's stacking pattern is shown in the lower right.

The rate of transgression during deposition of this unit was extremely rapid. This led to an overall thin unit (less than 20') with dramatically backstepping facies associations.

Overall Fiddler Creek

As in the Clareton system, the Fiddler Creek system displays an overall record of transgression through its depositional history. However, other than this similarity, the Fiddler Creek system recorded a very different filling history from that of the Clareton system. Unlike the Clareton system, fluvial facies are present in the distal portion of the lowest member of the Fiddler Creek system, namely the Upper Recluse member (figure 33 and 37). The sandstones in all four members of the Fiddler Creek system are thin and discontinuous in comparison to the Clareton system (figures 37 and 38).

Also, unlike the Clareton system, the older members of the Fiddler Creek system do not produce petroleum. The only member of the Fiddler Creek system that produces oil is the Ute member (figures 26 and 35). In fact, in the Fiddler Creek valley-fill the Ute member is composed primarily of continuous TFC facies association in the up-dip and mid sections of the member, and BHD facies association in the down-dip portion of the member (figure 35). In this stratigraphic interval the facies association TFC and BHD are very sand-rich compared to other members of the Fiddler Creek. The sandstones range from five to twelve feet thick (figure 26). Just as in the Clareton incised valley-fill, the Springen Ranch member does not produce oil (figures 29, 36, 37 and 38).

The most striking characteristic of the Fiddler Creek system is its change in depositional pathway mid-way through valley-filling (figures 37 and 38). The

Figure 37:

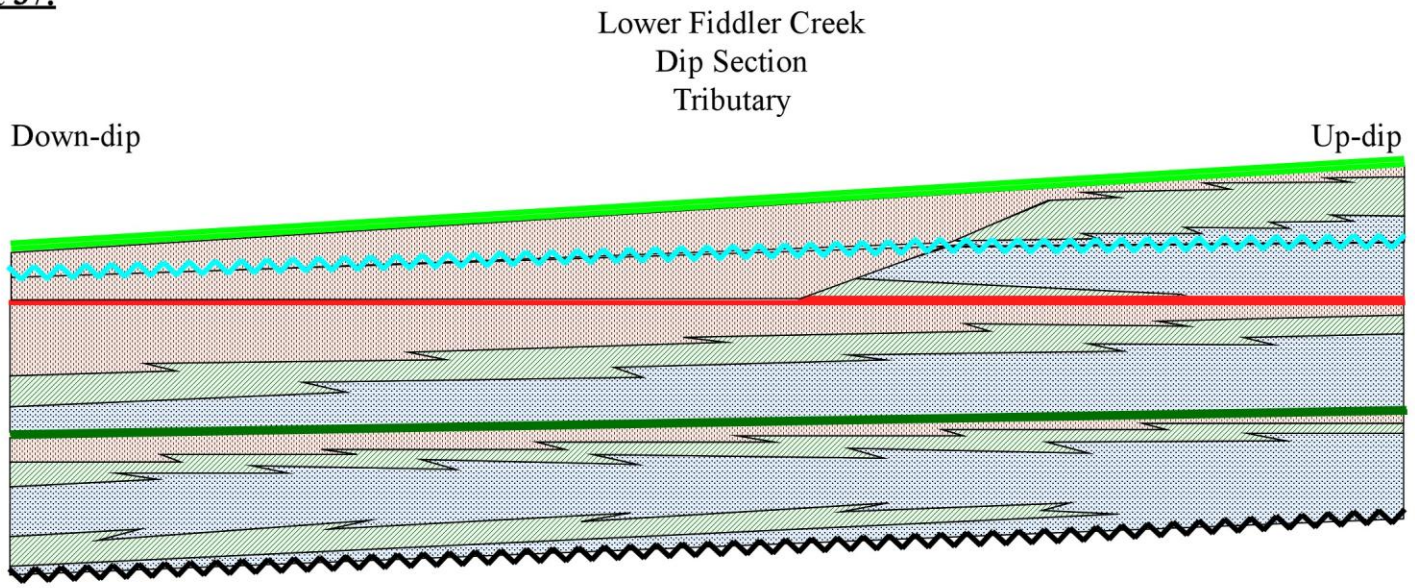

Fiddler Creek Tributary Dip Cross Section.

Dip cross section of the Fiddler Creek system showing the dip facies stacking pattern before the system has evulsed and become a through-going system. The Ute and Springen Ranch members thin significantly down-dip which is the record the interfluve between the two valleys in the down-dip portion of the section. Note that in the sea level curve for the Fiddler Creek, the rise and fall recorded in the Lower Recluse member is missing.

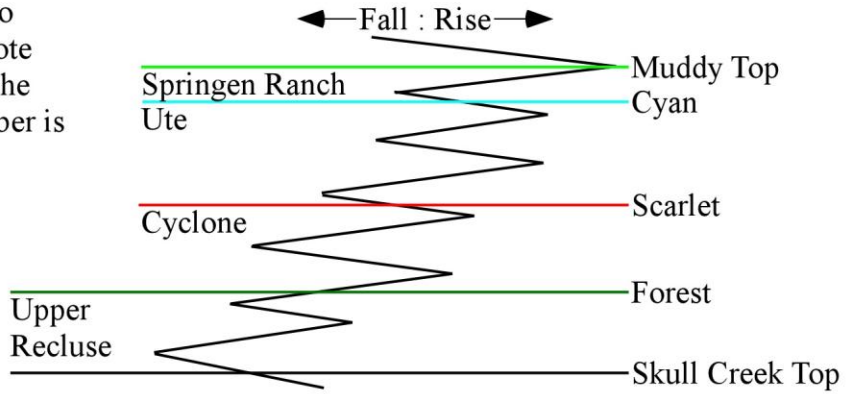

Key:

- FB and TFC associations
- BHD association
- CB and MM associations

Figure 38:

Upper Fiddler Creek
Dip Section
Through-going

Down-dip Up-dip

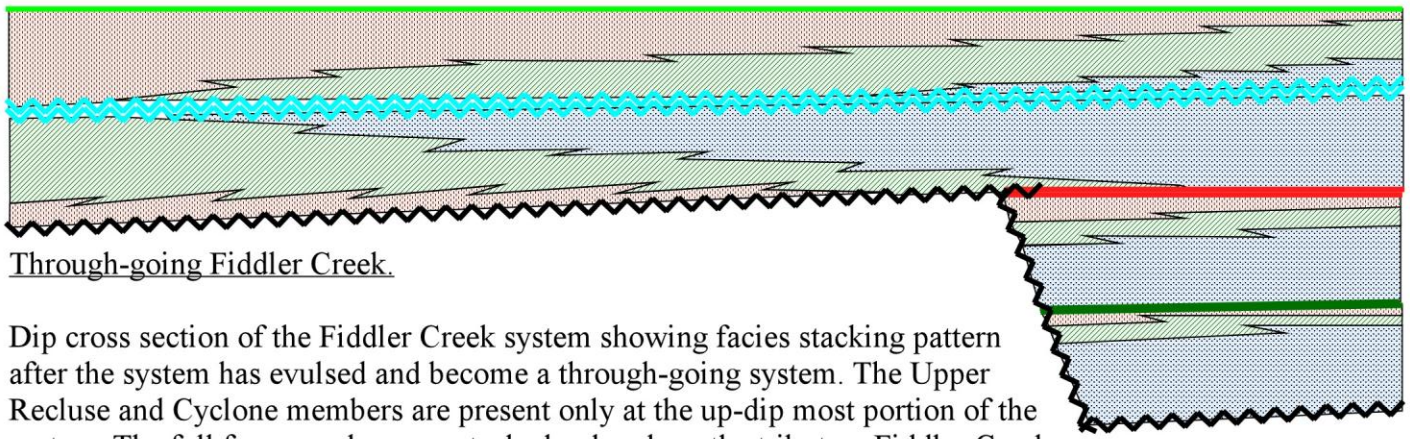

Through-going Fiddler Creek.

Dip cross section of the Fiddler Creek system showing facies stacking pattern after the system has evulsed and become a through-going system. The Upper Recluse and Cyclone members are present only at the up-dip most portion of the system. The full four members are stacked only where the tributary Fiddler Creek system, and the through-going Fiddler Creek system were deposited in the same place. Note that in the sea level curve for the Fiddler Creek, the rise and fall recorded in the Lower Recluse member is missing.

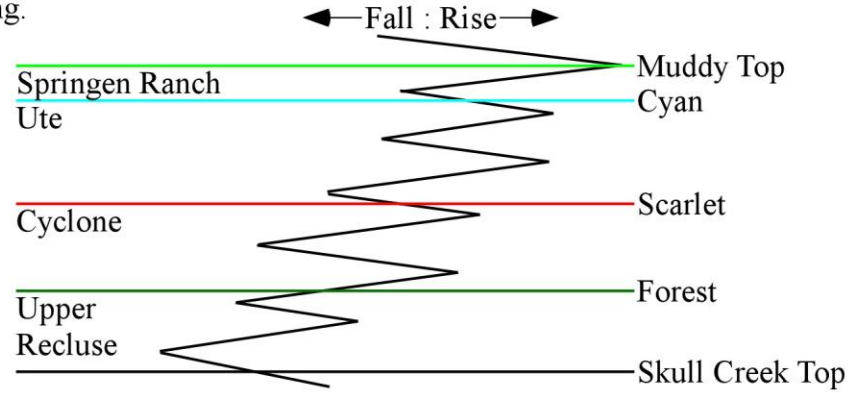

Key:

- FB and TFC associations
- BHD association
- CB and MM associations

stratigraphic architecture indicates that the initial Fiddler Creek erosional feature was filled by the end of deposition of the Cyclone member (figure 37, 23, and 26). In fact, the change in tributary point to the Clareton system after the Upper Recluse member indicates that the valley-fill was almost entirely filled during deposition of the Upper Recluse member (figure 37 and 20). After the erosional feature had been filled, the depositional pathway migrated and ceased being a tributary to the Clareton system. It was also at the onset of the new depositional pathway that the 'uncharacteristically sand-rich' TFC and BHD facies were deposited. This anomaly will be discussed in farther detail in the upcoming chapter.

Sequence Stratigraphy

By correlating the series of stacking patterns through the members in both depositional systems the overall sea level curve can be extrapolated. As is expected with all incised valley-fills, the deposits record an overall long-term sea level rise punctuated with a series of minor rises and falls. The beginning of deposition in the valleys appears to have begun at or near the high order turnaround from fall to rise. This explains the extreme erosive event which marked the end of deposition of the Lower Recluse in the Clareton system, and completely eliminated any Lower Recluse deposits which may have been deposited during this stratigraphic interval in the Fiddler Creek.

As the overall sea level curve continued to rise, the smaller fluctuations began to preferentially preserve the transgressive deposits rather than regressive surfaces. This is demonstrated in the trend of the older bounding surfaces in the features (Muddy Sandstone base, and Orange) are erosional surfaces, and younger surfaces (Scarlet, Shell Creek Shale base) are flooding surfaces.

The general sea level curve and generalized stacking patterns for each system are shown in figures 32, 37, and 38. This study has not determined if the cause of the minor regressions was due to a fall in sea-level, a decrease in the rate of sea-level rise, a decrease in the amount, or rate, of tectonic subsidence, or an increase in sediment supply to the system.

7. DISCUSSION AND CONCLUSIONS

Discussion

Incised Valley-Fills

In order to evaluate these features as incised valley-fills (IVF), we must first establish that the two features evaluated in this study are indeed incised valley-fills. To do this we compiled rigorous criteria for establishing what constitutes an incised valley-fill, as opposed to other incised and/or erosional features. For the purpose of this study the definition of incised valley-fills fits that described in Dalrymple et al.'s 1994 publication *Incised-valley systems: origin and sedimentary sequences* (SEPM Special Publication No. 51). Specifically, proper recognition of incised valley-fills must include the following criteria:

1. Lower bounding surface with:
    a. Observable truncation of underlying beds from erosion.
    b. The ability to correlate underlying within-feature surface of erosion (i.e. valley floor) with concurrent outer-feature surface of erosion (i.e. interfluve). The outer-feature surface of erosion may have been altered by the subsequent transgression.
    c. Within-feature surface of erosion must be *at least* one order of magnitude larger than coeval channel-fills.
    d. Surface of erosion must represent a significant gap in time, which cannot be explained with geomorphic rates of deposition.
2. And sediment fill with:

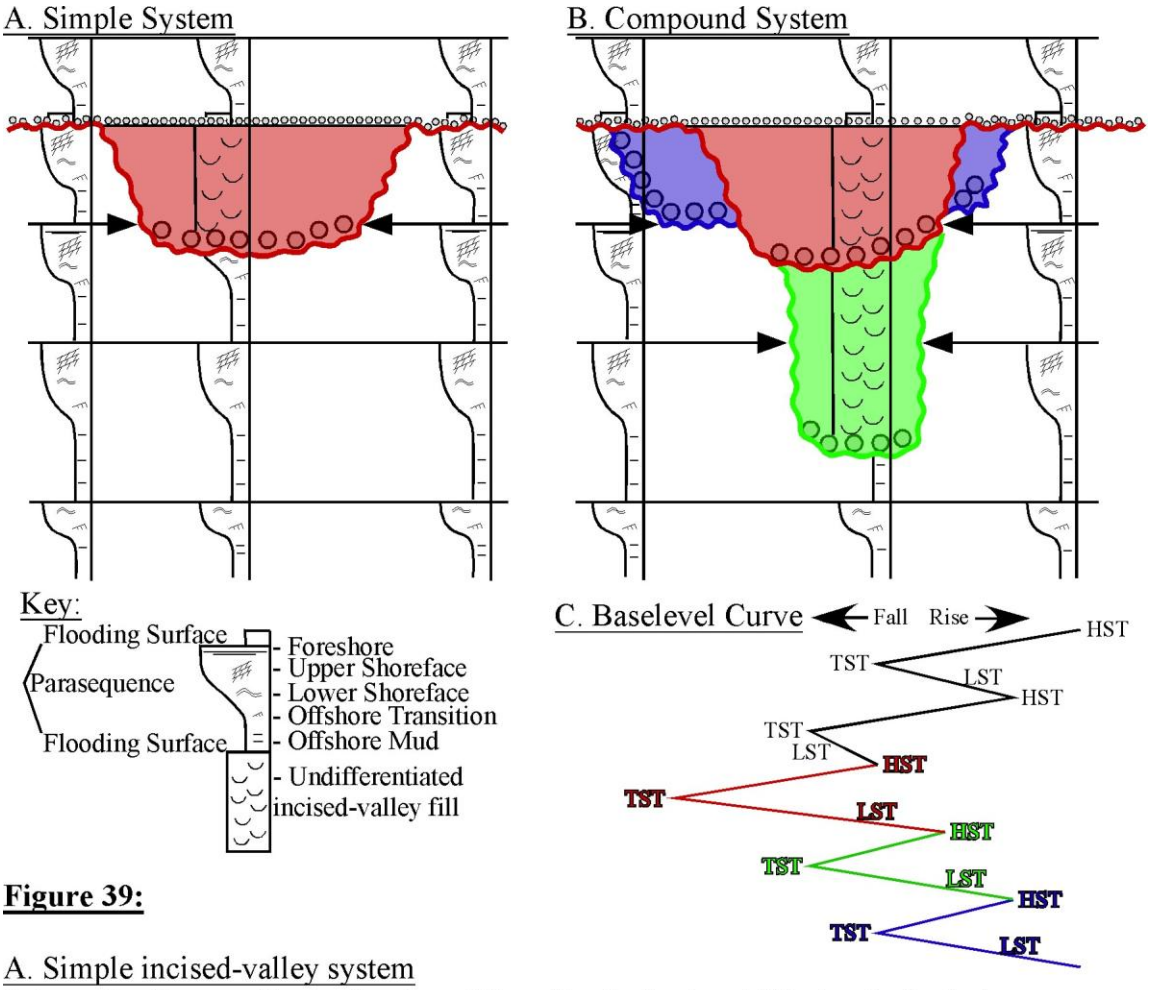

Figure 39:

A. Simple incised-valley system
Schematic diagram illustrating how this valley incised and filled entirely during one lowstand, transgressive, highstand sequence. In this case, the system incised and filled entirely in the red sequence shown on the baselevel curve in C. Aarows indicate truncation of underlying beds. Modify after Zaitlin et al. 1994.

B. Compound incised-valley system
This system incised and filled over three different lowstand, transgressive, highstand sequences. The first, in blue on both the baselevel curve (C) and diagram (B), the second sequence in green, and the final incision and fill in red. Aarows indicate truncation of underlying beds. Modified after Zaitlin et al. 1994.

C. Baselevel Curve
Example of possible baselevel curve which would explain periods of incision and fill in both A and B. LST = Lowstand Systems Tract; TST = Transgressive Systems Tract; HST = Highstand Systems Tract. In this diagram, incision of the valleys would take place during the LST, and subsequent valley-fill would begin during TST and continue through HST. LST, TST and HST all *sensu* Van Wagoner et al. 1990.

a. A recognizable juxtaposition of facies illustrating a basinward shift of proximal-facies over distal-facies.

b. Observable onlap and sidelap of surfaces onto the within-feature surface of erosion.

c. A change from fluvial facies at its base to estuarine facies above.[8]

(Summarized from Dalrymple et al. 1994, and Gardner, 2001)

Once a feature has been satisfactorily interpreted as an incised valley-fill, it then falls into one of two categories, simple (figure 39a), or compound fill (figure 39b). Simple systems result from an incision and fill which occur during a single lowstand - transgressive - highstand sequence (Figure 4a and 4c). Conversely compound systems result from incision and fill which occur during multiple lowstand - transgressive - highstand sequences (figure 4b and 4c) (Zaitlin et al. 1994).

Finally, the features are classed according to the geomorphic setting of its sediment source. In other words, if a valley-fill sources the hinterlands it is a piedmont incised valley, whereas if the valley-fill only sources the coastal plain it is a coastal plain incised valley (Zaitlin et al. 1994).[9]

Clareton

---

[8] This criterion applies only to those incised valley-fill features which are directly influenced by sea-level and which can, therefore, be correlated using sequence stratigraphy. Dalrymple et al. 1994 deems non-sea-level related incised valley-fills 'class two' valleys. Only 'class one' valleys will be evaluated as part of this study.

[9] This distinction can be applied to both modern and paleovalley features.

The Clareton system displays distinct lower bounding erosion surface with distinct truncation of underlying Skull Creek units. This surface of erosion is extensive and can be correlated in incised valleys, and between incised valleys through nearly all equivalent deposits in the Powder River, Denver and Williston basins (eg. Berg and Davies 1968; Gustason et al 1988; Farmer 1981; Emme 1981; Graham 2000; Higley et al 2003; Leckie et al 2004; and others). In addition, the Clareton feature is several orders of magnitude larger than a single channel fill (figure 40), as demonstrated by the multiple TFC and FB within each member of the Clareton valley-fill (see Chapter 6).

The fill comprising the Muddy Sandstone in the Clareton system displays a distinct juxtaposition of more proximal facies CB, BHD, FB, and TFC, over the distal MA facies of the underlying Skull Creek shale. The internal stratigraphic surfaces, specifically Forest, Scarlet, and Cyan surfaces, clearly onlap and sidelap onto the valley walls as is demonstrated by the progressive widening of deposits through time shown in the top structure and net sandstone maps of Chapter 6 (figures 17 through 31).

In light of this, the Clareton feature clearly fits the afore mentioned criteria and is indeed an incised valley-fill. The significant period of erosion which followed deposition of the Lower Recluse member and is marked by the Orange surface in addition to other multiple members bound by flood or erosion surfaces are evidence that the Clareton incised valley-fill is a compound fill, which recorded the deposition of multiple lowstand, transgressive, highstand sequences. Also, as previously mentioned in this work, the Clareton system is a piedmont system, whose sediment was sourced in the emerging Black Hills region to the west (Cupps 1964; Emme 1981; Farmer 1981; and Slack 1981).

Lower Fiddler Creek (tributary)

In the lower Fiddler Creek tributary section (Upper Recluse and Cyclone members) there is clear truncation of the underlying Skull Creek Shale beds demonstrated by multiple cross-sections from wireline well logs (appendix B), and the basal surface of erosion can be correlated with that of the Clareton incised valley-fill. Also, according to the member stacking pattern diagrams, which correlate to this segment of the system (figures 33 and 34), the incision is larger than that of a single channel.

The fill of the lower segment of the Fiddler Creek system appears to onlap and sidelap onto the erosion boundary, and displays a distinct transgression of facies in a landward direction. Also the onset of deposition in the Upper Recluse member, the lowest depositional member in the Lower Fiddler Creek, demonstrates an abrupt stacking of proximal facies over the distal facies of the Skull Creek Shale (figure 40). Therefore the Lower Fiddler Creek matches the definition of an incised valley-fill.

Since the source of sediment supply for this system was the coastal plain, and not the hinterlands as with the Clareton IVF, the lower Fiddler Creek is a coastal plain IVF. The lack of preservation of the Lower Recluse member, and ease of correlation of the Fiddler Creek erosional base with the Clareton IVF erosional base indicates that the lower Fiddler Creek is the result of a compound valley-fill.

Upper Fiddler Creek (through going)

The through-going Upper Fiddler Creek (Ute and Springen Ranch members) is bound at its base by the same surface of erosion as both Clareton and Lower Fiddler Creek IVF's (figure 40). However, well logs and isochore maps do not indicate that the

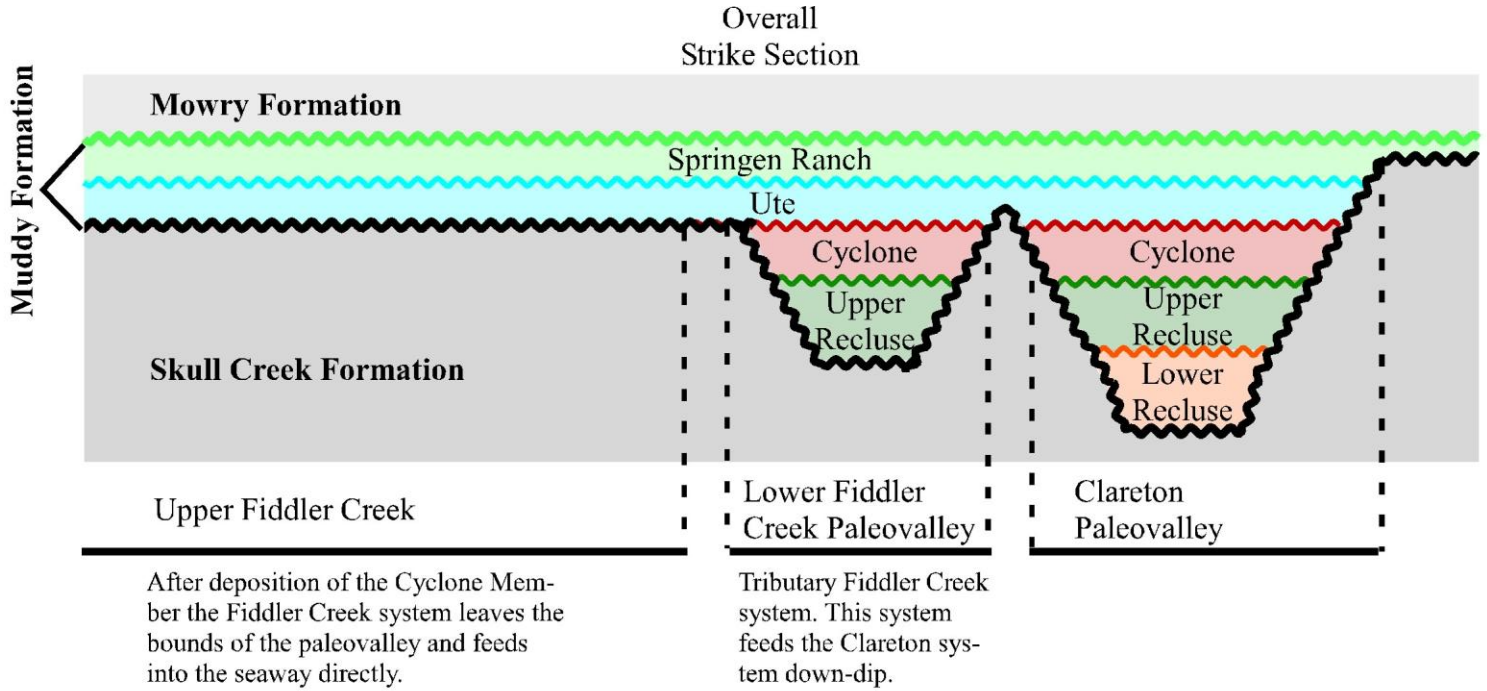

Figure 40:

Overall Strike Stacking Pattern:

Final stacking pattern of the Fiddler Creek and Clareton Paleovalleys in strike section. This figure displays how the after deposition of the Lower Fiddler Creek system (middle) the system avulsed out of the valley bounds and became a distributive system rather than a tributary to the Clareton Paleovalley. The Clareton remains confined by valley bounds until the end of deposition in the Springen Ranch member, at which time both valleys have been completely filled and are no longer incised valley fills. The top of the Muddy Formation is marked by a regional flooding surface which is recognized as the beginning of deposition of the Mowry Formation.

amount of incision in the Upper Fiddler Creek is greater than erosion caused by a single channel package.

The fill of the Upper Fiddler Creek does demonstrate a landward progression of facies, and has deposited proximal FB, TFC, and BHD facies over Skull Creek MA. However, in this depositional sequence, onlap and sidelap of internal surfaces onto the erosional surface are absent.

While the Upper Fiddler Creek does meet most of the criteria of an incised valley-fill, it is lacking two significant features. First, the amount of incision is not greater than that of a single channel erosion feature. Second, the internal stratigraphy does not onlap or sidelap onto the bounding erosion surface. Because of these two unmet criteria, the Upper Fiddler Creek is not an IVF, but is instead an erosional channel feature.

This relationship between the Lower and Upper Fiddler Creek is most clearly demonstrated in figure 40. In this figure you can see that the Fiddler Creek and Clareton systems began filling with the same onlap and sidelap relationship onto bounding valley walls. However after deposition of the Cyclone member, the Fiddler Creek avulses out of the valley bounds, and begins depositing as a distributive system during the Ute and Springen Ranch members. During this time, deposition in the Clareton system is still influenced by valley walls, and therefore still an IVF according to the criterion laid out in this work.

Stratigraphic Architecture

Overall, the depositional environments of the Clareton IVF, Lower Fiddler Creek IVF and Upper Fiddler Creek channel system fit the expected depositional patterns of

wave dominated estuarine incised valley-fills (Reading and Collinson 2004; Dalrymple et al 1994) with one major exception. Barrier facies association deposits are not present in any of the cores, well logs, or interpreted sections.

There are four possible explanations for this lack of an entire facies association. First, that the mouths of the incised valleys were very narrow and restricted the availability of sandstone into the system. While this is a possible explanation, even with a restricted valley mouth, some sandstone should still have been deposited within the system from the sandy transgressing shoreline. Since there is a complete lack of sand influence from the marine system, this hypothesis is not plausible.

Second, Barrier facies were deposited at the mouth of the incised valleys, but the extent of the study area does not contain this portion of the system. If this were the case, then as sea-level rose, and the shoreline transgressed we should see a forward stepping progression of facies. In fact, a distinct forward stepping pattern of facies is present in all three systems evaluated in this study; therefore if a barrier environment existed it should be present in the uppermost members of the systems. Since barrier deposits are not present in any level of the system this explanation is not probable.

Third, the barrier facies were preferentially eroded during subsequent sea-level falls leaving no record of their deposition. While erosive surfaces are undeniably common in this system, preferential erosion of the entirety of a single association is not logical. In addition, if this were the case, we would expect to see more extensive erosion of all other associations in the systems. Since this is not the case, this interpretation is not possible.

Finally, fourth that the depositional environment of the transgressing shoreline was extremely muddy and therefore no sand was available to be deposited in a barrier facies. This hypothesis is the most probable explanation for the lack of a barrier facies in any of the systems. Since there is not any sandstone deposited in the seaward segment of the valleys, no barrier facies are present in the uppermost members of the systems when all associations have migrated landward, and there is no evidence that specific erosion of these facies took place the most credible explanation is that the barrier facies were never deposited in the first place. Therefore the explanation for the lack of barrier facies at the mouth of the valleys is a muddy shoreline that had no sand to transport into the mouth of the valley's estuary.

Control of Sediment Supply

One of the primary questions of this thesis is what, if any, affect does sediment supply have on stratigraphic architecture in IVFs. The Clareton system, as previously discussed, was a piedmont system with a high rate of sandy sediment supply. In this system there are extensive fluvial facies, with relatively connected, continuous packages of sandstone in all five members. In the oldest members in the valley-fill, Lower and Upper Recluse, fluvial facies are connective nearly through the entire valley. Also the system experienced erosion events prior to filling which resulted in up to 100 feet of valley incision.

Throughout its filling history, sedimentation rate kept pace with the accommodation created in the Clareton system. Facies stacking patterns display periods of aggredation prior to final incursion marking the end of deposition of a member. Two

progradational packages are present in the Lower Recluse member of the Clareton system which likely represent periods when the rate of accommodation creation slowed, either by tectonic or eustatic control, and the high rate of sedimentation allowed for basinward progradation of facies. The rate of accommodation being created increased through time, which formed the overall landward step in facies association through all five members.

The Lower Fiddler Creek system has less significant fluvial deposits than the Clareton system. Less porous BHD are more common and more continuous in this system. The BHD in the Lower Fiddler Creek are present in each member as a relatively continuous deposit from head to toe of the system, and uniformly overlay the generally thin fluvial packages forming a stratigraphic cap. Valley incision does not exceed 50 feet in any place, and as a result, the system was completely filled after incursion of the Upper Recluse and Cyclone members.

It has been previously established that the rate of sedimentation, as well as overall system energy in the Fiddler Creek system was markedly less than that of the Clareton system. The result of the low rate of sedimentation resulted in half as much primary valley incision in the Lower Fiddler Creek system than in the Clareton system[10]. Because of the lower rate of sedimentation, the filling of the Lower Fiddler Creek system could not keep pace with the rate of accommodation creation and therefore backstepped at a much greater rate than did the Clareton. This rapid backstepping can be seen by comparing the facies associations figure from the Lower Fiddler Creek system (figure 37) to the Clareton system (figure 32). As a result, TFC sandstone packages are thinner than

[10] Fifty feet of incision as compared to 100 feet.

in the Clareton system, and tend to be reworked at the top by BHD tide and wave processes.

The Ute member of the Upper Fiddler Creek system displays only a progradational package. The missing retrogradational package was probably deposited, but eroded away during the period that formed the Cyan surface. The Upper Fiddler Creek displays the same rapid backstepping of facies in the Springen Ranch member as the Lower Fiddler Creek and Clareton units. There is no primary valley incision present in this section, and the entire unit is never more than 25 feet thick.

Simply because the Upper Fiddler Creek system is not an incised valley-fill does not mean that it cannot be useful in determining how sediment supply affects stratigraphic architecture. Once again, in the Upper Fiddler Creek associations are much more laterally extensive than in the Clareton system. Facies associations extend from the head of the valley to the toe, displaying relatively rapid rates of progradation. Erosion surfaces are also more common in this unit. For example, in the Clareton system, the Cyan surface is slightly erosional, but overall is the record of a flood that followed a period of transgression and retrogradation. In the Upper Fiddler Creek system the Cyan surface represents not only the period of retrogradation present in the Clareton system, but also the ensuing flooding event, and next regressive event. In other words, the surfaces in the Upper Fiddler Creek record more time than they do in the Clareton.

Overall, when the members of the Clareton system are compared to the members of the Fiddler Creek system it is apparent that equivalent changes in accommodation are recorded in considerably different ways. In the Clareton system changes in accommodation are recorded by progradational and retrogradational packages within

each member. In the Fiddler Creek, the same changes in accommodation resulted in the deposition of much more laterally extensive packages of facies. In other words, high rates of sediment supply tend to preferentially preserve progradational – retrogradational packages, where low sediment supply rates tend to preserve one or the other. Thus, surfaces in low sediment supply systems are more significant time stratigraphically as they represent larger amounts of time than equivalent surfaces in high sediment supply systems (see example from the Cyan surface above).

Sequestration

The final question to be answered is whether or not these systems are candidates for CO_2 sequestration. However, we must first determine criteria for a system to be considered a candidate for CO_2 sequestration. First a system must be sufficiently characterized in terms of sequestration integrity of the sequestration reservoir, and surrounding units. Sequestration integrity is determined by calculating potential storage volumes, porosity and permeability pathways within the reservoir, integrity of the trap and seal, degree of fracturing, well penetration, and existing infrastructure.

In addition, potential sequestration sites must meet certain pressure, temperature requirements. For maximum efficiency in sequestration CO_2 is sequestered in a supercritical phase. In a supercritical phase CO_2 has physical properties, and will therefore behave, similar to both a gas and a liquid. Like a gas CO_2 will effectively fill available pore volume, yet maintain a liquid-like density, which increases storage efficiency and decreases buoyancy, and therefore tendency to migrate (Bachu 2003). To maintain CO_2 in a supercritical phase it must be kept at temperatures $\geq 32°C$ ($\approx 88°F$)

and pressures ≥ 7.38 MPa (≈ 73.8 Bars, or ≈ 1070 psi). At higher pressures, the density of CO_2 increases which further decreases buoyancy forces and increases storage capacity. Assuming a general hydrostatic pressure gradient and geothermal gradient of 25°C/km (Holloway and Savage 1993) CO_2 should be stored at depths of at least 800 m (≈ 2625 ft), however supercritical zones can vary from basin to basin and even within a single basin.

If CO_2 is allowed to migrate out of the supercritical zone the consequences are undesirable at best. As the CO_2 moves upward into zones of lower pressure and temperature, its density decreases and therefore its buoyancy increases, which increases CO_2's propensity to migrate. This self-perpetuating process can lead to catastrophic blow-out as the CO_2 expands to less-dense gaseous phases (Bachu 2003, Bachu and Grobe 2006).

As previously determined by the stratigraphic architecture, porosity and permeability pathways in these systems are extremely laterally connected. In the Clareton incised valley-fill the lower most members have permeability pathways from head to toe of the feature. The upper members, while less laterally connective, still contain large producing reservoirs. In the Lower Fiddler Creek, porosity pathways extend from the head of the valley to the tributary connection with the Clareton, and are effectively sealed with CB and MA facies. Finally the Upper Fiddler Creek has connective porosity pathways from head to toe of the system much like the lower members of the Clareton. It is underlain by MA facies of the Skull Creek Shale, and overlain by its own CB facies of the Springen Ranch member.

Any of these systems contain the necessary connectivity and capacity to sequester and store CO_2. Nonetheless, none of these systems are candidates for CO_2 sequestration.

As mentioned previously, CO_2 must be stored in a supercritical phase, which requires specific pressure and temperature. While the lower most portions of the Clareton system meet the minimum pressure temperature requirements, the sandstone packages at the base of the system are connected with sandstone packages that outcrop near Newcastle Wyoming. If CO_2 were ever injected into the lower reservoirs for storage, it would quickly migrate, expand and leak out of outcrops.

Another potential problem with these systems is the existing infrastructure. In the sixty-four square townships that comprise this study area, there are over 6,000 wells that penetrate to, or past, the study interval. While this was not a part of this study specifically, in the event these systems were to be used for CO_2 sequestration, each well would need to be checked for leakage potential and recapped if necessary.

It is also important to note, in some areas of the Powder River basin, namely the Bell Creek field, the Skull Creek Shale produces oil out of a delta system at the top of the formation (Berg 1968). While this porous facies does not appear to be present in this area, a more detailed study should be done of the Skull Creek specifically in this area to evaluate any leakage potential through valley walls to potentially porous media in the Skull Creek Shale. If porous media are present and if leakage did occur, how far could contamination extend and what would be the impacts.

Even though these systems are not candidates for long term CO_2 sequestration, they are useful as proxies for similar systems, which may be candidates. The differences in stratigraphic architecture between the two systems, which resulted in three distinct depositional reservoir packages is a distinct new model for these two systems. This new

model uniquely explains the observed discrepancy between the isochore maps of the Muddy Sandstone, and observed well trends in the system.

Conclusions

1. The Clareton system is the record of a compound through-going piedmont incised valley.
2. The Fiddler Creek system should be separated into two systems, a tributary system (Lower Fiddler Creek system) in which the Fiddler Creek paleovalley-fill is a tributary to the piedmont Clareton system, and a coastal plain system (Upper Fiddler Creek system), where the Fiddler Creek drainage connected directly to the transgressing shoreline of the western interior Cretaceous seaway.
    a. The Lower Fiddler Creek system displays the necessary juxtaposition of facies, correlation and truncation of surfaces, and significant scale of erosion to be considered an incised valley-fill. However, this incised valley-fill's sediment source was a muddy coastal plain and is therefore a coastal plain incised valley-fill.
    b. The Upper Fiddler Creek do not display the necessary stratigraphic surface relationships to be classified as an IVF. Its source was also a muddy coastal plain and is a coastal plain distributary system.
3. Deposition of the members within the Clareton system, Upper, and Lower Fiddler Creek systems were characterized by a muddy shoreline that resulted in the lack of deposition of a barrier facies association in any of the units.

4. Similar changes in accommodation recorded considerably different stratigraphic architectures. The difference in stratigraphic architecture is the result of the differing sediment supply between the Clareton and Fiddler Creek systems.
    a. High rates of sediment supply result in preferential preservation of progradational - retrogradational packages, less time as a surface, and more narrow up-dip, down-dip deposition of facies.
    b. Low rates of sediment supply result in preferential preservation of erosionally bound retrogradational packages, more time as a surface, and more extensive up-dip to down-dip spread of facies.
5. None of the three depositional units in this study are candidates for CO_2 sequestration. However they are all useful as proxies for sequestration in other incised valley systems.

BIBLIOGRAPHY

Aldinucci, M., M. Ghinassi, and F. Sandrelli, 2007, Climatic and tectonic signature in the fluvial infill of late Pliocene valley (Siena basin, northern Apennines, Italy): Journal of Sedimentary Research, 77, 398-414.

Anthony, E. J., J. Lang, L. M. Oyede, 1996, Sedimentation in a tropical, microtidal, wave-dominated coastal-plain estuary: Sedimentology, 43, 665-675.

Aubrey, W. M., 1989, Mid-Cretaceous alluvial-plain incision related to eustasy, southeastern Colorado Plateau: Bulletin of the Geological Society of America, 101, 443-449.

Bachu, S. (2001), 'Geological sequestration of anthropogenic carbon dioxide: applicability and current issues', *in* Gerhard, L. C., W. E. Harrison, and B. M. Hanson (eds.), *Geological perspectives of global climate change*, 285-303.

Bachu, S. and M. Grobe, 2006, Characterization of sites for geological storage of carbon dioxide: Environmental Geosciences, 13 (2), 67-70.

Bachu, S., 2003, Screening and ranking of sedimentary basins for sequestration of CO(sub 2) in geological media in response to climate change: Environmental Geology, 44, 277-289.

Baines, D., D. G. Smith, D. G. Froese, P. Bauman, and G. Nimeck, 2002, Electrical resistivity ground imaging (ERGI): a new tool for mapping lithology and geometry of channel-belts and valley-fills: Sedimentology, 49, 441-449.

Baker, D. R., 1962, The Newcastle Formation in Weston County, Wyoming: A non-marine (alluvial) plain deposit: Wyoming Geological Association, Seventeenth Annual Field Conference Guidebook, 148-162.

Berg, R. R. and D. K. Davies, 1968, Origin of lower Cretaceous Muddy Sandstone at Bell Creek field, Montana: AAPG Bulletin, 52 (10), (10), 1888-1898.

Bhattacharya, J. P. and B. J. Willis, 2001, Lowstand deltas in the Frontier formation, Powder River basin, Wyoming: implications for sequence stratigraphic models: AAPG Bulletin, 85 (2), 261-294.

Bowen, D. W. and P. Weimer, 2004, Reservoir geology of Nicholas and Liverpool Cemetery fields (lower Pennsylvanian), Stanton County, Kansas, and their significance to the regional interpretation of the Morrow Formation incised-valley-fill systems in eastern Colorado and western Kansas: AAPG Bulletin, 88 (1), 47-70.

———, 2005, Regional sequence stratigraphic setting and reservoir geology of Morrow incised-valley sandstones (lower Pennsylvanian), eastern Colorado and western

Kansas: AAPG Bulletin, 87 (5), 781-815.

Cant, D. J., 1995, Sequence stratigraphic analysis of individual depositional successions: effects of marine/nonmarine sediment partitioning and longitudinal sediment transport, Mannville group, Alberta foreland basin, Canada: AAPG Bulletin, 79 (5), 749-762.

———, 1996, Sedimentological and sequence stratigraphic organization of a foreland basin clastic wedge, Manville Group, western Canada basin: Journal of Sedimentary Research, 66 (6), 1137-1147.

Capuzzo, N. and A. Wetzel, 2004, Facies and basin architecture of the late Carboniferous Salvan-Dorenaz continental basin (Western Alps, Switzerland/France): Sedimentology, 51, 675-697.

Cobban, W. A. and J. B. Reeside, 1962, Correlation of the Cretaceous formations of the western interior of the United States: AAPG Bulletin, 63, 1011-1044.

Cotter, E. and S. G. Driese, 1998, Incised-valley fills and other evidence of sea-level fluctuations affecting deposition of the catskill formation (Upper Devonian), Appalachian foreland basin, Pennsylvania: Journal of Sedimentary Research, 68 (2), 347-361.

Crowley, A. J., 1951, Possible lower Cretaceous uplifting of Black Hills, Wyoming and South Dakota: AAPG Bulletin, 35 (1), 83-107.

Cupps, C. Q., J. Fry, and R. F. Zaffarano, 1964, Areal variation in reservoir oil characteristics, Newcastle sandstone, greater Clareton area, Wyo.: U.S. Bureau of Mines, Report of investigations, 6389, 34.

Dalrymple, R. W., B. A. Zaitlin, and R. Boyd, 1992, Estuarine facies models: conceptual basis and stratigraphic implications: Journal of Sedimentary Petrology, 62 (6), 1130-1146.

Dalrymple, R. W., R. Boyd, and B. A. Zaitlin, (1994), 'History of research, types and internal organization of incised-valley systems: introduction to the volume', *in* Dalrymple, R. W., R. Boyd, and B. A. Zaitlin (eds.), *Incised-valley systems: origin and sedimentary sequences* (SEPM Special Publication No. 51, Tulsa Oklahoma: SEPM Society for Sedimentary Geology), 3-10.

———, (eds.), 1994, Incised-valley systems: origin and sedimentary sequences: SEPM Special Publication No. 51, Tulsa Oklahoma: SEPM Society for Sedimentary Geology, 385.

Dalrymple, R. W. and B. A. Zaitlin, 1994, High-resolution sequence stratigraphy of a

complex, incised valley succession, Cobequid Bay - Salmon River estuary, Bay of Fundy, Canada: Sedimentology, 41, 1069-1091.

Dalrymple, R. W. (2006), 'Incised valleys in time and space: an introduction to the volume and an examination of the controls on valley formation and filling', *in* Dalrymple, R. W., D. A. Leckie, and R. W. Tillman (eds.), *Incised valleys in time and space* (SEPM Special Publication No. 85, Tulsa Oklahoma: SEPM Society for Sedimentary Geology), 5-12.

de Freitas, C. R., 2002, Are observed changes in the concentration of carbon dioxide in the atmosphere really dangerous?: Bulletin of Canadian Petroleum Geology, 50 (2), 297-327.

Dolson, J., D. Muller, M. J. Evetts, and J. A. Stein, 1991, Regional paleotopographic trends and production, Muddy Sandstone (lower Cretaceous), central and northern Rocky Mountains: AAPG Bulletin, 75 (3), 409-435.

Dominici, S. and M. Zuschin, 2007, Sea-level change and the structure of marine ecosystems: Palaios, 22, 225-227.

Doughty, C. and K. Pruess, 2004, Modeling supercritical carbon dioxide injection in heterogeneous porous media: Vadose Zone Journal, 3, 837-847.

Dutton, S. P. and B. J. Willis, 1998, Comparison of outcrop and subsurface sandstone permeability distribution, lower Cretaceous Fall River Formation: Journal of Sedimentary Research, 68 (5), 890-900.

Eberth, D. A., 1996, Origin and significance of mud-filled incised valleys (Upper Cretaceous) in southern Alberta, Canada: Sedimentology, 43, 459-477.

Egbert, R. L. and E. F. Armstrong, 1970, The use of computer prepared residual maps as an aid in determining sedimentary environments of the Muddy Formation, northeastern Wyoming: The Mountain Geologist, 7 (4), 253-268.

Emme, J. J., 1981, Tectonic influence on sedimentation, lower Cretaceous strata, Osage - Newcastle area, Powder River Basin, Wyoming: Masters Thesis, Colorado School of Mines, 186.

Farmer, C. L., 1981, Tectonics and sedimentation, Newcastle Formation (Lower Cretaceous), southwestern flank Black Hills uplift, Wyoming and South Dakota: Masters Thesis, Colorado School of Mines, 195.

Foyle, A. M. and G. F. Oertl, 1997, Transgressive systems tract development and incised-valley fills within a Quaternary estuary-shelf system: Virginia inner shelf, USA: Marine Geology, 137, 227-249.

Friedman, G. M. and J. E. Sanders, 2000, Comments about the relationships between new ideas and geologic terms in stratigraphy and sequence stratigraphy with suggested modification: AAPG Bulletin, 84 (9), 1274-1280.

Gardner, M. H., 2001, Spectrum of fluvial architectural styles related to accommodation-sediment supply changes: field guide to selected outcrops of the lower Cretaceous Fall River Formation and Muddy Sandstone, Black Hills, Wyoming and South Dakota: American Association of Petroleum Geologists National Meeting, Denver, Colorado, 193.

Grace, R.M., 1952, Stratigraphy of the Newcastle formation, Black Hills region, Wyoming and South Dakota: Wyoming Geological Survey Bulletin, no. 44, 44.

Graham, J. P., 2000, Revised stratigraphy, depositional systems, and hydrocarbon exploration potential for the lower Cretaceous Muddy Sandstone, Northern Denver basin: AAPG Bulletin, 84 (2), 183-209.

Greene, D. L., A. B. Rodriguez, and J. B. Anderson, 2007, Seaward-branching coastal-plain and piedmont incised-valley systems through multiple sea-level cycles: late Quaternary examples from Mobil Bay and Mississippi Sound, USA: Journal of Sedimentary Research, 77, 139-158.

Gries, J. P., 1954, Cretaceous rocks of Williston Basin: AAPG Bulletin, 38, 443-453.

Hajash, A., 1980, Regional diagenetic trends in the lower Cretaceous Muddy sandstone, Powder River basin - Discussion: 679-681.

Hancock, E.T., 1920, The Mule Creek oil field, Wyoming, IN Contributions to economic geology, 1920; part 2, Mineral fuels: U.S. Geological Survey Bulletin, 716-C, C35-C53.

Harshman, E. N., 1972, Geology and uranium deposits, Shirley Basin area, Wyoming: Geological Survey Professional Paper, 745, 82.

Haq, B. U., J. Hardenbol, and P. R. Vail, 1987, Chronology of fluctuating sea levels since the Triassic: Science, 235 (4793), 1156-1167.

Higley, D. K., D. O. Cox, and R. J. Weimer, 2003, Petroleum system and production characteristics of the Muddy (J) Sandstone (lower Cretaceous) Wattenberg continuous gas field, Denver basin, Colorado: AAPG Bulletin, 87 (1), 15-37.

Hintze, F. F., 1915, The Basin and Greybull oil and gas fields: Wyoming Geologist's Office Bulletin, v.10, 62.

Holbrook, J., 2001, Origin, genetic interrelationships, and stratigraphy over the continuum of fluvial channel-form bounding surfaces: an illustration from middle Cretaceous strata, southeastern Colorado: Sedimentary Geology, 144, 179-222.

Jackson, M. D., S. Yoshida, A. H. Muggeridge, and H. D. Johnson, 2005, Three-dimensional reservoir characterization and flow simulation of heterolithic tidal sandstones: AAPG Bulletin, 89 (4), 507-528.

Kidney, R. L. and T. L. Davis, Tectonic influence on depositional patterns of lower Cretaceous strata, Newcastle, Wyoming area, eastern Powder River basin:

Kvale, E. P. and A. W. Archer, 2007, Paleovalley fills: trunk vs. tributary: AAPG Bulletin, 91 (6), 809-821.

Leckie, D. A., K. E. Wallace-Dudley, N. A. Vanbeselaere, and D. P. James, 2004, Sedimentation in a low-accommodation setting: nonmarine (Cretaceous) Mannville and marine (Jurassic) Ellis groups, Manyberries field, southeastern Alberta: AAPG Bulletin, 88 (10), 1391-1418.

MacDonald, A. C., L. M. Falt, and A. L. Hektoen, 1998, Stochastic modeling of incised valley geometries: AAPG Bulletin, 83 (6), 1156-1172.

MacEachern, J. A. and S. G. Pemberton, 1994, 'Ichnological aspects of incised-valley fill systems from the Viking Formation of the western Canada sedimentary basin, Alberta, Canada', *in* Dalrymple, R. W., R. Boyd, and B. A. Zaitlin (eds.), *Incised-valley systems: origin and sedimentary sequences* (SEPM Special Publication No. 51, Tulsa Oklahoma: SEPM Society for Sedimentary Geology), 129-157.

MacKenzie, D. B., 1965, Depositional environments of Muddy Sandstone, western Denver basin, Colorado: AAPG Bulletin, 49 (2), 186-206.

Martinsen, O. J., 1994, 'Evolution of an incised-valley fill, the Pine Ridge Sandstone of southeastern Wyoming, U.S.A.: systematic sedimentary response to relative sea-level change', *in* Dalrymple, R. W., R. Boyd, and B. A. Zaitlin (eds.), *Incised-valley systems: origin and sedimentary sequences* (SEPM Special Publication No. 51, Tulsa Oklahoma: SEPM Society for Sedimentary Geology), 109-128.

Martinsen, R. S. (1994), 'Stratigraphic compartmentation of reservoir sandstones: examples from the Muddy Sandstone, Powder River basin, Wyoming', *Basin compartments and seals: AAPG memoir 61*, 273-296.

———, 2003, Depositional remnants, part 1: common components of the stratigraphic record with important implications for hydrocarbon exploration and production: AAPG Bulletin, 87 (12),1869-1882.

———, 2003, Depositional remnants, part 2: examples from the western interior Cretaceous basin of North America: AAPG Bulletin, 87 (12), 1883-1909.

Mattheus, C. R., A. B. Rodriguez, D. L. J. Greene, A. R. Simms, and J. B. Anderson, 2007, Control of upstream variables on incised-valley dimension: Journal of Sedimentary Research, 77, 213-224.

McCarthy, P. J. and A. G. Plint, 1998, Recognition of interfluve sequence boundaries: integrating paleopedology and sequence stratigraphy: Geology, 26 (5), 387-390.

Melick, J. J., and M. H. Gardner, 2007, Demonstrating the value of combining geologic carbon dioxide sequestration with enhanced oil recovery: Powder River basin, Wyoming and Montana: AAPG Annual Meeting 2007 – Long Beach, CA, Oral Presentation.

Miall, A. D., 1985, Architectural-element analysis: A new method of facies analysis applied to fluvial deposits: Earth-Science Reviews, 22, 261-308.

———, 1999, Sequence stratigraphy and chronostratigraphy problems of definition and precision in correlation and the implications for global eustasy: Paleocene, 7, 261-286.

———, 2000, Suggestions for researching and publishing regional stratigraphic research: Sedimentary Geology, 132, 1-3.

———, 2006, Reconstructing the architecture and sequence stratigraphy of the preserved fluvial record as a tool for reservoir development: a reality check: AAPG Bulletin, 90 (7), 989-1002.

Miller, K. G., M. A. Kominz, J. V. Browning, J. D. Wright, G. S. Mountain, M. E. Katz, P. J. Sugarman, B. S. Cramer, N. Christie-Blick, and S. F. Pekar, 2005, The Phanerozoic record of global sea-level change: Science, 310, 1293-1298.

Montgomery, S. L., D. S. Schechter, and J. Lorenz, 2000, Advanced reservoir characterization to evaluate carbon dioxide flooding, Spraberry trend, Midland basin, Texas: AAPG Bulletin, 84 (9), 1247-1273.

Newell, N. D. and L. Marcus, 1987, Carbon dioxide and people: Palaios, 2, 101-103.

Nichols, M. M., G. H. Johnson, P. C. Peeples, 1991, Modern sediments and facies model for a microtidal coastal plain estuary, the James Estuary, Virginia: Journal of Sedimentary Petrology, 61 (6), 883-899.

Nordfjord, S., J. A. Goff, J. A. Austin, and S. P. S. Gulick, 2006, Seismic facies of incised-valley fills, New Jersey continental shelf: implications for erosion and

preservation processes acting during latest Pleistocene-Holocene transgression: Journal of Sedimentary Research, 76, 1284-1303.

Obradovich, J.D., and Cobban, W.A., 1978, K-Ar dating of the Albian, IN Geological Survey research 1978: U.S. Geological Survery Professional Paper, 1100, p. 191.

Oduolowu, O., 1976, A case study of the recoverable hydrocarbon volumes for the Minnelusa and Muddy sands, Powder River basin, Wyoming: The Log Analyst: a journal of formation evaluation and reservoir description, 17 (2), 24-32.

Pederson, K. H., and D. W. Bowen, 2007, Stratigraphic architecture of two incised valley fills: Fiddler Creek and Clareton fields, Wyoming: AAPG Annual Meeting 2007 – Long Beach, CA, Poster.

Peppers, R. A., 1959, Stratigraphy of the Muddy (Newcastle) Formation of the Powder River Basin, Wyoming and Montana: Masters Thesis, University of Illinois, 183.

Plint, A. G. and J. A. Wadsworth, 2003, Sedimentology and palaeogeomorphology of four large valley systems incising delta plains, western Canada Foreland Basin: implications for mid-Cretaceous sea-level changes: Sedimentology, 50, 1147-1186.

Posamentier, H. W., 2001, Lowstand alluvial bypass systems: incised vs. unincised: AAPG Bulletin, 85 (10), 1771-1793.

Reishus, M., 1968, The Newcastle Formation in the Williston basin of North Dakota: North Dakota Geological Survey Report of Investigations, no. 47, 26.

Rice, D. D. (1976), 'Revision of Cretaceous nomenclature of the northern Great Plains in Montana, North Dakota, and South Dakota', *in* Cohee, G. V. and W. B. Wright (eds.), *Changes in stratigraphic nomenclature by the U.S. Geological Survey* (U.S. Geological Survey Bulletin, U.S. Geological Survey), A66-A67.

Robinson, C. S., W. J. Mapel, and W. A. Cobban, 1959, Pierre shale along western and northern flanks of Black Hills, Wyoming and Montana: AAPG Bulletin, 43, 101-123.

Robinson, C.S., Mapel, W.J., and Bergendahl, M.H., 1964, Stratigraphy and structure of the northern and western flanks of the Black Hills uplift, Wyoming, Montana, and South Dakota: U.S. Geological Survey Professional Paper, 404, 134 p.

Rolinak, P., 1984, The allure of Muddy and Minnelusa: Western Oil Reporter, 41 (8), 53-55.

Shelton, J. W., 1972, Correlation sections and log maps in determination of sandstone trends: AAPG Bulletin, 56 (8), 1541-1544.

Siguaw, S. G., J. E. Estes-Jackson, S. E. Ingraham, and D. W. Shewmake, 2001, An integrated 3-D reservoir characterization at Riverton Dome field, Wyoming: The Leading Edge, 1226-1238.

Skolnick, H., 1958, Stratigraphy of some lower Cretaceous rocks of Black Hills area: AAPG Bulletin, 42 (4), 787-815.

Slack, P. B., 1981, Paleotectonics and hydrocarbon accumulation, Powder River basin, Wyoming: AAPG Bulletin, 730-743.

Sminchak, J. and N. Gupta, 2003, Aspects of induced seismic activity and deep-well sequestration of carbon dioxide: Environmental Geosciences, 10 (2), 81-89.

Stephen, K. D. and M. Dalrymple, 2002, Reservoir simulations developed from an outcrop of incised valley fill strata: AAPG Bulletin, 86 (5), 797-822.

Stone, W. D., 1972, Stratigraphy and exploration of the lower Cretaceous Muddy Formation northern Powder River basin, Wyoming and Montana: The Mountain Geologist, 9 (4), 355-378.

Szpakiewicz, M., K. McGee, and B. Sharma, 1987, Geologic problems related to characterization of clastic reservoirs for EOR: SPE formation evaluation, 2 (4), 449-460.

Thorne, J. (1994), 'Constraints on riverine valley incision and the response to sea-level change based on fluid mechanics', *in* Dalrymple, R. W., R. Boyd, and B. A. Zaitlin (eds.), *Incised-valley systems: origin and sedimentary sequences* (SEPM Special Publication No. 51, Tulsa Oklahoma: SEPM Society for Sedimentary Geology), 29-43.

Tysdal, R. G., T. S. Dyman, and D. J. Nichols, 1989, Lower Cretaceous bentonitic strata in southwestern Montana assigned to Vaughn Member of Mowry Shale (east) and of Blackleaf Formation (west): The Mountain Geologist, 26 (2), 53-61.

Van Wagoner, J. C., R. M. Mitchum, K. M. Campion, and V. D. Rahmanian, 1990, Siliciclastic Sequence Stratigraphy in well logs, cores and outcrops: AAPG Methods in Exploration, no. 7.

Vuke, S., 1981, Depositional environments of the early Cretaceous seaway, northwestern United States: Northwest Geologist, 10, 1-12.

Waage, K. M., 1955, Dakota Group in northern Front Range foothills, Colorado: Geological Survey Professional Paper, 274 (B), 51.

Weimer, R.J., 1988, Record of relative sea-level changes, Cretaceous of Western Interior, USA: SEPM Special Publication, 42, 285-288.

White, C. M., B. R. Strazisar, E. J. Granite, J. S. Hoffman, and H. W. Pennline, 2003, Separation and capture of CO2 from large stationary sources and sequestration in geological formations -- coalbeds and deep saline aquifers: Journal of the Air and Waste Management Association, 53, 645-715.

Willis, B. J., 1997, Architecture of fluvial-dominated valley-fill deposits in the Cretaceous Fall River formation: Sedimentology, 44, 735-757.

Wulf, G. R., 1962, Eroded oscillation ripple marks in Cretaceous Newcastle Sandstone, Wyoming and South Dakota: Journal of Sedimentary Research, 32 (3), 327-329.

———, 1962, Lower Cretaceous Albian rocks in north Great Plains: AAPG Bulletin, v.46, no. 8, 1371-1415.

Zaitlin, B. A., R. W. Dalrymple, and R. Boyd (1994), 'The stratigraphic organization of incised-valley systems associated with relative sea-level changes', *in* Dalrymple, R. W., R. Boyd, and B. A. Zaitlin (eds.), *Incised-valley systems: origin and sedimentary sequences* (SEPM Special Publication No. 51, Tulsa Oklahoma: SEPM Society for Sedimentary Geology), 45-60.

Zhang, Y., C. M. Oldenburg, and S. M. Benson, 2004, Vadose zone remediation of carbon dioxide leakage from geologic carbon dioxide sequestration sites: Vadose Zone Journal, 3, 858-866.

APPENDICES

APPENDIX A:

WELL LOG CORRELATIONS

Map of cross sections through Fiddler Creek and Clareton fields:

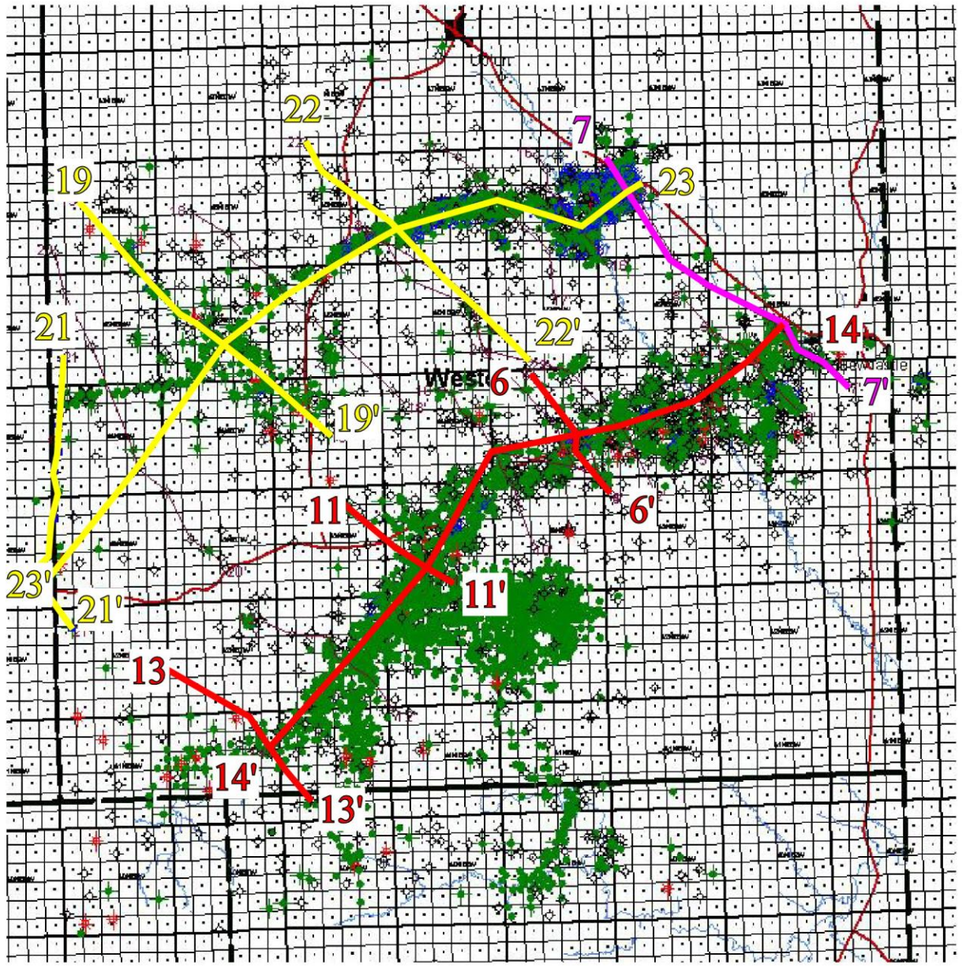

Left: Map showing location of cross section in fiddler creek and clareton friels. Red lines depict Clareton cross sections. Yellow lines depict Fiddler Creek cross sections. Purple line indicates the single strike cross section with goes through both the Fiddler Creek and Clareton fields.

Bottom: Full cross section #7. Cross section 7 is a strike section which crosses both the Fiddler Creek Field and Clareton Fields. Purple line indicates the boundary between each field. Cross section is hung on the top of the Muddy Sandstone, indicated by a green line. Note there is not a preserved interfluve between the two fields. This is most likely due to the final transgressive surface which capped the valleys, eroding any interfluve or paleosol deposits there.

- Top Muddy Sandstone, all cross sections hung on this surface.
- Top Ute Member.
- Top Cyclone Member.
- Top Upper Recluse Member.
- Top Lower Recluse Member.
- Top Skull Creek Shale. Base of valley erosion.

Clareton and Fiddler Creek Strike Section 7:

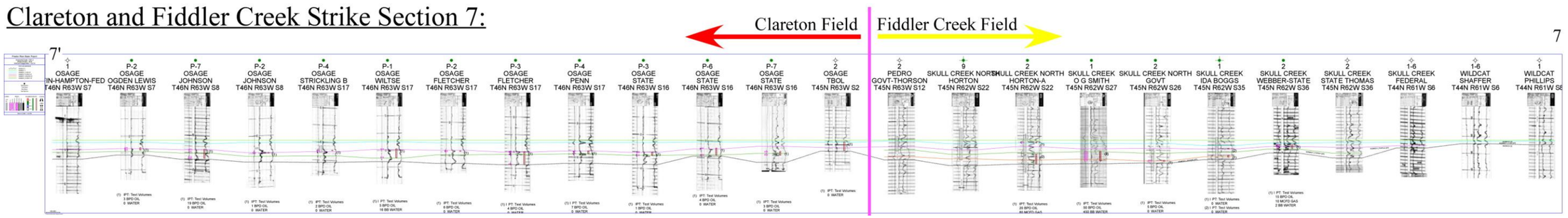

Clareton Dip Section 14:

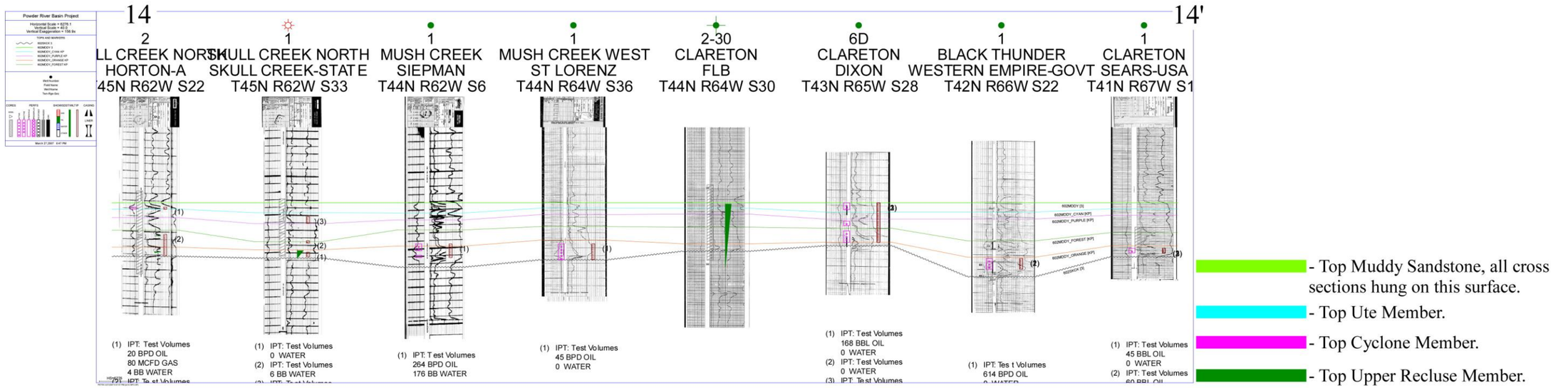

Clareton Strike 6:

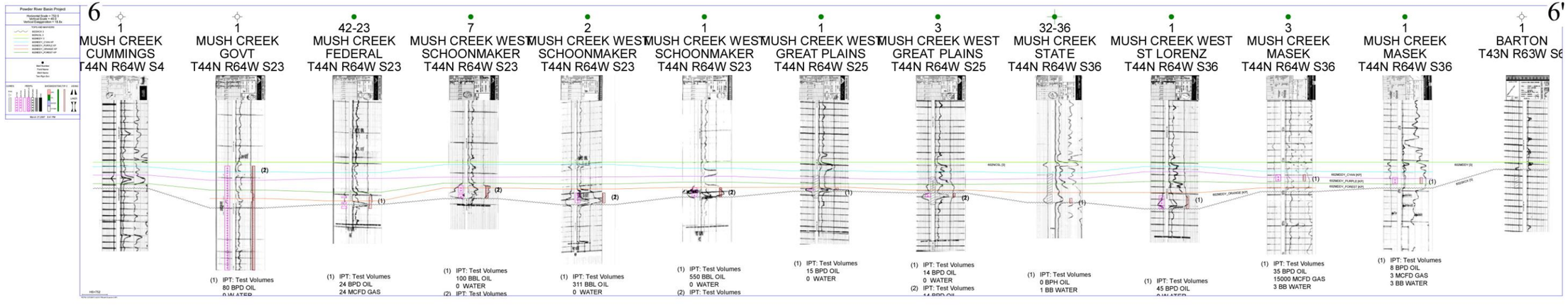

Clareton Strike 13:

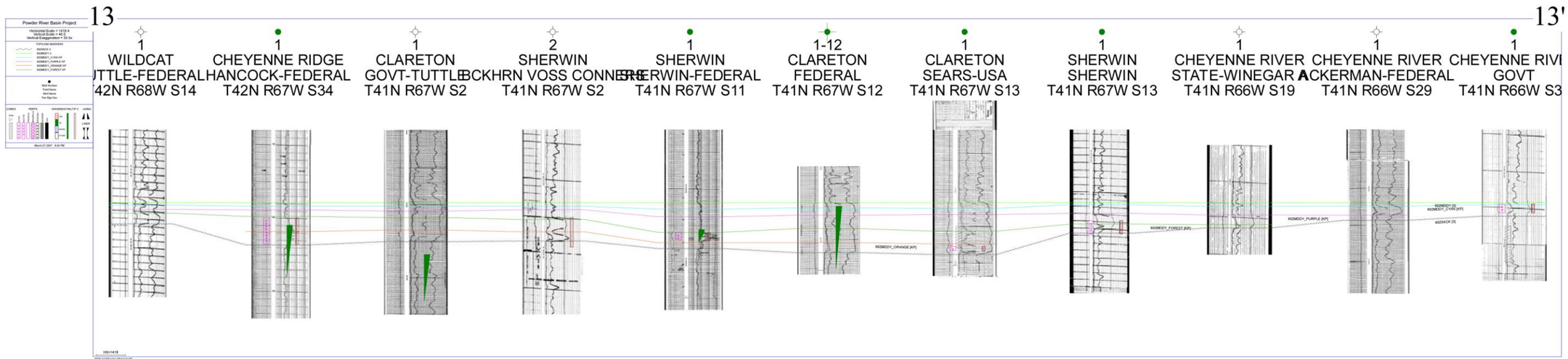

- Top Muddy Sandstone, all cross sections hung on this surface.
- Top Ute Member.
- Top Cyclone Member.
- Top Upper Recluse Member.
- Top Lower Recluse Member.
- Top Skull Creek Shale. Base of valley erosion.

Clareton Strike 11:

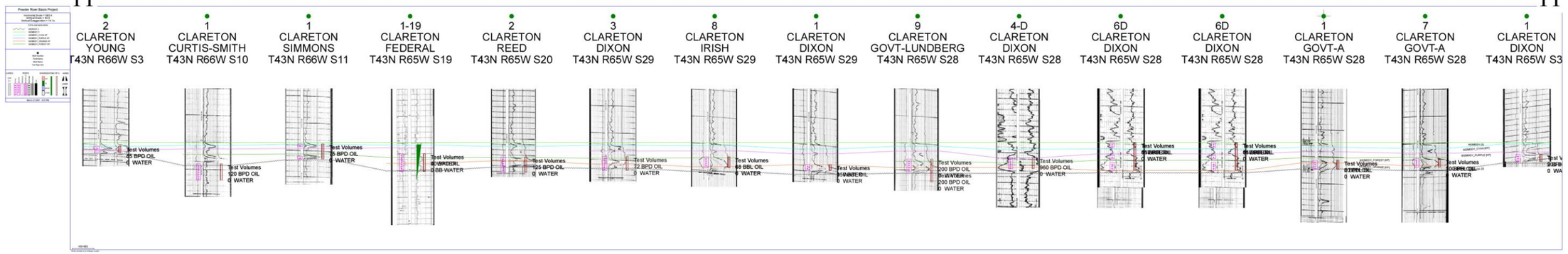

Fiddler Creek Dip Section 23:

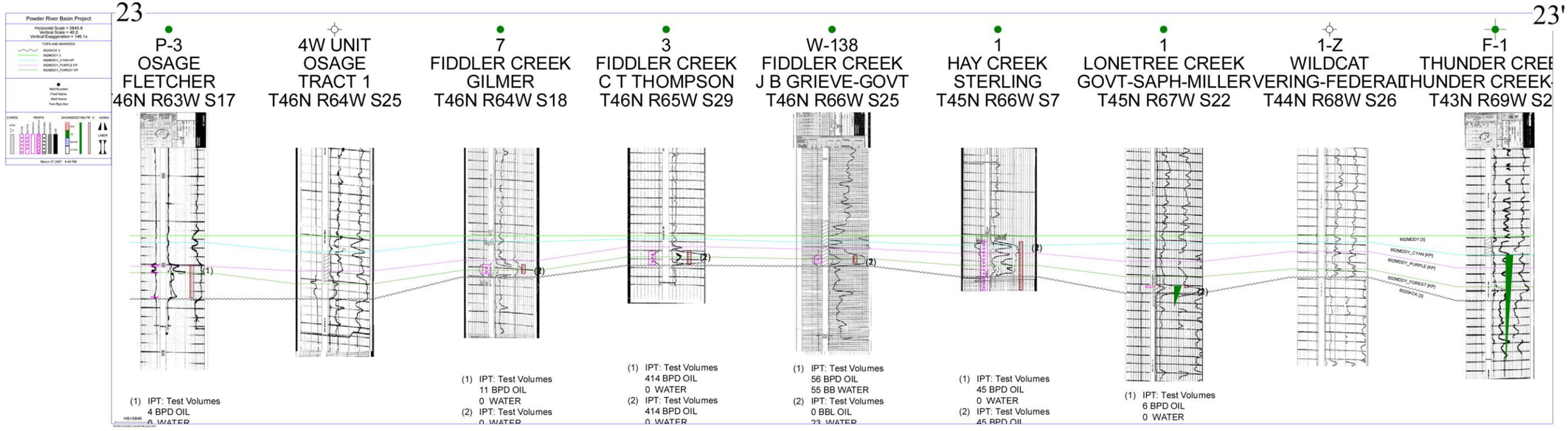

- Top Muddy Sandstone, all cross sections hung on this surface.
- Top Ute Member.
- Top Cyclone Member.
- Top Upper Recluse Member.
- Top Lower Recluse Member.
- Top Skull Creek Shale. Base of valley erosion.

Fiddler Creek Strike Section 19:

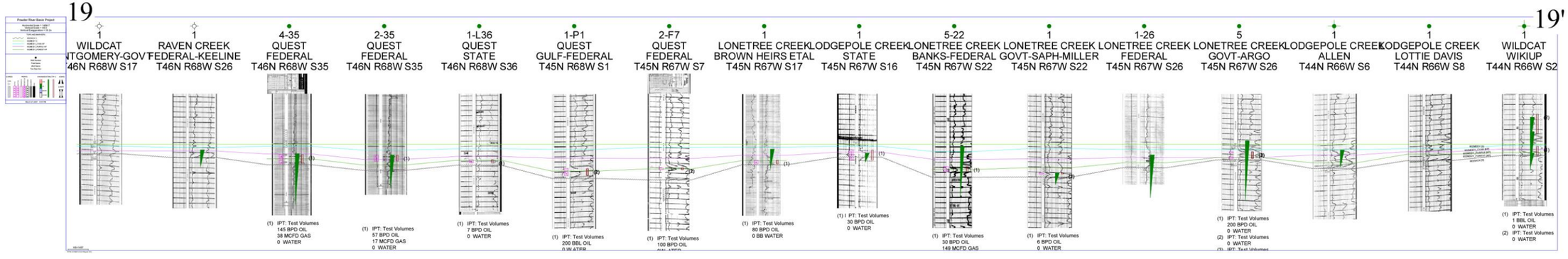

Fiddler Creek Strike Section 21:

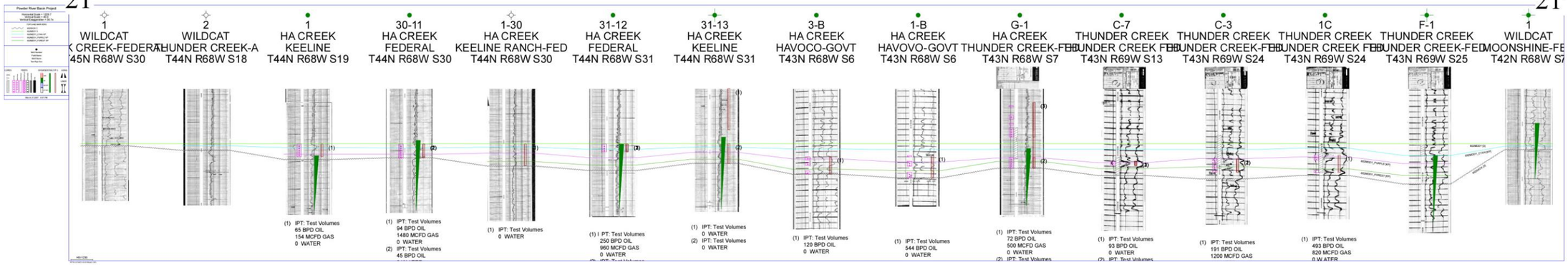

- Top Muddy Sandstone, all cross sections hung on this surface.
- Top Ute Member.
- Top Cyclone Member.
- Top Upper Recluse Member.
- Top Lower Recluse Member.
- Top Skull Creek Shale. Base of valley erosion.

Fiddler Creek Strike Section 22:

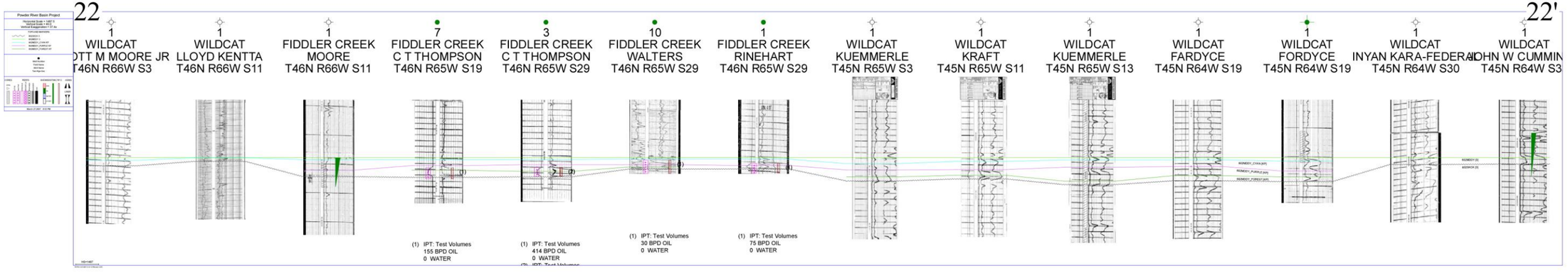

APPENDIX B:

CORE DESCRIPTIONS

Core Description Appendix Introduction

The cores are described form those available at the USGS Core Laboratory in Denver Colorado. The cores are labeled at the top of the core description by USGS Library number (e.g. S601), by RPI number from the well log (e.g. 4904521773), and by well name (e.g. Frank Walsh #2).

Bioturbation in the core is not broken out into specific ichnologies, but rather ranked on a scale of low bioturbation, labeled by +, to high bioturbation, labeled with +++. Low bioturbation (+) has between 5% and 20% of the core bioturbated, sedimentary structures are preserved and individual burrows are clearly identifiable. High bioturbation (+++) has between 60% and completely bioturbated. At this level of bioturbation sedimentary structures have been nearly, or completely destroyed and are unrecognizable. Individual burrows may be identifiable, but are likely too churned by subsequent bioturbation to be identified. Bioturbation is also sorted by whether the burrow is vertical or horizontal, whether the burrow is in sandstone or mudstone, and whether the burrow is filled with sandstone or mudstone.

Company Davis Oil / MSU
Well #1 Patrick Walsh Federal/ 4904521730
Field Clareton Core # S601
Date 18 Jan. 2008 By KHP Page 1 of 1
Location 41N 67W Sec. 20 Wyoming
Unit/Age Muddy Sandstone

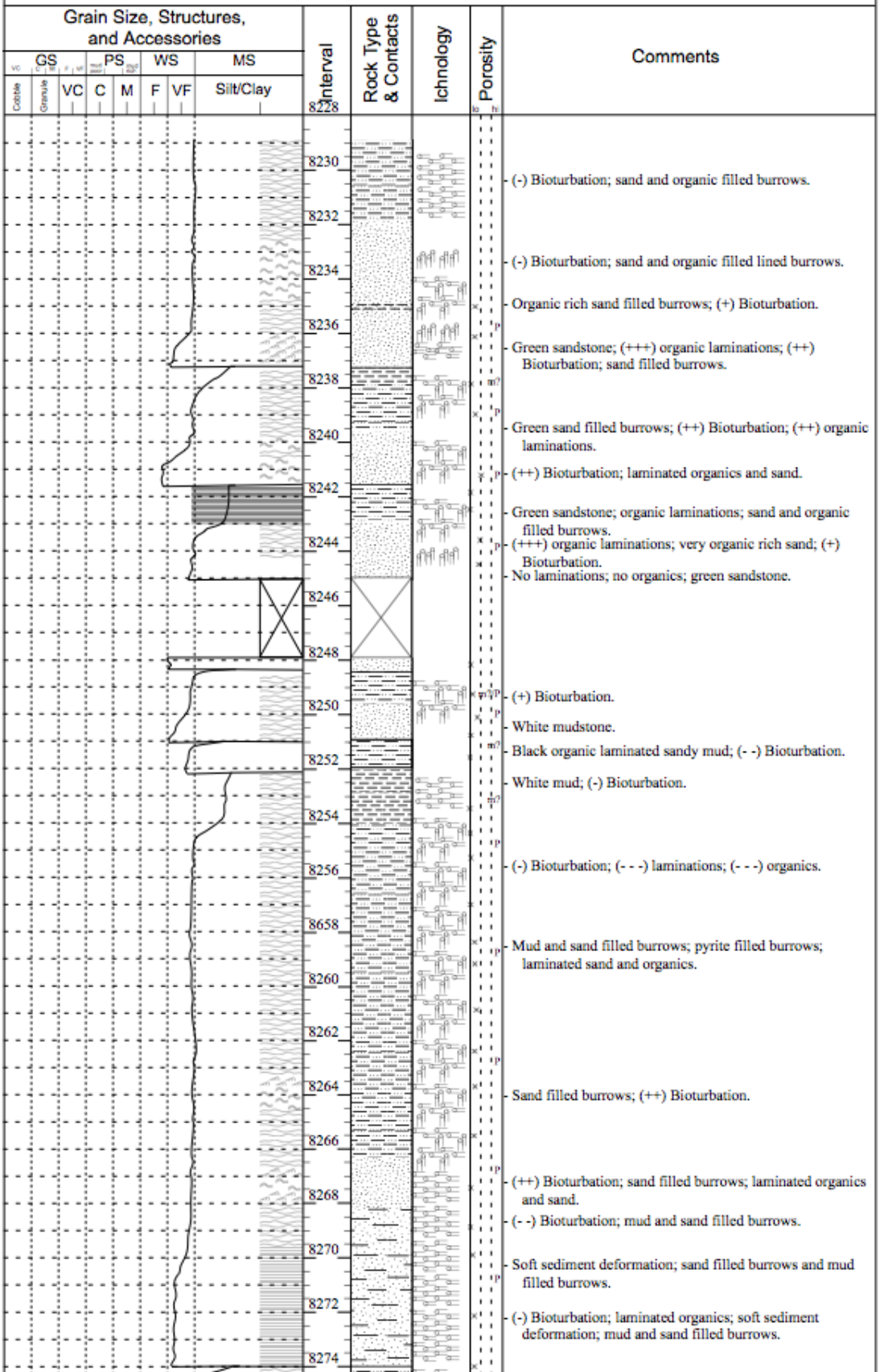

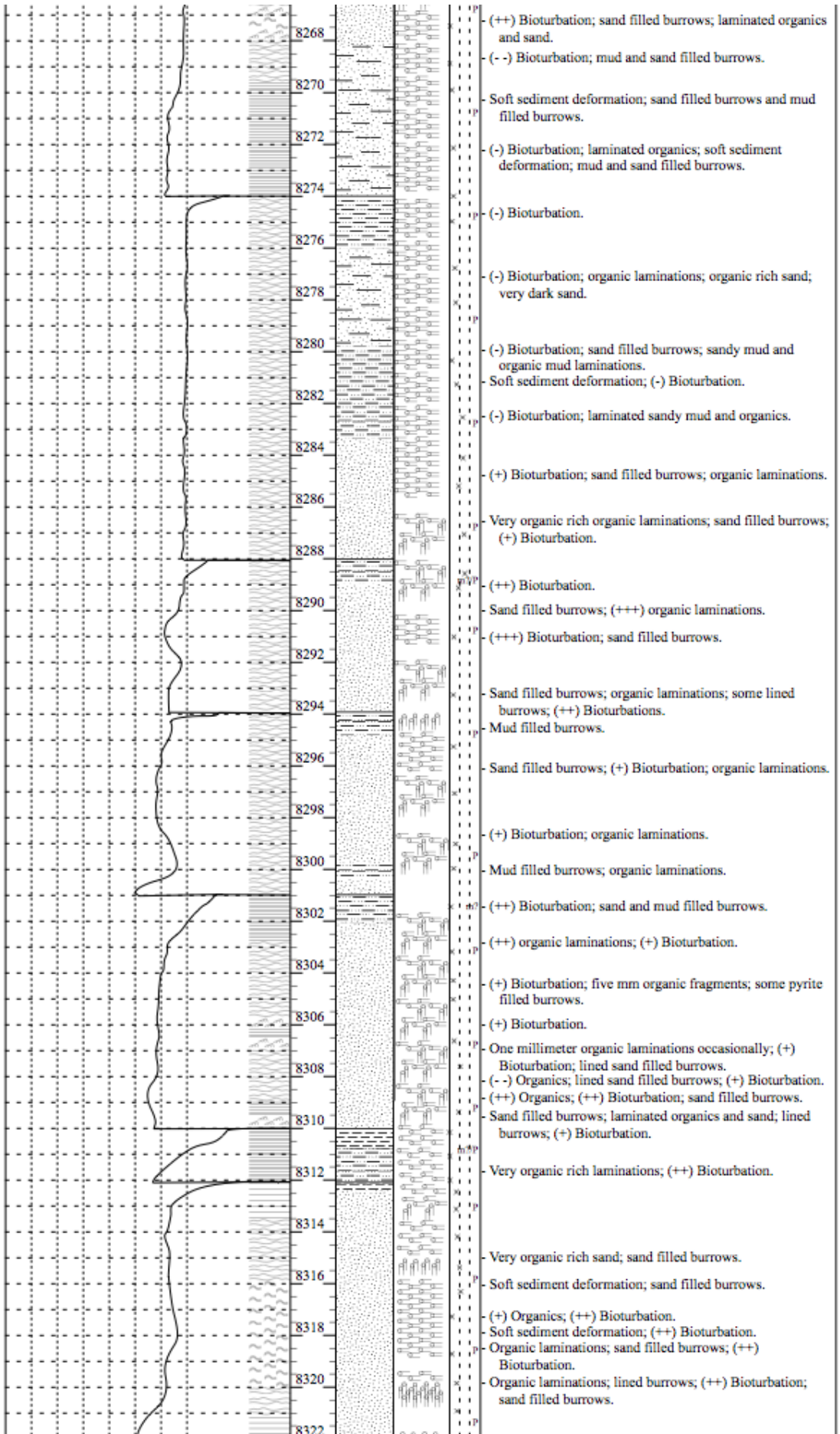
8268
8270
8272
8274
8276
8278
8280
8282
8284
8286
8288
8290
8292
8294
8296
8298
8300
8302
8304
8306
8308
8310
8312
8314
8316
8318
8320
8322
(++) Bioturbation; sand filled burrows; laminated organics and sand.
(- -) Bioturbation; mud and sand filled burrows.
Soft sediment deformation; sand filled burrows and mud filled burrows.
(-) Bioturbation; laminated organics; soft sediment deformation; mud and sand filled burrows.
(-) Bioturbation.
(-) Bioturbation; organic laminations; organic rich sand; very dark sand.
(-) Bioturbation; sand filled burrows; sandy mud and organic mud laminations.
Soft sediment deformation; (-) Bioturbation.
(-) Bioturbation; laminated sandy mud and organics.
(+) Bioturbation; sand filled burrows; organic laminations.
Very organic rich organic laminations; sand filled burrows; (+) Bioturbation.
(++) Bioturbation.
Sand filled burrows; (+++) organic laminations.
(+++) Bioturbation; sand filled burrows.
Sand filled burrows; organic laminations; some lined burrows; (++) Bioturbations.
Mud filled burrows.
Sand filled burrows; (+) Bioturbation; organic laminations.
(+) Bioturbation; organic laminations.
Mud filled burrows; organic laminations.
(++) Bioturbation; sand and mud filled burrows.
(++) organic laminations; (+) Bioturbation.
(+) Bioturbation; five mm organic fragments; some pyrite filled burrows.
(+) Bioturbation.
One millimeter organic laminations occasionally; (+) Bioturbation; lined sand filled burrows.
(- -) Organics; lined sand filled burrows; (+) Bioturbation.
(++) Organics; (++) Bioturbation; sand filled burrows.
Sand filled burrows; laminated organics and sand; lined burrows; (+) Bioturbation.
Very organic rich laminations; (++) Bioturbation.
Very organic rich sand; sand filled burrows.
Soft sediment deformation; sand filled burrows.
(+) Organics; (++) Bioturbation.
Soft sediment deformation; (++) Bioturbation.
Organic laminations; sand filled burrows; (++) Bioturbation.
Organic laminations; lined burrows; (++) Bioturbation; sand filled burrows.

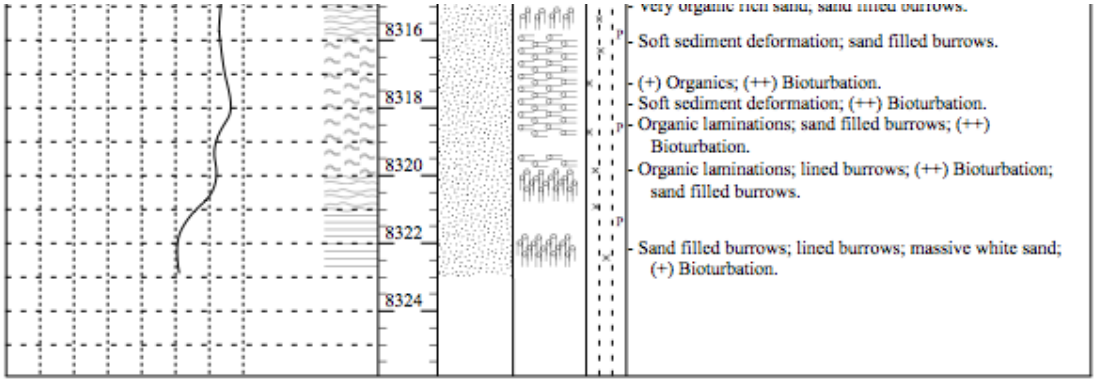
8316
8318
8320
8322
8324
Very organic rich sand; sand filled burrows.
Soft sediment deformation; sand filled burrows.
(+) Organics; (++) Bioturbation.
Soft sediment deformation; (++) Bioturbation.
Organic laminations; sand filled burrows; (++) Bioturbation.
Organic laminations; lined burrows; (++) Bioturbation; sand filled burrows.
Sand filled burrows; lined burrows; massive white sand; (+) Bioturbation.

Company Surtek Inc. / MSU
Well 12-5 LAK Ranch / 4904522507
Field Clareton Core # S311

Date 12 Dec. 2007 By KHP Page 1 of 1
Location 41N 61W Sec. 12 Wyoming
Unit/Age Mowry to Skull Creek

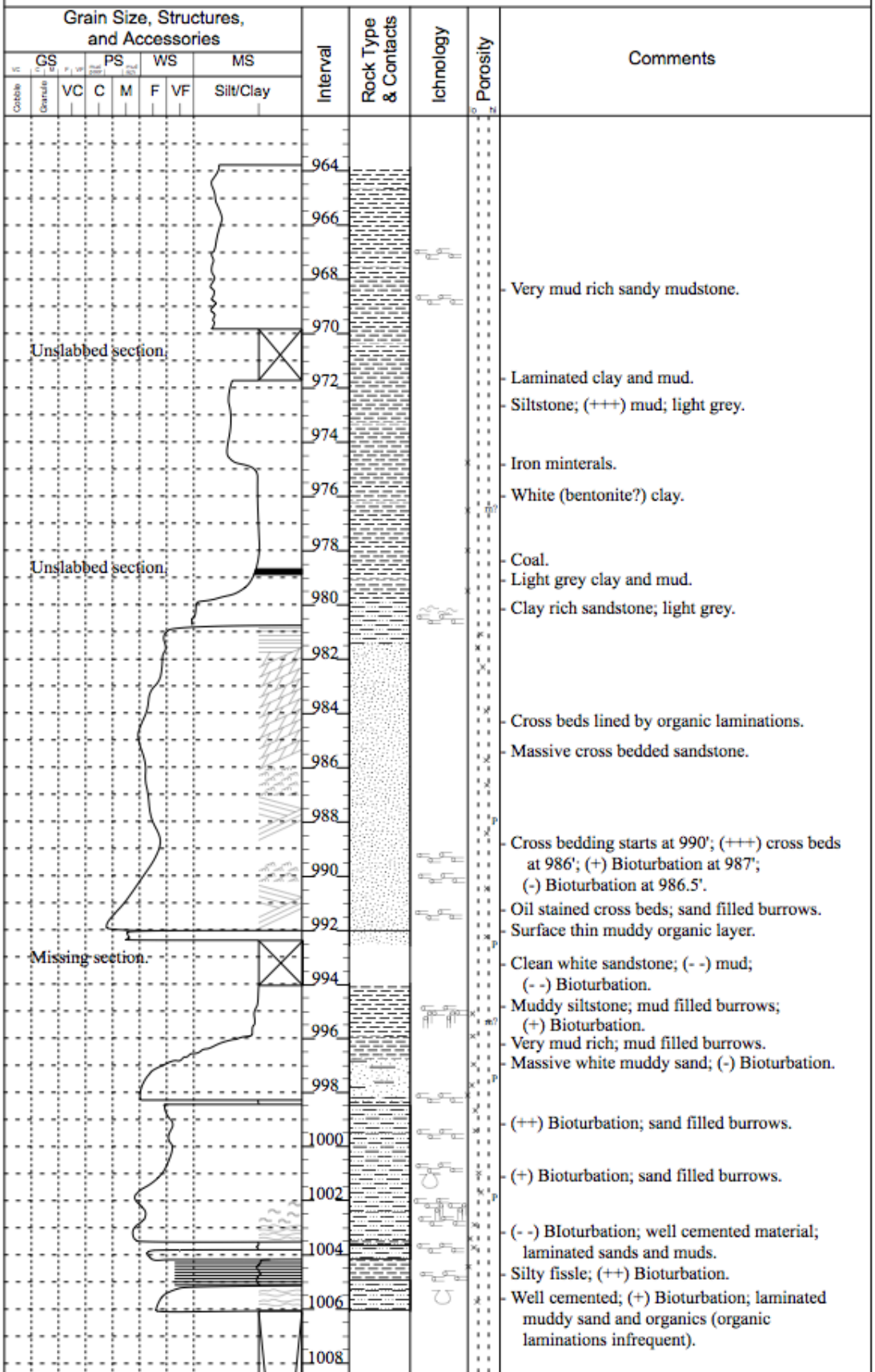

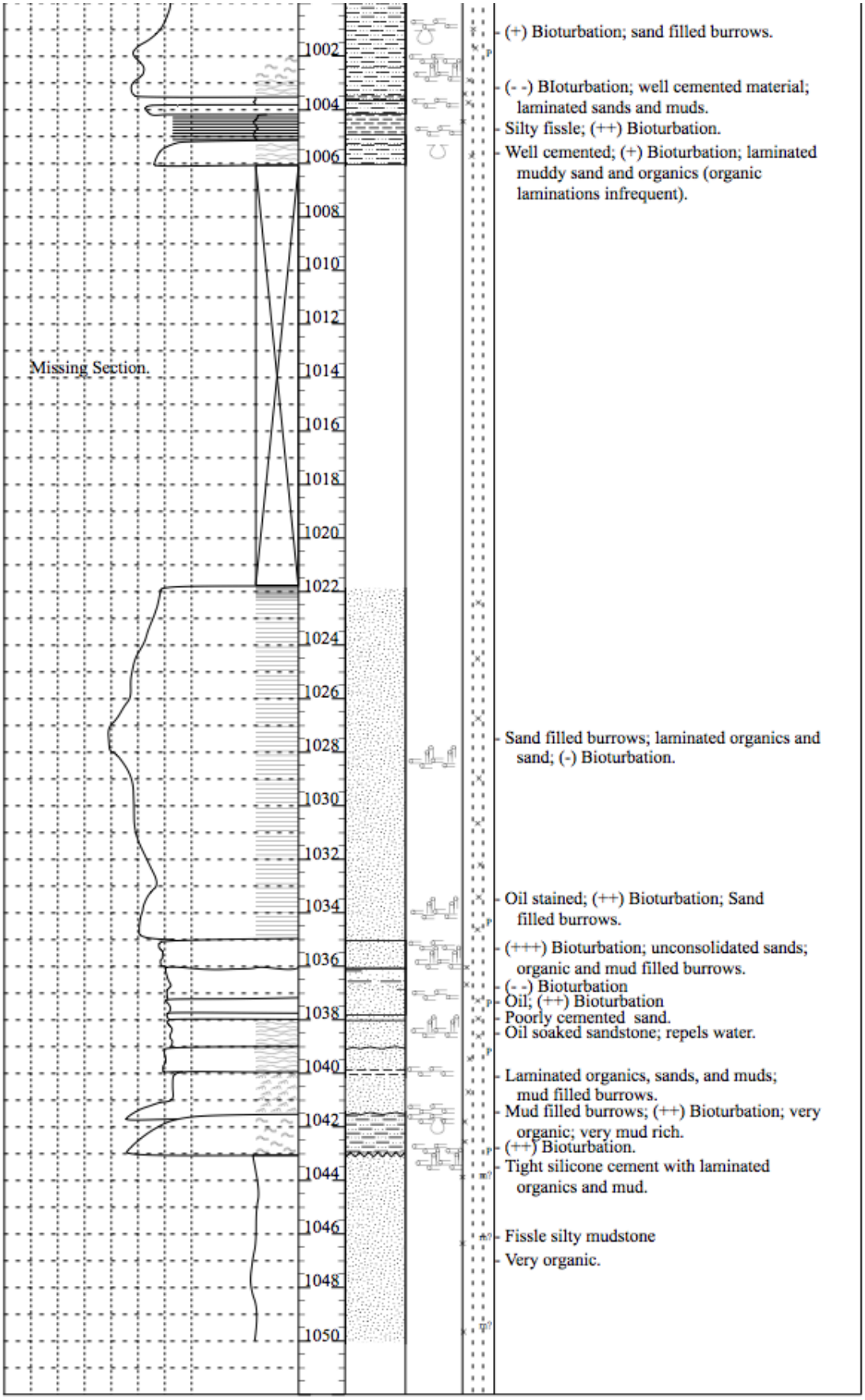
1002
1004
1006
1008
1010
1012
1014
1016
1018
1020
1022
1024
1026
1028
1030
1032
1034
1036
1038
1040
1042
1044
1046
1048
1050
Missing Section.
(+) Bioturbation; sand filled burrows.
(- -) BIoturbation; well cemented material; laminated sands and muds.
Silty fissle; (++) Bioturbation.
Well cemented; (+) Bioturbation; laminated muddy sand and organics (organic laminations infrequent).
Sand filled burrows; laminated organics and sand; (-) Bioturbation.
Oil stained; (++) Bioturbation; Sand filled burrows.
(+++) Bioturbation; unconsolidated sands; organic and mud filled burrows.
(- -) Bioturbation
Oil; (++) Bioturbation
Poorly cemented sand.
Oil soaked sandstone; repels water.
Laminated organics, sands, and muds; mud filled burrows.
Mud filled burrows; (++) Bioturbation; very organic; very mud rich.
(++) Bioturbation.
Tight silicone cement with laminated organics and mud.
Fissle silty mudstone
Very organic.

Company Davis Oil Company / MSU
Well #1 Bitterroot State / 4904521559
Field Clareton Core # R309

Date 17 Jan. 2008 By KHP Page 1 of 1
Location 41N 67W Sec. 28 Wyoming
Unit/Age Mowry to Skull Creek

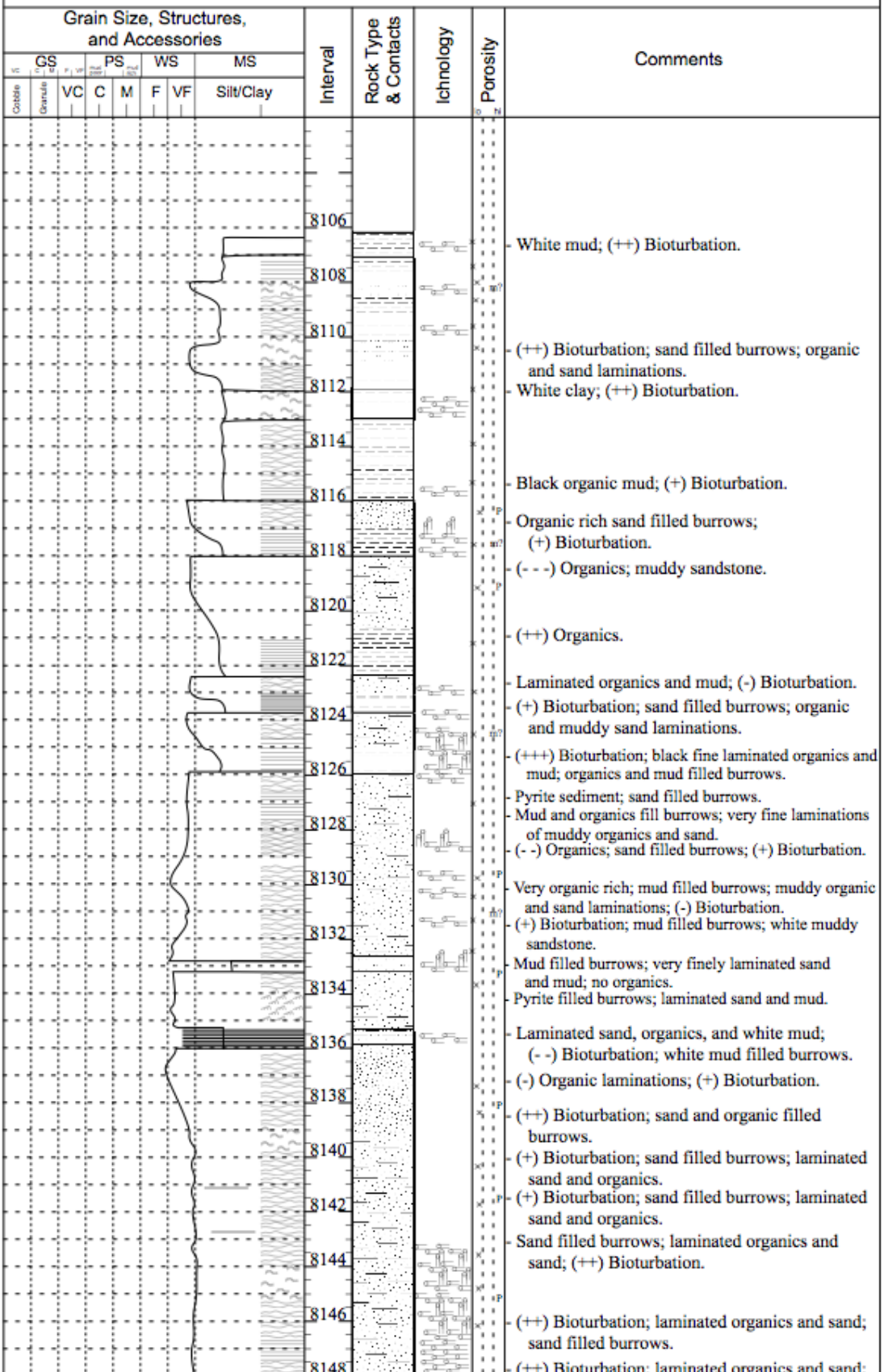

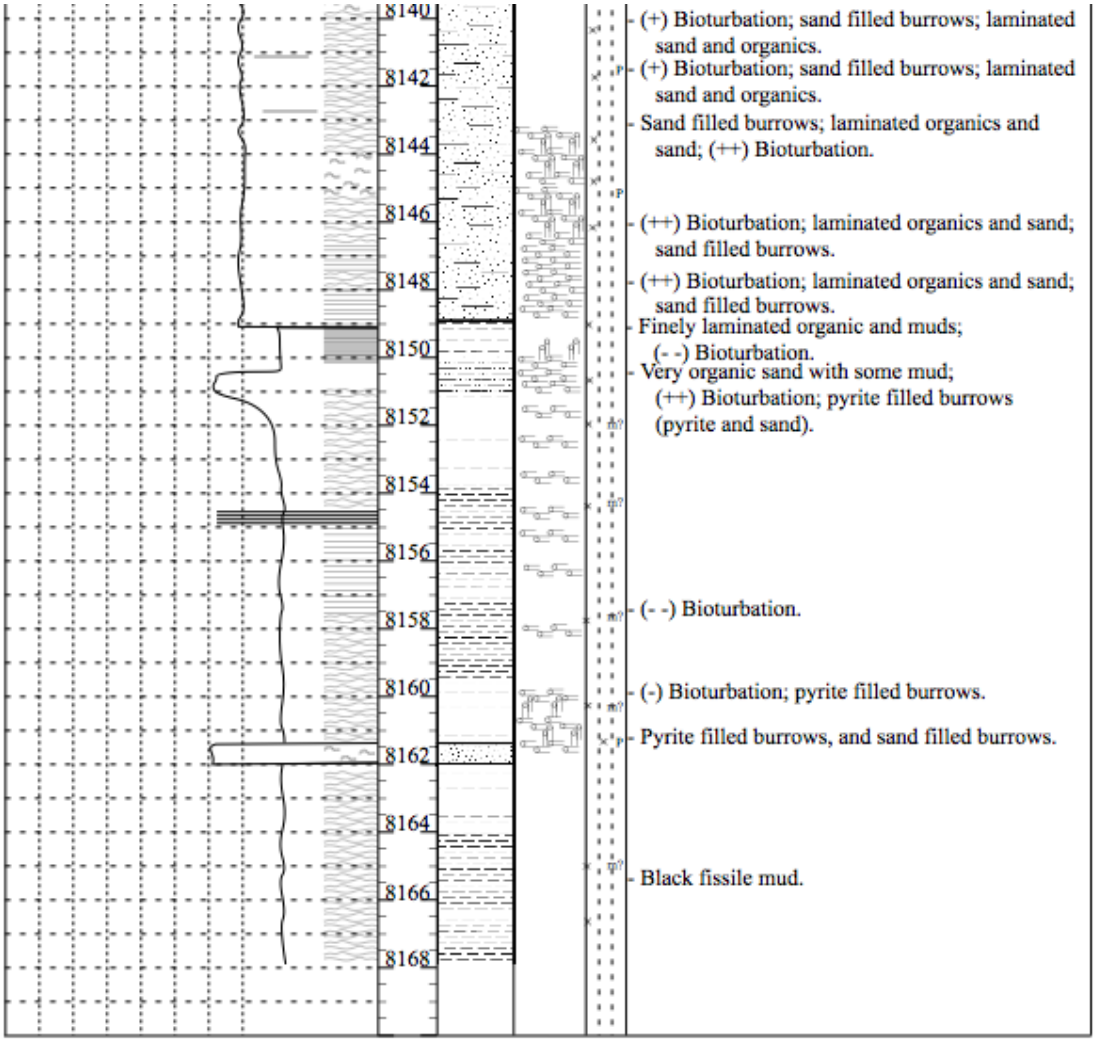
8140
8142
8144
8146
8148
8150
8152
8154
8156
8158
8160
8162
8164
8166
8168
- (+) Bioturbation; sand filled burrows; laminated sand and organics.
- (+) Bioturbation; sand filled burrows; laminated sand and organics.
- Sand filled burrows; laminated organics and sand; (++) Bioturbation.
- (++) Bioturbation; laminated organics and sand; sand filled burrows.
- (++) Bioturbation; laminated organics and sand; sand filled burrows.
- Finely laminated organic and muds; (- -) Bioturbation.
- Very organic sand with some mud; (++) Bioturbation; pyrite filled burrows (pyrite and sand).
- (- -) Bioturbation.
- (-) Bioturbation; pyrite filled burrows.
- Pyrite filled burrows, and sand filled burrows.
- Black fissile mud.

Company Enstar Petroleum / MSU
Well 41 Skull Creek Unit / 4904522253
Field Clareton Core # E366
Date 10 Dec. 2007 By KHP Page 1 of 1
Location 44N 62W Sec. 22 Wyoming
Unit/Age Muddy Sandstone (Newcastle)

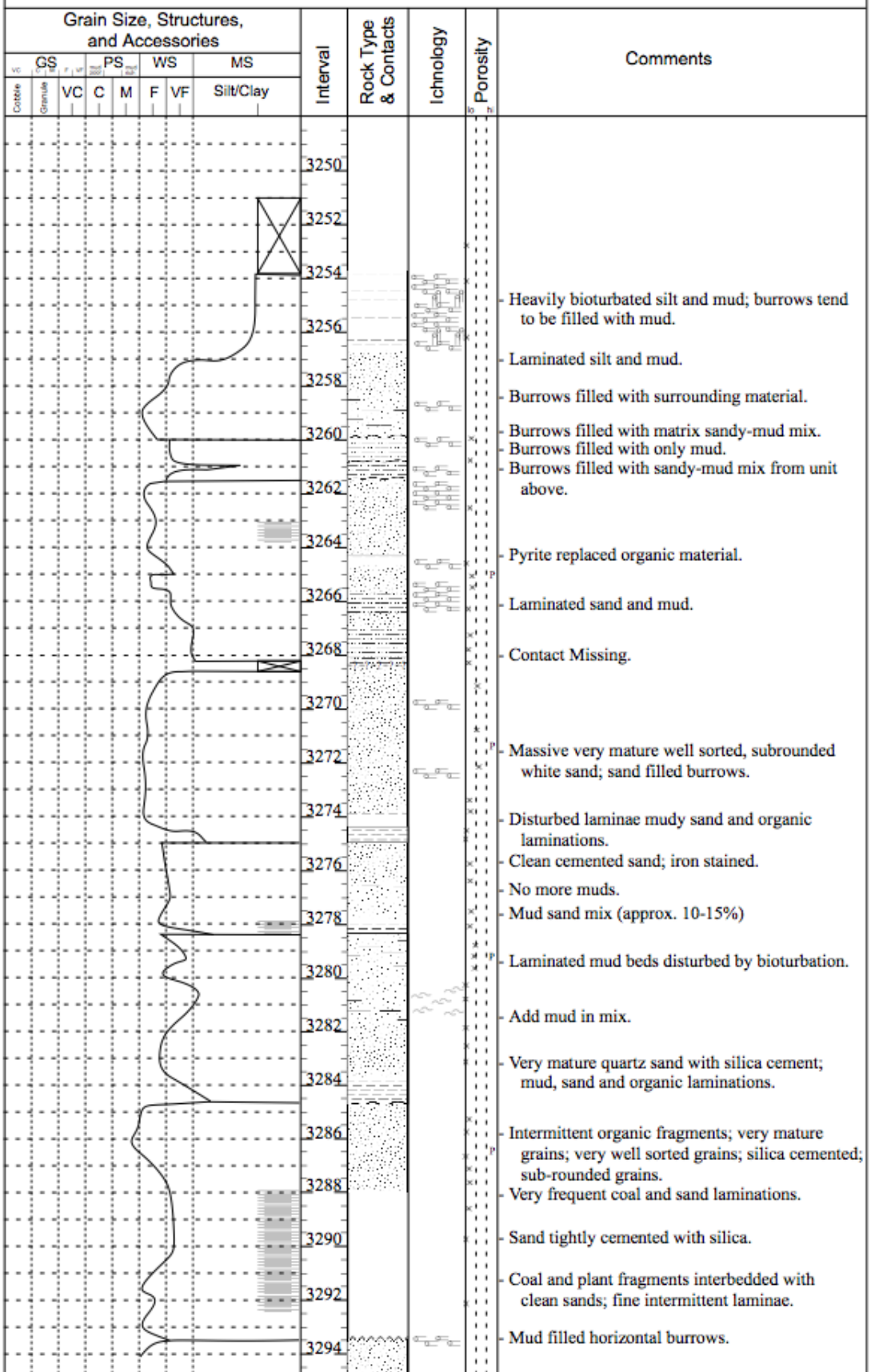

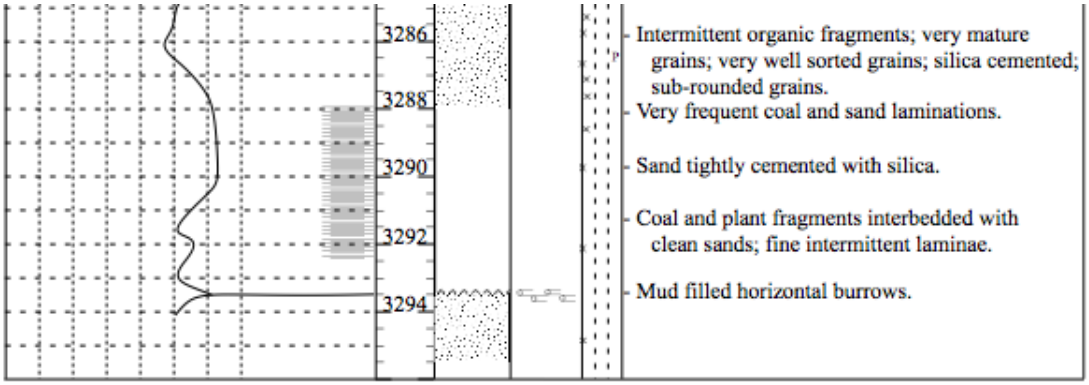
3286
3288
3290
3292
3294
Intermittent organic fragments; very mature grains; very well sorted grains; silica cemented; sub-rounded grains.
Very frequent coal and sand laminations.
Sand tightly cemented with silica.
Coal and plant fragments interbedded with clean sands; fine intermittent laminae.
Mud filled horizontal burrows.

Company Davis Oil / MSU
Well #1 Gregg Federal / 4904521737
Field Clareton Core # USGS/C811
Date 11 Dec. 2007 By KHP Page 1 of 1
Location 41N 66W Sec 8 Wyoming
Unit/Age Muddy Sandstone

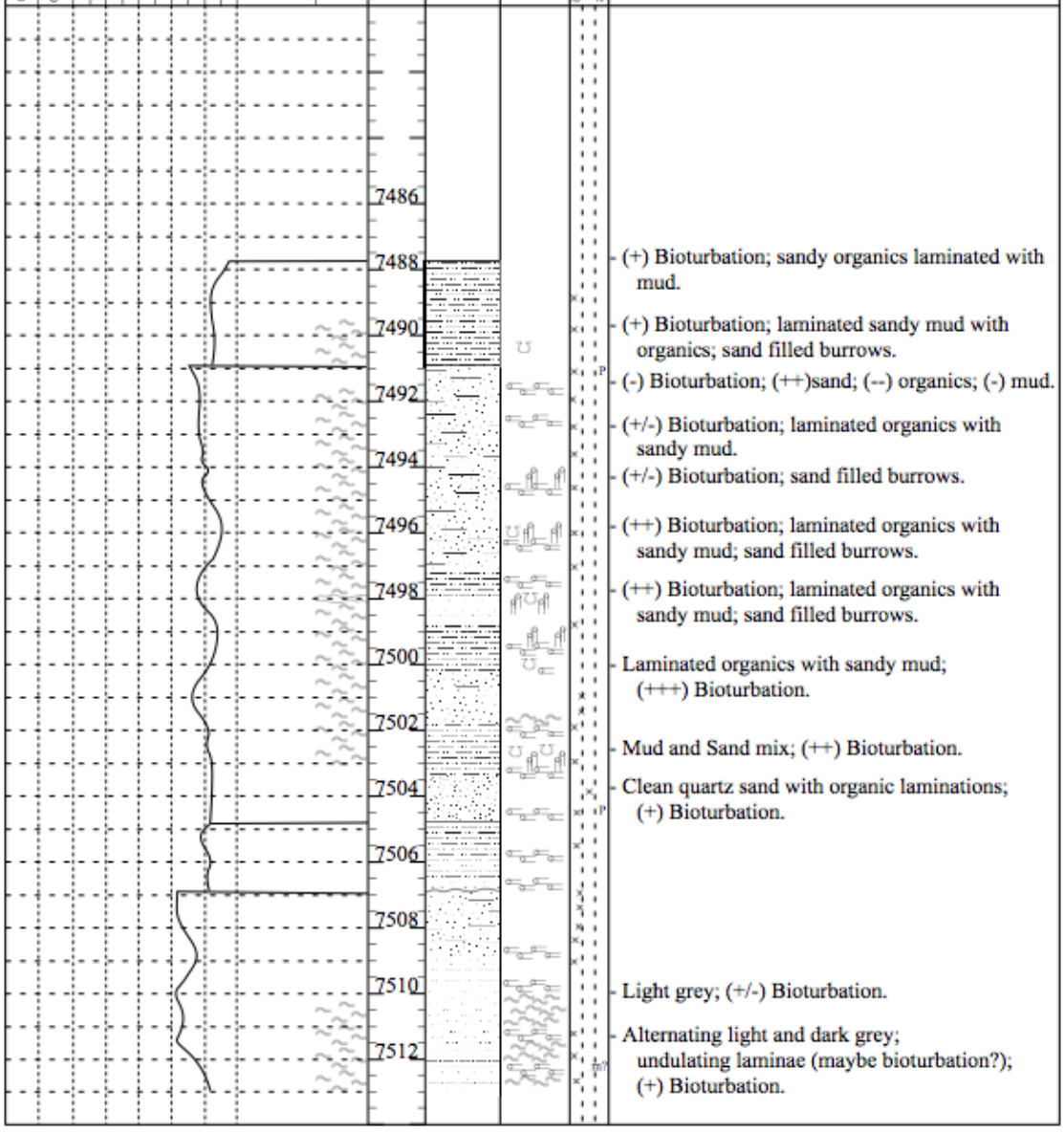

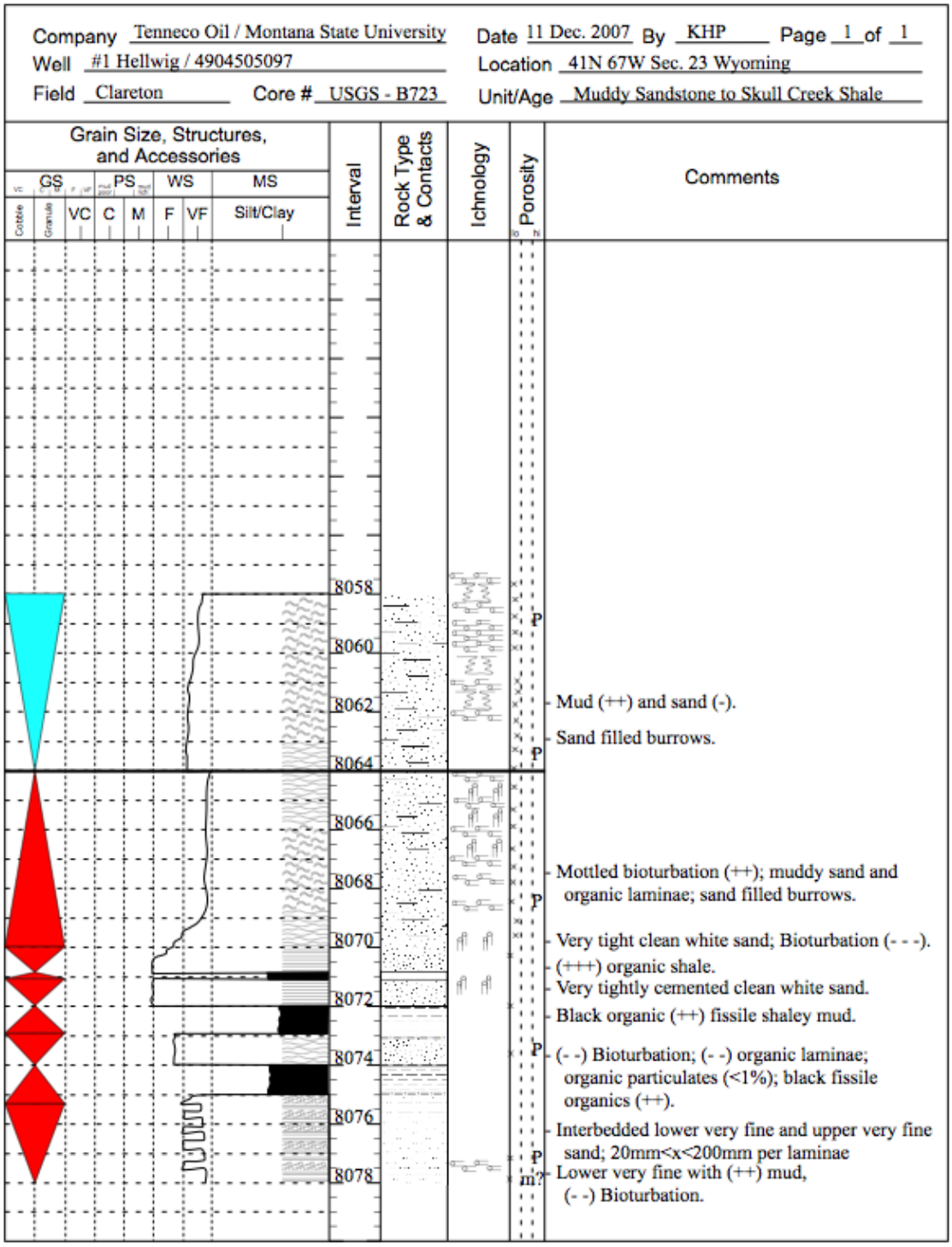
Company Tenneco Oil / Montana State University
Date 11 Dec. 2007 By KHP Page 1 of 1
Well #1 Hellwig / 4904505097
Location 41N 67W Sec. 23 Wyoming
Field Clareton
Core # USGS - B723
Unit/Age Muddy Sandstone to Skull Creek Shale
Grain Size, Structures, and Accessories
GS
PS
WS
MS
Cobble
Granule
VC
C
M
F
VF
Silt/Clay
Interval
Rock Type & Contacts
Ichnology
Porosity
Comments
8058
8060
8062
8064
8066
8068
8070
8072
8074
8076
8078
P
P
P
P
m?
Mud (++) and sand (-).
Sand filled burrows.
Mottled bioturbation (++); muddy sand and organic laminae; sand filled burrows.
Very tight clean white sand; Bioturbation (- - -).
(+++) organic shale.
Very tightly cemented clean white sand.
Black organic (++) fissile shaley mud.
(- -) Bioturbation; (- -) organic laminae; organic particulates (<1%); black fissile organics (++).
Interbedded lower very fine and upper very fine sand; 20mm<x<200mm per laminae
Lower very fine with (++) mud, (- -) Bioturbation.

Company Tenneco / MSU
Well #1 Sears USA / 4904520579
Field Clareton Core # B424
Date 17 Jan. 2008 By KHP Page 1 of 1
Location 41N 67W Sec 13 Wyoming
Unit/Age Muddy Sandstone

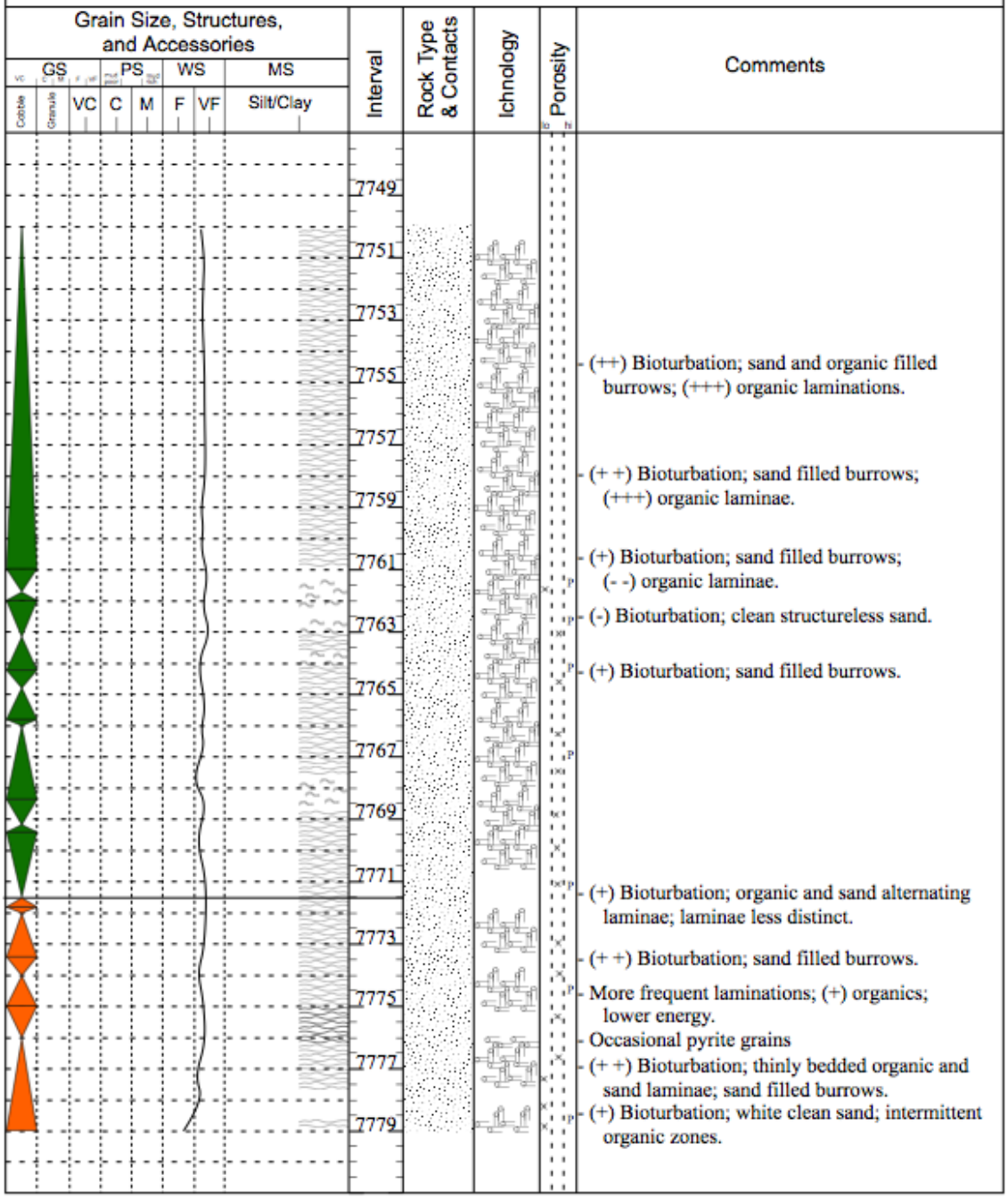

Company Tenneco Oil / MSU Date 12/12/07 By KHP Page 1 of 1

Well # 4-A Hellwig / 4904520565 Location 41N-67W Sec 13, WY

Field Clareton Core # USGS / B377 Unit/Age Muddy Sandstone

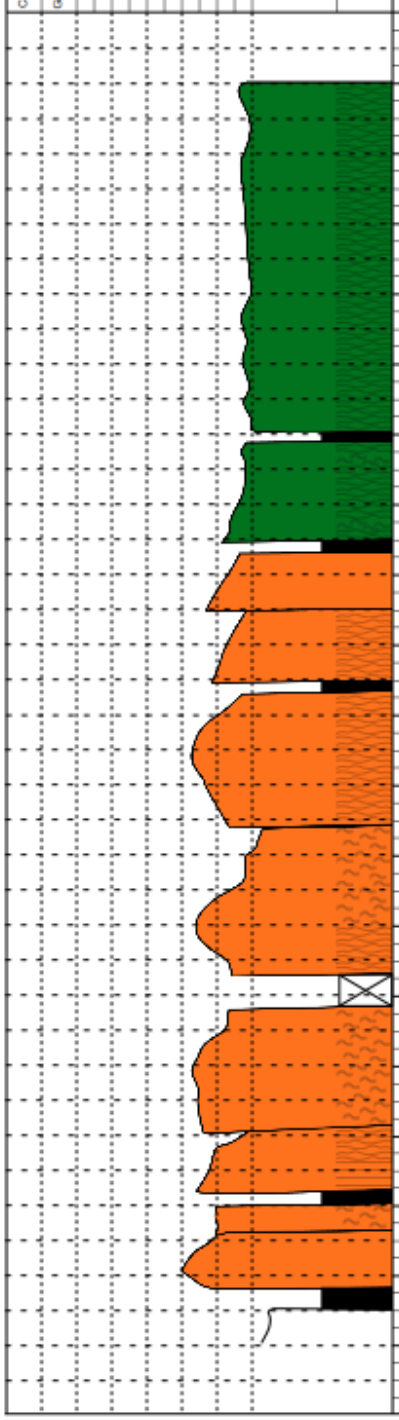

Comments

- Very finely laminated organic rich mud and sand; sand filled burrows.
- Very organic rich; (++) Bioturbation.
- (+) Bioturbation; laminated organic rich mud and sand.
- Clean sand; (- -) Bioturbation.
- Intermittent organic rich mud and sand laminations.
- (++) Bioturbation; sand filled burrows.
- Laminated organic rich mud and sand; sand filled burrows; (+) Bioturbations.
- Massive clean sandstone; (- -) organic fragments (1mm>).
- Lined and unlined burrows filled with sand.
- Tight clean sandstone 2mm (>) organic fragments.
- Very fine laminated sand, mud and organics.
- Very tightly cemented sandstone.
- Clean sandstone; intermittent unconsolidated organic laminations.
- Clean sandstone; lined sand filled burrows; intermittent minor organic laminations.
- (++) Organic fragments (<1mm); sand filled burrows.
- Black fissile shale.
- (+) Bioturbation; (-) laminated mud; organic fragments; sand filled burrows.
- Massive white sandstone; mud filled Burrows.
- Black laminated silt and sandstone.

Company Davis Oil / Montana State University Date 11 Dec 2007 By KHP Page 1 of 1
Well #1 Frog Creek State / 4900921092 Location T41N R68W SEC 36
Field Clareton Core # USGS A647 Unit/Age Mid-Muddy to Skull Creek

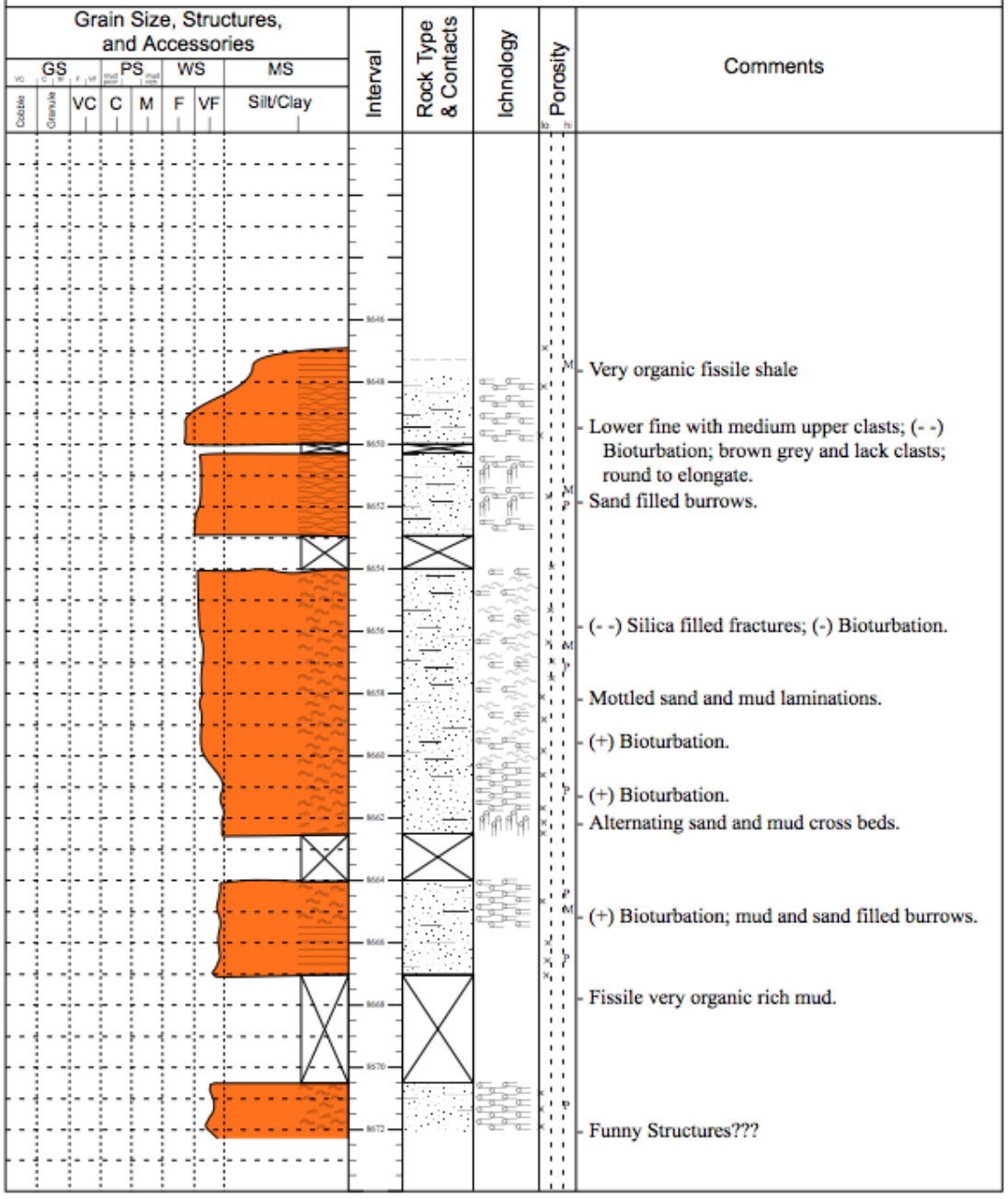

Company Union Oil / MSU
Well 1-J7 Federsal Weinehel / 4904520823
Field Fiddler Creek Core # A019

Date 15 Jan. 2008 By KHP Page 1 of 1
Location 45N 67W Sec. 7 Wyoming
Unit/Age Muddy - Below Skull Creek to Above Cyan

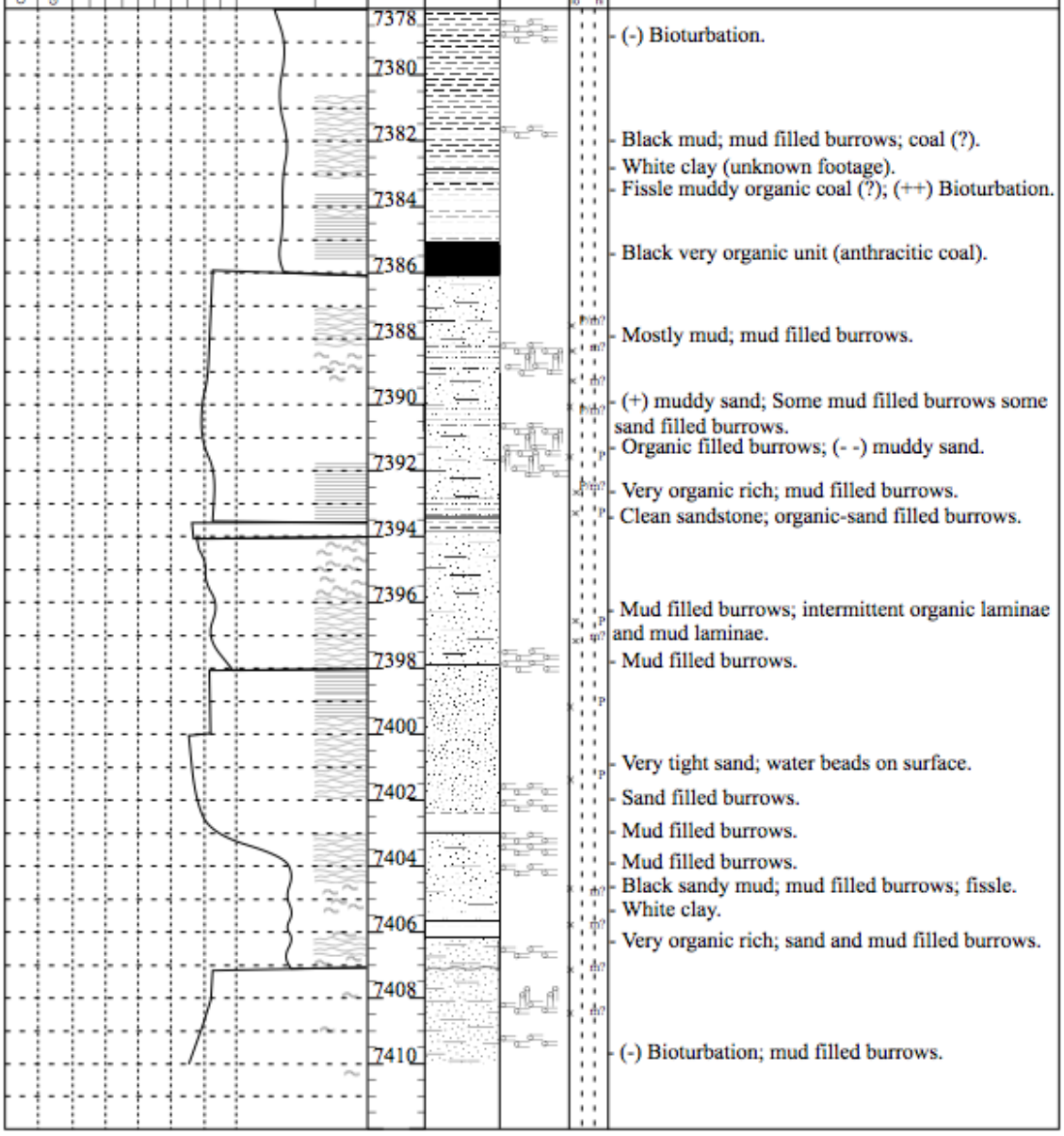

Company Union Oil / MSU
Well Cook USA #1 - H12 / 4904520781
Field Fiddler Creek Core # A016

Date 16 Jan. 2008 By KHP Page 1 of 1
Location 45N 68W Sec 12 Wyoming
Unit/Age Muddy Sandstone

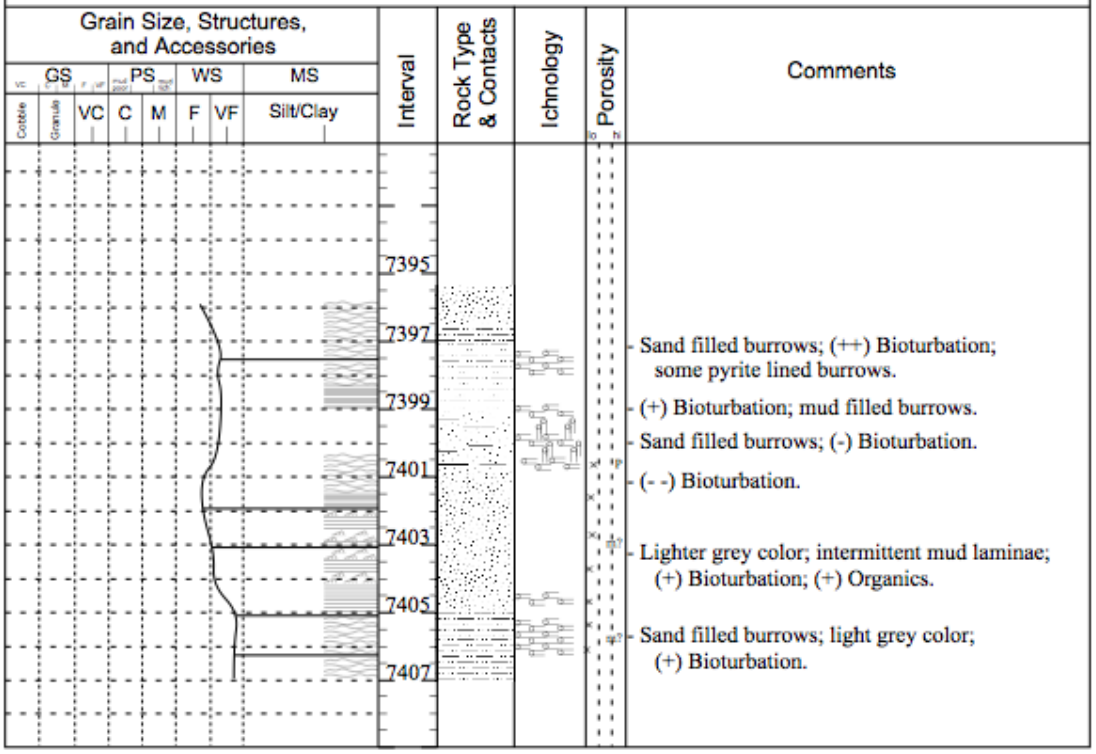

Appendix B

Table showing statistics generated from Petra database and resulting analog facies values from running IF-THEN script

Facies	Name	grainsize	sorting	primary struct	bed/bedset thickness (cm)	NTG (%)	perm		Φ	
SS	Sandstone	> 0.0625								
MR	Mudrock	< 0.0625								
CL	Claystone									
CM	Cemented									
SS1	Coarse lag	med SS - granule	poor	aligned grains, planar lam	<10	100	0.1	100	12	20
SS2	Clast-rich to conglom SS	Med - coarse SS	poor	Structureless, planar lam	20-50	100	0.1	0.3	4	6
SS3	Amalgamated cross-bedded SS	UF - coarse SS	mod well - well	Trough X cross	>100	100	0.01	20	2	14
SS4	Cross bedded SS	UF - coarse SS	mod well - well	Trough X cross	<100	100	0.1	150	4	23
SS5	Muddy cross beds	F-Med SS	mod - mod poor	Trough X cross, mud drapes	20-80	100	0.05	0.1	4	6
SS6	Soft sed deformed SS	F-Med SS	mod - mod poor	dewatering/load structures	20-100+	95	0.02	0.05	2	4
SS7	Structureless SS	Uf - med SS	mod - mod poor	structureless	20-100+	100	0.01	50	2	17
SS8	Plane parallel SS	Uf - med SS	mod well - well	planar laminations	10-50	100	0.01	150	2	15
SS9	Swaley SS	Fine SS	mod well - well	plane parallel to low angle strat with reactivation surfaces	20-40	100	0.1	0.1	3	12
SS10	Hummocky SS	Fine SS	mod well - well	plane parallel to low angle strata	10-30	100	0.01	150	4	18
SS11	Isolated SS	VF - Fine SS	mod - well	plane parallel, structureless	5-20	100	0.01	40	1	11
SS12	Faintly stratified amalgamated SS	F SS	mod - mod poor	Fait plane parallel, wispy discontinuous mud drapes	100-200	95	0.01	2	1	14
SS13	Interbedded deformed/bioturbated SS	VF - Fine SS	mod poor - poor	Burrows, loads, rip up clasts	2-5, 1-2	85	0.01	1	2	12
SS14	Amalgamated bioturbated SS	VF - Fine SS	mod poor - poor	Diverse and abundant burrows	10-200+	95	0.01	2	5	12
SS15	Ripple laminated SS	VF - Fine SS	well	Ripple laminations	1-20	100	0.6	50	1	23
SS16	Interbedded thinly laminated SS with mud drapes	VF - Fine SS	mod well - well	Planar laminated, mud drapes	1-3, 100+	70-90	0.01	100	2	20
SS17	Bioturbated SS and mud	VF - Fine SS	mod poor - poor	Diverse and abundant burrows	20-200+	80-100	0.1	0.1	13.5	13.5
MR19	Bioturbated mud and SS	Shale - silt				60-80	0.01	15	8	17
MR20	Shale with thin SS beds	Shale - silt				<50	0.08	2	2	2
CM23	cemented	variable	na							

Facies	GR-low	GR-hi	RHOB-lo	RHOB-hi	NPHI-lo	NPHI-hi	DT-lo	DT-hi
SS	30	80	2.3	2.5	0.10	0.17	60	74
MR	80	150	2.5	2.7	0.17	0.30	74	95
CL	150	400	2	2.3	0.30	0.50	95	150
CM	0	60	2.7	3	0.00	0.10	0	60
SS1	40	80	2.35	2.42	***11.5***	***15.5***	***66***	***74***
SS2	35	55	***2.55***	***2.60***	***8.5***	***12.5***	***60***	***65***
SS3	30	80	***2.43***	***2.54***	***10.5***	***16.5***	***60***	***70***
SS4	40	85	***2.46***	***2.53***	***10.5***	***15***	***69***	***75***
SS5	45	55	2.55	2.65	5	10	60	65
SS6	35	45	2.63	2.65	5	7	55	60
SS7	30	85	***2.45***	***2.58***	***7***	***15***	***66.5***	***78***
SS8	30	85	***2.46***	***2.57***	***10.5***	***18***	***71.5***	***77.5***
SS9	40	85	***2.48***	***2.55***	***13.5***	***16.5***	***67.5***	***72***
SS10	40	85	2.40	2.63	***12***	***15***	62	70
SS11	35	85	***2.47***	***2.56***	***9.5***	***16.5***	***71***	***81***
SS12	35	95	***2.49***	***2.58***	***9.5***	***15.5***	***67.5***	***74***
SS13	40	85	***2.48***	***2.62***	***10.5***	***16***	***68.5***	***74***
SS14	65	100	2.39	2.47	***11.5***	***14.5***	75	80
SS15	53	100	***2.39***	***2.56***	***12***	***21***	***65***	***80***
SS16	53	90	***2.43***	***2.63***	***12.5***	***21***	***72.5***	***81***
SS17	80	105	***2.54***	***2.61***	***14.5***	***18.5***	***65***	***80***
MR19	85	110	2.46	2.56	18	26	70	85
MR20	85	115	***2.43***	***2.61***	***18***	***26***	70	87
CM23	30	60	2.45	2.70	5	11	40	70

		GR-low	GR-hi	RHOB-lo	RHOB-hi	NPHI-lo	NPHI-hi	DT-lo	DT-hi	REST-lo	REST-hi
2	Stratified or thick bedded SS Higher energy facies	30	85	2.4	2.7	0.1	0.165	60	75	3	200
3	Interbedded or bioturbated SS/mud Lower energy facies	60	100	2.4	2.7	0.12	0.18	70	120	1	100
4	Interbedded or bioturbated mud/SS	85	400	0	2.625	0.16	1	70	120	0	50
1	Cemented SS	0	60	2.45	3	0	0.11	0	70	1	299

Appendix C

Transition from ZERT I to ZERT II

ZERT II FY2010 Quarter 4 Report

ZERT II Quarterly Technical Report
Investigating the Fundamental Scientific Issues Affecting the Long-term Geologic Storage of Carbon Dioxide

Second Revised Fiscal Year 2010 Quarter Four Report: July 1 – September 30, 2010

DOE Program Officer: William Aljoe
DOE Award #: DE-FE0000397
Zero Emission Research and Technology (ZERT II)
Principal Investigator: Lee H. Spangler –Montana State University

Report Date: February 7, 2011

Executive Summary

This report will cover the ZERT II activities for this past quarter and address which tasks were brought forward from the ZERT I project.

The goal of the ZERT Center is to develop a comprehensive approach to measurement, monitoring, mitigation, and risk assessment for geologic sequestration. This entails the fundamental studies of geophysical and geochemical interactions of CO_2 with formation waters and minerals, and development of individual new monitoring methods, as well as strategic use of suites of methods, parameterization of potential leakage/seepage mechanisms and assessment of reservoirs relevant to these mechanisms.

Effectively modeling elastic-plastic deformation is one of the critical needs in porous media fluid flow applications including CO_2 sequestration. LANL has developed an approach for modeling plastic deformation using von Mises plasticity model and have developed an algorithm in MATLAB. They are currently in the process of implementing this model in FEHM and have also initiated development of stress-dependent permeability models in FEHM.

Due to the late arrival of funding, LANL's ZERT activities were not initiated until the FY2010 Quarter 2. This quarterly report focuses on the work related to advances in the coupled flow-stress simulation capabilities in LANL's FEHM simulator, recent modeling work related to their Chimayo analog studies on CO_2 impact on shallow aquifer geochemistry and lattice Boltzmaan simulations for multi-phase CO_2-brine flow in porous media. Results of the Chimayo work were presented at the 10th Greenhouse Gas Technology Conference in Amsterdam.

LBNL simulated a large-scale CO_2 migration and fault-leakage test problem using the new TOUGH2/ECO2M which can simulate all phase combinations of CO_2; modeled cyclic leakage phenomena associated with phase interference and Joule-Thomson cooling; completed the sample problems and user guide to accompany the beta release of TOUGHREACT V2 that occurred in FY10; carried out accumulation chamber soil-gas CO_2 flux surveys at the MSU release facility; published a paper on

modeling pore scale phenomena and microtomography. LBNL's laboratory and modeling studies of pore occupancy demonstrated that heterogeneity affects CO_2 invasion at multiple scales.

LLNL completed the analysis of the 2009 field studies which used remote sensing techniques and real-time soil CO_2 probes to detect the concentrations and isotopic values and influence of CO_2 leakage on biogeochemical soil processes and vegetation at the MSU field site, including completion and publication of a peer-review technical paper.

Appendices

Los Alamos National Laboratory ZERT II FY2010 Quarter 2 Report
Los Alamos National Laboratory ZERT II FY2010 Quarter 3 Report
Los Alamos National Laboratory ZERT II FY2010 Quarter 4 Report
Lawrence Berkeley National Laboratory ZERT II FY2010 Quarter 4 Report
Lawrence Livermore National Laboratory ZERT II FY2010 Quarter 4 Report
Pacific Northwest National Laboratory ZERT II FY2010 Quarter 4 Report

Description of Tasks discontinued in ZERT I and Continued in ZERT II

Biofilms and Biomineralization

This ZERT project is conducting both batch as well as packed sand column experiments aimed at assessing the potential of microorganisms for enhancing Carbon Capture and Storage (CCS) by plugging porous media flow paths with biofilm and biomineralized calcium carbonate. The goal of these experiments is to develop an injection strategy which results in a spatially uniform distribution of calcium carbonate along the flow path. During ZERT I significant progress has been toward this goal by demonstrating uniform biomineralization plugging along the flow path of a 61 cm long packed sand column (along with other supporting experiments described in the tasks below). Several ZERT I tasks will be continued under ZERT II as indicated. The method of injecting the various constituents into the column as ultimately developed under ZERT I and ZERT II represents a starting point for a field injection strategy at CCS projects.

ZERT I Tasks

- Observation and quantification of biomineralization phenomena (i.e. ammonia production and calcite precipitation) in model core under high pressure (1150 psi) and elevated temperature (33 degrees C). *Status: Task completed January 2008.*
- Batch screening to identify ureolytic bacteria capable of using nitrate as an electron acceptor. S*tatus: Task completed September 2009.*
- Development of kinetic parameters for biofilm and biomineralization in porous media modeling conducted at the University of Stuttgart. *Status: Completed October 2009*
- Observation and characterization of biomineralization in a 2.54 diameter, 6 cm long packed sand column under pulsed flow conditions. *Status: Task completed December 2009.*
- Observation and characterization of biomineralization in a 2.54 cm diameter, 61 cm long packed sand column. First run completed June 2010, second run completed July 2010. *Status: This task is continued under ZERT II in order to continue with more sand column experiments. The ultimate goal of this task is to develop an optimized protocol for creating biomineral deposits of uniform density along the flow path through porous media. This goal was not reached during ZERT I and will therefore be continued under ZERT II, subtask 2.2.*

ZERT II Tasks

- Conduct experiments wherein CO_2 biomineralization deposits on flat coupons and in porous media bead packs are challenged with 1) formation brine and 2) supercritical CO_2 ($ScCO_2$). These challenge experiments will determine if the biomineralization deposits (i.e. calcium carbonate) are adversely affected by exposure to either challenge fluid. Also we will determine if the challenges significantly increase the porous media permeability in biomineralized bead packs. New subtask under ZERT II.
- Develop method to control the deposition rate of biomineralized calcium carbonate with distance along a porous media flow path. A series of packed bead column

experiments will be conducted in which key parameters governing biomineralization will be varied so as to achieve a uniform thickness of calcium carbonate with distance along the flow path. Key parameters which will be examined include column flow rate (pulsed vs. continuous), along with temporal sequences of the addition of urea (to manipulate pH increase), and the addition of calcium to initiate calcium carbonate precipitation. We hypothesize that these experiments will determine a procedure which will facilitate control of the rate and extent of mineral deposition along the flow path. Continuation of ZERT I task.

Ongoing research at the CBE has identified at least two microbially mediated processes by which CO_2 can possibly be sequestered in a mineral matrix or in biomass. The following subtasks will develop strategies for microbially-mediated sequestration of CO_2.

- Optimize biomineralization of isotopically labeled CO_2 carbon under variable head space pressure. Preliminary experiments show that the carbon contained in isotopically labeled CO_2 can be incorporated into the calcium carbonate mineral matrix during ureolytic biomineralization. This subtask will examine how the percentage of labeled CO_2 carbon appearing in deposited calcium carbonate varies with head space pressure in batch systems. New subtask under ZERT II.
- Evaluate the potential for coal-bed mediated CO_2 sequestration. Preliminary experiments indicate that by applying a carefully designed nutrient recipe coal can be stimulated resulting in a more diverse and active microbial biofilm community resulting in increased CO_2 uptake and enhanced methane production. Specifically this subtask will evaluate the rates of CO_2 uptake and methane production in batch experiments containing nutrient, coal slurry, and microbial inoculum recovered from groundwater wells in coal formations in the Powder River Basin in eastern Montana. New subtask under ZERT II.
- Construct a system capable of flowing supercritical fluids through the bore of the magnet of the NMR spectrometer. New subtask under ZERT II.
- Evaluate transport phenomena for brine and supercritical CO_2 in circular cross section cylindrical tubes using magnetic resonance techniques. Magnetic resonance microscopy (MRM) techniques will be used to determine propagators over a range of observation times, velocity maps, relaxation maps, and spin echo imaging. New subtask under ZERT II.
- Evaluate transport phenomena for brine and supercritical CO_2 in a bead pack or other model porous media. Observations will be made on non-flowing and flowing fluid. MRM will be used for diffusion properties, relaxation maps, spin echo imaging, propagators, and velocity maps for the respective flowing or non-flowing regimes. New subtask under ZERT II.

Natural Analogs of Escape Mechanisms

ZERT I Tasks

- Fully constrain the 2-d and 3-d geometry of Big Elk and Black Mountain anticlines using surface and subsurface data integrated in to Midland Valley's 2D and 3D-Move software applications for cross-section balancing.

  This subtask will roll-over into ZERT II because new structural-balancing software was obtained from LithoTect (Geo-Logic Systems). This new software is more robust and user-friendly than Midland Valley's balancing software, and Geo-Logic offers much better service in terms of user support. In addition, Midland Valley wanted to charge us for their software on an on-going basis, whereas LithoTect was donated to the university with a free academic license. The use of balanced cross-sections in structural analysis is integral to the outcome of objectives for both ZERT I and II, so this application is viewed as a seamless roll-over. A new cadre of graduate students will be trained in the use of LithoTect in January 2011. *Status*: *This task is continued under ZERT II.*

- Characterize the main reservoir rocks in the Salt River Range where they are well-exposed and accessible. Characterization will include measured sections, analysis of fracture pathways and other structural fabrics, and possible diagenetic and/or geochemical signatures of CO_2 infiltration and migration.

  Parts of this subtask will roll-over into ZERT II as we expand our structural analysis from SE Idaho eastward through the Absaroka, Darby and Prospect thrust sheets. Although we have largely completed field work in the Northern Salt River Range, we will revisit a couple of key outcrops that were discovered at the end of the 2010 field season for more sampling and fracture data. In addition, we are in the process of interpreting a large amount of structural data (fracture and fault measurements) collected in the Northern Salt River Range during the previous field season, coupled with on-going analyses of rock samples collected last year (e.g., thin-section microscopy; carbonate mineral staining; acetate peels; SEM; XRD; etc.). Isotopic analyses of carbonate cements will also overlap with ZERT II (this will actually be more efficient). *Status: This task is continued under ZERT II.*

- Collect field samples of fault materials from regions expected to have been exposed to CO_2 as well as regions expected to be unexposed.

  This is an on-going objective of both ZERT I and ZERT II. We are seeking to understand the preferred pathways of CO_2 migration in the subsurface of SE Idaho and western Wyoming, the diagenetic history of permeable conduits and the timing of CO_2 brine migration, and most importantly understand under what geologic conditions was CO_2 leakage augmented versus those conditions of CO_2 confinement. Therefore, we will continue to sample fault materials and measure/describe fracture systems across the width of the Idaho-Wyoming fold-and-thrust belt, in order to better understand long-distance migration of CO_2 and "CO_2-charging" of the Moxa arch in western Wyoming. *Status: This task is continued under ZERT II.*

- Microscopy for characterization of samples.

This objective will continue from ZERT I to ZERT II. Petrographic microscopy is a fundamental tool used in the description and diagenetic analysis of rocks, particularly so for carbonate rocks. *Status: This task is continued under ZERT II.*

- Fully constrain the 2-d and 3-d geometry of Big Elk and Black Mountain anticlines using surface and subsurface data integrated in to Midland Valley's 2D and 3D-Move software applications for cross-section balancing.

  This objective will continue from ZERT I to ZERT II. Petrographic microscopy is a fundamental tool used in the description and diagenetic analysis of rocks, particularly so for carbonate rocks. *Status: This task is continued under ZERT II.*

- Characterize the main reservoir rocks in the Salt River Range where they are well exposed and accessible. Characterization will include measured sections, analysis of fracture pathways and other structural fabrics, and possible diagenetic and/or geochemical signatures of CO_2 infiltration and migration.

  This objective will continue from ZERT I to ZERT II. Petrographic microscopy is a fundamental tool used in the description and diagenetic analysis of rocks, particularly so for carbonate rocks. *Status: This task is continued under ZERT II.*

ZERT II Tasks

- Leakage versus Confinement Associated with Subsurface Migration of Natural CO2 Across Faults and Fracture Networks

  The overarching goal of this subtask is to better understand the geologic processes that accompanied migration of CO_2 through this region.

  Dr. Erin Campbell-Stone will be utilized for task 3.0. She is uniquely qualified as a consultant because of her strong background in structural geology and particularly her on-going research in carbon sequestration in western Wyoming. Dr. Campbel-Stone's combination of expertise in structural geology (faults and fractures) and carbon sequestration with a solid knowledge of the local and regional geology of western Wyoming is unmatched.

- Ancient Hydrothermal Plumes as a Natural Analog of Hydrofracing Caprocks and Geochemical Healing Mechanisms

  The objective of this research task is to characterize the physical, mineralogical, and geochemical characteristics of hydrothermal plume related rocks in outcrop as natural analogs of breached and healed caprocks for carbon sequestration.

  Two geologic consultants, a petrographic analyst and a hydrothermal geologist, will be contracted for this subtask. They will assist the principal investigator in the collection of outcrop data and samples. Both will participate in interpretation of the data and final report preparation.

Optical Detection for Carbon Sequestration Site Monitoring

ZERT I Tasks

Above Ground Laser Based Sensor

The above ground laser based sensor for carbon dioxide (CO_2) monitoring began by exploring the possibility of generating a tunable continuous wave (cw) source of light with a nominal wavelength of 2.004μm. A cw Raman laser was first developed and tested along with a temperature tunable distributed feedback (DFB) laser. A cw differential absorption instrument was then developed and tested at the ZERT field sight during two summer field experiments demonstrating the capability of the cw differential absorption instrument to successfully measure CO_2 concentrations needed for sequestration site monitoring. Building on this work and other remote sensing development, researchers at Montana State modeled the performance of a pulsed differential absorption lidar (DIAL) for spatially mapping CO_2 concentrations over several km^2.

The successful demonstration of the cw differential absorption instrument and the modeling of the CO_2 DIAL instrument allowed researchers at Montana State University to seek and obtain competitive research funding to develop and build a CO_2 DIAL instrument. This funding, provided by the Department of Energy, has allowed a prototype CO_2 DIAL instrument to be constructed. This prototype is currently under test. The above ground laser based sensor work started under the auspices of the ZERT Phase I effort have progressed enough to finding outside funding for further instrument development and a PHASE I SBIR proposal has been submitted to the Department of Energy to begin the commercialization efforts. For this reason, this work will not be carried over into the ZERT Phase II effort. *Status: ZERT I tasks were completed and subsequent work is supported by commercialization funding.*

Flight Based Hyperspectral Imaging

The hyperspectral research efforts were funded in part by the ZERT Phase I effort and through a separate grant funded by NASA. During the first year of this research effort, a ground based study of Alfalfa was completed using a time series of hyperspctral data that was classified using a classification tree analysis. The results of this study indicated that hyperspectral imaging can detect the change in reflectance spectra resulting from plat stress due to the elevated sub-surface CO_2 levels resulting from the underground CO_2 release. This result led to a second field experiment during the following summer in which flight based hyperspectral imaging was conducted. The flight based data indicated that the classification tree analysis was capable of detecting the elevated subsurface CO_2 levels resulting from the underground release via changes in the reflectance spectra of the stressed vegetation.

The successful demonstration of the flight based hyperspectral imaging funded by the ZERT Phase I effort allowed competitive follow on funding to be obtain to continue this research effort and to begin moving towards commercialization. Funding by the Montana Board of Research and Commercialization Technology (MBRCT) was obtain that allowed further flight based hyperspectral imaging work for carbon sequestration site monitoring and noxious weed mapping to be conducted. Commercialization of flight based hyperspectral imaging for large area monitoring of carbon sequestration sites is also underway with a successful Phase I STTR project and a funded Phase II STTR

project by the Department of Energy. The funding by the ZERT Phase I effort for the hyperspectral imaging allowed follow on funding to be obtain for further basic research and to begin moving this monitoring technique into the commercial sector. For this reason, further funding for flight based hyperspectral imaging from the ZERT Phase II effort was not asked for. *Status: ZERT I tasks were completed and subsequent work is supported by commercialization funding.*

Fiber Based Subsurface Detectors

During the ZERT Phase I effort, a subsurface laser based sensor was developed for monitoring soil CO_2 concentrations. This sensor utilized the tunable DFB laser and a below ground absorption cell for monitoring the CO_2 concentration. This instrument was very successful at monitoring subsurface CO_2 concentrations during three summer field experiments at the ZERT field site. Work with the underground fiber sensor funded by the ZERT Phase I effort has lead to further funding through the Department of Energy and commercialization of the fiber sensor is underway through a Phase I SBIR project funded through the Environmental Protection Agency. The fiber sensor array currently under development and commercialization utilizes an array of underground probes connected via a fiber optic switch to a single laser and two detectors in a send/call geometry for large area monitoring of carbon sequestration sites. The successful demonstration of the subsurface fiber based sensor array, which begun under the ZERT Phase I effort is well on its way to commercialization. *Status: ZERT I tasks were completed and subsequent work is supported by commercialization funding.*

Inexpensive Normalized Differential Vegetation Detector

This subtask explored the use of relatively inexpensive multispectral imagers for detecting near-surface carbon dioxide through changes induced in the reflectance spectrum of overlying vegetation. This work used a commercial multi-spectral imager and showed a statistically significant correlation between the temporal-spatial distribution of carbon dioxide gas fluxes and the temporal changes in vegetation reflectance. This work used both band-averaged reflectance, as well as the Normalized Difference Vegetation Index (NDVI), a remote sensing parameter that indicates vegetation health through the use of red and near infrared reflectances. This preliminary study has been completed, although the instrument developed in this task continues to be used in continuing ZERT II studies. *Status: Task completed; instrument use continues in ZERT II.*

Construct Multispectral Imaging System and Test during Summer 2009 Field Experiment

Our work in this subtask was to design and test a custom, low-cost multispectral imaging system that could be deployed and operated remotely through the use of solar power and wireless communication. A prototype system was developed in 2009 and tested briefly alongside the original multispectral imaging system described in the immediately above task. This new system was further refined and deployed for actual carbon dioxide detection during the summer 2010 release experiment at the ZERT site in Bozeman, Montana. This system reduces the cost of the commercial system by a factor of approximately five, reduces the size by factor of approximately two, and incorporates solar power and wireless communication. *Status: This task is continued in ZERT II.*

ZERT II Tasks

The ZERT Phase II research effort is aimed at exploring the possibility of using a photonic bandgap (PBG) fiber as part of an inline fiber sensor for subsurface CO_2 monitoring. The geometry proposed for this fiber sensor is new and the ZERT Phase II effort is proving funding to begin exploring if the inline fiber sensor is feasible. The inline fiber sensor geometry will utilize a section of PBG fiber fusion spliced to a single mode fiber. The far end of the PBG fiber will have a small air gap causing a reflection of light from this interface. The light not reflected at this interface will be coupled into another section of single mode fiber, which has another section of PBG fusion spliced. This geometry will allow a series of inline CO_2 concentration measurements to be made using a series of absorption cells created with the PBG fiber.

- Underground Fiber Optic Sensors

  Set up the laboratory experiment demonstrating one segment of an in-line fiber sensor based on photonic bandgap PBG fibers.

  Demonstrate the ability to re-launch light into subsequent fiber sections when an air gap is left between the sections. The air gap is necessary to permit diffusion of CO_2 into the PBG fiber sections.

- Ultra-Compact Thermal Infrared Imagers

  The following subtasks will develop and deploy custom multispectral imager:

  Design multispectral imager using custom wide-angle optics.
  Build prototype of multispectral imager.
  Test prototype multispectral imager at ZERT site.

  This subtask begins an exploration of ultracompact thermal infrared imagers as a supplementary tool to operate alongside the previously developed low-cost multispectral imager. The hypothesis is that vegetation stressed by leaking carbon dioxide will not thermo-regulate as well as healthy vegetation, leading to larger temporal swings of vegetation radiation temperature observed in the long-wave infrared. During the summer 2010 carbon dioxide release experiment at the Bozeman, Montana ZERT site, we deployed a thermal infrared imager alongside the new low-cost and original multispectral imagers which was developed in the ZERT I project.

  The following subtasks will conduct experiments to assess the utility of thermal IR imagers for detecting plant stress:

  Package pre-existing thermal IR imager for field deployment.
  Conduct field tests at ZERT site.

Validation of Near-surface CO_2 Detection Techniques and Transport Models

ZERT I Tasks

All these tasks from ZERT I will be continued into ZERT II. The completion of all of these subtasks is necessary to ensure experimental work at the MSU field site can be

continued. This will maintain access to an experimental site with a known source term of CO_2 for researchers to prove sensing technologies and determine detection limits. Maintaining the availability of the field site permits instrument developers to bring subsequent generations of instruments back to an environment studied in previous years thus allowing them to assess the success of modifications. Having sustained access to the same field site also provides inter-year comparison which is important for characterizing natural variability. *Status: This task is continued under ZERT II.*

- Seasonal Site Preparation.
- Coordinate experimental season with ZERT team.
- Collect data in support of ZERT research project goals.
- Investigate opportunities for greater involvement outside of the ZERT team.

ZERT II Tasks

- Seasonal Site Preparation - In mid-Spring we will begin site preparation for the next experimental season.
- Coordinate experimental season with ZERT team. - Conduct conference calls and meetings to coordinate experimental operations on the site including experimental layout and CO2 flow periods to maximize participation and minimize conflict between detection methods. Assist visitors with local logistics, schedule use of the field site, oversee access, and serve as a point of contact.
- Collect data in support of ZERT research project goals. - Deploy commercial instrumentation to monitor quantities such as soil moisture, CO2 soil concentration, and soil CO2 flux relevant to geological carbon sequestration research.
- Investigate opportunities for greater involvement outside of the ZERT team. - Contact private sector entities, academics, and foreign personnel who are developing new detection techniques to invite participation if it does not have a deleterious effect on on-going activities.
- Provide meteorological support to the optical remote sensing group, provide optical sensing expertise, and develop and deploy optical imaging systems for detecting carbon dioxide.
- Provide bee hives and sampling for pollen capture of tracers experiments:

  The above two tasks includes a wide range of scientific support provided at the ZERT site, primarily involving remote deployment of meteorological and optical sensors operated with solar power and streaming data to an online webpage via wireless communication. Beehives and pollen collection, is included here because we previously operated beehives in a nearby field for a separate project. We have already begun operation of meteorological sensors at the ZERT site.

Tracking Emerging Issues That Could Influence CCS Research Needs

ZERT performs basic research in support of CCS programmatic needs. In order to identify relevant research gaps and to make certain that research results that are relevant to topical issues get communicated, it is important for ZERT management to stay informed on issues being considered by decision makers both domestically and internationally. *Status: This task is continued under ZERT II.*

Subtask 6.1 Provide timely information on relevant issues under consideration at the state, federal and international levels.

Subtask 6.2 Provide timely information on relevant issues under consideration by NGOs, industry groups, and professional groups relevant to CCS.

Sequestration of Carbon Dioxide in Appalachian Coal Deposits
Status: This task is continued in ZERT II.

LA-UR-10-02503

FY10-Q2 Quarterly Report

Project Title: Los Alamos National Laboratory Activities
for the Center for Zero Emission Research and Technology II (ZERT-II)

LANL Principal Investigator: ***Rajesh Pawar***
LANL Program Manager: ***Melissa Fox***

Research Team: Bill Carey, Elizabeth Keating, Sharad Kelkar, Quinjun Kang, Peter Lichtner, Saikiran Rapaka, Hari Viswanathan, Giday WoldeGabriel, George Zyvoloski

Date of Report: 15 April 2010
Period Covered by Report: 2nd Quarter FY10 (Jan-Mar 2010)

NETL Project Manager: William Aljoe

Executive Summary

Los Alamos National Laboratory's (LANL) ongoing activities for the Center for Zero Emission Research and Technology–II (ZERT-II) are focused on the scientific basis for predicting the performance of engineered geologic CO_2 storage sites. LANL's approach involves using theory, observation, experiment and simulation to characterize the fundamental processes that control the long-term fate of CO_2 in the subsurface. Specifically, LANL's activities are primarily focused on three topics:

- Application of lattice-Boltzmann methods (LBM) to characterize multi-phase CO_2-water fluid-flow
- Coupled fluid-flow and stress simulations to characterize geo-mechanical response of CO_2 injection
- Characterization of impact of CO_2 and deeper brines on groundwater quality

Due to the late arrival of funding, LANL's ZERT activities were not initiated until the FY10 2nd quarter. This quarterly report focuses on the work related to advances in the coupled flow-stress simulation capabilities in LANL's FEHM simulator. As part of this effort we are developing capabilities that can be used to simulate rock materials with non-linear mechanical behavior as well as plastic deformation. Results of this work will be presented during the Ninth Annual Conference on CO_2 Sequestration to be held in May 2010 in Pittsburgh, PA.

1. Development of capabilities to simulate non-linear geo-mechanical response in FEHM (Task 3.0):

As had been mentioned in earlier ZERT reports, understanding and characterizing the geo-mechanical response during large-scale CO_2 injection is one of the major needs for determining risks as well as developing guidelines for safely operating sequestration sites. As part of LANL's earlier ZERT effort, we have extended LANL's FEHM simulator for modeling coupled flow-stress simulations of CO_2 sequestration sites. These earlier developments were focused on building capabilities to simulate geo-mechanical

response of rocks using linear elastic mechanical models. As part of the ZERT II effort, we are extending the stress modeling capabilities to non-linear and elasto-plastic regime. This report provides summary of our effort related to developing non-linear elastic models in FEHM (sub-task 3.1) as described below.

The force balance equation for a linear elastic material for infinitesimal strain with homogeneous, isotropic material properties is

$$(\lambda+2G)\frac{\partial^2 u}{\partial x^2}+G\left(\frac{\partial^2 u}{\partial y^2}+\frac{\partial^2 u_1}{\partial z^2}\right)+(\lambda+G)\left(\frac{\partial^2 v}{\partial x\,\partial y}+\frac{\partial^2 w}{\partial x\,\partial z}\right)- \quad \textbf{(Eq. 1)}$$
$$3K*\left(\alpha\Delta\frac{\partial T}{\partial x}+\frac{1}{3H}\Delta\frac{\partial P}{\partial x}\right)=0$$

where,
E = young's modulus
$\upsilon = Poisson's\ ratio$
λ and G are Lame's paramteres given by

$$G=\frac{E}{2(1+\upsilon)} \text{ and } \lambda=\frac{\upsilon.E}{(1+\upsilon)(1-2\upsilon)}$$

(u,v,w)= displacements respectively in the (x,y,z) directions
α = coefficient of linear thermal expansion

$$\text{K = bulk modulus = } \frac{E}{3(1-2\upsilon)}$$

$\frac{1}{3H}$ = Biot's coefficient

The weak form of this equation using iso-parametric, nodal finite element shape functions, and allowing the material properties to be position dependant (either directly due to inhomogeniety or through functionality with respect to independent variables such as displacements and temperature) becomes:

$$\sum_J \int\left[\frac{\partial N_I}{\partial x}.(\lambda+2G).\frac{\partial N_J}{\partial x}d\Omega+\frac{\partial N_I}{\partial y}.G\ .\frac{\partial N_J}{\partial y}d\Omega+\frac{\partial N_I}{\partial z}.G\ .\frac{\partial N_J}{\partial z}d\Omega\right].u_J$$
$$+\sum_J \int\left[\frac{\partial N_I}{\partial x}.\lambda.\frac{\partial N_J}{\partial y}d\Omega+\frac{\partial N_I}{\partial y}.G\ .\frac{\partial N_J}{\partial x}d\Omega\right].v_J \quad \textbf{…(Eq. 2)}$$
$$+\sum_J \int\left[\frac{\partial N_I}{\partial x}.\lambda.\frac{\partial N_J}{\partial z}d\Omega+\frac{\partial N_I}{\partial z}.G\ .\frac{\partial N_J}{\partial x}d\Omega\right].w_J$$

+pore pressure terms + thermal stress terms +Boundary terms + body force terms = 0

Similar equations are developed for the y and z directions.

The focus of the development in this quarter is on the internal force terms written out in detail in the above equation. The pore pressure and thermal stress terms will be developed in detail as a part of the work in the next quarter. The boundary terms arise from the various boundary conditions imposed on the system. The body force terms are gravitational force terms. These terms are already incorporated in the FEHM stress module.

A material nonlinearity is generally represented as a function of the independent variables at a given point in the material; e.g. E=f(p(x)), where f is a function of the variable p at a location x in the model domain. In FEHM, the integrals in the equation above involving shape functions are approximated by taking the material coefficients out of the integral leaving only geometric functions under the integration, and multiplying the integral by an 'effective value' of the material coefficient. In FEHM, the 'effective' value of the material coefficient is related to the nodal values most often using the harmonic average between the pair of nodes i, j. For example, the first term in the equation 2 becomes:

$$\int \frac{\partial N_i}{\partial x}.(\lambda+2G).\frac{\partial N_j}{\partial x}\,d\Omega \cong \overline{(\lambda+2G).}_{ij} \int \frac{\partial N_i}{\partial x}.\frac{\partial N_j}{\partial x}\,d\Omega$$

Where $\overline{(\lambda+2G).}_{ij}$ is the effective value of $(\lambda+2G)$ over the overlapping region of the control volumes of the nodes i and j.

This approach results in considerable computational savings and has been proved to work well in many other highly nonlinear problems involving heat transfer, multiphase flow and phase transitions. In the stress balance equations, this term represents the material behavior in some 'effective' sense over the overlapping control volume domains of the nodes i and j. Hence, to represent the nonlinear material response of an isotropic material, it is not unreasonable to select a relationship of the form

$$C_{ij} = C_{ij-0} * f\left(\partial(\overline{u_i} - \overline{u_k})\right)$$

where, C_{ij} stands for any of the coefficients, C_{ij-0} is the intial value of C_{ij}, i stands for the node under consideration, the indices 'j' and 'k' run over all the nodes connected to node i. $f\{\}$ indicates functional dependence, and $\partial(\overline{u_i} - \overline{u_j})$ denotes the change in the displacement vector from the node i to node j..

This form depends only on the displacements at the nodes directly connected to the node under consideration. This has the advantage of not averaging over too large a computational volume, which can be a concern in regions with steep gradients, as well as keeping the bandwidth of the stiffness matrix to a minimum. The next step of the approach taken in FEHM is to form residual equations. For example, the residual form of the force balance equation in the x-direction at the node 'i' is:

$$R_x = \sum_J \begin{bmatrix} (\overline{e_1}\cdot SixSjx + \overline{G}.SiySjy + \overline{G}SizSjz)\cdot \delta u_{IJ} \\ +(\overline{G}SiySjx + \overline{\lambda}\ SixSjy)\cdot \delta v_{IJ} \\ +(\overline{G}SizSjx + \overline{\lambda}SixSjz)\cdot \delta w_{IJ} \end{bmatrix} \ldots\ldots\ldots\ldots\ldots\ldots\ldots\ldots (Eq.3)$$

$$+ \text{pore pressure terms} + \text{thermal stress terms} + \text{Boundary terms} + \text{body force terms}$$

where, $e_1 = \lambda + 2G$, and the bar over the quantity, i.e. $\overline{e_1}$, indicates an effective value (such as the harmonic mean) over the control volume overlap between the nodes 'i' and 'j'.

$$SixSjx = \int \frac{\partial N_I}{\partial x}\frac{\partial N_J}{\partial x} d\Omega$$

$$SiySjy = \int \frac{\partial N_I}{\partial y}\frac{\partial N_J}{\partial y} d\Omega$$

$$SizSjz = \int \frac{\partial N_I}{\partial z}\frac{\partial N_J}{\partial z} d\Omega$$

$$SiySjx = \int \frac{\partial N_I}{\partial x}\frac{\partial N_J}{\partial y} d\Omega$$

$$SizSjx = \int \frac{\partial N_I}{\partial x}\frac{\partial N_J}{\partial z} d\Omega$$

$$\delta u_{IJ} = u_I - u_J$$

$$\delta v_{IJ} = v_I = v_J, and$$

$$\delta w_{IJ} = w_I - w_J$$

The set of residual equations above are in general nonlinear with respect to the independent variables, and the Newton-Raphson method is used to solve these equations. In order to do so, derivatives of the residuals with respect to the independent variables need to be formed. For example, the derivative of the x-force balance equation at node 'i' (given above) with respect to the displacement at node J in the x-direction is:

$$\frac{\partial R_{Ix}}{\partial u_J} = \left\{\frac{\partial R_{Ix}}{\partial u_J}\right\}_{linear} + (\frac{\partial \overline{e_1}}{\partial u_J}\cdot SixSjx + \frac{\partial \overline{G}}{\partial u_J}\cdot SiySjy + \frac{\partial \overline{G}}{\partial u_J}\cdot SizSjz)\cdot(u_J - u_I)$$

$$+(\frac{\partial \overline{G}}{\partial u_J}\cdot SiySjx + \frac{\partial \overline{\lambda}}{\partial u_J}\cdot SixSjy)\cdot(v_J - v_I)$$

$$+(\frac{\partial \overline{G}}{\partial u_J}\cdot SizSjx + \frac{\partial \overline{\lambda}}{\partial u_J}\cdot SixSjz)\cdot(w_J - w_I)$$

Where $\left\{\frac{\partial R_{Ix}}{\partial u_J}\right\}_{linear}$ is the derivate for the case of constant material coefficients, already incorporated in the FEHM code. Two more sets of equations result for the derivatives with respect to the y and z displacements (v and w). Similar suites of equations describe

the variations of the residuals for the force balance equations in the 'y' and 'z' directions. If variations in the material properties with respect to temperature and pore pressure were to be taken into account, more equations would result.

In order to investigate the merits of this approach, an independent simplified stress-strain code is being developed in the MATLAB computational environment. This code utilizes the four-point quadrature formulae which are common in the traditional finite-element approaches. The purpose of this code would be to test the accuracy, speed and convergence properties of the FEHM algorithm when compared to traditional Finite-Element techniques. The MATLAB environment provides an intuitive programming language along with extremely powerful built-in linear solvers, visualization tools and code profilers resulting in a very fast code development cycle. This code has been successfully tested against analytical solutions for a range of two-dimensional and three-dimensional problems.

One of the problems considered is that of steady-state nonlinear heat conduction in a slab with imposed temperatures on two opposite sides. The thermal conductivity of the material is taken to vary linearly with the local temperature. The governing equations for this problem are:

$$\nabla \bullet k(T)\nabla T = 0$$

$$T(x=0)=1, T(x=1)=0, \frac{\partial T}{\partial y}(y=0,1)=0$$

$$k(T)=1+\alpha T$$

Being a single variable, single parameter system where the nonlinearity can be tuned easily by varying the magnitude of α, this problem can serve as an effective benchmarking solution to compute the accuracy of FEHM algorithms as a function of the degree of nonlinearity. This problem is endowed with an analytical solution given by

$$T(x) = \frac{-1+\sqrt{1+\alpha(2+\alpha)(1-x)}}{\alpha}, \qquad \alpha > 0$$
$$= 1-x \qquad\qquad \alpha = 0$$

In Fig.(1), we show the grid used for the MATLAB finite-element solution, as well as the computed temperature profile for the case of $\alpha = 10^5$. Even for a highly nonlinear problem such as this one, with the thermal conductivity varying by 5 orders of magnitude, the Newton method converged in 8 iterations.

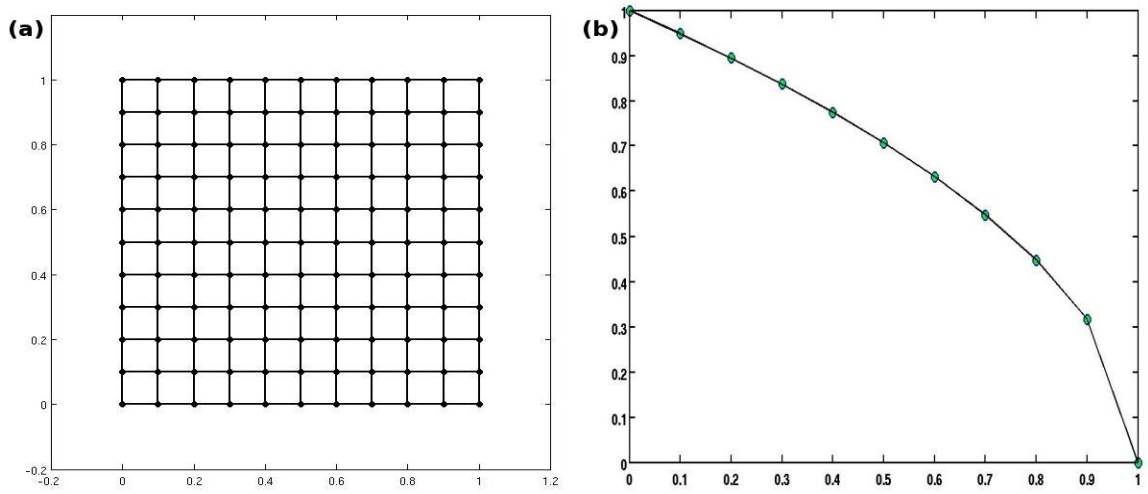

Fig. (1): (a) The 11x11 node grid used to simulate the heat conduction problem and (b) Comparison of the MATLAB solution (symbols) to the analytical solution (solid line). Simulations were conducted with $\alpha = 10^5$ and converged in 8 iterations.

A second test case is that of an internally pressurized cylindrical hull of finite thickness. The governing equations for this problem are the same as those shown in Eqn.(1). This test case was run using FEHM's linear elasticity module, but is of interest as this is one of the few problems where an analytical solution is available for elasto-plastic deformation when the material follows a von Mises model. In Fig.(2), we show the radial displacement of the cylinder computed using FEHM's linear elasticity module and the analytical solution for the problem.

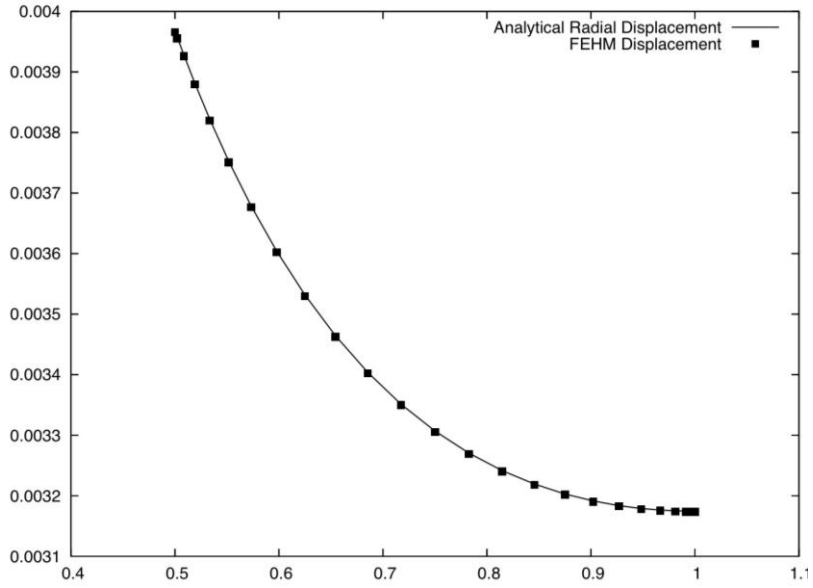

Fig.(2). Comparison between the radial displacement of an internally pressurized cylindrical hull computed using FEHM's linear elasticity module with the analytical solution.

The FEHM result can be seen to match the analytical solution extremely well. A grid convergence test was conducted using 5, 10 and 20 elements in the radial direction, and the max-norm of the error was found to converge quadratically with the grid spacing.

The code also incorporates a simple elasto-plasticity module which will be used to study the convergence properties of the FEHM algorithm for problems involving elastic-plastic transitions. In this regard, the emphasis during this quarter was on developing a von Mises J2-model for elasto-plasticity. This work will be extended to more complex models (such as Mohr-Coulomb and Drucker-Prager models) during the next quarter. As next steps, we are planning to complete the developments in FEHM based on the modeling approach described above. First, we will develop a non-linear elastic model that includes temperature dependence followed by displacement dependence. We will verify implementation of these models through verification problems.

3. Summary

Initiation of LANL activities for Center for Zero Emission Research & Technology (ZERT II) was delayed due to late arrival of funding. We have initiated our work associated with Task 3, "Advancing coupled flow-stress simulation capability in FEHM" and Task 4, "Characterization of impact of CO_2 and deeper brines on groundwater quality".

4. Publications/presentations:

None.

5. Milestones:

The table below tracks milestone status for FY10.

Milestone #/ Task Activity	PIP Quarter	Start Date	Target End Date	Milestone	Milestone Completed
M 1 / Task 4	FY10 Q3	1 Jan 10	30 Jun 10	Complete the simulations of CO_2/deeper brine flow through well at Chimayo and complete a journal manuscript for the work	
M 2/ Task 3	FY10 Q4	1 Jan 10	30 Sep 10	Complete development of capability to solve the stress equations for radial geometry in FEHM	

5. Summary of Significant Accomplishments:

None.

Issues and Planned Resolutions

None.

Technology Transfer Activities

Not applicable.

LA-UR-10-04927

FY10-Q3 Quarterly Report

Project Title: Los Alamos National Laboratory Activities
for the Center for Zero Emission Research and Technology II (ZERT-II)

LANL Principal Investigator: ***Rajesh Pawar***
LANL Program Manager: ***Melissa Fox***

Research Team: Bill Carey, Elizabeth Keating, Sharad Kelkar, Quinjun Kang, Saikiran Rapaka, Hari Viswanathan, George Zyvoloski

Date of Report: 15 July 2010
Period Covered by Report: 3rd Quarter FY10 (Apr-Jun 2010)

NETL Project Manager: William Aljoe

Executive Summary

Los Alamos National Laboratory's (LANL) ongoing activities for the Center for Zero Emission Research and Technology–II (ZERT-II) are focused on the scientific basis for predicting the performance of engineered geologic CO_2 storage sites. LANL's approach involves using theory, observation, experiment and simulation to characterize the fundamental processes that control the long-term fate of CO_2 in the subsurface. Specifically, LANL's activities are primarily focused on three topics:

- Application of lattice-Boltzmann methods (LBM) to characterize multi-phase CO_2-water fluid-flow
- Coupled fluid-flow and stress simulations to characterize geo-mechanical response of CO_2 injection
- Characterization of impact of CO_2 and deeper brines on groundwater quality

Due to the late arrival of funding, LANL's ZERT activities were not initiated until the FY10 2nd quarter. This quarterly report focuses on the work related to advances in the coupled flow-stress simulation capabilities in LANL's FEHM simulator. As part of this effort we are developing capabilities that can be used to simulate rock materials with non-linear mechanical behavior as well as plastic deformation. Results of this work were presented during the Ninth Annual Conference on CO_2 Sequestration held in May 2010 in Pittsburgh, PA.

1. Development of capabilities to simulate non-linear geo-mechanical response in FEHM (Task 3.0):

As had been mentioned in earlier ZERT reports, understanding and characterizing the geo-mechanical response during large-scale CO_2 injection is one of the major needs for determining risks as well as developing guidelines for safely operating sequestration sites. As part of LANL's earlier ZERT effort, we have extended LANL's FEHM simulator for modeling coupled flow-stress simulations of CO_2 sequestration sites. These earlier developments were focused on building capabilities to simulate geo-mechanical

response of rocks using linear elastic mechanical models. As part of the ZERT II effort, we are extending the stress modeling capabilities to non-linear and elasto-plastic regime. This report provides summary of our effort related to developing elastic-plastic deformation modeling capabilities that can be potentially applicable specifically to CO_2 sequestration application and in general in fluid flow in porous media.

Modular computation of the stiffness matrix

We begin by considering the statement of mechanical equilibrium, written in the form:

$$\nabla \bullet \sigma + F_b = 0 \tag{1}$$

where, σ is the stress in the solid and F_b are the applied body forces (for instance, gravitational terms). The discrete weak-form statement for this problem can be written in the standard form:

$$\left[\int B^T D B\right] u = F \tag{2}$$

where, the term in parenthesis is the *global stiffness matrix (K)* and u is the vector of nodal displacements. The matrix B in the above equation contains derivatives of the shape functions and D is a symmetric fourth order tensor (represented as a matrix using Voigt notation) containing the material properties that relate stresses to strains. For instance, for a linearly elastic, isotropic rock, the tensor D can be given using index notation as:

$$D_{ijkl} = \lambda \delta_{ij} \delta_{kl} + 2G \delta_{ik} \delta_{jl} \tag{3}$$

where, λ and G are the Lame's constants of the rock. In traditional quadrature-based finite element methods the global stiffness matrix is assembled during each iteration by performing a summation of the integral over the quadrature points in the element. The algorithm is simplified considerably in FEHM, where the integrals over the shape functions are pre-computed to save a significant amount of computation:

$$\begin{aligned} K_{ij} &= \int \sum_{l,p} B_{il}^T D_{lp} B_{pj} d\Omega \\ &= \sum_{l,p} D_{lp}^* \int B_{il}^T B_{pj} d\Omega \end{aligned} \tag{4}$$

where, the integral is only over the geometric terms involving shape functions, and needs to be computed just once during initialization and D* is a suitable defined average of the material properties (i.e. arithmetic or harmonic) of the neighboring nodes. We are investigating various schemes for evaluating D* in terms of nodal values regarding convergence and accuracy. This increase in computational speed is obtained at the cost of increased memory usage for saving the integrals at every node. However, in most finite element meshes, a large number of nodes have very similar nodal connectivity patterns

and savings in memory can be achieved by saving the integrals only once for each class of elements with a similar connectivity structure.

The algorithm can be understood by looking at the (1,1) term of the K matrix for 8-noded "hex" elements:

$$\begin{aligned} K_{11} = D_{11} \int \frac{\partial N_i}{\partial x}\frac{\partial N_j}{\partial x} d\Omega + D_{14} \int \frac{\partial N_i}{\partial x}\frac{\partial N_j}{\partial y} d\Omega + D_{16} \int \frac{\partial N_i}{\partial x}\frac{\partial N_j}{\partial z} d\Omega \\ + D_{41} \int \frac{\partial N_i}{\partial y}\frac{\partial N_j}{\partial x} d\Omega + D_{44} \int \frac{\partial N_i}{\partial y}\frac{\partial N_j}{\partial y} d\Omega + D_{46} \int \frac{\partial N_i}{\partial y}\frac{\partial N_j}{\partial z} d\Omega \\ + D_{61} \int \frac{\partial N_i}{\partial z}\frac{\partial N_j}{\partial x} d\Omega + D_{64} \int \frac{\partial N_i}{\partial z}\frac{\partial N_j}{\partial y} d\Omega + D_{66} \int \frac{\partial N_i}{\partial z}\frac{\partial N_j}{\partial z} d\Omega \end{aligned} \tag{5}$$

where, i is the node under consideration and j is a connected neighboring node. In this representation, the integrals only depend on the underlying grid and do not change during the course of the simulation. However, the coefficients in the matrix "D" can be functions of the independent variables and can change from one iteration to the next. For instance, for a material obeying von Mises' J2 plasticity model, the elasto-plastic "D" matrix can be given as:

$$D^{(ep)} = D^{(e)} - \frac{(D^{(e)} : N) \otimes (D^{(e)} : N)}{N : D^{(e)} : N} \tag{6}$$

where, N is the *flow vector* for plastic material deformation. Saving the integrals reduces the computational cost significantly, as the evaluation of each term in the stiffness matrix only involves 9 multiplications and additions.

During this quarter, the code in FEHM was modularized so as to utilize any arbitrary, symmetric "D" matrix to produce the consistent global stiffness matrix. Once the shape function integrals are computed and saved, it is necessary to tabulate which entries in the "D" matrix couple with each shape function integral, for every term in the nodal stiffness matrix. For example, looking at the (1,1) entry of the K matrix above, we need to tabulate that the (1,1) entry of D always multiplies the integral with both x-derivatives and so on. These indices were saved into two arrays, which provide the corresponding row and column entry into the "D" matrix needed for the $(i,j)^{th}$ entry of the nodal stiffness matrix. The assembly of the global stiffness matrix is then simplified as:

$$K_{ij} = \sum_{l,p=1}^{3} D^{*}_{row(l),col(p)} I_{lp} \tag{7}$$

$$I_{lp} = \int \frac{\partial N_i}{\partial x_l}\frac{\partial N_j}{\partial x_p} d\Omega \tag{8}$$

Material-dependent stress update and residual computation

Once the converged displacements are obtained, the stresses at every node need to be updated. In the current version of FEHM, the solid rock material is assumed to have linear elastic mechanical properties, and the computation of stress explicitly used this information. To facilitate ease of adding newer material models in the future, it is highly desirable to have flexibility where material properties can be updated based on the model for the mechanical behavior of the material (that may or may not be explicitly user-defined). During the FY10 second quarter, we included a new macro in FEHM to specify different materials in the simulation, each potentially obeying a different constitutive equation. The only places where the material properties are explicitly needed are during the computation of stresses from the current value of displacements and the global stiffness matrix.

For non-linear material models (for instance, elasto-plastic materials), the relationship between stresses and displacements can be quite complex. For instance, during an iteration of a plastic model, the material's new state can cross the yield surface and require an iterative solution to perform the return mapping to the yield surface. In this case, the computation of stresses is strongly dependent on the kind of model used to represent the material, as well as the specific algorithm used to perform the return mapping. For the sake of generality, the part of the code that depends on these specific material properties should be coded separately from the main algorithm that assembles the residual and stiffness matrix and computes the displacements. During the FY10 second quarter, we developed a framework for separating the material specific parts of the code from the general finite element algorithm.

We also made small changes to the residual computation routines. In the previous version of FEHM, the residual was being computed explicitly using the material properties. However, once the stresses are updated the residual can be computed directly from the stresses without using the material specific properties. We modified the part of the code that computes the residual to compute it directly using the stresses as:

$$R = \int B^T \sigma d\Omega \tag{9}$$

Development of a von Mises plasticity solver in MATLAB

We extended the work done in the previous quarter by implementing a basic plasticity model in the finite-element solver implemented using the MATLAB environment. The von Mises plasticity model is characterized by a yield surface that depends on the J2 invariant of the stress tensor:

$$\Phi(\sigma) = \sqrt{3J_2(\sigma)} - \sigma_y \tag{10}$$

where σ_y is the yield stress. This model is one of the simplest plasticity models in the sense that the (radial) return mapping algorithm does not need iterations and the updated stress can be computed exactly. The flow rule was assumed to be associative, resulting in

the flow vector being a scaled version of the deviatoric stress tensor. The plastic multiplier can be shown to be:

$$\Delta\gamma = \frac{N : D^{(e)} : \Delta\varepsilon}{N : D^{(e)} : N} \tag{11}$$

For the specific model implemented, we did not consider any hardening properties. However, hardening can be introduced with very minor changes to the existing code. The algorithm with radial return mapping is summarized in Figure 1.

Fig. 1: Stress update algorithm for the von Mises plasticity model

1. Given incremental displacements Δu, compute incremental strain $\Delta\varepsilon = B\Delta u$
2. Compute incremental stress $\Delta\sigma = D^e\Delta\varepsilon$
3. Obtain the trial stress $\sigma^{trial} = \sigma + \Delta\sigma$
4. If σ^{trial} < yield stress,
   4.1 Set the trial stress as the new converged stress and exit
   Else
   4.1. Compute the plastic multiplier $\Delta\gamma$
   4.2. Update the elastic and plastic strains
   4.3. Update the stress using only the elastic component of strain

To test the model, we set up a simple experiment where a block of material was uni-axially compressed (along the x-axis) with increasing loads. When the applied stress exceeds the yield stress, the material deigns to deform plastically. It can be shown using theoretical arguments that the normal stress in the direction orthogonal to the applied load increases with increasing plastic strain. The limiting value of the ratio of this stress (in z-direction) to that in the x-direction can be shown to reach 0.5 at which time the material fails. In Figure 2, we show the results from the MATLAB simulation along with the limiting value of 0.5 (dashed line). We used two different algorithms to simulate the problem – the first is a traditional element-based quadrature computation (shown using solid line), and the second is the simulation using an algorithm similar to the one used in FEHM but programmed in MATLAB (shown using blue squares). The accuracy of the FEHM algorithm to be able to predict plastic deformation can be seen from Figure 2. As the plastic strain slowly increases, the increment in the applied force has to be reduced to obtain convergence of iterations. It can be seen that the ratio of z-stress to the x-stress is reaching 0.5 asymptotically, as expected. These results have given us confidence in the current plastic deformation modeling algorithm implemented in MATLAB and we are using it to guide the development of plastic deformation simulation capability in FEHM. The MATLAB implementation also has an added advantage of developing a set of test problems that can be used to compare results of FEHM simulations.

Development of Stress Dependant Permeability Models

Shear failure can occur at much lower fluid pressures than tensile failure. It is expected that shear failure may be one potential failure in CO_2 sequestration reservoirs where

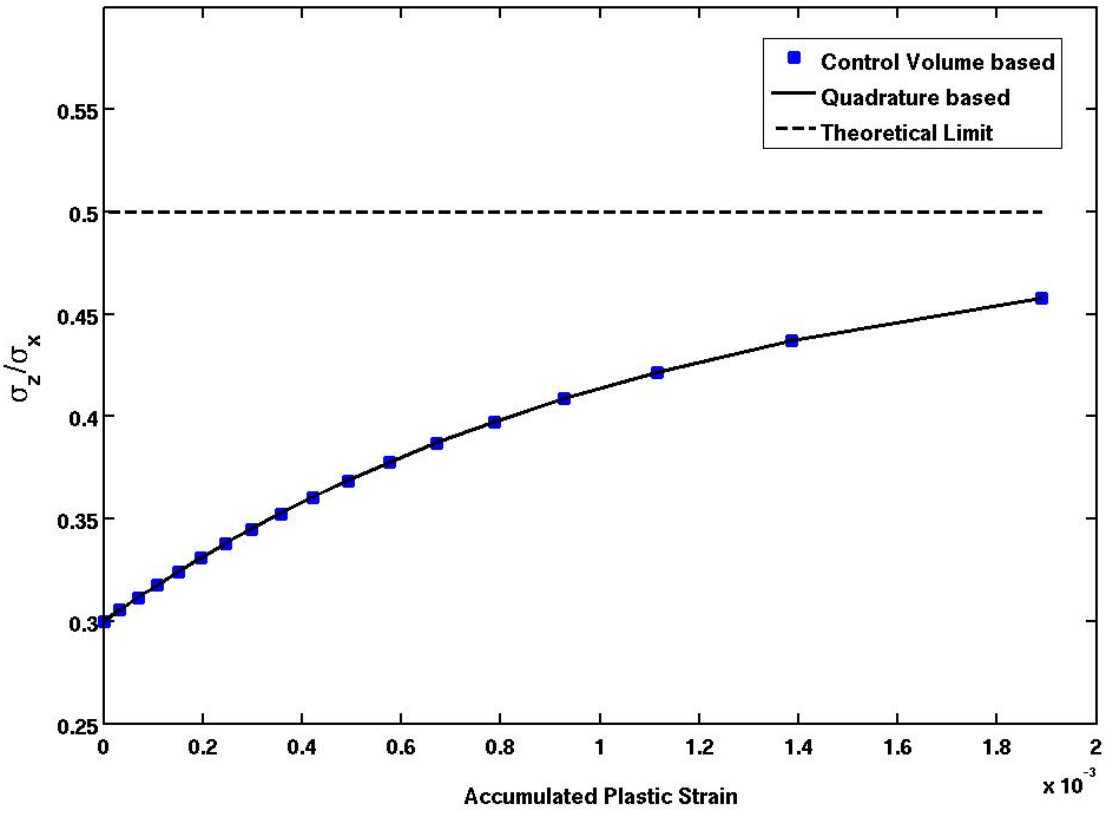

Fig. 2: Ratio of stresses in the z and x directions for a block uni-axially compressed along the x-axis. The limiting value of 0.5 can be predicted from theory (Hill, 1954)

changes in the in-situ stress field resulting from the injection of large volumes of CO_2 over long time spans can create conditions in the formation and/or caprock that are favorable to shear failure along preexisting (or induced) faults and planes of weakness. Shear failure can lead to permeability increase by as much as two orders of magnitude (Lee and Cho 2002, Min et al 2004). FEHM is currently being modified to handle such permeability changes. Mohr-Coulomb criterion (Jaeger and Cook 1979) is used for determining the model regions where conditions for shear failure are satisfied and then permeabilities and mechanical moduli are multiplied by user specified factors in directions normal and parallel to the plane of shear. The failure criteria is computed either on a plane with user specified orientation (such as a natural fault which may be present) or on the planes oriented optimally to satisfy the failure criteria (such as in a medium with ubiquitous fracturing). This development will be continued in the next quarter.

3. Summary

Effectively modeling elastic-plastic deformation is one of the critical needs in porous media fluid flow applications including CO_2 sequestration. We have developed an approach for modeling plastic deformation using von Mises plasticity model and have developed an algorithm in MATLAB. We are currently in the process of implementing

this model in FEHM. We have also initiated development of stress-dependent permeability models in FEHM.

4. Publications/presentations:

"Non-linear geomechanical modeling with the Finite Element Heat and Mass transfer (FEHM) code", Saikiran Rapaka, Sharad Kelkar, George Zyvoloski and Rajesh Pawar, Presented at the Ninth Annual CO_2 Sequestration Conference, May 11-13, 2010, Pittsburgh, PA.

5. Milestones:

The table below tracks milestone status for FY10.

Milestone #/ Task Activity	PIP Quarter	Start Date	Target End Date	Milestone	Milestone Completed
M 1 / Task 4	FY10 Q3	1 Jan 10	30 Jun 10	Complete the simulations of CO_2/deeper brine flow through well at Chimayo and complete a journal manuscript for the work	
M 2/ Task 3	FY10 Q4	1 Jan 10	30 Sep 10	Complete development of capability to solve the stress equations for radial geometry in FEHM	

5. Summary of Significant Accomplishments:

None.

Issues and Planned Resolutions

None.

Technology Transfer Activities

Not applicable.

REFERENCES

Jaeger J.C., and Cook N.G.W., 1979. Fundamentals of rock mechanics. Chapman and Hall, Publishers, New York, New York.

Lee H.S., Cho T.F., 2002. Hydraulic Characteristics of Rough Fractures in Linear Flow under Normal and Shear Load. Rock Mech. Rock Engng (2002) 35 (4), 299-318.

Min K.B., Rutqvist J., Tsang C.F., and Jing L., 2004. Stress-dependant permeability of fractured rock amsses: a numerical study. Int. J. Rock Mech. & Min. Sci., 41 (2004) 1191-1210.

LA-UR-10-07696

FY10-Q4 Quarterly Report

Project Title: Los Alamos National Laboratory Activities
for the Center for Zero Emission Research and Technology II (ZERT-II)

LANL Principal Investigator: **Rajesh Pawar**
LANL Program Manager: ***Melissa Fox***

Research Team: Bill Carey, Elizabeth Keating, Sharad Kelkar, Quinjun Kang, Saikiran Rapaka, Hari Viswanathan, George Zyvoloski

Date of Report: 8 November, 2010
Period Covered by Report: 4th Quarter FY10 (Jul-sep 2010)

NETL Project Manager: William Aljoe

Executive Summary

Los Alamos National Laboratory's (LANL) ongoing activities for the Center for Zero Emission Research and Technology–II (ZERT-II) are focused on the scientific basis for predicting the performance of engineered geologic CO_2 storage sites. LANL's approach involves using theory, observation, experiment and simulation to characterize the fundamental processes that control the long-term fate of CO_2 in the subsurface. Specifically, LANL's activities are primarily focused on three topics:

- Application of lattice-Boltzmann methods (LBM) to characterize multi-phase CO_2-water fluid-flow
- Coupled fluid-flow and stress simulations to characterize geo-mechanical response of CO_2 injection
- Characterization of impact of CO_2 and deeper brines on groundwater quality

Due to the late arrival of funding, LANL's ZERT activities were not initiated until the FY10 2nd Quarter. This quarterly report focuses on the work related to advances in the coupled flow-stress simulation capabilities in LANL's FEHM simulator, recent modeling work related to our Chimayo analog studies on CO_2 impact on shallow aquifer geochemistry and lattice Boltzmaan simulations for multi-phase CO_2-brine flow in porous media. Results of the Chimayo work were presented at the 10th Greenhouse Gas Technology Conference in Amsterdam.

1. Advancement of capabilities to simulate non-linear & plastic geo-mechanical response in FEHM:

1.1 Finite displacement boundary conditions in FEHM

As of the end of the previous quarter, FEHM supported zero-displacement boundary conditions and applied forces on the surface, as they are the natural conditions that arise in most mechanical problems. The functionality needed to specify fixed, but non-zero displacements at the boundary

was not available. However, in some cases it is useful to specify finite displacements, especially when driving plastic deformation problems using strain. During this quarter, we added this functionality to FEHM and tested it extensively.

1.2 New macro for traditional element based computations

As described in previous reports, the algorithm used in FEHM uses a novel factorization technique that separates the geometric (grid-dependent) component and the material-properties specific part of the stiffness matrix assembly computations. This results in a significant savings of computational time, as the shape-function integrals do not need to be computed during each iteration – the integrations can be performed just once during initialization and saved for subsequent use. However, for the sake of testing and verification, it is also useful to have the time-tested, traditional finite-element algorithm available as a user-specified option. During this quarter, we introduced a new macro "fem" which drives the computation using the standard formulation. All integrals are computed using Gauss Quadrature element-by-element and assembled into the global stiffness matrix.

1.3 Comparison of plasticity code with commercial software

In the previous quarter, we reported on the development of an Elasto-plastic mechanical deformation module for FEHM that utilizes a modular algorithm for computing the stiffness matrix and the residuals. The algorithm is independent of the material model being used. The material modules are only expected to return a physically consistent material stiffness matrix (the "D" matrix) and perform the stress updates for a given increment of strain. FEHM in turn uses the mechanical stiffness matrix to assemble the global stiffness matrix and the residuals, and solves for the updated displacements and strains.

In this quarter, we tested the mechanical deformation module using problems with a simple elasto-plastic model. The code was tested by comparing the results with those obtained using ABAQUS, an established commercial code. A beam of material was compressed under uniaxial strain conditions until irreversible plastic strains develop in the material. As the material is compressed further, we track the buildup of plastic strains, and the changes in the state of stress in the material. These results were compared with a simulation done under the same conditions using ABAQUS. The results were found to agree with each other closely.

1.4 Accuracy improvements for highly non-orthogonal grids

The quality of the grid plays a big role in the errors associated with numerical simulators. Most numerical schemes get higher errors and lower rates of convergence with distorted grids. However, for many geological applications, the grid is necessarily quite complex as it has to follow the features of the medium. Further, large changes in material properties can take place across the elements, leading to an amplification of errors. The jumps in material properties can lead to numerical "wiggles" in the solution, which can be a serious concern in nonlinear problems requiring many iterations.

We introduced many modifications into the code over this quarter to increase the accuracy when the grids are highly non-orthogonal, and with large changes in material properties. The calculation of control volumes associated with each node was made more accurate resulting in significantly better performance for lithostatic problems. In Figure 1, we show an example computation of thermal expansion of rock with elastic modulus varying over 2 orders of magnitude, over a very complex grid. It can be seen that the displacement matches the analytically expected linear profile very closely. We have also tested the code for problems involving time-dependent heating and observed that the results match the expected solutions very well.

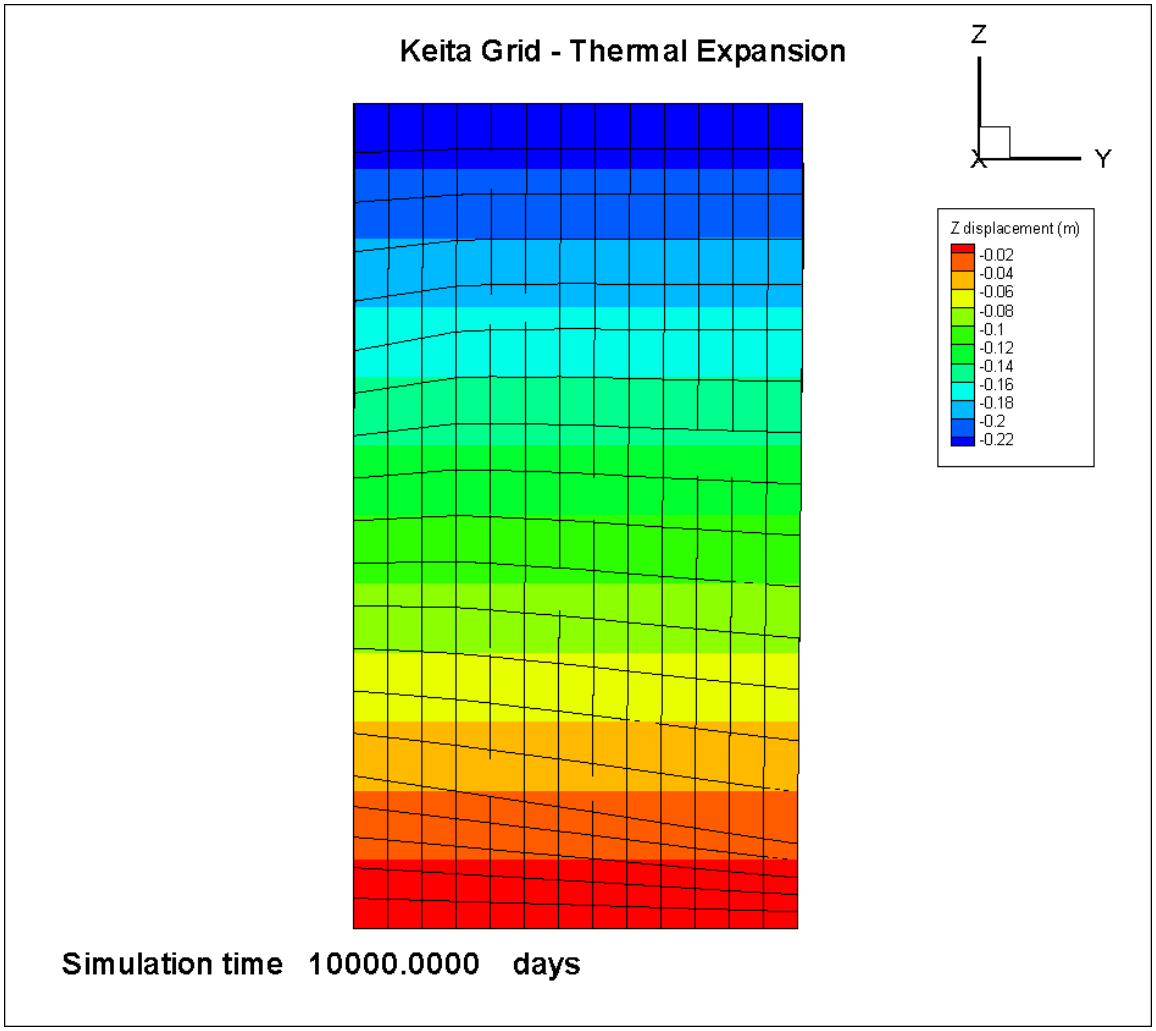

Figure 1. Displacements from thermal expansion on non orthogonal grid.

2. Progress on the natural analog study at Chimayo

Our recent progress in research at the Chimayo natural analog site has focused on developing site-specific batch, 1 and 3-D reactive transport models, informed by information collected at the site and also by laboratory experiments performed here at LANL (Bill Carey and others) and at NETL (Jaqueline Hakala). Much of this work was presented at the 2010 Annual Conference on

Carbon Capture & Sequestration conference (Viswanathan et al., 2010) and at the Greenhouse Gas Control Technology (GHGT-10) conference (Keating et al., 2010). A short paper was published as part of the GHGT-10 proceedings and is included as an appendix to this report. We also provided support to a third paper by collaborators at the U. of Pittsburgh (Gardiner et al., 2010) focusing on Sr isotope data collected at the site. We expect this collective work to culminate in several full papers in peer-reviewed journals in the next 12 months.

There are several broad goals for our modeling. One goal is to establish the extent to which laboratory and field-scale observations can be reconciled with a consistent model. Potential barriers to reconciliation include well-known discrepancies between field and laboratory estimated reaction kinetics, and the importance of physical and chemical heterogeneity at the field scale. Understanding the relationship between field and laboratory datasets will help future site characterization efforts design the appropriate scale of data collection. The second goal is to identify the key mechanisms affecting water quality in this particular shallow aquifer which is exposed to CO_2. Many of the mechanisms identified here may be important at other sites. Although mechanisms have been proposed based on field data collection (Keating et al, 2009), these need to be quantitatively tested through both modeling and laboratory analysis.

Experiments were conducted at LANL (Carey et al., 2009) to expose saturated sediments collected in Chimayo to CO_2 and measure resulting changes in water (see Figure 2).

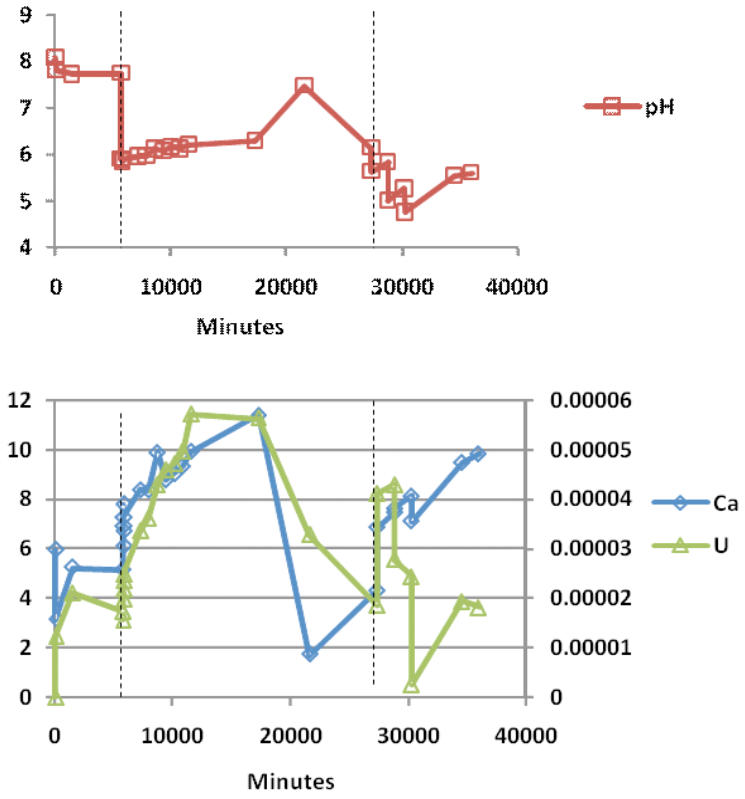

Figure 2. Experimental results.

The experiments conducted at NETL were designed to determine the types of reactions that would control trace metal release when exposed to CO_2. Both these sets of experiments were informative. We chose to focus initially on developing models for uranium, since uranium is a common trace element in this aquifer and has clear implications for human health.

Our first modeling goal was to reproduce the batch laboratory experimental results generated by Carey et al. (2009). Clay-rich sediments and quartz-rich sediments were collected from the Chimayo site. Batch experiments were conducted in which synthetic Chimayo groundwater was brought into contact with these sediments. CO_2 was then introduced into the system to determine how the aqueous geochemistry of the system was affected. One interesting trend that was observed showed that uranium and arsenic concentrations temporarily increased in the clay-rich sediments once CO_2 was introduced into the system. No increase was observed for the quartz-rich sediments.

In order to help determine what mechanisms may be responsible for the elevated trace metal concentrations, we performed forward geochemical modeling of the batch system. Several simplifying assumptions about the system were made. We assumed that the system was in equilibrium with calcite and that all aqueous speciation reactions were at equilibrium. We expected there to be multiple conceptual models that, when incorporated into a 1-D numerical model, could match the data.

2.1 Equilibrium with uraninite minerals

For the first attempt, we assumed that uraninite was the source of the uranium in solution and that the solution was in equilibrium with this mineral, as well as smectite and calcite. PHREEQC was used to titrate CO_2 into the system and predict the resulting water chemistry. Figure 3 shows the comparison between the experiment and model before CO_2 was injected and after it was injected, respectively.

The figures show that general trends in pH and the major ion chemistry were captured. However, uranium was greatly over-predicted by the model. These results lead us to believe that either uraninite is not the source of uranium or that the reaction is kinetically limited. Other possibilities exist such as ion exchange reactions with the clays that could also be causing the elevated uranium concentrations. Another mineral uranophane could also be a source for the uranium. Finally, a uranium-carbonate solid solution could also release U when exposed to CO_2.

2.2 Sorption reactions

Next, we explored the possibility that sorption reactions were controlling the chemistry. There have been numerous sorption models proposed in the literature for uranium. Because of the emphasis on carbonate chemistry, which is clearly important at Chimayo (and will be important in any CO_2-leakage scenario), we focused on the reactions proposed by Dong et al. (2005) and Hsi and Langmuir (1985). In laboratory experiments, Dong et al. (2005) found that in the presence of Ca, U-sorption is strongly pH-dependent due to the formation of specific U-Ca-CO_3 complexes which form at different pH values suppress sorption.

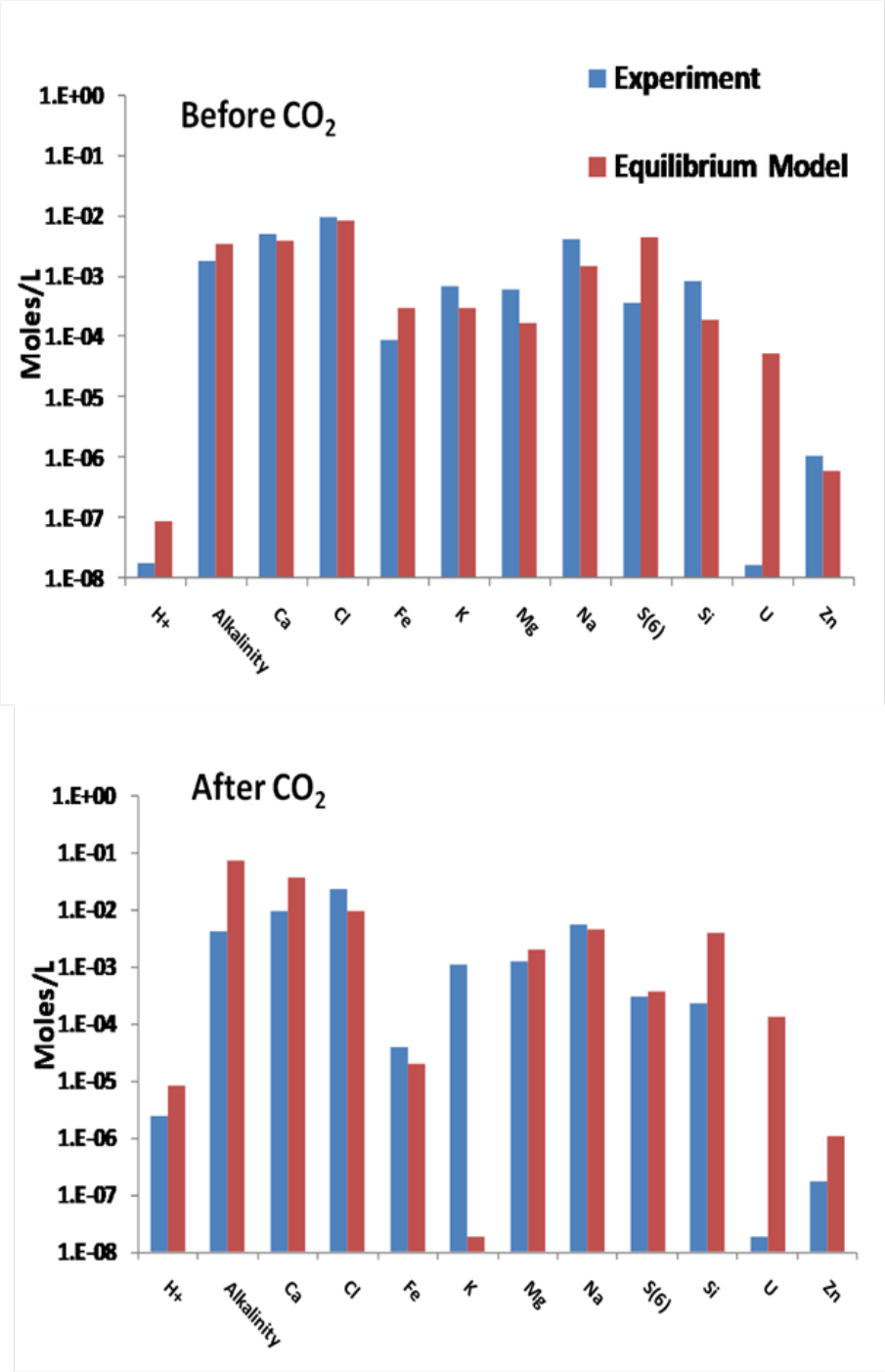

Figure 3. Comparison of measured and simulated water chemistry.

We incorporated these aqueous complexes into a reactive transport model using the code FEHM (Zyvoloski, 1997). (for all species and reactions considered, see Table 1). We found that under typical 'background' water chemistry conditions at Chimayo (as defined by groundwater samples reported in Keating et al., 2010) and the range of pH values measured during the LANL experiments (Carey et al., 2009), U sorption was never favored. Under all circumstances,

aqueous U was dominated by the $Ca_2UO_2(CO_3)_3$ complex, which were shown by Dong et al. (2005) to suppress U sorption.

Table 1. Solutes and reactions considered.

Solutes: H^+, H_2CO_3,Ca^{2+}, Cl^-, UO_2^{2+}, $Mg^{2+,}$ Na^+

Aqueous complexes

	H^+	H_2CO_3	Ca^{2+}	Cl^-	UO_2^{2+}	Mg^{2+}	Na^+	Log (K_{eq})
HCO_3-	-1	1	0	0	0	0	0	-6.3
CO_3^{2-}	-2	1	0	0	0	0	0	-16.6
OH-	-1	0	0	0	0	0	0	-14
$CaHCO_3^+$	-1	1	1	0	0	0	0	-5.245
$UO_2(CO_3)_2^{-2}$	-4	2	0	0	0	0	0	-16.3
$UO_2(CO_3)_2^{-4}$	-6	3	0	0	1	0	0	-28.41
UO_2CO_3	-2	1	0	0	1	0	0	-7.053
$Ca_2UO_2(CO_3)_3$	-6	3	2	0	1	0	0	-20.24
UO_2OH^+	-1	0	0	0	1	0	0	-5.0273

Calcite Minerals.

	H^+	H_2CO_3	Ca^{2+}	Cl^-	UO_2^{2+}	Mg^{2+}	Na^+	K_{sp}
Shallow aquifer	-2	1	1	0	2.E-7	0	0	2.14E8
Deep aquifer	-2	1	0	0	1.E-6	0	0	2.14E8

This result suggests U sorption/desorption reactions cannot explain the changes in U measured during the experiments when the sediments were exposed to CO_2. Another line of evidence is the correlation between the measured increase in [Ca] and [U] after exposure to CO_2 (see Figure 2). This suggests dissolution of a U-$CaCO_3$ solid-solution mineral. Geochemical models of the groundwater samples collected at Chimayo (Keating et al., 2010) also suggested that $CaCO_3$ dissolution is an important process at this site. Furthermore, sequential extraction experiments performed by NETL Hakala on sediment samples from Chimayo showed that U is either be desorbed from mineral surfaces (e.g., "exchangeable" fraction) or released through dissolution of carbonate minerals. Since desorption appears unlikely, we suspect dissolution of carbonate minerals.

2.3 1-D models of Chimayo, assuming solid solution U-$CaCO_3$ dissolution

Next, we developed 1-D models designed to reproduce the key features of the Chimayó aquifer: deep brine and CO_2 upwelling along a fault into a shallow sandstone aquifer, in accordance with the conceptual model of groundwater flow presented in Cumming (1997) and Keating et al. (2009, Figure 2). We assign initial water chemistry to the two layers in accordance with measured field data from the sandstone aquifer and inferred carbonate/brine water from geochemical models constrained by field data (Keating et al. (2009), Table 1).

Because the experimental data suggests that some or all the U is released from carbonate minerals, we simulated a solid-solution U-carbonate mineral with a molar ratio of U:Ca equal to that measured in the NETL sequential extraction experiments: ~2.E-7. This is a reasonable estimate of carbonate composition in the sandstone cements, but may underestimate the amount present in carbonates in the deeper layers. We assume the solid-solution carbonate mineral has the same K_{eq} as pure calcite. We include the aqueous uranium complexes considered by Dong et al. (2005) and Hsi and Langmuir (1985). We neglected redox reactions, since field data suggests that most waters are oxiding. CO_2 was only considered in the dissolved phase.

In Figure 4, we show the predicted evolution of [U] in the column. Interestingly, U concentrations in the upper nodes, corresponding to the shallow sandstone aquifer, initially decline. This is due to carbonate mineral *precipitation*, as a result of upward advection of the higher pH/high alkalinity water below and disequilibrium with the local water. This precipitation, in fact, continues throughout the simulation. However, after about 100 days the [U] increases above the initial conditions, due to advection of higher [U] concentration water originating below. The dominance of advective transport of [U], in contrast to *in situ* reaction–driven changes, suggested by this simulation result, is consistent with interpretation of field data trends presented in Keating et al. (2010).

To investigate the sensitivity of this result to assumptions about the U content of the deeper carbonate layer, we increased the molar ratio U:Ca to 10^{-6} in the deep layer. The results are shown in Figure 5. There are several interesting differences between this and the previous figure. First, the peak concentrations are much larger than the previous results. This is a direct consequence of the higher assumed U content of the deeper rock. Second, the highest concentrations only persist during intermediate times.

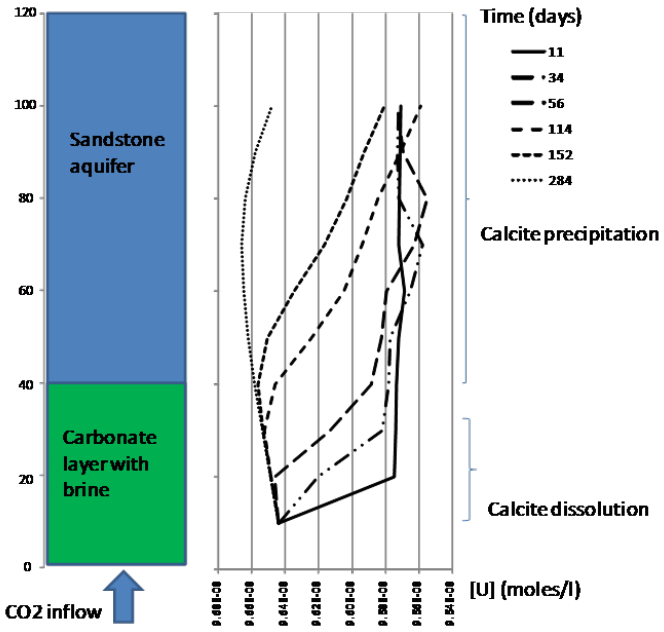

Figure 4. Results of 1-D simulation.

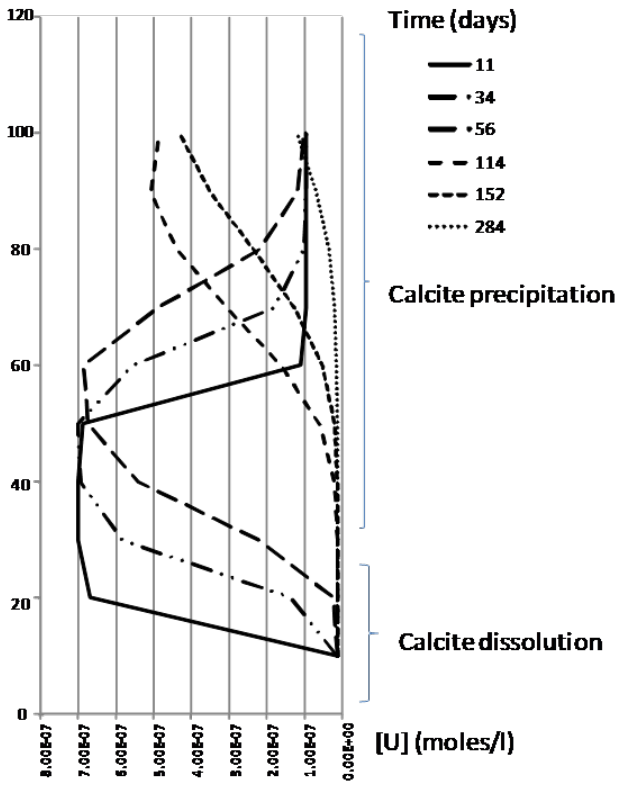

Figure 5. Simulation results for higher U:Ca molar ratio presumed for lower carbonate rocks.

At later times, this pulse has left the system and concentrations return to pre-leak levels. The length of time the high concentrations persist is related to many variables, including the molar ratio assumed for the deep layer.

2.4 3-D Models

Finally, we are beginning to develop 3-D models of the site, utilizing the approaches described above for the 1-D model. The model represents a two-layer system, corresponding to a deep carbonate layer and a shallow sandstone aquifer separated by a thin confining unit. The confining unit is breached in one location by a vertical, transmissive fault. In the shallow aquifer, flow is east-to-west with a hydraulic gradient approximately equal to that measured at the site (Cumming, 1997, Figure 10). Fresh water recharges the aquifer from the west and along the top at nodes corresponding to the Santa Cruz river (specified flux boundaries). The deep aquifer is recharged to the west with saline water. Both aquifers discharge at shallow nodes at the eastern edge of the model. This configuration is illustrated in Figures 6 and 7. The presumed water chemistry and reactions are shown in Table 3.

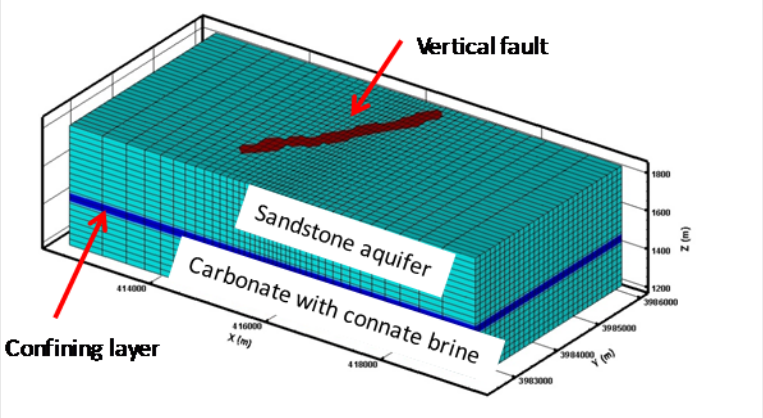

Figure 6 Hydrochemical model.

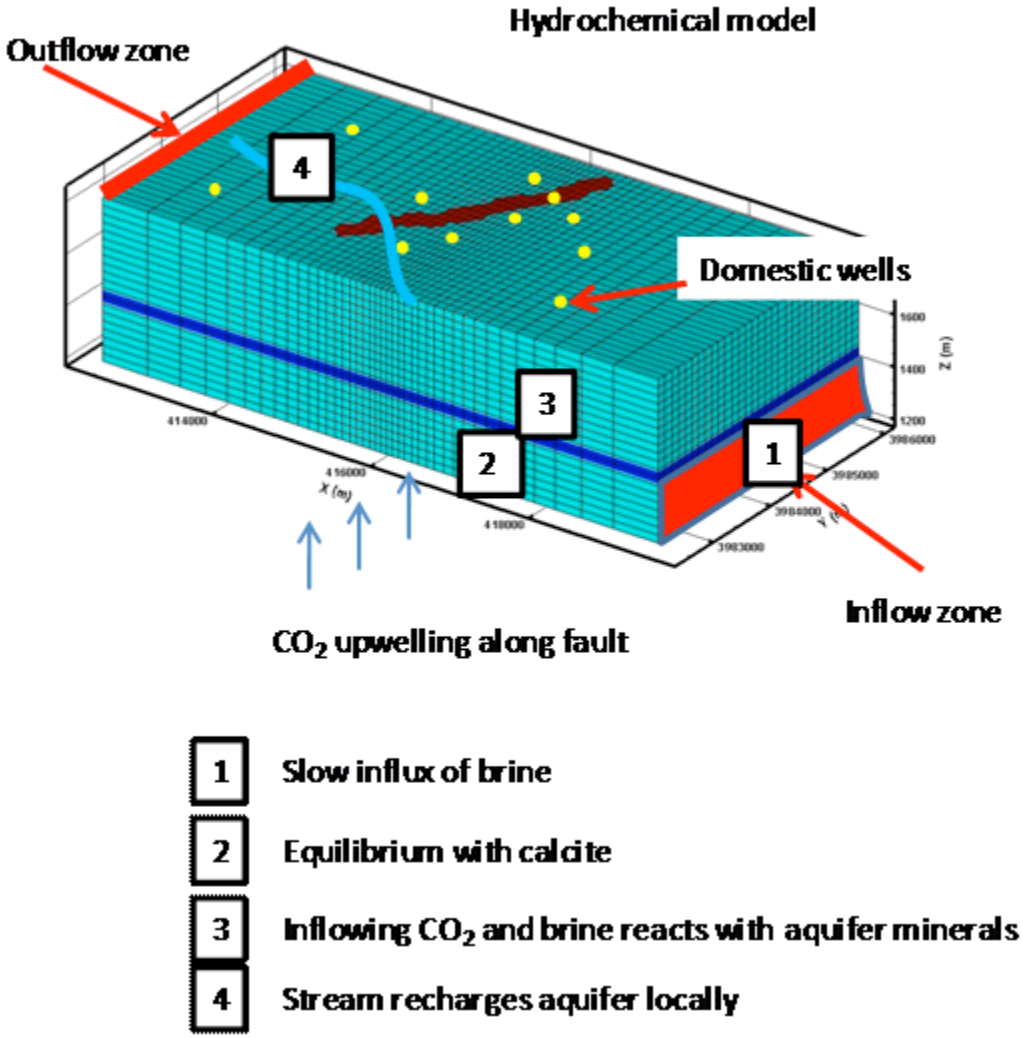

Figure 7 Hydrochemical model.

Table 3. Initial and boundary conditions for reactive-transport models. All units in moles/l except pH.

Inflow boundaries	Solute	Stream	Base of fault
	Ca	8.19E-07	8.19E-07
	Cl	0.00062	6.2E-07
	H+	6.5	6
	H2CO3	0	0.05516
	Na	0.000058	0.000058
	U	9.57E-12	7E-09
Initial conditions		Saline aquifer and confining unit	Shallow aquifer
	Ca	8.19E-05	0.002587
	Cl	0.01524	0.00062
	H+	7.6	6.806
	H2CO3	0.05516	0.009367
	Na	0.00058	0.04741
	U	7E-07	9.57E-08

Note: inflow nodes at upstream boundaries in saline aquifer and shallow aquifer are set equal to initial conditions.

At time = 0 a source of CO_2 is applied at the base of the fault. The CO_2 source is modeled indirectly as a source of H+ and HCO_3; no gas phase is present. We are in a very preliminary phase of this modeling. As shown in Figure 8, at early times the CO_2 displaces saline water in the fault which emerges at the base of the aquifer and elevates [U]. The plume of elevated [U] near the base of the shallow aquifer grows in time, but is eventually displaced by the relatively 'clean' (low [U]) water moving up from the base of the fault. Any changes in shallow groundwater chemistry caused by in-situ reactions are overwhelmed by advection of water up from the lower layers.

2.5 Preliminary conclusions and next steps

The modeling studies to date indicate that U-$CaCO_3$ dissolution is the most likely mechanism causing [U] to temporarily rise in the laboratory when sediments are exposed to CO_2. This is consistent with the results of sequential extraction experiments conducted by Hakala at NETL. There is, of course, uncertainty in the exact composition of the U-$CaCO_3$ solid solution and the kinetics of its dissolution/precipitation.

The simulations so far support the hypothesis proposed by Keating et al. (2009) that advection of trace elements via saline waters at depth overwhelms any in-situ reactions that may be controlling trace element chemistry. This hypothesis needs further examination and testing.

We plan to continue using the 1-D models to try to better match the measured U concentrations during the LANL experiments. We also plan to further develop the 3-D model by

- Varying the composition of the saline water in the carbonate layer
- Varying the composition of the upwelling, CO2-infused, water at the base of the fault
- Implementing two-phase flow
- Adding isotopes (C and Sr) to the simulations.
- Making quantitative comparisons between model results and field samples

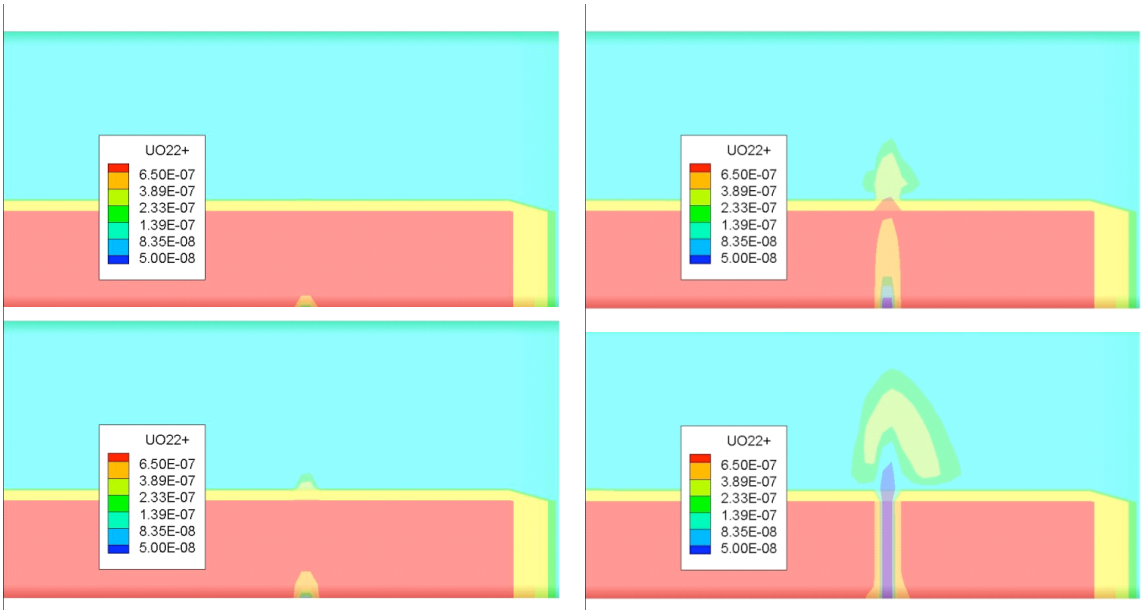

Figure 8. 3-D model results, shown along a N-S cross-section near the fault.

3. Pore-scale modeling of supercritical CO_2-water-rock multiphase system

Multiphase flow in natural and man-made porous media is ubiquitous, particularly in various energy, Earth, and environment systems. One example is the geological CO_2 sequestration, one of the most promising near-term solutions to the problem of reducing carbon emissions into the atmosphere. In this problem, the key processes are ultimately governed by the pore-scale interfacial phenomena, which occur at scales of microns. However, because of the wide disparity in length scales, it is virtually impossible to solve the pore-scale governing equations at the scale of interest. As a result, a continuum formulation (macroscopic approach) of multiphase flow in porous media based on spatial averages and empirical parameters (such as relative permeability) is often employed. As the spatial averaging is taken over length scales much larger than typical pore and grain sizes, spatial heterogeneities at smaller scales are unresolved. These unresolved heterogeneities, together with the empirical parameters often unrelated to physical properties, lead to significant uncertainties in multiphase flow modeling at the larger scale. Additionally, for CO_2-water multiphase systems, little experimentally measured data is available for relative permeability functions used in the continuum scale simulation. Therefore, to reduce uncertainties in the numerical modeling at the scale of interest, it is imperative to better understand these processes at the pore scale and to derive more physics-based constitutive relation for the continuum models.

However, at the pore scale, the multiphase flow in a confined system with fluid-fluid-solid interfaces is a moving contact-line problem, the theoretical analyses of which, on the basis of the classical hydrodynamics approach, with a sharp interface and no-slip boundary condition, lead to a non-integrable stress singularity at the contact line. Because of the kinetic nature of the lattice Boltzmann (LB) equations, however, there is no such singularity in the LB simulation of moving contact-line problems while the no-slip condition is still satisfied. The contact-line motion is achieved through the relative diffusion of the two fluid components in the vicinity of the contact line, which leads to effective slip of the interface of finite width at the contact line.

In the past a few months, we have simulated two-phase flow through porous media with various microstructures and have investigated the effect of pore-scale heterogeneity on relative permeability.

Figure 9 shows the dependence of relative permeability on wetting phase (WP) saturation for co-current two-phase flow through three different microstructures, including granular, fibrous, and network structures.

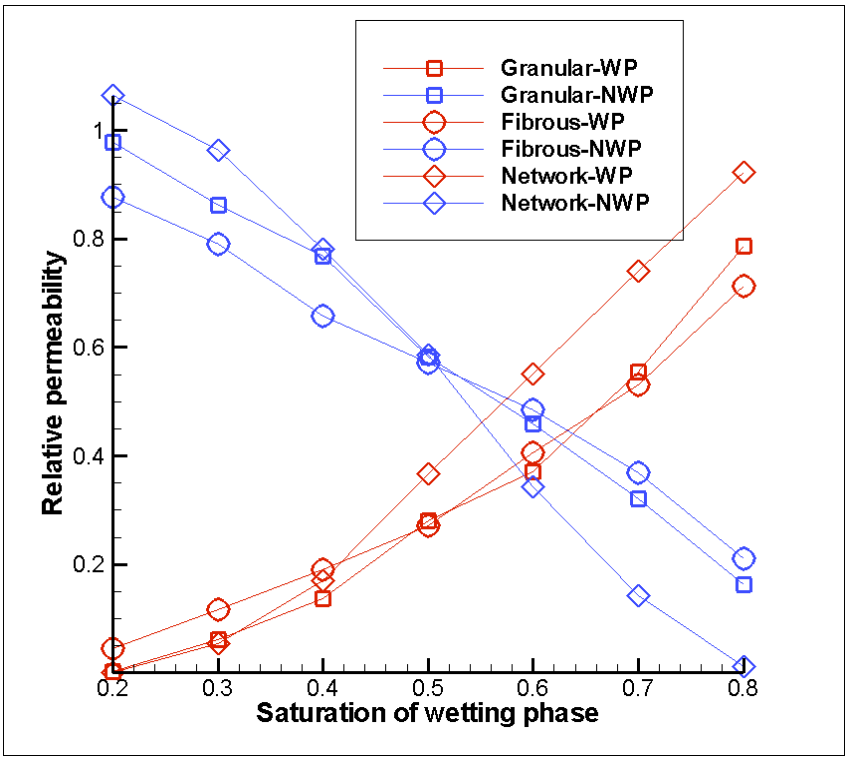

Figure 9. Relative permeability vs WP saturation for co-current two-phase flow through three different microstructures

Clearly, for a WP saturation smaller than 0.5, the network medium has the highest non-wetting phase (NWP) relative permeability, while the fibrous medium has the lowest. However, this trend is reversed when the WP saturation is greater than 0.5. Also, at the smallest WP saturation, the NWP relative permeability for the network medium exceeds one. This is counter-intuitive. It can be either physically correctly, or may be caused by numerical errors. One possible

explanation is that the small amount of WP fluid forms a thin film along the solid surface, which acts like a lubricating fluid, reducing the friction between the NWP and the solid walls. As a result, the flux of the NWP fluid is actually increased compared to the case where only one such fluid is in the system. However, more careful numerical studies and analyses on fluid-fluid and fluid-solid interfacial areas need to be carried out to better understand this phenomenon.

Figure 10 shows the steady-state distribution of the NWP at different WP saturations for the three different porous media.

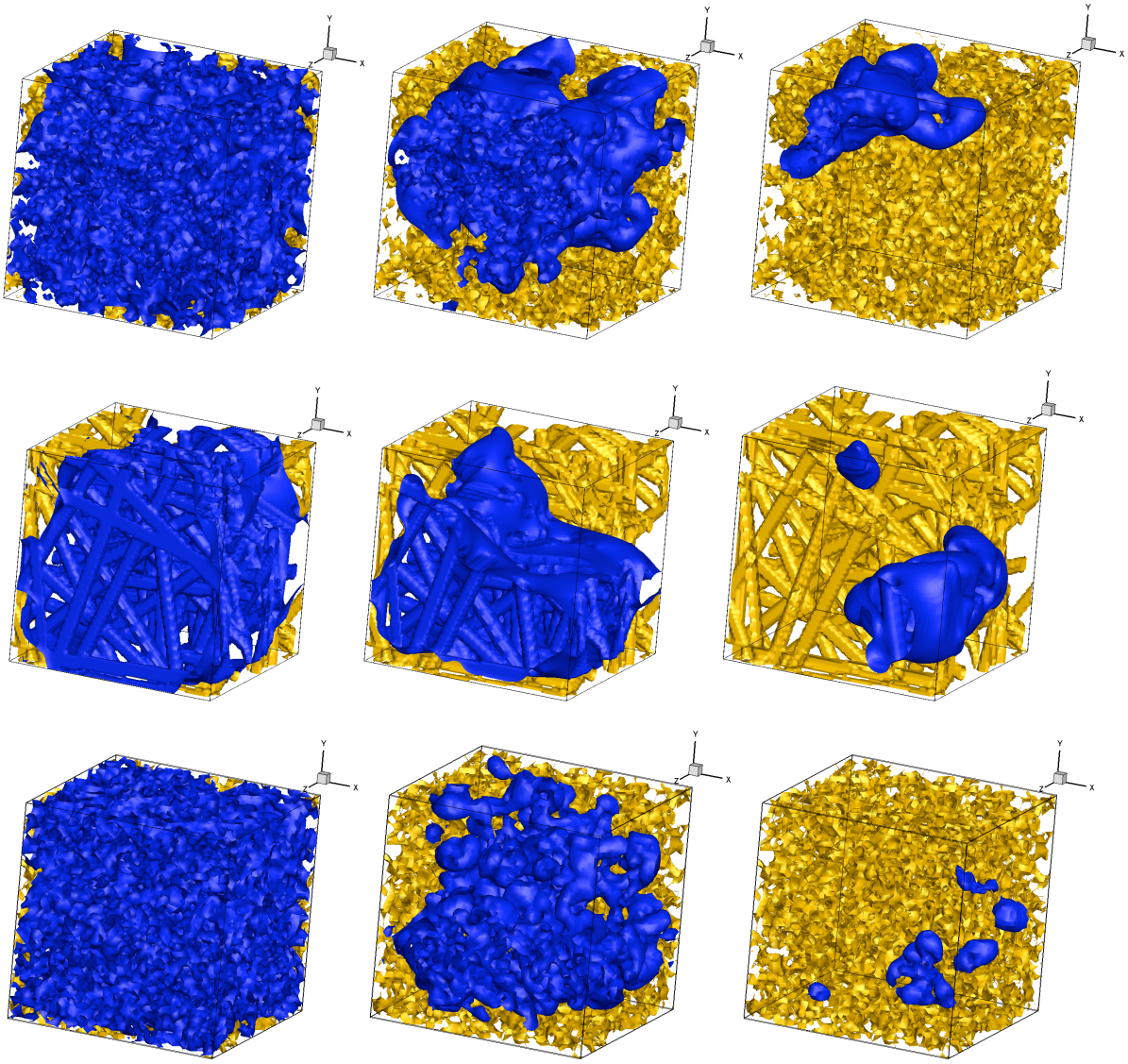

Figure 10. Steady-state distribution of the NWP (blue) at different WP saturations (0.2, 0.5, and 0.8 from left to right) for the three different porous media (granular, fibrous, and network from top to bottom). Yellow regions represent the solid phase.

In these simulations, the WP and NWP have the same density and viscosity. The results may be applicable to CO_2-water-rock multiphase system if the capillary forces are dominant, and therefore both the density and viscosity ratios are not important. Otherwise, the realistic ratios for

such a system should be accounted for in the numerical simulations. This can be achieved by using a multiple relaxation time (MRT) LBM instead of a single relaxation time (SRT) LBM and consists of the work for the next fiscal year.

4. Publications/presentations:

Keating, Elizabeth H., Hakala, J.A., Viswanathan, H., Capo, R., Stewart, B, Gardiner, J., Guthrie, G., Carey, J.W., Fessenden, J., 2010, The challenge of predicting groundwater quality impacts in a CO_2 leakage scenario: Results from field, laboratory, and modeling studies at a natural analog site in New Mexico, U.S.A. Energy Procedia, *in press*.

5. Milestones:

The table below tracks milestone status for FY10.

Milestone #/ Activity	PIP Quarter	Start Date	Target End Date	Milestone	Milestone Completed
M1/ Task 4	FY10 Q3	1 Jan 10	30 Jun 10	Complete the simulations of CO_2/deeper brine flow through well at Chimayo and publish a peer-reviewed paper	30 Sep 10
M 2/ Task 3	FY10 Q4	1 Jan 10	30 Sep 10	Complete development of capability to solve the stress equations for radial geometry in FEHM	

6. Summary of Significant Accomplishments:

None.

Issues and Planned Resolutions

None.

Technology Transfer Activities

Not applicable.

REFERENCES

1. Carey, J. W., Williams, M. R.; Hakala, A.; Fessenden, J. E.; Keating, E. H., Experimental study of sediment-CO2 reactions with application to changes in groundwater quality due to leakage of sequestered CO2. American Geophysical Union, Fall Meeting, **2009**, abstract #H13A-0913

2. Cumming, K.A., Hydrogeochemistry of groundwater in Chimayó, New Mexico, M.S., Northern Arizona University, **1997**, Flagstaff, AZ.
3. Dong, W. et al. , W.P. Ball, C. Liu, Z. Wang, A. Stone, J. Bai, J.M. Zachara, Influence of Calcite and Dissolved Calcium on Uranium(VI) Sorption to a Hanford Subsurface Sediment. Environ. Sci. Technol., **2005**, 39, 7949-7955.
4. Hsi, C-K D., L. Langmuir, Adsorption of uranyl onto ferric oxyhydroxides: Application of the surface complexation site-binding model, *Geochemica Cosmica Arm,* **1985**, *Vol. 49. pp. 193*
5. Gardiner, J. B., Stewart, B. W., Capo, R. C., Hakala, J. A., Keating, E. H. , Tracking CO_2 migration through a sandstone aquifer using Sr isotopes: Chimayó, New Mexico, USA., Goldschmidt Conference Abstracts, Geochim. Cosmochim. Acta , **2010**, 74: 11 (suppl. 1), A320.
6. Keating, Elizabeth H., Hakala, J.A., Viswanathan, H., Capo, R., Stewart, B, Gardiner, J., Guthrie, G., Carey, J.W., Fessenden, J., 2010, The challenge of predicting groundwater quality impacts in a CO_2 leakage scenario: Results from field, laboratory, and modeling studies at a natural analog site in New Mexico, U.S.A. Energy Procedia, *in press*.
7. Keating, E.H., Fessenden, J., , Kanjorski, N., Koning, D., Pawar , R., The impact of CO_2 on shallow groundwater chemistry: observations at a natural analog site and implications for carbon sequestration, Environmental Environmental Earth Science, **2009**, DOI 10.1007/s12665-009-0192-4
8. Viswanathan, H., Keating, Elizabeth H., Hakala, Carey, J.W., J., Guthrie, G., Reactive Transport Modeling and Field Observations of CO_2 Impacts on Shallow Groundwater Chemistry in Chimayo, New Mexico, 2010, Hari Viswanathan, Elizabeth Keating, Jaqueline Hakala, J. William Carey and George Guthrie Proceedings, 2010 Annual Conference on Carbon Capture & Sequestration conference, Pittsburg, PA.

9. Zyvoloski, G. A., et al. ,1997, Summary of the Models and Methods for the {FEHM} Application --- A Finite-Element Heat- and Mass-Transfer Code, 72 pp, Los Alamos National Laboratory.

ZERT II Quarterly Report:

July 1 – September 30, 2010 (Q4 FY2010)

Contact:
Curtis M. Oldenburg

Contributors in alphabetical order:
Christine Doughty
Timothy J. Kneafsey
Jennifer L. Lewicki
Curtis M. Oldenburg
Karsten Pruess
Matthew Reagan
Dmitriy Silin
Tianfu Xu

Earth Sciences Division
Lawrence Berkeley National Laboratory
1 Cyclotron Rd., MS 90-1116
510-486-7419; cmoldenburg@lbl.gov

DOE Program Manager: William Aljoe, 412-386-6569

October 12, 2010

Highlights

- A large-scale CO_2 migration and fault-leakage test problem was simulated using the new TOUGH2/ECO2M which can simulate all phase combinations of CO_2. Cyclic leakage phenomena associated with phase interference and Joule-Thomson cooling were modeled.
- Completed the sample problems and user guide to accompany the beta release of TOUGHREACT V2 that occurred in FY10.
- Carried out accumulation chamber soil-gas CO_2 flux surveys at the MSU release facility.
- Published paper on modeling pore scale phenomena and microtomography.
- Laboratory and modeling studies of pore occupancy demonstrated that heterogeneity affects CO_2 invasion at multiple scales.

Project Milestones for FY10

Milestone	Due Date	Delivery Date
Release of TOUGHREACT V2	Sept. 30, 2010	Sept. 30, 2010 as documented in this quarterly report under Task 2b.
Journal article on monitoring at ZERT facility	June 30, 2010	March, 2010 (Lewicki et al., published in *Env. Earth Sci.* (see publication list)
Reporting on pore occupancy and residual gas trapping	Sept. 30, 2010	Sept. 30, 2010, as documented in this quarterly report under Task 4a.

Research Progress Report

Task 1. Project Management, Planning, and Reporting

Goal: Maintain the Project Management Plan, including its revision(s), and report on activities in accordance with the plan.

This project consists of three technical tasks aimed at improving performance prediction of geologic carbon sequestration, developing approaches to monitor and verify storage, and improving understanding of trapping processes. The approaches used include computer modeling, field investigations at the ZERT shallow-release facility in Montana, and laboratory work. The project is organized into three technical Tasks 2-4 with a single task lead assigned to each task. The tasks share findings and models, particularly between Tasks 2 and 3, and 2 and 4 as computer models (Task 2) are used in Task 3 for predicting CO_2 leakage fluxes, and Task 4

generates data on relative permeability that can be used in computer models (Task 2). There is heavy interaction with Montana State University in Task 3 during the summer months when field experiments are carried out. Despite the seasonality of injection experiments, the spending profile for all tasks is nearly flat through the year because Tasks 2 and 4 do not involve field work, and data analysis and modeling occur in Task 3 during the non-summer months. In this Task 1, management and reporting of the project will be carried out.

Task 2. Performance prediction for underground fate and transport of CO_2
Goal: To develop reliable techniques to predict and model CO_2 migration and trapping mechanisms.

The TOUGH codes will be further developed to accurately simulate the fate and transport of CO_2 in the subsurface. TOUGH2 and TOUGHREACT are available to the public through the Department of Energy's National Energy Software Technology Center. The TOUGH2 simulator ("**t**ransport **o**f **u**nsaturated **g**roundwater and **h**eat") is a multi-dimensional numerical model for simulating the coupled transport of water, vapor, gas components, and heat in porous and fractured media. TOUGH2 offers added capabilities and user features, including the flexibility to handle different fluid mixtures through a wide variety of EOS (equation of state) modules. TOUGH2 uses an integral finite difference method for space discretization, and first-order fully implicit time stepping. Various preconditioned conjugate gradient and direct sparse matrix solvers are available for linear equation solution. Thermophysical properties of water are represented, within experimental accuracy, by steam table equations provided by the International Formulation Committee. The program provides options for specifying injection or withdrawal of heat and fluids. Double-porosity, dual-permeability, and multiple interacting continua (MINC) methods are available for modeling flow in fractured porous media. TOUGH2 takes account of fluid flow in both liquid and gaseous phases occurring under pressure, viscous, and gravity forces according to Darcy's law. Interference between the phases is represented by means of relative permeability functions. The code includes Klinkenberg effects and binary diffusion in the gas phase, and capillary and phase adsorption effects for the liquid phase. Heat transport occurs by means of conduction (with thermal conductivity dependent on water saturation), convection, and binary diffusion, which includes both sensible and latent heat.

TOUGHREACT uses the same basic architecture as TOUGH2, but includes geochemical reactions between CO_2, water, solutes and rock. Both equilibrium and kinetic calculations of mineral dissolution and precipitation can be carried out, thus allowing evaluation of mineral trapping.

Task 2a. Long-term CO_2 migration and leakage

Migration of CO_2 away from the storage reservoir remains a primary concern for geologic CO_2 storage. As free-phase CO_2 migrates upwards from the storage reservoir towards the land surface it decompresses and changes from a supercritical to gaseous phase. The pressure decreases can lead to cooling of the CO_2 and surrounding rock. This has been shown to create complex periodic migration behavior which has the tendency to self-limit rates of upward migration.. CO_2 injection may cause formation dry-out, which may be accompanied by precipitation of solids, and reduction in porosity, permeability and injectivity. In this task, we

develop and quantify scenarios for CO_2 migration to develop greater understanding of both self-limiting and self-enhancing processes controlling CO_2 migration. Additional capabilities will be added to TOUGH2 where needed.

Deliverable: None for this quarter.

Task 2b. TOUGHREACT V2

Add new capabilities to TOUGHREACT, improve existing treatments of processes, correct I/O problems, develop new sample problems, test the code and write up user guide. The recently implemented Pitzer ion-interaction model will be added later following in-depth testing.

Deliverable: Completion of TOUGHREACT V2 user guide, release of beta version of TOUGHREACT V2.

Task 2c. Hysteresis and Heterogeneity

In this task, we will investigate the effects of heterogeneity and scale (from core to reservoir scale) on the long-term residual gas trapping of CO_2. Relative permeability (the fundamental property that allows for residual phase trapping) in multiphase systems such as supercritical CO_2 and brine is dependent on the history of fluid-phase occupancy. For example, porous media that is draining (water exiting, CO_2 entering) has a different permeability to water and CO_2 than porous media that is imbibing (water entering, CO_2 exiting) as occurs when CO_2 migrates over long time periods up dip.

Deliverable: None for this quarter.

Task 2d. Near-surface modeling

CO_2 in the shallow subsurface will encounter soil gas that is predominantly air. For modeling near-surface CO_2 leakage and seepage, we have developed a module called EOS7CA where the CA stands for CO_2 and Air. Although we have applied this module extensively to the ZERT shallow-release experiment, we have not developed a user guide or set of test problems to make it accessible to others. In this task, we will develop test problems and write a user guide for EOS7CA.

Deliverable: None for this quarter.

Task 2 Results and Discussion

Task 2a. Long-term CO_2 migration and leakage

Long-term behavior of CO_2 plumes

We analyzed a variation of our previous scenario of plume migration beneath a sloping caprock, in which we assume that the storage aquifer has a vertical fault zone that extends all the way to

the ground surface (Figure 1; not to scale). The model domain as shown in Figure 1 has a tilt angle of $\alpha = 1.5^{o}$.

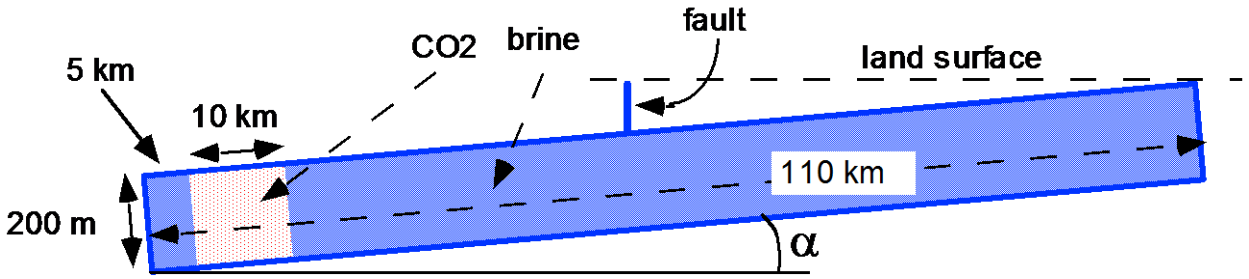

Figure 1. *Geometric dimensions of the flow system modeled. The initial CO_2 plume is shown by light shading. The fault intercepts the aquifer at a distance of 50 km from the left boundary.*

The simulation uses our new fluid property module ECO2M for TOUGH2, which can represent all possible phase combinations in the CO_2-brine system, including transitions between super- and sub-critical conditions, and phase change between liquid and gaseous CO_2. This allows a seamless modeling of CO_2 storage and leakage, all the way from a deep storage reservoir to the land surface.

Results are given in Figures 2-4. The CO_2 plume reaches the fault zone after about 185 years, at which time CO_2 begins to flow up the fault while water flow changes from small upflow to downflow. Subsequently, both CO_2 and water fluxes show cyclic variations (Figures. 2, 3), which arise from an interplay of three different processes with different time constants, (1) multiphase flow of CO_2 and water in the fault zone, that is accompanied by strong cooling effects from liquid CO_2 boiling into gas, and gaseous CO_2 expanding on approach to the land surface (Joule-Thomson effect), (2) heat exchange between fluids in the fault zone and the surrounding wall rocks, and (3) multiphase flow in the storage aquifer. Fig. 4 shows that the advancement of the CO_2 plume stalls when the fault zone is reached, but after a period of about 50 years, plume advancement continues with the same speed as for the case without a leaky fault. This behavior can be understood by noting that the leading edge of the plume is rather thin, so that fault zone leakage initially amounts to a large fraction of total updip CO_2 flow. Over time the CO_2 plume at the bottom of the fault thickens, so that leakage becomes a small fraction of total CO_2 flow, and impacts on the speed of plume advancement become small.

A first presentation of these results was made at the 10th International Conference on Greenhouse Gas Control Technologies (GHGT10; Pruess, 2010). Simulations and analysis of fault leakage are continuing.

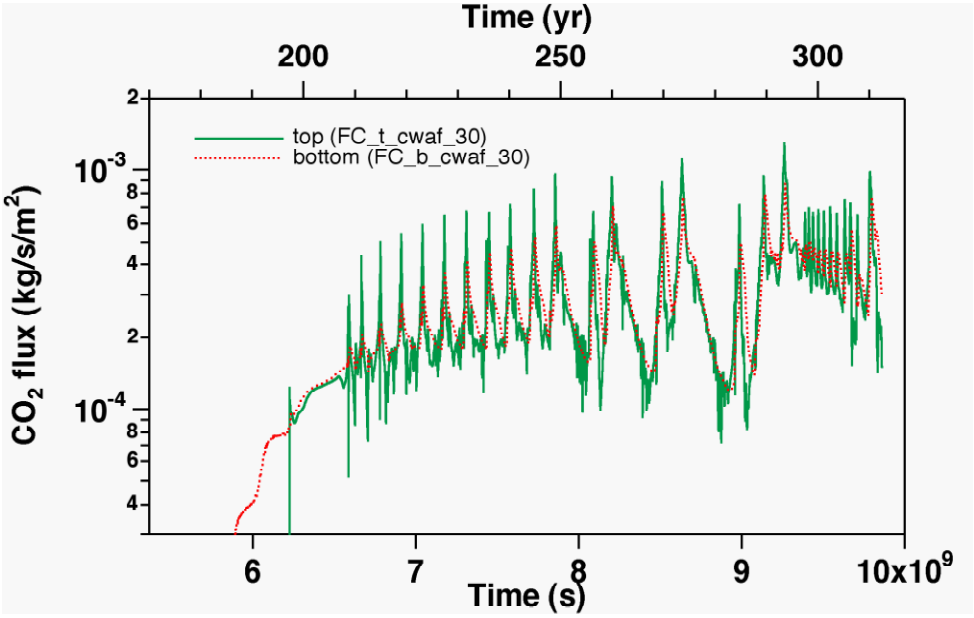

Figure 2. *CO_2 fluxes at the bottom and the top of the fault.*

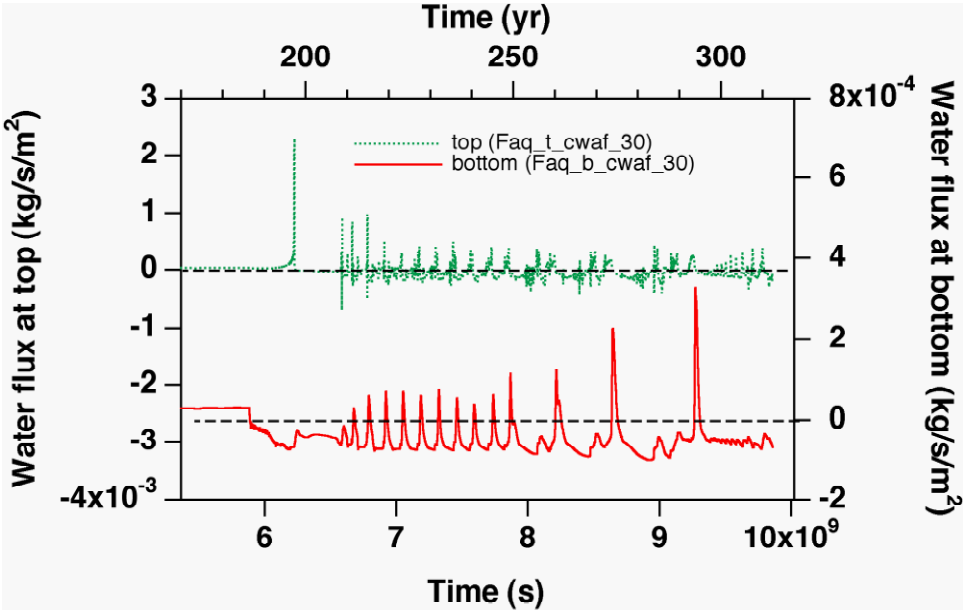

Figure 3. *Water fluxes at the top and bottom of the fault.*

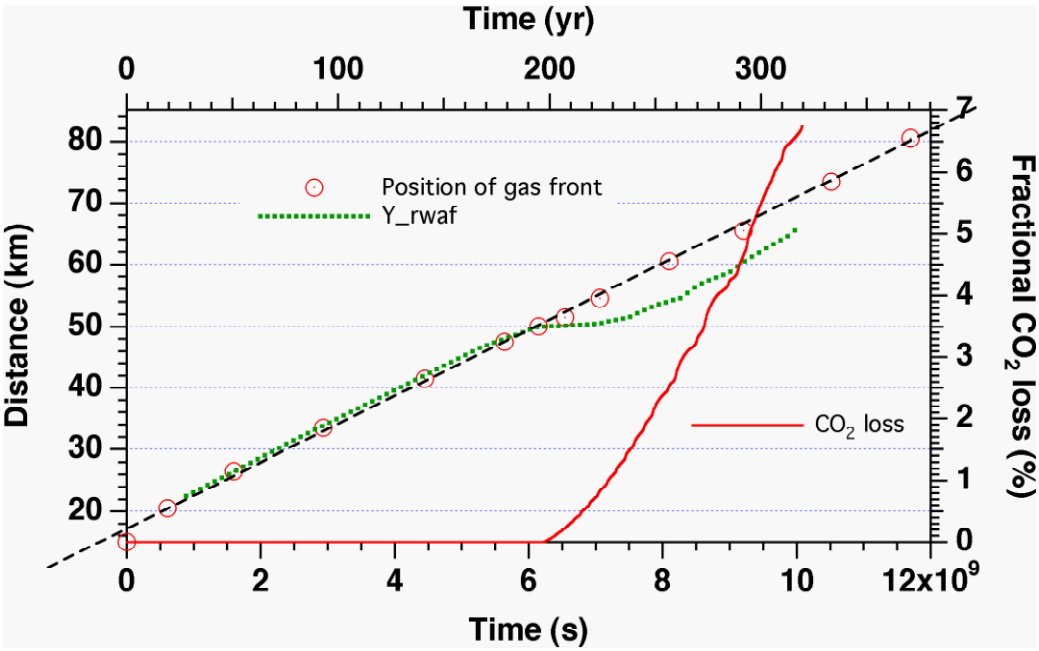

Figure 4. *Updip advancement of the CO_2 plume. Open circles are for the case without a fault, while the dotted line is with a fault zone present. CO_2 loss from the fault zone is also shown.*

Task 2b. TOUGHREACT V2

Sample problems and user guide of TOUGHREACT Version 2 have been completed. The two-dimensional sample problem reported last Quarter for long-term fate of injected CO_2 has been refined and included in the manual. The TOUGHREACT V2 beta code has been released to collaborators at the USGS (Palguta), Iceland (Etta), and multiple internal LBNL users.

Task 2c. Hysteresis and Heterogeneity

The TOUGH2 formulation for hysteretic relative permeability and capillary pressure curves are based on the van Genuchten (1980) functions, which are widely used for two-phase flow problems, and have enough degrees of freedom to enable them to be fit to a wide variety of experimental data. In the past, most of this experimental data came from the petroleum literature, but recently experiments have been conducted on two-phase mixtures of brine and supercritical CO_2 (Bachu and Bennion, 2008; Lee et al., 2010; Benson et al., 2006). Laboratory findings for two key features of the relative permeability functions are discussed here, along with their implications for numerical modeling.

The first parameter is k_{rgmax}, the value the gas relative permeability k_{rg} takes when liquid saturation S_l is reduced to its "irreducible" value S_{lr}. Irreducible is in quotes because it is not really the minimum value S_l can take, but is the value at which the liquid phase becomes immobile. Liquid saturation can decrease below this value by evaporation. Laboratory studies typically only measure relative permeability values for $S_l > S_{lr}$, thus the maximum k_{rg} value they provide is k_{rgmax}. In early studies of GCS, $k_{rgmax} = 1$ was commonly used, but the laboratory

results show a large range of k_{rgmax} values, from 0.01 to 0.91, with an average of 0.26. Small values of k_{rgmax} thus appear very likely, and will result in larger pressure increases accompanying CO_2 injection than would be predicted by a model using $k_{rgmax} = 1$.

The second parameter examined is the m parameter in van Genuchten's relative liquid permeability k_{rl} function, which controls the concavity of k_{rl}. Small values of m produce a highly concave function, resulting in k_{rl} values that are very small for most values of S_l. At the other extreme, using a value of m = 0.9 in van Genuchten's k_{rl} function makes it roughly equivalent to a cubic function, which yields a larger value of k_{rl} than do most commonly-used expressions for k_{rl}. For example, the Corey (1954) k_{rl} curve is a power-law function with exponent 4 and is comparable to m = 0.78. Using even smaller values of m has been common in code comparison and other modeling studies of CO_2 geologic storage (e.g., Pruess et al., 2002), and a regression of experimental soil moisture data produced m values in the range 0.083 – 0.627 (Carsel and Parrish, 1988). However, recent experimental measurements of CO_2/brine relative permeability functions using core samples from a variety of deep saline formations (Bachu and Bennion, 2008) shows k_{rl} functions that are well fit with power-laws using exponents ranging from 1.4 to 3.5, comparable to m ranging from 1.4 to 0.83. Hence, large values of m appear to be plausible. One important consequence of using large m values is that within the two-phase CO_2 plume, liquid brine is very mobile. Thus, when drawn by capillary forces, it can flow strongly toward the injection well, where the water evaporates into the supercritical CO_2 phase and dissolved salt precipitates. This can cause significant permeability reduction in the vicinity of the injection well.

The studies of the parameters of the relative permeability and capillary pressure curves used in TOUGH2 for CO_2/brine systems are at an early stage, and much further analysis of laboratory results remains to be done.

References

Bachu, S. and B. Bennion, Effects of in-situ conditions on relative permeability characteristics of CO_2/brine systems, Environmental Geology, 54, 8, 1707-1722, 2008.

Benson S.M., Tomutsa, L., Silin, D., Kneafsy, T. Core Scale and Pore Scale Studies of Carbon Dioxide Migration in Saline Formations. GHGT-8, Trondheim, Norway, June 2006.

Carsel, R.F. and R.S. Parrish, Developing joint probability distributions of soil water retention characteristics, Water Resources Res., 24, 5, 755-769, 1988

Corey, A.T., The interrelation between gas and oil relative permeabilities, Producers Monthly, 19,1, 38-41, 1954.

Lee, Y.S., K.H. Kim, T.H. Lee, W.M. Sung, Y.C. Park, and J.H. Lee, Analysis of CO_2 endpoint relative permeability and injectivity by change in pressure temperature, and phase in saline aquifer, Energy Sources, Part A, 32, 83-99, 2010.

Pruess, K., J. García, T. Kovscek, C. Oldenburg, J. Rutzvist, C. Steefel, and T. Xu, Intercomparison of numerical simulation codes for geologic disposal of CO_2, Rep. LBNL-51813, Lawrence Berkeley National Laboratory, Berkeley, CA, 2002.

van Genuchten,M. Th., A closed-form equation for predicting the hydraulic conductivity of unsaturated soils, Soil Sci. Soc. Am. J., 44, 5, 892-898, 1980.

Task 2d. Near-surface modeling

No activity to report for this quarter.

Task 2 (supplemental). WebGasEOS Usage Report

WebGasEOS is an online tool we developed for outside users to calculate properties of CO_2 gas mixtures. Its development was supported by ZERT and here we report on usage statistics.

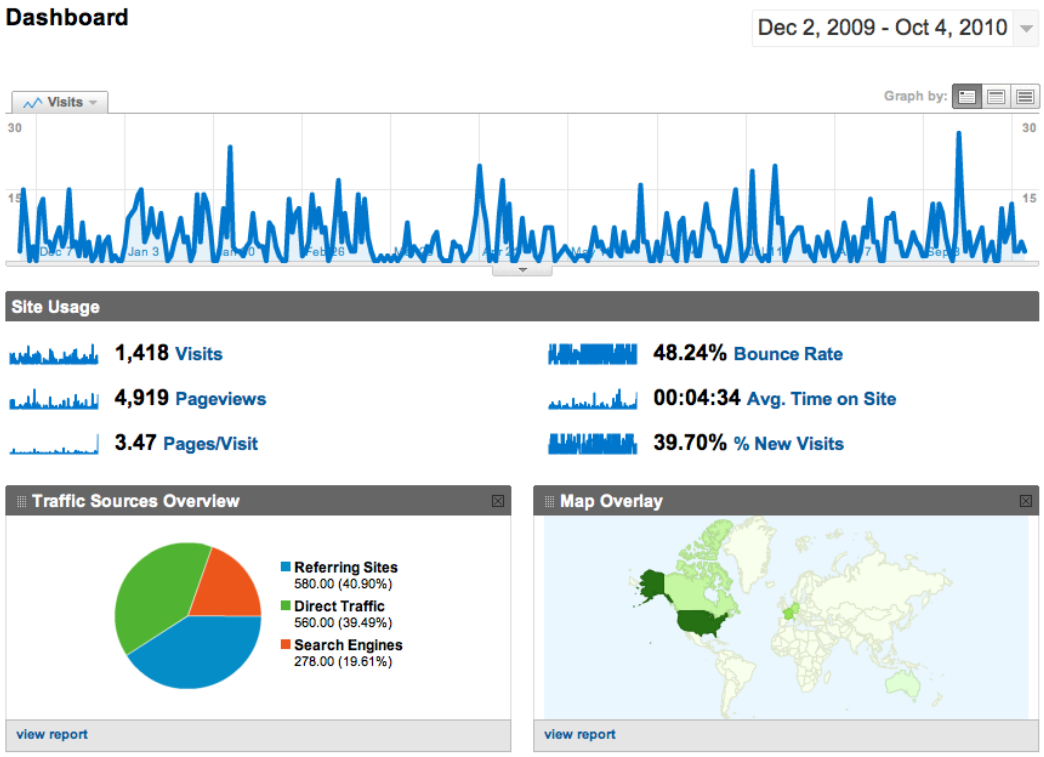

Figure 5. *Google Analytics summary of WebGasEOS activity for 2010*

Total WebGasEOS Site Traffic

From December 2, 2009 through October 4, 2010, the WebGasEOS site experienced continuous and substantial usage. A total of 4,919 requests for pages from the server were recorded for WebGasEOS site content.

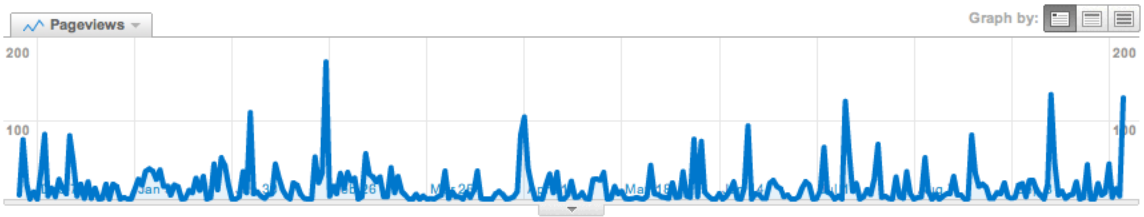

Figure 6. *WebGasEOS site usage (pageviews) for 2010*

These pageviews may be broken down into 1,448 "visits" (estimates of a user entering the site and accessing any number of pages) made by 637 unique visitors, for an average usage of 4.3 visits per day. During periods of heavy use, the site has experienced up to 20 visits per day, with frequent periods of 10 or more visits per day. 39.5% of these visits were via direct access (i.e., a user who types the URL or has bookmarked the site), 40.9% were from referrals (links from other websites or links within emails), and 19.6% from searches. Popular search terms used to find the site included *gaseos*, *webgaseos*, *gaseos berkeley*, *esdtools,* and *gas hydrates*.

Although usage is down from 2009, this reflects the decline in usage and subsequent recovery that occurred due to site downtime in March 2010. The original ESDTools server reached the end of its usable life, and the WebGasEOS software was moved to a new, multiprocessor server. Since many users were accessing WebGasEOS using outdated references in the Google database (which had stored the unaliased address "lnx.lbl.gov" despite our requests to correct the entry), there was some delay in users re-finding the program and correcting their bookmarks. Heavy use resumed within a month's time.

Significant numbers of visits were recorded from many academic and commercial institutions, including the University of Texas at Austin, Bureau de Recherches Geologiques et Minieres (BRGM), Shell International, Chevron, Amoco, Stanford University, University of Montana, ConocoPhillips, Halliburton, Schlumberger, Texas A&M, Korea Institute of Geoscience and Mineral Resources (KIGAM), Helmholtz-Zentrum Potsdam Deutsches Geoforschung, Universita di Firenze, Universita di Bologna, Southwest Research Institute, Instanbul Technical University, Natural Resources Canada, University of Bergen, University of Utah, and Institut Francais du Petrole.

WebGasEOS Usage

Within the 1,418 visits to the WebGasEOS site, the WebGasEOS tool itself was invoked (results generated and reported) 2,373 times by 522 unique users. 85.7% of these uses were from locations outside of the LBNL network. Peak usage reached 88 invocations per day. Compared to 2009, the number of invocations per unique user has increased, and usage has been more consistent over time.

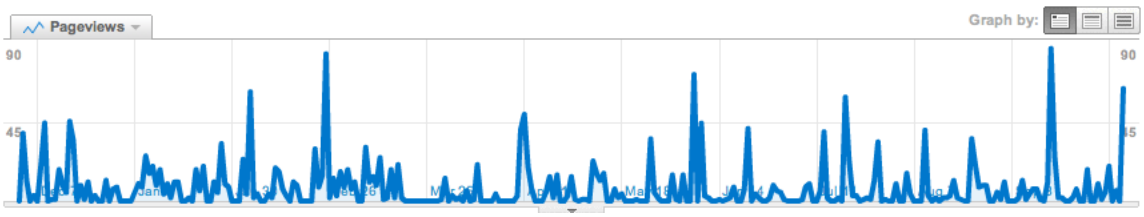

Figure 7. *WebGasEOS usage (invocations) for 2010*

Users of the tool came from 47 countries, with 62.2% of the visits coming from users outside the USA. In terms of numbers of unique visitors, the top countries from which WebGasEOS was accessed included: USA, France, Germany, Canada, Australia, the UK, Italy, Japan, Norway, Spain, and China.

Task 2 Summary of Noteworthy Accomplishments (Q4, FY2010)

- A large-scale CO_2 migration and fault-leakage test problem was simulated using the new TOUGH2/ECO2M which can simulate all phase combinations of CO_2. Cyclic leakage phenomena associated with phase interference and Joule-Thomson cooling were modeled.
- Completed the sample problems and user guide to accompany the beta release of TOUGHREACT V2 that occurred in FY10.

Conclusions. Work is on-going.

Milestones met. TOUGHREACT V2 manual was completed and the code was released as a beta version to multiple TOUGHREACT users.

Actual or Anticipated Problems or Delays. None

Task 3. Measurement and monitoring to verify storage and track migration of CO_2
Goal: To develop reliable techniques to demonstrate storage effectiveness and quantify migration out of the storage formation and release rates at the surface.

A combination of surface and subsurface methods will be developed for verifying storage effectiveness. Specifically, for surface monitoring we will investigate deployment and sensitivity of eddy-covariance methods, flux chamber measurements, and soil gas sampling. We will continue to support and conduct the ZERT shallow-release field test, coordinated with all of the ZERT partners, to develop, evaluate, and optimize the methods.

All assessments will be made in the context of quantifying "significant" releases from the storage structure, e.g., those that would compromise the effectiveness of geologic storage or cause unacceptable environmental impacts.

Task 3a. Assess detection limits and optimal deployment strategies for CO_2 leakage monitoring in subsurface and surface environments using eddy covariance, accumulation chamber, optical technology, and novel methods

Theoretical, modeling, and field studies will be performed to assess the sensitivity and detection limits of various methods for surface monitoring. This work will inform studies aimed at deployment strategies to optimize detection, quantification, and locating surface seepage. Preferred approaches will be recommended and described in papers.

Deliverable: Published paper on monitoring and detection of CO_2 leakage.

Task 3b. Perform simulations of CO_2 migration in support of the ZERT shallow-release experiment

Calculations using TOUGH2/EOS7CA, COMSOL multiphysics, and other approaches will be carried out in support of the ZERT shallow-release experiment. Modeling of saturated zone, vadose zone, and above-ground transport of CO_2 will be carried out. The results will be used to design experimental releases, sensor deployment for monitoring at the MSU site, and analyzing data from the shallow-release experiment.

Deliverable: None for this quarter.

Task 3c. Support field activities at the MSU shallow-release facility

In cooperation with the other ZERT partners, support field activities related to the ZERT shallow-release experiment. The site is pasture-land west of the main campus of MSU. We will actively contribute to the design and execution of the test. LBNL will provide a packer and tubing system to deliver CO_2 to the horizontal well that provides the source term for the experiment.

Deliverable: None for this quarter.

Task 3d. Conduct field experiments to verify surface monitoring techniques

In cooperation with the other ZERT partners, surface monitoring and verification experiments will be conducted to test and improve our ability to detect, locate and quantify seepage. CO_2 will be delivered through tubing to packed-off sections of the horizontal well. Eddy covariance, accumulation chamber, and novel approaches will be used to monitor the shallow release.

Deliverable: None for this quarter.

Task 3 Results and Discussion

Task 3a. Assess detection limits and optimal deployment strategies for CO_2 leakage monitoring in subsurface and surface environments using eddy covariance, accumulation chamber, optical technology, and novel methods

A CO_2 release was conducted from the horizontal well at the ZERT site from 19 July to 16 August 2010 (0.15 t CO_2 d^{-1}). We made measurements of soil CO_2 fluxes using the accumulation chamber method to characterize the spatial distribution of surface CO_2 leakage fluxes during the release. Measurements were made during the second week of the release, when surface CO_2 leakage fluxes should have been approximately at steady state. Measurements were made at 1-m spacing along the surface trace of the horizontal well on 28 July (Figure 8) and on a grid surrounding the release well on 27 and 29 July (Figure 9). The spatial distribution of surface CO_2 leakage fluxes was similar to that observed in previous years, characterized by 5-6 focused zones of elevated CO_2 emissions ("hot spots"), aligned along the surface trace of the well (Figures 8 and 9). Following the methods of *Lewicki et al*. [2007], we estimated the CO_2 leakage discharge based on grid measurements made on 27 and 29 July 2010 (Figure 9) as 0.13 and 0.14 t d^{-1}. These estimates are 87 and 93%, respectively, of the actual CO_2 release rate from the well.

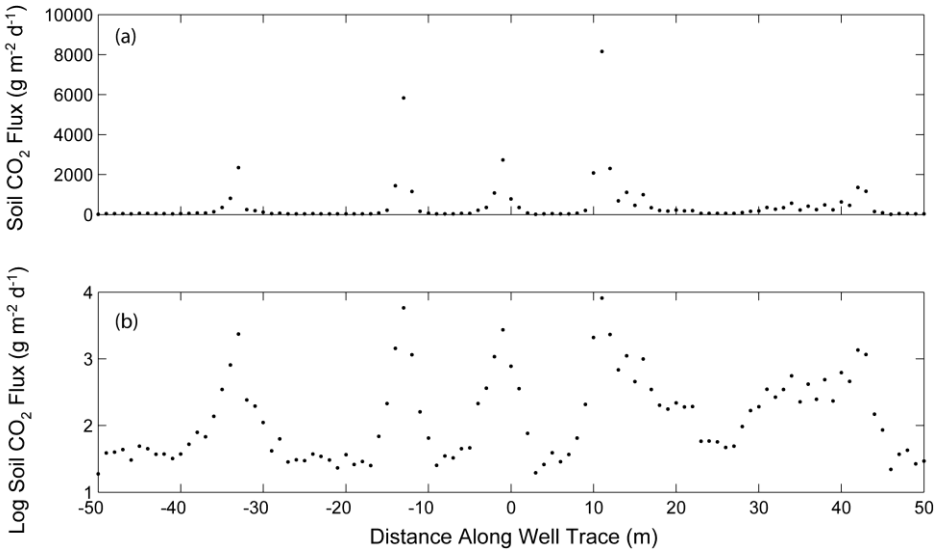

Figure 8. *Plots of (a) soil CO_2 flux and (b) log soil CO_2 flux measured using the accumulation chamber technique along the surface trace of the release well on 28 July 2010.*

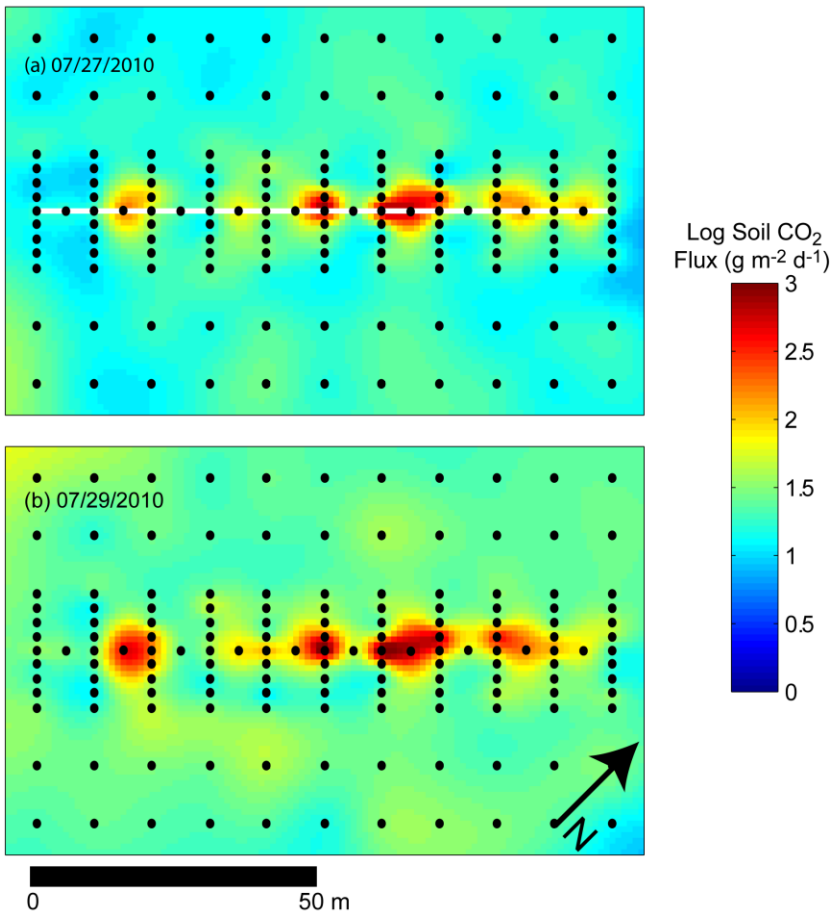

Figure 9. *Maps of log soil CO_2 flux, interpolated based on measurements made at the black dots on (a) 27 July 2010 and (b) 29 July 2010. White line on (a) shows surface trace of release well.*

Reference

Lewicki, J.L., C.M. Oldenburg, L. Dobeck, and L. Spangler, Surface CO_2 leakage during two shallow subsurface CO_2 releases, *Geophysical Research Letters, 34*, L24402, doi:101029/2007GL032047, 2007.

Task 3b. Perform simulations of CO_2 migration in support of the ZERT shallow-release experiment.

No activity to report for this quarter.

Task 3c. Support field activities at the MSU shallow-release facility

Carried out measurements and data analysis in support of field activities at the MSU facility.

Task 3d. Conduct field experiments to verify surface monitoring techniques

Conducted surveys of CO_2 flux during the July 2010 field experiment at the MSU facility.

Conclusions. Work is on-going.

Milestones: June 30, 2010, publish paper on monitoring CO_2 leakage. This paper was published in the March 2010 volume of Env. Earth Sci. (see publication list).

Actual or Anticipated Problems or Delays. None

Task 3 Summary of Noteworthy Accomplishments (Q4, FY2010)

- Carried out accumulation chamber soil-gas CO_2 flux surveys at the MSU release facility.

Task 4. Fundamental geochemical and hydrological investigations of CO_2 storage
Goal: To develop understanding and confidence in solubility trapping, residual gas trapping and mineral trapping, and to identify new trapping mechanisms that can contribute to even greater storage security.

Theory and experiments will be used to develop a greater understanding of solubility trapping, residual gas trapping and mineral trapping and to identify new trapping mechanisms that can provide even greater storage security.

Experiments to improve our understanding of residual gas trapping will be conducted in a high pressure 1-D column with X-Ray CT scanning capability. These experiments are designed to allow monitoring the evolution of trapped gas over time and as fluid slowly dissolves the trapped gas. Theoretical studies and numerical simulation will be used to interpret and generalize the results from these experiments. Planning to include measurements to correlate gas-water saturation with geophysical properties (e.g., acoustic wave speed, electrical conductivity) will be undertaken for future investigation in this task.

Task 4a. Core flow-through and scanning

Theory and laboratory experiments will be used to develop a greater understanding of solubility trapping, residual gas trapping, and mineral trapping to identify new trapping mechanisms that can provide even greater storage security over long time scales. Experiments to improve our understanding of residual gas trapping will be conducted in a high pressure 1-D column with X-Ray CT scanning capability. These experiments will monitor the evolution of trapped gas over time and as fluid slowly dissolves the trapped gas. Theoretical studies and numerical simulation will be used to interpret and generalize the results from these experiments.

Deliverable: Reporting on pore occupancy and residual trapping.

Task 4b. Interfacial tension studies

Interfacial tension of $scCO_2$ relative to water is the key property controlling residual gas trapping. We will initiate planning of investigations to measure and model the effects of co-injected gases (e.g., N_2, Ar, H_2S, SO_x, etc.) on interfacial tension for CO_2 mixtures.

Deliverable: None for this quarter.

Task 4c. Evolution of rock flow properties by mineral trapping

Mineral trapping of carbon dioxide is a promising mechanism of geologic storage of the green-house gas. It modifies the pore space geometry that affects the flow properties of the rock. The evolution of the relative permeabilities and the capillary pressure will affect both the flow near the wellbore, and the long-term trapping of gas. Experiments are difficult and time consuming. Modeling can provide useful insights by simulating various what-if scenarios. We will use the Maximal Inscribed Spheres method to simulate the flow in the changing pore-space geometry and quantify the impact of mineralization on the two-phase flow properties of the rock. The simulations will rely on the micro-CT images of rock samples obtained earlier within this task. Micro-CT studies of rock mineralization will be used for calibration and verification of the models. Results of this effort can be used as input data in the TOUGH2 simulations mentioned in Task 1.

Deliverable: None for this quarter.

Task 4 Results and Discussion

Task 4a. Core flow-through and scanning

Report on pore occupancy and residual gas trapping

Introduction

As a non-aqueous phase fluid, carbon dioxide (CO_2) in its supercritical, liquid, or gaseous states will invade a porous medium as governed by viscous interfacial, buoyancy, and pressure-gradient (e.g., injection pressure) forces. All target reservoirs for geologic carbon dioxide storage exhibit heterogeneity at a variety of scales including reservoir scale (e.g., caprock versus reservoir rock), unit scale (e.g., distal versus proximal deposition in fan deposits), strata scale (e.g. property variations between sand layers due to locally varying depositional pattern) and the pore scale (e.g., variation in packing of grains and grain shape). All of these heterogeneities will strongly impact the flow of injected CO_2, and ultimately the capacity of the reservoir, as some of the connate water will ultimately remain.

Upon introduction, CO_2 will first travel through regions most able to transport the displaced brine away from the flow and having the largest permeability to CO_2 . These high-permeability regions will only partially fill with CO_2 however, as heterogeneity on the pore scale will govern where the CO_2 ultimately goes, and it will govern CO_2 trapping. We are investigating the relation between pore occupancy and CO_2 trapping on the pore scale by modeling and by laboratory studies involving pore-scale imaging of CO_2 and brine flow and trapping, and also the effect of subcore-scale heterogeneity on CO_2 flow and brine displacement.

Effect of pore-scale heterogeneity

In a recent study, Silin and coworkers [*Silin et al.*, 2010] examined CO_2 invading the pores of a sandstone sample using x-ray microtomography (micro CT) at the Advanced Light Source at

Lawrence Berkeley National Laboratory. Figure 10 shows a micro CT image in which the invading CO_2 is dark, the brine is white, and the mineral sandstone medium is gray, next to a prediction of phase occupancy computed using the method of Maximal Inscribed Spheres (MIS). From the micro CT image, one can clearly see that the invading CO_2 occupies the larger porespaces as expected, while the smaller pores are brine-filled. Silin and coworkers used this data and the MIS technique to compute capillary pressure saturation curves for the sample, which compared favorably with curves measured using other techniques.

Figure 11 shows the porespace and the mineral frame of a Frio sandstone sample from the micro CT imaging. Using the MIS method, the CO_2 distribution at two water saturations was computed and shown in Figure 12. Note the presence of isolated CO_2 bubbles that are not connected with other bubbles, particularly at the higher water saturation. Although these computations were performed without any particular fluid displacement scenario, these CO_2 bubbles are indicative of trapped CO_2 in the pore space.

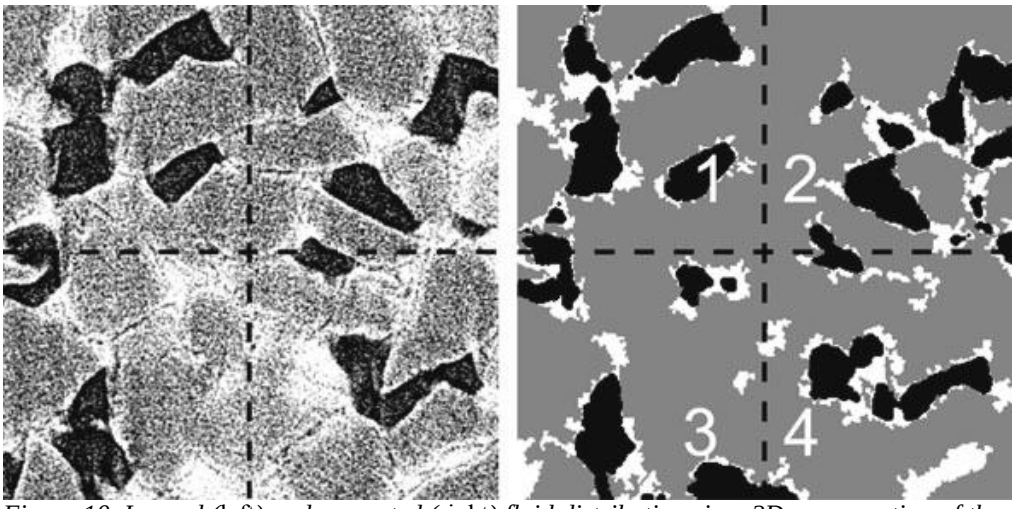

*Figure 10. Imaged (*left*) and computed (*right*) fluid distributions in a 2D cross-section of the sandstone sample. The black color denotes gas, the white color denotes brine, and the* gray *color denotes solid skeleton. Figure from Silin et al. (2010).*

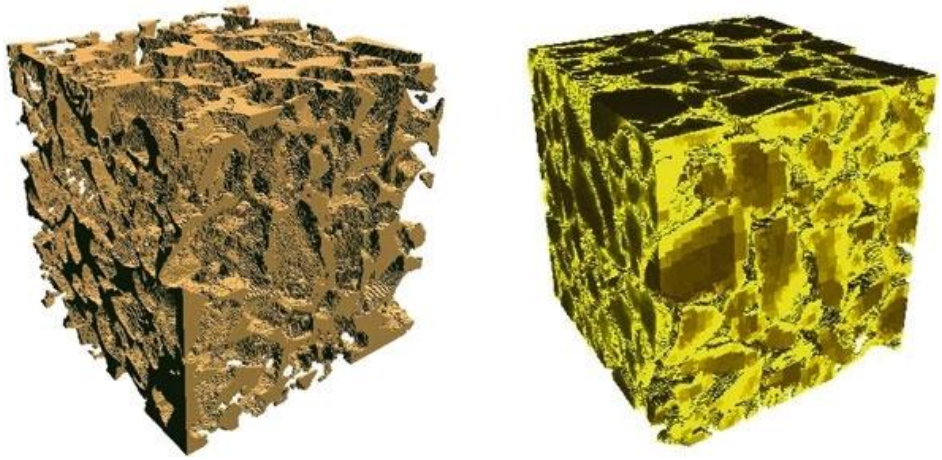

Figure 11. An image of the pore space and the skeleton of a 0.9 x 0.9 x 0.9 mm Frio sandstone sample. Figure from Silin et al. (2010).

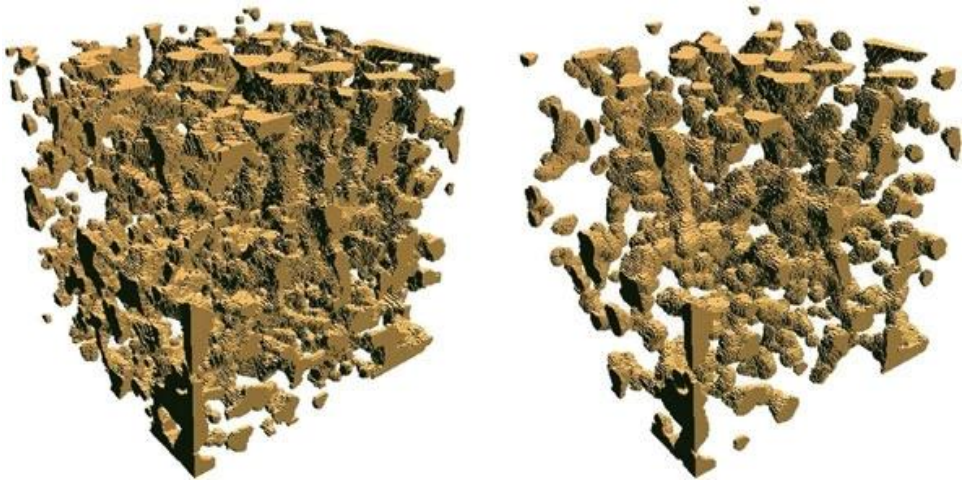

Figure 12. Distributions of CO_2in the pore space shown above at two water saturations: Sw = 27% and Sw = 55%. Figure from Silin et al. (2010).

In this sample, heterogeneity of two-phase saturation was observed not only at the pore scale. For instance, two-phase fluid distribution in a few-centimeters core sample also can be very non-uniform [*Perrin and Benson*, 2010].

Effect of subcore-scale heterogeneity

Several studies have been and are being performed to examine the effect of subcore-scale heterogeneity on CO_2 trapping. Figure 13 shows results from four studies that have used x-ray computed tomography (CT) to observe CO_2 occupancy in natural porous media cores (typically about 3.7 cm in diameter and varying lengths). Figure 13a (unpublished data, Kneafsey and Nakagawa, 2010) shows CO_2 invasion into a fairly tight clay-bearing sandstone (Germany). The bright color indicates the presence of CO_2. It is clear that CO_2 preferentially occupies certain regions, and not others. Figure 13b shows the CO_2 invasion into Tako sandstone (Japan) [*Shi et al.*, 2010]. These results also clearly show the effect of laminations and heterogeneity in the core affecting the flow of CO_2. The lower right image, presenting the final condition, shows both the resulting heterogeneous CO_2 distribution and the relative amount of CO_2 present as the regions with the higher CO_2 saturation only containing over 40%. This overall low saturation is the result of pore-scale heterogeneities. Figure 13c shows the CO_2 invasion of a relatively uniform Berea (USA) sandstone core (unpublished data, Kneafsey and Nakagawa, 2010). In this core, there is evidence of gravity override, the effect of subcore scale heterogeneity, and a distinct CO_2 saturation gradient from the inlet to the outlet of the core. Figure 13d presents the region of CO_2 presence in a very highly permeable Frio sandstone core (USA) (unpublished data, Tomutsa, 2005) resulting from a CO_2 flood of a brine-saturated sample. Again, a distinct CO_2 saturation gradient exists from the inlet to the outlet, and upon CO_2 breakthrough, this region remained unchanged.

a.

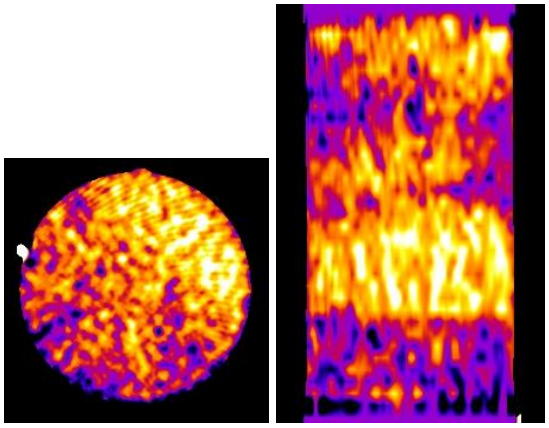

b.

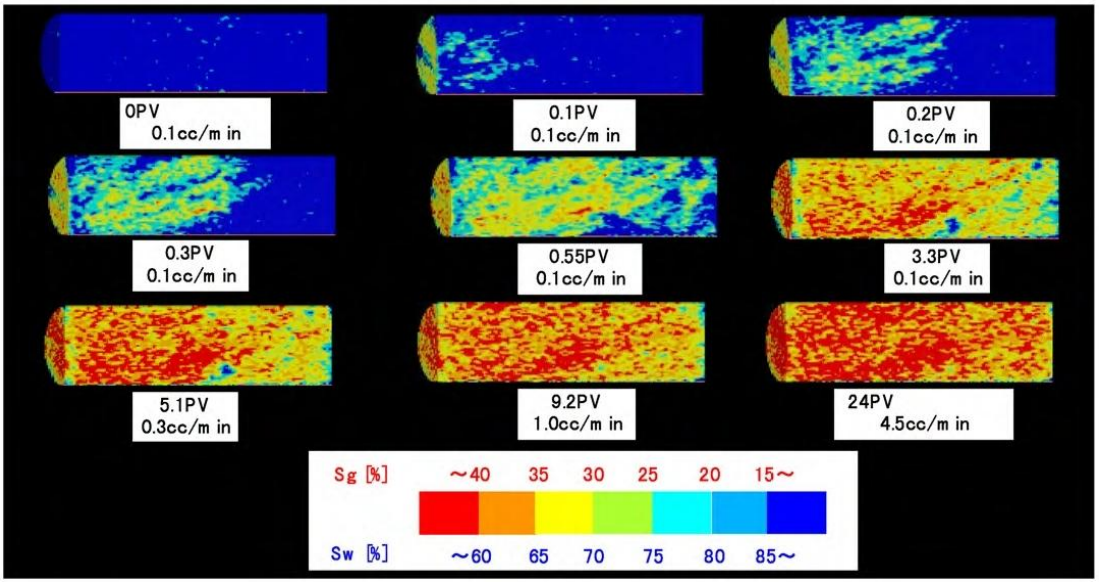
0PV
0.1cc/m in
0.1PV
0.1cc/m in
0.2PV
0.1cc/m in
0.3PV
0.1cc/m in
0.55PV
0.1cc/m in
3.3PV
0.1cc/m in
5.1PV
0.3cc/m in
9.2PV
1.0cc/m in
24PV
4.5cc/m in
Sg [%] ～40 35 30 25 20 15～
Sw [%] ～60 65 70 75 80 85～

c.

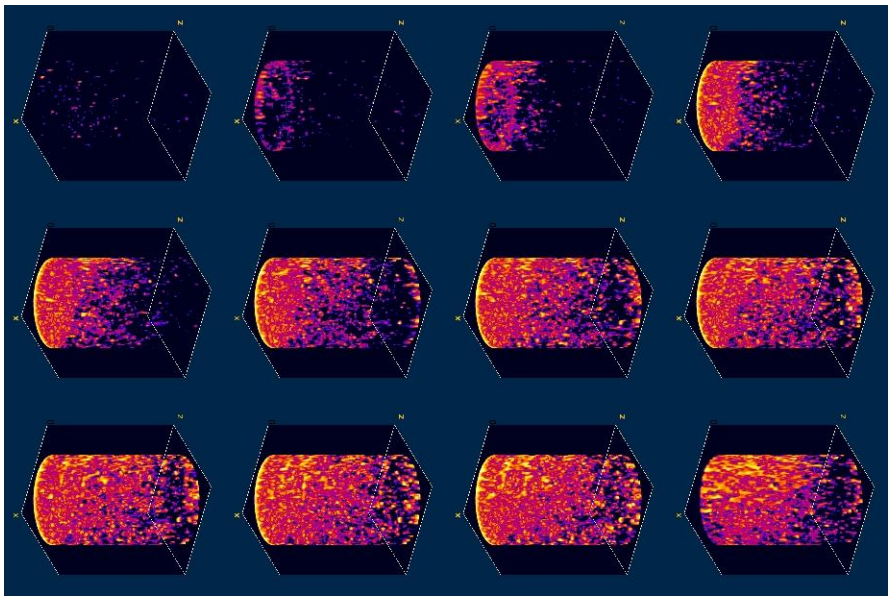

d. 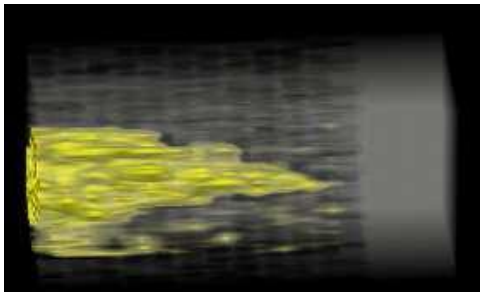

Figure 13. Results of x-ray CT observations of CO_2 invading brine-saturated sandstone samples. a. tight sandstone (Germany) – brighter colors indicate higher CO_2 saturation (Kneafsey and Nakagawa, 2010, LBNL unpublished data), b. Tako sandstone (Japan) [Shi et al., 2010], c. Berea sandstone (USA) – brighter colors indicate higher CO_2 saturation (Kneafsey and Nakagawa, 2010, LBNL unpublished data), and d. Frio sandstone (USA) – yellow indicates region where CO_2 is present (Tomutsa, LBNL unpublished data, 2005)

Examining one case in greater detail, (Figure 13c.) we show the CO_2 saturation along the core as the CO_2 flood occurred. As expected, the CO_2 saturation increased at the injection end first (lowest curve in Figure 14). As the CO_2 invasion continued, the saturation gradient from inlet to outlet continued to grow in extent. When the CO_2 front reached the end of the core, the CO_2 pooled there until enough was present to overcome the elevation of the exit port. After a number of pore volumes of CO_2 were introduced, the CO_2 saturation profile changed little, as there was little impetus for pore invasion to occur throughout the sample once breakthrough occurred. These results are not in complete agreement with the results of Shi et al., 2010, as their CO_2 saturations in the Tako sandstone were somewhat uniform across the length of the core. This may be due to the difference in heterogeneity in the two samples with the additional heterogeneity causing more CO_2 to be trapped [*Han et al.*, 2010].

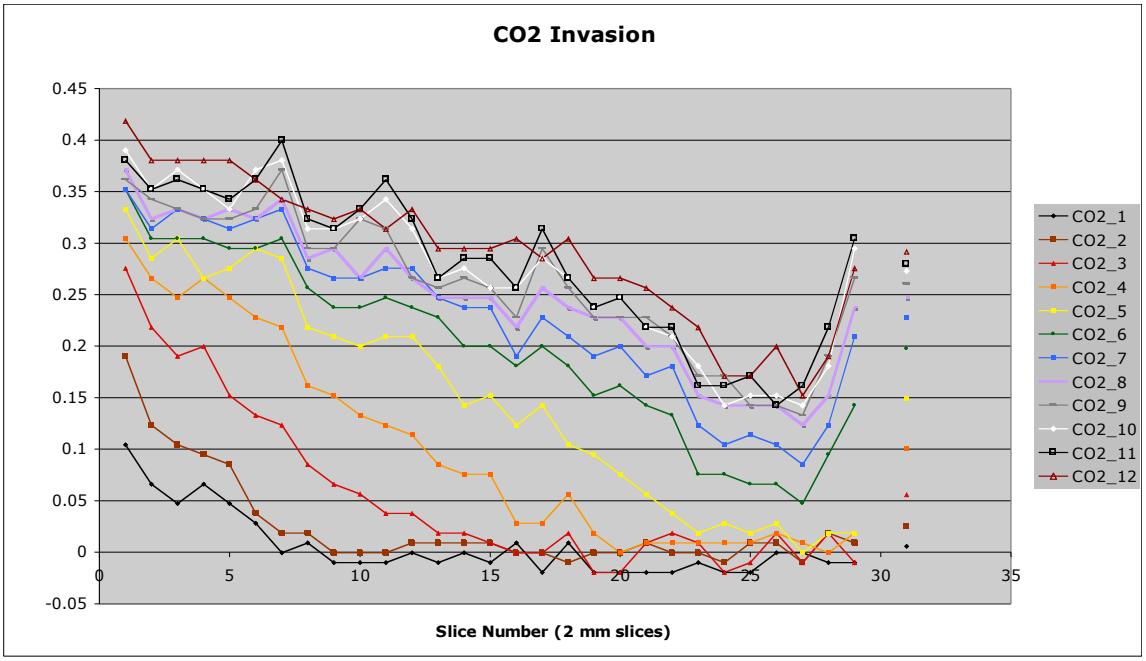

Figure 14. CO_2 saturation along the Berea sandstone core shown in Figure 13c during CO_2 injection. The unconnected dots at the right of the figure are the average CO_2 saturation values.

Conclusions

Heterogeneity affects CO_2 invasion at multiple scales. At the pore scale, interfacial forces and pore network heterogeneity as well as imposed pressure gradients affect pore invasion. These effects have been observed using micro CT, and can be modeled using MIS. The agreement between the modeling and observations, while not perfect, indicates that the processes of pore-scale invasion are largely understood, however the nature of pore spaces can be quite complicated and difficult to describe mathematically.

At the subcore scale, heterogeneity also strongly affects the invasion of CO_2. In some cores, the CO_2 invaded large regions that appeared similar to surrounding regions, and was not displaced from these regions. In others, the porosity variation was more obvious, and its effects dramatic. In all cases, complete replacement of brine by CO_2 was not achieved, with displacements on the order of several tens of percent being typical.

References

Han, W. S., et al. (2010), Effects of permeability on CO_2 trapping mechanisms and buoyancy-driven CO_2 migration in saline formations, *Water Resour. Res.*, *46*(7), W07510.

Kneafsey and Nakagawa, 2010, unpublished data, Supercritical CO_2 floods of brine saturated cores under reservoir conditions: X-ray CT and geophysical observations, Lawrence Berkeley National Laboratory.

Perrin, J.-C., and S. Benson (2010), An Experimental Study on the Influence of Sub-Core Scale Heterogeneities on CO_2; Distribution in Reservoir Rocks, *Transport in Porous Media*, *82*(1), 93-109.

Shi, J.-Q., et al. (2010), Supercritical CO_2 core flooding and imbibition in Tako sandstone--Influence of sub-core scale heterogeneity, *International Journal of Greenhouse Gas Control*, *In Press, Corrected Proof*.

Silin, D., et al. (2010), Microtomography and Pore-Scale Modeling of Two-Phase Fluid Distribution, *Transport in Porous Media*, 1-21.

Tomutsa, 2005, unpublished data, Supercritical CO_2 flood of brine saturated Frio sandstone: X-ray CT and hydrological observations, Lawrence Berkeley National Laboratory.

Task 4b. Interfacial tension studies

No specific activity this quarter.

Task 4c. Evolution of rock flow properties by mineral trapping

No Activity for this quarter.

Conclusions. Work is ongoing.

Milestones: *Reporting on pore occupancy and residual trapping. See Write up under Task 4a.*

Actual or Anticipated Problems or Delays. None.

Task 4 Summary of Noteworthy Accomplishments (Q4, FY2010)

- Laboratory and modeling studies of pore occupancy demonstrated that heterogeneity affects CO_2 invasion at multiple scales.

Publications Q4, FY2010 (Peer Reviewed)

Silin, D., Tomutsa, L., Benson, S. and Patzek, T, (2010). Microtomography and pore-scale modeling of two-phase fluid distribution, Transport in Porous Media, 1–21, 10.1007/s11242-010-9636-2.

Xu, T., E. Sonnenthal, N. Spycher, G. Zhang, L. Zheng, and K. Pruess, TOUGHREACT Version 2.0: A simulator for subsurface reactive transport under non-isothermal multiphase flow conditions, Computers&Geosciences. In press, 2010 (updated reference from last quarter).

Complete List of ZERT Publications to Date (FY2010) (Peer Reviewed)

Lewicki, J.L. and G.E. Hilley, Eddy covariance mapping and quantification of surface CO_2 leakage fluxes. Geophysical Research Letters, 36, L21802, doi:10.1029/2009GL040775, 2009.

Lewicki, J. L., G.E. Hilley, L. Dobeck, and L. Spangler, Dynamics of CO_2 fluxes and concentrations during a shallow subsurface CO_2 release, Environmental Earth Sciences, 60, 285-297, doi:, 10.1007/s12665-009-0396-7, 2010.

Male, E.J., W.L. Pickles, E.I. Silver, G.D. Hoffmann, J. Lewicki, M. Apple, K. Repasky, and E.A. Burton, Using hyperspectral plant signatures for leak detection during the 2008 ZERT CO_2 sequestration field experiment in Bozeman, MT. Environmental Earth Sciences, 60, 251-261, doi: 10.1007/s12665-009-0372-2, 2010.

Oldenburg, C.M., J.L. Lewicki, L. Pan, L. Dobeck, and L. Spangler, Origin of the Patchy Emission Pattern at the ZERT CO_2 Release Test, *Env. Earth Sci.*, 60, 241-250, 2010, LBNL-3063E.

Oldenburg, C.M., J.L. Lewicki, L. Dobeck, and L. Spangler, Modeling Gas Transport in the Shallow Subsurface During the ZERT CO_2 Release Test, Transport in Porous Media, 82(1), p. 77-92, 2010, DOI 10.1007/s11242-009-9361-x, LBNL-1529E.

Oldenburg, C.M., and C. Doughty, Injection, Flow, and Mixing of CO_2 in Porous Media with Residual Gas, *Transport in Porous Media*, submitted.

Pan, L., J.L. Lewicki, C.M. Oldenburg, and M.L. Fisher, Time-Windows-Based Filtering Method for Near-Surface Detection of Leakage from Geologic Carbon Sequestration Sites, Env. Earth Sci., 60(2), 359-369, 2010, LBNL- 3349E.

Pruess, K. and J. Nordbotten. Numerical Simulation Studies of the Long-term Evolution of a CO_2 Plume in a Saline Aquifer with a Sloping Caprock, submitted to *Transport in Porous Media,* January 2010.

Rouse, J.H., J.A. Shaw, R.L. Lawrence, J.L. Lewicki, L.M. Dobeck, K.S. Repasky, and L.H. Spangler, Multi-spectral imaging of vegetation for detecting CO_2 leaking from underground. Environmental Earth Sciences, 60, 313-323, doi:10.1007/s12665-010-0483-9, 2010.

Silin, D., Tomutsa, L., Benson, S. and Patzek, T, (2010). Microtomography and pore-scale modeling of two-phase fluid distribution, Transport in Porous Media, 1–21, 10.1007/s11242-010-9636-2.

Spangler, L.H., L.M. Dobeck, K.S. Repasky, A.R. Nehrir, S.D. Humphries, J.L. Barr, C.J. Keith, J.A. Shaw, J.H. Rouse, A.B. Cunningham, S.M. Benson, C.M. Oldenburg, J.L. Lewicki, A.W. Wells, J.R. Diehl, B.R. Strazisar, J.E. Fessenden, T.A. Rahn, J.E. Amonette, J.L. Barr, W.L. Pickles, J.D. Jacobson, E.A. Silver, E.J. Male, H.W. Rauch, K.S. Gullickson, R. Trautz, Y. Kharaka, J. Birkholzer and L. Wielopolski, A shallow subsurface controlled release

facility in Bozeman, Montana, USA, for testing near surface CO_2 detection techniques and transport models, Env. Earth Sci., doi10.1007/s12665-009-0400-2, 2009, LBNL-78319.

Xu, T., E. Sonnenthal, N. Spycher, G. Zhang, L. Zheng, and K. Pruess, TOUGHREACT Version 2.0: A simulator for subsurface reactive transport under non-isothermal multiphase flow conditions, Computers&Geosciences. In press, 2010 (updated reference from last quarter).

Seminars and Presentations (FY2010)

Lewicki, J.L., G.E. Hilley, L. Dobeck, and L. Spangler (2010), Micrometeorological mapping and quantification of surface CO_2 flux leakage signals. *9th Annual Conferenece on Carbon Capture and Sequestration*, May 10-13, 2010.

Lewicki, J.L. (2010) Invited talk at the U.S. Geological Survey Cascades Volcano Observatory in Vancouver, WA, entitled "Eddy Covariance Applications to Surface CO_2 Emissions Monitoring".

Lewicki, J.L., G.E. Hilley, L. Dobeck, and L. Spangler, Monitoring near-surface leakage during controleld releases of CO_2. Berkeley-Stanford-Beijing Workshop on Carbon Capture and Sequestration, 2009.

Lewicki, J.L., G.E. Hilley, M.L. Fischer, L. Dobeck, and L. Spangler, Eddy Covariance Detection, Mapping, and Quantification of Surface CO_2 Leakage Fluxes: Examples from Mammoth Mountain, CA and the ZERT CO_2 Release Facility, MT. American Geophysical Union Fall Meeting, 2009.

Oldenburg, C.M. and C. Doughty, Injection, Flow, and Mixing of CO_2 in Porous Media with Residual Gas, *9th Annual Conferenece on Carbon Capture and Sequestration*, May 10-13, 2010, Pittsburgh, PA.

Pruess, K. Modeling CO_2 Leakage Scenarios, including Transitions between Super- and Sub-Critical Conditions, and Phase Change between Liquid and Gaseous CO_2, presented at 10th International Conference on Greenhouse Gas Control Technologies (GHGT10), Amsterdam, The Netherlands, September 19-23, 2010.

Pruess, K. On the Long-term Evolution of a CO_2 Plume Under a Sloping Caprock, paper presented at XVIII International Conference on Computational Methods in Water Resources (CMWR 2010), Barcelona/Spain, June 21-24, 2010.

Pruess, K. Coupling of Processes, invited presentation at IEA Workshop on CO_2 Geologic Storage Modeling, University of Utah, Salt Lake City, Utah, February 2010.

Pruess, K. Numerical Modeling of Coupled Processes in Aquifer Storage of Greenhouse Gases - Recent Results and Open Challenges, invited seminar, Stanford University, 2 February 2010.

Xu, T., Invited lecture, Subsurface reactive transport modeling: From CO_2 Geological Sequestration to Geothermal Energy Development, Colorado School of Mines, February 19, 2010.

Xu, T., Keynote Speaker, Reactive transport modelling for CO_2 Geological Sequestration, AAPG Workshop on CO_2 Capture and Storage, Golden, Colorado, August 9-12, 2010.

LBNL ZERT I-II Transition Report

Earth Sciences Division
Lawrence Berkeley National Laboratory
December 1, 2010

The ZERT I project funded research at LBNL in three principal areas related to geologic carbon sequestration: (1) Performance prediction (model development and applications); (2) Measurement and monitoring; and (3) Fundamental laboratory investigations. The ZERT II project continues research in these three areas with some changes reflecting advances and accomplishments. Note that we use below the ZERT II task numbering reflecting the addition of a Task 1 on management (not present in the earlier ZERT I) as follows:

Task 1.0 Project Management, Planning, and Reporting
Task 2.0 Performance prediction for long-term fate and transport of injected CO_2.
Task 3.0 Measurement and monitoring techniques to verify storage and track migration of CO_2.
Task 4.0 Fundamental geochemical and hydrological investigations of long-term CO_2 storage.
.

Task 2. Performance prediction for long-term fate and transport of injected CO_2

In ZERT II, we continue to develop TOUGH2 and TOUGHREACT capabilities while also applying the new capabilities to significant problems related to long-term fate and transport of injected CO_2. For example, in Subtask 2.1 of ZERT I, the ECO2N equation-of-state module for TOUGH2 was developed and released to the community. In ZERT II, we are developing, testing, and applying a new module called ECO2M which extends the earlier module to include transitions to liquid CO_2 across the gas-liquid phase boundary. In Subtask 2.2, TOUGHREACT V2.0 was released to outside users for testing. In ZERT II, updates in response to user questions and applications of the new capabilities will be carried out to demonstrate the advanced capabilities of this unique capability to the geologic carbon sequestration community. Similarly, hysteresis models have been developed for TOUGH2/ECO2N in Subtask 2.3 of ZERT I, and they will continue to be tested and applied in ZERT II to better understand residual gas trapping. The near-surface modeling and simulation of Subtask 2.4 is another area of effort that will continue in ZERT II with production of a user guide for the TOUGH2 module that was used extensively in applications to the ZERT shallow-release test that were part of Subtask 3.2.

Task 3. Measurement and monitoring techniques to verify storage and track migration of CO_2

There are two theoretical and modeling subtasks (Subtasks 3.2 and 3.3) and two field-related subtasks (Subtasks 3.4 and 3.5) that we have been working on in ZERT I. We will continue focused effort in ZERT II in Subtask 3.1 on the theoretical and modeling subtasks and provide support in the field-related subtasks as required by need at the ZERT shallow-release experiment. As in ZERT I, research on assessing detection limits extends to a variety of approaches with

main emphasis on the eddy covariance method. In ZERT II, advances in modeling eddy covariance to improve locating sources will be pursued, accompanied by atmospheric dispersion modeling if needed. New monitoring methods capable of discriminating between connected and disconnected CO_2 saturation in porous media will also be evaluated. In Subtask 3.2 of ZERT I, we carried out extensive simulations for design and interpretation related to the ZERT shallow-release experiment. Effort in ZERT II in this subtask will be dictated by the needs of the field project. Similarly for Subtasks 3.3 and 3.4, in which we provided extensive field support under ZERT I for the ZERT shallow-release test, work in these tasks will depend on the extent of field activity in the ZERT II project.

Task 4. Fundamental geochemical and hydrological investigations of CO_2 storage

The three subtasks of Task 4 in ZERT I will continue in ZERT II. In the ZERT I period, CO_2 and brine flow-through experiments were conducted and images of phase saturation were produced in Subtask 4.1. Analyses and modeling of pore occupancy were also carried out and these will be continued in ZERT II. These efforts pointed to the importance of interfacial tension, the topic of Subtask 4.2. In ZERT II, a new effort that makes use of a capillary pressure (CP) cell will be initiated as part of Subtask 4.2. The interfacial tensions efforts are aimed at better understanding of interfacial tension related to residual gas trapping and the effects of contaminants and mixed wettability. The long time scales associated with mineral trapping motivate the use of modeling to simulate changes in pore structure related to mineral reactions. Hence, effort in Subtask 4.3 will be aimed at using micro-CT images and modeling to study impacts of mineral trapping on rock flow properties.

ZERT Quarterly Report: LLNL
July 1, 2010 – September 30, 2010

Contact: Jeff Wagoner
Lawrence Livermore National Laboratory
7000 East Ave
P.O. Box 808
Livermore, CA 94551
925-422-1374
wagoner1@llnl.gov

DOE Work Proposal # FEW 0137
DOE Program Manager: William Aljoe

Highlights

Highlights of this quarter include completion of the analysis of the 2009 field studies which used remote sensing techniques and real-time soil CO_2 probes to detect the concentrations and isotopic values and influence of CO_2 leakage on biogeochemical soil processes and vegetation at the MSU field site, including completion and publication of a peer-review technical paper.

Project Objectives

This research effort utilizes existing LLNL capabilities and relationships with the University of California, specifically UC Santa Cruz. The specific tasks are creating products that support and underscore the research of other organizations working with ZERT and NETL on carbon sequestration science. There are three overarching objectives to LLNL's role within ZERT: (1) Reduce the uncertainty involved in subsurface storage; (2) Improve characterization of risk elements, specifically assessment and monitoring of leakage; (3) Identify strategies to reduce risk elements.

Progress to Date

In the ZERT experiment conducted at Montana State University, a horizontal, segmented, underground well at a few meters depth and 100 meters long is injected with CO_2, giving ZERT partners opportunities to test a variety of techniques to detect the spread of the CO_2 in the soil as a function of distance from the well and duration of injection during the experiment. LLNL participated in assessment of hyperspectral

imaging and other remote sensing techniques and in providing real-time CO_2 soil sensors, which were deployed in the field by UCSC and LBNL.

A key and as yet unanswered question is whether viable remote sensing techniques exist for monitoring for leakage and verification of CO_2 storage sites. Results from 2008a and 2009 indicate that a minimum CO_2 concentration is needed in soil to stress vegetation, which appears to be between 4% and 8% CO_2 by volume. Plant stress becomes evident in spectral signatures within days of exposure to excess CO_2. In light of these results, and the correspondence between the ground measurements and spectral measurement made by Resonon, Inc. in 2008, the team sought two sources of remote data to compare with field measurements: additional airborne data and satellite data.

The results from 2008 and 2009 represent an important milestone in the proof-of-concept of hyperspectral data as a convenient and powerful monitoring and verification technology. Satellite data sources were identified and plans are being made to compare appropriate ground-based and airplane ZERT datasets with the Japanese satellite, IBUKI (GOSAT) datasets for future field sessions.

Project Deliverables

FY2009 work and planning for FY2010 were completed by UC Santa Cruz under subcontract using FY2008 funds carried over. A peer-reviewed paper is being delivered as a separate file, along with this quarterly report. No other deliverables were due for this quarter.

Project Milestones

The project milestones were defined for FY2011. Funding was received for FY 2011 in September 2010.

Transition from ZERT I to ZERT II

In FY2011, the UC Santa Cruz and LLNL team will explore the potential usefulness of satellites such as OCO 2 and GOSAT for monitoring possible elevated CO_2 above CO_2 sequestration sites worldwide. This is a continuation of the effort supported by ZERT I. The important issue for CO_2 sequestration monitoring is how much excess CO_2 can be reliably detected from satellite for various site conditions and seasons. We will do what we can to leapfrog development of analysis methods for the Orbiting Carbon Observatory -2 (OCO-2), due to be launched in February 2013, by using Japanese GOSAT data which is currently available.

We will work with the NASA-funded effort at JPL called “Atmospheric Carbon Observations from Space” or ACOS, which focuses on the analysis of GOSAT data. We believe that if we can use ground truth at the Bozeman ZERT release site (during FY2011) simultaneous with data collected by the GOSAT, analysis of that data would establish the methodology to use OCO-2 data for monitoring sequestration sites for leakage.

As a separate task under ZERT II, will perform modeling and analysis of applications to CCS of risk assessment techniques from other analogous industries. In particular, we propose to do a test case study of predictive modeling capabilities for CO_2 leakage by history matching documented gas leaks through abandoned wells and faults in oil and gas fields in the United States. This builds on work LLNL has done previously to investigate analog sites that might be useful in informing CO_2 sequestration R&D. There are several historical examples where natural gas was injected into a depleted oil and gas fields and, after a certain period of time, the gas was detected at the ground surface. Gas migrated upward through both known and unknown wellbores, as well as other natural features (faults). We will create an 3D geological model that will be used as a basis for simulating these past natural gas leaks, and use the same tools that we collectively are using to characterize and simulate potential CO_2 sequestration plume movement and leakage risk.

Zero Emission Research & Technology Center II
FWP 58882 - Pacific Northwest National Laboratory Contribution

Q4 (July – September) FY2010

Executive Summary

More than half of the anthropogenic carbon dioxide emissions worldwide are due to transportation energy and electrical power generation. New technologies hold great promise to significantly reduce these emissions from fossil fuels, but the engineering, economic, and environmental viability of these zero emission fossil energy technologies must be validated. Demonstrating clean and economically viable hydrogen and electricity production from coal as well as acceptance of the concept of carbon sequestration by the public and the power industry are of critical importance to meeting the global climate change challenge. For this reason, the Zero Emission Research and Technology (ZERT II) Center has been created.

Research Results During Reporting Period

Task 4 (Under ZERT I): Thermodynamic Data Assessment for Geochemical Modeling of CO_2-Sequestration

During Q4, the report "Thermodynamic Data for Geochemical Modeling of Carbonate Reactions Associated with CO_2 Sequestration – Literature Review" was completed.

Transition from ZERT I to ZERT II

This task was not continued in ZERT II as it was considered complete by issuing the report.

Task 1: Project Management

PNNL's ZERT I project under FWP 46379 was closed on April 30, 2010 and a new ZERT II project opened on May 1 under the new FWP 58882.

Task 2: Scalable Computing

The principal objective of this task is the development and demonstrated application of a scalable numerical simulator for geologic sequestration of greenhouse gases with capabilities for coupled process modeling. The geologic sequestration simulator being developed at the Pacific Northwest National Laboratory (PNNL) is actually a suite of operational modes of the STOMP (Subsurface Transport Over Multiple Phases) simulator (i.e., STOMP-CO2, STOMP-CO2e, STOMP-CO2ae). STOMP-CO2 is the isothermal version, STOMP-CO2e is the nonisothermal version, and STOMP-CO2ae is the nonisothermal version for ground-surface interaction. All of these simulators include the possibility of coupling in the Equilibrium, Conservation, Kinetic Equation Chemistry (ECKChem) reactive transport module for modeling geochemistry.

Scalable refers to the ability of the simulator to execute on multiple-processor computers, realizing a scaled reduction in compute time with an increasing number of processors for a given problem. At the beginning of the ZERT program (i.e., November 2004), the supercomputer at PNNL, Mpp2, had 1936 cores and was a tera-scale computer, with a maximum rating of 8.6 TFlops. The scalable version of the STOMP-CO2 suite at the beginning of the ZERT program, typically executed on less than 256 processors for problems involving less than 3 million unknowns. Parallelization of the simulator at the start of the ZERT program was implemented by embedding directives into a serial code that were interpreted by a preprocessor,

that rewrote the simulator, using MPI to handle inter-processor communication. Today, (November 2010), the supercomputer at PNNL, Chinook, has 18,176 cores, with a maximum rating of 97 TFlops. The new scalable version of STOMP-CO2 being tested has been executed on Jaguar, a peta-scale computer with 224,162 cores and a peak rating of 1.8 PFlops, using 16,000 processors on a problem approaching 1 billion unknowns. The new version of the scalable simulator is uses the Global Arrays (GA) software, developed at PNNL, for inter-processor communication.

Coupled process modeling refers to the ability to address interdisciplinary processes in a coupled fashion within one simulator. Currently for geologic sequestration interdisciplinary processes are multiphase flow (H), heat transport (T), reactive transport (C), and geomechanics (M). Geologic sequestration of greenhouse gases in deep saline reservoirs generally involves two immiscible phases (i.e., supercritical CO_2 and brine), but could involve three immiscible phases for enhanced oil recovery or transcritical situations (i.e., leakage of CO2 to the ground surface). Subsurface simulators with capabilities for multiphase flow processes track the flow of each phase independently, accounting for phase interference, and the possibility of nonwetting fluid entrapment. More advanced simulators additionally consider the possibility of wettability transformations. The temperature of CO_2 injected into geologic reservoirs will vary with surface ambient conditions, injection rates, and injection pressure and generally will not match the subsurface temperatures. Additionally migration of CO_2 to lower pressure regions yield fluid expansion and associated cooling. As supercritical CO_2 properties are a strong function of temperature, heat transport and thermal effects are critical to simulating geologic sequestration. Mineralization of injected CO_2 depends on the mineral assemblage of the reservoir formation and co-injectants (e.g., SO_x, NO_x). Mineralization rates vary from less than 100 years for basalt reservoirs to more than 100,000 years for some sedimentary formations. Recent research on mineralization mechanisms and rates for supercritical CO_2 in contact with the reservoir formation suggest a new role for water the geochemistry of CO_2 mineralization. As carbonates are a relatively stable entrapment form for sequestering CO_2 the ability to numerically simulate the geochemistry of both aqueous and supercritical CO_2 phase mineralization reactions is an essential component of coupled process modeling. Injecting CO_2 into a geologic formation will change the stress state of the system via pressure and thermal changes and geochemical alteration. Geomechanical modeling translates changes in system stress and material strength into displacements, allowing the prediction of induced seismicity, caprock fracture, fault movement, and surface topography changes. As the geomechanical response of a geologic sequestration repository is dependent on pressure, temperature, and geochemical alteration, its critical geomechanics simulation be coupled to the simulation of multiple fluid flow, heat transport, and reactive transport.

The initial isothermal version of STOMP-CO2, a multiple fluid simulator, was developed with internal funding at the PNNL through its Laboratory Directed Research and Development (LDRD) program, prior to the start of the ZERT program. The original mechanism (i.e., interpreted directives translated into MPI-based coding) for converting the simulator from a sequential to scalable implementation was also developed with PNNL LDRD funding. From these core scalable simulation capabilities developed by PNNL using internal funding, the ZERT program has allowed the STOMP-CO2 suite of simulators to expand in coupled process modeling capabilities. The stage for this development was set at the ZERT sponsored and PNNL lead Computational Topical Workshop, entitled "Advancing Sequestration Science via Collaboration," held August 6-7, 2006 in Winter Park, Colorado. Over the course of the ZERT

program funding the STOMP-CO2 simulator has seen a number of advancements: 1) kinetic dissolution model, 2) coupled heat transport for non-isothermal environments, 3) geochemical reactive transport through the development of the ECKEChem module, 4) super-critical to sub-critical transition and near-surface processes, including air, 5) pressure-limited injection well model, and 6) boundary-fitted orthogonal grid systems. These advancements have transformed the STOMP-CO2 simulator from a single H-process simulator to a coupled HTC-process simulator. Concurrently ZERT funding was used to implement these capabilities into a scalable form of the simulator. Whereas the ZERT program has significantly advanced the STOMP-CO2 suite of simulators, the code is lacking in coupled geomechanical capabilities. Implementing coupled geomechanical simulation capability will be the focus of the ZERT II effort on this Task.

Transition from ZERT I to ZERT II

The ZERT II program will allow the full objectives for the STOMP-CO2 suite of simulators to be realized (i.e., HTCM coupled process modeling and scalable computing). This funding will move STOMP-CO2 from a scalable simulator with capabilities for HTC coupled process modeling, developed with support from ZERT I to one with full HTCM coupled process capabilities. There are essentially three options for implementing geomechanical capabilities in STOMP-CO2: 1) loose coupling with a third-party simulator, 2) full development of a geomechanical simulator, and 3) incorporation of an existing open-source software package for geomechanics. The loose coupling with a third-party simulator is the most direct method for providing coupled geomechanics capabilities in STOMP, and could be accomplished using commercial software (e.g., FLAC3D, ABAQUS). With the loose coupling scheme, HTC results generated with STOMP-CO2 would be passed to the geomechanics model via file transfer and vis-a-versa. This approach would probably be sufficient for smaller problems without strong HTCM coupling, but generally would not an appropriate for execution on multiple-processor computing. The full development approach would allow for complete flexibility in coupling HTC and M processes, and would permit a scalable implementation. But it would be an expensive code development effort. The third option, incorporation of existing open-source software, is attractive from both coupling and scaling perspectives. Two open-source geomechanical codes have been identified as possibilities for incorporation into the STOMP-CO2 simulators.

During this quarter we investigated source codes that could be incorporated into STOMP. The two most promising options are 1) to collaborate with Dr. George Zyvoloski at LANL, working with the geomechanical system in FEHM, and 2) to implement the geomechanical simulator developed by Dr. Yilin Fang, now part of the eSTOMP development team at PNNL. The first option would provide mature geomechanical capabilities, but would require a meshing interface between the FEHM finite-element formulation and the STOMP structured orthogonal integral volume formulation. The second option avoids the meshing interface as the code developed by Dr. Fang uses an arbitrary mesh interface element method. Although the geomechanical code offered by the second option is not nearly as mature, the advantages offered by not having to translate meshes and having the source code and developer on the STOMP development team, makes this option more attractive for more immediate implementation of coupled geomechanics into STOMP-CO2. Because of the long-term advantages of having and integrated geomechanics capability that can solve strongly coupled HTCM problems, a decision was made to proceed with implementation of Dr. Fang's code into STOMP-CO2.

Task 3: Fundamental Studies

Planning and construction of the tubular Soret/Raman cell is on schedule. We anticipate receiving the key components of the assembly, custom sapphire tubes with dimensions suitable for the UV-Raman microprobe studies, within a few months. Preliminary testing in a mock setup was completed on "rough" sapphire tube samples with similar specifications and a simulant for the supercritical fluid. Results gave acceptable spatial resolution for observing the Soret effect in a $scCO_2/H_2O$ mixture assuming the variation in concentrations between the thermal reservoirs is of a magnitude previously predicted.

Temperature gradients will be induced from mixing of $scCO_2$ and H_2O under conditions found in deep saline formations. Such gradients could, in turn, induce coupled feedback effects on the rate of convective mixing through nonlinear thermal diffusion or a Soret effect. The Soret effect is the tendency of a mixture of two or more components to separate under the influence of a temperature gradient.

The goal of this work is to determine, in a single experiment, the molecular diffusion coefficient of CO_2 and the Soret coefficient for water-CO_2 and brine-CO_2 mixtures after an equilibrium temperature gradient is established and a steady-state concentration profile achieved. PNNL has been investigating an application of scanning laser Raman spectrometry to directly probe the chemical state and monitor the time and spatial variation of dissolved CO_2 in a pressure cell coincident with time-dependent temperature measurements using micromachined thermocouples set along the center of the same cell. While successful on a qualitative level, attempts to determine Soret coefficients (measured ratios of the ordinary and thermal diffusion coefficient, important in quantifying the Soret effect) were compromised by uncontrollable thermal anomalies in the cell and the convection currents that resulted from "hot" (or "cold") spots. The thermal anomalies were largely due to the relatively massive cell windows and some portions of the cell that did not equilibrate properly with the temperature gradient that was imposed during the experiment. Modifications to the cell to correct these problems were not successful.

In work to be performed this year, a new, improved, approach and cell for Raman studies of the Soret effect in $scCO_2/H_2O$ mixtures will be constructed that will address deficiencies in the previous design. A conceptualization of this Raman cell and the scattering configuration is shown in Figure 1.

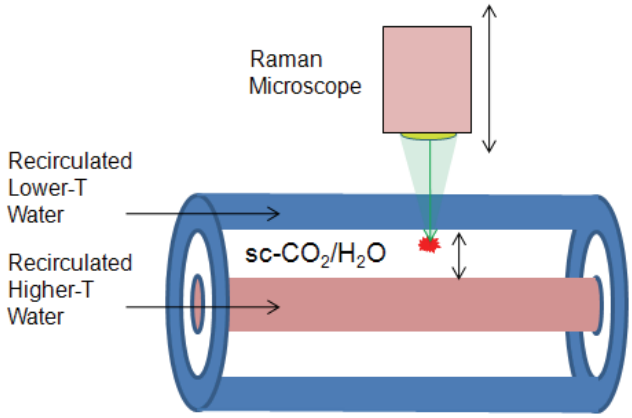

Figure 1. Conceptual model of Raman cell and the scattering configuration?

A high resolution UV-Raman microprobe system will be used in this study. The beam will be focused within the bulk of a static $scCO_2/H_2O$ fluid contained in a sapphire chamber occupying the middle of three concentric tubes that, in turn, are positioned directly under the Raman microscope. The inner and outer chambers will contain water at near-ambient pressure recirculated between two thermostatically

controlled temperature baths, separated in temperature by the desired gradient for the Soret study. The result will be a temperature gradient imposed across the fluid without the presence of thermally unregulated windows. Using the microscope, Raman spectra will be collected as a function of depth, or distance between the walls of the two temperature-controlled chambers. From these measurements, composition (CO_2/H_2O) profiles within the sc fluid across the annulus will be determined and, from the imposed temperature gradient, the Soret coefficient for the fluid calculated.

The depth resolution of Raman microscopes have improved significantly over the past few years, particularly with the advent of UV-Raman spectroscopy. A JY-Horiba LabRAM HR high resolution UV-Raman system that PNNL acquired in 2009 is particularly suited for these measurements. This instrument, which has all reflective optics providing excellent quality Raman spectra with minimal signal distortion and resolution of +/- 2 cm^{-1}, also has distinct advantages in depth profiling. Studies on polished Si have demonstrated precise penetration depths on the order of microns are achievable, depending on the excitation wavelength (shorter is better and our system uses deep-UV excitation at 244 nm), the characteristics of the material under study and the configuration of the optics, especially the size of the pinhole used for confocal measurements. With this fine depth resolution, it should be possible to obtain numerous Raman spectra as a function of distance between the two temperature reservoirs. Each spectrum will provide information on CO_2/H_2O ratio as a function of position between the two thermal reservoirs and, provided the sensitivity is sufficient to allow us to determine, through its variation as a function of position, the Soret coefficient (quantification of the effect) for the supercritical fluid mixture. Repeating the experiment as a function of solution composition (e.g. brine concentration) and temperature gradient will help provide needed input regarding the concentration profiles of reactive species to support simulation of temperature gradient effects for CO2 mixing in geological formations.

A preliminary design of the tubular Soret/Raman cell was completed with most of the current effort focused on the dimensions and properties of the concentric sapphire tubes. An assessment of the pressure/temperature ratings of the cell was performed, and optimal diameters and wall thicknesses were determined. Two suppliers were identified for the sapphire tubing. One of these, Saint-Gobain, committed to sending relatively inexpensive samples of tubes to our specifications quickly, although these tubes were not of sufficiently high optical quality for precise measurements. Nevertheless, the tubes were ordered with the intention of performing some preliminary studies, including design modification of end caps and fittings, as well as pressure testing. The Saint-Gobain tubes were received in early November 2010. One of these was also used in a set of preliminary optical measurements reported below. The second supplier, Rayotech, is our source for the final, optical quality, tubes that will be used in the actual Soret/Raman studies to be formed later this FY. The tubes were ordered from Rayotech early in November 2010 with an expected delivery time of 2-3 months.

The Saint-Gobain sapphire tubes were transparent but of relatively poor optical quality, appearing foggy under inspection with visible light. Nevertheless, the UV-laser beam in the Raman spectrometer was able to penetrate them, so preliminary UV-Raman studies were performed to assess the spatial resolution (in the z-direction, i.e. side-to-interior) possible using our setup.

The largest sapphire tube is the tube that will be used to contain the supercritical fluid, specifically within the annulus between its inside wall and the outer wall of the smaller tube to be contained within it. The larger tube has a wall thickness of approximately 3 mm and an ID = 13.5 mm. It is 15.2 cm long. During the Soret/Raman measurements that will be performed, the Raman microscope will focus the UV laser beam at different positions between the inner wall of this tube and the outer wall of the smaller tube inside. This is in the region where the supercritical fluid will be contained. Each measurement in this region will interrogate a finite region of volume. The smaller this interrogation volume is, the more precise the measurement. As a preliminary assessment of this resolution, a simulated Raman cell/sample was used (see Figure 2). The large tube was filled with an aqueous solution saturated with Na2SO4 and a smaller tube of Teflon was placed within it. The Teflon tube had an OD = 10 mm. This left an annulus, now containing the Na_2SO_4 solution, with a "thickness" of 3.5 mm. The assembly was placed under the Raman microscope and spectra were obtained, focusing first on the outer surface of the sapphire tube, then through the tube wall, then within the sulfate solution and, finally up to and below the surface of the Teflon tube. Since sapphire, aqueous sulfate and Teflon all have strong characteristic Raman bands, the exercise was intended to show the amount of spatial resolution (in the z-direction) possible in this setup. Spectra were obtained using 244-nm excitation, confocal pinhole settings at both 400 µm and 50 µm, and at a series of positions in the z direction.

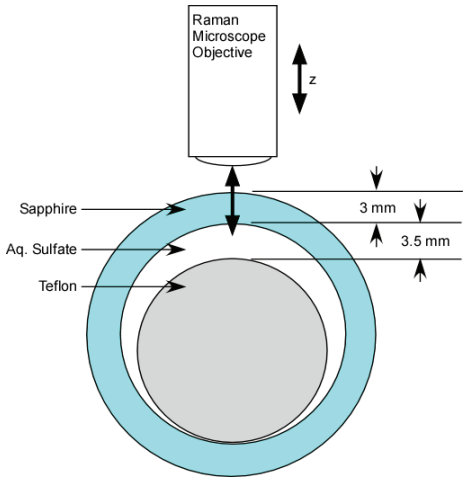

Figure 2. Setup for preliminary Raman study using sapphire tube.

Results for the two pinhole settings are shown in Figure 3. In both graphs, normalized intensities of principal Raman bands arising from sapphire, sulfate and Teflon are shown. Both sapphire and Teflon have two characteristic bands that are plotted. Of initial importance was the absolute intensities (not shown) of the Raman band from the sulfate (indicating the signal strengths relative to the detection limits for the species contained in the annulus). Both pinhole sizes gave satisfactory intensities for this band using typical spectra acquisition times, even through the 3 mm thick tube with relatively poor optical quality was used. Spectral counts for the band were on the order of 10,000's and 1000's for the 400 µm and 50 µm pinholes, respectively.

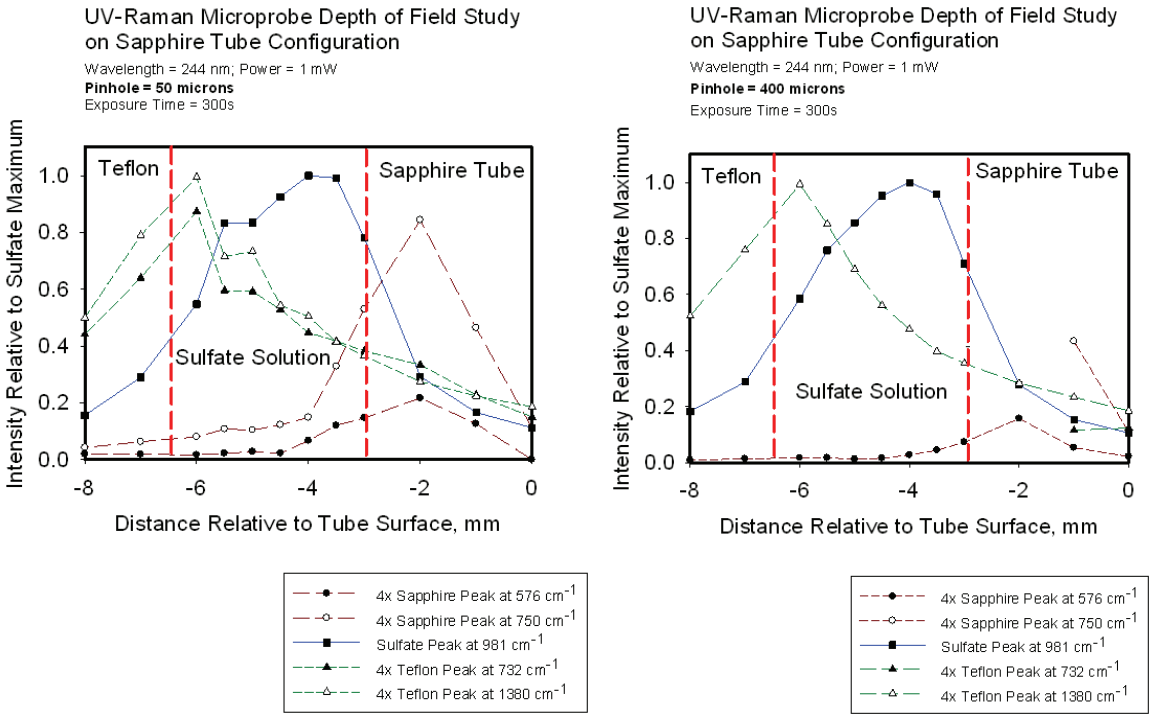

Figure 3. Variation in characteristic Raman peaks for sapphire, sulfate and Teflon. Zero position on the x-axis is the outer surface of the large sapphire tube. Red dotted lines mark the phase boundaries (sapphire|sulfate and sulfate|Teflon).

As shown in Figure 3, the variations with depth (z-direction) of relative intensities of bands from the three components are not as sharp at the phase boundaries (sapphire|sulfate and sulfate|Teflon) as hoped, even when the smallest pinhole was used. Of the two phase boundaries, the sapphire|sulfate is more reliable because both phases are transparent. The phase boundary with the "white" Teflon gives rise to a much higher amount of both elastic and inelastic backscattering, even when the focus is further away from the phase boundary. So, the wider persistence of signal (over the z-distance) from the Teflon surface is not unexpected. Taking the spatial resolution in the z-direction as the distance where the peak intensity varies significantly across a phase boundary and focusing on the sapphire|sulfate boundary, spatial (z-direction) resolution is estimated to be +/- 1 mm with the current configuration. The resolution is not optimized however, and we expect it to improve with the reduction in diffuse scattering anticipated for the Rayotech tubes (on order) that will have better optical clarity. However, even with the 1-mm spatial resolution afforded by these preliminary studies, the ability to see variations in relative CO_2/H_2O concentrations should be realizable. As indicated in previous quarterly reports, S_T is expected to be 10-100, indicating very significant variation in the concentration ratio across the annulus. Between the boundaries of the homogeneous supercritical fluid phase, much like between the boundaries of the homogeneous sulfate solution in this study, variations in relative intensities accompanying concentration variation of this magnitude should be discernable.

As a final note, the use of the smaller 50 μm pinhole improved the resolution of the Raman frequencies significantly. As shown in Figure 3, despite the lower intensities of the bands, we were able to resolve the bands at 732 cm^{-1} (from Teflon) and 750 cm^{-1} (from sapphire) across the full range of positions, and calculate their intensities from Gaussian fits to the spectra in this

region. In contrast, this was only possible at two positions when using the larger 400 μm pinhole size. At other positions (where contribution from either Teflon or sapphire was much greater than the other) when using the larger pinhole, the frequencies of the bands were too close to permit de-convolution.

Planning and construction of the tubular Soret/Raman cell is on schedule. Pressure testing and further preliminary measurements should be performed next quarter using the sapphire tubes from Saint-Gobain. Preliminary measurements on the special resolution possible in a Raman cell using the tubular design and our current optical setup were promising. Although not as quantitative as hoped for this first assessment, marked improvements are expected with the tubes of higher optical quality that were purchased from Rayotech. Even with the lower-quality tubes, however, we were able to obtain remarkably strong signals from a good Raman scatterer inside of the large tube annulus in a configuration similar to that to be used with $scCO_2$, also a good Raman scatterer. Variations in concentration (e.g. CO_2/H_2O ratio) along the z-direction within the annulus should be discernable using this setup, provided the magnitude of S_T is on the order expected from previous estimates.

Transition from ZERT I to ZERT II

The primary goal of Fundamental Studies task in ZERT I was to use Raman spectroscopy in conjunction with a specially designed high pressure optical cell to measure the molecular diffusion coefficient of $scCO_2$ and the Soret coefficient for water-$scCO_2$ and brine-$scCO_2$ mixtures. While successful on a qualitative level, attempts to determine Soret coefficients (measured ratios of the ordinary and thermal diffusion coefficient, important in quantifying the Soret effect) were compromised by uncontrollable thermal anomalies in the cell and the convection currents that resulted from "hot" (or "cold") spots. The thermal anomalies were largely due to the relatively massive cell windows and some portions of the cell that did not equilibrate properly with the temperature gradient that was imposed during the experiment. Modifications to the cell to correct these problems were not successful. In ZERT II, an alternate approach and redesigned cell for Raman studies of the Soret effect in $scCO_2/H_2O$ mixtures will be constructed that will address deficiencies in the previous design. The ZERT II cell will consist of a set of concentric sapphire tubes with the $scCO_2/H_2O$ fluid in the annulus between two flowing thermal reservoirs. The laser probe beam for the Raman measurements will be directed perpendicular to the tubes and focused with a microscope objective as a function of position within the annulus. This new arrangement will give better control of temperature at the boundaries of the supercritical fluid and contain less fluid mass through which unwanted convection could occur. Additional details of the ZERT II cell design are provided in the revised statement of work and quarterly reports.

Task 4: Monitoring Capability Development and Field Testing

In this quarter we successfully deployed and field-tested the new CO_2 and soil-moisture detection system during the mid-July injection at the ZERT site (Figure **4**). We set up an array of 25 steady-state flow-through chambers to sample a 4-m x 10-m zone located with one of the long sides directly above a known "hot spot" (in the center foreground of Figure 4). The mean volumetric soil-moisture content in the top 15 cm of soil was monitored continuously by a pair of

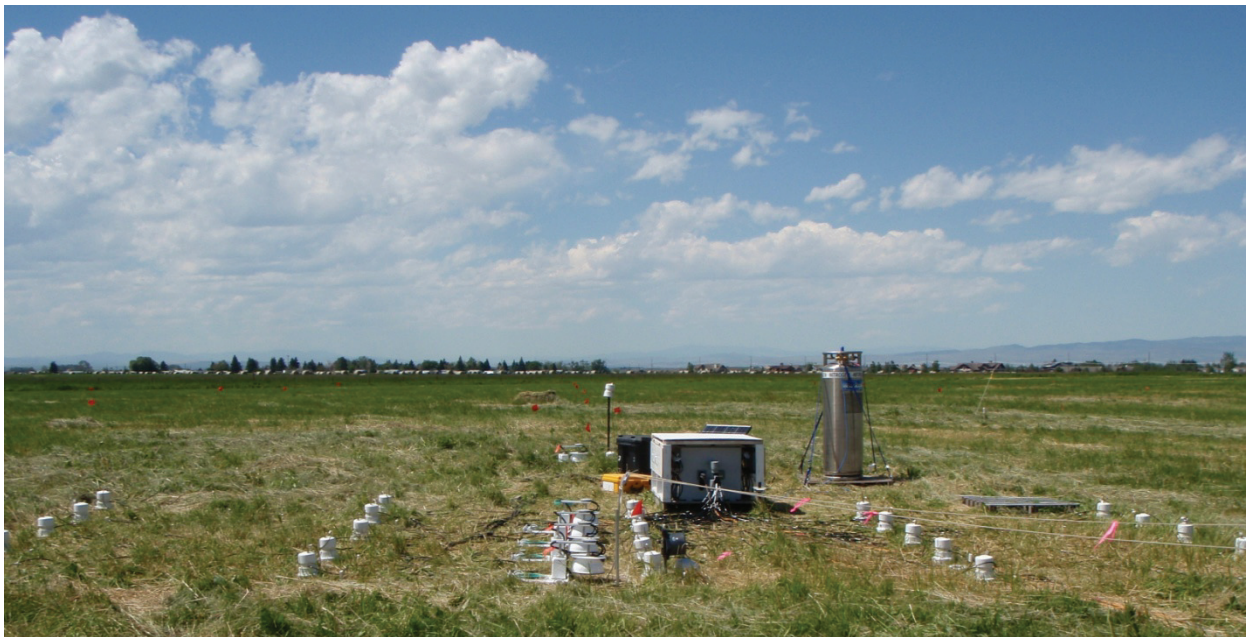

Figure 4. View of PNNL experiment at the ZERT field site taken on 16 July, two days before the start of the injection.

time-domain reflectometry (TDR) sensors located at each chamber, one inside the chamber (VMin) and one in the soil adjacent to the chamber (VMout). The entire experiment operated unattended for two months, with only a change of the nitrogen purge-gas cylinder mid-way through the experiment.

Data were collected and managed remotely using the SMADA web-based software developed in FY2009, which was further enhanced for this year's experiment. Unfortunately, a datalogger programming error prevented storage of data during the first two weeks of the injection. However, data for the remainder of the experiment were saved and so we will be able to follow the decay of CO_2 after the injection.

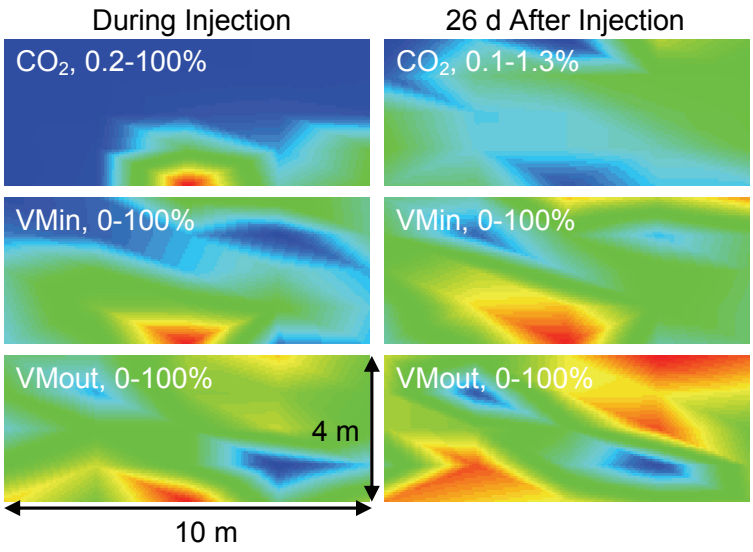

Figure 5. Selected data from the ZERT field experiment showing concentration contours for CO_2, VMin and VMout during (left) and after (right) the injection.

Two sets of results for CO_2, VMin, and VMout are shown in Figure 5, one collected during the injection and the other just before the system was demobilized about 4 weeks after the end of the injection. The CO_2 hot spot is clearly visible during the injection, whereas several weeks later it yields no signal. The moisture contents both within and adjacent to the chambers (VMin and VMout, respectively) correlate well with the location of the hot spot, suggesting that significant amounts

of moisture are carried into the soil by the CO_2 as a result of it being released below the water table. In contrast to the CO_2, however, a significant memory effect is seen for VMin after the injection ceases. A different pattern, however, is seen for VMout. These results show that the moisture contents within and adjacent to the chambers vary somewhat independently due to the different degrees of exposure to ambient air. We will be interpreting the entire experimental dataset, and incorporating meteorological data into our analysis during the first quarter of 2010.

Transition from ZERT I to ZERT II

This task will continue into ZERT II provided field work at the site continues.

Task 5: Geopotential Monitoring

In this quarter, the second gravity survey was completed at Pendleton, Oregon. In regards to the interferograms, nothing new has been done since the 3rd quarter report due to a delay in the signature of a contract with Jet Propulsion Laboratory (JPL). The final processing of interferograms is scheduled to begin in October.

After the processing of the first gravity data set collected in June along the four profiles defined close to the two main injection wells active this year (Figure **6**), it appeared that their quality could be improved if the interval between two returns at main bases is reduced. A new strategy for data collection has been tested during a 2nd survey mid August. With water filling in the reservoir at an intermediate level, the four profiles have been re-done between August 17 and 19th. Each point was measured three times at different times to get a better estimate of the instrumental drift. One more day is needed to complete the survey with this sampling strategy which much better and reliable observations.

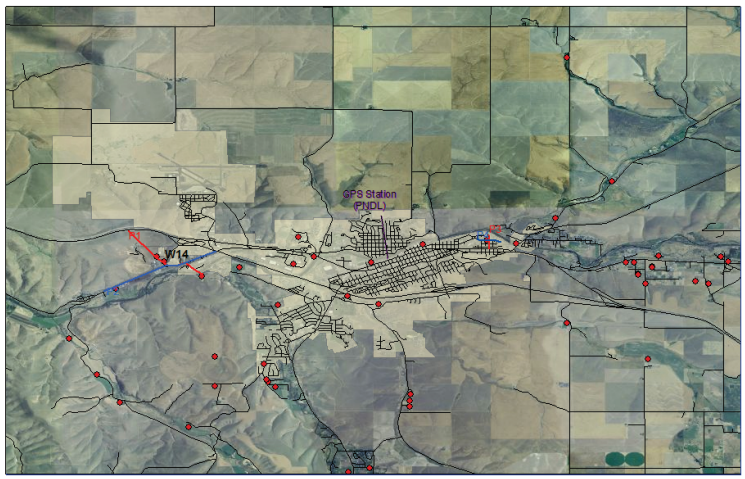

Figure 6. Overview of injection sit

The gravimeter was the same one used during the first survey, a Lacoste and Romberg model G rented from Exploration Instruments LLC, Austin, Texas. The two profiles have been tied to the base station Pendleton 39 located at the main Post Office. In order to accurately reoccupy the same gravity measurement stations between surveys, Real-Time Kinematic (RTK) positioning has been performed on each station.

A crew of 3 people (2 gravity and 1 for GPS) is needed for each survey. Mark Sweeney is the engineer supervising the instrument preparation and field operations. Jeffrey Dermond, an under-graduated student working full time on the project since July, is also participating in the field surveys and is in charge of data processing. The stations will be reoccupied again at the end of October 2010 to measure the end of the reservoir withdrawal. A first report on the temporal variations of the gravity during this first period will be presented in the next quarterly report.

Transition from ZERT I to ZERT II

This is a new task under ZERT II.

Publications and Presentations

Krupka, KM, KJ Cantrell, BP McGrail. 2010. "Thermodynamic Data for Geochemical Modeling of Carbonate Reactions Associated with CO_2 Sequestration –Literature Review". PNNL-19766, Pacific Northwest National Laboratory, Richland, Washington.

Appendix D

LLNL Technical Paper

Environ Earth Sci (2010) 60:251–261
DOI 10.1007/s12665-009-0372-2

SPECIAL ISSUE

Using hyperspectral plant signatures for CO_2 leak detection during the 2008 ZERT CO_2 sequestration field experiment in Bozeman, Montana

Erin Jing Male · William L. Pickles · Eli A. Silver · Gary D. Hoffmann · Jennifer Lewicki · Martha Apple · Kevin Repasky · Elizabeth A. Burton

Received: 3 April 2009 / Accepted: 17 November 2009 / Published online: 13 January 2010

Abstract Hyperspectral plant signatures can be used as a short-term, as well as long-term (100-year timescale) monitoring technique to verify that CO_2 sequestration fields have not been compromised. An influx of CO_2 gas into the soil can stress vegetation, which causes changes in the visible to near-infrared reflectance spectral signature of the vegetation. For 29 days, beginning on July 9, 2008, pure carbon dioxide gas was released through a 100-m long horizontal injection well, at a flow rate of 300 kg day^{-1}. Spectral signatures were recorded almost daily from an unmown patch of plants over the injection with a "FieldSpec Pro" spectrometer by Analytical Spectral Devices, Inc. Measurements were taken both inside and outside of the CO_2 leak zone to normalize observations for other environmental factors affecting the plants. Four to five days after the injection began, stress was observed in the spectral signatures of plants within 1 m of the well. After approximately 10 days, moderate to high amounts of stress were measured out to 2.5 m from the well. This spatial distribution corresponded to areas of high CO_2 flux from the injection. Airborne hyperspectral imagery, acquired by Resonon, Inc. of Bozeman, MT using their hyperspectral camera, also showed the same pattern of plant stress. Spectral signatures of the plants were also compared to the CO_2 concentrations in the soil, which indicated that the lower limit of soil CO_2 needed to stress vegetation is between 4 and 8% by volume.

Keywords Geologic carbon sequestration · Hyperspectral plant signatures · Reflectance spectra · CO_2 leak detection · Surface monitoring of carbon sequestration

E. J. Male (✉) · W. L. Pickles · E. A. Silver · G. D. Hoffmann
Earth and Planetary Sciences,
University of California-Santa Cruz,
Santa Cruz, CA 95064, USA
e-mail: emale@ucsc.edu

J. Lewicki
Lawrence Berkeley National Laboratory,
Berkeley, CA 94720, USA

M. Apple
Montana Tech of The University of Montana, Butte,
MT 50701, USA

K. Repasky
Department of Electrical and Computer Engineering,
Montana State University, Bozeman, MT 59717, USA

E. A. Burton
Lawrence Livermore National Laboratory,
Livermore, CA 94550, USA

Introduction

With the effects of climate change on the rise, reduction of the amount of CO_2 released into the atmosphere is crucial. Injection of CO_2 into deep underground formations, known as geologic carbon sequestration, can be an effective method of mitigation by preventing the CO_2 injected into underground sequestration formations from entering the atmosphere. In order for geologic sequestration to be successful, methods of verification are important to maintain the sequestered CO_2 and to assure the public that the sequestration operation is safe. It is therefore important to develop techniques for long-term CO_2 leak detection at the surfaces of the CO_2 sequestration fields (Pickles and Cover 2005).

Analyzing hyperspectral plant signatures over CO_2 sequestration fields can confirm that the sequestration fields have not been compromised. If a leak were to occur, the

excess amount of CO_2 in the top layers of soil near the surface would stress the vegetation above the sequestration field, which can be seen as changes in their spectral signatures. CO_2-induced stress has been recognized in the spectral signature of plants over volcanic CO_2 vents at the Latera (Bateson et al. 2008) and Long Valley (De Jong 1996; Hausback et al. 1998; Martini et al. 2000) calderas, as well as in laboratory experiments (Noomen and Skidmore 2009). Conversely, if vegetation over a sequestration field has healthy spectral signatures, it would indicate that CO_2 is being sequestered effectively. Because the basic requirement of this technique is just the presence of healthy vegetation over the sequestration field, hyperspectral plant signatures are particularly useful tool for monitoring sequestration fields for years to centuries (Pickles and Cover 2005).

This technique was studied during a shallow underground leak experiment held at Montana State University (MSU) in Bozeman, Montana. Pure CO_2 gas was released for 29 days from a 100-m long, horizontal CO_2 injection well, located about 1–2.5 m underground. During this time, the health of vegetation over the west end of the injection well was determined by measuring their hyperspectral reflectance signatures with a field spectrometer. In addition, airborne hyperspectral imagery was acquired from a low-flying aircraft using a hyperspectral camera system developed by Resonon, Inc. of Bozeman, MT (www.resonon.com). The spectral signatures of the plants were also correlated with variations in soil CO_2 concentrations measured directly over, and at 2.5, 5, 7.5, and 10 m from the well by Lewicki et al. (2009, this volume).

Plant stress and spectral signatures

The term "plant stress" tends to be used in numerous ways because monitoring plant health has many applications. In a general sense, plant stress occurs when environmental conditions are unfavorable for optimal plant growth. Some of the conditions that can cause stress are drought, extreme heat or cold, insect infestation, waterlogging, bacterial diseases, oxygen depletion, nutrient deficiencies, or acidic soil (Lichtenthaler 1998). Although excess CO_2 has also been shown to negatively affect plants, the exact mechanism(s) by which it harms vegetation is not known. Most likely, the CO_2 gas displaces oxygen to the roots of the plant, which occurs in natural gas leaks (Noomen et al. 2008). Other possibilities are that large amounts of CO_2 could change the pH and redox potential of soil or alter natural microbial environments (Noomen et al. 2006). The result of vegetation experiencing stress over long periods can be stunted growth, reduced water content, or a decrease in leaf chlorophyll concentrations. This can lead to replacement by other more tolerant plant species which then becomes habitat modification (Pickles and Cover 2005). We used the decrease in chlorophyll concentrations as an indicator of plant stress because it is a typical response regardless of species of vegetation or cause of stress (Carter 1993). In addition, chlorophyll can be readily estimated in the reflectance spectra of the vegetation (Carter and Knapp 2000; Hill 2004; Zhang et al. 2008; Moorthy et al. 2008).

When light contacts a leaf, the various wavelengths can be absorbed, reflected, or transmitted based on the leaf's chemical and physical structure. This interaction results in a distinctive spectrum of reflected light. Healthy plants tend to have relatively low reflectance in the visible ($\sim$400 to 720 nm) with a peak in the green range ($\sim$550 nm) and high reflectance in the near-infrared (NIR) ($\sim$700–1,400 nm). The spectral signature of plants in the visible is caused by the various pigments they contain, such as carotenoid and chlorophyll compounds. Chlorophyll gives a healthy plant its green color because chlorophyll reflects light in the green and absorbs light elsewhere in the visible (Blackburn 2007). Specifically, chlorophyll causes a strong absorption feature in healthy plant spectra from approximately 600 to 700 nm. The size and detailed shape of this absorption feature have been found to correlate with the amount of chlorophyll in a plant because a decrease in the amount chlorophyll would also decrease the plant leaf's overall absorptivity in the range of the absorption feature (Carter 1993, Carter and Knapp 2001; Smith et al. 2004; Noomen et al. 2006; Noomen and Skidmore 2009). Therefore, if a particular plant is stressed by excess CO_2 from a faulty sequestration field, the chlorophyll concentrations will decrease, and the chlorophyll absorption feature of its spectral signature will change accordingly.

Even though hyperspectral signatures can be used to estimate the amount of plant stress, it is unable to distinguish between the different causes of stress. This uncertainty can be problematic when testing for CO_2 leaks. A sequestration field could appear unhealthy spectrally, but the stress could be caused by something unrelated to escaping CO_2. To reduce the number of possible false positives, it is important to normalize measurements by comparing plant spectra to identical environmental conditions outside the sequestration field. Normalization can help determine if the identified stress is seasonal (for example, high summer heat), which would affect vegetation regionally. The spatial distribution of stressed vegetation may also yield information about the pathways by which CO_2 migrates from depth to the surface. In addition, knowing the location of CO_2 pipelines and other potential leak sites would be extremely useful since the CO_2 stress would probably be located near by. Thus, hyperspectral plant signatures could still be used to verify that the sequestration fields have not leaked (with healthy spectral

signatures across the field) or at least focus ground-based CO_2 monitoring techniques on potential leak sites.

Methods

Field design

In a MSU agricultural field, a 100-m long, horizontal CO_2 injection well was installed at depth varying between approximately 1 and 2.5 m. Pure CO_2 gas was injected for 29 days from July 9 to August 7, 2008 at a flow rate of 300 kg day^{-1} (Spangler et al. 2009, this volume). Prior to the start of the injection, a 20- by 30-m patch of vegetation, centered over the west end of the horizontal injection well, was selected for the plant stress experiment. This section of the field was left unmown except for access paths and was not disturbed for the duration of the experiment (Fig. 1). Within the plant study area, 68 sites were chosen where plant spectral measurements were taken daily. Measurements started 2 days before the start of the injection until 1 week after the CO_2 injection was shut off (July 5 to August 11, 2008). Measurement sites ranged in position from directly over the injection well out to 10 m from the well horizontally. In addition, 24 measurement sites were located at 1-m intervals directly above the injection well (Fig. 2). This array gave plant reflection spectra both within and outside of the injected CO_2 leak zones so the observations could be normalized for other environmental factors affecting the plants. The plant species within the field consisted primarily of various species of short and tall grasses, alfalfa, dandelions, and a variety of clovers. Each measurement site contained random mixes of vegetation species. Table 1 contains a full list of plant types with their scientific names that were identified on July 30, 2008. This

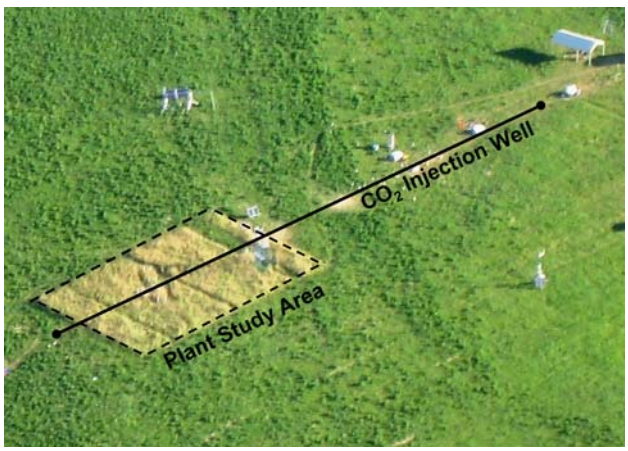

Fig. 1 Aerial photo of field site, taken August 5, 2008 by Resonon Inc

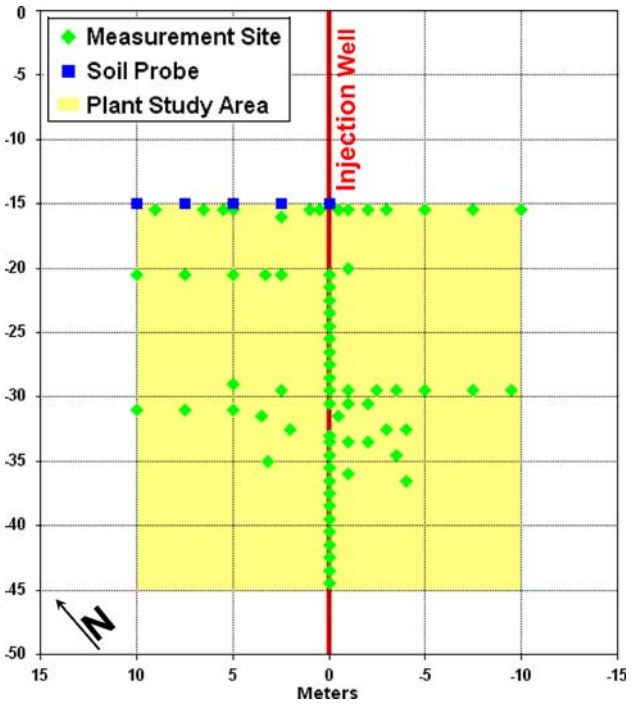

Fig. 2 Schematic representation of plant study area. Distances are measured relative to the center of the injection well

Table 1 Plant species identified at field site

Composite family—Asteraceae
Western salsify (*Tragopogon dubius*)
Dandelion (*Taraxacum officinale*)
Canada thistle (*Cirsium arvense*)
Legume family—Leguminaceae
Alfalfa (*Medicago sativa*)
Birdsfoot trefoil (*Lotus corniculatus*)
Yellow blossom sweet clover (*Meliotus officinalis*)
Red clover (*Trifolium pretense*)
Lupine (*Lupinus argenteus*)
Grass family—Poaceae
Quackgrass (*Agropyron repens*)
Orchard grass (*Dactylis glomerata*)
Timothy (*Phleum pretense*)
Tall fescue (*Festuca pratensis*)
Kentucky bluegrass (*Poa pratensis*)
Field brome (*Bromus arvensis*)
Smooth brome (*Bromus inermis*)

list may not be complete as some species may have been dormant at the time.

Field spectrometer measurement techniques

Plant spectral signatures were measured using a "FieldSpec Pro" spectrometer by ASD, Inc., (www.asdi.com). It was a

full range spectrometer that measured reflectance spectra from 350 to 2,500 nm with a 1-nm bandwidth. The spectrometer was connected to a fiber optic cable fitted with a 5° lens. The lens was held approximately 1 m above the ground from a nadir position, which resulted in the spectrometer having a field-of-view of approximately 10 cm. To reduce noise in the spectra, the spectrometer was programed to give a final spectral measurement that was the average of 100 spectra taken continuously at each site. This spectrometer was also designed to self-regulate many of the settings. To optimize this feature, the lens of the spectrometer was held over the vegetation to be measured for approximately 3 s prior to acquiring each spectral signature. This time allowed the spectrometer to self-adjust its settings before taking each measurement. Precautions were also made not to expose the lens of the spectrometer to extreme bright light or darkness. These techniques appeared to reduce noise and increased the reproducibility of the data significantly.

Several procedures were used to eliminate illumination and atmospheric factors that would affect the data. A "Spectralon" white "reflectance plate" provided the solar reference spectrum used to calculate reflectance spectra from the raw collected spectra. A white plate reference spectrum was measured before collecting any plant signatures and re-measured it after every few spectral readings. In addition, spectral readings were only acquired under cloud-free skies with minimal haze. Each day, data were collected in the same sequence as close to solar noon as possible, typically between 9:30 am and 1:30 pm. This approach gave a consistent solar intensity and angle at each measurement site throughout the experiment.

Classification of hyperspectral plant signatures

To aid in analyzing patterns of plant stress, the hyperspectral plant spectra were classified using the software program ENVI 4.5 (www.ittvis.com). As a first step, we created a computer program to compile the individual spectra recorded by the FieldSpec Pro spectrometer into data cubes, thereby creating artificial images of the plant study area. The artificial images show the discrete spectral measurements taken on a given day with their true relative orientations. The images have a 0.5-m pixel size. Each pixel contains either the spectra measured by the FieldSpec Pro at that site or were assigned a spectrum with zero reflectance and were ignored in subsequent analysis. These artificial images were created for each day of the experiment. They are oriented with the east edge of the plant study area at the top of the artificial image with the CO_2 injection well running along the center of the image (Fig. 3).

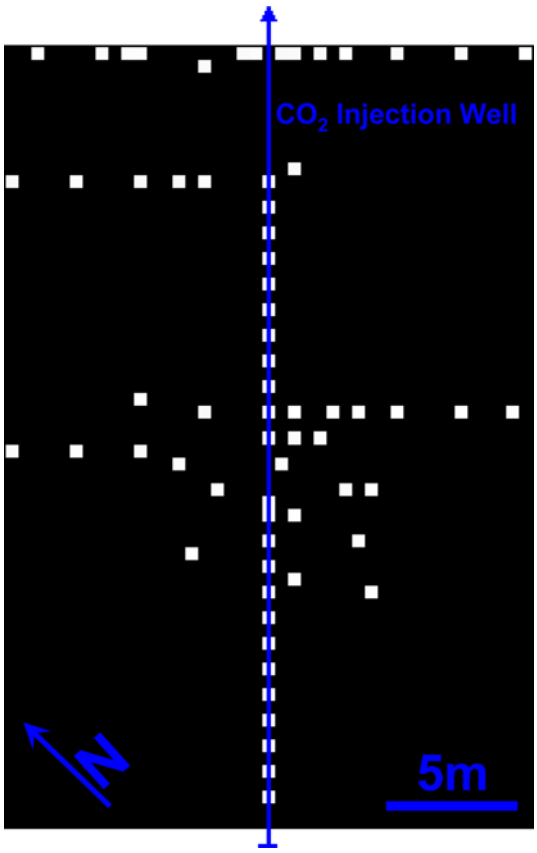

Fig. 3 Example artificial image created from data collected from FieldSpec Pro Spectrometer. *Black* area represents the plant study area. *White* pixels are measurement sites. The east edge of the plant study area is the top of the image

Each artificial image of the field was processed with an ENVI classification tool called Spectral Angle Mapper (SAM). This method classifies measured spectra to reference endmember spectra based on how closely the observed and reference spectra compare (Kruse et al. 1990). This technique has been found to be relatively insensitive to illumination effects caused by atmospheric conditions or differences in leaf angle relative to the spectrometer lens line of sight (Sohn and Rebello 2002).

The SAM classification utilized more of the spectral signature than other simple indices of plant health, which may only compare reflectance at select wavelengths. The supervised SAM classification was based on spectral signatures from 350 to 800 nm. The spectra were divided into three classes: Healthy Vegetation, Moderate to Highly Stressed Vegetation, and Extremely Stressed Vegetation. A total of nine spectra were chosen as endmembers for the SAM classification, with four endmembers as "Healthy Vegetation", two as "Moderately to Highly Stressed Vegetation", and three as "Extremely Stressed Vegetation". Endmembers were based on the overall shape of the spectra, variety of vegetation, quality of spectral signal,

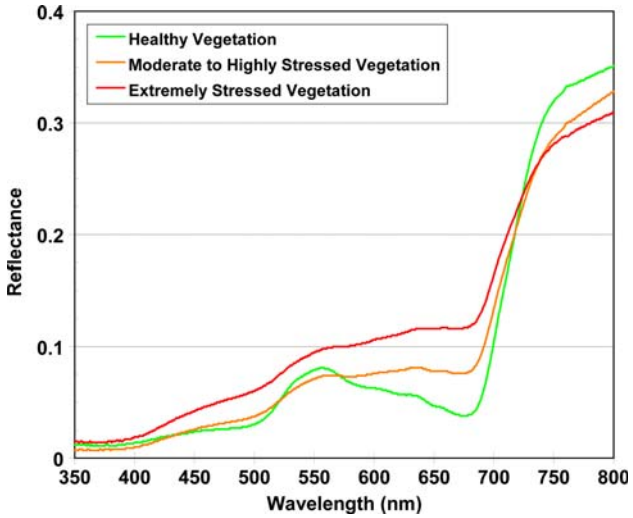

Fig. 4 Graph of representative spectra for each endmember class used to classify artificial images

and on the depth of their chlorophyll absorption feature from approximately 600 to 700 nm. The depth of this absorption feature was estimated by subtracting the maximum reflectance, between 525 and 575 nm, from the minimum reflectance, between 675 and 700 nm. A relatively large absorption depth was considered to be "Healthy Vegetation," whereas an absorption depth very close to zero (either positive or negative) was "Moderate to Highly Stressed Vegetation" and a large negative absorption value was "Extremely Stressed Vegetation". While measuring the depth of this chlorophyll absorption feature gives an estimation of stress level, it was not used as a final classifier because we wanted to utilize the entire spectral signature. Figure 4 shows representative endmember spectra for each class.

Aerial hyperspectral imagery

On August 5, 2008 (after 27 days of CO_2 injection), a hyperspectral image was acquired of the entire injection well from a low-flying aircraft. The spectrometer, developed by Resonon, Inc. of Bozeman, MT, had a spectral range of 400–880 nm with a wavelength resolution of approximately 6 nm. ENVI's supervised classification tool with Spectral Angle Mapper was used to analyze the image over the spectrometer's full spectral range. Reference endmember spectra were determined on the basis of spectral shape, particularly the depth of the chlorophyll absorption feature, as well as on plant species. The image was classified into five categories: High stress, Moderate stress, Low or Seasonal Stress, Healthy Vegetation (grasses), and Healthy Vegetation (herbaceous legumes). Figure 5 is the hyperspectral imagery shown in true color.

Fig. 5 Aerial hyperspectral imagery of field site shown in true color. Imagery was acquired after 27 days of the CO_2 injection

Results

By comparing changes in shape of the hyperspectral plant signatures, stress could be identified in some of the plants close to the well after 4–5 days of CO_2 injection (Fig. 6). After 14 days, the spatial extent of plant stress reached a maximum with two discrete, identifiable zones of plant stress. One zone was located over the injection well, along the eastern edge of the vegetation study area. It extended out to at least 2.5 m on the north side of the injection well and out to approximately 1 m on the south side. The second zone of plant stress was in the center of the vegetation study area approximately 20 m from the east edge. It was also located over the injection well and extended out to at least 2.5 m in all directions.

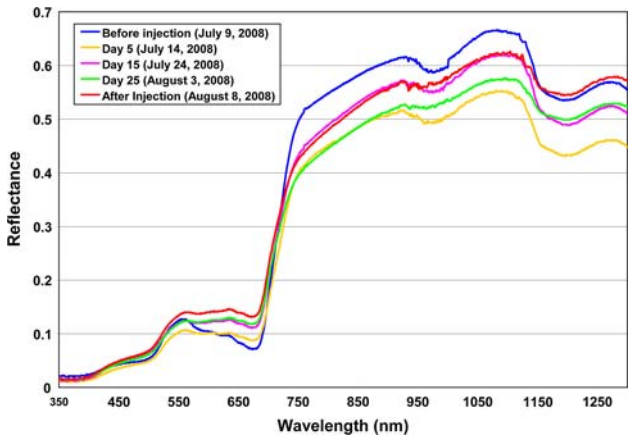

Fig. 6 Spectral signatures throughout experiment of vegetation 0.5-m north of injection well, at the eastern edge of plant study area. Note the changes in absorption features between 550 and 750 nm

Fig. 7 Photos of vegetation 0.5 m north of injection well, at east edge of plant study area. *Top* photo was taken before injection (July 8, 2008). *Bottom* photo taken 4 days after end of injection (August 11, 2008)

Because hyperspectral plant signatures are very sensitive to environmental changes, this method indicated plant stress using before changes in vegetation were visible to the eye. Large decreases in chlorophyll can make vegetation appear more yellow or brown (Fig. 7). However, changes in the spectral signature can indicate chlorophyll decreases even when there are only small deceases in chlorophyll and the vegetation is still green. In addition, the amount of stress measured during the experiment seemed to be species dependent. The tall grasses and alfalfa in the field reacted quickly, whereas dandelion and some naturally short grasses appeared to be more resistant to stress.

Spectral measurements were collected for 1 week past the end of the injection. It was unclear whether the extremely stressed vegetation began to recover during this time. It was likely that the prolonged exposure to the high amount of CO_2 applied enough stress to irreparably damage the vegetation. However, new vegetation, specifically orchard grass and dandelions, began to grow anew in zones of extreme plant stress, which may suggest that certain species of vegetation are more capable of growing under CO_2 stress.

Classification results: field spectrometer artificial images

The classification from the artificial images of the field also shows two locations of plant stress by the end of the CO_2 injection: (1) on the east edge and (2) in the center of the plant study area. Figure 8a–f is the classification images at the start of the injection, at 10, 14, 16, and 23 days of injection, and 1 day following the end of the injection, respectively. According to the classifications, plants began to experience moderate to high amounts of stress after approximately 6 days of the injection. The size and intensity of the plant stress zones increased throughout the duration of the injection. Near the end of the experiment (early August), the entire field appears to be stressed to some degree (Fig. 8f), which was due to natural changes in the grasses lifecycle and/or by extreme weather (for example, excessive heat or the hail storm on July 22, 2008). Despite seeing this trend of increasing stress across the field, the pattern of two zones of extreme stress is still identifiable. This is an additional benefit for CO_2 sequestration monitoring, because it shows that stress from an influx of CO_2 can be distinguished from seasonal or other environmental stressors.

Classification results: aerial hyperspectral imagery

Figure 9 is the SAM classification of the hyperspectral imagery, which was acquired after 27 days of CO_2

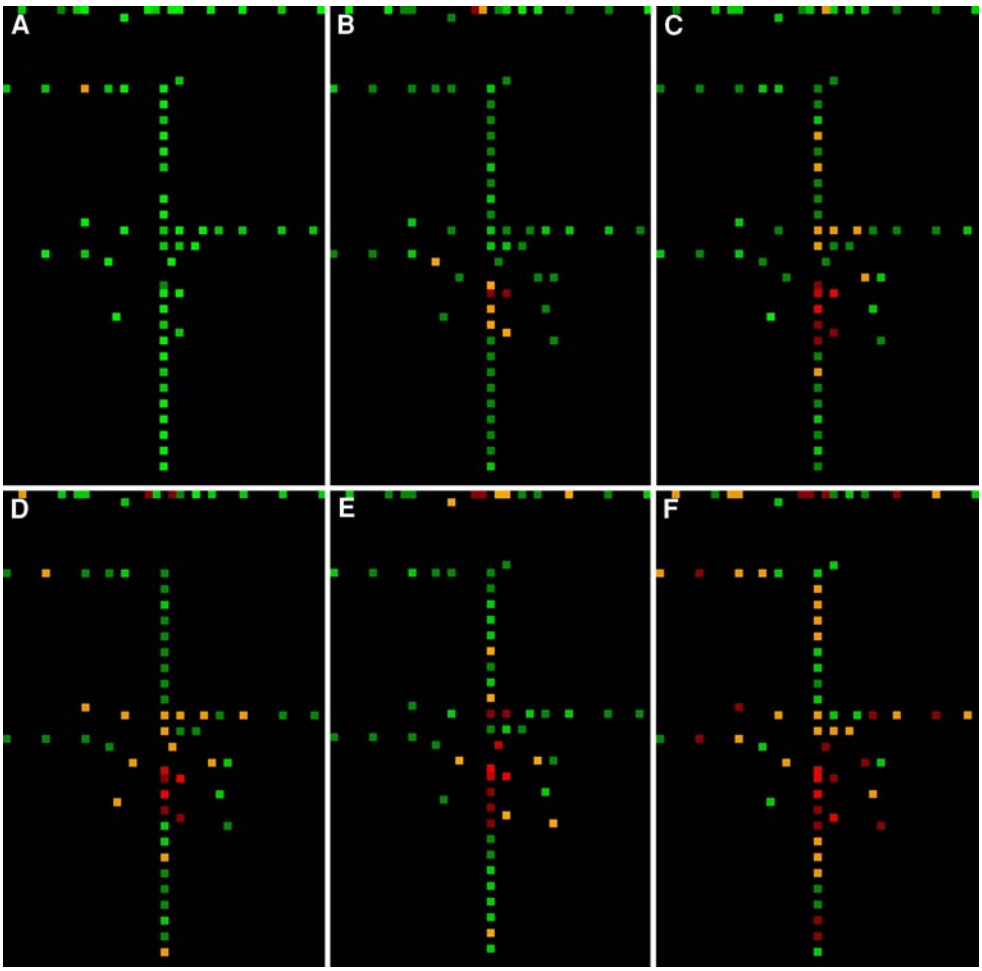

Fig. 8 Classifications of artificial image using ENVI Spectral Angle Mapper algorithms. *Green* Healthy vegetation, *orange* moderately to highly stressed vegetation, *red* extremely stressed vegetation. **a** Before injection (July 9, 2008); **b** after 10 days (July 19, 2008); **c** after 14 days (July 23, 2008); **d** After 16 days (July 25, 2008); **e** 23 days (August 1, 2008); **f** 1 day after end of the 29-day injection (August 8, 2008)

injection (August 5, 2008). The classification figure (Fig. 9) also shows the two same zones of plant stress, each measuring approximately 2 m in diameter. Similar-sized zones of plant stress are also found along the length of the entire injection well. These other zones were in mown grass that was approximately 15 cm tall. This demonstrates how this monitoring technique was capable of detecting CO_2 leaks over areas with different types of vegetation. One zone of plant stress is difficult to distinguish at the north end of the injection well (Fig. 9). It appears similar to zones of low plant stress caused by frequent foot traffic. However, its location directly over the injection well suggests that the plant stress is connected to the CO_2 injection. There are also areas that have been classified as high plant stress that were actually caused by disturbances from equipment from other participants of this experiment that can be seen in the true color aerial image (Fig. 8a). Comparing the locations of plant stress with locations of potential leak site (pipelines, for example) and artificial structures helped indentify the various causes of plant stress.

In addition to identifying zones of plant stress, different types of vegetation could be distinguished in the image. Because the tall grasses of the plant study area were left unmown, there were dried seeds on top of the grass stalks. Although that was normal for those species of grass during late summer, it made the unmown area appear slightly stressed. This effect occurs because the aerial spectrometer looks vertically onto the vegetation, seeing mainly the dried seed pods. Outside of the plant study area, the vegetation had been mown prior to the start of the experiment and fresh and healthy vegetation was growing in. This image also demonstrates the effect of plant structure on the hyperspectral signature. Across the MSU agricultural site, the vegetation is typically some variety of either grass or herbaceous legume (Alfalfa, clover, or bird's foot trefoil). Even if both categories of vegetation are considered healthy, their spectral signatures may be distinct because of the differences in their physical leaf structures, specifically vertical blades of grass compared to more horizontal wide leaves. These differences in spectral signatures were identified using ENVI's classification algorithms. It is also

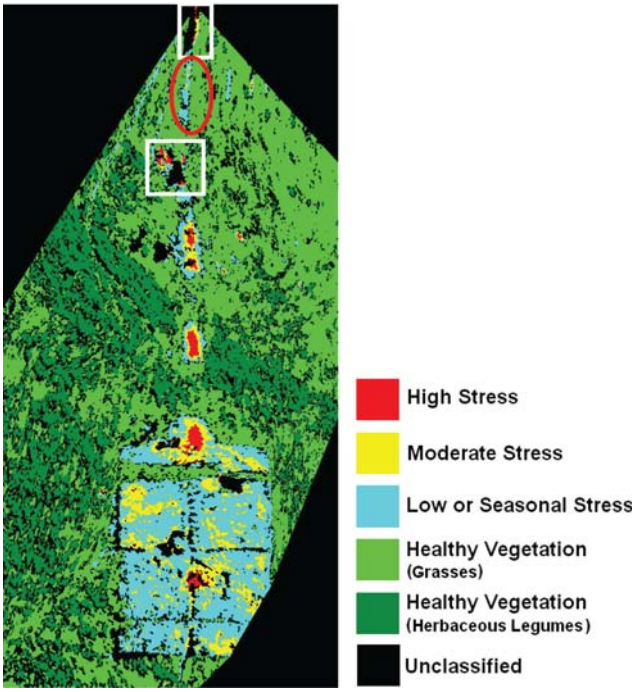

Fig. 9 Classification of Aerial Hyperspectral Imagery acquired by Resonon Inc. Classification was performed using ENVI Spectral Angle Mapper algorithms. *White boxes* show locations of areas of apparent plant stress caused by equipment from outside experiments. The *red circle* indicates location of the subtle fifth zone of plant stress caused by the injected CO_2

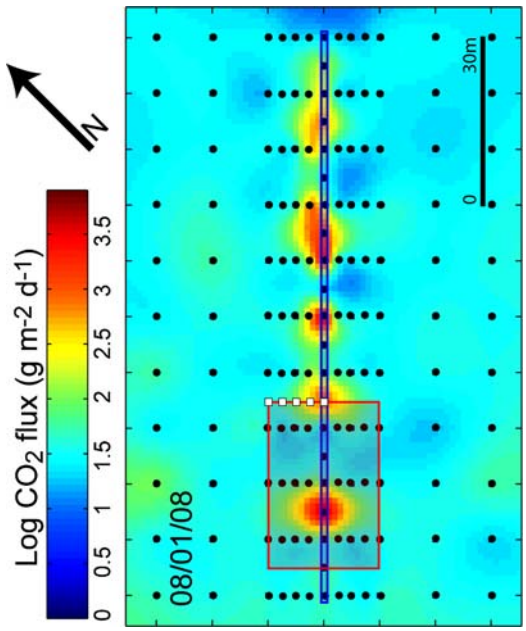

Fig. 10 Map of log soil CO_2 flux, interpolated based on measurements made at the black dots [modified from Lewicki et al. 2009, (this volume)]. The blue rectangle represents the CO_2 injection well. The red rectangle marks the plant study area. White squares are soil CO_2 concentration probes. Note the two zones of high CO_2 flux at the east edge and in the center of the plant study area

important to note that these effects from leaf structure are mostly pronounced outside the chlorophyll absorption feature and do not significantly affect the ability to detect stress from the spectral signatures.

Associated observations

Soil CO_2 fluxes

Soil CO_2 fluxes were measured using the accumulation chamber method on a grid repeatedly on a daily basis during the injection by Lewicki et al. (2009, this volume). Figure 10 shows an example of a map of log soil CO_2 flux, interpolated based on measurements made on August 1, 2008 (23 days of CO_2 injection). The location of the plant study area is shown for reference. Five separate zones of relatively high CO_2 flux can be seen, which are approximately 2–3 orders of magnitude above background levels. They are roughly circular to elliptical in shape ranging from approximately 5 to 15 m in diameter. Within the boundaries of the plant study area, there are two zones of high CO_2 flux, located in the center of the plant study area and at the eastern edge.

Soil CO_2 fluxes were also measured at 1-m intervals along the surface trace of the injection well on July 14, 2008 (5 days of CO_2 injection) by Lewicki et al. (2009, this volume). Figure 11 shows the same five zones of high flux along the injection well, two of which were located within the plant stress area. One high CO_2 flux zone, located in the center of the plant study area, is approximately 6 m in diameter and has a maximum flux of approximately 3,700 g m^{-2} day^{-1}. The other maximum, at 6,500 g m^{-2} day^{-1}, is located 2 m northeast of the eastern edge of the plant study area, while CO_2 flux is about 700 g m^{-2} day^{-1} at the edge of the plant study area.

Soil CO_2 concentrations

Soil CO_2 concentrations were measured at 30 cm depth at distances of 0, 2.5, 5, 7.5 and 10 m northwest of the injection well (Fig. 9) using non-dispersive infrared gas analyzers every 1 s and averaged over half-hour periods (Lewicki et al. 2009, this volume) (see Figs. 2, 10 for locations). Figure 12 shows time series of the soil CO_2 concentrations. Over the injection well, soil CO_2 concentrations rose to approximately 13–14% CO_2 by volume. The plants over the injection well also began to show stress after 4 days. CO_2 concentrations measured 2.5 m from the well ranged from 6 to 10%, averaging approximately 8% CO_2 by volume. Nearby plants showed stress after 14 days.

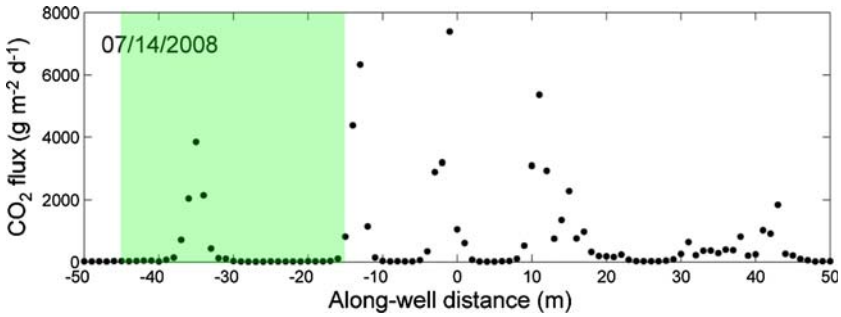

Fig. 11 Soil CO_2 fluxes measured along the surface trace of the horizontal well [modified from Lewicki et al. 2009, (this volume)]. The area of the plant study area is indicated by the shaded region

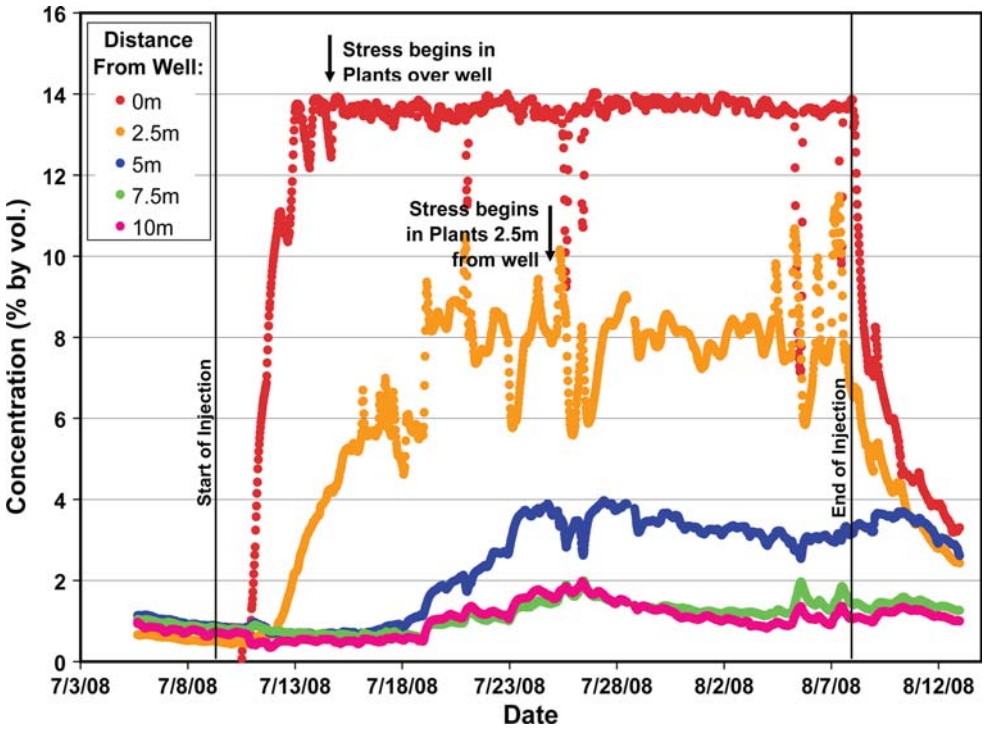

Fig. 12 Time series of soil CO_2 concentrations [Lewicki et al. 2009, (this volume)]. Soil probes were located at east edge of plant study area at varying distances from CO_2 injection well

At 5 m from the well, soil CO_2 concentrations rose to a maximum of 3–4%. At 7.5 and 10 m from the injection well, soil CO_2 concentrations did not rise significantly during the injection, staying close to 1–2% CO_2 by volume. None of the plants at 5, 7.5, or 10 m showed significant signs of stress. From these observations, the lower limit of the CO_2 concentration needed in the soil to begin to stress vegetation could be inferred. Because plants at 2.5 m were stressed, but those at 5 m were not, the lower limit of soil CO_2 concentration can be estimated to be between 4 and 8% by volume, which was approximately 3–4 times greater than background levels. Bateson et al. (2008) performed a leak detection experiment over natural volcanic CO_2 vents in Italy by monitoring plant health using various remote sensing techniques. The minimum soil CO_2 concentration of their detected gas vents was 5.6% which falls within the range determined in this experiment. In a greenhouse experiment on maize plants, Noomen and Skidmore (2009) found a correlation between high percentages of CO_2 in soil and decreases in chlorophyll content and plant growth. However, 50% CO_2 was the minimum CO_2 concentration to give statistically different results.

Discussion

Everywhere high CO_2 flux was measured, it was associated with a corresponding zone of plant stress. This result shows the potential of using hyperspectral plant signatures for CO_2 leak detection. Both the field spectrometer and the airborne hyperspectral imager measured the same two discrete zones of plant stress, on the eastern edge and in the center of the plant study area. These zones coincided with areas of high measured CO_2 flux. The airborne

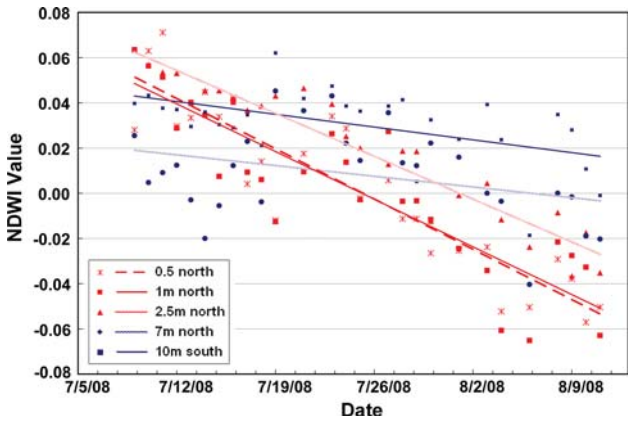

Fig. 13 Plot of Normalized Difference Water Index (NDWI) values. Vegetation is located along east edge of plant study area at various distances from the injection well. Vegetation in the CO_2 leak zone is plotted in *red*. Background values are in *blue*. NDWI = (ρ860 − ρ1240)/(ρ860 + ρ1230), ρ = reflectance at given wavelength in nm

hyperspectral imagery also shows three additional zones of plant stress outside the plant study area, whose locations match the zones of high CO_2 flux measured along the entire injection well (Fig. 9). The high similarity between the distinctive distributions of extremely stressed vegetation and high CO_2 flux indicated that injected CO_2 is the cause of the plant stress.

One difficulty of this leak detection method is in the ability to recognize stress caused by excess CO_2 independent of other environmental stressors. However, the spatial distribution of relative stress across a sequestration field can help to identify the possible causes for the identified plant stress. In this experiment, two zones of plant stress were located that were focused and sharply delineated from the rest of the field in circular patterns that were centered over the leaks in the injection well. This pattern would not be expected for stress caused by weather, infestation, or poor soil which would act on a regional scale. In addition, the size of plant stress zones remained consistent during changing environmental conditions. For instance, several days of consistent rainfall did not appear to alleviate stressed vegetation, indicating that dehydration was not the cause of the plant stress. The signal of extreme plant stress was also distinct enough not to be clouded by seasonal stress at the end of the summer, showing that seasonal stress was not the only stressor present. The link between injected CO_2 and zones of plant stress became evident after ruling out these other environmental possibilities for stress.

It can also be possible to use the spectral signature of vegetation to eliminate drought or prolonged exposure to high heat as possible stressors. Leaf water content strongly influences hyperspectral plant signatures outside the visible spectra (Carter 1991). Because this experiment took place during the end of a hot summer, there was a possibility that the vegetation was showing stress because they were simply drying out. To investigate this possibility, the Normalized Difference Water Index (NDWI) was calculated over the course of the injection for vegetation at various measurement sites across the east edge of the plant study area. NDWI values are calculated by the difference of the reflectance at 860 and 1,240 nm divided by their sum. NDWI has been found to correlate with water content of vegetation (Gao 1995). Figure 13 is a graph of NDWI for vegetation on the east edge of the plant study area located 0.5-, 1-, 2.5-, 7.5-m north, as well as 10-m south, of the injection well. Measurements from vegetation at 7.5 and 10 m from the injection well were outside the CO_2 leaks and can be considered as background values. Figure 13 shows an overall decrease in water content for all vegetation across the field, suggesting that high summer heat has affected the water content of all the plants. However, the water content in vegetation within 2.5 m of the injection well decreased at a faster rate than background vegetation. This result indicates an additional stress, besides high heat, was acting on these plants because the temperature and precipitation were consistent between all areas of the field. In this experiment, the additional stress can be linked to the high CO_2 flux within 2.5 m of the injection well because it is the only different factor known between the vegetation. However, in general, this connection cannot be made since the CO_2 flux is usually unknown. Normalizing for water content can at least eliminate some stressors and reduce the chance of false positives for CO_2 leaks. It is possible that other stressors could be eliminated similarly. Therefore, it is important to acquire hyperspectral data over an entire region and not just over pipelines and other potential leak sites of sequestration fields.

Conclusions and recommendations

CO_2 leaks through the soil could successfully be identified by hyperspectral signatures to determine the health of overlying vegetation. The plant spectra began to show signs of stress within 4 days of the CO_2 injection. The lower limit of soil CO_2 concentration needed to induce this stress can be estimated to be between 4 and 8% CO_2 by volume. The spatial extent of plant stress, as determined by spectrometers in the field and from the air, match the locations of high measured CO_2 flux from the injection.

There are also many additional benefits to this monitoring technique, such as a quick response time. Vegetation is very sensitive to stress, so a suspected leak could be identified within days. Also, the actual spectral measurements can be collected and processed rapidly by acquiring

airborne hyperspectral imagery, which will have no impact on the sequestration field itself. More importantly, this monitoring technique can be utilized long term, even on 100-year timescales, as it would require little to no maintenance of the sequestration field. The only requirement is simply the presence of vegetation. With these benefits, analyzing hyperspectral plant signatures for stress is an efficient method to verify that sequestration fields are successful in retaining injected CO_2.

Future work will focus on monitoring CO_2 leaks with various instruments, particularly on airborne and/or satellite platforms. Work will also go toward determining the specific mechanisms that cause plant stress due to changes in soil ecosystems from a CO_2 leak. In addition, the species dependence of the plant stress caused by elevated CO_2 soil concentrations is another topic to be investigated.

Acknowledgments We thank Laura Dobeck and Kadie Gullickson of Montana State University for their help with the experiment layout. We also thank Lee Spangler of Montana State University and Rand Swanson of Resonon, Inc., in Bozeman, Montana. We acknowledge the Montana Board of Research and Commercialization Technology (Grant No. 08–44) and NASA (Grant No. NNX06AD11G) for funding of the airborne hyperspectral imagery. Martha Apple acknowledges support by the US Department of Energy EPSCoR program under (Grant No. DE-FG02-08ER46527) for plant response research.

References

Bateson L, Vellico M, Beaubien SE, Pearce JM, Annunziatellis A, Ciotoli G, Coren F, Lombardi S, Marsh S (2008) The application of remote-sensing techniques to monitor CO_2-storage sites for surface leakage: method development and testing at Latera (Italy) where naturally produced CO_2 is leaking to the atmosphere. Int J Greenhouse Gas Control 2:388–400. doi:10.1016/j.ijggc.2007.12.005

Blackburn GA (2007) Hyperspectral remote sensing of plant pigments. J Exp Bot 58:855–867. doi:10.1093/jxb/erl123

Carter GA (1991) Primary and secondary effects of water content on the spectral reflectance of leaves. Am J Bot 78:916–924. doi:10.2307/2445170

Carter GA (1993) Responses of leaf spectral reflectance to plant stress. Am J Bot 80:239–243. doi:10.2307/2445346

Carter GA, Knapp AK (2001) Leaf optical properties in higher plants: linking spectral characteristics to stress and chlorophyll concentration. Am J Bot 88:677–684. doi:10.2307/2657068

De Jong SM (1996) Surveying dead trees and CO_2-induced stressed trees using AVIRIS in the Long Valley Caldera. In: Summaries of the sixth annual JPL airborne earth science workshop. JPL Publication 96, pp 67–74

Gao B (1995) Normalized difference water index for remote sensing of vegetation liquid water from space. Proc SPIE 2480:225. doi:10.1117/12.210877

Hausback BP, Strong M, Farrar C, Pieri D (1998) Monitoring of volcanogenic CO_2-induced tree kills with AVIRIS image data at Mammoth Mountain, California. In: Summaries of the seventh annual JPL airborne earth science workshop. JPL Publication 98

Hill M (2004) Grazing agriculture: managed pasture, grassland, and rangeland. In: Ustin S (ed) Remote sensing for natural resources management and environmental monitoring: manual of remote sensing, vol 4, 3rd edn. Wiley, Hoboken, pp 449–530

Kruse FA, Keirein-Young KS, Boardman JW (1990) Mineral mapping at Cuprite, Nevada, with a 63-channel imaging spectrometer. Photogramm Eng Rem S 56:83–92

Lewicki JL, Hilley GE, Dobeck L, Spangler L (2009, this volume) Dynamics of CO_2 fluxes and concentrations during a shallow subsurface CO_2 release. Env Geol

Lichtenthaler HK (1998) The stress concept in plants: an introduction. Ann NY Acad Sci 851:187–198. doi:10.1111/j.1749-6632.1998.tb08993.x

Martini BA, Silver EA, Potts DC, Pickles WL (2000) Geological and geobotanical studies of Long Valley Caldera, CA, USA utilizing new 5 m hyperspectral imagery. Geoscience and remote sensing symposium, 2000 proceedings. IGARSS 2000. IEEE 2000 International 4:1376–1378. doi:10.1109/IGARSS.2000.857212

Moorthy I, Miller JR, Noland TL (2008) Estimating chlorophyll concentration in conifer needles with hyperspectral data: an assessment at the needle and canopy level. Remote Sens Environ 112:2824–2838. doi:10.1016/j.rse.2008.01.013

Noomen MF, Skidmore AK (2009) The effects of high soil CO_2 concentrations on leaf reflectance of maize plants. Int J Remote Sens 30:481–497. doi:10.1080/01431160802339431

Noomen MF, Skidmore AK, Van Der Meer FD, Prins HH (2006) Continuum removed band depth analysis for detecting the effects of natural gas, methane and ethane on maize reflectance. Remote Sens Environ 105:262–270. doi:10.1016/j.rse.2006.07.009

Noomen MF, Smith KL, Colls JJ, Steven MD, Skidmore AK, Van Der Meer FD (2008) Hyperspectral indices for detecting changes in canopy reflectance as a result of underground natural gas leakage. Int J Remote Sens 29:5987–6008. doi:10.1080/01431160801961383

Pickles WL, Cover WA (2005) Hyperspectral geobotanical remote sensing for CO_2 storage monitoring. In: Thomas DC, Benson S (eds) Carbon dioxide capture for storage in deep geologic formations—results from the CO_2 capture project capture and separation of carbon dioxide from combustion sources, vol 2. Elsevier, San Diego, pp 1045–1070 (ISBN: 0-08-044570-5)

Smith KL, Steven MD, Colls JJ (2004) Use of hyperspectral derivatives ratios in the red-edge region to identify plant stress responses to gas leaks. Remote Sens Environ 92:207–217. doi:10.1016/j.rse.2004.06.002

Sohn Y, Rebello NS (2002) Supervised and unsupervised spectral angle classifiers. Photogramm Eng Rem S 68:1271–1280

Spangler LH, Dobeck L et al (2009) A controlled field pilot in Bozeman, Montana, USA, for testing near surface CO_2 detection techniques and transport models. Env Geol

Zhang Y, Chen JM, Miller JR, Noland TL (2008) Leaf chlorophyll content retrieval from airborne hyperspectral remote sensing imagery. Remote Sens Environ 112:3234–3247. doi:10.1016/j.rse.2008.04.005

Appendix E

List of Publications and Presentations

Publications

1. Steefel, C.I. and Lagasa, A.C., *A Coupled Model for Transport of Multiple Chemical Species and Kinetic Precipitation/Dissolution Reactions with Applications to Reactive flow in Single Phase Hydrothermal System.* American Journal of Science, 1994. **294**: p. 529-592.

2. Chilakapati, A., *RAFT: A Simulator for Reactive Flow and Transport of Groundwater Contaminants.* 1995, Pacific Northwest National Laboratory: Richland, WA.

3. Steefel, C.I., *GIMRT, Version 1.2: Software for Modeling Multicomponent, Multidimensional Reactive Transport: User's Guide*. 2001, Lawrence Livermore National Laboratory: Livermore, CA.

4. Fang, Y., Yeh, G.-T., and Burgos, W.D., *A General Paradigm to Model Reaction-Based Biogeochemical Processes in Batch Systems.* Water Resources Research, 2003. **39**(4): p. 1183-1107.

5. Bacon, D.H., White, M.D., and McGrail, B.P., *Subsurface Transport Over Reactive Multiphases (STORM): A Parallel, Coupled, Nonisothermal Multiphase Flow and Reactive Transport, and Porous Medium Alteration Simulator, Version 3.0*. 2004, Pacific Northwest National Laboratory: Richland, WA.

6. Pruess, K. Numerical simulation of CO_2 leakage from a geologic disposal reservoir, including transitions from super- to sub-critical conditions, and boiling of liquid CO_2. LBNL52423. Soc. Pet. Eng. J., 237-248, June 2004

7. Rockhold, M.L., Bacon, D.H., Brockman, F.J., Truex, M.J., and White, M.D., *Evaluation of Engineered Bioremediation vs. Natural Attenuation* in *Environmental Technology Division LDRD Annual Report (Unpublished)*. 2004, Pacific Northwest National Laboratory (PNNL): Richland, WA.

8. Xu, T., Apps, J.A., and Pruess, K., *Numerical Simulation of* CO_2 *Disposal by mineral Trapping in Deep Aquifers.* Applied Geochemistry, 2004. **19**: p. 917-936.

9. Lomesh, D., Nuttall, E., Cunningham, A.B., James, G., and Hiebert, R., *In Situ Biofilm barriers: Case Study of a Nitrate Ground water Plume, Alburquerque, New Mexico.* Remediation, Wiley Interscience, 2005. **2005**(Autumn).

10. Pruess, K., *E*CO_2*N: A TOUGH2 Fluid Property Module for Mixtures of Water, NaCl, and* CO_2, in *Lawrence Berkeley National Laboratory Report*. 2005, Lawrence Berkely National Laboratory: Berkeley, CA.

11. Sharp, R.S., James, G., Cunningham, A.B., and Komlos, J., *Novel Subsurface Biobarriers to Contain and Remediate Contaminated Ground Water.* Contaminated Soils, 2005. **10**.

12. Sharp, R.S., Stoodley, P., Adgie, M., Gerlach, R., and Cunningham, A.B., *Visualization and Characterization of Dynamic Patterns of Flow, Growth and Activity of Biofilms Growing in Porous Media.* Water Science and Technology, 2005. **52**(7): p. 85-90.

13. Spycher, N. and Pruess, K., CO_2*-H2o Mixtures in the Geologic Sequestration of* CO_2*. II. Partitioning in Chloride Brines at 12-100*C and up and up to 600 bar.* Geochim Cosmochim. Acta, 2005. **69**(13): p. 3309-3320.

14. Tomutsa, L., Silin, D., Benson, S.M., and Patzek, T., *Synchrotron Microtomography in* CO_2 *Geosequestration Research.* EOS Transactions, 2005. **82**(52).

15. Benson, S.M., *Monitoring Geological Storage of Carbon Dioxide*, in *Carbon Capture and Geologic Sequestration: Integration Technology, Monitoring and Regulation*, E.J. Wilson and D. Gerard, Editors. 2006, Blackwell Scientific Publishing: Ames, Iowa.

16. Pruess, K., *On* CO_2 *behavior in the subsurface, following leakage from a geologic storage reservoir*. 2006, LBNL: Berkely, CA.

17. Reagan, M.T. and Oldenburg, C.M., *WebGasEOS v1.0 user Guide*. 2006, LBNL: Berkely, CA.

18. Repasky, K.S., Humphries, S.D., and Carlsten, J.L., *Differential Absorption Measurements of Carbon Dioxide Using a Temperature Tunable Distributed Feedback Diode Laser.* Review of Scientific Instruments, 2006. **77**(11).

19. Repasky, K.S., Nehrir, A.R., Hawthorne, J.T., Switzer, G.W., and Carlsten, J.L., *Extending the Continuous Tuning Range of an External Cavity Diode Laser.* Applied Optics, 2006. **45**(35): p. 9013-9020.

20. Zhang, K., Doughty, C., Wu, Y.S., and Pruess, K., *Efficient parallel simulation of* CO_2 *geologic sequestration in saline aquifers.* SPE Journal (submitted), 2006.

21. Audigane, P., Gaus, I., Czernichowski-Lauriol, I., Pruess, K., and Xu, T., *Two-dimensional Reactive Transport Modeling of* CO_2 *Injection in a Saline Aquifer at the Sleipner Site, North Sea.* American Journal of Science, 2007. **307**: p. 974-1008.

22. Cunningham, A.B., Sharp, R.S., Caccavo Jr., F., and Gerlach, R., *Effects of Starvation on Bacterial Transport Through Porous Media.* Advances in Water Resources, 2007. **30**(6-7): p. 1583-1592.

23. Doughty, C., *Modeling geologic storage of carbon dioxide: Comparison of hysteretic and non-hysteretic curves.* Energy Conversion and Management, 2007. **48**(6): p. 1768-1871.

24. Doughty, C., *Predictions of long-term* CO_2 *Plume Behavior for Geologic Carbon Storage in a Saline Formation.* Transport in Porous Media: Special Issue on Geologic Carbon Storage, 2007. **Submitted**.

25. Gherardi, F, T Xu and K Pruess. Numerical Modeling of Self-limiting and Self-enhancing Caprock Alteration Induced by CO_2 Storage in a Depleted Gas Reservoir, Chem. Geol., 244, 103–129, 2007.

26. Lewicki, J.L., Hilley, G.E., Tosha, T., Aoyaga, R., Yamamoto, H., and Benson, S.M., *Dynamic coupling of volcanic* CO_2 *Flow and Wind at the Horeshoe Lake Tree Kill, Mammoth Mountain, CA.* Geophysical Research Letters, 2007. **34**.

27. Lewicki, J.L., Oldenburg, C.M., Dobeck, L., and Spangler, L., *Surface* CO_2 *Leakage During Two Shallow Subsurface* CO_2 *Releases.* Geophysical Research Letters, 2007. **34**.

28. Oldenburg, C.M. and Thomson, J., *Cooling due to* CO_2 *Injection into natural Gas Reservoirs.* Energy Conversion and Management, 2007. **48**: p. 1808-1815.

29. Pruess, K. and Spycher, N., *E*CO_2*N - A fluid property module for the TOUGH2 code for studies of* CO_2 *Storage in saline aquifers.* Energy Conversion and Management, 2007. **48**: p. 1761-1767.

30. Xu, T, JA Apps, K Pruess and H Yamamoto. Numerical modeling of injection and mineral trapping of CO_2 with H_2S and SO_2 in a sandstone formation. LBNL57426. Chemical Geology, 242 (3-4), 319-346, 2007.

31. Xu, T., Apps, J.A., Pruess, K., and Yamamoto, H., *Numerical modelin of injection and mineral trapping of* CO_2 *with H2S and So2 in a saline sandstone formation.* Chemical Geology, 2007. **242**(3-4): p. 319-346.

32. Cortis A, CM Oldenburg and SM Benson. The role of optimality in characterizing CO_2 seepage from geologic carbon sequestration sites, LBNL 1417E. Int. J. Greenhouse Gas Control, 2, 640-652, 10.1016/ j.ijggc.2008.04.008, 2008.

33. Doughty C. Estimating plume volume for geologic storage of CO_2 in saline aquifers. LBNL 656E. Ground Water, 46 (6), 810-813, 2008.

34. Doughty, C., *Estimating Plume Volume for Geologic Storage of* CO_2 *in Saline Aquifers.* Ground Water, 2008. **46**(6): p. 810-813.

35. Gherardi, F., Xu, T., Sakurai, M., and Sekine, K., *Numerical Modeling of Self-limiting and Self-enhancing Caprock Alteration Induced by* CO_2 *Storage in a Depleted Gas Reservoir.* Chemical Geology, 2008.

36. Humphries, S.D., Nehrir, A.R., Keith, C.J., Repasky, K.S., Dobeck, L., Carlsten, L., and Spangler, L., *Testing Carbon Sequestration Site Monitoring Instruments Using a Controlled Carbon Dioxide Release Facility.* Applied Optics, 2008. **47**(4): p. 548-555.

37. Ito, T., Xu, T., Sakurai, M., and Sekine, K., *A Concept of in-situ Reaction Method to Remedy Leakage from Geological* CO_2 *Storage Reservoirs.* Greenhouse Gas Control Technologies, 2008. **Submitted**.

38. Lewicki, J.L., Fischer, M.L., and Hilley, G.E., *Six-week Time Series of Eddy Covariance* CO_2 *Flux at Mammoth Mountain, California: Performance evaluation and role of meteorological forcing.* Journal of Volcanology and Geothermal Research, 2008: p. 178-190.

39. Lewicki, J.L., Oldenburg, C.M., Dobeck, L., and Spangler, L., *Surface* CO_2 *Leakage During the First Shallow Subsurface* CO_2 *Release Experiment.* Geophysical Research Letters, 2008. **34**.

40. Male, E.J., Pickles, W.L., Silver, E.A., Lewicki, J.L., Apple, M., and Burton, E.A., CO_2 *Leak Detection Using Hyperspectral Plant Signatures During the 2008 ZERT* CO_2 *Sequestration Field Experiment in Bozeman, MT.* EOS Transactions, 2008. **89**(53).

41. Mitchell, A., Phillips, A., Hamilton, M., Gerlach, R., Kuszuba, J., and Cunningham, A.B., *Resilience of Bacillus Mojavensis Planktonic and Biofilm Communities to Supercritical* CO_2*.* The Journal of Supercritical Fluids, 2008. **47**(2): p. 318-325.

42. Mitchell, A., Phillips, A., Hamilton, M., Gerlach, R., Kuszuba, J., and Cunningham, A.B., *Resilience of planktonic and biofilm communities to supercritical* CO_2*.* The Journal of Supercritical Fluids, 2008. **47**(2): p. 318-325.

43. Mitchell, A.C., Phillips, A., Kaszuba, J., Hollis, W.K., Gerlach, R., and Cunningham, A.B., *A Microbially Enhanced Carbonate Mineralization and Containment of* CO_2*.* Geochemica et Cosmochimica Acta, 2008. **72**(12): p. A636.

44. Mullholland, T., Cunningham, A.B., Kania, B.G., Osterlund, M.T., and Stewart, F.M., *Floating islands as an alternative to constructed wetlands for treatment of excess nutrients from agricultural and municipal wastes – results of laboratory-scale tests.* Land Contamination and Reclamation, 2008. **16**(1): p. 25-33.

45. Oldenburg, C.M., Lewicki, J.L., Dobeck, L., and Spangler, L., *Modeling Gas Transport in the Shallow Subsurface During the ZERT* CO_2 *Release Test.* Transport in Porous Media, 2008. **82**(1): p. 77-92.

46. Pruess, K. On CO_2 fluid flow and heat transfer behavior in the subsurface following leakage from a geologic storage reservoir, LBNL60076. Env. Geol., 54 (8), 1677–1686, DOI 10.1007/s00254-007-0945-x, June 2008.

47. Pruess, K., *Leakage of* CO_2 *from Geologic Storage: Role of Secondary Accumulation at Shallow Depth.* International Journal of Greenhouse Gas Control, 2008. **In press**: p. 37-46.

48. Pruess, K., *On* CO_2 *Fluid Flow and Heat Transfer Behavior in the Subsurface, Following Leakage from a Geologic Storage Reservoir.* Environmental Geology, 2008. **54**(8): p. 1677-1686.

49. Silin, D., Patzek, T., and Benson, S.M., *A modeling of buoyant gas plume migration.* International Journal of Greenhouse Gas Control, 2008.

50. Stauffer, P.H., Viswanathan, H.S., Pawar, R.J., and Guthrie, G.D., *A system model for geologic sequestration of* CO_2*.* Environmental Science & Technology Journal, 2008. **43**(3): p. 565-570.

51. Viamajala, S., Gerlach, R., Sivaswamy, V., Peytion, B.M., Apel, W.A., Cunningham, A.B., and Peterson, J.N., *Permeable reactive biobarriers for in-situ Cr(VI) reduction: Bench scale tests using Cellulomonas sp. strain ES6.* Biotechnology and Bioengineering, 2008. **101**(6): p. 1150-1162.

52. Xu, T. and Pruess, K., *Enhanced Solubility Trapping, Convection Mixing, and Mineral Trapping for Long-Term* CO_2 *Storage in a Saline Sandstone Formation.* Transport in Porous Media: Special Issue on Geologic Carbon Storage, 2008. **Submitted**.

53. Xu, T., *TOUGHREACT testing in high ionic strength brine sandstone systems*. 2008, LBNL: Berkeley, CA.

54. Amonette, J.E. and Barr, J.L., *Multi-Channel Auto-Dilution System for Remote Continuous Monitoring of High Soil-*CO_2 *Fluxes*. 2009, Pacific Northwest National Laboratory: Richland, WA.

55. Cortis A and CM Oldenburg. Short-range atmospheric dispersion of carbon dioxide, LBNL2964E, Boundary-Layer Meteorology, 133, 17-34, 2009.

56. Doughty, C. and Myer, L.R., *Scoping calculations on leakage of* CO_2 *in geologic storage.* Science and Technology of Carbon Sequestration, 2009.

57. Doughty, C., *User's guide for hysteretic capillary pressure and relative permeability functions in iTOUGH2*. 2009, Lawrence Berkeley National Laboratory: Berkeley, CA.

58. Gerlach, R. and Cunningham, A.B., *Influence of Biofilms on Porous Media Hydrodynamics*, in *Porous Media: Applications in Biological Systems and Biotechnology*, K. Vafai, Editor. 2009, Taylor Francis.

59. Hansen, L., *Design and experimental testing of a high pressure, high temperature flow-through rock core reactor using supercritical carbon dioxide*, in *Earth Sciences*. 2009, Montana State University: Bozeman, Montana.

60. Keith, C.J., Repasky, K.S., Lawrence, R.L., Jay, S.C., and Carlsten, J.L., *Monitoring Effects of a Controlled Subsurface Carbon Dioxide Release on Vegetation Using a Hyperspectral Imager.* International Journal of Greenhouse Gas Control, 2009. **3**(5): p. 626-632.

61. Kharaka, YK, JJ Thordsen, E Kakouros, G Ambats, et al. Changes in the Chemistry of Shallow Groundwater Related to the 2008 Injection of CO_2 at the ZERT Field Site, Bozeman, Montana, Environmental Earth Sciences, Environmental Geology , published online, DOI 10.1007/s12665-009-0401-1, 2009.

62. Lewicki, J.L. and Hilley, G.E., *Eddy covariance mapping and quantification of surface* CO_2 *leakage fluxes.* Geophysical Research Letters, 2009. **36**(L21802).

63. Lewicki, J.L., Hilley, G.E., Fischer, M.L., Pan, L., Oldenburg, C.M., Dobeck, L., and Spangler, L., *Eddy Covariance Observations of Surface Leakage During Shallow Subsurface* CO_2 *Releases.* Journal of Geophysical Research - Atmospheres, 2009. **114, D12302**.

64. Mitchell, A.C., Phillips, R., Hiebert, R., Gerlach, R., and Cunningham, A.B., *Biofilm Enhanced Subsurface Sequestration of Supercritical* CO_2*.* International Journal of Greenhouse Gas Control, 2009. **3**(1): p. 90-99.

65. Ogretim, E., Gray, D., and Bromhal, G., *Effects of Water Table and Topography on the Near-Surface Migration of a* CO_2 *Leak.* Vadose Zone Journal, 2009. **Submitted**.

66. Oldenburg, C.M., Lewicki, J.L., Pan, L., Dobeck, L., and Spangler, L., *Origin of the Patchy Emission Pattern at the ZERT* CO_2 *Release Test.* Environmental Earth Sciences, 2009. **82**(2): p. 241-250.

67. Pruess, K. and Muller, N., *Formation Dry-Out from* CO_2 *Injection into Saline Aquifers. Part 1, Effects of Solids Precipitation and their Mitigation.* Water Resources Research, 2009. **45**(W03402, (LBNL-1584E)).

68. Pruess, K., *Formation Dry-Out from* CO_2 *Injection into Saline Aquifers. Part 2, Analytical Model for Salt Precipitation.* Water Resources Research, 2009. **45**(W03403, doi:10.1029/2008WR007102 (LBNL-1584E-Pt2)).

69. Pruess, K., *Numerical Simulation Experiments on the Long-Term Evolution of a* CO_2 *Plume under a Sloping Caprock*. 2009, Lawrence Berkeley National Laboratory: Berkeley, CA.

70. Schultz, L., Pitts, B., Mitchell, A., Cunningham, A.B., and Gerlach, R., *Imaging Biologically-Induced Mineralization in Fully Hydrated Flow Systems.* Microscopy Today, 2009. **Accepted**.

71. Seymour, J.D., Fridjonsson, E.O., Schultz, L., Gerlach, R., Cunningham, A.B., and Codd, S.L., *NMR Measurements of Hydrodynamic Dispersion in Porous Media Subject to Biofilm Mediated Precipitation Reactions.* Journal of Containment Hydrology, 2009. **Accepted**.

72. Silin, D., Patzek, T., and Benson, S.M., *A Model of Buoyancy-Driven Two-Phase Countercurrent Fluid Flow.* Transport in Porous Media 2009. **76**(3): p. 449-469.

73. Silin, D., Patzek, T., and Benson, S.M., *A one-dimensional model of vertical gas plume migration through a heterogeneous porous medium.* International Journal on Greenhouse Gas Control, 2009. **3**: p. 300-310.

74. Spangler, L., Dobeck, L., Repasky, K.S., Nehrir, A.R., Humphries, S.D., Barr, J.L., Keith, A., Shaw, J.A., Rouse, J.H., Cunningham, A.B., Benson, S.M., Oldenburg, C.M., Lewicki, J.L., Wells, A., Diehl, J.R., Strazisar, B., Fessenden, J., Rahn, T., Amonette, J.E., Pickles, W.L.,

Jacobson, J.D., Silver, E.A., Male, E.J., Rauch, H., Gullickson, K.S., Trautz, R., Kharaka, Y., Birkholzer, J., and Wielopolski, L., *A shallow subsurface controlled release facility in Bozeman, Montana, USA, for testing near surface* CO_2 *detection techniques and transport models.* Environmental Earth Sciences, 2009. **60**(2): p. 227-239.

75. Spangler, LH, LM Dobeck, A Nehrir, S Humphries, et al. A controlled field pilot in Bozeman, Montana, USA, for testing near surface CO_2 detection techniques and transport models, Environmental Earth Sciences, published online, Journal of Environmental Geology, doi:10.1016/j.egypro.2009.01.279, 2009.

76. Spycher, N. and Pruess, K., *A Phase-Partitioning Model for* CO_2*-Brine Mixtures at Elevated Temperatures and Pressures: Application to* CO_2*-Enhanced Geothermal Systems.* Transport in Porous Media, 2009(July).

77. Strazisar, Brian R., Arthur W. Wells, and J. Rodney Diehl, "Near Surface Monitoring for the ZERT Shallow CO2 Injection Project " International Journal of Greenhouse Gas Control, 2009. 3(6): p. 736-744.

78. Todaka, N., Nakanishi, S., Xu, T., and Pruess, K., *Hydrogeochemical modeling for natural analogue study of* CO_2 *leakage due to Matsushiro Earthquake Swarm.* Energy Procedia, Elsevier, 2009. **1**: p. 2413-2420.

79. Xiao, Y., Xu, T., and Pruess, K., *The effects of gas-fluid-rock interactions on* CO_2 *injection and storage: Insights from reactive transport modeling.* Energy Procedia, Elsevier, 2009. **1**: p. 1783-1790.

80. Xu, T., Zhang, K., and Pruess, K., *Reaction-driven aqueous density increase and convective mixing during long-term* CO_2 *storage in a saline sandstone formation.* Transport in Porous Media, 2009. **Special issues on** CO_2 **geological sequestration, re-submitted after revision**.

81. Zhang, K., Li, Y., Xu, T., Cheng, H., Zheng, Y., and Xiong, P., *Long-term variations of* CO_2 *trapped in different mechanisms in deep saline formations: A case study of the Songliao Basin, China.* International Journal of Greenhouse Gas Control, 2009. **3**(2): p. 161-180.

82. Apps, J, L Zheng, Y Zhang, T Xu, and JT Birkholzer. Evaluation of groundwater chemistry changes in response to CO_2 leakage from deep geological storage. LBNL2931E. Transport in Porous Media: Special Issue on Geologic Carbon Storage, published online, DOI 10.1007/s11242-009-9509-8, Springer, 2010.

83. Doughty, C., *Investigation of* CO_2 *plume behavior for a large-scale pilot test of geologic carbon storage in a saline formation.* Transport in Porous Media, 2010. **82**(1): p. 49-76.

84. Ebibo, A., Helmig, R., Cunningham, A.B., Class, H., and Gerlach, R., *Modeling biofilm growth in the presence of carbon dioxide and water flow in the subsurface.* Advances in Water Resources, 2010. **33**(7): p. 762-781.

85. Lewicki, J.L., Hilley, G.E., Dobeck, L., and Spangler, L., *Dynamics of* CO_2 *fluxes and concentrations during a shallow subsurface* CO_2 *release.* Environmental Earth Sciences, 2010. **60**: p. 285-297.

86. Male, E.J., Pickles, W.L., I., S.E., Hoffman, G.D., Lewicki, J.L., Apple, M., Repasky, K.S., and Burton, E.A., *Using hyperspectral plant signatures for leak detection during the 2008 ZERT* CO_2 *sequestration field experiment in Bozeman, MT.* Environmental Earth Sciences, 2010. **60**: p. 251-261.

87. Mathias, SA, JG Gluyas, CM Oldenburg and C-F.Tsang. Analytical solution for Joule-Thomson cooling during CO_2 geo-sequestration in depleted oil and gas reservoirs. LBNL3660E. Int. J. Greenhouse Gas Control, 4(5), 806-810, doi:10.1016/j.ijggc.2010.05.008, 2010.

88. Melick, J.J., Gardner, M.H., and Uland, M.J., *Geologic Heterogeneity in Basin-Scale Geologic Carbon Storage: Examples from the Powder River Basin, NE Wyoming and SE Montana.* Society of Petroleum Engineers International, 2010. **Submitted**.

89. Mitchell, A., Dideriksen, K., Skidmore, M., Kaszuba, J., Spangler, L., Cunningham, A.B., and Gerlach, R., *Microbially enhanced carbon capture and storage by mineral-trapping and solubility-trapping.* Environmental Science and Technology, 2010. **44**(13): p. 5270–5276.

90. Oldenburg, C.M. and Doughty, C., *Injection, Flow, and Mixing of* CO_2 *in Porous Media with Residual Gas.* Transport in Porous Media, 2010. **In Preparation**.

91. Pan, L., Lewicki, J.L., Oldenburg, C.M., and Fischer, M.L., *Time-Windows-Based Filtering Method for Near-Surface Detection of Leakage from Geologic Carbon Sequestration Sites.* Environmental Earth Sciences, 2010. **60**(2): p. 359-369.

92. Pederson, K.H., *Stratigraphic Framework and Reservoir Characterization of Clareton and Fiddler Creek Fields, Early Cretaceous Muddy Sandstone Formation, Powder River Basin, Wyoming: Effects of Sediment Supply on Incised Valley-fill System Architecture*, in *Earth Sciences*. 2010, Montana State University: Bozeman, MT. p. 156.

93. Pruess, K. and Nordbotten, J., *Numerical Simulation Studies of the Long-term Evolution of a* CO_2 *Plume in a Saline Aquifer with a Sloping Caprock.* Transport in Porous Media, 2010. **submitted**.

94. Rouse, J.H., Shaw, J.A., Lawrence, R.L., Lewicki, J.L., Dobeck, L., Repasky, K.S., and Spangler, L., *Multi-spectral imaging of vegetation for detecting* CO_2 *leaking from underground.* Environmental Earth Sciences, 2010. **60**(2): p. 313-323.

95. Silin, D, L Tomutsa, SM Benson and T Patzek. Microtomography and pore-scale modeling of two-phase fluid distribution, Transport in Porous Media, 1–21, 10.1007/s11242-010-9636-2, 2010.

96. Wells, Arthur, Brian Strazisar, J. Rodney Diehl, and Garret Veloski, "Atmospheric Tracer Monitoring and Surface Plume Development at the ZERT Pilot Test in Bozeman, Montana,

USA" Environmental Earth Science, March 2010, 60(2), 299-305 DOI: 10.1007/s12665-009-0371-3.

97. Xu, T, E Sonnenthal, N Spycher, G Zhang, L Zheng and K Pruess. TOUGHREACT Version 2.0: A simulator for subsurface reactive transport under non-isothermal multiphase flow conditions, Computers & Geosciences. In press, 2010.

98. Barr, J.L., Humphries, S.D., Nehrir, A.R., Repasky, K.S., Dobeck, L., Carlsten, J.L., and Spangler, L., *Laser Based Carbon Dioxide Monitoring Instrument Testing During a Thirty Day Controlled Underground Carbon Release Field Experiment.* International Journal of Greenhouse Gas Control, 2011. **5**(1): p. 138-145.

99. Natalie Pekney, Arthur Wells, J. Rodney Diehl,Matthew McNeil, Natalie Lesko, James Armstrong Atmospheric monitoring of a perfluorocarbon tracer at the 2009 ZERT Center experiment in Bozeman, Montana, USA Submitted to Atmospheric Environment, June 2011.

Presentations

1. Benson, S.M., *Introduction to Geologic* CO_2 *Storage, Leak Detection and Mitigation*, in *Research Experience in Carbon Sequestration (RECS) Workshop*. 2005: Santa Fe, NM.

2. Benson, S.M., *IPCC Special Report on Carbon Dioxide Capture and Storage: Storage in Deep Underground Geological Formations*, in *6th Annual MIT Carbon Sequestration Forum*. 2005: Massachusetts Institute of Technology, Cambridge, MA.

3. Benson, S.M., *Monitoring and Verification of Subsurface* CO_2, in *Global Climate and Energy Project (GCEP) International Workshop*. 2005: Beijing, China.

4. Cunningham, A.B., Gerlach, R., Phillips, A., and Spangler, L., *Microbially Enhanced Geologic Sequestration of Supercritical* CO_2, in *USDOE Fourth Annual Conference on Carbon Capture and Sequestration*. 2005: Hilton Alexandria Mark Center, Alexandria, VA.

5. Lewicki, J.L., Hilley, G.E., and Oldenburg, C.M., *An Improved Strategy to Detect Carbon Dioxide Leakage for Verification of Geologic Carbon Sequestration*, in *AGU Fall Meeting*. 2005: San Francisco, CA.

6. Pruess, K., *Capabilities of TOUGH Codes for Modeling Geologic Sequestration and Leakage of* CO_2. , in *Workshop on Leakage Modeling*. 2005: Princeton University, Princeton, NJ.

7. Pruess, K., *Geologic storage of greenhouse gases: Multiphase and non-isothermal effects, and implications for leakage behavior*, in *Modelling Coupled Processes in Porous Media*. 2005: University of Utrecht, Utrecht, The Netherlands.

8. Pruess, K., *Geologic Storage of Greenhouse Gasses: Multiphase and Non-isothermal Effects and Implications for Leakage Behavior*, in *Workshop on Modeling Coupled Processes*. 2005: Utrecht, The Netherlands.

9. Pruess, K., *International Workshop on Modeling Coupled Processes in Porous Media*. 2005: University of Utreck, The Netherlands.

10. Pruess, K., *Numerical Studies of* CO_2 *Leakage from Geologic Storage Reservoirs*, in *AGU Fall Meeting*. 2005: San Francisco, CA.

11. Pruess, K., *Paper on Capabilities of the TOUGH Codes for* CO_2 *Sequestration and Leakage Modeling*. 2005: Princeton University, Princeton, NJ.

12. Benson, S.M., *Sensitivity of Pressure Measurements For Detecting Leakage of Carbon Dioxide from a Geological Storage Site*, in *Fifth Annual Conference on Carbon Capture & Sequestration*. 2006: Alexandria, VA.

13. Benson, S.M., *Sensitivity of Pressure Measurements for Leakage Detection*, in *Groundwater Protection Council*. 2006: Austin, TX.

14. Benson, S.M., *Sitting and Monitoring Geological Storage Projects*, in *World Resources Institute Stakeholder Workshop*. 2006: Washington D.C.

15. Benson, S.M., *The Role of* CO_2 *Capture and Storage in Decarbonizing the US Economy*, in *AAAS Annual Meeting*. 2006: St. Louis, MS.

16. Benson, S.M., Tomutsa, L., Silin, D., Kneafsey, T., and Miljkovic, L., *Core Scale and Pore Scale Studies of Carbon Dioxide Migration in Saline Formations*, in *8th International Conference on Greenhouse Gas Control Technologies (GHGT8)*. 2006: Trondheim, Norway.

17. Cunningham, A.B. and Phillips, A., *A High-Pressure Core Testing System for Investigating Biotic and Abiotic Issues Associated with Geologic Sequestration of* CO_2, in *Zero Emissions Research and Technology Seminar Series*. 2006: Montana State University, Bozeman, MT.

18. Cunningham, A.B. and Phillips, A., CO_2 *Sequestration: Opportunities for Biofilm Research*, in *Center for Biofilm Engineering Seminar Series*. 2006: Montana State University, Bozeman, MT.

19. Cunningham, A.B. and Spangler, L., *Opportunities for International Collaboration with the Zero Emissions Research and Technology (ZERT) Program*. 2006: Institute of Hydraulic Engineering, University of Stuttgart, Stuttgart, Germany.

20. Cunningham, A.B., *Microbial Considerations in the Geologic Sequestration of Supercritical* CO_2, in *Seminar for the University of Stuttgart Water Resources Department*. 2006: University of Stuttgart, Stuttgart, Germany.

21. Cunningham, A.B., *Microbially Enhanced Geologic Sequestration of Supercritical* CO_2, in *Fifth Annual Conference on Carbon Capture & Sequestration*. 2006: Alexandria, VA.

22. Gardner, M.H., *Understanding the Complexity and Capacity for Geologic Storage of Greenhouse Gases*, in *United States Geological Survey (USGS) Earth Sciences Seminar*. 2006: Montana State University, Bozeman, MT.

23. Hansen, L., Skidmore, M., Bowen, D., and Gardner, M.H., *Experimental Studies using Supercritical* CO_2 *to Challenge Brine Aquifer Reservoir Rocks*, in *American Geophysical Union 2006 Fall Meeting*. 2006: San Francisco, CA.

24. Hoversten, M., Gasperikova, E., and Benson, S.M., *Theoretical Limits for Seismic Detection of Small Accumulations of Carbon Dioxide in the Subsurface*, in *8th International Conference on Greenhouse Gas Control Technologies (GHGT8)*. 2006: Trondheim, Norway.

25. Humphries, S.D., *Laser Based Differential Absorption Carbon Dioxide Sensor*, in *Fifth Annual Conference on Carbon Capture & Sequestration*. 2006: Alexandria, VA.

26. Humphries, S.D., Nehrir, A.R., Repasky, K.S., Carlsten, J.L., Shaw, J.A., and Spangler, L., *Differential Absorption Measurements of Carbon Dioxide and Diatomic Oxygen*, in *Fifth Annual Conference on Carbon Capture & Sequestration*. 2006: Alexandria, VA.

27. Jalali, J., CO_2 *Sequestration in Appalachian Coal Seams using Pinnate Well Patterns*, in *Fifth Annual Conference on Carbon Capture & Sequestration*. 2006: Alexandria, VA.

28. Kaszuba, J., *Dawsonite Reactivity in Geologic Carbon Sequestration* in *Fifth Annual Conference on Carbon Capture & Sequestration*. 2006: Alexandria, VA.

29. Melick, J.J. and Gardner, M.H., *Geologic Implications of Basin- and Gigaton-Scale Storage of Greenhouse Gases: Modeling the Powder River Basin for Economic EOR,* CO_2 *and Leakage*, in *American Association of Petroleum Geologist/ Rocky Mountain Section*. 2006: Billings, MT.

30. Melick, J.J., *The Giganton Greenhouse Gas Problem: Modeling the Powder River Basin for CO_2 Sequestration*, in *First Annual Earth Science Student Colloquium Poster*. 2006: Montana State University, Bozeman, MT.

31. Pruess, K., Ennis-King, J., and Zhang, K., *The role of dissoluition-induced aqueous phase convections in the long-term fate of CO_2 stored in saline formations*, in *AGU Fall Meeting*. 2006: San Francisco, CA.

32. Pruess, K., *On the Feasibility of Using Supercritical CO_2 as Heat Transmission Fluid in an Engineered Hot Dry Rock Geothermal System*, in *Stanford Geothermal Workshop*. 2006: Stanford University, Stanford, CA.

33. Smirnov, A., *Modeling of Long Term Carbon Sequestration in Different Coal Seams*, in *Fifth Annual Conference on Carbon Capture & Sequestration*. 2006: Alexandria, VA.

34. Tomutsa, L., *Synchrotron Microtomography in CO_2 Geosequestration Research*, in *Fifth Annual Conference on Carbon Capture & Sequestration*. 2006: Alexandria, VA.

35. Tomutsa, L., *Synchrotron Radiation Microtomography for Characterizing Multiphase Flow of CO_2 in Rocks*, in *ALS Users Meeting*. 2006: Berkely, CA.

36. Viswanathan, H.S., *CO_2-PENS: A CO_2 Sequestration Systems Model for Geologic Sequestration*, in *Fifth Annual Conference on Carbon Capture & Sequestration*. 2006: Alexandria, VA.

37. Benson, S.M., Miljkovic, L., Tomutsa, L., and Doughty, C., *Relative permeability and capillary pressure controls on CO_2 migration and brine displacement - Elucidating fundamental mechanisms by laboratory experiments and simulation*, in *National Energy Technology Lab*. 2007: Pittsburgh, PA.

38. Cortis, A., Oldenburg, C.M., and Benson, S.M., *On the optimality of above-ground monitoring networks for Carbon Capture and Sequestration*, in *NETL Sixth Annual Meeting on Carbon Sequestration* 2007: Pittsburgh, PA.

39. Cortis, A., Oldenburg, C.M., and Benson, S.M., *The Role of Optimality in Characterizing CO_2 Seepage from Geological Carbon Sequestration Sites*, in *EOS Transactions of the American Geophysical Union 2007 Fall Meeting*. 2007: San Francisco, CA.

40. Cortis, A., Oldenburg, C.M., and Benson, S.M., *The Role of Optimality in Characterizing CO_2 Seepage from Geological Carbon Sequestration Sites*, in *American Geophysical Union 2007 Fall Meeting*. 2007: San Francisco, CA.

41. Cunningham, A.B., *Biofilm Applications to Geologic Carbon Sequestration*. 2007: Department of Applied Mathematics, University of Bergen, Bergen, Norway.

42. Hansen, L., Skidmore, M., Bowen, D., and Gardner, M.H., *Experimental Studies Using Supercritical CO_2 to Challenge Brine Aquifer Rocks*, in *Sixth Annual Conference on Carbon Capture and Sequestration*. 2007: Pittsburgh, PA.

43. Hansen, L., Skidmore, M., Bowen, D., Gardner, M.H., and Brox, T., *Experimental Studies Using Supercritical CO_2 to Challenge Brine Aquifer Rocks*, in *Geological Society of America, Annual General Meeting*. 2007: Denver, CO.

44. Humphries, S.D., Nehrir, A.R., Repasky, K.S., Carlsten, J.L., Shaw, J.A., and Spangler, L., *Atmospheric Carbon Dioxide Measurements Using a Tunable Laser Based System*, in *Sixth Annual Conference on Carbon Capture & Sequestration*. 2007: Pittsburg, PA.

45. Humphries, S.D., Nehrir, A.R., Repasky, K.S., Carlsten, J.L., Spangler, L., and Shaw, J.A., *Differential Absorption Measurements of Carbon Dioxide For Carbon Sequestration Site Monitoring Using a Temperature Tunable Diode Laser*, in *American Geophysical Union Annual Meeting*. 2007: San Francisco, CA.

46. Lewicki, J.L., Hilley, G.E., Fischer, M.L., Tosha, T., Aoyaga, R., Yamamoto, H., and Benson, S.M., *Monitoring spatio-temporal variablilty of surface* CO_2 *emissions at the Horseshoe Lake tree kill, Mammoth Mountain CA*, in *NETL Sixth Annual Meeting on Carbon Sequestration*. 2007: Pittsburgh, PA.

47. Melick, J.J. and Gardner, M.H., *Demonstrating the Value of Combining Geologic Carbon Dioxide Sequestration with Enhanced Oil Recovery: Powder River Basin, Wyoming and Montana*, in *Zero Emission Research & Technology Seminar Series*. 2007: Montana State University, Bozeman, MT.

48. Melick, J.J. and Gardner, M.H., *Demonstrating the Value of Combining Geologic Carbon Dioxide Sequestration with Enhanced Oil Recovery: Powder River Basin, Wyoming and Montana*, in *United States Geologic Survey (USGS) Earth Sciences Seminar*. 2007: Montana State University, Bozeman, MT.

49. Melick, J.J. and Gardner, M.H., *Demonstrating the Value of Combining Geologic Carbon Dioxide Sequestration with Enhanced Oil Recovery: Powder River Basin, Wyoming and Montana*, in *American Association of Petroleum Geologist National Convention*. 2007: Long Beach, CA.

50. Melick, J.J., *Basin Modeling and Gigaton-scale* CO_2 *Sequestration, Powder River Basin: Reservoir Characterization and Co-optimization of Geologic Storage with Enhanced Oil & Gas Recovery Practices*, in *Department of Earth Sciences Proposal Defense*. 2007: Montana State University, Bozeman, MT.

51. Mitchell, A.C., Phillips, A., Hiebert, R., Gerlach, R., Kaszuba, J., Spangler, L., and Cunningham, A.B., *Biofilm Enhanced Subsurface Sequestration of Supercritical* CO_2, in *2007 American Geophysical Union (AGU) Fall Meeting*. 2007: San Francisco, CA.

52. Muller, N. and Pruess, K., *Halite Precipitation During* CO_2 *Injection*, in *The 4th Trondheim Conference on* CO_2 *Capture, Transport and Storage*. 2007: Trondheim, Norway.

53. Nehrir, A.R., Humphries, S.D., Repasky, K.S., Carlsten, J.L., Spangler, L., and Dobeck, L., *Underground Fiber-Optic Differential Absorption Instrument for Monitoring Carbon Dioxide Soil Gas Concentration for Carbon Sequestration Site Monitoring*, in *American Geophysical Union Annual Meeting*. 2007: San Francisco, CA.

54. Oldenburg, C.M., Dobeck, L., and Spangler, L., *Modeling Near-Surface Carbon Dioxide Migration from a Shallow Horizontal Well*, in *EOS Transactions of the American Geophysical Union 2007 Fall Meeting*. 2007: San Francisco, CA.

55. Phillips, A., Cunningham, A.B., and Gerlach, R., *Supercritical CO_2 Disinfection*, in *Center for Biofilm Engineering Technical Advisory Conference*. 2007: Montana State University, Bozeman, MT.

56. Pickles, W.L., Jacobson, J.R., Silver, E.A., Fresssenden, J.E., Lewicki, J.L., Dobeck, L., Repasky, K.S., and Keith, C.J., *Summary of Hyperspectral, Carbon Isotope, and Soil CO_2 Flux Measurements Made During the Plant Stress Part of the July 2007 ZERT CO_2 Sequestration Field Experiment*, in *American Geophysical Union Annual Meeting*. 2007: San Francisco, CA.

57. Pruess, K. and Muller, N., *Formation Dry-out and Salt Precipitation During Injection of CO_2 into Saline Aquifers*, in *Annual Fall Meeting of the American Geophysical Union (AGU)*. 2007: San Francisco, CA.

58. Pruess, K., *Non-linear Feedback Processes During CO_2 Leakage involving a secondary accumulation at shallow depth*, in *Sixth Annual Conference on Carbon Capture & Sequestration*. 2007: Pittsburgh, PA.

59. Silin, D., Patzek, T., and Benson, S.M., *Modeling evolution of leaking gas plume migration*, in *2007 Ground Water Protection Council Annual Forum, Ground Water Protection Council (GWPC)*. 2007: San Diego, CA.

60. Spangler, L. and Dobeck, L., *A Controlled Field Pilot for Testing Near Surface CO_2 Detection Techniques and Transport Models*, in *American Geophysical Union Fall Meeting*. 2007: San Francisco, CA.

61. Wilson, T. and Siriwardane, H., *Carbon Sequestration and Leakage risk in Unminable Coals: Northern Appalachian Coal Basin*, in *Society of Exploration Geophysics Japan Annual Convention*. 2007: Tokyo, Japan.

62. Wilson, T. and Siriwardane, H., *Leakage risks associated with coal sequestration in some areas of the central Appalachians: Subsurface, seismic and geomechanical simulations*, in *American Association of Petroleum Geologists Annual Convention*. 2007: Denver, CO.

63. Xu, T. and Pruess, K., *Mineral Dissolution, Enhanced CO_2 Solubility Trapping and Convective Mixing* in *American Geophysical Union 2007 Fall Meeting*. 2007: San Francisco, CA.

64. Xu, T. and Pruess, K., *Mineral Dissolution, Enhanced CO_2 Solubility Trapping and Convective Mixing*, in *American Geophysical Union (AGU) 2007 Fall Meeting*. 2007: San Francisco, CA.

65. Barr, J.L. and Amonette, J.E., *Multi-channel auto-dilution system for remote continuous monitoring of high soil-CO_2 fluxes*, in *American Geophysical Union 2008 Fall Meeting*. 2008: San Francisco, CA.

66. Cunningham, A.B., Dobeck, L., and Spangler, L., *Overview of the Zero Emissions Research & Technology (ZERT)*, in *Presentation to Montana Congressman Denny Rehberg, Dustin Frost, and Mike Dennison*. 2008: Montana State University ZERT Field Site, Bozeman, MT.

67. Cunningham, A.B., Gerlach, R., Spangler, L., Schultz, L., and Mitchell, A.C. *Microbially Enhanced Geologic Containment of Sequestered Supercritical CO_2*. in *Proceedings of the Nineth*

International Conference on Greenhouse Gas Technologies. 2008. Omni Shorehouse Hotel, Washington D.C.

68. Cunningham, A.B., Mitchell, A., Gerlach, R., Wheeler, L., Shultz, L., and Spangler, L., *Microbially Enhanced Geologic Carbon Storage*, in *Workshop on Numerical Models for Carbon Dioxide Storage in Geological Formations*. 2008: University of Stuttgart, Stuttgart, Germany.

69. Cunningham, A.B., *Overview of the Zero Emissions Research & Technology (ZERT)*, in *Presentation to Representatives from the Montana State Office of Higher Education Commission and Montana State Legislature*. 2008.

70. Daley, T.M., Ajo-Franklin, J., and Doughty, C., *Integration of Crosswell CASSM (Continuous Active Source Seismic Monitoring) and Flow Modeling for Imaging of a* CO_2 *lume in a Brine Aquifer*, in *SEG Annual Meeting* 2008: Las Vegas, NV.

71. Doughty, C., Myer, L.R., and Oldenburg, C.M., *Predictions of Long-term Behavior of a Large-Volume Pilot Test for* CO_2 *Geological Storage in a Saline Formation in the Central Valley, California*, in *GHGT-9 Conference*. 2008: Washington, D.C.

72. Ebibo, A., Cunningham, A.B., and Helmig, R., *Modeling Microbial Clogging in the Subsurface*, in *Workshop on Numerical Models for Carbon Dioxide Storage in Geological Formations*. 2008: University of Stuttgart, Stuttgart, Germany.

73. Gerlach, R., Mitchell, A., Schultz, L., Spangler, L., and Cunningham, A.B., *Microbially Mediated Biomineralization: Fundamentals and Possible Applications*, in *Center for Biofilm Engineering Technical Advisory Conference* 2008: Montana State University, Bozeman, MT.

74. Glezakau, V.A., Dang, L.X., and McGrail, B.P., *Spontaneous activation of* CO_2 *and Corrosion Pathways on Fe(100) (submitted)*, in *2008 American Conference on Theoretical Chemistry*. 2008: Northwestern University, Evenston, IL.

75. Hansen, L., Skidmore, M., and Brox, T., *Experimental Analysis of Supercritical* CO_2*-Brine-Rock Interactions using a flow-through Reactor*, in *The Geochemical Society 18th V. M. Goldschmidt Conference From See to Sky*. 2008: Vancouver, Canada.

76. Hansen, L., Skidmore, M., and Brox, T., *Experimental Studies on Supercritical* CO_2 *Challenge to Brine Aquifer Rocks*, in *Third Annual Earth Science Student Colloquium Presentation*. 2008: Montana State University, Bozeman, MT.

77. Jordan, P. and Doughty, C., *Sensitivity of* CO_2 *Migration Estimation on Reservoir Temperature and Pressure Uncertainty*, in *GHGT-9 Conference*. 2008: Washington D.C.

78. Keating, E., Fessenden, J., and Pawar, R.J., *Field observations and geochemical modeling of* CO_2 *impacts on shallow groundwater chemistry in Chimayo, New Mexico*, in *American Geophysical Union 2008 Fall Meeting*. 2008: San Francisco, CA.

79. Lewicki, J.L., Fischer, M.L., Rahn, T., Dobeck, L., and Spangler, L., *Monitoring Surface* CO_2 *Fluxes During Shallow Subsurface* CO_2 *Release Experiments*, in *American Geophysical Union 2007 Fall Meeting*. 2008: San Francisco, CA.

80. Lewicki, J.L., Hilley, G.E., Dobeck, L., and Spangler, L., *Dynamics of* CO_2 *Concentrations and Fluxes During the 2008 ZERT Project Shallow Subsurface* CO_2 *Release*, in *American Geophysical Union Fall Meeting*. 2008: San Fransisco, CA

81. Lewicki, J.L., Hilley, G.E., Fischer, M.L., Pan, L., Oldenburg, C.M., Dobeck, L., and Spangler, L., *Detection of* CO_2 *Leakage by Eddy Covariance during the ZERT Project's* CO_2 *Release Experiments*, in *GHGT-9 Conference*. 2008: Washington D.C.

82. Lewicki, J.L., *Monitoring Surface* CO_2 *Fluxes During Two Shallow Subsurface* CO_2 *Releases*, in *Groundwater Protection Council - U.S. Environmental Protection Agency MMV Workshop*. 2008: New Orleans, LA.

83. Lewicki, J.L., Oldenburg, C.M., Dobeck, L., and Spangler, L., *Integrated Monitoring and Modeling of* CO_2 *Leakage During the ZERT Project* CO_2 *Release Experiments*, in *National Energy Technology Laboratory (NETL) Seventh Annual Conference on Carbon Capture and Sequestration*. 2008: Pittsburg, PA.

84. McGrail, B.P., Schaef, H.T., Dang, L.X., Glezakau, V.A., Martin, P.F., and Owen, A.T., *Water Reactivity in the Liquid and Supercritical* CO_2 *Phase: Has half of the story been neglected?*, in *Ninth International Conference on Greenhouse Gas Technologies (GHGT-9).* 2008: Washington, DC.

85. McGrail, B.P., Schaef, H.T., Glezakau, V.A., Dang, L.X., Martin, P.F., and Owen, A.T., *Water Reactivity in the Liquid and Supercritical* CO_2 *Phase: Has Half the Story been Neglected?*, in *GHGT-9 Conference*. 2008: Washington D.C.

86. Melick, J.J. and Gardner, M.H., *Geologic Storage at the Basin Scale: Region-Based Basin Modeling, Powder River Basin (PRB), NE Wyoming and SE Montana*, in *American Geophysical Union Fall Meeting*. 2008: San Francisco, CA.

87. Melick, J.J. and Gardner, M.H., *Predicting Connected Pore Volume at the Basin Scale Using Environments of Deposition, Powder River Basin, NE Wyoming and SE Montana*, in *Third Annual Earth Science Student Colloquium Poster*. 2008: Montana State University, Bozeman, MT.

88. Melick, J.J. and Gardner, M.H., *Predicting Connected Pore Volume at the Basin Scale Using Environments of Deposition, Powder River Basin, NE Wyoming and SE Montana*, in *3rd Annual Earth Science Student Colloquium Poster Session*. 2008: Montana State University, Bozeman, MT.

89. Melick, J.J. and Gardner, M.H., *Region-based Basin Modeling: Correlation Environment of Deposition to Connected Pore Volume, Powder River Basin, NE Wyoming and SE Montana*, in *25th Annual MSU Student Research Celebration*. 2008: Montana State University, Bozeman, MT.

90. Melick, J.J. and Gardner, M.H., *Region-based Basin Modeling: Correlating Depositional Environment to Connected Pore Volume, Powder River Basin, NE Wyoming and SE Montana* in *American Association of Petroleum Geologists/ Rocky Mountain Section Annual Meeting*. 2008: Denver, CO.

91. Melick, J.J. and Gardner, M.H., *Region-based Basin Modeling: Correlating Environment of Deposition to Connected Pore Volume, Powder River Basin, NE Wyoming and SE Montana*, in *Annual Montana State University Student Research Celebration*. 2008: Montana State University, Bozeman, MT.

92. Melick, J.J. and Gardner, M.H., *Region-based Basin modeling: Correlating Depositional Environment to Connect Pore Volume, Powder River Basin, NE Wyoming and SE Montana*, in *American Association of Petroleum Geologist/ Rocky Mountain Section Annual Meeting*. 2008: Denver, CO.

93. Melick, J.J. and Gardner, M.H., *Region-based Basin Modeling: Correlating Depositional Environment to Connect Pore Volume, Wall Creek Example, Powder River Basin (PRB), NE Wyoming and SE Montana*, in *Wyoming Geological Association Annual Meeting*. 2008: Laramie, WY.

94. Mitchell, A., Cunningham, A.B., Gerlach, R., Schultz, L., Wheeler, L., and Spangler, L., *Microbially Enhanced Geologic Containment of Sequestered Supercritical* CO_2 *(Poster number 826)*, in *Seventh Annual Carbon Capture and Sequestration Conference*. 2008: Pittsburgh, PA.

95. Mitchell, A., Phillips, A., Kaszuba, J., Hollis, W.K., Spangler, L., Cunningham, A.B., and Gerlach, R., *Microbially Enhanced Carbonate Mineralization and the Geologic Containment of* CO_2, in *The Geochemical Society 18th V. M. Goldschmidt Conference From See to Sky*. 2008: Vancouver, Canada.

96. Muller, N., Qi, R., and Pruess, K., CO_2 *Sequestration:* CO_2 *Injection Impairment due to Halite Precipitation*, in *Ninth International Conference on Greenhouse Gas Technologies (GHGT-9)*. 2008: Washington, D.C.

97. Myer, L.R., Surles, T., Oldenburg, C.M., Doughty, C., and Wagoner, J., *WESTCARB Large Volume CCS Test*, in *GHGT-9 Conference* 2008: Washington, D.C. .

98. Ogretim, E., Gray, D., and Bromhal, G., *Effects of Water Table and Topography on the Migration of a* CO_2 *Leak*, in *U.S. Department of Energy Annual Carbon Capture and Storage Meeting*. 2008: Pittsburgh, PA.

99. Oldenburg, C.M., Lewicki, J.L., Dobeck, L., and Spangler, L., *On Modeling near-Surface Migration of* CO_2 *from a Shallow-Release Test: Results from the Vandose and Saturated Zones*, in *Computational Methods in Water Resources*. 2008: San Francisco, CA.

100. Pawar, R.J., Watson, T.L., and Gable, C.W., *Numerical Simulation of* CO_2 *Leakage through Abandoned Wells: Model for an Abandoned Site with Observed Gas Migration in Alberta, Canada*, in *Ninth Greenhouse Gas Technology Conference*. 2008: Washington, DC.

101. Pruess, K., *Numerical Modeling of Coupled Processes in Geologic Storage of Greenhouse Gases - Recent Results and Open Challenges*. 2008: Columbia University, New York City, NY

102. Pruess, K., *Numerical Modeling of Coupled Processes in Geologic Storage of Greenhouse Gases - Recent Results and Open Challenges*, in *Workshop on Numerical Models for Carbon Dioxide Storage in Geological Formations*. 2008: Stuttgart, Germany.

103. Pruess, K., *Numerical Modeling of Coupled Processes in Geologic Storage of Greenhouse Gases - Recent Results*, in *Seminar at Oregon State University & Stanford University*. 2008: Oregon State University & Washington State University.

104. Pruess, K., *On Leakage of* CO_2 *from an open Wellbore: Predictions from the Drift Flux Model (submitted)*, in *Computational Methods in Water Resources XVII International Conference*. 2008: San Francisco, CA.

105. Silin, D., Tomutsa, L., Benson, S.M., and Patzek, T., *Pore-scale analysis of microtomography images of the rock in geosequestration research* in *American Geophysical Union Fall Meeting*. 2008: San Francisco, CA.

106. Small, M., Yang, Y.-M., Gray, D., Ogretim, E., Bromhal, G., Wells, A., and Strazisar, B., *Use of Bayesian Belief Network in Designing Sequestration Monitoring Systems that Incorporate Multiple Technologies*, in *GHGT-9*. 2008: Washington, D.C.

107. Stauffer, P.H., Pawar, R.J., Han, J., and McPherson, B.J., *Assessing the leakage potential of* CO_2 *into groundwater resources at SACROC, West Texas*, in *American Geophysical Union 2008 Fall Meeting*. 2008: San Francisco, CA.

108. Todaka, N., Shigetaka, N., Xu, T., and Pruess, K., *Hydrogeochemical Modeling for Natural Analogue Study of* CO_2 *Leakage due to Matsushiro Earthquake Swarm*, in *9th International Conference on Greenhouse Gas Control Technologies (GHGT-9)* 2008: Washington, D.C. .

109. Wilson, E.J. and Siriwardane, H., *Distribution of Unminable Coals along the Eastern Margin of the Rome Trough in Central West Virginia with COnsiderations of Carbon Sequestration Potential and Risk*, in *25th Annual Pittsburgh International Coal Conference*. 2008.

110. Wilson, T. and Siriwardane, H. *Distribution of Unminable Coals along the Eastern Margin of the Rome Trough in Central West Virginia with Considerations of Carbon Sequestration Potential and Risk* in *Proceedings of the 25h Annual Pittsburgh International Coal Conference* 2008. Pittsburgh, PA.

111. Xiao, Y., Xu, T., and Pruess, K., *The Effects of gas-fluid-rock Interactions on* CO_2 *Iinjection and Storage: Insights from Reactive Transport Modeling*, in *9th International Conference on Greenhouse Gas Control Technologies (GHGT-9)*. 2008: Washington D.C. .

112. Xu, T. and Ito, T., *Numerical modeling of in-situ reaction barrier by injection of Ca(OH)2 solution for* CO_2 *geological storage*, in *American Geophysical Union 2008 Fall Meeting*. 2008: San Francisco, CA.

113. Xu, T. and Pruess, K., *Issues of* CO_2 *Storage in Deep Saline Formations Addressed by Geochemical Transport Modeling: Recent Advances and Open Challenges (submitted)*, in *33rd International Geological Congress*. 2008: Oslo, Norway.

114. Xu, T. and Pruess, K., *Numerical Studies on Enhanced* CO_2 *Dissolution and Mineral Trapping due to Formation of Aqueous Complexes (submitted)*, in *Computational Methods in Water Resources XVII International Conference*. 2008: San Francisco, CA.

115. Xu, T., *Issues of* CO_2 *Geological Storage in Saline Formations Addressed by Geochemical Transport Modeling: Recent Advances and Open Challenges*. 2008: Tohoku University, Japan.

116. Zyvoloski, G.A., Pawar, R.J., and Kelkar, S., *Simulating coupled fluid mechanical processes during* CO_2 *injection*, in *American Geophysical Union 2008 Fall Meeting*. 2008: San Francisco, CA.

117. Apple, M., Prince, J.B., Bradley, A.R., Zhou, V.R., Lakkaraju, V.R., Male, E.J., Pickles, W.L., Thordsen, J.J., Dobeck, L., Cunningham, A.B., and Spangler, L., *An In-Situ Root-Imaging System in the Context of Surface Detection of* CO_2, in *American Geophysical Union Fall Meeting*. 2009: San Francisco, CA.

118. Barr, J.L., Humphries, S.D., Nehrir, A.R., Repasky, K.S., Carlsten, J.L., Spangler, L., and Dobeck, L., *Laser Based Direct Detection of Carbon Dioxide for Surface and Subsurface Monitoring of Carbon Sequestration Sites*, in *Carbon Sequestration Conference*. 2009: Pittsburgh, PA.

119. Birkholzer, J., Bromhal, G., Brown, C.F., Carroll, S., Edenborn, H., Fessenden, J., Guthrie, G.D., Hakala, A., Keating, E., Spycher, N., Strazisar, B., and Thompson, A., *National Risk Assessment Program: Potential Effects on Groundwater Resources*, in *Eighth Annual Conference on Carbon Capture and Sequestration*. 2009: Pittsburgh, PA.

120. Cunningham, A.B., Schultz, L., Gerlach, R., Kaszuba, J., Spangler, L., Mitchell, A., and Parks, S., *Microbially Enhanced Carbonate Mineralization and Geologic Containment of Sequestered Supercritical* CO_2, in *Eighth Annual Conference on Carbon Capture & Sequestration* 2009: Pittsburgh, PA.

121. Doughty, C., Myer, L.R., and Oldenburg, C.M., *Predictions of long-term behavior of a large volume pilot test for* CO_2 *geological storage in a saline formation in the Central Valley, California*, in *Eighth National Conference on Carbon Capture and Sequestration, National Energy Technology Laboratory*. 2009: Pittsburgh, PA.

122. Gerlach, R., Cunningham, A.B., and Mitchell, A., *Utility of Biofilms in Geological Carbon Sequestration*, in *Fifth AMS Conference on Biofilms*. 2009: Cancun, Mexico.

123. Gerlach, R., Mitchell, A., Schultz, L., and Cunningham, A.B., *Metal and carbon dioxide sequestration through biologically induced mineral precipitation: Influence of hydrodynamics*, in *American Chemical Society 237th National Meeting Division of Geochemistry*. 2009: Salt Lake City, UT.

124. Gerlach, R., Mitchell, A., Schultz, L., Cunningham, A.B., and Schultz, L., *Biofilm mediated calcite precipitation: controlling hydraulic conductivity, carbon sequestration, and the transport of radionuclides*, in *Center for Biofilm Engineering Technical Advisory Conference*. 2009: Montana State University, Bozeman, MT.

125. Gerlach, R., Schultz, L., Mitchell, A., and Cunningham, A.B., *Bacterially Induced Calcite Precipitation and Strontium Co-Precipitation under Flow Conditions in a Porous Media System (Poster)*, in *American Geophysical Union Fall Meeting*. 2009: San Francisco, CA.

126. Gerlach, R., Schultz, L., Mitchell, A., and Cunningham, A.B., *Bacterially Induced Calcite Precipitation and Strontium Co-Precipitation under Flow Conditions in a Porous Media System (Poster)*, in *Biofilm Science and Technology Meeting, Center for Biofilm Engineering*. 2009: Bozeman, MT.

127. Hakala and al, e., *Effect of* CO_2 *on groundwater geochemistry in unconsolidated sand and gravel aquifers: experimental results from a natural analog site*, in *Eighth Annual* CO_2 *Capture & Sequestration Conference*. 2009: Pittsburgh, PH.

128. Hansen, L., Skidmore, M., and Brox, T., *Experimental* CO_2*-brine and* CO_2*-brine-rock interactions using Mississippian carbonates from the Powder River Basin, USA*, in *Tenth International Conference on Greenhouse Gas Control Technologies*. 2009: RAI, Amsterdam, Netherlands.

129. Jordan, P. and Doughty, C., *Considerations for scale-up between the Kimberlina Phase III Pilot and full deployment*, in *Eighth National Conference on Carbon Capture and Sequestration, National Energy Technology Laboratory*. 2009: Pittsburgh, PA.

130. Keating, E. and al, e., *Assessing our ability to predict impacts of a* CO_2 *leak on shallow aquifer resources: reconciling model predictions with field observations at natural analog site* in *Eighth Annual* CO_2 *Capture & Sequestration Conference* 2009: Pittsburgh, PA.

131. Lewicki, J.L., Hilley, G.E., Dobeck, L., and Spangler, L., *Monitoring near-surface leakage during controleld releases of* CO_2, in *Berkeley-Stanford-Beijing Workshop on Carbon Capture and Sequestration*. 2009.

132. Lewicki, J.L., Hilley, G.E., Fischer, M.L., Dobeck, L., and Spangler, L., *Eddy Covariance Detection, Mapping, and Quantification of Surface* CO_2 *Leakage Fluxes: Examples from Mammoth Mountain, CA and the ZERT* CO_2 *Release Facility, MT*, in *Fall Meeting American Geophysical Union*. 2009.

133. Male, E.J., Pickles, W.L., Silver, E.A., Hoffman, G.D., Lewicki, J.L., Apple, M., Repasky, K.S., Dobeck, L., and Burton, E.A., *Monitoring Surface* CO_2 *Leaks Using Hyperspectral Plant Signatures During the 2008 and 2009 ZERT Shallow Subsurface* CO_2 *Release Experiment in Bozeman, MT*, in *American Geophysical Union Fall Meeting*. 2009: San Francisco, CA.

134. McGrail, B.P., *Integrated* CO_2 *Capture and Sequestration Systems: Lessons Learned from Commercial-Scale Design Studies*, in *Regional Meeting of the National Academy of Engineering*. 2009: University of Washington, Seattle, Washington.

135. Melick, J.J. and Gardner, M.H., *Consequences of Simplified Geologic Models for* CO_2 *Sequestration: Example from the Powder River Basin, NE Wyoming and SE Montana*, in *AAPG/SEG/SPE Hedberg Research Conference, Geological Carbon Sequestration: Prediction and Verification*. 2009: Vancouver, BC, Canada.

136. Melick, J.J. and Gardner, M.H., *Critical Geo-details in a Basin-scale Geologic Model for* CO_2 *Sequestration: Powder River Basin (PRB), NE Wyoming and SE Montana*, in *Eighth Annual Conference on Carbon Capture & Sequestration*. 2009: Pittsburgh, PA.

137. Melick, J.J. and Gardner, M.H., *Model for* CO_2 *Sequestration: Powder River Basin (PRB), NE Wyoming and SE Montana*, in *Eighth Annual Conference on Carbon Capture & Sequestration*. 2009: Pittsburgh, PA.

138. Melick, J.J., Gardner, M.H., and Uland, M.J., *Incorporating Geologic Heterogeneity in 3D Basin-Scale Models for* CO_2 *Sequestration: Examples from the Powder River Basin, NE*

Wyoming and SE Montana, in *First Annual SPE International Conference on* CO_2 *Capture, Storage and Utilization*. 2009: San Diego, CA.

139. Pruess, K., Nordbotten, J., and Zhang, K., *Long-term Evolution of a* CO_2 *Plume under a Sloping Caprock*, in *TOUGH Symposium 2009*. 2009: Berkeley, CA.

140. Pruess, K., *Numerical Modeling of Coupled Processes in Aquifer Storage of Greenhouse Gases - Recent Results and Open Challenges*, in *International Conference on Deep Saline Aquifers for Geological Storage of* CO_2 *and Energy*. 2009: Rueil-Malmaison, France.

141. Pruess, K., *On the Role of Multi-Scale Processes in* CO_2 *Storage Security and Integrity*, in *American Geophysical Union Annual Fall Meeting*. 2009: San Francisco, CA.

142. Pruess, K., *The Potential for Operating Enhanced Geothermal Systems (EGS) with* CO_2 *as Heat Transmission Fluid*, in *Eighth Annual Conference on Carbon Capture and Sequestration*. 2009: Pittsburgh, PA.

143. Rau, G.H., McAlexander, W.I., Burton, E.A., Dobeck, L., and Spangler, L., *Grassland Soil and Fossil* CO_2 *Fluxes Monitored Using Continuous CELS Measurements of [*CO_2*] and δ13C*, in *American Geophysical Union Fall Meeting*. 2009: San Francisco, CA.

144. Schultz, L., Cunningham, A.B., and Gerlach, R., *Image and Tracer Analysis of Biofilm and Mineral Affected Porous Media*, in *Biofilm Science and Technology Meeting, Center for Biofilm Engineering, Montana State University*. 2009: Bozeman, MT.

145. Schultz, L., Gerlach, R., Mitchell, A., Parks, S., and Cunningham, A.B., *Biofilm Mediated Calcite Precipitation: Controlling Hydraulic Conductivity, Carbon Sequestration, and the Transport of Radionuclides (Poster)*, in *Center for Biofilm Engineering Technical Advisory Conference*. 2009: Montana State University, Bozeman, MT.

146. Schultz, L., Pitts, B., and Gerlach, R., *Imaging biomineralization in flow systems (Platform Presentation)*, in *Microscopy and Microanalysis Conference*. 2009: Richmond, VA.

147. Spangler, L., *Filling Gaps in the Carbon Sequestration Research Portfolio; Activities in the Zero Emissions Research and Technology Center*, in *Earth and Environmental Sciences (EES) Division Frontiers in Geoscience Colloquia*. 2009: Los Alamos National Laboratory.

148. Viswanathan, H.S. and al, e., *The evolution of damage zones due to geo-mechanical and chemical effects caused by* CO_2 *injection*, in *Eighth Annual* CO_2 *Capture & Sequestration Conference*. 2009: Pittsburgh, PA.

149. Wilson, T., Bajura, R., Winschel, R.A., Srivastava, R.S., Scandrol, R., Wells, A., and Patchen, D., *Geophysical Characterization of the Marshall County West Virginia Pilot Sequestration Site*, in *International Pittsburgh Coal Conference*. 2009: Pittsburgh, PA.

150. Cunningham, A.B., Gerlach, R., Spangler, L., Mitchell, A., Parks, S., and Phillips, A., *Reducing the risk of well bore leakage of* CO_2 *using engineered biomineralization barriers*, in *GHGT10 Conference*. 2010: Amsterdam, The Netherlands.

151. Gerlach, R. and Cunningham, A.B. *Influence of Microbial Biofilms on Reactive Transport in Porous Media*. in *Third International Conference on Porous Media and its Applications in Science, Engineering and Industry*. 2010: Montecatini, Italy.

152. Gerlach, R., *Influence of Microbial Biofilms on Reactive Transport in Porous Media*, in *Third International Conference on Porous Media and its Applications in Science, Engineering and Industry*. 2010: Montecatini, Italy.

153. Gerlach, R., Mitchell, A., Spangler, L., and Cunningham, A.B. *Bacterially Induced Calcite Precipitation and Strontium Co-Precipitation under Flow Conditions in a Porous Media System*. in *European Geosciences Union General Assembly 2010*. 2010: Vienna, Austria.

154. Gerlach, R., Mitchell, A., Spangler, L., and Cunningham, A.B., *Biologically Enhanced Geologic Carbon Sequestration*, in *European Geosciences Union General Assembly 2010*. 2010: Vienna, Austria.

155. Gerlach, R., Mitchell, A., Spangler, L., and Cunningham, A.B., *Role of Biofilms in Geological Carbon Sequestration*, in *European Geosciences Union General Assembly 2010*. 2010: Vienna, Austria.

156. Lewicki, J.L., *Eddy Covariance Applications to Surface* CO_2 *Emissions Monitoring*. 2010: Invited Talk, U.S. Geological Survey Cascades Volcano Observatory, Vancouver, WA.

157. Lewicki, J.L., Hilley, G.E., Dobeck, L., and Spangler, L., *Micrometeorological mapping and quantification of surface* CO_2 *flux leakage signals*, in 9^{th} *Annual Conferenece on Carbon Capture and Sequestration*. 2010: Pittsburgh, PA.

158. Lynn, H.B. and Lageson, D.R. *Hydrocarbon and* CO_2 *entrapment in the Stewart Peak culmination, northern Salt River Range, Wyoming: Migration pathways and reservoir characterization*. in *Undergraduate/Graduate Scholars Research Program and Celebration*. 2010. Montana State University, Bozeman, MT.

159. Melick, J.J. and Gardner, M.H., *The distinction between modern and ancient deltas*, in *Fifth Annual MSU Earth Sciences Colloquium*. 2010: Bozeman, MT.

160. Pekney, Natalie, Arthur Wells, J. Rodney Diehl, Kara Comley, Matthew McNeil, Natalie Lesko, James Armstrong, *Atmospheric Monitoring of a Perfluorocarbon Tracer at the ZERT Center 2009 Experiment in Bozeman, Montana, USA* in The Ninth Annual Conference On Carbon Capture & Sequestration, 2010: Pittsburgh, PA.

161. Pruess, K., *Coupling of Processes*, in *IEA Workshop on* CO_2 *Geologic Storage Modeling*. 2010: University of Utah, Salt Lake City, UT.

162. Pruess, K., *Numerical Modeling of Coupled Processes in Aquifer Storage of Greenhouse Gases - Recent Results and Open Challenges*, in *Invited Seminar*. 2010: Stanford University, Stanford, CA.

163. Pruess, K., *On the Long-term Evolution of a* CO_2 *Plume Under a Sloping Caprock*, in *XVIII International Conference on Computational Methods in Water Resources (CMWR 2010)*. 2010: Barcelona, Spain.

164. Rauch, H. and Hega, B., CO_2 *Sequestration in Unminable Coal with Enhanced Coal Bed Methane Recovery: The Marshall County Project*, in *2010 International Pittsburgh Coal Conference*. 2010: Istanbul, Turkey.

165. Small, Mitchell, Ya-Mei Yang, Donald Gray, Egemen Ogretim, Gavin Liu, Grant Bromhal, Arthur Wells, Brian Strazisar, *Integrating CO_2 and Tracer Transport Models to Predict Leak Detection Probabilities for a Monitoring Network,* in The Ninth Annual Conference On Carbon Capture & Sequestration, 2010: Pittsburgh, PA.

166. Spane, F.A., *Hydrologic Testing Strategies for Reservoir Property Characterization*, in *Workshop on Geological Carbon Sequestration Site Integrity: Characterization and Monitoring Science and Technology*. 2010: Columbus, OH.

167. Spangler, L., *Carbon Sequestration Research in Zero Emission Technology Center (ZERT) and the Big Sky Carbon Sequestration Partnership*. 2010: Norwegian Geotechnical Institute, Oslo, Norway.

168. Spangler, L., *Carbon Sequestration Research in Zero Emission Technology Center (ZERT) and the Big Sky Carbon Sequestration Partnership*. 2010: SINTEF, Tronhdeim, Norway.

169. Spangler, L., *ZERT Near Surface Detection Experiment*. 2010: Norwegian Geotechnical Institute, Oslo, Norway.

170. Sullivan, E.C., *Geophysical Potential Fields: An Often Overlooked Technology for Characterization of CCS Sites*, in *Workshop on Geological Carbon Sequestration Site Integrity: Characterization and Monitoring Science and Technology*. 2010: Columbus, OH.

171. Treadway, W.A. and Lageson, D.R., *Geological factors that lead to CO_2 leakage at the surface, Idaho-Wyoming fold-and-thrust belt*, in *Undergraduate/Graduate Scholars Research Program and Celebration*. 2010: Montana State University, Bozeman, MT.

172. Xu, T., *Subsurface reactive transport modeling: From CO_2 Geological Sequestration to Geothermal Energy Development*, in *Invited Lecture*. 2010: Colorado School of Mines, Golden, CO.

173. Yang, Ya-Mei, Mitchell J. Small, Egemen O. Ogretim, Donald D. Gray, *Integrated Leakage Detection Using Multiple Near-surface Monitoring Techniques Applied to Hypothetical Leaks at the ZERT site* in The Ninth Annual Conference On Carbon Capture & Sequestration, 2010: Pittsburgh, PA.

Appendix F

Copyright Permissions

Permission To Copy or To Use Copyrighted Material

Keriann Hope Pederson provides MSU permission to copy and use copyrighted materials listed below for the purposes of the ZERT I final report by MSU. This material will be used solely for nonprofit educational or research purposes in accordance with the mission of Montana State University. The copied material will not be sold.

This permission is non-exclusive, royalty-free (no cost to the Montana State University), world-wide, and perpetual.

By giving MSU permission to use the copyrighted material, permission is also granted to the Department of Energy and the U.S. Government to use the copyrighted material. The Government reserves for itself and others acting on its behalf a royalty-free, nonexclusive, irrevocable, worldwide license for Governmental purposes to publish, distribute, translate, duplicate, exhibit, and perform this copyrighted paper.

Please sign the release form below to signify agreement.

Permission for use only as stated above is granted.

Keriann H Pederson — Copyright Holder's Signature

7 Sept 2011 — Date

Permission extends to the following materials:

Pederson, K.H., *Stratigraphic Framework and Reservoir Characterization of Clareton and Fiddler Creek Fields, Early Cretaceous Muddy Sandstone Formation, Powder River Basin, Wyoming: Effects of Sediment Supply on Incised Valley-fill System Architecture*, in *Earth Sciences*. 2010, Montana State University: Bozeman, MT. p. 156. Thesis.

Permission To Copy or To Use Copyrighted Material

Martha Apple provides MSU permission to copy and use copyrighted materials listed below for the purposes of the ZERT I final report by MSU. This material will be used solely for nonprofit educational or research purposes in accordance with the mission of Montana State University. The copied material will not be sold.

This permission is non-exclusive, royalty-free (no cost to the Montana State University), world-wide, and perpetual.

By giving MSU permission to use the copyrighted material, permission is also granted to the Department of Energy and the U.S. Government to use the copyrighted material. The Government reserves for itself and others acting on its behalf a royalty-free, nonexclusive, irrevocable, worldwide license for Governmental purposes to publish, distribute, translate, duplicate, exhibit, and perform this copyrighted paper.

Please sign the release form below to signify agreement.

Permission for use only as stated above is granted.

Martha E. Apple

Copyright Holder's Signature

July 19th, 2011

Date

Permission extends to the following materials:

Male, E.J., Pickles, W.L., Silver, E.I., Hoffman, G.D., Lewicki, J.L., Apple, M., Repasky, K.S., and Burton, E.A., *Using hyperspectral plant signatures for leak detection during the 2008 ZERT CO_2 sequestration field experiment in Bozeman, MT.* Environmental Earth Sciences, 2010. **60**: p. 251-261.

Permission To Copy or To Use Copyrighted Material

Elizabeth A. Burton provides MSU permission to copy and use copyrighted materials listed below for the purposes of the ZERT I final report by MSU. This material will be used solely for nonprofit educational or research purposes in accordance with the mission of Montana State University. The copied material will not be sold.

This permission is non-exclusive, royalty-free (no cost to the Montana State University), world-wide, and perpetual.

By giving MSU permission to use the copyrighted material, permission is also granted to the Department of Energy and the U.S. Government to use the copyrighted material. The Government reserves for itself and others acting on its behalf a royalty-free, nonexclusive, irrevocable, worldwide *license for Governmental purposes to publish*, distribute, translate, duplicate, exhibit, and perform this copyrighted paper.

Please sign the release form below to signify agreement.

Permission for use only as stated above is granted.

Elizabeth A Burton — 7/31/11

Copyright Holder's Signature — Date

Permission extends to the following materials:

Male, E.J., Pickles, W.L., Silver, E.I., Hoffman, G.D., Lewicki, J.L., Apple, M., Repasky, K.S., and Burton, E.A., *Using hyperspectral plant signatures for leak detection during the 2008 ZERT CO_2 sequestration field experiment in Bozeman, MT.* Environmental Earth Sciences, 2010. **60**: p. 251-261.

Permission To Copy or To Use Copyrighted Material

Gary D. Hoffmann provides MSU permission to copy and use copyrighted materials listed below for the purposes of the ZERT I final report by MSU. This material will be used solely for nonprofit educational or research purposes in accordance with the mission of Montana State University. The copied material will not be sold.

This permission is non-exclusive, royalty-free (no cost to the Montana State University), world-wide, and perpetual.

By giving MSU permission to use the copyrighted material, permission is also granted to the Department of Energy and the U.S. Government to use the copyrighted material. The Government reserves for itself and others acting on its behalf a royalty-free, nonexclusive, irrevocable, worldwide license for Governmental purposes to publish, distribute, translate, duplicate, exhibit, and perform this copyrighted paper.

Please sign the release form below to signify agreement.

Permission for use only as stated above is granted.

Copyright Holder's Signature

Date 7/27/11

Permission extends to the following materials:

Male, E.J., Pickles, W.L., Silver, E.I., Hoffmann, G.D., Lewicki, J.L., Apple, M., Repasky, K.S., and Burton, E.A., *Using hyperspectral plant signatures for leak detection during the 2008 ZERT CO_2 sequestration field experiment in Bozeman, MT.* Environmental Earth Sciences, 2010. **60**: p. 251-261.

Jennifer Lewicki is listed as author for the appended publication:

Male, E.J., Pickles, W.L., Silver, E.I., Hoffman, G.D., Lewicki, J.L., Apple, M., Repasky, K.S., and Burton, E.A., Using hyperspectral plant signatures for leak detection during the 2008 ZERT CO2 sequestration field experiment in Bozeman, MT. Environmental Earth Sciences, 2010. 60: p. 251-261.

Permission To Copy or To Use Copyrighted Material

Erin Jing Male provides MSU permission to copy and use copyrighted materials listed below for the purposes of the ZERT I final report by MSU. This material will be used solely for nonprofit educational or research purposes in accordance with the mission of Montana State University. The copied material will not be sold.

This permission is non-exclusive, royalty-free (no cost to the Montana State University), world-wide, and perpetual.

By giving MSU permission to use the copyrighted material, permission is also granted to the Department of Energy and the U.S. Government to use the copyrighted material. The Government reserves for itself and others acting on its behalf a royalty-free, nonexclusive, irrevocable, worldwide license for Governmental purposes to publish, distribute, translate, duplicate, exhibit, and perform this copyrighted paper.

Please sign the release form below to signify agreement.

Permission for use only as stated above is granted.

_____ __7/22/2011___

Copyright Holder's Signature Date

Permission extends to the following materials:

Male, E.J., Pickles, W.L., I., S.E., Hoffman, G.D., Lewicki, J.L., Apple, M., Repasky, K.S., and Burton, E.A., *Using hyperspectral plant signatures for leak detection during the 2008 ZERT CO2 sequestration field experiment in Bozeman, MT.* Environmental Earth Sciences, 2010. **60**: p. 251-261.

Permission To Copy or To Use Copyrighted Material

I, Patricia Medsker (William L. Pickles' heir(s)) provides MSU permission to copy and use copyrighted materials listed below for the purposes of the ZERT I final report by MSU. This material will be used solely for nonprofit educational or research purposes in accordance with the mission of Montana State University. The copied material will not be sold.

This permission is non-exclusive, royalty-free (no cost to the Montana State University), world-wide, and perpetual.

By giving MSU permission to use the copyrighted material, permission is also granted to the Department of Energy and the U.S. Government to use the copyrighted material. The Government reserves for itself and others acting on its behalf a royalty-free, nonexclusive, irrevocable, worldwide license for Governmental purposes to publish, distribute, translate, duplicate, exhibit, and perform this copyrighted paper.

Please sign the release form below to signify agreement.

Permission for use only as stated above is granted.

Patricia M. Medsker — July 22, 2011

Copyright Holder's Signature — Date

Permission extends to the following materials:

Male, E.J., Pickles, W.L., Silver, E.I., Hoffman, G.D., Lewicki, J.L., Apple, M., Repasky, K.S., and Burton, E.A., *Using hyperspectral plant signatures for leak detection during the 2008 ZERT CO_2 sequestration field experiment in Bozeman, MT.* Environmental Earth Sciences, 2010. **60**: p. 251-261.

Permission To Copy or To Use Copyrighted Material

Kevin Repasky provides MSU permission to copy and use copyrighted materials listed below for the purposes of the ZERT I final report by MSU. This material will be used solely for nonprofit educational or research purposes in accordance with the mission of Montana State University. The copied material will not be sold.

This permission is non-exclusive, royalty-free (no cost to the Montana State University), world-wide, and perpetual.

By giving MSU permission to use the copyrighted material, permission is also granted to the Department of Energy and the U.S. Government to use the copyrighted material. The Government reserves for itself and others acting on its behalf a royalty-free, nonexclusive, irrevocable, worldwide license for Governmental purposes to publish, distribute, translate, duplicate, exhibit, and perform this copyrighted paper.

Please sign the release form below to signify agreement.

Permission for use only as stated above is granted.

Copyright Holder's Signature

7-13-2011
Date

Permission extends to the following materials:

Male, E.J., Pickles, W.L., Silver, E.I., Hoffman, G.D., Lewicki, J.L., Apple, M., Repasky, K.S., and Burton, E.A., *Using hyperspectral plant signatures for leak detection during the 2008 ZERT CO_2 sequestration field experiment in Bozeman, MT.* Environmental Earth Sciences, 2010. **60**: p. 251-261.

Permission To Copy or To Use Copyrighted Material

Eli Silver provides MSU permission to copy and use copyrighted materials listed below for the purposes of the ZERT I final report by MSU. This material will be used solely for nonprofit educational or research purposes in accordance with the mission of Montana State University. The copied material will not be sold.

This permission is non-exclusive, royalty-free (no cost to the Montana State University), world-wide, and perpetual.

By giving MSU permission to use the copyrighted material, permission is also granted to the Department of Energy and the U.S. Government to use the copyrighted material. The Government reserves for itself and others acting on its behalf a royalty-free, nonexclusive, irrevocable, worldwide license for Governmental purposes to publish, distribute, translate, duplicate, exhibit, and perform this copyrighted paper.

Please sign the release form below to signify agreement.

Permission for use only as stated above is granted.

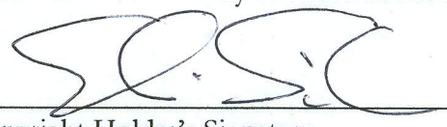

Copyright Holder's Signature

2/12/11

Date

Permission extends to the following materials:

Male, E.J., Pickles, W.L., Silver, E.I., Hoffman, G.D., Lewicki, J.L., Apple, M., Repasky, K.S., and Burton, E.A., *Using hyperspectral plant signatures for leak detection during the 2008 ZERT CO2 sequestration field experiment in Bozeman, MT.* Environmental Earth Sciences, 2010. **60**: p. 251-261.